LATE QUATERNARY HYDROLOGICAL, PALEOENVIRONMENTAL AND GEOMORPHOLOGICAL PROCESSES IN THE TIBETAN PLATEAU AND ITS ADJACENT AREAS

EDITED BY: Xiangjun Liu, Xiangzhong Li, Zhongping Lai and Feng Cheng
PUBLISHED IN: Frontiers in Earth Science

frontiers Research Topics

frontiers

ISSN 1664-8714
ISBN 978-2-88974-507-4
DOI 10.3389/978-2-88974-507-4

About Frontiers

Frontiers is more than just an open-access publisher of scholarly articles: it is a pioneering approach to the world of academia, radically improving the way scholarly research is managed. The grand vision of Frontiers is a world where all people have an equal opportunity to seek, share and generate knowledge. Frontiers provides immediate and permanent online open access to all its publications, but this alone is not enough to realize our grand goals.

Frontiers Journal Series

The Frontiers Journal Series is a multi-tier and interdisciplinary set of open-access, online journals, promising a paradigm shift from the current review, selection and dissemination processes in academic publishing. All Frontiers journals are driven by researchers for researchers; therefore, they constitute a service to the scholarly community. At the same time, the Frontiers Journal Series operates on a revolutionary invention, the tiered publishing system, initially addressing specific communities of scholars, and gradually climbing up to broader public understanding, thus serving the interests of the lay society, too.

Dedication to Quality

Each Frontiers article is a landmark of the highest quality, thanks to genuinely collaborative interactions between authors and review editors, who include some of the world's best academicians. Research must be certified by peers before entering a stream of knowledge that may eventually reach the public - and shape society; therefore, Frontiers only applies the most rigorous and unbiased reviews.
Frontiers revolutionizes research publishing by freely delivering the most outstanding research, evaluated with no bias from both the academic and social point of view. By applying the most advanced information technologies, Frontiers is catapulting scholarly publishing into a new generation.

What are Frontiers Research Topics?

Frontiers Research Topics are very popular trademarks of the Frontiers Journals Series: they are collections of at least ten articles, all centered on a particular subject. With their unique mix of varied contributions from Original Research to Review Articles, Frontiers Research Topics unify the most influential researchers, the latest key findings and historical advances in a hot research area! Find out more on how to host your own Frontiers Research Topic or contribute to one as an author by contacting the Frontiers Editorial Office: frontiersin.org/about/contact

LATE QUATERNARY HYDROLOGICAL, PALEOENVIRONMENTAL AND GEOMORPHOLOGICAL PROCESSES IN THE TIBETAN PLATEAU AND ITS ADJACENT AREAS

Topic Editors:
Xiangjun Liu, Jiaying University, China
Xiangzhong Li, Yunnan University, China
Zhongping Lai, Shantou University, China
Feng Cheng, University of Nevada, United States

Citation: Liu, X., Li, X., Lai, Z., Cheng, F., eds. (2022). Late Quaternary Hydrological, Paleoenvironmental and Geomorphological Processes in the Tibetan Plateau and Its Adjacent Areas. Lausanne: Frontiers Media SA.
doi: 10.3389/978-2-88974-507-4

Table of Contents

frontiers in Earth Science

EDITORIAL
published: 26 January 2022
doi: 10.3389/feart.2022.839663

Editorial: Late Quaternary Hydrological, Paleoenvironmental and Geomorphological Processes in the Tibetan Plateau and Its Adjacent Areas

Xiangjun Liu[1,2]**, *Xiangzhong Li*[3]**, *Zhongping Lai*[4]** and *Feng Cheng*[5]**

[1]School of Geography and Tourism, Jiaying University, Meizhou, China, [2]College of Geography and Environmental Science, Northwest Normal University, Lanzhou, China, [3]Yunnan Key Laboratory of Earth System Science, Yunnan University, Kunming, China, [4]Guangdong Provincial Key Laboratory of Marine Biotechnology, Shantou University, Shantong, China, [5]Nevada Bureau of Mines and Geology, Reno, NV, United States

Keywords: Tibetan Plateau and its adjacent areas, hydrological and surficial processes, geomorphological processes, paleoenvironments, late quaternary

Editorial on the Research Topic

Late Quaternary Hydrological, Paleoenvironmental and Geomorphological Processes in the Tibetan Plateau and Its Adjacent Areas

Edited and reviewed by:
Steven L. Forman,
Baylor University, United States

****Correspondence:***
Xiangjun Liu
xiangjunliu@126.com
Xiangzhong Li
xzhli04@163.com
Zhongping Lai
zhongping.lai@yahoo.com
Feng Cheng
cfcf.chengfeng@gmail.com

Specialty section:
This article was submitted to Quaternary Science, Geomorphology and Paleoenvironment, a section of the journal Frontiers in Earth Science

Received: *20 December 2021*
Accepted: *11 January 2022*
Published: *26 January 2022*

Citation:
Liu X, Li X, Lai Z and Cheng F (2022) Editorial: Late Quaternary Hydrological, Paleoenvironmental and Geomorphological Processes in the Tibetan Plateau and Its Adjacent Areas.
Front. Earth Sci. 10:839663.
doi: 10.3389/feart.2022.839663

The Tibetan Plateau (TP) has essential impacts on the climate in Asia and even in the Northern Hemisphere. It serves as the headwaters for at least ten large rivers that provide sustaining waters for >1 billion people, and is a dust source for downwind areas from the Chinese Loess Plateau to the Pacific Ocean and Greenland. Over the last few decades, many new datasets have been published on the surficial processes of this area during the late Quaternary, including chronologic, organic, and inorganic environmental proxies. The integration of these datasets enable us to have improved understanding of the surficial evolution of the TP and its adjacent areas; and provides insights for current and future climate variability.

This research topic focuses on new advances in late Quaternary hydrological, paleoenvironmental and geomorphological processes in the TP and adjacent areas. This collection includes 20 papers covering research fields such as lake evolution, fluvial and alluvial sedimentation and dating, aeolian processes and chronology, archaeology, salt lake evolution and diagenesis, tectonic processes, and reconstruction of paleoclimate from the applications of the established and new environmental proxies.

Eleven papers in this research topic focused on the geomorphological evolution, lake level variability, salt lake evolution and diagenesis, and archaeological aspects for the TP. Luo et al. dated an archaeological site near Seling Co (at south-central TP) which was previously thought to be 30–40 ka years old. Their Optically Stimulated Luminescence (OSL) dating results indicate the Seling Co site is not earlier than the early Holocene, much younger than the former estimated age. The revised age of Seling Co site is consistent with the warm and humid climate conditions on the central TP during early Holocene. Liu et al. reported that lakes in western inner TP expanded more extensively than those to the east during the early Holocene lake expansion stage. The driving force was the intensification of the Indian summer Monsoon in response to a northward shift of the tropical convergence zone, in combination with the positive phase of the Atlantic Multidecadal Oscillation that resulted in the intensification of southwesterly winds on the southwest flank of the TP. Meanwhile, westerly winds over the TP weakened, resulting in added water vapor transported to the inner TP through the "up-and-over" moisture transport route and then stuck in there. The amount of enhanced precipitation decreased from the southwestern to northeastern inner TP that further enhanced high lake levels in western inner TP. Liu et al. found a linear relationship between excess topography and mean erosion rate in drainage basins in southeastern TP, which indicates that hillslope erosion, especially landslides, is the main erosion process. They propose that excess topography is a better metric than slope to describe the spatial distribution of the erosion rates in southeastern TP.

Determining precise ages of lacustrine sediment in TP lakes is difficult due to the complex nature of lake reservoir effects. Cong et al. dated a lacustrine sediment profile near the Zhari Namco (at south-central TP). They found that radiocarbon ages of the same sampling units are divergent between bulk organic matter and grass leaves, and OSL ages, which yield more reliable ages than radiocarbon dating. Yang et al. provide chronology and multiple proxies of an typical aeolian section in Gannan to reconstruct aeolian deposition history in the eastern TP during the Holocene. Their results showed that aeolian deposition occurred in the eastern TP since the early Holocene.

An et al. investigated alluvial sequences in the drainage basins on the northeastern TP based on geomorphic and stratigraphic investigations and OSL chronologies. They found that the development of alluvial fans was driven by glacier activities, and the dynamics of alluvial processes had paleoclimatic origins rather than tectonic. Shen et al. collected two hundred and thirty-four surface pollen samples from moss polsters, top soil, lake surface sediments, shrublands, shrub meadows, meadows, steppes, and deserts in the TP to explore the relationship between modern pollen rain and vegetation. They found main vegetation types can be distinguished by their modern pollen rain. Sun et al. conducted OSL dating of ceramic and tile remains from three ancient cities in Qinghai Lake Basin (at northeastern TP). They found that the warm and humid climate at cal. 2 ka was an important driver of immigration to this region that led to the construction of cities in the Qinghai Lake area during the late Western Han Dynasty. Wende et al. presented human impact on the paleo-environment through the expansion and development of agriculture on the northeast margin of TP, they found that large scale deforestation occurred due to both agricultural practice and pottery production. Primitive natural vegetation was replaced by cultivated land and possibly environmental degradation has occurred due to early grazing. Ma et al. dated a natural section in the salt lake in Qaidam Basin (at northeastern TP) by using OSL dating, they reported the formation periods of the brine lithium deposits and discussed the contemporary paleoenvironmental conditions. Li et al. measured the chemical composition of fluid inclusions in primary halite that collected from the ISL1A borehole in Qarhan Salt Lake (at south-central Qaidam Basin), the analysis results showed that Ca-Cl type deep brine and tectonic activities have huge impact on the evolution of the Qarhan Salt Lake and the formation of potassium salt.

Five papers in this research topic explored lake level changes, sand dune formations, tectonic processes, and salt mine formations adjacent to the TP. Huang and Chun reconstructed the lake-level variations of Daihai at the marginal region of the East Asian summer monsoon influencing area in north China during the Holocene. Their results revealed the high lake level of Daihai began to develop at 8.1 ka and reached the maximum at 5.2 ka (~40 m higher than present), following the enhanced monsoon precipitation during the mid-Holocene. Wang et al. analyzed elements and colors of lacustrine sediments from Chagan Nur at the southern Mongolian Plateau to constrain the lake environmental changes during the Holocene. Their results showed that stable element contents like Ti are more related to surface erosion and vegetation coverage, and the variations of Sr are related to lake level changes. Zhu et al. reported that dune sands in the Hexi Corridor are mainly "sediments of *in-situ* rising" that originated from alluvial or fluvial deposits, lacustrine deposits, and aeolian deposits in the erosion zone of the forelands of the Qilian Mountains and the north-neighboring deserts. Their research reveals that the interaction between wind and water dynamics is significant in the formation and evolution of aeolian landforms in terms of geomorphic genesis in these arid areas. Li et al. constructed a vertical land motion model based on the latest leveling observations adjacent to the West Qinling orogen and analyzed the modern crustal deformation pattern in this region. They found strain transformation plays a key role in controlling the tectonic uplift in the West Qinling orogen. Hussain et al. combined mineralogy, geochemistry, and fluid inclusion and chlorine stable isotope compositions to discuss the origin and evolution of the Eocene halite in Kohat Basin (in Western Pakistan), they then reconstructed the paleoclimate that was prevailing in Asia during the Eocene.

Four papers in this research topic focus on diatom transfer function to quantitative paleoclimatic reconstruction, loess and Old Red Sand in southern China, and theory for the dynamics of ice age cycles. Zou et al. selected an alpine lake in Southwest China, investigated the seasonal succession of modern diatom assemblages to produce a mean surface water temperature transfer function, and produced a diatom-water depth transfer function by exploring the spatial pattern of surface diatom assemblages with water depth. After being validated by meteorology data, they proposed diatom transfer functions based on modern observations of the same lakes. These functions have a high environmental sensitivity and can be used for the quantitative reconstruction of regional climate change on various timescales. Fan et al. used grain size data and quartz grain surface microtexture observations to identify the provenance for the Xiashu loess in southern China, they concluded that floodplains in the lower reaches of the Yangtze River, the alluvial plains of the Huai River, and the Yellow River to the north are the dominant source areas. Fan et al. studied the origin and paleoenvironmental significance of the Old Red Sand (ORS) on the southeast coast of China. They reported that the grain size of the ORS shows typical aeolian features, the quartz grain surface microtexture of the ORS shows both aeolian features and subaqueous environment characteristics. At last, Lai et al. proposed a new theory for the dynamics of ice age cycles focusing on the saw-tooth patterns and related changes in the energy balance of the Earth. By analyzing global temperature archives reconstructed from various proxies, they suggest the cooling of ice ages is associated with slow Northern Hemisphere high-latitude processes, while deglacial warming is associated with fast heat release from the deep ocean. This “bimodal forcing” hypothesis poses questions to the previous single forcing theories which suggest the control of Northern Hemisphere high latitude areas and pave a new way to understand the dynamics of ice ages.

AUTHOR CONTRIBUTIONS

All authors listed have made a substantial, direct, and intellectual contribution to the work and approved it for publication.

FUNDING

We acknowledge the supports from the Second Tibetan Plateau Scientific Expedition and Research Program (2019QZKK0202) and the National Natural Science Foundation of China (41671006).

ACKNOWLEDGMENTS

We appreciate the Editorial office of Frontiers in Earth Science for their timely support during organizing and managing the topic, and all the reviewers for their selfless contributions during the reviewing processes that substantially improved the qualities of these published papers.

Conflict of Interest: The authors declare that the research was conducted in the absence of any commercial or financial relationships that could be construed as a potential conflict of interest.

frontiers
in Earth Science

ORIGINAL RESEARCH
published: 08 April 2021
doi: 10.3389/feart.2021.644485

Origin and Evolution of Eocene Rock Salts in Pakistan and Implications for Paleoclimate Studies: Insights From Chemistry and Cl Stable Isotopes

Syed Asim Hussain[1,2,3,4]*, *Feng Qing Han*[2,3]*, *Zhe Ma*[2,3], *Amjad Hussain*[5], *Muhammad Saleem Mughal*[6], *Jibin Han*[2,3], *Abdullah Alhassan*[7] *and David Widory*[8]

[1]Key Laboratory of Comprehensive and Highly Efficient Utilization of Salt Lake Resources, Qinghai Institute of Salt Lakes, Chinese Academy of Science, Xining, China, [2]Qinghai Provincial Key Laboratory of Geology and Environment of Salt Lakes, Xining, China, [3]University of Chinese Academy of Sciences, Beijing, China, [4]Department of Earth Sciences, Karakoram International University, Gilgit-Baltistan, Pakistan, [5]State Key Laboratory of Geological Processes and Mineral Resources, China University of Geosciences, Wuhan, China, [6]Institute of Geology, University of Azad Jammu and Kashmir, Muzaffarabad, Pakistan, [7]State Key Laboratory of Biogeology and Environmental Geology, China University of Geosciences, Wuhan, China, [8]GEOTOP/Earth and Atmosphere Sciences Department, UQAM, Montréal, QC, Canada

The Kohat Basin (KB) lies on the Himalayan Foothills and is of scientific importance as it directly recorded the closure of the Tethys Sea and the Himalayan collision between India, Asia, and a number of other small plates. During the Eocene, after the collision between the Indian and Eurasian plates terminated the Tethys Sea, thick-bedded marine evaporite sequences developed in the KB. In this study, we combined mineralogy, geochemistry, fluid inclusion and chlorine stable isotope compositions to discuss the origin and evolution of the KB Eocene halite deposits with the ultimate objective of defining the paleoclimate that was prevailing in Asia during the Eocene. Our results showed that halite samples were SO_4^{2-} rich ($225–370.10^3$ ppm) and Br^- poor (<3 ppm). Cl^-, B^+, Mg^{2+}, K^+, SO_4^{2-} and very low Br concentrations as well as the (Br/Cl) ratios indicated that halite resulted of a mixture of solutions with variable compositions and that dissolution, recrystallization and a progressive decrease in dolomitization were the mechanisms leading to the formation of these evaporites. A Br/Cl vs Cl plot revealed that the end members involved were: seawater (sw), saline waters and/or freshwaters. The recrystallization process prevented identifying the primary structures and primary fluid-inclusions. Most of Cl isotope compositions ($-0.54‰ < \delta^{37}Cl < 0.83‰$) were within the usual range ($0 \pm 0.5‰$) associated to seawater as the initial source for the halite. The higher isotope compositions ($\delta^{37}Cl \geq 0.83‰$) comforted the hypothesis of the genesis by mixing of solutions of different origins as well as the involvement of recrystallization. Based on our results, we are proposing the following to explain the regional paleoclimate sequence: 1) shallow water conditions; 2) halite precipitation induced by evaporation, 3) unstable paleoclimatic conditions that resulted in the morphing from an evaporite basin into a terrestrial foreland basin. All these events were controlled by regional tectonic and linked to both the overall uplift times of the NW Indian Craton and the Eocene thermal maximum one during the Eocene-Oligocene period.

OPEN ACCESS

Edited by:
Xiangjun Liu,
Northwest Normal University, China

Reviewed by:
Tadeusz Marek,
Polish Geological Institute, Poland
Xiangru Zhang,
Guangxi Normal University, China

Correspondence:
Syed Asim Hussain
s.asim_110@yahoo.com
Feng Qing Han
hanfq@isl.ac.cn

Specialty section:
This article was submitted to
Quaternary Science, Geomorphology
and Paleoenvironment,
a section of the journal
Frontiers in Earth Science

Received: *21 December 2020*
Accepted: *18 February 2021*
Published: *08 April 2021*

Citation:
Hussain SA, Han FQ, Ma Z, Hussain A, Mughal MS, Han J, Alhassan A and Widory D (2021) Origin and Evolution of Eocene Rock Salts in Pakistan and Implications for Paleoclimate Studies: Insights From Chemistry and Cl Stable Isotopes.
Front. Earth Sci. 9:644485.
doi: 10.3389/feart.2021.644485

Keywords: kohat-plateau, marine halite, geochemistry, paleoclimate, Cl stable isotopes

INTRODUCTION

The collision tectonic events leading to the final closure of the Tethys Sea during the Cenozoic formed mountain chains that prolong from the Mediterranean region to Asia (Potter and Szatmari, 2009). These events were recorded *by* the Paleocene–Pleistocene sedimentary rocks present in India, Nepal and Pakistan (Najman et al., 2017). These events most probably debuted after the Indian plate broke away from Gondwanaland, began moving north towards Eurasia, and ended with the subduction of the Tethys Sea (Khan et al., 1987; Ahmad et al., 2002). The continent-continent collision between the Indo-Pakistan and the Eurasian plates not only led to the Himalayan orogeny but also provided enough marine sediments and source material for the development of thick-bedded evaporites in Pakistan (Pivnik and Wells, 1996). The major rock salts deposits in Pakistan are located in the Salt Range area and in the Kohat basin (KB) (e.g. Hussain et al., 2019; Hussain et al., 2020a; Hussain et al., 2020b; Hussain et al., 2021). The Precambrian Salt Range is considered as the main and oldest salt deposits in the sub-continent. The younger salt deposits (Eocene age) are found in the northwestern KB with the main deposits located in the central part of the basin. Deposits contain halite along with variable amounts of gypsum dolomite and clays, and limited layers of potash and magnesium salts. In comparison, the KB salts are thin compared to the Salt Range Formation and can be observed at different locations (Jatta, Karak and Bahadurkhel) of the KB (**Figure 1**). Just like the SR Fm. the base of the KB is not exposed but its thickness is variable, with a maximum of 700 m (Asrarullah, 1963; Pivnik and Wells., 1996). Records of marine sedimentation ranging from the Paleocene to younger ages can be observed at the Kohat Plateau (KP; NW Pakistan), also known as the Kohat Fold and Thrust Belt (KFTB) (Hussain and Zhang, 2018). These sedimentary rocks are mainly constituted of complex groups of sulfate, evaporite, shale/sandstone, and conglomerates (Meissner et al., 1975). The KP lies within 100 km of the western Himalayan Foothills (Pivnik and Wells, 1996) and is assumed to be the main Himalayan depocenter at the time of the collision between the Indian and Asian plates (Gardezi, 2016). The KP is restricted by the Main Boundary Thrust (MBT) on its northern part and by the Trans-Indus Salt Ranges and the Bannu Plain on its southern border. The Indus River and the Kurram Fault mark (**Figure 1**) its eastern and western boundaries (Kazmi and Rana, 1982).

The KP encompasses Cenozoic sedimentary rocks and previous studies have shown that during the Paleocene (early Eocene) the formation of thick-bedded evaporites in the region was facilitated by the submergence of the NW Indian continental shelf that separated from both the Tethys Sea and the Persian Gulf (e.g. Pivnik and Wells, 1996). Thick-bedded evaporites and particularly brines are common geological features worldwide (Warren, 2006; Guo et al., 2017) that have been vastly investigated (e.g. Gee, 1938; Krishnan, 1966; Hsü et al., 1973; Hsü and Bernoulli, 1978; Alsop, 1996; Hardie and Lowenstein, 2004). Studies have particularly focused on evaporites strictly related to source rocks in sedimentary environments (e.g. Hussain and Warren, 1991; Warren, 2010; Hussain et al., 2021). However, due the lack of modern equivalents, the origin, evolution and the depositional background of these evaporites is still subject to debate (e.g. Guo et al., 2017; Hussain et al., 2020a). Classical chemistry and isotope systematics have already demonstrated their added value to better constrain the sources and processes leading to the formation of these evaporites (Han et al., 2019; Hussain et al., 2020a; Hussain et al., 2021). For example, the Br/Cl ratio and Na-Cl-Br concentrations measured in evaporites can be used to characterize the formation and evolution, including recrystallizsation, dissolution and redeposition processes, of basin fluids (e.g. Walter et al., 1990). The Cl/Br ratio is a common proxy used to study changes during the late phases of halite deposition (e.g. Eggenkamp et al., 2019a; Hussain et al., 2021), the origin of saline waters (e.g. Alcala and Custodio, 2004; Alcala and Custodio, 2008; Katz et al., 2011) as well as dissolved mineral components in deep fluids (Heinrich et al., 1993; Sonney et al., 2010) and paleoenvironment of evaporites (Ercan et al., 2019). On the other hand, the use of Cl stable isotope compositions (noted δ^{37}Cl) has proved to be a reliable tracer for ancient evaporites (Eggenkamp et al., 2018; Eggenkamp et al., 2019a; Eggenkamp et al., 2019b), to identify the origin of modern brines (Eggenkamp, 2014; Luo et al., 2014), and to characterize the geochemical development of connate waters in sedimentary basins (Tomascak et al., 2016; Hanlon et al., 2017). δ^{37}Cl is good at fingerprinting the origin of mixed magmatic–basinal brines and it can differentiate between marine and non-marine environment and depositional conditions (Chiaradia et al., 2006). Recently it has also been proved that δ^{37}Cl can be used to evaluate the evaporation rate at the time of the salt formation (Luo et al., 2014, Luo et al., 2016; Hussain et al., 2019).

The rock salt deposits in Pakistan were early characterized (e.g. Wynne 1875, Wynne 1878, Wynne 1880). Gee (1945) created two inches to one-mile geological maps. Asrarullah, 1962; Asrarullah, 1963 and Alam and Asrarullah (1973) estimated the volumes of Pakistan rock salt resources. While most of this research was focusing on understanding the stratigraphy and geology of the KB (Eames, 1952; Meissner et al., 1974; Meissner et al., 1975; Shah, 1977; Wells, 1984; Pivnik and Sercombe 1993a; Pivnik and Wells 1996), the vast deposits of halite, sulfate and other salts present in the Eocene Kohat Fold and Thrust Belt and their corresponding sources and evolution have never been investigated using chemistry and isotope systematics due to a complex assemblage of these evaporites. The objectives of this study were: 1) to geochemically characterize the Kohat salt (also known as the Bahadur Kel salt) deposits 2) to define the origin and evolution of the ancient halites and ultimately to discuss the paleoclimate prevailing during their deposition. To fulfill these objectives, we decided to couple the classical geochemical, mineralogical and lithological approach with the use of the (Br/Cl) ratios and δ37Cl isotope compositions. To our knowledge, this represents the first study using Cl isotopes to

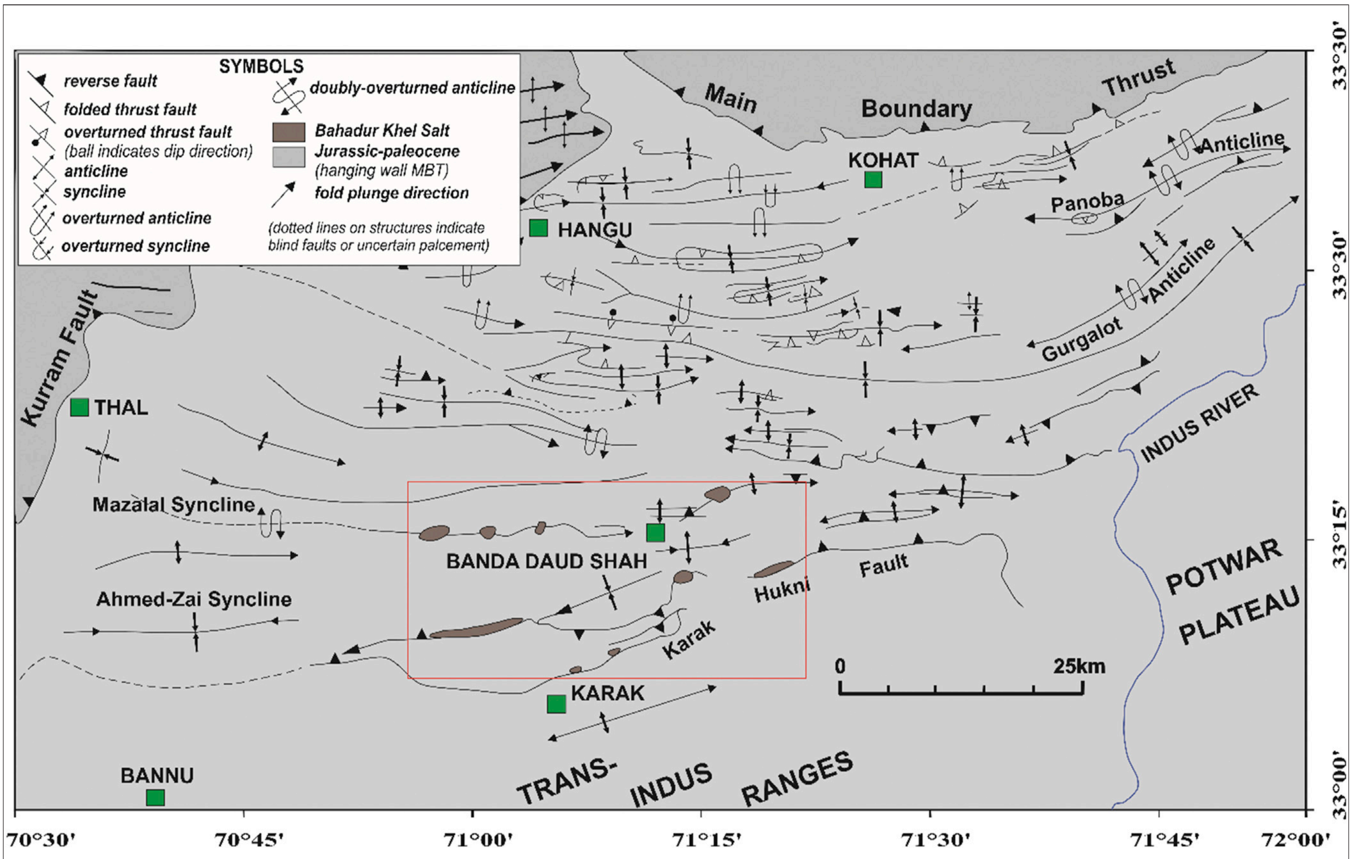

FIGURE 1 | Structural map of the Kohat Plateau (modified after Pivnik and Wells, 1996). The map indicates the major structural boundaries as well as the locations of the thick-bedded salt rock deposits.

better understand the regional geology, and lays a basis for future isotope investigations of the KFTB.

GEOLOGY AND STRATIGRAPHY

The Great Himalaya emerged because of a N-S crustal shortening and thickening, resulting from the junction between the Indian and Eurasian Plates and their later impaction (Gansser, 1964; Le Fort, 1975). In the Early Miocene, these tectonic movements formed the Tibetan Plateau (TP) as well as thrust structures such as the KP, which are parts of the Indo-Gangetic foreland (Ahmad et al., 2006), comprising Tertiary sedimentary rocks. Previous studies (Gee 1938; Meissner et al., 1974; Meissner et al., 1975; Shah, 1977; Wells, 1984; Pivnik and Sercombe 1993b; Pivnik and Wells 1996) indicated that the surface rocks are mainly from the Eocene and present an unconformable relationship to the overlying Miocene or younger rocks (Gee, 1945; Fatmi, 1973; Shah, 2009). The strata deposited under restricted marine conditions and represents the first record of the Himalayan collision (Pivnik and Wells 1996). The KFTB was cut off from the Tethys Sea and developed a complex assemblage of evaporites, carbonates and clastic rocks generated by tectonic forces during the later stages of the Himalayan orogeny.

Structurally, the KP represents both compressional and transpression tectonics (Pivnik and Sercombe, 1993b); many features are linked to imbricated thrusts; and associated folds are linked to the oblique convergence and subsequent formation of an hybrid terrain (Paracha, 2004). Seismic data from the Northern Potowar Deformation Zone (NPDZ) and KP revealed that both regions shares parallel structure histories (Pivnik and Sercombe, 1993a). Pop-ups, wide synclines, narrow faults, and evaporite anticlines are the most common structural features of the KFBT. They indicate a high-level translation of a large thrust mass along the Eocene evaporites (Hussain and Zhang, 2018) resulting from the northward clockwise tectonic movement of the Indian plate (Gardezi, 2016).

Figure 2 reports the detailed stratigraphy of the KFBT studied and shows that the Paleozoic and Mesozoic rocks deposited on the north Indian passive continental margin, which facilitated a southern shoreline to the Tethys sea (Pivnik and Wells 1996). The oldest exposed rocks are of Eocene age and consist of evaporites (halite and gypsum) and shales. Drill hole data from hydrocarbon exploration suggest that early Jurassic rocks are the unexposed oldest rocks (Gardezi, 2016). In this study, we are focusing on the Eocene halite deposit that was developed between the NW Indian continental margin, the southern Asian margin, and at least one

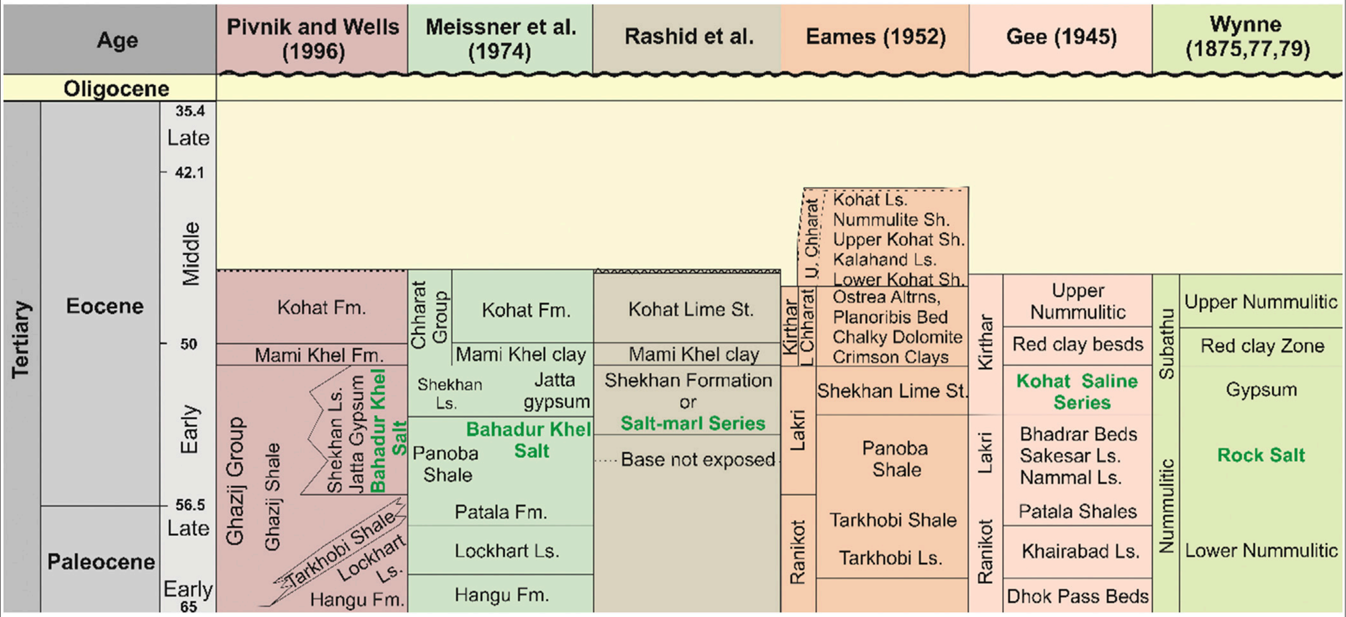

FIGURE 2 | Stratigraphic column of the Kohat Plateau (KP), showing major formations and corresponding ages.

TABLE 1 | δ^{37}Cl and ion compositions of the salt deposits from the Kohat basin: Jatta, Karrak, and Bahadur Khel deposits.

Reion	Sample	Cl^- ppm	Br^- ppm	B^{3+} ppm	Ca^{2+} ppm	K^+ ppm	Li^+ ppm	Mg^{2+} ppm	Na+ ppm	SO_4^{2-} ppm	δ^{37}Cl ‰	Error ‰
Jatta	A–1	591,110.4	2.25	<0.0072	2,749.78	104.12	3.71	20.05	383,061.7	5,919.19	–0.15	0.05
	A–2	592,647.9	2.21	<0.0072	2,179.82	113.21	3.88	20.41	384,097.2	4,646.17	–0.03	0.04
	A–3	550,320.7	2.11	<0.0072	9,214.54	113.04	4.41	18.16	356,155.2	20,479.94	–0.54	0.06
	B–1	599,593.2	2.33	<0.0072	88.44	118.33	3.47	23.94	390,451	225.4	0.69	0.13
	B–2	558,776.3	2.05	<0.0072	8,458.22	185.09	2.64	35.57	361,712.8	18,976.26	0.29	0.12
	B–3	558,080.4	2.17	<0.0072	8,326.75	155.82	4.2	63.12	361,253.6	18,717.9	0.39	0.15
	C–1	545,489.1	2.26	<0.0072	9,763.02	155.16	3.48	29.96	352,658.3	21,135.75	–0.32	0.03
	C–2	565,499.6	2.05	<0.0072	6,600.86	126.44	3.34	9.38	367,752.6	17,853.88	–0.16	0.08
	C–3	582,439.4	1.3	<0.0072	4,817.71	111.16	3.76	126.54	377,306	11,029.13	–0.24	0.05
Karrak	D–1	473,510.6	2.22	<0.0072	9,796.43	179.15	2.72	57.1	305,864.4	21,147.7	–0.06	0.05
	D–2	526,668.4	2.14	<0.0072	10,396.13	507.73	2.96	125.26	341,049.3	24,716.07	–0.25	0.12
	D–3	540,145	2.37	<0.0072	11,473.05	145.15	4.13	29.83	349,166.7	25,167.27	–0.18	0.26
	D–4	496,278.5	2.04	<0.0072	13,025.51	168.52	2.52	33.22	321,023.1	29,584.64	–0.46	0.05
	E–1	558,421.5	2.12	<0.0072	9,066.92	139.22	3.49	11	361,596.7	20,518.82	0.83	0.17
	E–2	561,922.5	2.23	<0.0072	6,777.26	123.19	3.05	13.46	363,923.9	15,141.28	–0.07	0.24
	E–3	550,577.1	1.76	<0.0072	11,036.04	130.97	4.01	13.92	355,285.6	22,686.3	–0.06	0.05
Bahadur khel	M4–1	577,665.2	1.94	13.65	7,750.18	82.51	0.77	32.51	373,962.7	17,133.25	–0.26	0.17
	M4–2	564,373.8	1.85	4.77	8,808.81	83.13	0.1	37.04	365,623	20,278.07	–0.2	0.05
	M4–3	576,612.1	1.71	2.57	6,585	105.7	1.31	24.5	373,436.7	14,667.23	–0.1	0.23
	M17–1	575,358.7	2.1	<0.0072	7,848.77	100.85	1.09	30.88	372,284	17,004.87	0.28	0.01
	M17–2	571,203.3	1.78	<0.0072	9,413.37	71.43	1.17	27.82	369,778.9	21,102.12	–0.14	0.31
	M17–3	532,018.8	1.92	1.29	8,654.4	174.19	0.14	42.14	344,216.4	19,171.54	–0.11	0.21
	M17–4	555,311.8	1.94	<0.0072	10,310.72	121.99	1.16	47	359,532.2	23,520.57	–0.26	0.17
	OA	561,138.9	2.01	<0.0072	7,248.57	123.74	1.01	15.86	363,103.7	15,629.58	–0.35	0.01

or more microplates that now constitute western Pakistan and eastern Afghanistan.

The Eocene halite in the KP is referred as the Kohat Saline Series (Gee, 1945) or the Bahadur Khel Salt (Meissner et al., 1974). It is exposed along anticlines with a general EW-trend and crops out in the central part of the KP near the Manzalai anticline and along the Karak-Hukni fault. The Jatta Gypsum confirmly lays on top of the Bahadur Khel Salt (BKS) but correlating its age with other units (e.g. the Ghazij Group) is rendered difficult due to the lack of local age control (Pivnik and Wells, 1996). The real thickness of the BKS is unknown as its base is not exposed. However, while Meissner et al. (1974) reported an exposed thickness of about 100 m, a hole drilled in the core of an anticline (in the Shakarkara village) yielded a thickness of about 700 m (Meissner et al., 1974). Regional geology and stratigraphy indicate that at the time of deposition the brine was most likely warm and deposited on sabkhas and in lagoons in its northeastern part and in a shallow water environment in its southern part (Pivnik and Wells, 1996). The Eocene regression forged the final small and limited basins.

MATERIALS AND METHODS

Sampling and Elemental Concentrations

In total, we collected 24 representative halite samples in 2018 from three distinct deposits (details are given in **Table 1**): nine samples from the Jatta deposit, seven from the Karrak one and eight from the Bahadur Khel one. For each halite sample, we measured the K^+, Na^+, Ca^{2+}, B^{3+}, Mg^{2+}, Li^{3+}, SO_4^{2-}, Br^-, Cl^- concentrations and corresponding Cl stable isotope compositions (noted $\delta^{37}Cl$). K^+, Ca^{2+}, Mg^{2+}, and B^{3+} concentrations were measured by ICP-OES (ICAP6500DUO, United States) with a precision better than 5%. Br^- and SO_4^{2-} were analyzed by Ion Chromatography (IC-5000+, Thermo Fisher, United States) and Cl^- was measured by chemical mercurimetry, with an accuracy higher than 0.3% (ISL, CAS, 1988). $\delta^{37}Cl$ was analyzed by Positive Thermal Ionization Mass Spectrometry (TIMS-TRITON, United States). All measurements were made at the Salt Lakes Analytical and Testing Department, Qinghai Institute of Salt Lakes, Chinese Academy of Sciences.

Isotope Sample Preparation and Analysis

Each halite sample was first dissolved in highly deionized water and then purified using the following two-step protocol (samples were purified to ultimately contain 5 g/L of Cl): 1) dissolved samples first passed through a polyethylene ion-exchange column (~0.5 cm diameter) filled with ~2 cm of Dowex 50WX8 H-cation exchange resin, and subsequently through 2) a second polyethylene ion-exchange column (~0.5 cm diameter) filled with ~1.6 cm of Cs-cation exchange resin. The pH of the solution was kept <7 throughout the procedure. Finally, the eluant was collected for further analysis by TIMS. As the halite samples presented low SO_4^{2-}/Cl^- and NO_3^-/Cl^- ratios, interferences by SO_4^{2-} and NO_3^- were considered negligible and therefore no additional purification step was needed (for details see Hussain et al., 2020b). A tantalum (Ta) filament was heated under vacuum for 1 h using a current of 2–3A, before being covered with 2.5 μl of a graphite slurry that contained 80% of ethanol and 80 μg of graphite. About 2 μl of the sample solution, having no less than 10 μg of Cl as CsCl, was deposited onto the filament. The filament was then dried using a current of 1 A for ~2.5 min and inserted into the TIMS (pressure at $\sim 2.5 \times 10^{-7}$ mbars). The Cs_2Cl^+ ion current generated was maintained at 4×10^{-12} A by adjusting the source current. Data were instantaneously collected on Faraday cup "C" and "H1" by using the ion flows from mass numbers 301 ($^{133}Cs_2{}^{35}Cl^+$) and 303 ($^{133}Cs_2{}^{37}Cl^+$). The average $^{37}Cl/^{35}Cl$ ratio we obtained for the IAEA ISL-354 NaCl standard was 0.319031 ± 0.000066 ($n = 12$), in agreement with the value of 0.31964 ± 0.00092 reported by Xiao et al., 1997. The corresponding $\delta^{37}Cl$ value was calculated as (error ≤ 0.09‰):

$$\delta^{37}Cl = \left[\frac{\frac{^{37}Cl}{^{35}Cl}_{sample}}{\frac{^{37}Cl}{^{35}Cl}_{ISL-354}}\right] \times 10^3$$

RESULTS AND DISCUSSION

Halite Mineralogical Characteristics

The $\delta^{37}Cl$ and elemental compositions of the halite samples are given in **Table 1**. Results show that Na^+ and Cl^- are the major ions, followed by SO_4^{2-} and $Ca^{2+\cdot}$ Trace elements, such as B^{3+} and Br^-, are usually negligible. $\delta^{37}Cl$ in our halite samples range from −0.54‰ −0.83‰ with an average isotope composition of −0.06 ± 0.33‰.

The main salt deposits in the KB can be observed at three localities: Jatta, Karak and Bahadur Khel (**Figure 1**). All deposits in the KB are stratigraphically considered as the Bahadur Khel Salt (Meissner et al., 1974; Pivnik and Wells, 1996). The general trend follows a NS direction and extends for up to 40 km. The KB salts are white to grayish in color, the later resulting of the intermixing of black bitumen/shale with rock salt, which in turn affects its purity. The halite thickness in the KB varies from one to hundreds of meters (Meissner et al., 1974). The exposed mineralization is massive and translucent for most of the deposits. Few thin layers are transparent and crystals vary between euhedral and anhedral. Primary textures were absent or difficult to detect and only secondary textures with secondary fluid inclusions were observed under microscopy (**Figure 3**).

Primary structures in halite, e.g. chevron and hopper structures, are generally interpreted as reflecting shallow lake brines (Salvany et al., 2007) deposited under stable environmental conditions (Warren 2006; Ercan et al., 2019). Although previous studies concluded that the KB brines were warm, shallow and developed within a passive continental margin (e.g. Pivnik and Wells, 1996; Pivnik and Wells, 1996), finding corresponding primary structures was not possible due to the recycling of the ancient halite. On the other hand, the recrystallization and dissolution processes during flooding (Shearman, 1970) and the alteration of the mineral morphologies by burial effects or by active capillary activities around older mineralization develop common secondary features (Ercan et al., 2019). Thus, this indicates that the KB halite either developed or evolved under variable conditions.

Halite Geochemistry

For all halite samples Mg^{2+}, Ca^{2+} and SO_4^{2-} ions yielded large variations in their concentrations (**Table 1**). Li^+ Br^-, Ca^{2+}, K^+, and B^+ concentrations varied among the different sites, and even within each sampling site (**Table 1**): the K^+ and Ca^{2+} contents in the Jatta and Bahadur Khel samples ranged from 104 to 185 ppm, from 88 to 9,763 ppm, from 71 to 174 ppm and from 6,585 to 10,310 ppm, respectively. The Karrak samples gave the highest

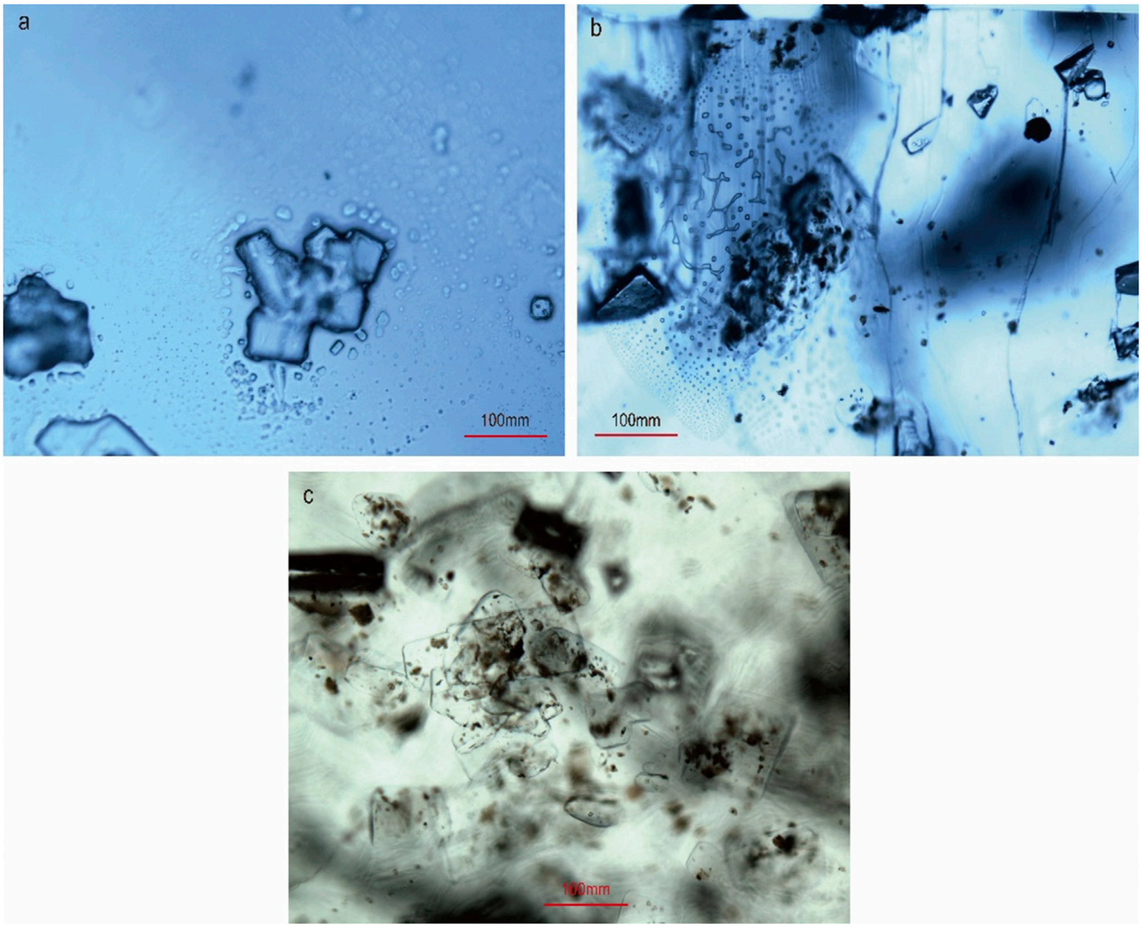

FIGURE 3 | Microscopy pictures of the halite samples: **(A)** random crystal of halite covered by secondary fluids, **(B)** washout structures, and **(C)** halite random crystals covered by (black) bituminous materials.

Ca^{2+} (6,777–13,025 ppm) and K^+ (123–507 ppm) concentrations. Mg^{2+} concentrations ranged between 15 and 47 ppm for the Bahadur Khel site, between 11 and 125 ppm for the Jatta site and from 9 to 126 ppm for the Jatta site. Li^+ and Br^- contents varied between 0.09 and 4.4 ppm and between 1.2 and 2.3 ppm, respectively. B^+ concentrations were very low (≤0.007 ppm) in most of the halite samples. SO_4^{2-} content were high in most samples with values between 225 and 29,584 ppm. The highest SO_4^{2-} concentrations were observed at the Karrak site.

During the late Eocene (37–34 Ma), seawater was Mg^{2+} and SO_4^{2-} rich (Holland, 2005), due to a progressive decrease in dolomitization. Between 93.5 and 36 Ma the SO_4^{2-} concentration was higher than that of Ca^{2+} (Timofeeff et al., 2006). **Figure 4** shows that for the KB $SO_4^{2-} > Ca^{2+}$, which indicates that the parent waters were SO_4^{2-} rich. While the K^+ concentration of Tertiary marine halite was constant at about 400 ppm (Holland, 1984), in our samples, it varied between 84 and 9,413 ppm, with an average value around 100 ppm (**Figure 4A**). As the Mami Khel clays overlay the Kohat salts these lower K^+ concentrations may thus be explained by the absorption of K^+ onto clay minerals. The Mg^{2+} content of the Eocene SW was lower (874 ppm) compared to the 1,336 ppm in present day SW (Brennan et al., 2013). In the KB halite the Mg content varied between 1 and 126 ppm (**Figure 4B**). The low Mg^{2+} are probably caused by permeable zones. The study area is highly faulted, with the Kurram Thrust Fault covering the western and northern parts of the area and overlaying the Mami Khel clays. It may form impermissible zones that prevent any water input. Brennan et al. (2013) reported that the Ca^{2+} content in present-day SW (264 ppm) is lower than during the Eocene (384 ppm), giving a negative relationship between Ca^{2+} and SO_4^{2-} (**Figure 4C**). In our study, the relationship between these two ions was linear with a positive slope (**Figure 4C**) that indicated that the controlling process is a global decrease in the dolomitization process (Holland and Zimmermann, 2000; Holland, 2005).

The Br^- concentration in the first halite precipitated from SW is ~75 ppm (Holser, 1979) and its value reaches up to 270 ppm in the advanced concentration stages, at the beginning of the Mg sulfate deposition (Kovalevych et al., 2006). The calculated Br^- residence time is ~100 million years (Holland, 1984). Therefore, the Br^- concentration in halite precipitated from the evaporation of Tertiary seawater must be about 75–270 ppm (Ercan et al.,

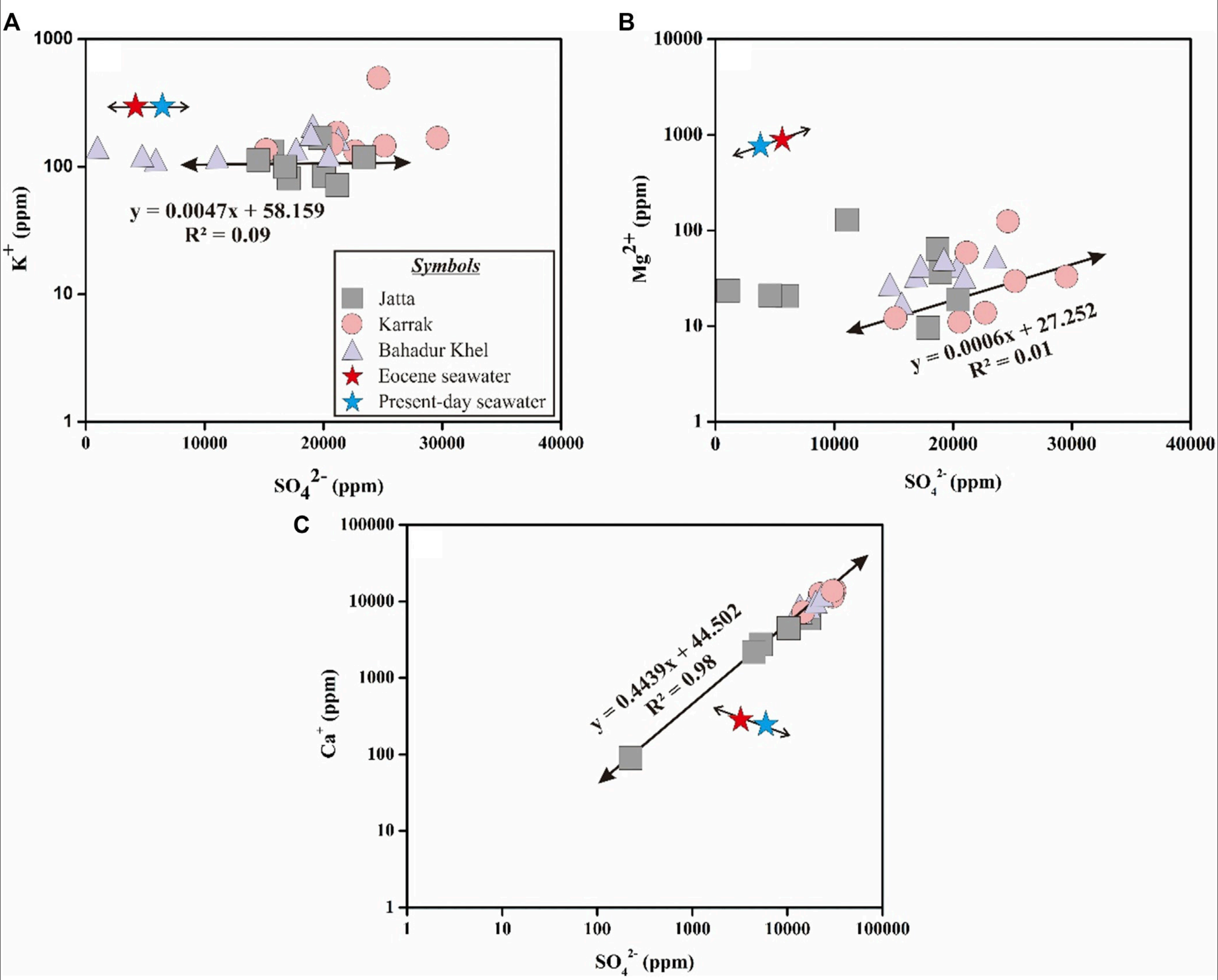

FIGURE 4 | Ion relationships observed in the Bahadur Khel salts: **(A)** SO_4^{2-} *vs* K^+, **(B)** SO_4^{2-} *vs* Mg^{2+} and (**C**) SO_4^{2-} *vs* Ca^{2+}. For each diagram the corresponding characteristics of the Eocene (data from Brennan et al., 2013) and present-day seawaters are given (data from Holland, 1984).

2019) but later changes (e.g. recrystallization, dissolution) can affect these concentrations (Eggenkamp et al., 2019a). For example, the Miocene halite of the Mediterranean region yields Br^- concentrations up to 40 ppm (Bloch, 1953) but also as low as ~5 ppm (e.g. Ercan et al., 2019). Brennan et al. (2013) reported Br^- concentrations of 11 ppm for halites from the Catalan sub-basin, whereas Moretto (1986) reported Br^- concentrations of 10 ppm for the Bresse Basin. The Eocene salts from Bhadur Khel have lower Br^- concentrations compared to the other Paleogene and Neogene basins (1.3–2.37 ppm) that indicate an entry of non-marine water (Shouakar-Stash, 2008) or the dissolution or recycling of ancient marine halite (Brennan et al., 2013; Han et al., 2019; Eggenkamp et al., 2019b). The study of the Cl/Br ratio has proved to be one of the most effective and sensitive indexes when defining the geological environment, brine concentrations and the depositional stages associated to the brine evaporation process (e.g. Han et al., 2019; Hussain et al., 2019). Experiments have demonstrated that this Cl/Br ratio is related to the brine and salt evolution (Braitsch, 1962): the more advanced brine solutions produce lower Cl/Br ratios in the precipitates (Eggenkamp et al., 2019a; Eggenkamp et al., 2019b). The Cl/Br ratio in SW (~300) is lower than at any halite stage as evaporites preferentially incorporate Cl^- compared to Br^- (Hussain et al., 2020b). **Figure 5** shows that our halite samples Br^- concentrations were low, yielding high Cl/Br ratios. This indicates that they have been dissolved by saline waters/non-marine waters as evaporites forming in basins having no or limited connections with the open sea are expected to episodically get waters and solutes from non-marine sources (Holland et al., 1984). Geology demonstrates that halite in the KB has a marine origin (Wells, 1984; Pivnik and Wells, 1996), resulting from the precipitation of the ancient Tethys Sea (Pivnik and Wells, 1996; Hussain and Zhang, 2018). Thus, the low Br^-

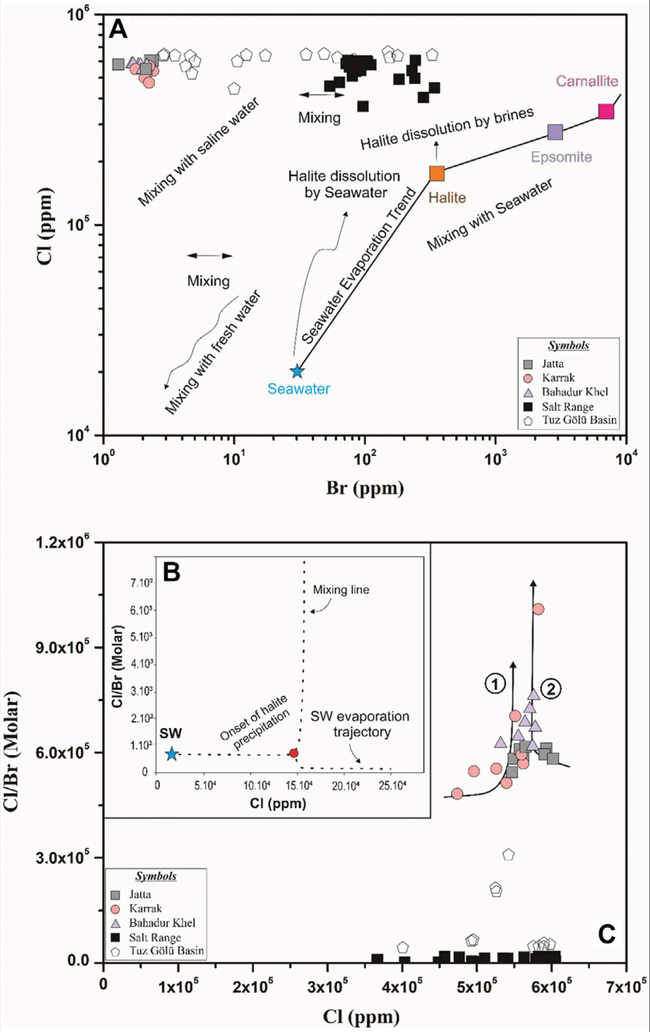

FIGURE 5 | Simplified models explaining the Cl and Br behaviors in halite from the Kohat Basin. **(A)** Cl vs Br ratios. Data are compared to those of the Salt Range (Pakistan) and Tuz Golu (Turkey) Basins. Precipitation data of variable evaporite minerals are from Matray, 1988, the seawater evaporation line is from Shouakar-Stash (2008) and Ercan et al. (2019). **(B)** Mixing model adapted from Grandia et al. (2003) and Ercan et al. (2019) where the dashed line represents the addition of highly evaporated brine that underwent dilution by a factor of seven to a fluid-dissolving halite. **(C)** Cl/Br ratio vs. Cl. Trends one and two represent variable evaporation trends.

concentrations can only be explained by multiple inputs of non-marine water.

The Cl/Br vs Cl diagram (**Figure 5**) shows that in our study area brines of different origins were mixed. The halite samples from our three locations plot along two distinct trends: 1) Most of the samples from the Karrak mine plot along trend 1 in **Figure 5** and indicated that they precipitated from two mixed Cl-rich salt waters that have dissimilar compositions, percentages or origins (e.g., SW, saline water or meteoric water). 2) Samples from Bahadur Khel and Jatta lay along trend 2 and agreed with the recrystallization of ancient halite (i.e. WRI; water-rock interaction). We also compared our values with those of two other salt basins (**Figure 5**): the Salt Range (Pakistan; Hussain et al., 2020a) and the Tuz Golu (Turkey; Ercan et al., 2019) basins. While the KB showed a trend similar (but with lower Br concentrations) to the Tuz Golu basin, the nearest Salt Range yielded significantly lower and homogenous Cl/Br ratios that may be explained by active tectonic and multiple halite dissolutions.

Cl Isotopes in Halite: Implications for Paleoclimate

δ^{37}Cl isotope compositions have been extensively studied in evaporites in order to explain the Cl stable isotope fractionations induced by the evaporation process (e.g. Vengosh et al., 1989; Xiao et al., 1997; Eggenkamp et al., 1995; Eastoe et al., 1999; Ying-Kai et al., 2000; Eastoe et al., 2001; Eastoe et al., 2007; Luo et al., 2012; Luo et al., 2014; Eastoe, 2016; Luo et al., 2016; Eggenkamp et al., 2019a; Eggenkamp et al., 2019b). Salt precipitation from marine brines follows the classic Rayleigh distillation law (Eggenkamp et al., 1995), inducing a decrease in the δ^{37}Cl coupled to an increase in the corresponding Br/Cl ratio (Eggenkamp et al., 2019a). **Figure 6** shows that the Bahadurkhel and Karrak samples are mostly characterized by rather constant δ^{37}Cl ~−0.2‰ but varying Br/Cl ratios, whereas the Jatta samples display somewhat positive δ^{37}Cl values with considerably constant Br/Cl ratios. This may be explained by frequent and multiple dissolution and precipitation processes as Br contents decline with successive recycling processes (Eggenkamp et al., 2019b; Han et al., 2019). It also indicated that the basin was disconnected from the main water reservoir (i.e. sea), allowing for multiple dissolution/precipitation and mixing to occur. Ultimately, this resulted in the halite showing various origins, in agreement with the findings of Holland, 1984.

Previous studies have shown that halite is generally enriched in the heavier ^{37}Cl isotope and that its final δ^{37}Cl is controlled by

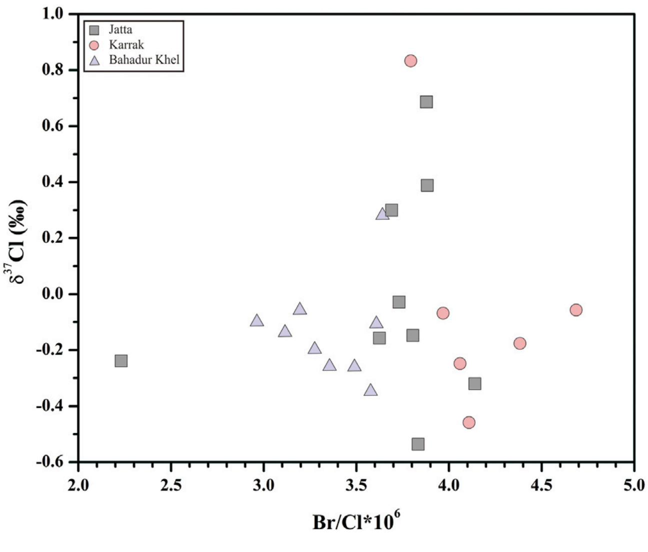

FIGURE 6 | Br/Cl ratio vs δ^{37}Cl of individual halite samples from the Kohat Basin.

the corresponding deposition conditions (e.g. Luo et al., 2016). The study of Cl stable isotope fractionations during salt precipitation (e.g. Eggenkamp et al., 1995; Luo et al., 2012; Luo et al., 2014; Eggenkamp et al., 2015; Luo et al., 2016; Eggenkamp et al., 2016) showed that the most negative δ^{37}Cl appear when bischofite ($MgCl_2{\bullet}6H_2O$) starts precipitating (Eggenkamp et al., 2018). Luo et al. (2014) also showed that δ^{37}Cl keep decreasing continuously with the precipitation of K-Mg salts. Thus, Cl isotopes are good proxies for characterizing the evaporation process: the continuous impoverishment in ^{37}Cl can be linked to the evaporation cycles (Luo et al., 2014; Eggenkamp et al., 2019a). Cl^- in the Kohat Basin results of the ancient marine water (Pivnik and Wells, 1996; Hussain and Zhang, 2018) that may be mixed with non-marine or meteoric waters, as demonstrated by the δ^{37}Cl values of its halite centered around 0‰ (Eastoe et al., 2001; Eastoe et al., 2007). The δ^{37}Cl for the KB Eocene marine halite ranged from −0.54‰ to 0.83‰, and most of these isotope compositions are within 0 ± 0.5‰, indicating that variable climatic conditions prevailed during deposition as well as the alternation of wet and dry periods climate. Under wetter conditions, dissolution of the already deposited halite is the main source of Cl. This dissolution is accompanied by higher δ^{37}Cl (Luo et al., 2016) compared to lake water. Under dry spell conditions, a limited quantity of Cl enters the basin and, coupled to the evaporation process, this continuously decreases δ^{37}Cl in the salt lakes. Consequently, lake waters during flooding have higher δ^{37}Cl compared to dry conditions. These higher δ^{37}Cl indicate thus both the state of the halite precipitation from the saline lake but also reveal a larger volume of lake water. For the KB, the highest δ^{37}Cl was 0.83‰, suggesting a sudden high-depth lake and thus important amounts of water entering the basin. On the other hand, as most of the δ^{37}Cl values were negative (**Figure 6**; lowest δ^{37}Cl = −0.54‰), this suggests that long dry and hot climatic conditions prevailed during the deposition of the halite.

Origin of the Eocene Halite in the Kohat Basin

Due to the events associated to the "Eocene thermal maximum 1(ETM1)" (also known as the "Paleocene–Eocene Thermal Maximum; PTEM"), Eocene was an evolving period. The PTEM was characterized by an extreme increase (5–8°C) of the global average temperature (Mcinerney and Wing, 2011). The ETM1 occurred about 56 Ma ago (Bowen et al., 2015) and this hot period remained for at least 200,000 years (Mcinerney and Wing, 2011). The ETM1 effect was recorded worldwide and the mid-latitude areas saw average temperatures of ~6°C (Hansen et al., 2013). Variations in the δ^{37}Cl and ion compositions of the Kohat Salts may have thus been controlled by the global sea level fluctuations caused by these climate variations during ETM1. The effects of the PTEM are more observable in the marine sedimentary section across the Paleocene/Eocene (P/E) margin in the adjacent Indus basin (Hanif et al., 2014). In this basin, the onset of the carbon and oxygen stable isotope excursion has proved that it's associated with the PETM (Hanif, 2011). Besides isotopic evidences, paleontological ones also support that the PTEM impacted the area neighboring the Salt Range (Afzal et al., 2011; Hanif et al., 2020) and indicate that the environment fluctuated (bathyal - shallow carbonate platform; Hanif et al., 2020). Still, to our knowledge, the studies about the PTEM effects in this region are still scarce, therefore arising the need for further investigations based on petrographic (e.g. halite homogenized temperature) and isotope approaches. **Figure 7** presents a simplified model detailing the successive events that led to the deposition of the KB Eocene halite. At the end of the Early Eocene, an extensive but short-time regression period occurred in the KB, evidenced by the presence of the Jatta gypsum and of the association of the gypsiferous shale with halite (Qadri, 1995). During the Middle Eocene, a widespread transgression formed marshes covering the whole KB. This is evidenced by the Mami Khel Formation that overlays the Chorgali Formation, that was deposited in a coastal or tidal saline/brackish water environment during a transgression event (Paracha, 2004). It comprises red to brownish fluvial and/or alluvial claystone and shale intervals which demonstrate the existence of a highly dry environment for a long period in the KB. The deposition of the Kohat Formation indicated transitional marine conditions about 50 Ma ago (Paracha, 2004). This ultimately established a foredeep basin between the Indian and Asian Plates. Later on, it morphed into a confined evaporite basin, followed by an early terrestrial foreland basin and an open marine basin. And lastly, during the Pliocene-Pleistocene times, it developed into an entirely terrestrial foreland basin (Pivnik and Khan, 1996; Paracha 2004). All these events were controlled by regional tectonic, i.e. the overall rise of the NW Indian Craton between the Eocene and Oligocene periods that formed an evaporite basin (**Figure 7**).

CONCLUSION

In this study, we used the mineralogy, geochemistry and isotope characteristics of Eocene halite samples from the Kohat Basin in northern Pakistan to discuss the origin and evolution of the evaporites and associated regional paleoclimate. Our results suggested that the source of the ancient halites is not only marine water but also included a combination of solutions having different compositions (e.g. seawater or saline water and meteoric water). Ion compositions (Br^-; <3 ppm) and stable high δ^{37}Cl values (+0.83‰) evidenced a non-marine water entry and/or multiple time dissolution/recrystallization by different waters. All samples yielded higher SO_4^{2-} concentrations compared to Ca^{2+}, which confirmed that halite precipitated from SO_4^{2-}-type waters. The high Mg^{2+} contents in the halite samples compared to the Eocene seawater supported a global decrease in the dolomitization process. The absence of primary fluid inclusion indicated that highly unstable regional paleoclimate prevailed during the different stages of the KB formation: 1) during the initial stages shallow seawater existed, which favored the establishment of an evaporite basin, 2) later on, this evaporite basin turned into a terrestrial foreland basin, followed by 3) an open marine basin, and ultimately 4) settled as a terrestrial foreland basin. All this basin sequence was

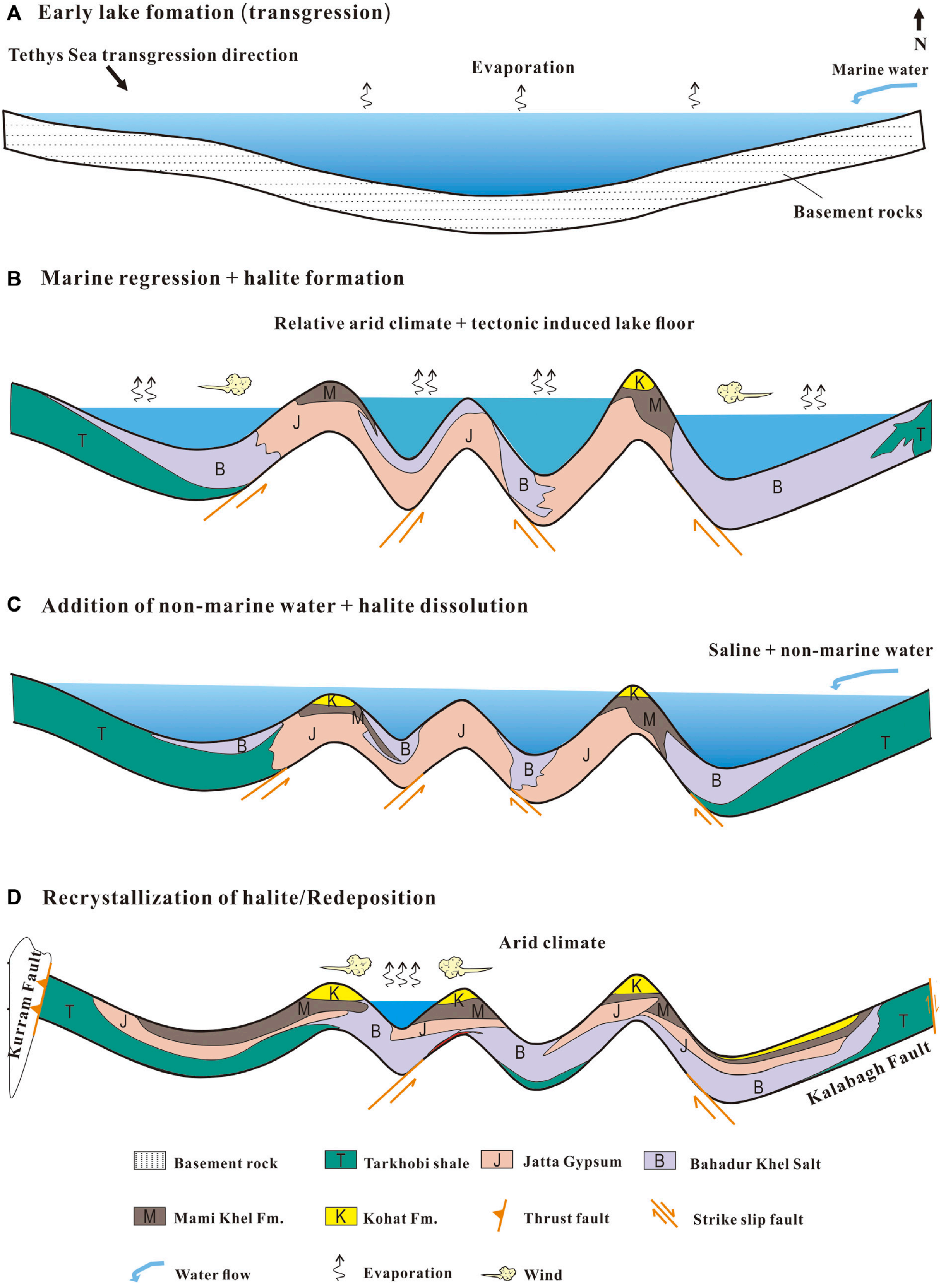

FIGURE 7 | Simplified conceptual lake model showing the origin and evolution of the Eocene halite in the Kohat Basin. **(A)** Lake formation during regression of Tethys sea, **(B)** marine transgression and halite precipitation, **(C)** saline and non-marine water input in the lake, and **(D)** gives recrystallization of halite.

controlled by an active tectonic system that was linked to the Himalayan orogeny and to the global sea-level fluctuations that were triggered by ETM1.

DATA AVAILABILITY STATEMENT

The original contributions presented in the study are included in the article/Supplementary Material, further inquiries can be directed to the corresponding authors.

AUTHOR CONTRIBUTIONS

Credit author statement: Conceptualization, SH; validation, FH; Software, AH and MM; Formal analysis and investigation, MZ, HJ and SH; Data curation, AA; writing—original draft preparation, SH; writing—review and editing, DW; supervision, FH, DW.

FUNDING

This scientific work was supported by the Qinghai Natural Science Foundation (grant No. 2019-ZJ-911), Natural Science Foundation of China (No. 42007169), the Fourth Batch of Qinghai Province “Thousand Talents Program for High-end Innovative Talents” (2020000051) and Funds for the Qinghai Province (No. 2020-ZJ-932Q; 2020-ZJ-732).

ACKNOWLEDGMENTS

We especially thank Ahsan-Ulla Khan & Engineer Shah Burhan-Uddin (Project Manager: PMDC, KPK site, Pakistan) for their help during sampling. We are also thankful to Zhang-Kuang Peng & Prof. Ma Yunqi for their help in the Cl isotope analysis, and the anonymous reviewers for their helpful comments.

REFERENCES

Afzal, J., Williams, M., Leng, M. J., Aldridge, R. J., and Stephenson, M. H. (2011). Evolution of Paleocene to early eocene larger benthic foraminifer assemblages of the Indus basin, Pakistan. *Lethaia* 44, 299–320. doi:10.1111/j.1502-3931.2010.00247.x

Ahmad, M., Akram, W., Ahmad, N., Tasneem, M. A., Rafiq, M., and Latif, Z. (2002). Assessment of reservoir temperatures of thermal springs of the northern areas of Pakistan by chemical and isotope geothermometry. *Geothermics* 31, 613–631. doi:10.1016/s0375-6505(02)00009-3

Ahmad, S., Ali, F., Khan, M. I., and Khan, A. A. (2006). Structural transect of the western Kohat Fold and thrust Belt between hangu and basia Khel, NWFP, Pakistan. *Pakistan J. Hydrocarbon Res.* 16, 22–35.

Alam, G. S., and Asrarullah (1973). *Potash deposits of salt mine, Khewra, Jhelum District, Punjab, Pakistan*. Director General, Geological Survey of Pakistan.

Alcalá, F. J., and Custodio, E. (2004). La deposición atmosférica de cloruro al terreno en España. *Boletín Geológico y Minero* 115 (5), 319–330.

Alcalá, F. J., and Custodio, E. (2008). Using the Cl/Br ratio as a tracer to identify the origin of salinity in aquifers in Spain and Portugal. *J. Hydrol.* 359, 189–207. doi:10.1016/j.jhydrol.2008.06.028

Alsop, G. I. (1996). Physical modelling of fold and fracture geometries associated with salt diapirism. *Geol. Soc. Lond. Spec. Publications.* 100, 227–241. doi:10.1144/gsl.sp.1996.100.01.14

Asrarullah (1962). *Rock salt resources of Pakistan*. Lahore, Pakistan: CENTO symposium.

Asrarullah (1963). Rock salt resources of Pakistan. *Pakistan Geographical Rev.* 18, 19–32.

Bloch, M. (1953). On the Cl^-/Br^- ratio and the distribution of Br ions in liquids and solids during evaporation of bromide-containing chloride solutions. *Bull. Res. Counc. Isr.*

Bowen, G. J., Maibauer, B. J., Kraus, M. J., Röhl, U., Westerhold, T., Steimke, A., et al. (2015). Two massive, rapid releases of carbon during the onset of the Palaeocene-Eocene thermal maximum. *Nat. Geosci.* 8, 44–47. doi:10.1038/ngeo2316

Brennan, S. T., Lowenstein, T. K., and Cendón, D. I. (2013). The major-ion composition of Cenozoic seawater: the past 36 million years from fluid inclusions in marine halite. *Am. J. Sci.* 313, 713–775. doi:10.2475/08.2013.01

Eames, F. (1952). A contribution to the study of Eocene in western Pakistan and western India, Part A. The geology of standard sections in the western Punjab and in the kobat district. *Geol.*

Eastoe, C. (2016). Stable chlorine isotopes in arid non-marine basins: Instances and possible fractionation mechanisms. *Appl. Geochem.* 74, 1–12.

Eastoe, C. J., Long, A., and Knauth, L. P. (1999). Stable chlorine isotopes in the Palo Duro Basin, Texas: evidence for preservation of Permian evaporite brines. *Geochimica et. Cosmochimica Acta.* 63, 1375–1382. doi:10.1016/s0016-7037(99)00186-6

Eastoe, C. J., Long, A., Land, L. S., and Kyle, J. R. (2001). Stable chlorine isotopes in halite and brine from the Gulf Coast Basin: brine genesis and evolution. *Chem. Geology.* 176, 343–360. doi:10.1016/s0009-2541(00)00374-0

Eastoe, C. J., Peryt, T. M., Petrychenko, O. Y., and Geisler-Cussey, D. (2007). Stable chlorine isotopes in Phanerozoic evaporites. *Appl. Geochem.* 22, 575–588. doi:10.1016/j.apgeochem.2006.12.012

Eggenkamp, H. G. M. (2015). Comment on "stable isotope fractionation of chlorine during the precipitation of single chloride minerals" by Luo, C.-g., Xiao, Y.-k., wen, H.-j., Ma, H.-z., Ma, Y.-q., Zhang, Y.-l., Zhang, Y.-x. And He, M.-y. [Applied geochemistry 47 (2014) 141-149]. *Appl. Geochem.* 54, 111–116. doi:10.1016/j.apgeochem.2014.11.018

Eggenkamp, H. G. M., Kreulen, R., and Koster Van Groos, A. F. (1995). Chlorine stable isotope fractionation in evaporites. *Geochimica et. Cosmochimica Acta.* 59, 5169–5175. doi:10.1016/0016-7037(95)00353-3

Eggenkamp, H. G. M., Louvat, P., Agrinier, P., Bonifacie, M., Bekker, A., Krupenik, V., et al. (2019a). The bromine and chlorine isotope composition of primary halite deposits and their significance for the secular isotope composition of seawater. *Geochimica et. Cosmochimica Acta.* 264, 13–29. doi:10.1016/j.gca.2019.08.005

Eggenkamp, H. G. M., Louvat, P., Griffioen, J., and Agrinier, P. (2019b). Chlorine and bromine isotope evolution within a fully developed Upper Permian natural salt sequence. *Geochimica et Cosmochimica Acta* 245, 316–326. doi:10.1016/j.gca.2018.11.010

Eggenkamp, H., Bonifacie, M., Ader, M., and Agrinier, P. (2016). Experimental determination of stable chlorine and bromine isotope fractionation during precipitation of salt from a saturated solution. *Chem. Geol.* 433, 46–56.

Eggenkamp, H., Griffioen, J., Louvat, P., and Agrinier, P. (2018). “Bromine stable isotope fractionation in evaporites,” in 20th EGU General Assembly, EGU2018, Proceedings from the conference, Vienna, Austria, April 4–13, 2018, 2536.

Eggenkamp, H. (2014). *The geochemistry of stable chlorine and bromine isotopes*. New York: Springer.

Ercan, H. Ü., Karakaya, M. Ç., Bozdağ, A., Karakaya, N., and Delikan, A. (2019). Origin and evolution of halite based on stable isotopes (δ37Cl, δ81Br, δ11B and δ7Li) and trace elements in Tuz Gölü Basin, Turkey. *Appl. Geochem.* 105, 17–30. doi:10.1016/j.apgeochem.2019.04.008

Fatmi, A. N. (1973). *Lithostratigraphic units of the Kohat-Potwar province, Indus basin*. Pakistan: Geological Survey of Pakistan.

Gansser, A. (1964). *Geology of the himalayas*.

Gardezi, S. a. H. (2016). “Geological constraints on central KOHAT FORELAND basin, Khyber PAKHTUNKHWA, Pakistan: implication from 2d and 3d structural modeling,” in *International conference and exhibition* Barcelona, Spain: Society of Exploration Geophysicists and American Association of Petroleum, 3–6.

Gee, E. (1938). The economic geology of the northern Punjab, with notes on adjoining portions of the North-West Frontier Province: India Mining Geol. *Metall. Inst. Trans.* 33, 263–350.

Gee, E. (1945). The age of the Saline Series of the Punjab and of Kohat. *Proceedings of the National Academy of Science India* 14, 269–310.

Grandia, F., Canals, A., Cardellach, E., Banks, D. A., and Perona, J. (2003). Origin of ore-forming brines in sediment-hosted Zn-Pb deposits of the Basque-Cantabrian Basin, Northern Spain. *Econ. Geology.* 98, 1397–1411. doi:10.2113/gsecongeo.98.7.1397

Guo, P., Liu, C., Huang, L., Wang, P., Wang, K., Yuan, H., et al. (2017). Genesis of the late Eocene bedded halite in the qaidam basin and its implication for paleoclimate in east Asia. *Palaeogeogr. Palaeoclimatol. Palaeoecol.* 487, 364–380. doi:10.1016/j.palaeo.2017.09.023

Han, J-L., Hussain, S-A., and Han, F-Q. (2019). Stable chlorine isotopes in saline springs from the Nangqen basin, Qinghai–Tibet Plateau: brine genesis and evolution. *J. Earth Syst. Sci.* 128, 206. doi:10.1007/s12040-019-1236-0

Hanif, M., Hart, M. B., Grimes, S. T., and Leng, M. J. (2014). Integrated stratigraphy and palaeoenvironment of the P/E boundary interval, Rakhi Nala section, Indus Basin (Pakistan). *Arab J. Geosci.* 7, 323–339. doi:10.1007/s12517-012-0812-2

Hanif, M., Sabba, M., Ali, N., Rahman, M. U., Ali, F., and Swati, M. a. F. (2020). A multi-proxy based high-resolution stratigraphical analysis of the possible Palaeocene–Eocene boundary interval, Salt Range, Pakistan. *Geol. J.* 56, 434–456. doi:10.1002/gj.3912

Hanif, M. (2011). *Stratigraphy and palaeoenvironment of the paleocene/eocene boundary interval in the Indus basin*. Pakistan: University of Plymouth.

Hanlon, C., Stotler, R., Frape, S., and Gwynne, R. (2017). Comparison of δ81Br and δ37Cl composition of volatiles, salt precipitates, and associated water in terrestrial evaporative saline lake systems. *Isotopes Environ. Health Stud.* 53, 446–465. doi:10.1080/10256016.2017.1324856

Hansen, J., Sato, M., Russell, G., and Kharecha, P. (2013). Climate sensitivity, sea level and atmospheric carbon dioxide. *Phil. Trans. R. Soc. A.* 371, 20120294. doi:10.1098/rsta.2012.0294

Hardie, L. A., and Lowenstein, T. K. (2004). Did the Mediterranean Sea dry out during the Miocene? A reassessment of the evaporite evidence from DSDP Legs 13 and 42A cores. *J. Sediment. Res.* 74, 453–461. doi:10.1306/112003740453

Heinrich, C. A., Bain, J. H. C., Fardy, J. J., and Waring, C. L. (1993). Br/Cl geochemistry of hydrothermal brines associated with Proterozoic metasediment-hosted copper mineralization at Mount Isa, northern Australia. *Geochimica et. Cosmochimica Acta.* 57, 2991–3000. doi:10.1016/0016-7037(93)90288-8

Holland, H. D. (2005). Sea level, sediments and the composition of seawater. *Am. J. Sci.* 305, 220–239. doi:10.2475/ajs.305.3.220

Holland, H. D. (1984). *The chemical evolution of the atmosphere and oceans*. New Jersey: Princeton University Press.

Holland, H. D., and Zimmermann, H. (2000). The dolomite problem Revisited1. *Int. Geology. Rev.* 42, 481–490. doi:10.1080/00206810009465093

Holland, O. B., Brown, H., Kuhnert, L., Fairchild, C., Risk, M., and Gomez-Sanchez, C. E. (1984). Further evaluation of saline infusion for the diagnosis of primary aldosteronism. *Hypertension* 6, 717–723. doi:10.1161/01.hyp.6.5.717

Holser, W. T. (1979). Trace elements and isotopes in evaporites. *Marine Minerals. Mineralogical Society of America Short Course Notes Washington, DC* doi:10.1515/9781501508646-013

Hsü, K. J., and Bernoulli, D. (1978). *Genesis of the Tethys and the mediterranean*. Boston, MA: US Government Printing Office.

Hsü, K. J., Ryan, W. B. F., and Cita, M. B. (1973). Late Miocene desiccation of the mediterranean. *Nature* 242, 240–244. doi:10.1038/242240a0

Hussain, H., and Shuangxi, Z. (2018). Structural evolution of the Kohat Fold and thrust Belt in the shakardarra area (south eastern Kohat, Pakistan). *Geosciences* 8, 311. doi:10.3390/geosciences8090311

Hussain, M., and Warren, J. K. (1991). Source rock potential of shallow-water evaporites: an investigation in holocenepleistocene Salt Flat sabkah (playa), west Texas-New Mexico. *Carbonates Evaporites* 6, 217–224. doi:10.1007/bf03174424

Hussain, S. A., Feng-Qing, H., Yunqi, M., Khan, H., Jian, Y., Hussain, G., et al. (2020a). *An overview of Pakistan rock salt resources and their chemical characterisation*. Pakistan Journal of Scientific and Industrial Research

Hussain, S. A., Han, F-Q., Han, J., Khan, H., and Widory, D. (2020b). Chlorine isotopes unravel conditions of formation of the Neoproterozoic rock salts from the Salt Range Formation, Pakistan. *Can. J. Earth Sci.* doi:10.1139/cjes-2019-0149

Hussain, S. A., Han, F-Q., Han, W., Rodríguez, A., Han, J-L., Han, J., et al. (2019). Climate change impact on the evolution of the saline lakes of the soan-sakaser valley (central salt range; Pakistan): evidences from hydrochemistry and water (δD, δ18O) and chlorine (δ37Cl) stable isotopes. *Water* 11, 912. doi:10.3390/w11050912

Hussain, S. A., Han, F-Q., Ma, Z., Hussain, A., Mughal, M. S., Han, J., et al. (2021). Unraveling sources and climate conditions prevailing during the deposition of neoproterozoic evaporites using coupled chemistry and boron isotope compositions (δ11B): the example of the salt range, Punjab, Pakistan. *Minerals* 11, 161. doi:10.3390/min11020161

Katz, B. G., Eberts, S. M., and Kauffman, L. J. (2011). Using Cl/Br ratios and other indicators to assess potential impacts on groundwater quality from septic systems: a review and examples from principal aquifers in the United States. *J. Hydrol.* 397, 151–166. doi:10.1016/j.jhydrol.2010.11.017

Kazmi, A. H., and Rana, R. A. (1982). *Tectonic map of Pakistan 1: 2 000 000: map showing structural features and tectonic stages in Pakistan*. Quetta: Geological Survey of Pakistan.

Khan, K., Khan, I., Leghari, A., and Khan, M. (1987). *Geology along the karakoram highway from hasan abdal to khunjerab pass*. Quetta: Geological Survey of Pakistan, 39–43.

Kovalevych, V., Marshall, T., Peryt, T., Petrychenko, O., and Zhukova, S. (2006). Chemical composition of seawater in neoproterozoic: results of fluid inclusion study of halite from salt range (Pakistan) and amadeus basin (Australia). *Precambrian Res.* 144, 39–51. doi:10.1016/j.precamres.2005.10.004

Krishnan, M. S. (1966). Salt tectonics in the Punjab salt range, Pakistan1. *Geol. Soc. America Bull.* 77, 115–122. doi:10.1130/0016-7606(1966)77[115:stitps]2.0.co;2

Le Fort, P. (1975). Himalayas: the collided range. Present knowledge of the continental arc. *Am. J. Sci.* 275, 1–44.

Luo, C., Wen, H., Xiao, Y., Ma, H., Fan, Q., Ma, Y., et al. (2016). Chlorine isotopes in sediments of the Qarhan Playa of China and their paleoclimatic significance. *Geochemistry.* 76, 149–156. doi:10.1016/j.chemer.2016.01.004

Luo, C., Xiao, Y., Ma, H., Ma, Y., Zhang, Y., and He, M. (2012). Stable isotope fractionation of chlorine during evaporation of brine from a saline lake. *Chinese Science Bulletin* 57 (15), 1833–1843.

Luo, C., Xiao, Y., Wen, H., Ma, H., Ma, Y., Zhang, Y., et al. (2014). Stable isotope fractionation of chlorine during the precipitation of single chloride minerals. *Appl. Geochem.* 47, 141–149. doi:10.1016/j.apgeochem.2014.06.005

Matray, J. (1988). *Hydrochimie et géochimie isotopique des eaux de réservoir pétrolier du Trias et du Dogger dans le Bassin de Paris. Tbbse de 36me cycle*, Orsay: Universit6 de Paris-Sud. 118.

Mcinerney, F. A., and Wing, S. L. (2011). The Paleocene-Eocene Thermal Maximum: a perturbation of carbon cycle, climate, and biosphere with implications for the future. *Annu. Rev. Earth Planet. Sci.* 39, 489–516. doi:10.1146/annurev-earth-040610-133431

Meissner, C. R., Jr, Hussain, M., Rashid, M., and Sethi, U. (1975). *Geology of the parachinar quadrangle*. Pakistana: US Govt. Print. Off.

Meissner, C. R., Jr, Master, J., Rashid, M., and Hussain, M. (1974). *Stratigraphy of the Kohat quadrangle*. Pakistan: US Govt. Print. Off.

Moretto, R. (1986). *Etude sédimentologique et géochimique des dépôts de la série salifère paléogène du bassin de Bourg-en-Bresse (France). Nancy 1.*

Najman, Y., Jenks, D., Godin, L., Boudagher-Fadel, M., Millar, I., Garzanti, E., et al. (2017). The Tethyan Himalayan detrital record shows that India-Asia terminal collision occurred by 54 Ma in the Western Himalaya. *Earth Planet. Sci. Lett.* 459, 301–310. doi:10.1016/j.epsl.2016.11.036

Paracha, W. (2004). *Kohat plateau with reference to Himalayan tectonic general study*. CSEG recorder.

Pivnik, D. A., and Khan, M. J. (1996). Transition from foreland- to piggyback-basin deposition, plio-pleistocene upper siwalik group, shinghar range, NW Pakistan. *Sedimentology.* 43, 631–646. doi:10.1111/j.1365-3091.1996.tb02018.x

Pivnik, D. A., and Sercombe, W. J. (1993a). Transpression-and compression-related, evaporite-controlled faulting and folding in the Kohat Plateau, NW Pakistan. *Himalayan Tectonics: Geol. Soc. Lond. Spec. Publications.*

Pivnik, D. A., and Sercombe, W. J. (1993b). Compression-and transpression-related deformation in the Kohat Plateau, NW Pakistan. *Geol. Soc. Lond. Spec. Publications.* 74(1), 559–580. doi:10.1144/gsl.sp.1993.074.01.37

Pivnik, D. A., and Wells, N. A. (1996). The transition from Tethys to the Himalaya as recorded in northwest Pakistan. *Geol. Soc. America Bull.* 108, 1295–1313. doi:10.1130/0016-7606(1996)108<1295:ttfttt>2.3.co;2

Potter, P. E., and Szatmari, P. (2009). Global Miocene tectonics and the modern world. *Earth-Science Rev.* 96, 279–295. doi:10.1016/j.earscirev.2009.07.003

Salvany, J. M., GARCÍA-VEIGAS, J., and OrtI, F. (2007). Glauberite–halite association of the Zaragoza Gypsum Formation (Lower Miocene, Ebro Basin, NE Spain). *Sedimentology* 54 (2), 443–467.

Shah, I. (1977). *Stratigraphy of Pakistan: geological survey of Pakistan memoirs*. Islamabad, Pakistan: Geol Surv Pakistan, 12.

Shah, S. (2009). *Stratigraphy of Pakistan: geological survey of Pakistan memoir*. Quetta: Pakistan: Geol Surv Pakistan., 22.

Shearman, D. J. (1970). *Recent halite rock, Baja California*. Mexico: Instition of Mining & Metallurgy.

Shouakar-Stash, O. (2008). Evaluation of stable chlorine and bromine isotopes in sedimentary formation fluids. PhD thesis. (Waterloo (Canada): University of Waterloo).

Sonney, R., Vuataz, F.-D., and Cattin, S. (2010). "Use of Cl/Br ratio to decipher the origin of dissolved mineral components in deep fluids from the Alps range and neighbouring areas", in *Proceedings World Geothermal Congress: Institut des sciences du langage et de la communication*. Bali, Indonesia: Université de Neuchâtel, 1–13.

Timofeeff, M. N., Lowenstein, T. K., Da Silva, M. A. M., and Harris, N. B. (2006). Secular variation in the major-ion chemistry of seawater: evidence from fluid inclusions in Cretaceous halites. *Geochimica et. Cosmochimica Acta.* 70, 1977–1994. doi:10.1016/j.gca.2006.01.020

Tomascak, P. B., Magna, T., and Dohmen, R. (2016). *Advances in lithium isotope geochemistry*. New York: Springer.

Vengosh, A., Chivas, A. R., and Mcculloch, M. T. (1989). Direct determination of boron and chlorine isotopic compositions in geological materials by negative thermal-ionization mass spectrometry. *Chem. Geology. Isotope Geosci. Section.* 79, 333–343. doi:10.1016/0168-9622(89)90039-0

Walter, L. M., Stueber, A. M., and Huston, T. J. (1990). Br-Cl-Na systematics in Illinois basin fluids: constraints on fluid origin and evolution. *Geol.* 18, 315–318. doi:10.1130/0091-7613(1990)018<0315:bcnsii>2.3.co;2

Warren, J. K. (2010). Evaporites through time: tectonic, climatic and eustatic controls in marine and nonmarine deposits. *Earth-Science Rev.* 98, 217–268. doi:10.1016/j.earscirev.2009.11.004

Warren, J. K. (2006). *Evaporites: sediments, resources and hydrocarbons*. Heidelberg, Germany: Springer Science & Business Media.

Wells, N. (1984). Marine and continental sedimentation in the early Cenozoic Kohat Basin and adjacent northwestern Indo-Pakistan. Ph. D. dissertation. (Ann Arbor: University of Michiga).

Wynne, A. (1875). *The Trans-Indus salt region in the Kohat district*. New Delhi, India: Government of India.

Wynne, A. (1878). On the geology of the salt range in the Punjab: mem. *Geol. Surv. India* 14, 98.

Wynne, A. (1880). *On the Trans-Indus extension of the Punjab salt Range*, Calcutta, India: Geological Survey of India, 17. 1–95.

Xiao, Y., Liu, W., Zhou, Y., and Sun, D. (1997). Isotopic compositions of chlorine in brine and saline minerals. *Chin.Sci.Bull.* 42, 406–409. doi:10.1007/bf02884233

Ying-Kai, X., Wei-Guo, L., Yin-Min, Z., Yun-Hui, W., and Shirodkar, P. V. (2000). Variations in isotopic compositions of chlorine in evaporation-controlled salt lake brines of Qaidam Basin, China. *Chin. J. Ocean. Limnol.* 18, 169–177. doi:10.1007/bf02842577

Conflict of Interest: The authors declare that the research was conducted in the absence of any commercial or financial relationships that could be construed as a potential conflict of interest.

frontiers
in Earth Science

ORIGINAL RESEARCH
published: 25 May 2021
doi: 10.3389/feart.2021.681361

Origin and Paleoenvironmental Significance of the Old Red Sand Along the Southeast Coast of China

Qingbin Fan[1,2], *Jie Liao*[1]*, *Yan Li*[3], *Wei Ye*[4], *Tao Wang*[1] *and Xiao Feng*[1,2]

[1]Key Laboratory of Desert and Desertification, Northwest Institute of Eco-Environment and Resources, Chinese Academy of Sciences, Lanzhou, China, [2]University of Chinese Academy of Sciences, Beijing, China, [3]College of Forestry, Nanjing Forestry University, Nanjing, China, [4]College of Geography and Environmental Sciences, Zhejiang Normal University, Jinhua, China

The "Old Red Sand" (ORS) along the southeast coast of China is of significant paleoclimatic and paleoenvironmental significance. However, its provenance remains controversial. In this study, grain size characteristics and quartz grain surface microtextures were analyzed to study the origin and paleoenvironmental significance of the ORS, the results show that the grain size of the ORS show typical aeolian features, the quartz grain surface microtextures of the ORS show both aeolian features and subaqueous environments characteristics. Combined with the latest OSL dating data, we suggest that the ORS was coastal aeolian sand dunes developed since the last interglacial period. The formation of the ORS was restricted jointly by climate changes of the coastal area and the distance from the shoreline that resulted from sea level changes.

Keywords: old red sand, aeolian activity, east Asian monsoon, climate changes, sea level changes

OPEN ACCESS

Edited by:
Xiangzhong Li,
Yunnan University, China

Reviewed by:
Xianyan Wang,
Nanjing University, China
Jianhui Jin,
Fujian Normal University, China

Correspondence:
Jie Liao
liaojie@lzb.ac.cn

Specialty section:
This article was submitted to Quaternary Science, Geomorphology and Paleoenvironment, a section of the journal Frontiers in Earth Science

Received: *16 March 2021*
Accepted: *05 May 2021*
Published: *25 May 2021*

Citation:
Fan Q, Liao J, Li Y, Ye W, Wang T and Feng X (2021) Origin and Paleoenvironmental Significance of the Old Red Sand Along the Southeast Coast of China.
Front. Earth Sci. 9:681361.
doi: 10.3389/feart.2021.681361

INTRODUCTION

Coastal dunes are common around the world and resulted from complex interactions related to prevailing winds, sand supply, climate changes and sea level fluctuations (Blumer et al., 2012). Red dunes are widespread in south Asia and east Asia, including Sri Lanka, India and the southeast coast of China, etc (Alappat et al., 2013). The "Old Red Sand" (ORS) refers to a Quaternary sediment of semi-cemented medium fine sand, mainly in red or brown red, and intermittently distributed along the southeast coast of China, its thickness can reach several meters to tens of meters (Wu et al., 1995; Zeng et al., 1999a; Li et al., 2012; Jin et al., 2018). The coastal area, as a special zone of interaction among lithosphere, hydrosphere and atmosphere, is very sensitive to climate and environment changes. The development of large areas of coastal dunes reflects the complex interaction among land, ocean and atmosphere, therefore, the origin and paleoenvironmental significance of the ORS is crucial for studying coastal climate and environment evolution along the southeast coast of China.

The large areas of red dunes had aroused great interests of geographers and geologists since the 1960s, researchers have done a lot of work on the ORS, however, there are still controversies on its origin nowadays. Firstly some researchers believed that the ORS belong to a marine deposit originated from beach sand in high sea level periods (Zeng and Huang, 1964; Zeng et al., 1999a; Li et al., 2012), while others considered it as a aeolian deposit derived from the exposed continental shelf plain in low sea level stages during glacial periods (Wu et al., 1995; Fangen et al., 2012; Jin et al., 2017). Different views on the origin of the ORS lead to contrasting environmental interpretations. The former interpretation implies that the development of the ORS resulted from more sand supply brought by rivers during high sea level stages in interglacial period (Zeng et al., 1999a; Li et al., 2012). The latter view indicates low sea level conditions and an intensified East Asian winter monsoon.

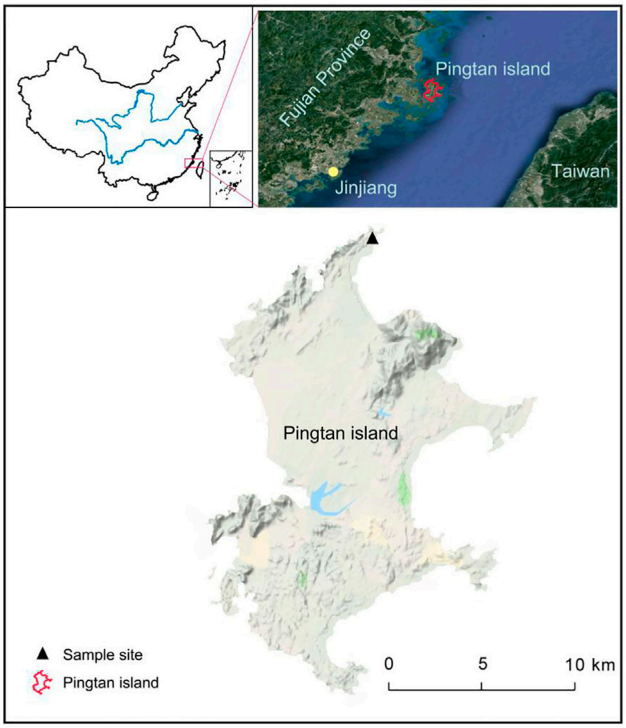

FIGURE 1 | Sample site of QF profile in Pingtan island, Fujian Province.

Therefore, identification the origin and paleoenvironmental significance of the ORS is helpful for studying regional climate and environment evolution along the southeast coast of China.

With regard to its chronology, firstly it is reported that the ORS was developed in Würm Glaciation (the last glacial period), and there are mainly two views on its chronology. One view holds that the ORS was formed in 50–40 and 20–10 Ka BP (Zhu et al., 1981; Wu and Wu, 1987); the other view believes that the ORS was formed in 60–40, 35–25, and 20–10 Ka BP (Feng et al., 1988; Wu and Wang, 2001), among which 60–40 Ka BP is the earliest period, and 20–10 Ka BP is the latest period of the ORS. Researchers believe that during the last glacial period, with global cooling, the sea level declined, the intensified East Asian winter monsoon provided enough power to transport the loose sand materials on the exposed continental shelf plain and deposit along the coast, which were stained red by a later strong weathering after deposition (Zhu et al., 1981; Wu and Wu, 1987; Feng et al., 1988; Wu and Wang, 2001).

In 2007, a new method of Optically Stimulated Luminescence (OSL) dating was applied to determine the chronology of the ORS, which promoted the study of the geochronology of the ORS to a new stage. OSL dating for the ORS in Jinjiang, Fujian Province show that the ORS was formed earlier than 77 Ka BP (Zhang et al., 2007), indicating that the ORS could be formed in the last interglacial period, which broke the upper limit of the ORS dating results reported (not earlier than 60 Ka BP). Subsequently by OSL dating, Jin Jianhui suggests that the ORS in Qingfeng, Fujian Province was formed in 110–33 Ka BP (Jin et al., 2017), Yu Mingtong suggests that the four layers of the ORS in Qingfeng, Pingtan island were formed in 122.5, 97.7, 83.1 and 61.9 Ka BP respectively (Yu et al., 2014). Hu Fangen suggests that the ORS in Jinjiang of Fujian Province was formed in 6 stages: 125–115, 105–97, 84–74, 61.5–52.0, 39–29 and 15–9 Ka BP respectively (Fangen et al., 2012), indicating that the ORS was formed since the last interglacial period, which promoted the study of the ORS to a new stage, that is, the ORS developed in both the last interglacial period and the last glacial period, but not occur in the LGM.

MATERIALS AND METHODS

The Study Area

Pingtan island (25°23′N–25°40′N, 119°41′E–119°52′E) (**Figure 1**), the most widely distributed area for the ORS (**Figure 2**), is located in the east coast of Fujian Province, adjacent to Taiwan Strait in the east and Pingtan Strait to the west, with an area of 278.61 km^2 (**Figure 1**). Aiming at the most controversial issue in study of the ORS, we take Qingfeng (QF) ORS profile on the coastal platform in the northeast corner of Pingtan island as an example. QF profile (25°36′46.7″N, 119°48′19.6″E) (**Figure 1**), a complete, thick and continuously deposited ORS profile, with an altitude of 48 m, a thickness of 13.94 m, according to its sedimentary characteristics (**Table 1**), the QF profile was divided into 7 layers (**Table 1**), A total of 70 samples were collected from bottom to top at equal intervals of 20 cm. Its grain size characteristics and quartz grain surface microtextures were analyzed, coupled with the latest dating results, the origin and environmental significance of the ORS were interpreted. Our results could provide further data for us to have a scientific understanding of the ORS and to support paleoenvironment reconstruction of southeast coast China.

Methods

Grain Size

Grain size characteristics of sediments are mainly controlled by the transportation mode and sedimentary environment. Therefore, grain size analysis is often used to identify sedimentation process and depositional environment (Yang et al., 2017; Purtill et al., 2019). The classification scheme used in this study is: Clay (0–4 μm), silt (4–63 μm), very fine sand (63–125 μm), fine sand (125–250 μm), medium sand (250–500 μm), coarse sand (500–1,000 μm) and extremely coarse sand (1,000–2,000 μm). The commonly used grain size parameters include average grain size (Mz), standard deviation (Sd), skewness (Sk) and kurtosis (Kg). The mathematical calculation formula of particle size parameters is as follows (Folk and Ward, 1957; Yang et al., 2017):

$$M_z = \frac{\sum_{i=1}^{n} x_i f_i}{100}$$

$$sd = \sqrt{\frac{\sum_{i=1}^{n} (x_i - Mz)^2 fi}{100}}$$

FIGURE 2 | The Old Red Sand in Pingtan island, Fujian Province.

TABLE 1 | Stratigraphic description of QF profile.

Layer	Depth (m)	Color of the ORS layers	description
1	0–4.8	Red sand	Sand (0–20 cm) is dry and hard, with plant roots; (20–260 cm) is uniform in color and compact; (260–480 cm) is loose and wet.
2	4.8–6.2	Yellowish brown sand	The sand is loose and wet.
3	6.2–7.0	Red sand	There are gradually increasing black spots in the vertical direction
4	7.0–8.3	Yellow sand	The sand is slightly tight with light yellow and black brown patches
5	8.3–9.9	Brow yellow sand	The upper sand is loose, containing iron plates (thickness about 4 cm) and gray yellow stripes; tight with black and grayish yellow spots in the middle and the lower part
6	9.9–11.74	Brown sand	The upper sand contains iron plates (thickness 4 cm); the middle sand contains black spots and black aggregates, which is relatively loose in texture
7	11.74–13.94	Gray sand	The sand layer contains black spots and is loose in texture

$$sk = \sqrt[3]{\frac{\sum_{i=1}^{n}(x_i - Mz)^3 fi}{100sd^3}}$$

$$Kg = \sqrt[4]{\frac{\sum_{i=1}^{n}(x_i - Mz)^4 fi}{100Sd^4}}$$

Grain size analysis was carried out at the geographic process laboratory, Zhejiang Normal University, using a Mastersizer 2000 laser grain size analyzer (Malvern, United Kingdom) with a measurement range of 0.01–2000 μm and an error of <2%. Samples for grain size analysis were pre-treated as follows. Samples were first boiled with 10% H_2O_2 and 10% HCl to remove the organic matter and carbonate, respectively. Next, 0.5 mol/L $(NaPO_3)_6$ was added as a dispersant, then the pretreated samples were ultrasonicated for 15 min before being analyzed.

Fisher linear discriminant analysis (FLDA), a common classification method in multivariate statistical analysis, is widely used to identify the origin of various sediments (Yang et al., 2017). In this study, we use FLDA to identify the origin of the ORS based on statistical analysis of hydraulic deposit (HD) and aeolian deposit (AD) grain size parameters. The function we created is as follows. $y = -1.138*\mathrm{Mz} + 1.58*\mathrm{Sd} - 0.781*\mathrm{Sk} + 0.805*\mathrm{Kg}$, the threshold level is −4.5744 (if $y > -4.5744$, it belongs to AD; if $y < -4.5744$, it belongs to HD) (Yang et al., 2017).

In this study, we selected a typical aeolian loess profile of Zeketai (ZKT) profile in Xinjiang provenance, which is considered as the provenance for the loess on the Chinese Loess Plateau (CLP) (Liu, 1985; Yang et al., 2014). We also selected Luochuan (LC) loess profile which was located on the central CLP, as well as Nantong (NT) profile (floodplain deposit) in the lower reaches of the Yangtze River. To test the linear discriminant function created above, 215 aeolian loess samples of ZKT profile and 33 typical floodplain deposits samples from NT profile were inputted into statistical software (SPSS) as AD and HD training sets respectively. All the significance probability values of the variable group mean are <0.001 (**Table 2**). Therefore, the four variables in this discriminant analysis are all effective.

The Box's *M* test assesses the assumption of homogeneity of covariance matrices. This test is very sensitive to meet the assumption of multivariate normality. The statistical value of Box's *M* is 738.71 (**Table 3**), far >0.05. Therefore, each of the

TABLE 2 | Equality test of group means.

Parameters	Wilks' Lambda	F	Significance probability
Mz	0.262	286.586	0
Sd	0.02	5079.284	0
Sk	0.042	2334.562	0
Kg	0.203	401.401	0

TABLE 3 | Box's *M* test results of equality covariance matrixes.

Boxe's *M*	*F*	
	Approx	Sig.
738.71	70.049	0

TABLE 4 | The verification of the discriminant function.

Profile codes	No. of samples	Actual category	Discriminant results		Accuracy (%)
			AD	HD	
ZKT	215	AD	215	0	100
NT	33	HD	0	33	100
LC	57	AD	57	0	100

covariance matrices can be considered equal. The significance probability of the *F*-test is 0.000, <0.05, indicating that the error judgment rate is minimal.

In order to verify the reliability of this model, sediment grain size parameters (Mz, Sd, Sk, and Kg) of 215 loess samples from ZKT profile, 33 floodplain deposit samples from NT profile, and 57 typical aeolian loess samples from LC profile were computed using the function. As shown in **Table 4**, all the aeolian loess samples from ZKT profile and LC profile were identified as AD, resulting in an accuracy of 100%. All the floodplain deposit samples from NT profile were identified as HD. Hence, the discriminant model is reliable.

Quartz Grain Surface Microtextures

Quartz grains have high hardness, stable chemical properties and strong weathering resistance, leading to a variety of microtextures that are well preserved on the quartz grains. These microtextures are considered to record the sedimentary history of quartz grains, including the parent rock, transportation process, and sedimentary environment. Therefore, many researchers have stated that quartz grain surface microtextures can be used to identify sedimentary environments (Liu, 1985; Pye, 1995; Helland et al., 1997; Mahaney and Kalm, 2000; Mahaney, 2002; Guo et al., 2002; Costa et al., 2012; Costa et al., 2013; Mahaney et al., 2014; Smith, et al., 2018; Chen et al., 2019; Li et al., 2021). It is suggested that dish-shaped depressions, crescentic depressions, pockmarked surfaces, upturned plates, meandering ridges are considered as typical features of aeolian quartz grains (Ying and Deonarine, 1985; Guo et al., 2002; Krinsley and Doornkamp, 2011; Costa et al., 2012; Costa et al., 2013). For example, dish-shaped depressions often develop in aeolian environments with high energies where quartz grains collide with each other, and densely distributed pockmarks result from collision with other grains during wind transportation, forming pockmarked surfaces. Meandering ridges mainly occur in aeolian environments as well (Costa et al., 2012; Costa et al., 2013; Mahaney, et al., 2014). On the other hand, conchoidal fractures, V-shaped cracks, polished surfaces, flat cleavage surfaces, parallel striations, grooves (straight or curved) are regarded as typical features of quartz grains from subaqueous environments (Ying and Deonarine, 1985; Mahaney et al., 2001; Guo et al., 2002; Mahaney et al., 2014; Vos et al., 2014). V-shaped cracks, which are triangular in shape and non-oriented, are likely to be caused by grain-to-grain collisions in subaqueous environments, parallel striations result from grain-to-grain scratches in subaqueous environments (Ying and Deonarine, 1985; Mahaney, 2002; Vos et al., 2014). Mahaney (2002) concluded that the feature which is the most common in subaqueous environments are V-shaped cracks. Here, 10 quartz grains were randomly selected in each sample of QF profile, and a total of 700 quartz grains were selected for Scanning Electron Microscope (SEM) observations.

Quartz grain surface textures were observed under an S-4800 high-resolution field emission scanning electron microscope (SEM) produced by Hitachi (Japan) at the Institute of Physical Chemistry, Zhejiang Normal University. The extraction method for quartz sand before SEM observation was as follows:

(1) To remove free iron, the dried sample was placed in centrifuge tube with sodium dithionite, sodium citrate (0.3 mol/L) and sodium bicarbonate solution (1 mol/L) and heated in a water bath. The solution was then separated by centrifuge until clear.
(2) The quartz minerals were separated and purified by the potassium pyrosulfate melting-fluorosilicic acid immersion method. After removing the free iron, the samples were mixed with potassium pyrosulfate powder and heated in a muffle furnace for 1 h (initial temperature 350°C, then 650°C from 20 min to the end). The heated samples were transferred to a beaker, and HCL solution (l:3) was added to the heating plate to dissolve the frit. After separation by centrifuge, the samples were dried in the oven. The samples were then soaked in fluorosilicic acid for 3 days. The solution was centrifuged and the clear liquid was removed three days later. The residue was dried, and the quartz grains with highest purity were extracted.

RESULTS

Grain Size Characteristics

The grain size characteristics of QF profile are as follows: the sand content ranges from 45.99 to 90.77% (mean 73.23%), the silt content varies from 6.25 to 34.18% (mean 17.34%), and the clay content ranges from 2.97 to 19.83% (mean 9.43%). The sand content is the first dominant grain size in QF profile, constituting the highest composition (**Tab.5**). In QF profile: (1) medium sand, fine sand and silt account for 30.17, 26.23 and 17.34% respectively; (2) coarse sand and clay are the second, with an average of 9.86 and 9.43%; (3) the content of extremely coarse sand is the least, with an average content of 0.97%. Whereas the beach sand in Pingtan island is mainly composed of medium sand, fine sand and coarse sand, with average contents of 48, 32.18, and 17.68% respectively, and almost without silt or clay (Zhang and Ming-Tong, 2014). Although beach sand is mainly composed of medium sand and fine sand, its contents of coarse sand and gravel is significantly higher than those in the ORS; in addition, the ORS contains more fine materials such as silt and

TABLE 5 | Grain size composition and Grain size parameters of QF profile.

Profile		Grain size composition/% (μm)							Grain size parameters			
		<4	4–63	>63	63–125	125–250	250–500	500–1,000	Mz	Sd	Sk	Kg
QF	Max	19.83	34.18	90.77	13.87	48.83	41.51	27.07	4.76	3.23	2.34	4.75
	Min	2.97	6.25	45.99	1.48	10.59	15.29	0.04	2.45	1.97	0.25	1.69
	Mean value	9.43	17.34	73.23	6.00	26.23	30.17	9.86	3.38	2.94	1.12	3.05

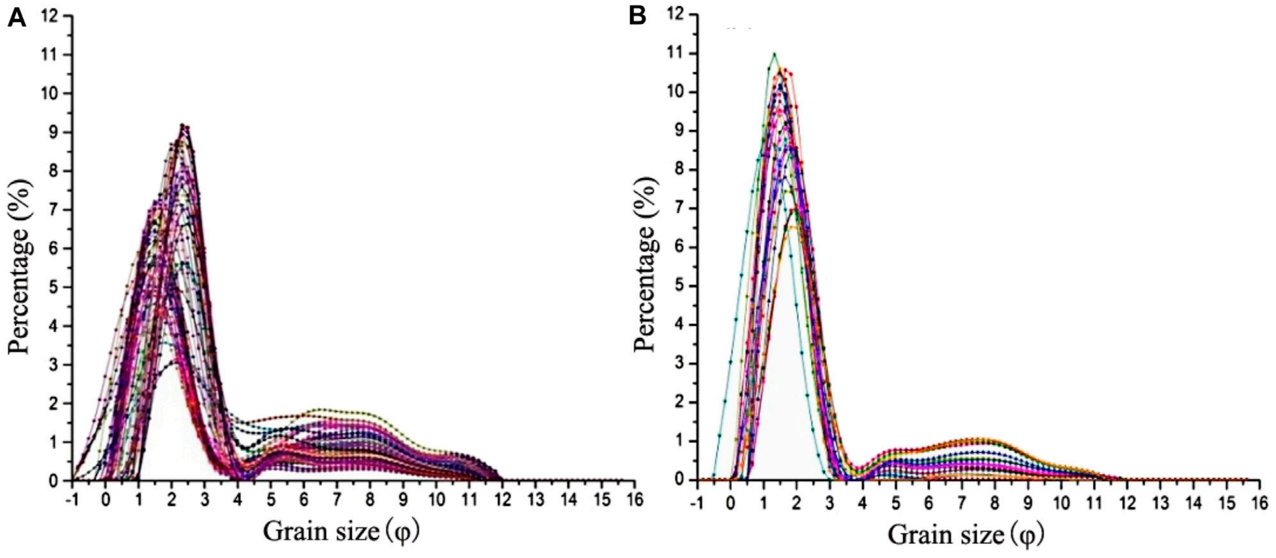

FIGURE 3 | The grain-size frequency curve of QF profile **(A)** and ZS profile **(B)**.

clay, while beach sand has little silt or clay. Shepard believes that the difference in clay content is one of the most significant differences between beach sand and aeolian sand (Shepard and Young, 1961). Wave disturbance makes the fine materials such as silt and clay in a suspension state, which are carried to the open sea by waves instead of depositing on the beach, while wind can transport and deposit these fine materials (Shepard and Young, 1961). According to Whalley's wind erosion quartz test, a small amount of fine materials such as silt and clay can be produced during the saltation process of sand grains transported by wind (Pye, 1983). The QF ORS profile contains more fine-grained materials, which is likely to be related to transport process of wind and the strong chemical weathering in a warm–humid subtropical monsoon climate after deposition.

The average grain size (Mz) of samples from QF profile varies 2.45–4.76*φ* (mean 3.38*φ*) (**Table 5**). Whereas the average grain size (Mz) of beach sand in coast of Fujian Province is 1.26–2.08*φ* (mean 1.76*φ*) (Zeng et al., 1999a). The sorting coefficient (Sd) ranges from 1.97 to 3.23 (mean 2.94*φ*), indicating a poor sorting. It is suggested that aeolian sand has a good sorting, while the sorting of modern coastal aeolian sand and beach sand are better than that of the ORS, this may be related to the chemical weathering in a warm–humid subtropical monsoon climate after deposition, which greatly increased the content of fine materials such as silt and clay; The skewness (Sk) varies from 2.34 to 0.25 (mean 1.12), Most of the samples show positive skewness, analogous to aeolian sand, while beach sand mostly show negative skewness (Zeng et al., 1999b). The kurtosis (Kg) ranges from 1.69 to 4.75 (mean 3.05), most samples are sharply peaked, analogous to aeolian sand, while beach sand mostly are medium to narrow peaked, without very narrow peaks (Zeng et al., 1999b). The grain-size frequency curve (**Figure 3A**) of QF profile is characterized by a single peak, a positive skewness and a long tail, which is very similar to that of a typical paleo-aeolian dune in Zhoushan (ZS) island, indicating QF profile a aeolian sand dune. The modal grain size is located near 2.5*φ*, and there is a small bulge from 4 to 12*φ*, indicating that the QF profile contains a certain amount of fine materials, namely silt and clay component, suggest an aeolian transportation and a strong chemical weathering process after deposition.

TABLE 6 | The identification result of the QF profile.

Profile codes	No. of samples	Actual category	Discriminant results	
			AD	HD
NT	33	HD	0	33
QF	70	AD	70	0

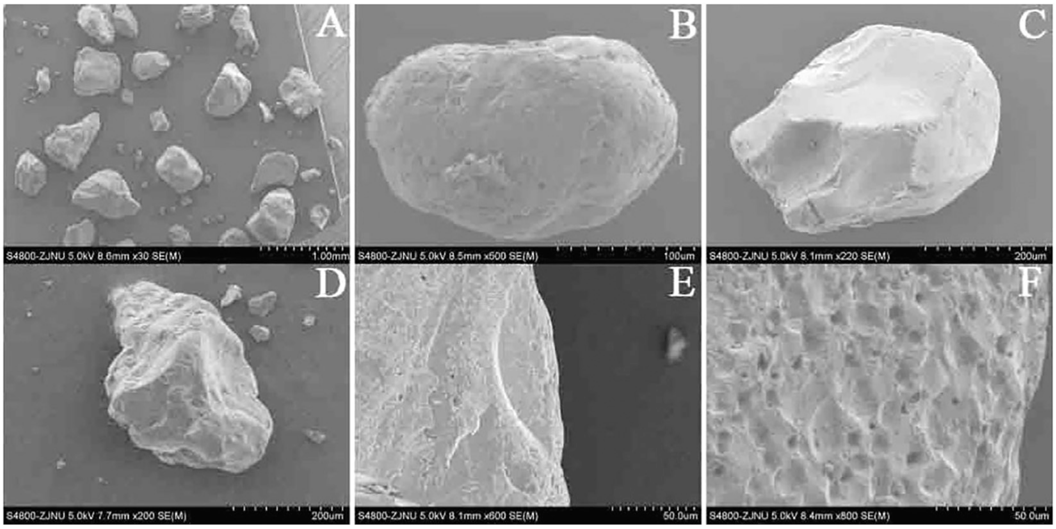

FIGURE 4 | (A) Quartz grains in XG profile. **(B)** Rounded grain. **(C, D)** Dish-shaped depressions. **(E)**. Crescentic marks. **(F)** Pockmarked surface.

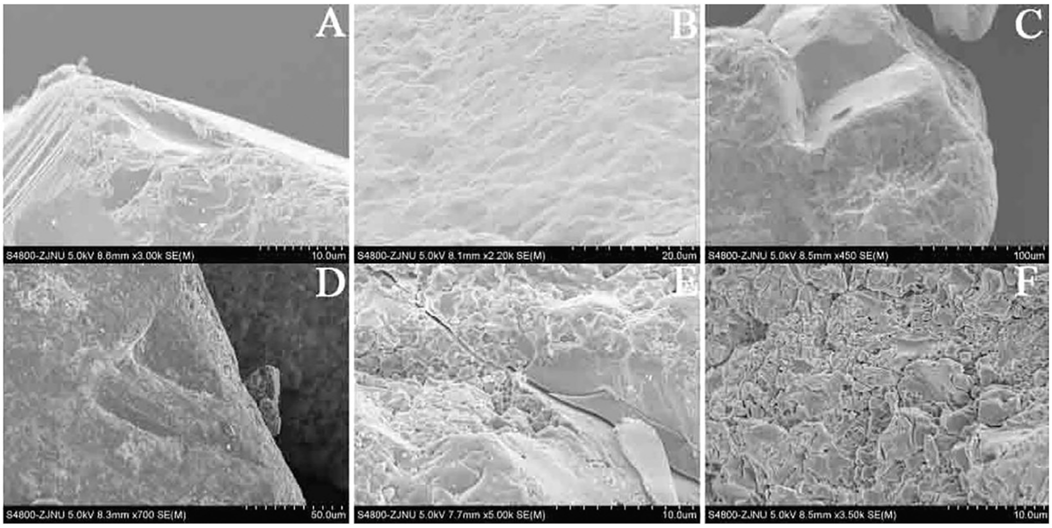

FIGURE 5 | (A) Conchoidal fractures. **(B, C)** V-shaped cracks. **(D)** Triangular cracks. **(E)** Solution crevasses. **(F)** Silica globules.

Seventy samples from QF profile were computed using the function, as shown in **Table 6**, all the ORS samples from QF profile were identified as AD, and all the floodplain deposit samples from NT profile were identified as HD. Therefore, the QF ORS profile is considered as an aeolian sediment.

Quartz Grain Surface Microtextures of QF Profile

SEM observations show that most quartz grains in QF profile are characterized by subrounded (57%) outlines (**Figure 4**; **Figure 5**; **Figure 6**), with a certain number of angular particles (10%) and round particles (16%) (**Figure 6**). Mechanically produced features in QF profile are abundant and varied, suggest that the quartz grains have experienced a range of external forces. Characteristics typical of aeolian quartz grains in QF profile are common (**Figures 4B–F**), for example dish-shaped depressions (**Figures 4C,D**) and crescentic depressions (**Figure 4E**) have occurrence rates of 72% (**Figure 6**) and 65% (**Figure 6**), respectively. Other aeolian features such as upturned plates and meandering ridges also occur on the grains, as well as pockmarks, formed pockmarked surfaces (**Figure 4F**), indicating obvious surface erosion during wind transportation. Meanwhile, many subaqueous features are also observed in QF quartz grains: for example, V-shaped cracks (**Figures 5B,C**), triangle cracks (**Figure 5D**), conchoidal fractures (**Figure 5A**), underwater polished surfaces (**Figure 5C**), grooves (**Figures 5A,D**), parallel striations caused by scratch (**Figure 5A**)

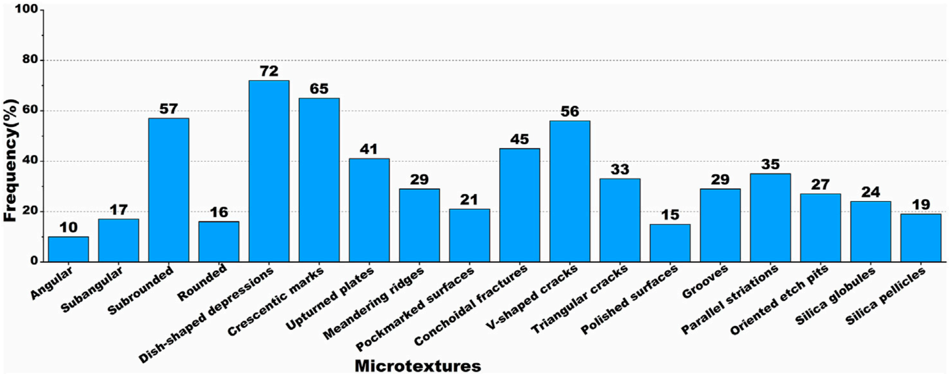

FIGURE 6 | Frequencies of microtextures identified in QF profile.

in subaqueous environments. V-shaped cracks, the most representative feature produced by grain-to-grain collisions in subaqueous environments (Mahaney, 2002; Krinsley and Doornkamp, 2011), reach an occurrence rate of 56% in QF ORS profile (**Figure 6**), indicating a subaqueous environment. A majority of quartz grains with abundant mechanical V-shaped cracks as well as parallel striations caused by scratches demonstrated that QF quartz grains have undergone a high-energy subaqueous transport. Some grains have surface microtextures typical of a subaqueous environment, on which dish-shaped depressions and pockmarked surfaces are superimposed: this combination suggests the quartz grains were abraded in a fluvial environment before undergoing aeolian transportation. In addition, the quartz grains in QF profile exhibit silica dissolution and silica precipitation textures indicative of chemical weathering as well. Silica dissolution mainly comprise oriented etch pits, solution pits and crevasses (**Figure 5E**). Oriented etch pits are usually oriented and aligned, mainly developed in rivers, lakes, and especially marine environments where the water affects the grains by dissolution (Mahaney, 2002), 27% of the quartz grains in QF profile show oriented etch pits, indicating a subaqueous environment. Silica precipitation suggest that the QF quartz grains have produced silica globules (**Figure 5F**), silica pellicles, some grains are even completely covered by silica pellicles, indicating that the quartz grains have undergone a strong chemical weathering after deposition.

DISCUSSION

Evidence of Aeolian Deposition

The QF ORS profile is mainly composed of medium sand, fine sand and silt, with more silt and clay components, the average grain size is fine; whereas beach sand is mainly composed of coarse sand, medium sand and fine sand, almost without silt or clay components, and the average grain size is much coarser than that of the ORS (Zeng et al., 1999a), indicating that the grain size composition of the ORS is obviously different from that of beach sand, but close to that of aeolian sand. On the other hand, it is suggested that aeolian sand dunes usually show positive skewness, while beach sand mostly show negative skewness (Zeng et al., 1999b), our results indicate that most samples of QF profile show positive skewness, suggest typical aeolian characteristics of the ORS. In addition, it is believed that aeolian sand dunes usually show narrow peaks, while beach sand mostly correspond to medium-narrow peaks, without very narrow peaks. Most samples from QF profile show very sharp peaks, suggest an aeolian origin. The QF profile contains more silt and clay materials than modern coastal aeolian sand and beach sand, but its sorting is not as good as those of modern coastal aeolian sand and beach sand grains, this is probably related to the strong chemical weathering in the warm–humid subtropical monsoon climate after deposition, which greatly increased the content of fine materials and resulted in a poor sorting. The grain-size frequency curve (**Figure 3A**) of QF profile is very similar to that of a typical paleo-aeolian dune profile in Zhoushan (ZS) island, indicating QF ORS a aeolian sand accumulation, and the QF samples were all identified as aeolian sand by FLDA. Finally, all grain size characteristics of QF profile are consistent with those of other reported ORS profiles along the southeast coast of China, including a fine grain size, more silt and clay component, positive skewness, a poor sorting, very sharp peaks etc, indicating that they share the same provenance (Zeng et al., 1999a; Zeng et al., 1999b; Zhang et al., 2007; Fangen et al., 2012; Yu et al., 2014; Jin et al., 2018). It is suggested that quartz grains >63 μm are difficult to be transported by wind for long distances and are regarded as near-source materials (Liu, 1985), in QF profile, sand content is the first dominant grain size, constituting the highest composition, indicating a near-source accumulation. Thus we suggest that the ORS should be aeolian deposit originated from river sand or beach sand nearby, which were transported and deposited by wind along the coast.

SEM observations show that quartz grains in QF profile are mainly characterized by subrounded (57%) outlines. Mechanically produced marks are abundant and varied, including both subaqueous environment features such as triangle marks, V-shaped cracks, and aeolian traces like dish-shaped depressions and pockmarked surfaces, suggest that the QF ORS quartz grains have experienced comprehensive effect of two external forces. It is suggested that triangle cracks, V-shaped cracks and dish-shaped depressions are typical or indicative characteristics of river sand, beach sand and aeolian sand respectively. Furthermore, river sand and beach sand are without aeolian features like dish-shaped depressions, crescentic marks etc (Wu et al., 1995). In addition, it is suggested that river sand and beach sand are characterized by subangular outlines, while aeolian sand are mostly characterized by subrounded outlines (Ying and Deonarine, 1985; Krinsley and Doornkamp, 2011). Our results show that most sand grains from QF profile are subrounded in outline, its roundness is much better than that of river sand and beach sand. Finally, some subaqueous environment marks of the sand grains from QF profile were transformed or rounded by later wind transportation. Comprehensive analysis show that the ORS should be aeolian sand dune originated from river sand or beach sand. The ORS is likely to have been transported by rivers or waves, and then transported and deposited by wind power, ultimately transformed by chemical weathering after deposition. The better roundness of the ORS resulted from the abrasion by the fluvial process and the later aeolian process.

Paleoenvironmental Significance of the ORS Along the Southeast Coast of China

Based on the results of our study and the latest reported dating results (Zhang et al., 2007; Fangen et al., 2012; Yu et al., 2014; Jin et al., 2017), we found that the ORS was aeolian deposit mainly developed in 6 stages: 125–115, 105–97, 84–74, 61.5–52.0, 39–29, and 15–9 ka. Therefore, we can draw the conclusion that the ORS developed in the warm–humid high sea level stages during the last interglacial period and in the relatively cold-dry low sea level stages during the last glacial period, but not occur in the lowest sea level stages during the LGM, the formation of the ORS was restricted jointly by climate changes of the source area and the distance from the shoreline that resulted from sea level changes. This result is consistent with previous studies that red dunes developed in high sea level stages and in relatively low sea level stages (Giannini et al., 2007; Tamura et al., 2011; Jayangondaperumal et al., 2012; Alappat et al., 2013). During the last interglacial period, under a warm–humid climate, the precipitation increased significantly, rivers transported sufficient sand supply to the coast, the intensified East Asian summer monsoon transported these sand materials and deposited along the coast. During the last glacial period, with the sea level declined, the exposed continental shelf plain provided abundant sand materials for aeolian activities, the intensified East Asian winter monsoon transported these loose materials and deposited along the coast, subsequently dune reddening could occur rapidly in areas with high rainfall and high temperature, the red coating of sands resulted from iron oxides formed by *in-situ* weathering of garnet over hundreds of years (Chase and Thomas, 2007; Alappat et al., 2013). However, it is not the case that aeolian activities are non-existent along the coast in the LGM, just because with the rapid rise of the sea level after 15 ka BP, the aeolian dunes were submerged by sea water, became paleodunes buried in seabed. It has been widely reported that aeolian dunes developed on the shelf during the LGM. For example, there were aeolian dunes on the west African shelf in the LGM (Shepard and Young, 1961). A drilling research shows that there are a large number of submerged aeolian dunes on the shelf of the South China Sea at a depth of 60–200 m (Wu and Wu, 1987; Wu et al., 1995), and the distribution area of the ORS in southeast China coastal areas have evolved into an inland denudation environment because it was too far away from the coastline.

CONCLUSION

Grain size characteristics and quartz grain surface microtextures were analyzed to study the origin and paleoenvironmental significance of the ORS, the results show that the ORS show typical aeolian features and subaqueous environments characteristics, combined with the latest OSL dating data, we suggest that the ORS should be coastal aeolian sand dunes developed since the last interglacial period. The formation of the ORS was restricted jointly by climate changes of the coastal area and the distance from the shoreline that resulted from sea level changes.

DATA AVAILABILITY STATEMENT

The original contributions presented in the study are included in the article/Supplementary Material, further inquiries can be directed to the corresponding author.

AUTHOR CONTRIBUTIONS

Investigation, QF and JL; methodology, QF and YL; data curation, QF and XF; writing original draft, QF; review and editing, JL and WY; funding acquisition, TW.

FUNDING

This research was funded by the National Key and Program of China (2016YFC0500909)" Key Techniques and Demonstration of Desertification Control in Semiarid Area in North China," and the National Key Research and Development Program of China (Grant No. 2017YFC0504804). We are very grateful to the reviewers for their constructive comments.

REFERENCES

Alappat, L., Seralathan, P., Shukla, A., Thrivikramji, K., and Singhvi, A. (2013). Chronology of Red Dune Aggradations of South India and its Palaeo-Environmental Significance. *Geochronometria* 40 (4), 274–282. doi:10.2478/s13386-013-0118-5

Blumer, B. E., Arbogast, A. F., and Forman, S. L. (2012). The OSL Chronology of Eolian Sand Deposition in a Perched Dune Field along the Northwestern Shore of Lower Michigan. *Quat. Res.* 77 (3), 445–455. doi:10.1016/j.yqres.2012.01.006

Chase, B. M., and Thomas, D. S. G. (2007). Multiphase Late Quaternary Aeolian Sediment Accumulation in Western South Africa: Timing and Relationship to Palaeoclimatic Changes Inferred from the Marine Record. *Quat. Int.* 166 (1), 29–41. doi:10.1016/j.quaint.2006.12.005

Chen, R., Chen, J., Ma, J., and Cui, Z. (2019). Quartz Grain Surface Microtextures of Dam-Break Flood Deposits from a Landslide-Dammed Lake: A Case Study. *Sediment. Geol.* 383, 238–247. doi:10.1016/j.sedgeo.2019.02.010

Costa, P. J. M., Andrade, C., Dawson, A. G., Mahaney, W. C., Freitas, M. C., Paris, R., et al. (2012). Microtextural Characteristics of Quartz Grains Transported and Deposited by Tsunamis and Storms. *Sedimentary Geol.* 275-276, 55–69. doi:10.1016/j.sedgeo.2012.07.013

Costa, P. J. M., Andrade, C., Mahaney, W. C., Marques da Silva, F., Freire, P., Freitas, M. C., et al. (2013). Aeolian Microtextures in Silica Spheres Induced in a Wind Tunnel Experiment: Comparison with Aeolian Quartz. *Geomorphology* 180-181, 120–129. doi:10.1016/j.geomorph.2012.09.011

Fangen, H., Zhizhong, L., Jianhui, J., et al. (2012). A Primary Research on Multiphase Development Pattern of Old Red Sand in Jinjiang Coast of Southeast Fujian. *Quat. Sci.* 32 (6), 1207–1220. doi:10.3724/sp.j.1226.2012.00462

Feng, W., Xue, W., and Yang, D. (1988). *The Geological Environment of Late Quaternary in the Northern South china Sea*. Guangzhou: Guangdong Technology Publishing House.

Folk, R. L., and Ward, W. C. (1957). Brazos River Bar [Texas]; a Study in the Significance of Grain Size Parameters. *J. Sediment. Res.* 27 (1), 3–26. doi:10.1306/74d70646-2b21-11d7-8648000102c1865d

Giannini, P. C. F., Sawakuchi, A. O., Martinho, C. T., and Tatumi, S. H. (2007). Eolian Depositional Episodes Controlled by Late Quaternary Relative Sea Level Changes on the Imbituba-Laguna Coast (Southern Brazil). *Mar. Geol.* 237, 143–168. doi:10.1016/j.margeo.2006.10.027

Guo, Z. T., Ruddiman, W. F., Hao, Q. Z., Wu, H. B., Qiao, Y. S., Zhu, R. X., et al. (2002). Onset of Asian Desertification by 22 Myr Ago Inferred from Loess Deposits in China. *Nature* 416, 159–163. doi:10.1038/416159a

Helland, P. E., Huang, P.-H., and Diffendal, R. F. (1997). SEM Analysis of Quartz Sand Grain Surface Textures Indicates Alluvial/Colluvial Origin of the Quaternary “Glacial” Boulder Clays at Huangshan (Yellow Mountain), East-Central China. *Quat. Res.* 48, 177–186. doi:10.1006/qres.1997.1916

Jayangondaperumal, R., Murari, M. K., Sivasubramanian, P., Chandrasekar, N. A. K., and Singhvi, A. K. (2012). Luminescence Dating of Fluvial and Coastal Red Sediments in the SE Coast, India, and Implications for Paleoenvironmental Changes and Dune Reddening. *Quat. Res.* 77 (3), 468–481. doi:10.1016/j.yqres.2012.01.010

Jin, J.-H., Li, Z.-Z., Cheng, Y., Xu, X.-L., Li, Z.-X., and Liu, X.-J. (2018). Late Pleistocene Aeolian Activity in Haitan Island, Southeast China: Insights from Optically Stimulated Luminescence Dating of Coastal Dunes on Marine Terraces. *J. Mt. Sci.* 15 (8), 1777–1788. doi:10.1007/s11629-018-4890-9

Jin, J., Li, Z., Lei, G., et al. (2017). Chronology and Environmental Significance of Old Red Sand in South China:Take the Old Red Sand in Qingfeng, Fujian as an Example. *Scientia Geographica Sinica* 37 (2), 301–310. doi:10.1007/bf02886083

Krinsley, D. H., and Doornkamp, J. C. (2011). *Atlas of Quartz Sand Surface Textures*. Cambridge: Cambridge University Press.

Li, Z. W., Dong, Y. X., and Li, B. S. (2012). Current Study and Prospect of the Old Red Sand along the Southeast Coast of China. *Sci. Cold Arid Regions* 4 (6), 0462–0471. doi:10.3724/sp.j.1226.2012.00462

Li, C., Peng, F., Lai, C., Xue, X., Yu, Q., Xiaojie, C., et al. (2021). Plant community changes determine the vegetation and soil δ13C and δ15N enrichment in degraded alpine grassland. *Land Degradation & Development* 32 (7), 2371–2382. doi:10.1002/ldr.3912

Liu, T. (1985). *Loess and the Environment*. Beijing: China Ocean Press.

Mahaney, W. (2002). *Atlas of Sand Grain Surface Textures and Applications*. USA: Oxford University Press.

Mahaney, W., and Kalm, V. (2000). Comparative Scanning Electron Microscopy Study of Oriented till Blocks, Glacial Grains and Devonian Sands in Estonia and Latvia. *Boreas* 29, 35–51. doi:10.4095/304896

Mahaney, W. C., Hancock, R. G. V., Milan, A., Pulleyblank, C., Costa, P. J. M., and Milner, M. W. (2014). Reconstruction of Wisconsinan-Age Ice Dynamics and Compositions of Southern Ontario Glacial Diamictons, Glaciofluvial/lacustrine, and Deltaic Sediment. *Geomorphology* 206, 421–439. doi:10.1016/j.geomorph.2013.10.014

Mahaney, W. C., Stewart, A., and Kalm, V. (2001). Quantification of SEM Microtextures Useful in Sedimentary Environmental Discrimination. *Boreas* 30, 165–171. doi:10.1080/030094801750203170

Purtill, M. P., Kite, J. S., and Forman, S. L. (2019). Geochronology and Depositional History of the Sandy Springs Aeolian Landscape in the Unglaciated Upper Ohio River Valley, United States. *Front. Earth Sci.* 7, 322. doi:10.3389/feart.2019.00322

Pye, K. (1983). Coastal Dune. *Prog. Phys. Geogr.* 7 (4), 431–557. doi:10.1177/030913338300700403

Pye, K. (1995). The Nature, Origin and Accumulation of Loess. *Quat. Sci. Rev.* 14, 653–667. doi:10.1016/0277-3791(95)00047-x

Shepard, F. P., and Young, R. (1961). Distinguishing between Beach and Dune Sands. *J. Sed. Petr.* 31 (2), 196–214.

Smith, C., Soreghan, G. S., and Ohta, T. (2018). Scanning Electron Microscope (SEM) Microtextural Analysis as a Paleoclimate Tool for Fluvial Deposits: a Modern Test. *Geol. Soc. Am. Bull.* 130, 1256–1272. doi:10.1130/b31692.1

Tamura, T., Kodama, Y., Bateman, M. D., et al. (2011). Coastal Barrier Dune Construction during Sea Level High Stands in MIS3 and 5a on Tottori Coast Line, Japan. *Palaeoecology* 308 (3-4), 492–501. doi:10.1016/j.palaeo.2011.05.054

Vos, K., Vandenberghe, N., and Elsen, J. (2014). Surface Textural Analysis of Quartz Grains by Scanning Electron Microscopy (SEM): from Sample Preparation to Environmental Interpretation. *Earth-Science Rev.* 128, 93–104. doi:10.1016/j.earscirev.2013.10.013

Wu, Z., Huang, S., and Hu, S. Z. (1995). *Research on the Landforms of the Wind-Drift Sand in South China Coast*. Beijing: Science Press, 114–118.

Wu, Z., and Wang, W. (2001). TL Dating of the Old “Red Sand”on the Coasts of Fujian and Guangdong. *J. Desert Res.* 21 (4), 328–332. doi:10.1007/bf02886083

Wu, Z., and Wu, K. G. (1987). Sedimentary Structure and Developing Model of Coastal Dunes along the Northeastern Coast of Hainan Island, China. *Acta Geogr. Sin.* 42 (2), 129–141.

Yang, L. H., Ye, W., Zheng, X. M., et al. (2014). The Discriminant Function with Grain Size of Floodplain and Aeolian Sediments and its Application in the Quaternary Red Clay. *Geographical Res.* 33 (10), 1848–1856. doi:10.1016/j.quaint.2012.08.2076

Yang, L.-H., Zheng, X.-M., Ye, W., et al. (2017). Sedimentary Environment of Vermicular Red Clay in South China. *J. Mt. Sci.* 14 (3), 513–526. doi:10.1007/s11629-016-3973-8

Ying, W., and Deonarine, B. (1985). *Model Atlas of Surface Textures of Quartz Sand [M]*. Beijing: Science Prees.

Yu, M. T., Zhang, H. Y., Gong, Z. Q., et al. (2014). The Monsoon Components in Qingfeng Old Red Sands and Their Formation Epoch, Pingtan Island, Fujian Province. *Scientia Geographica Sinica* 34 (3), 352–357. doi:10.1088/1755-1315/17/1/012075

Zeng, C. S., Chen, J. Z., and Wu, Y. G. (1999a). *Research of Old Red Sad in Southeast Fujian*. Beijing: Geology Publishing House, 35–39.

Zeng, C. S., Chen, J. Z., and Wu, Y. G. (1999b). The “Old Red Sands” along the Coast of Southeast Fujian and Environmental Evolution during Late Quaternary. *J. desert Res.* 19 (2), 110–114.

Zeng, Z. X., and Huang, S. M. (1964). “The Discussion on "Old Red Sand" along the South China Sea,” in *Chinese Society of Quaternary SciencesThe Collection of Second Academic Session Papers*. Beijing, 162–163.

Zhang, H. Y., and Ming-Tong, Y. U. (2014). Tracer Analysis of Old Red Sand Source in QF Section from Pingtan Island of Fujian Province. *Journal of Subtropical Resources & Environment* 9 (1), 815. doi:10.19687/j.cnki.1673-7105.2014.01.002

Zhang, J. F., Yuan, B. Y., and Zhou, L. P. (2007). Luminescence Chronology of “Old Red Sand” in Jinjiang and its Implications for Optical Dating of Sediments in South China. *Chin. Sci. Bull.* 52 (22), 2646–2654. doi:10.1007/s11434-008-0001-6

Zhu, Y., Zeng, C., and Jin, C. (1981). The Sea Level Change of East China Sea Continental Shelf since the Late Pleistocene[J]. *Chin. Sci. Bull.* 26 (19), 1195–1198.

Conflict of Interest: The authors declare that the research was conducted in the absence of any commercial or financial relationships that could be construed as a potential conflict of interest.

frontiers
in Earth Science

ORIGINAL RESEARCH
published: 25 May 2021
doi: 10.3389/feart.2021.681995

Reconstruction of Cultivated Land in the Northeast Margin of Qinghai–Tibetan Plateau and Anthropogenic Impacts on Palaeo-Environment During the Mid-Holocene

Zhuoma Wende[1], *Guangliang Hou*[1,2]*, *Jingyi Gao*[1], *Xiaoliang Chen*[1], *Sunmei Jin*[1] and *Zhuoma Lancuo*[1]

[1]*School of Geographic Science, Qinghai Normal University, Xining City, China,* [2]*Academy of Plateau Science and Sustainability, Qinghai Normal University, Xining, China*

OPEN ACCESS

Edited by:
Xiangzhong Li,
Yunnan University, China

Reviewed by:
John Dodson,
Chinese Academy of Sciences, China
Xin Jia,
Nanjing Normal University, China

***Correspondence:**
Guangliang Hou
hgl20@163.com

Specialty section:
This article was submitted to Quaternary Science, Geomorphology and Paleoenvironment, a section of the journal Frontiers in Earth Science

Received: *17 March 2021*
Accepted: *29 April 2021*
Published: *25 May 2021*

Citation:
Wende Z, Hou G, Gao J, Chen X, Jin S and Lancuo Z (2021) Reconstruction of Cultivated Land in the Northeast Margin of Qinghai–Tibetan Plateau and Anthropogenic Impacts on Palaeo-Environment During the Mid-Holocene. Front. Earth Sci. 9:681995. doi: 10.3389/feart.2021.681995

The study of past global change is paramount to comprehending the present and future, as well as to better understand the mechanisms and influences of human–land interactions in a given region. The northeastern margin of the Qinghai–Tibetan Plateau has complex natural environments, sensitive to global change, and renowned for its long history of human occupancy. This makes it an ideal region for the study of anthropogenic impacts on the paleo-natural environment. This paper reconstructed the prehistoric temporal and spatial distribution of cultivated lands on the northeast margin of Qinghai–Tibetan Plateau, and analyzed the Dianziping pollen assemblage to disclose the anthropogenic impacts on the paleo-environment. The results demonstrated that around 4.3–4.0 cal ka BP, the rapid development of the Majiayao culture boosted the population to approximately 39,200 people, over 460 km^2 of the land area was converted to cropland, concomitantly, evidence of tree pollen decreased significantly. This marked the earliest identification of anthropogenic impacts on vegetation through agricultural activity in this region. At 4.0–3.6 cal ka BP, the population appeared to have diminished in conjunction with the cultivated land area. Nevertheless, forested areas continued to decrease, primarily due to adverse climatic conditions, but, anthropogenic activities played an undeniable role. Dianziping profile demonstrated the existence of natural forest in the Hehuang Valley during Qijia cultural Period. There was also evidence for the occurrence of regional fire events, suggesting large-scale burning of land cover in the area. This further illustrates anthropogenic impacts. At 3.6–2.6 cal ka BP, populations reached approximately 61,300 people, coinciding with the peak of cropland expansion. Consequently, more of the natural vegetation were converted to crops, and the superimposed influences of farming and grazing aggravated the process of deforestation and vegetation succession. Likewise, deforestation during the historical period can be explained, mostly by human driven causes with limited influence from climatic factors. The extensive exploitation of forest and expansion of cropland consequently resulted in extensive land deterioration, leaving the region with forest islands scattered in less populated, mountainous regions.

Keywords: cultivated land reconstruction, pollen analysis, Qinghai–Tibetan plateau, vegetation destruction, mid-late Holocene, anthropogenic impact

INTRODUCTION

Understanding the temporal and spatial evolution of land use as well as the resulting implications for ecological systems from the past may contribute to our understanding of global change, human–land interactions, and sustainable land use (Gaillard et al., 2018). Since the Holocene, land use and cover change driven by anthropogenic activities, primarily cultivation and grazing, have profoundly influenced surface vegetation patterns, and even the entire terrestrial ecosystems that persisted until today, consequently, humans have changed the physical, ecological, and biological components of the Earth's planetary systems (Goldewijk et al., 2007; Pielke et al., 2011; Zhang et al., 2012; Ellis et al., 2013; Gaillard et al., 2018; Fang et al., 2019). The extent to which human activities modified the palaeoecological environment may prove vital in explaining the current environmental conditions. As such, the study of the human dimensions of global change is considered an integral part of palaeoecological environmental research (Miehe et al., 2014).

The northeast margin of the Qinghai Tibet Plateau (QTP) is densely populated and extensively cultivated. Relative to the rest of the plateau, it receives more precipitation and experiences warmer temperature. Denisova, an argumentum prima facie for early human footprints on the QTP, actively demonstrates that hunter-gatherers occupied this part of the world from the late Pleistocene (Zhang et al., 2020a, b). The palaeo-anthropogenic impacts on the natural vegetation on the northeast margin of the QTP are not known in detail. Agriculture is widely considered to be one of the most striking impacts humans have exerted on the natural ecosystem (Pongratz et al., 2008). In the northeast margin of the QTP, the climate was relatively warm and humid during the mid-Holocene (Cheng et al., 2013; Li et al., 2014), and provided a suitable environment for the introduction of agriculture in the area (Dong et al., 2012). Farming tools, such as stone knives and axes have been excavated (Xie, 2002). Moreover, charred seeds of millet were discovered in the Majiayao cultural sites (Jia et al., 2013). These provide unquestionable evidence for the onset of cultivation in this area. The ways in which agriculture may have transformed the natural environment in this part of the world, have yet to be studied in depth.

Agriculture emerged following the hunting and gathering culture and developed rapidly over time (Harlan, 1971; Bellwood et al., 2005). Agricultural activities have been a driving force for humans to adapt and modify the environment (Edwards, 1991; Cavalli-Sforza et al., 1993). Palynological and archaeological evidence have been used to reconstruct past environments (Zhou et al., 2011; Wei H.-c. et al., 2020; Miehe et al., 2021). In Europe, land cover change in the form of cropland expansion, caused severe deforestation as early as approximately 7 cal ka BP (Lowe and Walker, 1997). Pongratz et al. (2008) reconstructed the spatial dispersion of global cultivated land and other past land usage using historical population data and modern land use patterns. The results indicated that broadleaf deciduous forests were severely affected by cropland expansion. Vitousek et al. (1997), found that terrestrial vegetation has been significantly altered by the rapid development of agriculture. Driven by sharp increases in human populations, over 30–50% of the Earth's land cover has been converted into agricultural land. The development of ancient Chinese civilization is entangled with the emergence of agriculture. During the mid-Holocene, a shrinking of forests across much of China was concomitant with the patterns of human settlement and cropland expansion (Ren, 2000). In the western Loess Plateau, the Yangshao people started millet cultivation around 6.0 cal ka BP, which developed rapidly, forming a complex farming structure with a variety of crops. The amplified intensity of farming resulted in a decrease in shrub and grassland coverage in the Longdon area (Zhou et al., 2011). Owing to the human disturbance, the coniferous and broadleaf mixed forests cover decreased markedly after 4.6 cal ka BP (Li et al., 2012). Hou et al. (2012) reconstructed prehistoric cultivated land areas in the middle and lower reaches of the Yellow River based on prehistoric population estimations and prehistoric sites. The results indicated that cropland expansion reduced area of the pristine forests along the lower reaches of the Yellow River. Based on those studies, it is clear that cultivation has had extensive consequences for the natural environment. To what extent this process has played out on the northeast margin of QTP is largely unknown. By reconstructing the prehistoric cropland area using palynological and archaeological evidence, this paper attempts to describe the impacts of anthropogenic activity on the natural vegetation in the northeastern margin of the QTP. In particular, this paper draws attention on changes in forests, as forest ecosystems are crucial components of the carbon cycle, biodiversity conservation, soil maintenance, water conservation, and climate regulation. In summary, this paper aims to better explain bio-physical environmental changes resulting from human intervention and make a contribution to the fields of palaeoecology, paleoenvironment, and paleo-climate.

STUDY AREA

Environmental Setting of the Study Area

The northeastern margin of QTP encompasses the eastern part of Qinghai Province, including the areas along the Huangshui River and upper reaches of the Yellow River from Tongde County to

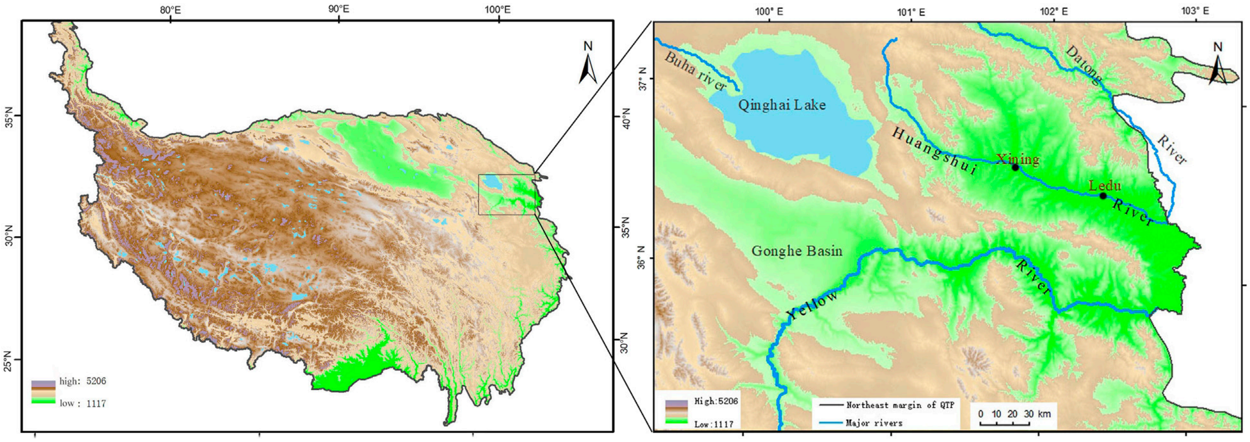

FIGURE 1 | Northeast margin of the QTP. Scope of this study.

Xunhua County, as well as the Gonghe Basin (**Figure 1**). This subregion is an important transitional zone between the QTP and Loess Plateau, marking the boundary between the East Asia summer monsoon and the northwest arid region. It features mostly north-south-oriented, high mountains, deep and broad valleys, well-developed river terraces, and elevations ranging between 1,650 and 5,206 m above sea level. The region is climatically sensitive and ecologically vulnerable. It is classified as having a temperate-arid and semi-arid continental climate, with mean annual precipitation between 252 and 535 mm, and mean annual temperature between 3 and 8°C (Jia et al., 2019). The dominant biome in this area is temperate grassland with distinctive vertical zonality. This area is typical of the agropastoral areas where river terraces are densely cultivated and it has one of the highest rates of agricultural land use on the QTP. In spite of the fact that this region accounts for only 5.18% of the province's total area, the population exceeds 70% of the province's total. Cropland area accounts for 73% of that found in the province (Zhao, 2016).

The Dianziping profile was collected from Gaomiao basin, Ledu County, Qinghai Province, which is characterized as having a temperate-plateau, semi-arid climate. The basin sits at an elevation of 1,870 m, has a mean temperature of 7.6°C and a mean precipitation of 333.7 mm annually. The Huangshui River runs through the basin from west to east. In the river valley, flat terrain and intact terraces are common. At present, cropland is widely distributed on terraces and slopes, and most of the plants observed in the valley are cultivated species such as *Triticum aestivum*, *Vicia faba*, *Pisum sativum*, *Juglans regia*, *Zanthoxylum bungeanum*, *Populus*, *Salix*, and others. In the foothills, temperate grasslands are dominant, with *Stipa bungeana* occurring as the dominating species; clustered *Stipa glareosa* and *artemisia gmelinii* are commonly observed. In the high mountains, shrub species such as *Potentilla fruticosa*, *Salix oritrepha*, *Rhododendron lapponicum*, and a few *Picea crassifolia*, *Picea wilsonii* are abundant. Mountain regions above 3,200 m are mainly *Kobresia* dominated alpine grassland.

Cultural Sequence

The scope of this study extends from the Neolithic Age to the historical time period (5.3–0.11 cal ka BP). This time frame coincides with the occurrence of the Majiayao, Qijia, Xindian, and the Kayue cultures. The Majiayao culture, renowned for its excellency in pottery, was centered in the Hehuang Valley and mainly practiced farming. Based on radiocarbon dating, the Majiayao culture can be categorized into three different subsets, the Majiayao type (5.3–4.5 cal ka BP), Banshan type (4.5–4.3 cal ka BP), and Machang type (4.3–4.0 cal ka BP). Around 4.2 cal ka BP, the Qijia culture (4.2–3.6 cal ka BP) replaced the Majiayao culture in the region, representing the onset of the Bronze Age. During the mid-late Bronze Age, people of the Kayue culture (3.6–2.7 cal ka BP), who practiced both farming and grazing, and the Xindian culture, which practiced farming, occupied the area. While the Kayue culture was mainly distributed in the western part of the study area, the Xindian Culture (3.6–2.6 cal ka BP) was found in the east (Xie, 2002; Chen et al., 2015).

MATERIALS AND METHODS

Agricultural intensity is inherently linked to population density (Vasey, 1992; Pongratz et al., 2008). As such, population sizes can be used as a proxy for agricultural activity. To estimate the population, and analyze the spatial distribution pattern of cultivated land, the prehistorical sites in the northeast of QTP were examined here. The data for prehistoric sites were primarily obtained from the Atlas of Chinese Relics. More recent discoveries are also incorporated. The study area includes approximately 280 sites of the Majiayao type, 90 sites of the Ban Shan type, 520 sites of the Machang type, 430 sites of the Qijia Culture, 1,700 sites of the Kayue Culture, and 350 sites of the Xindian Culture (Bureau of National Cultural Relics, 1996; Zhang and Dong, 2017).

Population

Prehistoric population sizes are estimated mainly by settlement archaeology, grave analysis, bio-archaeology, relics study, and other analytical methods (Fang, 2007). In this study settlement archaeology and grave analysis were used for population estimation. Calculation of the prehistoric population was based on both the sizes of prehistoric sites (settlement archaeology) and the number of graves excavated at each site (grave analysis). In light of the fact that there were no record of prehistoric population and former studies of the specific human population, we used the data attained from officially excavated sites. Uncertainty around the population estimates are the result of inaccuracies in grave numbers due to both natural, and human disturbances such as grave robbery and village construction. These disturbances have resulted in an inaccurate number of recorded graves and excavated human bones. Consequently, the population estimates for this study are likely low, but provides a reasonable approximation of the population and general population growth trends, if used consistently across all sites.

Settlement Archeology

For the prehistoric sites identified within a specified area, settlement archaeology was used, and the following equation was adopted:

$$Pi = s{*}d$$

In this, Pi stands for the total population of the prehistoric site i; s represents the area size, and d provides the population density. Since the prehistoric population density of northeast QTP was unavailable, the prehistoric population density of the Yangshao culture ($d = 0.005625$ person/m^2) was applied (Qiao, 2010). The Yangshao culture expanded to the east of QTP and established the early Majiayao culture. The sites of these two cultures were similar in terms of geographical settings; the Yangshao culture sites were located along the western fringe of the Loess Plateau which is connected to the northeast fringe of the QTP. Both sites exhibited similar climatic conditions as both were strongly influenced by continental monsoon and both cultures practiced millet farming. As such, the population density of the Yangshao culture was seemed applicable for estimating the population density of the Majiayao culture.

Grave Analysis

For the prehistoric sites with unspecified size area, grave analysis was adopted. The number of graves and human bones excavated at each typical cultural site was used as a reference for the total population of that particular cultural site. The life span, which was estimated from the study of human bones, was obtained from other studies (**Table 1**). Thus, the residential populations (annual population in a cultural site) for each cultural site were obtained using the following equation:

$$Pri = \frac{Pi{*}Li}{Ti}$$

Here, Pri stands for the residential population of the site i: Pi gives the total population of the site i; Li is the estimated life span of the site i; Ti stands for the time span of the cultural site i (**Table 1**).

The total population of a cultural/type was estimated using the formula

$$Pt = \sum_{i=1}^{n} \frac{Li{*}Pi}{Ti} = \sum_{i=1}^{n} Pri$$

The populations of all cultural sites with the same cultural types were summarized to obtain the total population (Pt) for each group.

Cultivated Land

The most distinct change in vegetation cover brought by anthropogenic activity is the conversion of natural to cultivated lands. The total area of the cropland can be used to estimate the extent of human disturbance to natural vegetation. Elevation, slope aspect, and gradient, as well as soil types, are considered as limiting factors for cultivation (Luo et al., 2015; Han et al., 2020). During the prehistoric time periods, the distance to the river was also considered a limiting factor for cultivation due to the lack of vehicles for transportation and undeveloped irrigation technology. Generally speaking, the suitable land area available for cultivation was limited by one social factor; population, and four natural factors; elevation, slope, water source, and soil type.

Natural Factors

Elevation, slope, water source, and soil type are considered the four natural factors affecting the suitability of cropland. Elevation greatly affects rainfall and temperature of the area. On the Tibetan Plateau precipitation and temperature are mostly at the edge of ecological limitation for forest. Slight elevation changes may lead to changes in the distribution of vegetation and even the entire ecosystem structure (Huang et al., 2008; Li D.-M. et al., 2008). Assuming that the topography of the prehistoric sites remained consistent with current landform, and millet was the main crop, three elevation zones were designated: 0–2,000 m, 2,000–2,800 m, >2,800 m. The high-altitude mountainous regions above 2,800 m are characterized by low temperatures, high precipitation, severe frost, low incidence of farming, and sparse vegetation cover (Zeng et al., 2012). They are, thus, considered unfavorable for cultivation. The major rivers along the settlement area provide a reliable water source for settlers within a 3 km or 1 h walking distance (Vita Finzi, 1969). Distance to a river (water source), in this case, has been identified as another limiting factor for cultivation. Slope gradient also greatly constrains the expansion of the cropland area (Han et al., 2020) and determines the potential for land erosion. It also influences the texture of the soil, and to an extent, the thickness of soil layers. A gradient of 20° is considered steep, prone to erosion, and hence, unsuitable for long-term cultivation (Li, 1978). The Tibetan Plateau is made up mostly of alpine desert and brown desert soil, which are not suitable for cultivation. Soil types that are suitable for cultivation, are relatively scarce. (**Table 2**).

Social Factor: Population

The extent of arable land use is determined, in part, by the population of the area and mode of production employed

TABLE 1 | Population and life span of each culture/type.

Age/time	5.0–4.5 cal ka BP	4.5–4.3 cal ka BP	4.3–4.0 cal ka BP	4.0–3.6 cal ka BP	3.4–2.6 cal ka BP	3.6–2.6 cal ka BP
Culture/type	Majiayao type	Banshan type	Machang type	Qijia culture	Xindian culture	Kayue culture
Site	Hetao Zhuang, Minhe County	Yangshan, Minhe County	Liuwan, Ledu County	Gamatai, Guinan County	Hetao Zhuang Minhe County	Shang Sunjiazhai Datong County
Approximate population estimate	180	215	890	55	75	1,080
Mean life span	30	35	40	35	30	30
References	1	2	3	4&5	1	6&7

1, Qinghai Province Cultural Relics Archaeological Institute, 2004; 2, Qinghai Province Cultural Relics Archaeological Institute, 1990; 3, Qinghai Province Cultural Relics Management Branch Archaeological team, Chinese Academy of Social Sciences, Institute of Archaeology, 1984; 4, Bureau of National Cultural Relics, 1996; 5, Ren, 1998; 6, Su et al., 2010; 7, Li and Lu, 1981.

∗The estimated results were rounded and kept to the nearest five.

TABLE 2 | Natural limiting factors in the reconstruction of cultivated farmland.

Type	Category	Value*	Type		Category	Value*
Soil	Chestnut soil and sierozem (suitable for cultivation)	1	Slope	Slope aspect	0–45	0
	Highland desert soil and Brown desert soil (unsuitable for cultivation)	0			45–225	1
					225–360	0
				Gradient	0–10	1
Water source	Distance to river ≤3 km	1			10–20	0.5
					>20	0
			Elevation		0–2,000 m	2
	Distance to river >3 km	0			2,000–2,800 m	1
					>2,800 m	0

**Value equals 0 is unsuitable for cultivation. Higher the value the more suitable it for cultivation.*

TABLE 3 | The estimated result of population.

Culture/type	Majiayao type	Banshan type	Machang type	Qijia culture	Xindian culture	Kayue culture
Residential population	35	40	70	50	70	30
Total population	9,900	3,710	39,200	22,790	6,930	54,400

∗The estimated results were rounded and kept to the nearest five.

(Chen Q. et al., 2019). In prehistoric times, a primitive method of cultivation was adopted whereby, land was burned prior to the planting of seeds. A similar strategy was also utilized during the Xia Dynasty and produced a grain yield of 37.5 kg/ha (Yang, 1998). The likeness in methodologies suggests that the grain production of the two may have been similar. The annual grain consumption of the Yangshao settlers was around 258 kg/person (Qiao, 2010), so, theoretically, the size of prehistorical cropland could be calculated through the following formula:

$$Si = \frac{Pi*C}{Y}$$

where Si stands for the theoretical size of cropland at prehistorical site i. Pi stands for the population size of the site i, and C stands for the grain consumption per person and Y stands for grain yield.

Estimates of the practical cropland area in use during each cultural time period were reconstructed using Arc-GIS. Assuming that cultivation would have taken place within a circle, with the prehistoric site in the center, the radius of the circle can be set as the measured range of cropland. The radius was based on the Si (site i theoretical cultivated land). Applying the buffer tool in Arc-GIS to that estimate, we obtained an approximation spatial distribution pattern of theoretical cropland area in each different culture. However, the distribution of cultivated land at any site is restricted by the natural factors of topography, as previously discussed. In areas where the sites are densely distributed, the actual cultivated land area may be smaller than that of the theoretical cultivated land area. The raster data was assessed again considering the natural limiting factors (**Table 2**). Areas were classified as; unsuitable (0–1) or more suitable (2–3) for crop cultivation. Superimposing the two estimated results and the new results ratings of three to four were considered to be practical for cropland area cultivated during the time period of a culture. In this way, the spatial distribution patterns and the sizes of practical cropland area for each culture were obtained. It is important to note that, during the Kayue cultural period, the mode of production was more diversified. Agriculture was the main subsistence strategy of the Kayue people living along the Yellow and Huangshui Rivers, but grazing and hunting supplemented their diets (Xie, 2002). The mean elevation of the Xindian sites is lower than that of the Kayue sites, thus the proportion of agriculture in the Xindian culture is higher than that of the Kayue culture. It follows that the grain in Xindian culture and Kayue culture accounts for approximately 80 and 60% of food consumption respectively. The radii for estimated cultivated land areas for the two cultures were approximately 535 and 320 m (rounded to the nearest five) respectively.

On-Site Profile for Pollen Analysis and Dating

A 3.5 m profile with intervals of 4 and 6 cm (280–311 cm) was collected from Dianziping (36°26′28″N, 102°34′51″E, 1,938 m.a.s.l.), Gaomiao basin for the purpose of dating and pollen analysis. Fifty samples were prepared according to standardized protocols and the experiment was carried out using standard procedures (Li et al., 1995). A known number of *Lycopodium* spores (27,637 ± 563 grain/slice) were added to each sample for calculating the values of pollen and charcoal concentration. Carbonate and silicate were removed with 10% hydrochloride and 40% hydrofluoric acid, respectively, and washed through 10 μm sieves. Five charcoal samples from the stratum were collected at depths of 108, 173, 194, 205, and 241 cm for AMS dating. These charcoal samples were sent to Quaternary Dating Laboratory for AMS14C dating in Peking University. Ages were calibrated using IntCal13 atmospheric curve (Reimer et al., 2013), using the program OxCal v4.2.4 (Bronk Ramsey, 2015).

RESULTS

Population

Table 3 illustrates the population estimations of the different cultures. The Neolithic residential population size increased from 40 people in the early stages of the Majiayao culture to approximately 70 people during the Machang type. The residential population dropped to 50 people during the Qijia cultural period, but recovered during the Xindian cultural period and augmented to a similar rate of the Machang type. This indicates that, in spite of low population, the Xindian sites were more densely populated. The total population of the Majiayao type reached 9,900 people but fell by nearly half during the Banshan period. During the Machang type, the population increased dramatically and reached the peak of the Neolithic Age with a total population of 39,200 people in the northeast part of the QTP. Numbers decreased significantly during the Qijia cultural period and reached 22,790 people. The study area was occupied by both the Xindian culture and the Kayue culture during the mid-late Bronze Age when the total population reached approximately 61,330 people. Around 2.0 cal ka BP, during the Han dynasty, Zhao Chongguo, an official in Hehuang Valley, reported in his letter to the emperor, that there were about fifty thousand Qiangs (refers to the Kayue people) in the area. This supports the estimated results of the Kayue population.

Cultivated Land

The statistical result of the reconstructed cultivated land showed that during the Majiayao culture, the cultivated land area grew from approximately 150–460 km^2 during the Machang type. However, this was decreased during the Banshan type, falling to approximately 25 km^2 (**Table 4**). During the Qijia Culture, it decreased slightly to 330 km^2 and then, was followed by an increase during the mid-late Bronze Age. During this period, cultivated land area expanded to approximately 1,080 km^2 in the west. In the eastern region of the study area, the cultivated land area was 80 km^2. The total cultivated land area in the northeast margin of the QTP reached 1,160 km^2.

Figure 2 illustrates the temporal and spatial distribution of cultivated land throughout the prehistoric time period. Rivers played a central role in the distribution patterns of the cultivated land area. During the early Majiayao culture, the cultivated lands were sparsely distributed along the two major rivers: the Huangshui and the Yellow Rivers. During the late Neolithic Age, the cultivated land area expanded along the Huangshui River and the east edge of QTP appeared to be heavily cultivated. In the mid-late Bronze Age, the cultivated land area expanded westward, to the source region of the Yellow River and its tributaries, and northward to the areas along the Beichuan River, a main tributary of the Huangshui River.

Palynology

Dating

The high precision $AMS^{14}C$ is reported as a mean age within a range of error. The results indicated that the 3.5 m section of Dianziping site captured a specific, concentrated time period between 4.0 and 3.7 cal ka BP (**Table 5**); classified as the Qijia cultural period. There was a small inversion of dates, suggesting anthropogenic disturbance to the stratum. The discovery of potsherds and ash pits in the stratum further testified the incidence of anthropogenic activity. Moreover, the potsherds were mainly reddish clay pottery and sand mixed pottery, finely polished. Some of the potsherds were painted with string-like greyish-black lines. These features strengthen the link to Qijia pottery and culture.

Pollen Records

Forty-nine pollen taxa were identified in the Dianziping section, including *Pinus*, *Picea*, *Betula*, *Ulmus*, *Carpinus*, *Alnus*, *Hippophae*, *Nitraria*, *Ephedra*, *Artemisia*, *Taraxacum*, Poaceae, Chenopodiaceae, Asteraceae, and Polypodiaceae. The pollen assemblage was largely dominated by arboreal pollen with *Pinus* accounting for ±62.6% of the total. Herbaceous plants accounted for ±26.6%, *Artemisia* (±9.9%) and Chenopodiaceae (±10.7%) were the most ubiquitous taxa. Three zones were recognized based on stratigraphically constrained cluster analysis (CONISS) (**Figure 3**). The three zones were as follows:

Zone A (240–350 cm) In this section, tree pollen, predominantly *Pinus* (±71.18%), *Picea* (±8.34%), and some *Betula* (±0.63%), accounted for ±80% of the total pollen assemblage. Herbaceous plants, consisted mostly of Chenopodiaceae (±5.64%) and *artemisia* (±8.66%), accounted for ±17.28% of the total.

Zone B (170–240 cm) This section included substantial cultural elements and was similarly characterized by trees as dominant. *Pinus* and *Picea* were prevalent, but their relative abundance had evidently decreased to ±58.24 and ±4.69% respectively. Herbs including *Artemisia* (±13.33%), Chenopodiaceae (±11.71%), and Poaceae (±4.26%) increased compared to Zone A. In total, trees accounted for ±64.4% and herbs accounted for ±33.41%.

TABLE 4 | Cultivated land area in the northeast margin of Qinghai Tibetan Plateau.

Culture/Type	Theoretical cropland area (km^2)	Theoretical cropland radius (km^2)	Land area suitable for cultivation (km^2)	Practical cropland area (km^2)
Majiayao	560,000	425	160	150
Banshan	576,000	430	60	25
Machang	1,120,000	560	630	465
Qijia	848,000	520	365	330
Kayue	326,400	325	1,300	1,080
Xindian	1,120,000	535	80	80

∗The estimated results were rounded and kept to the nearest five.

Zone C (60–170 cm) In this section, the tree pollen was mainly *Pinus* (±60.72%) and *Picea* (±5.68%). The concentration of *Ephedra* increased substantially compared to the previous stage. Herbaceous plants mainly consisted of *artemisia* and Chenopodiaceae, particularly Chenopodiaceae increased appreciably to ±14.07% of the total.

In summary, there was a clear indication of anthropogenic activity in Zone B as judged by increases of Poaceae, *Artemisia*, Chenopodiaceae, Asteraceae, *Taraxacum*, and a notable decrease in tree pollen.

Charcoal Analysis

Charcoal particles provided reliable evidence for fire. Small charcoal particles could be transported across long distances by wind, especially in dry areas (Huang et al., 2006). These small particles provided evidence for regional fires. Alternatively, large charcoal particles tended to travel only short distances, and serve as a good indicator for local fires (Patterson et al., 1987; Clark, 1988; Miao et al., 2017). Charcoal particles exceeding 100 μm are considered too massive to be suspended and transported over long distances by wind (Clark, 1988). Dianziping site charcoal analyses reveal a concentration of charcoal particles <50, 50–100, and >100 μm at 200–225, 200–250, and 200–210 cm respectively. These findings indicate the occurrence of regional fire events at a period represented at 200–250 cm, and local fire events at 200–210 cm, suggesting increased anthropogenic activity around 3.8–3.9 cal ka BP. The regional fire events appear to have occurred within the cultural layer, while evidence is absent from other layers. It is, thus reasonable to equate the high concentration of charcoal particles during this period as an indication of human activity. In addition, a sharp increase of Poaceae pollen was also observed in this section, which may further suggest that human intervention to the natural vegetation had occurred.

DISCUSSION

Anthropogenic Impact on the Land Cover During the Late Neolithic Age (5.3–4.0 cal Ka BP)

In the early Majiayao culture, the population density was low, and a relatively small area of land was cultivated. These areas were sparsely distributed along the Yellow and Huangshui Rivers. At this point, the anthropogenic impacts on natural vegetation was small. However, in the late Majiayao culture, the population increased dramatically, and agriculture became the primary means of sustenance (Xie, 2002). Notably, the population had increased three to four-folds and reached 39,200 during the Machang period. Concomitantly, the area of cultivated land increased exponentially and reached a peak of 465 km^2. Although the cultivated land had decreased during the Banshan Type, the cultivation intensity, attained by dividing the cropland area with the duration of that culture and area of that particular culture (Zhuo et al., 2013), had steadily increased since the beginning of the Majiayao Culture. This trend indicates that, despite the decreasing population, the settlement areas were still densely populated, and surrounding areas were intensely cultivated, even during the Banshan period. Disturbance to the neighboring area continued by expanded areas of cultivation (**Figure 4**).

During the mid-Holocene climatic optimum, coniferous and broadleaf forests grew abundantly in northeast QTP (Zhou et al., 2011). However, shifts in arboreal pollen were recorded around the Changning region (Dong et al., 2012). Around 5.1 cal ka BP, tree pollen such as *Picea*, *Ulmus*, and *Betula* accounted for ±33% of the total, while plant taxa associated with human activity such as Poaceae, Asteraceae, Brassicaceae, Apiaceae, Fabaceae, and Rosaceae (Li Y. Y. et al., 2008) only accounted for ±13%. Around 5.0 cal ka BP, tree pollen decreased and at around 4.2 cal ka BP, reached a low point with approximately ±10% in relative abundance. In contrast, synanthropic species significantly increased during that period, and reached a peak of ±43% of the total pollen assemblage, and in which, Poaceae accounted for ±41% (**Figure 5**). The decrease in tree pollen was associated with an increase in human-indicator species, especially in Poaceae during the optimum climate condition of mid-Holocene. This was also highly correlated with the population growth and expansion of cropland, as well as the high intensity of cultivation, suggesting human-induced deforestation and land cover change (**Figure 4**). Anthropogenic disturbance to the original vegetation was evident. The farmers of the Neolithic Age actively deforested neighboring areas to create cropland and to meet the needs of an increasing population. In short, anthropogenic impacts on the environment were initially apparent at approximately 4.3–4.0 cal ka BP on this part of the plateau.

In addition, the firing of pottery and utilization of wood resources also likely accelerated deforestation. Pottery-making technology during the Majiayao culture was highly developed, and this culture was renowned for its exquisite pottery. According to previous research, a temperature of 800°C is required for the firing of pottery (Papachristodoulou et al., 2006). Wood might have been the most attainable source for fuel at that time and a substantial number of trees utilized for pottery making. Additionally, among the excavated tombs of the Majiayao culture, wooden coffins (coffin made

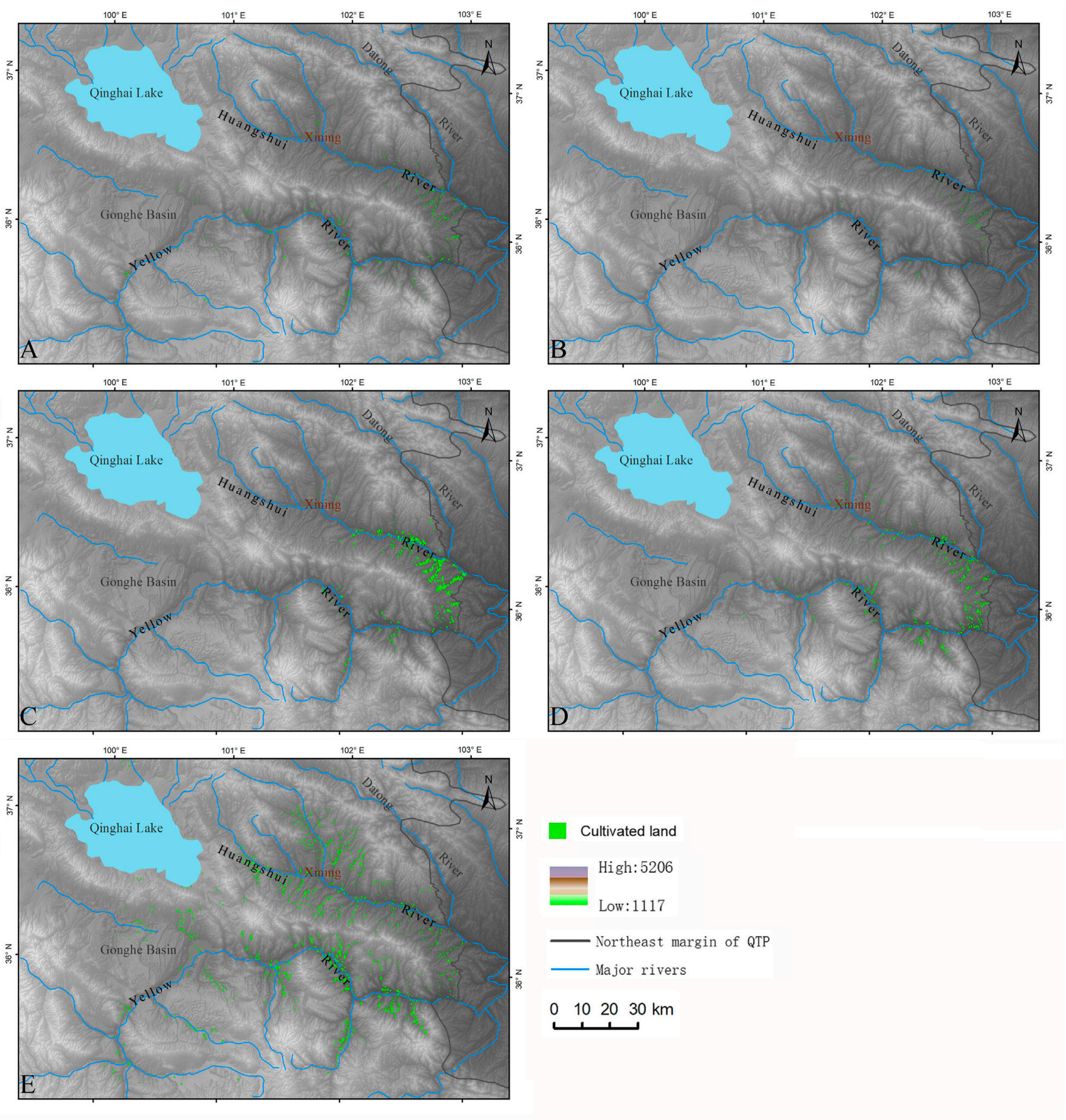

FIGURE 2 | Temporal and spatial distribution of cultivated land during each culture/type. **(A)** Distribution of cultivated land during the Majiayao type. **(B)** Distribution of cultivated land during the Banshan type. **(C)** Distribution of cultivated land during the Machang type. **(D)** Distribution of cultivated land during the Qijia Culture. **(E)** Distribution of cultivated land during the Xindian and Kayue Cultures.

of wood) accounted for 84% of the burials (Qinghai Province Cultural Relics Management Branch Archaeological team, Chinese Academy of Social Sciences, Institute of Archaeology, 1984). To sum up, it appears that tree resources were abundant during the early Majiayao culture. Cropland areas may have been previously forested, but, trees were definitely logged for various of wood usage. It is thus reasonable to conclude that large areas of forests were brought down during this period.

Anthropogenic Impacts on the Natural Vegetation During the Early Bronze Age (4.0–3.6 ka BP)

Qijia culture represents an early period of the Bronze Age. During this period, the overall climate of the QTP gradually shifted from the mid-Holocene’s warm and wet to drier and colder climate (Liu, 2016; Wei H. et al., 2020). This transition

TABLE 5 | Charcoal testing result from Dianziping stratum.

Lab number	Depth (cm)	AMS^{14}C age	Calibrated age (cal a BP)
BA160517	108	3,570 ± 25	3,878 ± 52
BA160516	173	3,525 ± 25	3,798 ± 82
BA160515	194	3,600 ± 30	3,908 ± 72
BA160518	205	3,555 ± 30	3,872 ± 58
BA160519	241	3,645 ± 25	3,944 ± 56

continued through the entire Qijia period on the QTP and was synchronous with increasing climatic instability and extreme weather events (Wang et al., 2021). According to Liu (2016), the Genggahai region received relatively low amounts of precipitation between 4.1 and 3.1 cal ka BP. The excavation of the Lajia site confirmed that the area was experiencing frequent mountain torrents, indicating an increase in severe rainstorms (Chui et al., 2019; Wang et al., 2021). Driven by the overall cooling, drying climate, and the increase of extreme weather events, the human population in the area declined slightly, and the production mode of the agricultural settlers also shifted during this period. Farmers appeared to have adopted grazing as an alternative means of sustenance (Xie, 2002; Chen T. et al., 2019). Evidence suggests that people were, at least partially, engaged in pastoralism. Burial objects unearthed during the Qijia culture shifted from pigs to sheep, implying the onset of pastoralism on the northeast margin of QTP (Liu, 2014). Consequently, the cultivation intensity demonstrated a dramatic fell during the Qijia culture (**Figure 4**). The area of cultivated land decreased compared to that of the Machang Type.

The Dianziping pollen analysis indicates that during the Qijia culture, pine and spruce forests, as well as deciduous broadleaf trees (birch and maple), had persisted in the area. Tree pollen accounted for ±70% and shrubs accounted for ±26.8% of the total pollen assemblage (**Figure 3**). Trees, especially coniferous taxa, appeared to have been abundant in the area while broadleaf trees were scarce. Therefore, climate change had caused vegetation succession in the high-altitude areas. However, forests in the lower elevation (~1,870 m) areas in the Hehuang Valley persisted indicating that these areas were still warm and wet enough for the growth of these tree species. Since cultivated land area was also concentrated in the eastern edge of Huangshui Valley. It seems that this part of the QTP was intensely cultivated despite its low human population numbers, which could be drawn from the relatively high intensity of cultivation (**Figure 4**). Meanwhile, analysis of the charcoal in Dianziping indicated that the incidence of regional fire was frequent between 3.9 and 3.8 cal ka BP (**Figure 3**). These fires were unlikely to be started naturally as lightning events are typically followed by thunderstorms and heavy precipitation on the QTP. As such, these findings further demonstrated anthropogenic disturbance during this period.

Based on series of archaeological excavations, there are approximately 366 graves of the Qijia culture, among which 288 (approximately 80%) graves used wooden coffins. Over half of these were made from a single cut of wood with diameters of approximately 50 cm. Although both the population and cultivated land area in the northeast margin of the QTP decreased during the Qijia culture, forest destruction in the region continued. Despite climate change being a major driving force for the reduction of deciduous broadleaf forests, human destruction to the forests, especially to the disappearance

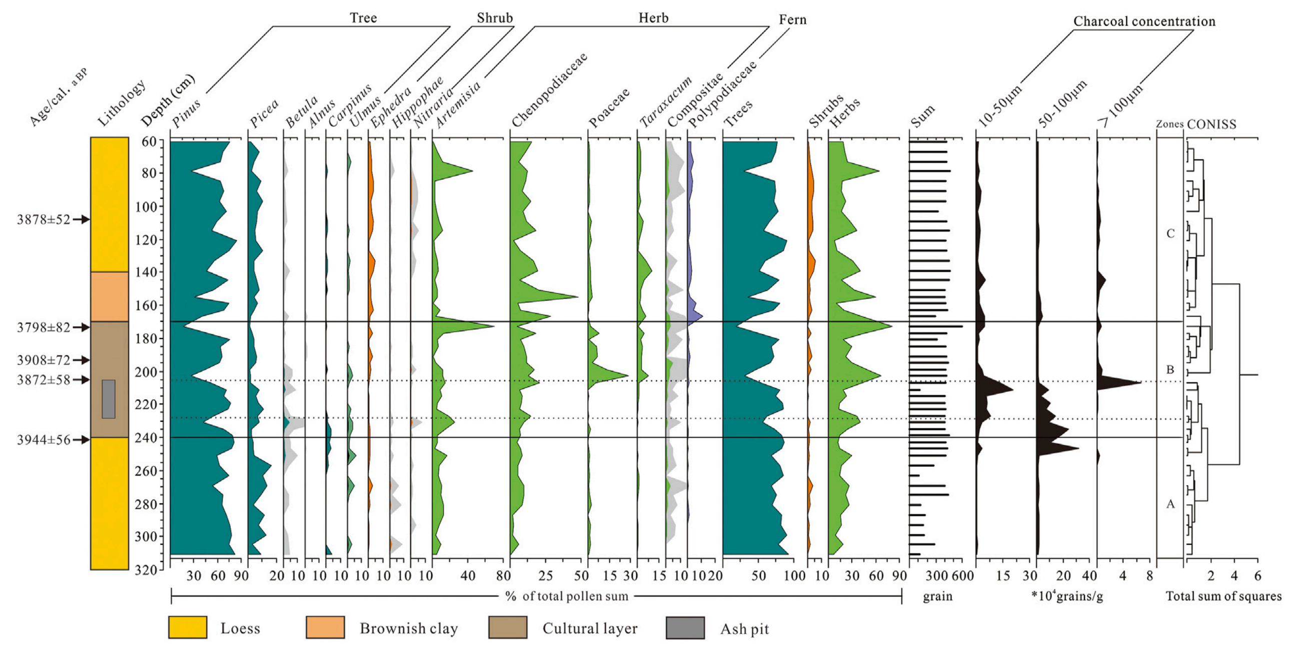

FIGURE 3 | Pollen assemblage diagram of Dianziping profile.

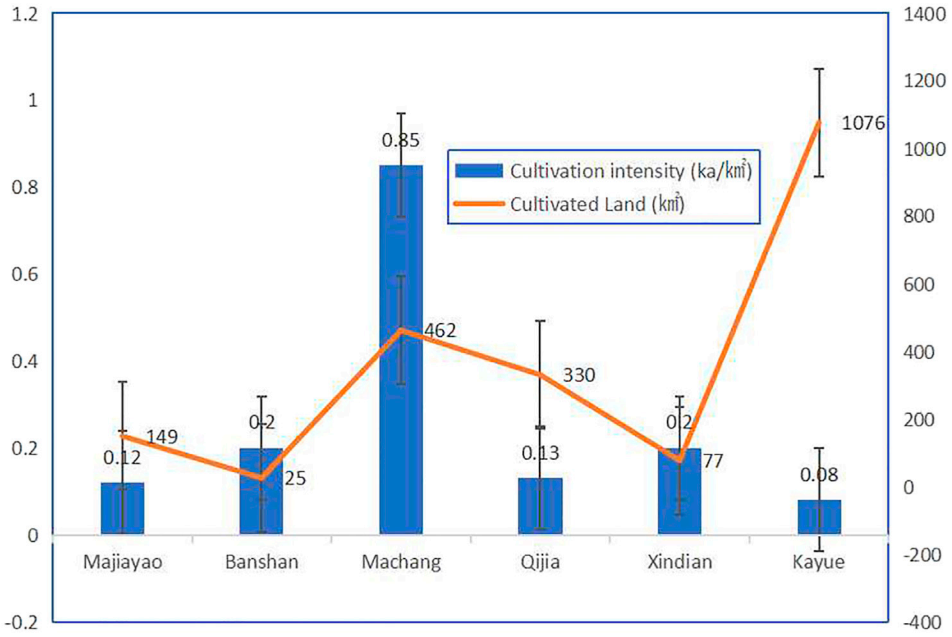

FIGURE 4 | Comparison of cultivation intensity and cultivated land area during each culture/type. Blue bar: Cultivation intensity during each culture/type (ka/km^2). Orange line: cultivated land (km^2).

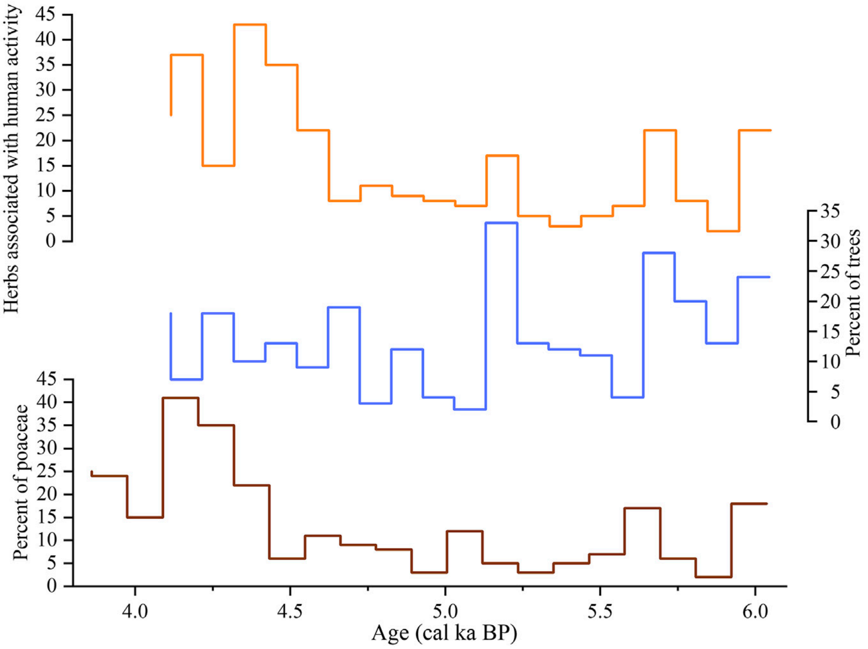

FIGURE 5 | Analysis of Changning pollen assemblage.

of coniferous forests on the river terraces in the valleys, are undeniable. In conclusion, it appears that during the Qijia culture, large scale ecological shifts were mainly driven by climatic changes. The changes obviously caused forest decline in high altitude areas and ecological succession in lower areas (Kramer et al., 2009a; Kramer et al., 2009b). On the other hand, intensive cultivation and lumber utilization in settlement areas accelerated the pace of deforestation at lower elevations.

Anthropogenic Impact on Natural Vegetation During Mid-Late Bronze Age (3.6–2.4 cal ka BP)

During the mid-late Bronze Age, the northeast QTP was occupied by people of the Xindian and Kayue cultures. The relatively cold and dry climate, dictated the people to undertake some changes concerning their means of sustenance (Jia, 2012; Dong et al., 2013; Chen et al., 2015; Ren et al., 2018). One such change to the farming practice was a shift from the monoculture of millet to developed multiple crops. Barley, as cold-resistant crop, became staple in the harsh highlands (Ma et al., 2016; Zhang and Dong, 2017). Sheep, as cold-tolerant livestock, were introduced into this region in the early Bronze Age via cross-mainland cultural exchange, and grazing livestock was broadly adopted (Dodson et al., 2013; Dong, 2018). In addition, the number of pigs associated with funeral sties began to decrease and were replaced by sheep, horses, and cattle (Liu, 2014), which implies the growing importance of grazing in the Kayue culture. The development of pastoralism allowed farming activities to expand from low altitude to high altitude areas despite the dry and cold climate, and to settle permanently in areas with elevations above three thousand meters (Chen et al., 2015). Consequently, Kayue culture developed quickly in the higher altitude areas, practicing both grazing and farming. The Xindian culture was mainly distributed at lower altitude areas in the east of the study area, and was sustained by traditional farming. The shifts in production structure boosted the population growth and the development of agriculture. The total population in the northeast margin of QTP reached approximately 61,330 people, and the cropland area amounted to over 1,160 km^2 (**Table 4**). These croplands were mainly distributed along the Yellow River, and its major tributaries, expanding into the upper reaches of the Yellow River. As figure four illustrates, the adoption of grazing reduced cultivation intensity but the exponential population growth enlarged the overall impacted area. The population growth and the subsequent cropland expansion significantly resulted in human-induced environmental destruction in the natural areas, especially at high altitudes. Furthermore, increasing charcoal concentration in Gonghe Basin during the Kayue culture was accompanied by increasing human imprints and disturbances to the high-altitude areas (Miao et al., 2017).

Wood was used as raw material for construction, production tools, and fuel for the fire (Wang et al., 2014). Generally, charcoal remains from the burning of dead wood were rich in *mycelium* (Marguerie and Hunot, 2009; Vidal-Matutano et al., 2017). In the charcoal analysis from the Kayue and the Xindian cultural sites, *mycelium* was rarely encountered (Liu, 2019). Based on the absence of *mycelium*, it can be inferred that the increasing population during the mid-late Bronze Age could have resulted in massive logging for fuel. In the Liuwan site, six graves of the Xindian culture were excavated, but none used wooden coffins (Qinghai Province Cultural Relics Management Branch Archaeological team, Chinese Academy of Social Sciences, Institute of Archaeology, 1984). The excavation of Hetao Zhuang grave, located along a tributary of Huangshui River in Milagou, revealed 342 graves, 102 of which used wood coffins (Qinghai Province Cultural Relics Archaeological Institute, 2004). In Guide Shan Pingtai site, along the Yellow River, 90 graves of the Kayue Culture were excavated, of which, 32 graves contained wooden coffins made of woods with diameter of only 10 cm. This suggests that forests along the Huangshui River were mostly exhausted. Trees were quite limited even along the upper reaches of Yellow River where only small trees and shrubs remained. Moreover, Liu (2019) states that *Pinus* was easily shaped, yet hard to corrode, making it a favorable choice for use by prehistoric humans. However, the number of broadleaf trees used by prehistoric Kayue people was significantly higher than that of coniferous species. Approximately two-thirds of the wood came from broadleaf trees. This demonstrates that the availability of conifers such as *Pinus* has been greatly reduced, but the climate still allowed the growth of deciduous broadleaf trees. In addition, the pollen assemblage from Fengtai site in Huzhu County disclosed a variety of Poaceae taxa that no longer existed in the area. This is a testament to the rich floral biodiversity in the region during the Kayue culture and that climate allowed their abundance (Jin et al., 2006). In sum, despite having a climate that was optimal for supporting the diversity of flora and growth of deciduous broadleaf trees during that time, the forest resources were being depleted. This is supported by both archaeological evidence of wood utilization and by the pollen assemblage from Dalianhai, which showed a decreasing trend of *Pinus* and *Picea* and steady increase of Poaceae (Cheng et al., 2013) (**Figure 6**).

Ecological studies conducted on the grasslands of the QTP show that grazing by domesticated livestock caused an increase of *Stellera chamaejasme* across the landscape (Huang et al., 2017; Wei H. et al., 2020; Wei H.-C. et al., 2020). This species is toxic and was not consumed by livestock. Grazing of other species accelerates the growth of *Stellera*, enabling it to eventually become the dominant species on the grassland (Liu et al., 2004). The increasing abundance of *Stellera chamaejasme,* therefore, is an indicator of overgrazing and grassland degradation (Miehe et al., 2014). The pollen assemblage from Genggahai illustrates a rapid proliferation of *Stellera chamaejasme* around 3.6–3.0 cal ka BP in the surrounding areas. This indicates intensive grazing activity resulting in the degradation of previously *Artemisia* dominated steppe (Huang et al., 2017). This is consistent with the results of a sediment core analysis in Lake Muge, where the occurrence of frequent anthropogenic fire events showed expansion of cropland and pasture. The resulting environmental impacts of these activities induced great alterations of the natural vegetation (Sun et al., 2016).

In all, during this period, both the human populations and the cultivated land areas had increased significantly due to a progression in environmental adaptability. The Kayue people had moved up to the middle and high-altitude areas and practiced grazing as a primary means of livelihood, and crop cultivation as alternative sustenance. As a result, the pristine forests in these areas were largely destroyed, and the grassland cover was disturbed by both cultivation and grazing activities. It appears that anthropogenic impacts had been the major driving force for land deterioration and forest decline during this period.

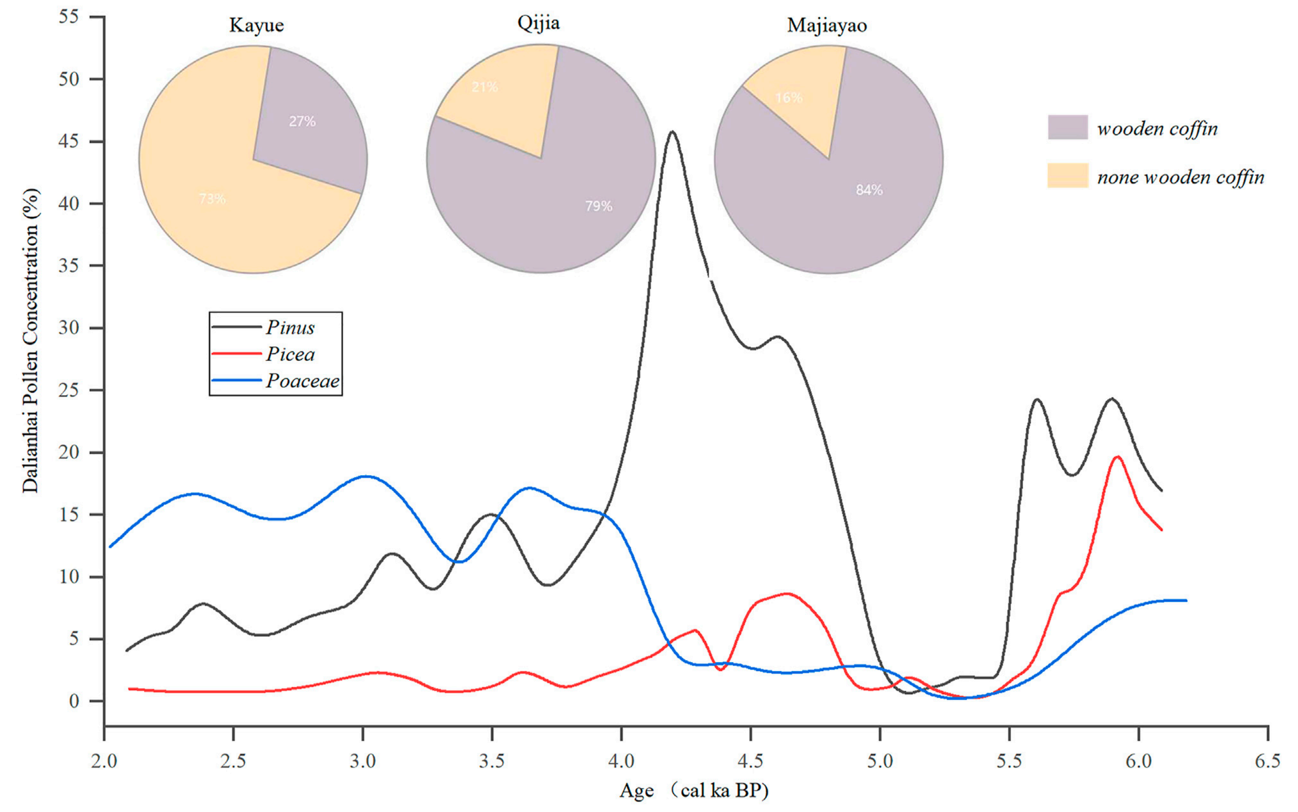

FIGURE 6 | Analysis of Dalianhai pollen assemblage and utilization of wood for construction of coffin.

Environmental Impacts During the Historical Time

The analysis of Genggahai and Dalianhai pollen assemblages show that since 1.6 cal ka BP, herbaceous pollen had increased, while tree pollen decreased (Cheng et al., 2013; Liu, 2016). In Genggahai region, the growth of herbaceous pollen, such as *Stellera*, *Artemisia*, and Chenopodiaceae was evident, and degradation of the grassland was apparent. The soil in the region was arid and low in organic matter, and the region was successively transformed into a desert steppe (Liu, 2016). In the Dalianhai area, at 1.4 cal ka BP, the humidity gradually increased, and the grassland began to expand. However, forested areas were not restored due to the slow succession rate of forest re-generation itself and the extensive deforestation that previously occurred in the area (Cheng et al., 2013). Soil water retention capacity was reduced, signs of soil erosion in the surrounding area were apparent, and grassland degradation was evident with the increasing growth of *Stellera*. It appears that anthropogenic activity, including over-grazing, was a driving force for land degradation.

The three main expansion periods of cultivation during the historical period in China occurred during the Han Dynasty, the Song Dynasty and mid-Qing Dynasty (Fang et al., 2019). In approximately 2.2 cal ka BP, the Han Dynasty colonized the areas along the Huangshui River and implemented "military cultivation" and "immigration garrison" policies to supply food to the military in the area (Gong, 2012). To ensure the implementation of these policies, over ten thousand soldiers were staged in the region to cultivate the barren land in Ledu (along the Huangshui River). Advanced iron plow techniques were introduced, and agriculture became highly developed (Gu, 2007). Postal stations and bridges were also constructed in the area during this period. According to the Legend of Zhao Chongguo and Xin Qingji, during the construction, over six thousand trees were logged from the adjacent mountains and transported along the Huangshui River. This depleted the forests in the Huangshui Valley, leaving trees mainly on the adjacent mountains. In the Tang Dynasty "military cultivation" and expansion of cropland in the Hehuang Valley reached approximately 321 km^2 (Wu et al., 2017). During the Song Dynasty, according to *Qing Tang Record*, only a few clusters of pine trees were observed along the Huangshui River. The total cropland area in Hehuang Valley was approximately 305 km^2, congruent with Tang Dynasty (Guo et al., 2021). By the Ming Dynasty, the population had increased rapidly in the area (Cui et al., 1999; Zhang et al., 2016). In the late Ming Dynasty, 1650AD, the cropland area in the Hehuang Valley reached approximately 433 km^2 (Zhao, 2016). The structure of forest vegetation in the valley had changed significantly, with poplar and birch replacing the original pine and spruce forests (Qinghai Local Chronicle Compilation Committee, 1993). By the Qing

Dynasty, dry farming had been widely developed and the cultivated land gradually expanded into the hills and mountains (Wang et al., 2000). In 1747AD, Yang Yingju recorded in *Annals of Xining Fu*, that most of the mountains along the middle reaches of the Huangshui River were barren lands (Yang and Wang, 1747). Timber for construction of *Xining Fu* had to be transported from distant mountains. By the late Qing Dynasty, in 1845AD, the cropland in Hehuang Valley reached approximately 1,505 km^2.

In conclusion, croplands were abandoned and re-cultivated frequently and expanded continually; forests and shrubs were heavily harvested. Cropland expansion increasingly pushed the carrying capacity of the land toward the edge of limitation. Large areas of barren hillsides were formed in Hehuang area. Soil erosion and landslides occurred more frequently following the deterioration of the natural vegetation. There were no major climate fluctuations during the historical period suggesting the destruction of vegetation cover was overtly induced by anthropogenic factors. Currently, natural forest in the area is patchy and scattered across the hills and slopes found at elevations ranging from 2,600 to 3,400 m (Zhou et al., 1986). This further demonstrates that the destruction of forests and the deterioration of grassland during the historical period were primarily due to anthropogenic forces.

CONCLUSION

(1) This paper addresses human impacts on the natural vegetation in the northeast margin of the QTP. The study explains the extent of anthropogenic influence on the natural land cover through cropland expansion, with the support of pollen records and archaeological data. Cultivated land areas were reconstructed using population estimates and prehistorical site reconstruction. Altitude, soil, distance to the river, slope aspect, and gradient are considered to be natural limiting factors for the expansion of cropland. The Dianziping pollen assemblage was analyzed and compared to previous pollen studies in the area.

(2) In the mid-Holocene climatic optimum, the reduction of tree pollen can be explained by the intrusion of Neolithic farmers and expansion of cropland, as well as heavy utilization of timber resources. The decline of forests and shift in vegetation composition, including a reduction of flora diversity during the early Bronze Age may be explained by adverse climatic impacts, but human exploitation of forests and destruction of land cover at low elevated rivers terraces were also evident. During the mid-late Bronze Age, climatic impacts appeared to be less influential, while the expansion of cropland and population growth likely resulted in the continued diminishing of forests. Humans likely drove the ecological succession of natural vegetation to the current pastureland. The current landscape, characterized by barren mountains and remnant forest islands can be explained by the large-scale deforestation that occurred throughout human history.

(3) A strong correlation was found to exist among the occurrence of population growth, cropland expansion, and reduction of tree pollen found at prehistoric sites. Population growth instigated a self-reinforcing cycle whereby more cropland was required to support inhabitants and more inhabitants cultivated more land, which in turn, boosted population growth. Consequently, extensive logging and burning of natural forest cover were performed for various human purposes and resulted in significant reductions in tree pollen.

(4) Neolithic farmers planted corps mainly on terraces in river valleys along the Huangshui River. In the late Bronze Age, the cultivated land area quickly expanded to the small hills and flat terrain at higher altitudes along the upper reaches of the Yellow River. The development of cropland along the Yellow River in the northeast margin of QTP occurred slightly later than that of the Huangshui River.

DATA AVAILABILITY STATEMENT

The raw data supporting the conclusions of this article will be made available by the authors, without undue reservation.

AUTHOR CONTRIBUTIONS

ZW and GH designed the study and wrote the paper, GH reconstructed the cultivated land, ZW and JG conducted the pollen analysis, SJ, XC, ZL conducted the field work.

FUNDING

This study was supported by Natural Science Fund of Qinghai Province, Grant No. 2021-ZJ-917.

REFERENCES

Bellwood, P., Gamble, C., Steven, A. L. B., Pluciennik, M., Richards, M., and Terrell, J. E. (2005). *First Farmers: The Origins of Agricultural Societies*. London, United Kingdom: Blackwell Publishing.

Bronk Ramsey, C. (2015). *OxCal Program v4.2.4*. Oxford, United Kingdom: Oxford Radiocarbon Accelerator Unit, Research Lab for Archaeology, University of Oxford. Available at: https://c14.arch.ox.ac.uk/oxcal/OxCal.html (Accessed March 15).

Bureau of National Cultural Relics (1996). *Atlas of Chinese Cultural Relics-Fascicule of Qinghai Province*. Beijing, China: China Cartographic Publishing Press.

Cavalli-Sforza, L., Menozzi, P., and Piazza, A. (1993). Demic Expansions and Human Evolution. *Science* 259, 639–646. doi:10.1126/science.8430313

Chen, F. H., Dong, G. H., Zhang, D. J., Liu, X. Y., Jia, X., An, C. B., et al. (2015). Agriculture Facilitated Permanent Human Occupation of the Tibetan Plateau after 3600 B.P. *Science* 347 (6219), 248–250. doi:10.1126/science.1259172

Chen, Q., Liu, F., Fang, X., Zhou, Q., Chen, Q., and Chen, R. (2019). Reconstruction of Cropland Distribution in the Late Neolithic Period in Northern China. *Geo. Res.* 38 (12), 2927–2940. doi:10.11821/dlyj020181293

Chen, T., Jia, X., Li, H., and Dong, G. (2019). The Analysis of Spatio Temporal Transformations of Agricultural and its Influence Factors During Qijia Culture Period in Gansu Qinghai Region. *Quat. Sci.* 39 (1), 132–144. doi:10.11928/j.issn.10017410.2019.01

Cheng, B., Chen, F., and Zhang, J. (2013). Palaeovegetational and Palaeoenvironmental Changes since the Last Deglacial in Gonghe Basin, Northeast Tibetan Plateau. *J. Geogr. Sci.* 23 (1), 136–146. doi:10.1007/s11442-013-0999-5

Chui, Y. D., Huang, C. C., Pang, J. L., Zhou, Y. L., Zhang, Y. Z., Guo, Y. Q., et al. (2019). Study of the Soil Sequence and the Dating of Prehistoric Mountain Torrent Disaster in La Jia Ruins, Qinghai Province. *Acta Geogra. Sinica* 74 (11), 2371–2384. doi:10.11821/dlxb201911013

Clark, J. S. (1988). Particle Motion and the Theory of Charcoal Analysis: Source Area, Transport, Deposition, and Sampling. *Quat. Res.* 30, 67–80. doi:10.1016/0033-5894(88)90088-9

Cui, Y. H., Zhang, D. Z., and Du, C. S. (1999). *General History of Qinghai*. Xining, China: Qinghai People's Publishing House.

Dodson, J. R., Li, X., Zhou, X., Zhao, K., Sun, N., and Atahan, P. (2013). Origin and Spread of Wheat in China. *Quat. Sci. Rev.* 72, 108–111. doi:10.1016/j.quascirev.2013.04.021

Dong, G. (2018). Understanding Past Human-Environment Interaction from an Interdisciplinary Perspective. *Sci. Bull.* 63 (16), 1023–1024. doi:10.2018-16-00310.1016/j.scib.2018.07.013

Dong, G., Jia, X., An, C., Chen, F., Zhao, Y., Tao, S., et al. (2012). Mid-Holocene Climate Change and its Effect on Prehistoric Cultural Evolution in Eastern Qinghai Province, China. *Quat. Res.* 77 (1), 23–30. doi:10.1016/j.yqres.2011.10.004

Dong, G., Jia, X., Elston, R., Chen, F., Li, S., Wang, L., et al. (2013). Spatial and Temporal Variety of Prehistoric Human Settlement and its Influencing Factors in the Upper Yellow River Valley, Qinghai Province, China. *J. Archaeol. Sci.* 40 (5), 2538–2546. doi:10.1016/j.jas.2012.10.002

Edwards, K. J., and MacDonald, G. M. (1991). Holocene Palynology: II Human Influence and Vegetation Change. *Prog. Phys. Geogr. Earth Environ.* 15, 364–391. doi:10.1177/030913339101500402

Ellis, E. C., Kaplan, J. O., Fuller, D. Q., Vavrus, S., Klein Goldewijk, K., and Verburg, P. H. (2013). Used Planet: A Global History. *Proc. Natl. Acad. Sci. U.S.A.* 110 (20), 7978–7985. doi:10.1073/pnas.1217241110

Fang, H. (2007). *Archaeological Theory and Practice in Settlement and Environment*. Shandong, China: Shandong University Publishing House.

Fang, X. Q., Ye, Y., Zhang, C. P., and Tang, C. C. (2019). Cropland Cover Change and its Environmental Impacts in the History of China. *J. Paleogeogr.* 21 (1), 160–174. doi:10.4135/9781446247501.n891

Gaillard, M.-J., Morrison, K. D., Madella, M., and Whitehouse, N. (2018). Past Land-Use and Land-Cover Change: The Challenge of Quantification at the Subcontinental to Global Scales. *PAGES Mag.* 26 (1), 1–44. doi:10.22498/pages.26.1.3

Goldewijk, K. K., Drecht, G. V., and Bouwman, A. F. (2007). Mapping Contemporary Global Cropland and Grassland Distributions on a 5 × 5 minute Resolution. *J. Land Use Sci.* 2 (3), 167–190. doi:10.1080/17474230701622940

Gong, S. (2012). *Book of Han·Book of the Later Han*. Chengdu, China: Bashu Press.

Gu, B. (2007). *Book of Han*. Beijing, China: Zhonghua Press.

Guo, R., Liu, F.-g., Chen, Q., Zhou, Q., Gu, X.-j., and Cai, X.-c.-m. (2021). Reconstruction of Cultivated Land Pattern in the Upper Reaches of the Yellow River in the Late Northern Song Dynasty:Take Hehuang Valley as an Example. *J. Nat. Resour.* 36 (1), 27–37. doi:10.31497/zrzyxb.20210102

Han, X. Y., Ying, H. S., and Wang, J. (2020). The Influencing Factors of Cultivated Land Utilization in Lv Liang Mountain Area. *J. Shanxi Agri. Sci.* 48 (10), 1679–1682+1692. doi:10.15405/epsbs.2020.10.02.33

Harlan, J. R. (1971). Agricultural Origins: Centers and Noncenters. *Science* 174, 468–474. doi:10.1126/science.174.4008.468

Hou, G., Lai, Z., Xiao, J., and Chongyi, E. (2012). Reconstruction of Cultivated Land during Mid- Holocene in the Middle and Lower Reaches of Yellow River and Human Impact on Vegetations. *J. Geogr. Sci.* 22 (5), 933–945. doi:10.1007/s11442-012-0974-6

Huang, C. C., Pang, J., Chen, S., Su, H., Han, J., Cao, Y., et al. (2006). Charcoal Records of Fire History in the Holocene Loess–Soil Sequences Over the Southern Loess Plateau of China. *Palaeogeogr. Palaeoclimatol. Palaeoecol.* 239 (1–2), 28–44. doi:10.1016/j.palaeo.2006.01.004

Huang, M., Ji, J. J., and Peng, L. L. (2008). The Response of Vegetation Net Primary Productivity to Climate Change During 1981- 2000 in the Tibetan Plateau. *Clim. Environ. Res.* 13 (5), 608–616. doi:10.1016/j.scitotenv.2012.12.014

Huang, X.-z., Liu, S.-s., Dong, G.-h., Qiang, M.-r., Bai, Z.-j., Zhao, Y., et al. (2017). Early Human Impacts on Vegetation on the Northeastern Qinghai–Tibetan Plateau during the Middle to Late Holocene. *Prog. Phys. Geogr. Earth Environ.* 41 (3), 286–301. doi:10.1177/0309133317703035

Jia, X. (2012). Study of the Cultural Evolution and Plant Remains of Neolithic-Bronze Age in Northeast Qinghai Province. Dissertation. Lanzhou (China): Lanzhou University.

Jia, X., Dong, G., Li, H., Brunson, K., Chen, F., Ma, M., et al. (2013). The Development of Agriculture and its Impact on Cultural Expansion during the Late Neolithic in the Western Loess Plateau, China. *The Holocene* 23 (1), 85–92. doi:10.1177/0959683612450203

Jia, X., Lee, F. L., Cui, M., Cheng, G., Zhao, Y., Ding, H., et al. (2019). Differentiations of Geographic Distribution and Subsistence Strategies Between Tibetan and Other Major Ethnic Groups are Determined by the Physical Environment in Hehuang Valley. *Sci. China Earth Sci.* 62 (2), 412–422. doi:10.1007/s11430-018-9301-5

Jin, G. Y., Wang, W., Wagner, M., and Tarasov, P. E. (2006). Palynology Analysis and Human Activities at the Kayue Cultural Site in Fengtai, Huzhu, Qinghai Province—Results of Fossil and Modern Topsoil Pollen Analysis. *Huaxia Archaeol.* 14 (3), 24–32. doi:10.16143/j.cnki.1001-9928.2006.03.004

Kramer, A., Herzschuh, U., Mischke, S., and Zhang, C. (2009a). Holocene Treeline Shifts and Monsoon Variability in the Hengduan Mountains (Southeastern Tibetan Plateau), Implications from Palynological Investigations. *Palaeogeogr. Palaeoclimatol. Palaeoecol.* 286 (2010), 23–41. doi:10.1016/j.palaeo.2009.12.001

Kramer, A., Herzschuh, U., Mischke, S., and Zhang, C. (2009b). Late Glacial Vegetation and Climate Oscillations on the Southeastern Tibetan Plateau Inferred from the Lake Naleng Pollen Profile. *Quat. Res.* 73 (2), 324–335. doi:10.1016/j.yqres.2009.12.003

Li, D.-M., Guo, Z.-G., and An, L.-Z. (2008). Assessment on Vegetation Restoration Capacity of Several Grassland Ecosystems under Destroyed Disturbance in Permafrost Regions of Qinghai-Tibet Plateau. *Ying Yong Sheng Tai Xue Bao* 19 (10), 2182–2188. doi:10.5194/tc-2015-218-rc2

Li, Y. Y., Zhou, L. P., and Cui, H. T. (2008). Indicative Pollen for Human Activity. *Sci. Briefings* 7 (9), 991–1002. doi:10.1007/s11434-008-0181-0

Li, G. L., and Lu, Y. G. (1981). Tombs of Kayue Culture. *Qinghai Archaeol. Soc.* 2 (3), 38–41.

Li, G. R., Chen, Y. Y., Niu, Q. F., Song, Y. R., and Wei, D. D. (2014). Particle Size Characteristics and Paleo-Environmental Significance of Dalianhai Sediments. *J. Qinghai Univ.* 32 (4), 65–83. doi:10.13901/j.cnki.qhwxxbzk.2014.04.012

Li, G. Y., Qian, Z. S., and Hu, J. (1995). *Palynological Analysis Manual*. Beijing, China: Geological Publishing House.

Li, M. S. (1978). Overview of Tibet Land Resource. *Nat. Resour.* 14 (2), 27–29.

Li, X., Sun, N., Dodson, J., and Zhou, X. (2012). Human Activity and its Impact on the Landscape at the Xishanping Site in the Western Loess Plateau during 4800–4300 cal yr BP Based on the Fossil Charcoal Record. *J. Archaeol. Sci.* 39 (2012), 3141–3147. doi:10.1016/j.jas.2012.04.052

Liu, F. W. (2019). Human Wood Utilization Strategy in the Northeast of Qinghai Tibetan Plateau During Neolithic and Bronze Age. Dissertation. Lanzhou (China): Lanzhou University.

Liu, S. S. (2016). Vegetation and Climate Change since the Last Deglaciation in the Northeast Qinghai–Tibetan Plateau Genggahai Region. Dissertation. Lanzhou (China): Lanzhou University.

Liu, Y., Long, R. J., and Yao, T. (2004). Research Progress on *Stellera chamajasme* L. on Grassland. *Pratacultural Sci.* 21 (6), 55–61. doi:10.3969/j.issn.1001-0629.2004.06.017

Liu, Z. H. (2014). Discussion of Climate Change and Cultural Evolution in Hehuang Area—Case of Majiayao, Qijia, Xindian and Kayue Cultures Were Investigated. *Theo. Res.* 20, 141–143. doi:10.1163/9789004322714_cclc_2015-0133-009

Lowe, J. J., and Walker, M. J. C. (1997). *Reconstructing Quaternary Environments*. 2nd ed. London, United Kingdom: Addison-Wesley.

Luo, J., Chen, Q., Liu, F. G., Zhang, Y. L., and Zhou, Q. (2015). Methods for Reconstructing Historical Cropland Spatial Distribution of the Yellow River-Huangshui River Valley in Tibetan Plateau. *Geo. Sci. Prog.* 21 (2), 207–216. doi:10.11820/dlkxjz.2015.02.00910.11820/dlkxjz.2015.02.009

Ma, M., Dong, G., Jia, X., Wang, H., Cui, Y., and Chen, F. (2016). Dietary Shift after 3600 Cal Yr BP and its Influencing Factors in Northwestern China: Evidence from Stable Isotopes. *Quat. Sci. Rev.* 145, 57–70. doi:10.1016/j.quascirev.2016.05.041

Marguerie, D., and Hunot, J.-Y. (2009). Charcoal Analysis and Dendrology: Data from Archaeological Sites in North-Western France. *J. Archaeol. Sci.* 34 (10), 1417–1433. doi:10.1016/j.jas.2006.10.032

Miao, Y. F., Zhang, D. J., Cai, X. M., Li, F., Jin, H. L., Wang, Y. P., et al. (2017). Holocene Fire on the Northeast Tibetan Plateau in Relation to Climate Change and Human Activity. *Quat. Int.* 443, 124–131. doi:10.1016/j.quaint.05.029

Miehe, G., Hasson, S., Glaser, B., Mischke, S., Böhner, J., van der Knaap, W. O., et al. (2021). Föhn, Fire and Grazing in Southern Tibet? A 20,000-Year Multi-Proxy Record in an Alpine Ecotonal Ecosystem. *Quat. Sci. Rev.* 256, 106817. doi:10.1016/J.QUASCIREV.2021.106817

Miehe, G., Miehe, S., Böhner, J., Kaiser, K., Hensen, I., Madsen, fnm., et al. (2014). How Old is the Human Footprint in the World's Largest Alpine Ecosystem? A Review of Multiproxy Records from the Tibetan Plateau from the Ecologists' Viewpoint. *Quat. Sci. Rev.* 86, 190–209. doi:10.1016/j.quascirev.2013.12.004

Papachristodoulou, C., Oikonomou, A., Ioannides, K., and Gravani, K. (2006). A Study of Ancient Pottery by Means of X-Ray Fluorescence Spectroscopy, Multivariate Statistics and Mineralogical Analysis. *Anal. Chim. Acta* 573–574, 347–353. doi:10.1016/j.aca.2006.02.012

Patterson, W. A., Edwards, K. J., and Maguire, D. J. (1987). Microscopic Charcoal as a Fossil Indicator of Fire. *Quat. Sci. Rev.* 6 (3), 3–23. doi:10.1016/0277-3791(87)90012-610.1525/9780520337404

Pielke, R. A., Pitman, A., Niyogi, D., Mahmood, R., McAlpine, C., Hossain, F., et al. (2011). Land Use/Land Cover Changes and Climate: Modeling Analysis and Observational Evidence. *WIREs Clim. Change* 2 (6), 828–850. doi:10.1002/wcc.144

Pongratz, J., Reick, C., Raddatz, T., and Claussen, M. (2008). A Reconstruction of Global Agricultural Areas and Land Cover for the Last Millennium. *Glob. Biogeochem. Cycles* 22 (3), GB3018. doi:10.1029/2007GB003153

Qiao, Y. (2010). The Evolutionary History of Complex Society in Yiluo Region between Peiligang to Erlitou Cultural Time. *Acta Aechaeol. Sinica* 45 (4), 423–454. doi:10.1017/cbo9781139034395.006

Qinghai Local Chronicle Compilation Committee (1993). *Chronicle of Qinghai Province: Forestry*. Xining, China: Qinghai People's Publishing House.

Qinghai Province Cultural Relics Archaeological Institute (2004). *Minhe He Tao Zhuang*. Beijing, China: Science Press.

Qinghai Province Cultural Relics Archaeological Institute (1990). *Minhe Yangshan*. Beijing: Heritage Press.

Qinghai Province Cultural Relics Management Branch Archaeological team, Chinese Academy of Social Sciences, Institute of Archaeology (1984). *Qinghai Liuwan*. Beijing, China: Heritage Press, 125–146.

Reimer, P. J., Bard, E., Bayliss, A., Beck, J. W., Blackwell, P. G., Ramsey, C. B., et al. (2013). IntCal13 and Marine13 Radiocarbon Age Calibration Curves 0-50,000 Years Cal BP. *Radiocarbon* 55, 1869–1887. doi:10.1017/S003382220004886410.2458/azu_js_rc.55.16947

Ren, G. (2000). Decline of the Mid- to Late Holocene Forests in China: Climatic Change or Human Impact?, *J. Quat. Sci.* 15 (3), 273–281. doi:10.1002/(SICI)1099-141710.1002/(sici)1099-1417(200003)15:3<273::aid-jqs504>3.0.co;2-2

Ren, L., Dong, G., Li, H., Rhode, D., Flad, R. K., Li, G., et al. (2018). Dating Human Settlement in the East-Central Tibetan Plateau During the Late Holocene. *Radiocarbon* 60, 137–150. doi:10.1017/RDC.2017.117

Ren, X. Y. (1998). *Random Notes of Gamatai Site Excavation, Compilation of the Committee on Learning and Literature and History of the CPPCC Qinghai Province, Archaeological Records of Qinghai*. Xining, China: Qinghai People's Publishing House, 65–73.

Su, B. Q., Zhang, Z. P., and Yan, W. M. (2010). *Ancient China*. Shanghai, China: Shanghai People's Publishing House.

Sun, W., Zhang, E., Shen, J., Chen, R., and Liu, E. (2016). Black Carbon Record of the Wildfire History of Western Sichuan Province in China over the Last 12.8 Ka. *Front. Earth Sci.* 10 (4), 634–643. doi:10.1007/s11707-015-0546-z

Vasey, D. E. (1992). *An Ecological History of Agriculture: 10,000 B. C.—A. D.* Ames, IA: Iowa State University Press, 363.

Vidal-Matutano, P., Henry, A., and Théry-Parisot, I. (2017). Dead Wood Gathering Among Neanderthal Groups: Charcoal evidence from Abric del Pastor and El Salt (Eastern Iberia). *J. Archaeol. Sci.* 80, 109–121. doi:10.1016/j.jas.2017.03.001

Vita Finzi, C. (1969). "Early Man and the Environment," in *Trends in Geography, an Introductory Survey*. Editors R. U. Cooke and J. H. Johnson (Oxford and New York, NY: Pergamon Press).

Vitousek, P. M., Mooney, H. A., Lubchenco, J., and Melillo, J. M. (1997). Human Domination of Earth's Ecosystems. *Science* 277, 494–499. doi:10.1007/978-0-387-73412-5_110.1126/science.277.5325.494

Wang, A. M., Liu, J. L., and Miao, L. L. (2000). The Historical Transformation of Man-Environment Relationship in the North-Eastern Border of Tibetan Plateau and its Surrounding Areas. *Hum. Geogr.* 15 (2), 58–63. doi:10.13959/j.issn.1003-2398.2000.02.015

Wang, H., Huang, C. C., Pang, J., ZhouCuan, Y. Y. D., Cuan, Y., Guo, Y., et al. (2021). Catastrophic Flashflood and Mudflow Events in the Pre-historical Lajia Ruins at the Northeast Margin of the Chinese Tibetan Plateau. *Quat. Sci. Rev.* 251, 106737. doi:10.1016/J.QUASCIREV.2020.106737

Wang, S. Z., Li, H., Zhang, L. R., Cheng, G. K., and WangZhao, P. Z. J. (2014). Tree Exploitation and Palaeo-Environment at Heishuiguo Xichengyi Site, Zhangye City, Gansu Province, Revealed with Excavated Charcoal Analysis. *Quat. Sci.* 2014, 43–50. doi:10.3969/j.issn.1001-7410.2014.06

Wei, H., Chongyi, E., Zhang, J., Sun, Y., Li, Q., Hou, G., et al. (2020). Climate Change and Anthropogenic Activities in Qinghai Lake Basin Over the Last 8500 Years Derived from Pollen and Charcoal Records in an Aeolian Section. *Catena* 193, 104616. doi:10.1016/j.catena.2020.104616

Wei, H.-c., Hou, G.-l., Fan, Q.-s., Madsen, D. B., Qin, Z.-j., Du, Y.-s., et al. (2020). Using Coprophilous Fungi to Reconstruct the History of Pastoralism in the Qinghai Lake Basin, Northeastern Qinghai–Tibetan Plateau. *Prog. Phys. Geogr. Earth Environ.* 44, 70–93. doi:10.1177/0309133319869596

Wu, Z. L., Liu, F. G., Chen, Q., Zhou, Q., and Yang, D. X. (2017). Reconstruction of Cropland Spatial Patterns in 733 AD along the Yellow River. *Res. Sci.* 39 (2), 252–262. doi:10.4324/9780203480243

Xie, D. J. (2002). *Prehistoric Archaeology in Ganqing Region*. Beijing, China: Cultural Relics Press.

Yang, G. (1998). Speculation on Yield Per Mu in Xia, Shang and Zhou Dynasties. *Agric. Hist. China* 13 (2), 24–26.

Yang, Y. J., and Wang, Y. (1747). *Xining Fu New Records*. Xining, China: Qinghai People's Publish House.

Zeng, Y. N., Jin, W. P., He, L. L., et al. (2012). Land Use Mapping Using Remote Sensing for Eastern Part of Qinghai Plateau. *Trans. Chin. Soc. Agric. Eng.* 28 (6), 225–231. doi:10.3969/j.issn.1002-6819.2012.16.035

Zhang, D. J., Dong, G. H., Wang, H., Ren, X. Y., Ha, B. B., Qiang, M. R., et al. (2016). History and Possible Mechanisms of Prehistoric Human Migration to the Tibetan Plateau). *Sci. China Earth Sci.* 46, 1007–1023. 10.1007/s11430-015-5482-x

Zhang, D. J., Shen, X. K., Cheng, T., Xia, H., Liu, W., Gao, X., et al. (2020a). New Progress in Prehistoric Human Activity in Qinghai-Tibet Plateau. *Chin. Sci. Bull.* 65 (6), 475–482. doi:10.1360/TB-2019-0382

Zhang, J., Yuan, M. S., Zhang, J., Li, H. W., Wang, J. W., Zhang, X., et al. (2020b). Responses of the NDVI of Alpine Grasslands on the Qinghai–Tibetan Plateau to Climate Change and Human Activities over the Last 30 Years. *Acta Ecol. Sin.* 40 (18), 6269–6281. doi:10.1007/s10584-006-9135-1

Zhang, S., and Dong, G. (2017). Human Adaptation Strategies to Different Altitude Environment During Mid-Late Bronze Age in Northeast Tibetan Plateau. *Quat. Res.* 37 (4), 696–708. doi:10.11928/j.issn.1001-7410.2017.04.03

Zhang, X., Wang, W.-C., Fang, X., Ye, Y., and Zheng, J. (2012). Agriculture Development-Induced Surface Albedo Changes and Climatic Implications Across Northeastern China. *Chin. Geogr. Sci.* 22 (3), 264–277. doi:10.1007/s11769-012-0535-z

Zhao, Y. J. (2016). Evolution of Settlement Pattern and Cultivated Land Change in Hehuang Valley in Ming Dynasty. Master's thesis. Xining (China): Qinghai Normal University.

Zhou, X., Li, X., Zhao, K., Dodson, J., Sun, N., and Yang, Q. (2011). Early Agricultural Development and Environmental Effects in the Neolithic Longdong Basin (Eastern Gansu). *Chin. Sci. Bull.* 56 (8), 762–771. doi:10.1007/s11434-010-4286-x

Zhou, X. M., Wang, Z. B., and Du, Q. (1986). *100~107*. Xining, China: Qinghai People's Publish House.

Zhuo, H. X., Liu, H. Y., Jia, X., and Sun, Y. G. (2013). A Preliminary Study on Human Activities in Sand Fields of Northern China and its Relationship with the Climatic Variations in Holocene. *Quat. Res.* 33, 303–313. doi:10.1177/095968369400400210

Conflict of Interest: The authors declare that the research was conducted in the absence of any commercial or financial relationships that could be construed as a potential conflict of interest.

frontiers in Earth Science

ORIGINAL RESEARCH
published: 28 May 2021
doi: 10.3389/feart.2021.640172

Radiocarbon and Luminescence Dating of Lacustrine Sediments in Zhari Namco, Southern Tibetan Plateau

Lu Cong[1,2,3], Yixuan Wang[1]*, Xiying Zhang[2], Tianyuan Chen[2], Donglin Gao[2] and Fuyuan An[4]

[1] Key Laboratory of Comprehensive and Highly Efficient Utilization of Salt Lake Resources, Qinghai Institute of Salt Lakes, Chinese Academy of Sciences, Xining, China, [2] Key Laboratory of Salt Lake Geology and Environment of Qinghai Province, Xining, China, [3] University of Chinese Academy of Sciences, Beijing, China, [4] Key Laboratory of Physical Geography and Environmental Processes of Qinghai Province, School of Geographical Science, Qinghai Normal University, Xining, China

There are more than 1,000 lakes within the Tibetan Plateau (TP), all of which are sensitive to changes in regional climate and local hydrology. Lacustrine sediments within these lakes preserve a good record of these changes. However, determining their precise ages is difficult due to the complex nature of lake reservoir effects (LRE), which limit our understanding of paleoenvironmental changes. Focusing on an exposed 600 cm thick lacustrine sediment profile located in western Zhari Namco, we used a combination of both radiocarbon and optically stimulated luminescence (OSL) dating methods in order to evaluate the carbon reservoirs of bulk organic matter (BOM) and aquatic plant remnants (APR), and to explore the age differences between ^{14}C and OSL and their respective reliability. We demonstrated that (i) OSL ages were changed in stratigraphic order, and the OSL age just below the beach gravel layer was consistent with previously reported paleoshoreline ages; (ii) ^{14}C ages were divergent between BOM and grass leaves; (iii) ^{14}C ages of BOM were older than ^{14}C ages of APR; and (iv) all ^{14}C ages were older than OSL ages. This could be attributed to changing LRE in the past, causing the ^{14}C ages to appear unstable during the deposition period. Although the ^{14}C ages of terrestrial plant remnants (TPR) were not affected by LRE, an analyzed twig nonetheless returned a ^{14}C age older than its respective layer's OSL age, suggesting it may have been preserved on land prior to transportation into the lake. Our study suggests that OSL ages are more reliable than ^{14}C ages with respect to Zhari Namco lacustrine sediments. We recommend caution when interpreting paleoenvironmental changes based on lacustrine sediment ^{14}C ages alone.

Keywords: lake reservoir effect, lacustrine sediments, optically stimulated luminescence, radiocarbon dating, Tibetan Plateau

Edited by:
Feng Cheng,
University of Nevada, Reno,
United States

Reviewed by:
Yougui Song,
Institute of Earth Environment,
Chinese Academy of Sciences, China
Maarten Blaauw,
Queen's University Belfast,
United Kingdom

****Correspondence:***
Yixuan Wang
yixuanwang@isl.ac.cn

Specialty section:
This article was submitted to Quaternary Science, Geomorphology and Paleoenvironment, a section of the journal Frontiers in Earth Science

Received: *10 December 2020*
Accepted: *20 April 2021*
Published: *28 May 2021*

Citation:
Cong L, Wang Y, Zhang X, Chen T, Gao D and An F (2021) Radiocarbon and Luminescence Dating of Lacustrine Sediments in Zhari Namco, Southern Tibetan Plateau. Front. Earth Sci. 9:640172. doi: 10.3389/feart.2021.640172

INTRODUCTION

The Tibetan Plateau (TP) is the largest and highest plateau on Earth, often regarded as the "Third Pole" due to both its high elevations and expansive *c.* 2.5 million km^2 coverage (Yao et al., 2012; Liu et al., 2019). Of the more than 1,400 lakes (larger than 1 km^2) distributed across the TP, *c.* 60% are within the endorheic TP (Zhang et al., 2020), and their lacustrine sediments preserve a wealth of information that helps researchers track past environmental and hydrological changes within the region (Hou et al., 2010; Long et al., 2014; Liu et al., 2018; Chongyi et al., 2018).

Radiocarbon (^{14}C) dating is the most commonly used method for dating lacustrine sediments within the TP (Shen et al., 2005; Hou et al., 2010; Chen H. et al., 2019; Wang H. et al., 2019), with most age frameworks for borehole lacustrine sediments constructed using ^{14}C ages (Hou et al., 2012). Terrestrial plant remnants (TPR), aquatic plant remnants (APR), and bulk organic matter (BOM) are typical materials for ^{14}C dating of lacustrine sediments within the TP (Zhang et al., 2007). Although ^{14}C dating is a mature dating technology with high precision, the harsh environmental conditions in the region limit overall biomass. This makes it difficult to find TPR in lacustrine sediments (Mischke et al., 2013). However, ^{14}C ages taken from the BOM and APR of lacustrine sediments ^{14}C ages are often influenced by the disequilibrium with atmospheric radiocarbon, thus causing the corresponding BOM and APR ^{14}C ages to appear older than the ^{14}C ages of contemporaneous TPR. This phenomenon is called the lake reservoir effect (LRE), which is commonly encountered during radiocarbon dating of lacustrine sediments within the TP. The accurate estimation of LRE is a crucial prerequisite for establishing reliable ^{14}C age-depth relationships (Stuiver and Braziunas, 1993; Ascough et al., 2011). Hou et al. (2012) and Mischke et al. (2013) summarized several approaches for evaluating LRE within the TP. These methods include: ^{14}C-based estimation of reservoir ages (RAs) using modern lacustrine sediments (Mischke et al., 2010), linear extrapolation of the ^{14}C age-depth model to the sediment-water interface depth (Fontes et al., 1996; Shen et al., 2005), geochemical models for ^{14}C reservoir correction (Wang et al., 2007; Yu et al., 2007), stratigraphic alignment (Liu et al., 2008), independent age determinations such as ^{210}Pb and ^{137}Cs dating (Zhu et al., 2008), optically stimulated luminescence (OSL) dating (Long et al., 2014; Wang Y. X. et al., 2019), U-series dating (Zhu et al., 2004), magnetic susceptibility comparison (Li et al., 2021), and varve counting (Zhou et al., 2011). In the above methods, OSL is unaffected by variations in LRE and lake hydrochemistry, and it is convenient for extracting dating materials (e.g., quartz and feldspar grains). Because of these advantages, OSL dating is frequently used for Quaternary sediments dating.

The OSL age of sediment directly reflects its time of burial, i.e., when it was last exposed to sunlight (Aitken, 1998). Recent studies have successfully applied the OSL dating method to TP loess (Liu et al., 2012, 2017; Wang et al., 2018; Kang et al., 2020; Li et al., 2020), dunes (Chen T. Y. et al., 2019), sand wedges (Liu et al., 2010; Liu and Lai, 2013), river sediments (An et al., 2018) and lacustrine sediments (Liu et al., 2011, 2015) in order to reveal their respective accumulation histories. Moreover, many recent studies have used a combination of ^{14}C and OSL dating to discuss the reliability of ages from lacustrine sediment cores. Zhang et al. (2007) used OSL and ^{14}C dating in organic-rich lacustrine sediments cored from Lake Gucheng (Jiangsu, China), and found the ^{14}C ages of BOM were *c.* 2,000 years (a) older than the OSL ages. Shen et al. (2008) applied OSL dating using fine silt quartz, together with ^{14}C dating of terrestrial plant macrofossils, which should not have been affected by the LRE, to establish a chronology for a lacustrine sediment core from Crummock Water (in the northwestern part of the English Lake District). Long et al. (2011) used OSL and ^{14}C dating of lacustrine sediments from Qingtu Lake (northern China); the apparent agreement between OSL and ^{14}C dating suggested that the RAs of ^{14}C samples in Qingtu Lake were much lower than in other lakes of northern China (e.g., Bangong Lake: 6,670 a, Fontes et al., 1996, Qinghai Lake: 1,039 a, Shen et al., 2005, Ahung Lake: 600–700 a, Morrill et al., 2006, Bositeng Lake: 1,140 a, Chen et al., 2006). However, only few studies of lacustrine sediments from the TP have used multi-dating approaches to establish age-depth models (Hu et al., 2017). Hu et al. (2017) used a combination of ^{210}Pb, ^{14}C, and OSL dating in Linggo Co (central TP) and found that the ^{210}Pb and OSL ages were roughly concordant, and all ^{14}C ages were much older than the ^{210}Pb and OSL ages at the same depths.

Therefore, a comparison between OSL and ^{14}C ages may help assess the reliability of the established chronology. In this study, ^{14}C ages sampled from different materials were compared with independently obtained OSL ages from Zhari Namco with the aim of determining their respective accuracy and reliability and to gain a better understanding of the intrinsic variability of the LRE.

STUDY AREA AND RESEARCH MATERIALS

Zhari Namco (30°44′–31°05′N, 85°20′–85°54′E) is a brackish lake located in the Cuoqin Basin, situated in the southern TP and possessing a cold and arid climate (**Figure 1**). The lake is formed by an east-west extending structural fault and is irregular in shape with narrow northern and southern banks, whereas its eastern and western banks are relatively wide. According to GPS measurements in the field, Zhari Namco sits at an elevation of 4,613 m above sea level (a.s.l.). With an overall length of 54.3 km from east to west, a length of 26.2 km from north to south, a present surface area of 996.9 km^2, and a catchment area of *c.* 15,433.2 km^2, it is the third-largest lake in Tibet after Siling Co and Namco. It is supplied mainly by precipitation and meltwater from snow and ice, with the Cuoqin Zangbo River—which drains into the lake from the south—representing the major water input. This river originates at the Gangdisê Mountains (*c.* 6,000 m a.s.l.) and has a total length of 253 km and a catchment area of about *c.* 9,930 km^2 (Wang and Dou, 1998).

An exposed section, named CQ (31°0′56.086″N, 85°8′51.238″E, elevation 4,664 m a.s.l.), was discovered in Cuoqin County, which is located on the west side of the lake. Section CQ (**Figure 2**) is composed of subsection CQ1 (**Figure 2A**) and CQ2 (**Figure 2B**). CQ1 is located at the top and is 400 cm thick. CQ2 is 200 cm thick and connects with the bottom of CQ1. The surface section of CQ is comprised mainly of modern soil and some gravels (0–5 cm). Moving up the section, the sediments change from fine to coarse, with the color undergoing an attendant change from dark to light. CQ can roughly be divided into five stratigraphic units: In the bottommost part (600–230 cm depth), the sediments are unstratified silty clay and fine sands with dark black coloration and exuding a strong smell of organic decay,

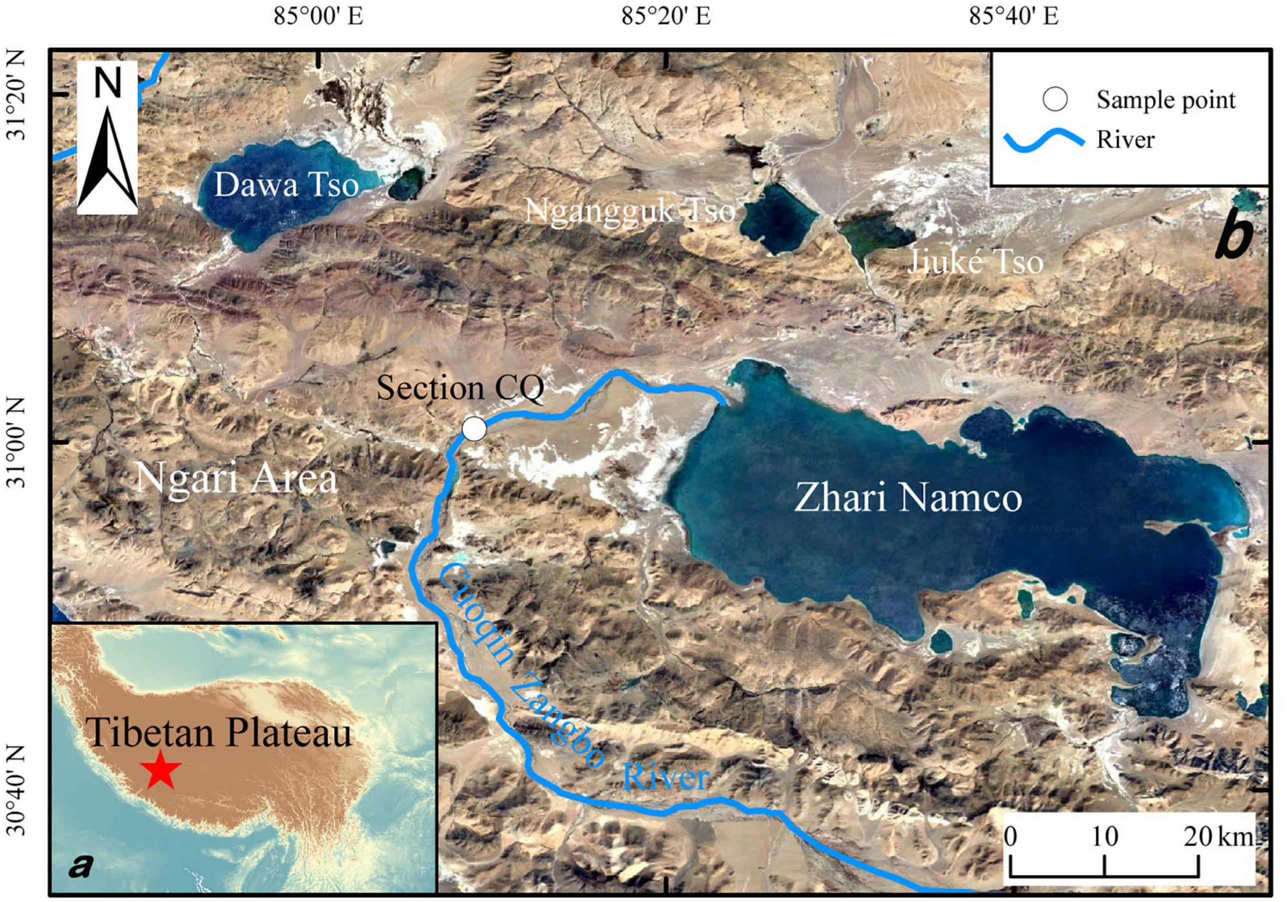

FIGURE 1 | (a) Location of Zhari Namco Lake within the Tibetan Plateau. **(b)** The position of section CQ (white circle) investigated in this study.

indicating continuous sedimentation within a deep and stable lake environment (**Figure 2a**). In the second part (230–150 cm depth), the sediments change from blackish to grayish medium-fine sands (**Figure 2b**). The third part (150–130 cm depth) is comprised of a layer of well-sorted, yellowish to grayish, medium-fine sands, indicating they were deposited at or near the lake shoreline (**Figure 2c**). The sediments of the fourth part (130–70 cm depth) consist of coarse sands and pebbles, which are round or dish-shaped with a long axis of 0.5 cm to 3 cm, indicative of a high-energy shoreline deposit (**Figure 2d**). Within the uppermost part (70–0 cm depth) the sediment is characterized by slope wash and colluvial deposits composed of soils and angular rock pieces (**Figure 2C**).

Samples for OSL dating were collected from both CQ subsections. The vertical sections were first cleaned and polished to ensure access to freshly exposed sediments. Stainless steel tubes (6 cm in diameter and 30 cm in length) were then inserted into the profile to obtain the samples. Once extracted from the profile, both the ends of the tube were immediately sealed by cotton and wrapped with dark-colored tape before being sealed in a black plastic bag in order to avoid light exposure and water loss. A total of five OSL samples were collected from section CQ (**Figure 2**). Additionally, radiocarbon dating samples were collected from the middle-lower parts of the profile. They included eight aquatic plant leaves along with a terrestrial plant twig (**Figure 3**), as well as three BOM samples.

OSL DATING

Sample Preparation and Measurement

We selected quartz as the dating material due to the ease with which it can be bleached compared to feldspar. All OSL sample preparation and luminescence measurements were conducted under subdued red light in the Luminescence Dating Laboratory at the Qinghai Institute of Salt Lakes, Chinese Academy of Sciences. Then the outer 3 cm of sediment at the end of each steel tube were scraped away and reserved for measurements of water content and environmental dose rate. The unexposed middle section of the tube was used for equivalent dose (D_e) determination. The five raw samples were first treated with 10% HCl and 30% H_2O_2 to remove carbonates and organic materials, followed by wet sieving to obtain three fractions: grains smaller than 38 μm, middle-grained quartz (MG, 38–63 μm), and coarse-grained quartz (CG, 90–125 μm). All grains smaller than 38 μm were treated in glass cylinders using Stokes' law in order to

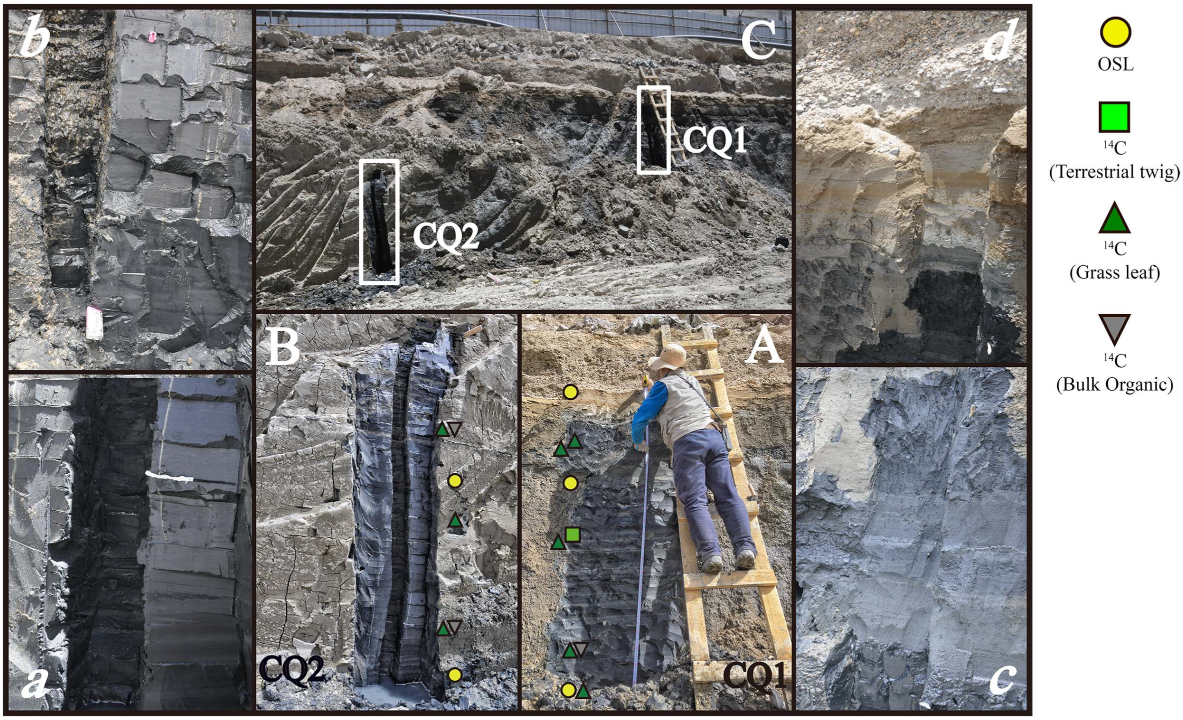

FIGURE 2 | Profile of section CQ. **(A)** section CQ1, **(B)** section CQ2, and **(C)** overall profile of section CQ. **(a–d)** are details of section CQ.

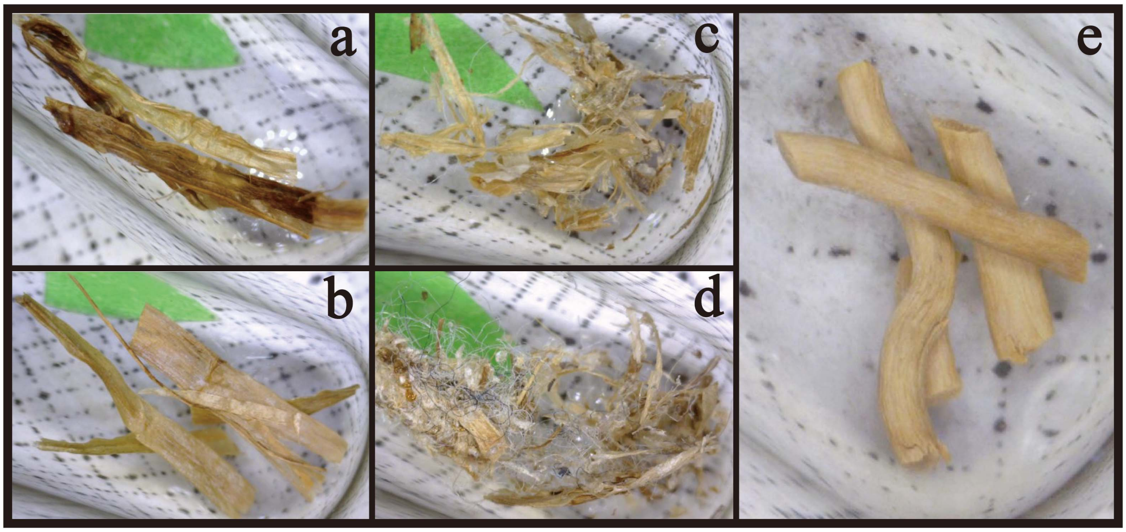

FIGURE 3 | Photos of radiocarbon dating samples. **(a–d)** Are aquatic plant remnants, **(e)** is terrestrial plant remnants.

obtain fine-grained quartz (FG, 4–11 μm). The MG and FG were treated with silica saturated fluorosilicic acid (H_2SiF_6) for about 2 weeks, whereas the CG was etched with 40% HF for 60 min. All three fractions were then treated with 10% HCl to remove any fluorides, followed by the use of a magnet to remove any magnetic minerals. The purity of the isolated quartz was tested via infrared (IR) stimulation, with samples that showed obvious infrared stimulated luminescence (IRSL) signals retreated with H_2SiF_6 or HF again until no obvious IRSL was observed in any sample. We also ensured that all feldspar was removed in order to protect against age underestimation (Duller, 2003; Roberts, 2007; Lai and Brückner, 2008). Finally, we chose sufficient fractions by the content of different grain sizes for D_e measurements (**Table 1**).

The quartz was mounted as a mono-layer on the central part (0.65 cm diameter) of a stainless-steel disc (0.97 cm diameter) using silicone oil. The OSL signal was measured using an

TABLE 1 | Luminescence dating results.

Sample ID	Depth (cm)	Grain size (μm)	K (%)	Th (μg/g)	U (μg/g)	Water content (%)	Dose rate (Gy/ka)	Number of aliquots	D_e (Gy)	Age (ka)	Age model
CQ1-A	145	90∼125	2.83 ± 0.04	16.22 ± 0.7	2.722 ± 0.4	20 ± 5	3.91 ± 0.29	73	8.23 ± 0.27	2.1 ± 0.2	MAM-3
CQ1-B	221	90∼125	2.86 ± 0.04	15.27 ± 0.7	2.21 ± 0.4	20 ± 5	3.74 ± 0.26	68	7.51 ± 0.52	2.0 ± 0.2	MAM-3
CQ1-91	375	38∼63	2.90 ± 0.04	15.12 ± 0.7	2.82 ± 0.4	45 ± 5	2.76 ± 0.20	84	8.50 ± 0.50	3.1 ± 0.3	MAM-3
CQ2-26	445	38∼63	2.93 ± 0.04	17.92 ± 0.7	3.19 ± 0.4	50 ± 5	2.65 ± 0.019	71	11.1 ± 1.04	4.2 ± 0.5	MAM-3
CQ2-60	552	4∼11	2.55 ± 0.04	15.66 ± 0.7	6.14 ± 0.5	60 ± 5	2.35 ± 0.15	65	12.09 ± 0.41	5.1 ± 0.4	MAM-3

automated Risø TL/OSL-DA-20 reader. Laboratory irradiation was carried out using ^{90}Sr/^{90}Y sources mounted within the reader, with a dose rate of 0.086 Gy/s. The OSL signal was obtained after passage through a U-340 filter, while the IRSL signal was detected using a photomultiplier tube with the IRSL passing through BG-39 and coring-759 filters.

The environmental dose rate was calculated by measuring the radioactive element concentrations of surrounding sediments with a small contribution from cosmic rays. For all samples, U and Th concentrations and K contents were determined using inductively coupled plasma mass spectrometry (ICP-MS) analysis at the Institute of Earth Environment, Chinese Academy of Sciences in Xian. The cosmic ray dose was estimated for each sample as a function of depth, elevation, and geomagnetic latitude (Prescott and Hutton, 1994). The water content was calculated from sample weights measured before and after drying in an oven. The measured water contents of three deep lake samples CQ1-91, CQ2-26, and CQ2-60 were 43.8, 48.1, and 61.8%, respectively, and for the two shoreline samples CQ1-A and CQ1-B, the measured water contents were 20.5 and 19.7%, respectively. Due to water content variability during the burial period and based on the measured water content, approximations of measured water content were used to calculate OSL ages; an error of 5% of the measured water content was applied given the uncertainty of water changes in the lake sediments after burial (**Table 1**). The α-value for fine-grained quartz and middle-grained quartz was taken as 0.035 ± 0.003 (Lai et al., 2008). Radionuclide concentrations, water content, and dose rates are summarized in **Table 1**. Lastly, we converted the elemental concentrations into annual dose rates according to Aitken (1998).

Luminescence Characteristics

The equivalent dose for each sample was measured using the single aliquot regenerative dose (SAR) protocol (Murray and Wintle, 2000). For each sample, at least 65 aliquots were measured by SAR. The OSL signal was calculated using the integral of the initial 0.64 s of the OSL signals minus the last 8 s. The characteristics of the quartz luminescence growth and decay curves for sample CQ1-A and CQ2–60 are shown in **Supplementary Figure 1**. It is important to investigate the influence of preheating on the charge transfer from light-insensitive traps to light-sensitive ones, a process called thermal transfer (Aitken, 1998). To select the appropriate preheat conditions for D_e determination using the SAR protocol, a preheat temperature plateau test was conducted for samples CQ1-A and CQ1-B. Preheat temperatures from 140 to 240°C at 20°C intervals for 10 s were tested and the cut-heat was 140°C for 10 s, using a heating rate of 5°C/s. As a plateau was observed from 160 to 200°C, we therefore selected a preheat temperature of 200°C for routine D_e determination (**Supplementary Figure 2**). The suitability of the SAR procedure for D_e determination was further checked with a "dose recovery test" (Murray and Wintle, 2003). The dose recovery test was performed on sample CQ1-A. Six natural aliquots were stimulated for *c.* 56 h under direct sunlight. The aliquots were then given a laboratory dose of 9.2 Gy, close to the natural D_e (9.19 Gy). The measured D_e was 9.4 ± 1.8 Gy. Thus, the ratio of the measured to the given D_e was *c.* 1.02, suggesting that the SAR conditions were appropriate for D_e determination.

For OSL age calculation, because the sediments in nearby lakes within the TP did not experience long-distance transport or multiple sedimentation-transportation cycles, samples drawn from these lakes may be partially bleached, and the stimulated signal intensities will be low when compared with sediments from other regions, such as the Chinese Loess Plateau (Lee et al., 2009). To reduce this impact, CQ1–90 removed one test aliquot with abnormal data, CQ2–60 and CQ2–26 removed two test aliquots with abnormal data. Because each sample had at least 65 aliquots, the influence of removed data on the results could be ignored. The abnormal data did not occur in CQ1-A and CQ1-B. **Supplementary Table 1** shows the raw data for D_es. Moreover, Arnold et al. (2007) proposed the single-aliquot age selection model to determine whether the 3-parameter minimum-age model (MAM-3) or the central-age model (CAM) was applied to calculate the D_es. We used the R-language-based luminescence data analysis package "numOSL" to select the suitable age model (Peng et al., 2013), with all the samples' D_es ultimately determined using MAM-3 (**Table 1**).

RADIOCARBON DATING

Radiocarbon dating of 12 samples took place at Beta Analytic Inc. (Miami, FL, United States). Eight samples were APR, three samples were BOM, and the final sample was a terrestrial plant twig. Three samples (BOM) were simply treated with acid washes to remove any carbonates, whereas the nine plant samples were pre-treated with acid/alkali/acid to remove carbonates and mobile humic acids. They were then subjected to accelerator mass spectrometry (AMS) to measure their ^{14}C ratios. The calibration of ^{14}C dates was performed using the "CALIB 8.1.0" program (Stuiver et al., 2021) and the IntCal20 calibration curve (Reimer et al., 2020). The ^{13}C/^{12}C ratios (δ^{13}C, ‰) of all dating materials were measured using an isotope ratio mass spectrometer (IRMS). All ^{14}C ages from section CQ are summarized in **Table 2**. Radiocarbon ages and OSL ages are shown together against the depth scale in **Figure 4**.

RESULTS AND DISCUSSION

OSL Ages

Our results showed that the ages for all five OSL samples increased with respect to their depth within the section, indicating that these lacustrine sediments were deposited between 5 and 2 ka BP (**Table 2**). The uppermost sample CQ1-A, just below the paleo-shoreline deposits, returned an OSL age of 2.1 ± 0.2 ka BP. Accordingly, the oldest OSL age was 5.1 ± 0.4 ka BP, which was from the sample collected from the bottom of section CQ (**Figure 2** and **Table 2**). The ages of the three mid-depth samples collected from 220, 375, and 445 cm were 2.0 ± 0.2 ka BP, 3.1 ± 0.3 ka BP, and 4.2 ± 0.5 ka BP, respectively (**Table 2**). We suggest that the lake level was higher than section CQ (4,664 m) during the interval from 5.1 to 3.1 ka BP on account of the lacustrine nature of the sediments, and because the paleo-shoreline deposits within the upper part of the section were deposited at *c.* 2 ka BP—the lake has further regressed since then. Our speculation is consistent with previous research indicating that the lake level of Zhari Namco declined by 42.5 m between 3.9 and 2.0 ka BP (from 4,680.6 to 4,637.9 m) (Chen et al., 2013).

Equivalent Dose and Dose Rate of OSL Ages

During the deposition process, the OSL signal bleaching degree is the key factor affecting the accuracy of D_e determination in lacustrine sediments. In different minerals, quartz is more easily bleached than feldspar (Long et al., 2010). According to the OSL dating results from other lacustrine sediments within the TP (Long et al., 2012), the OSL signal of lacustrine sediments was well bleached during the deposition. In our study, the OSL signal quickly decreased to background levels within the first 2 s (**Supplementary Figure 1**), indicating that it was dominated by the fast component (Singarayer and Bailey, 2003). It also suggested that the quartz in our samples was relatively bright, which should have bleached easily when the grains were exposed to sunlight. Even so, our samples showed broad D_e distributions that may have been heterogeneously bleached before deposition (**Supplementary Figure 3**). To mitigate the influence of partial bleaching on age estimation, we used MAM-3 to calculate D_es. Moreover, in D_e determination using the SAR protocol, inaccuracies may have been caused by improper heating conditions. However, dose recovery tests and preheat temperature plateau tests showed that D_es was measured correctly for all samples from the CQ section using the SAR protocol (Aitken, 1998; Murray and Wintle, 2003). Therefore, we concluded that the OSL dating correctly measured and calculated D_e in this study.

The dose rate is determined by the content of the radionuclides in the sediments. It is usually assumed the dose rate of a sample is constant during the burial period in OSL dating (Zhang et al., 2007). Cupper (2006) measured sediment radioactivity from three salt lakes within southeastern Australia, finding it was in secular equilibrium from one of the salt lakes. Sediment radioactivity was in disequilibrium in the other two salt lakes, but this had a minimal effect on the dose rate. As shown in **Table 1**, the radionuclides contents of our samples were roughly constant, similar to other lacustrine sediments within the TP (Long et al., 2014; Hu et al., 2017). This suggests that radionuclides disequilibrium was likely to be absent in our samples (Long et al., 2015).

Water content is also the main factor affecting dose rate except for radionuclides. The water molecules in the sediments will absorb some radiation energy from the environment, reducing the absorption of the radiation energy by the sediments themselves (Zhang et al., 2007). In the field, we found that sediments in the profile were well preserved in a permanently frozen condition (the elevation of the site was *c.* 4,664 m), the water content was stable throughout their burial stage, and

TABLE 2 | Radiocarbon dating results.

Lab code	Sample code	Depth (cm)	Materials	δ^{13}C (‰)	Pmc	Conventional ^{14}C age (a BP)	Calibrated 2σ age range* (Cal a BP)
Beta-498519	CQ1-24	178	Grass leaf	−8.7	58.19 ± 0.22	4,350 ± 30	4,849–5,027
Beta-498520	CQ1-27	184	Grass leaf	−10.7	56.90 ± 0.21	4,530 ± 30	5,052–5,313
Beta-498521	CQ1-61	258	Terrestrial twig	−23	61.62 ± 0.23	3,890 ± 30	4,189–4,417
Beta-498522	CQ1-88B	339	Bulk organic	−23.1	46.04 ± 0.17	6,230 ± 30	7,011–7,253
Beta-498523	CQ2-16G	400	Grass leaf	−11.5	57.11 ± 0.21	4,500 ± 30	5,046–5,301
Beta-498524	CQ2-16B	400	Bulk organic	−22.4	43.92 ± 0.16	6,610 ± 30	7,431–7,569
Beta-498528	CQ2-2B	525	Bulk organic	−21.8	45.19 ± 0.17	6,380 ± 30	7,177–7,421
Beta-499906	CQ1-88G	339	Grass leaf	−4.3	56.97 ± 0.21	4,520 ± 30	5,051–5,309
Beta-501268	CQ1-64	267	Grass leaf	−9	56.05 ± 0.21	4,650 ± 30	5,315–5,466
Beta-501269	CQ1-100	375	Grass leaf	−7.3	55.64 ± 0.21	4,710 ± 30	5,324–5,575
Beta-501270	CQ2-1	475	Grass leaf	−15.5	55.08 ± 0.21	4,790 ± 30	5,475–5,588
Beta-501271	CQ2-2G	525	Grass leaf	−9.5	52.61 ± 0.20	5,160 ± 30	5,766–5,994

**The ^{14}C ages were calibrated to calendar years using the CALIB 8.1.0 program (Stuiver et al., 2021) with the internationally agreed IntCal20 data set (Reimer et al., 2020).*

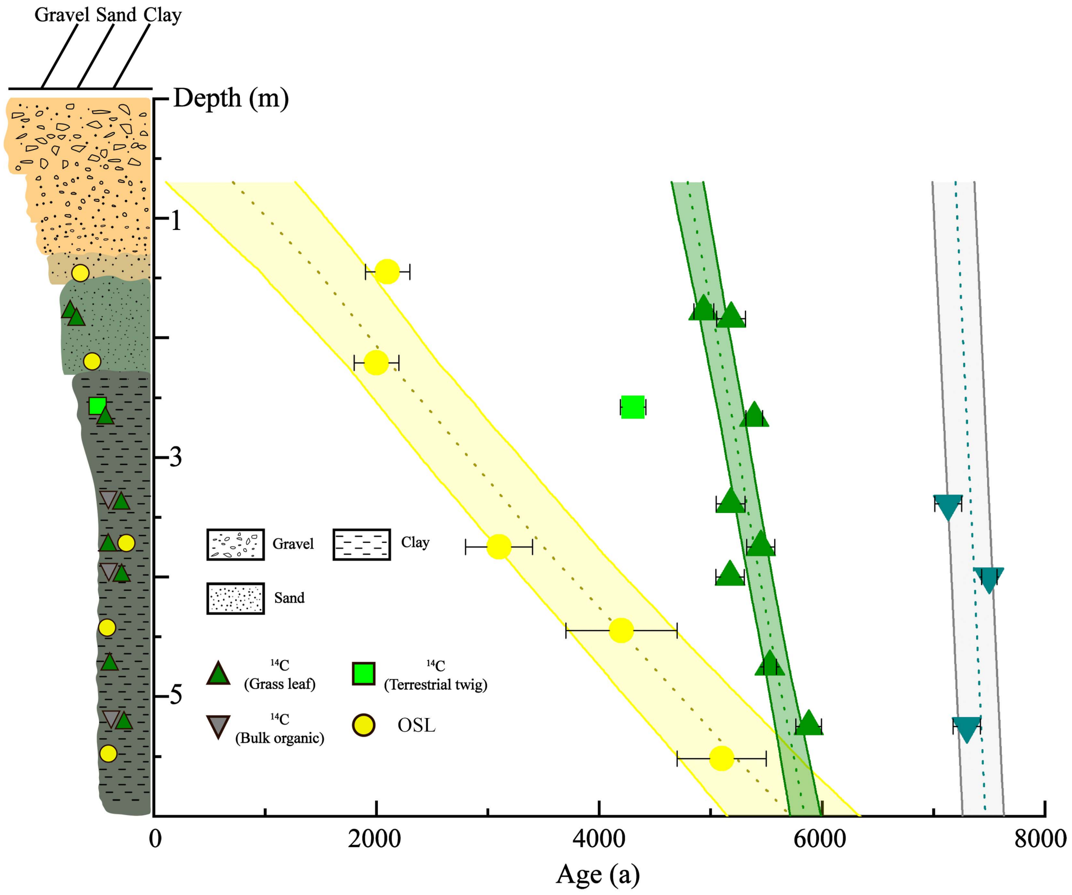

FIGURE 4 | Stratigraphy of the lacustrine sediment sequences and the ages of section CQ discussed in the text. The three shaded areas are the age-depth models of lacustrine sediment. The yellow shaded area is the OSL age-depth model, and the green and gray shaded areas are the age-depths of aquatic plant remnants and bulk organic matter, respectively. Three dotted lines are the median ages. Because there was only one ^{14}C age of TPR, we did not use it to build the age-depth model.

no evidence of a disturbance was observed from the structural features of the profile. Therefore, the measured water content at present could represent the real water content of sediments from section CQ during the burial period.

^{14}C Ages

The twig, with a depth of 258 cm (CQ1–61), had a ^{14}C age of 4,189–4,417 Cal a BP. The aquatic plant leaf, although coming from a similar depth of 267 cm (CQ1–64), returned a ^{14}C age of 5,315–5,466 Cal a BP. Moreover, at depths of 339, 400, and 525 cm, the ^{14}C ages of these aquatic plant leaf samples were 5,051–5,309, 5,046–5,301, and 5,766–5,994 Cal a BP, respectively. However, at a similar depth, the ^{14}C ages of BOM were 7,011–7,253, 7,431–7,569, and 7,177–7,421 Cal a BP. The rest of aquatic plant leaves were sampled at depths of 178, 184, 375, and 475 cm, with reported ^{14}C ages of 4,849–5,027, 5,052–5,313, 5,324–5,575, and 5,475-5,588 Cal a BP, respectively.

^{14}C Ages of Terrestrial Plant Remnants

In general, the ^{14}C ages of TPR are not affected by LRE, and their ages are often considered to be consistent with those of the sedimentary horizons in which they are found (Hou et al., 2012). However, the ^{14}C age of the terrestrial twig (CQ1–61, 4,372 a) was roughly 2.3 ka older than the OSL sample (CQ1-B, 2.0 ± 0.2 ka BP) taken at a similar stratigraphic depth in section CQ. It is worth noting, however, that this discrepancy could possibly be explained due to a delay between the death of the twig and its ultimate transportation to, and burial within, the lacustrine sediments of the lake (Chen et al., 2017).

^{14}C Ages of Aquatic Plant Remnants

As shown in **Table 2** and **Figure 4**, the ^{14}C ages of APR were older than the OSL ages at similar depths, an inconsistency that was possibly due to the influence of LRE. This line of reasoning is supported, firstly, by the massive marine carbonate rocks which are widely distributed throughout the Coqen Basin (Zhong et al., 2010). These rocks have been eroded by precipitation runoff recharge and glacial meltwater from the catchment area, which enters the lake as dissolved inorganic carbon (DIC). In addition to DIC, dissolved organic carbon (DOC) and particulate organic carbon (POC) enters the lake by various means (Chen H. et al., 2019; Meng et al., 2020), with some underground brine water also infiltrating the lake via underlying faults (Fontes et al., 1996). Secondly, Zhari Namco is centrally located within the TP, which is one of the coldest and most arid regions. Extensive evaporation has resulted in a high concentration of carbon ions in the water, with the lake struggling to maintain equilibrium with atmospheric carbon (Zhou et al., 2020). Aquatic plants are therefore absorbing greater quantities of old or dead carbon (Olsson, 2009; Meng et al., 2020), possibly leading to inflated age estimates.

^{14}C Ages of Bulk Organic Matter

The ^{14}C ages for BOM were consistently older than that of OSL and ^{14}C ages for APR of similar depth (**Figure 4**). However, determining the precise LRE to explain this discrepancy was complicated by the complex nature of BOM. Firstly, in addition to the carbon disequilibrium between water and atmosphere, as well as the abundance of old and dead carbon from the catchment area, microalgae and bacteria which lived in Zhari Namco represent yet another source of LRE affecting BOM (Meyers and Ishiwatari, 1993; Li et al., 2015; Chen H. et al., 2019). Secondly, bulk masses of terrestrial organic matter and external POC can be directly deposited without dissolution in lacustrine sediments, which can also produce inflated ^{14}C age estimates for BOM (Meng et al., 2020). Moreover, HCL washing, which is typically used to remove carbonate during the preparation of BOM samples, sometimes has the unintended corollary of mixing carbonate remnants into the organic material, which can also make the age of the sample appear older than it actually is (Harkness, 1975; Gilet-Blein et al., 1980). However, because all ^{14}C samples were pretreated and dated in Beta's laboratory, we did not know the exact details for this performance, hence this factor could not easily be estimated in this study. In conclusion, the ^{14}C ages of BOM from Zhari Namco were also clearly subject to a host of LRE, and caution should be taken before drawing inferences from ^{14}C ages based on this material.

Implications for Lacustrine Sediments Dating in Zhari Namco

Although the error margins for radiocarbon dating are lower compared with luminescence dating, and TPR are generally exempt from the influence of LRE (Hou et al., 2012), TPR are nonetheless rare in the lacustrine sediments of the TP due to low vegetation cover. Additionally, as terrestrial plants typically grow on the land surrounding the lake, they are not necessarily deposited directly into the lake upon death. This means that the timing of both their death and their retention on land remains uncertain (Chen et al., 2017), further illustrating the caution required when using the ^{14}C ages of TPR. Most ^{14}C ages from loess sediments (Wang et al., 2014; Song et al., 2015; Song et al., 2017; Cheng et al., 2019) have underestimated ages. In contrast, due to the effects of LRE, the ^{14}C ages of APR and BOM are overestimated in Zhari Namco. This phenomenon has also been

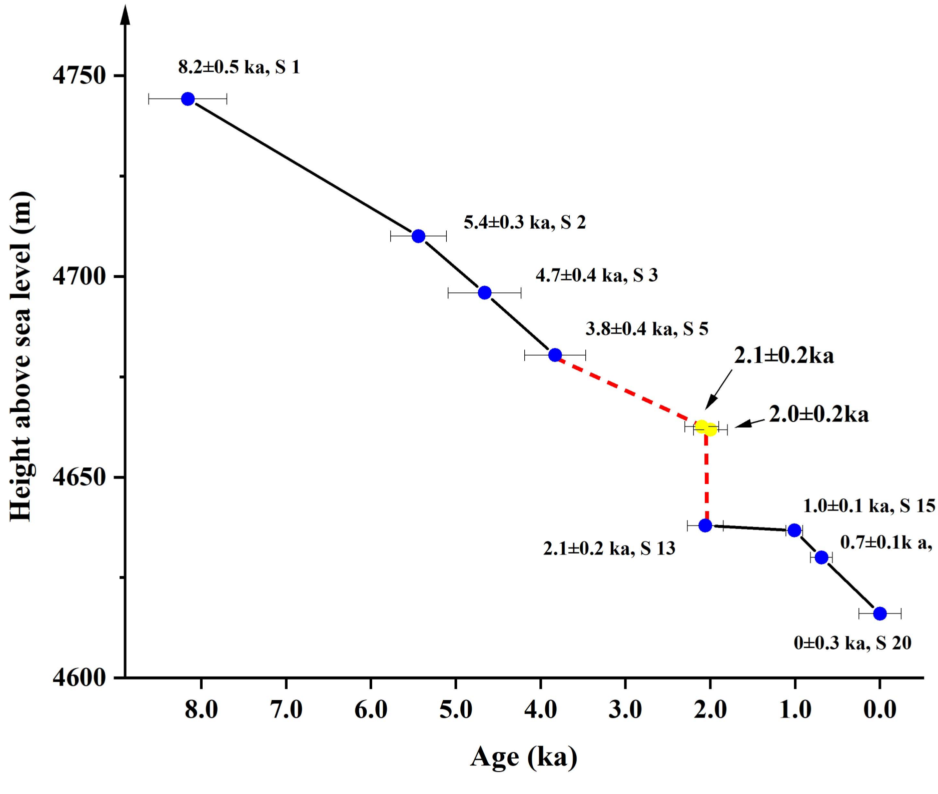

FIGURE 5 | OSL ages plotted against elevation for the 10 paleo-shorelines sediments of Zhari Namco. Blue circles are the ages of each shoreline from Chen et al. (2013). Yellow circles are the OSL ages of the CQ section.

observed in QingHai Lake (Meng et al., 2020), Tangra Yumco (Long et al., 2014), and Linggo Co (Hu et al., 2017), all of which contain BOM with ^{14}C ages older than that of stratigraphically associated aquatic plant material, and all ^{14}C ages of APR and BOM appearing older than its actual age.

OSL dating is not affected by the LRE of lacustrine sediments. The equivalent dose and dose rate used in the calculation of OSL age in this study were reliable. The OSL ages were in stratigraphic sequence order, with no age reversals, and we used MAM-3 to mitigate the influence of partial bleaching on age estimation and to make sure that any overestimation of the equivalent dose had less impact on OSL ages (Peng et al., 2013; Shi et al., 2017). An age-depth model for the CQ section's lacustrine sediments was established using the Bacon age-depth modeling package in "R" software (Blaauw and Christen, 2011) for five OSL ages, eight ^{14}C ages of APR, and three ^{14}C ages of BOM. As shown in **Figure 4**, age-depth model for OSL calculations found that for the ^{14}C ages of APR and ^{14}C ages of BOM, the average sedimentation rates of section CQ section *c.* 1.06 mm·a^{-1}, *c.* 5.03 mm·a^{-1}, *c.* 19.8 mm·a^{-1}. The average sedimentation rate was *c.* 1.03 mm·a^{-1} within Linggo Co (Hu et al., 2017), which was also similar to the average sedimentation rate found by using OSL age from section CQ. Due to this convergence in multiple lines of evidence, we are confident of the general reliability of OSL ages in section CQ.

The chronology framework for a series of paleo-shorelines and section CQ in Zhari Namco showed that lake level dropped by 128 m since *c.* 8.2 ka BP (Chen et al., 2013) (**Figure 5**). Notably, there was a "dog-leg" change in **Figure 5**. Based on the OSL ages and the sedimentary facies of section CQ, the sediments from the bottom experienced continuous sedimentation within a deep and stable lake environment. As depth decreased, sediments changed to a high-energy shoreline deposition (**Figure 4**). This meant that the lake level of Zhari Namco dropped rapidly between *c.* 5.1 ka BP and *c.* 2.0 ka BP, which was also consistent with a similarly rapid decline in the levels of Seling Co Lake and Zabuye Lake—reported as occurring during the late Holocene (Shi et al., 2017; Jonell et al., 2020). Therefore, we suggested that the rapidly dropping lake level caused the "dog-leg" change. Another possible cause might be that section CQ was located at the mountainous area far from the lakefront area, with undulating landforms and significant elevation change.

The major reason behind the dropping lake level may have been the weakening Indian summer monsoon, which caused the climate in Zhari Namco to change from relatively warm-humid to cold-arid during this period (Chen et al., 2013). Because of this, the recharge of the catchment area into the lake also underwent a gradual decrease during this period. Moreover, it was clear that the RAs were not constant, neither in APR nor in BOM (**Figure 6**). This was probably related to the drop in lake level. From stratigraphy and age fluctuation, during *c.* 5.1 ka BP to *c.* 2 ka BP, Zhari Namco experienced a drop in lake level. With this decrease, the RAs of APR increased from *c.* 0.1 ka to *c.* 4.1 ka

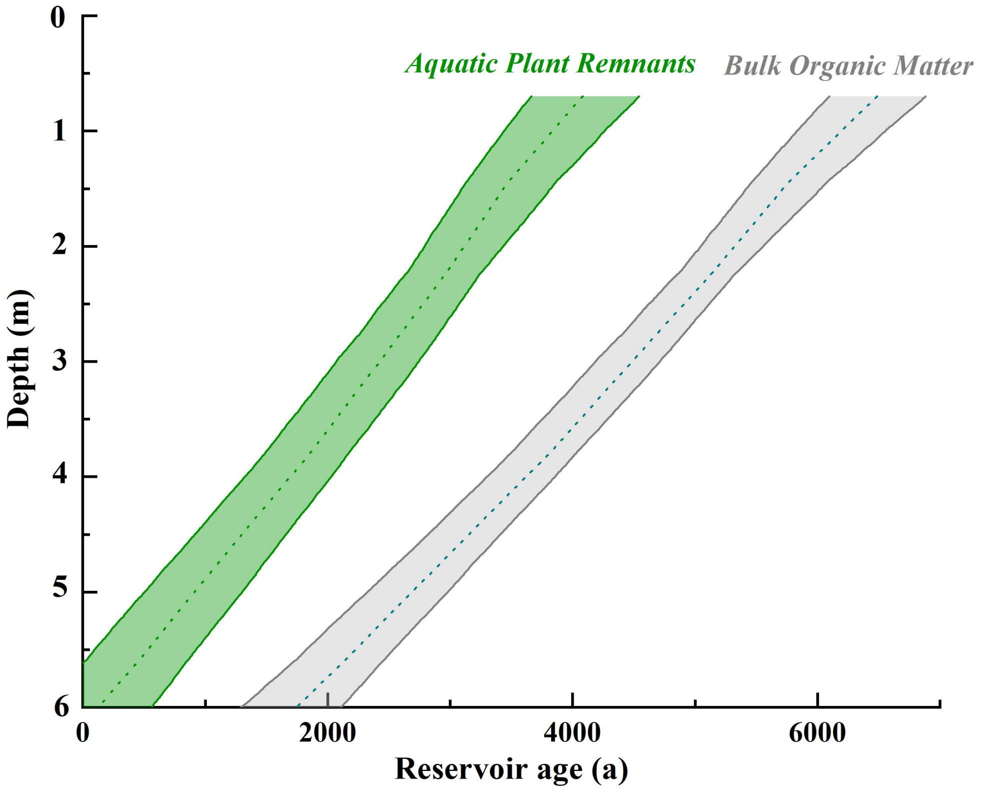

FIGURE 6 | The two shaded areas are the RAs-depth models. The green shaded area is the RAs-depth model for aquatic plant remnants, the gray shaded area is the RAs-depth of bulk organic matter. The two dotted lines represent the RAs median values.

(6–0.7 m core depth), and the RAs of BOM increased from *c.* 1.7 ka to *c.* 6.5 ka (6–0.7 m core depth). We suggest that the major contributor to LRE variation in Zhari Namco is salinity. Salinity, in addition to being associated with climate-driven fluctuations in lake capacity and level (Fontes et al., 1996; Wu et al., 2007), has been tightly influenced by changes in carbon ion concentration (Xu et al., 2006; Lei et al., 2010; Li and Liu, 2012, 2014; Li et al., 2015; Batanero et al., 2017; Zhou et al., 2020), causing RAs to increase or decrease in different periods. During warm-humid periods and the attendant increase in lake capacity and water level, lake desalination would occur, which, accompanied by a decrease in carbon ion concentration (Yu et al., 2016), caused a concomitant decrease in RAs. However, the opposite situation occurred during cold-arid periods, which caused RAs to increase. Similar results were found in Qinghai Lake: Chongyi et al. (2018) suggested that the highest RAs may have occurred when the lake had its highest salinity and lowest water levels. In addition, the RAs of BOM were greater than APR, possibly due to the increased complexity of the LRE sources acting on it (Gilet-Blein et al., 1980). Either way, because of the noted influence of LRE, the ^{14}C age estimates of APR and BOM cannot be considered to be wholly accurate.

CONCLUSION

In this study, radiocarbon and OSL dating were used to date lacustrine sediments from Zhari Namco Lake in the southern Tibetan Plateau. Through the comparison and analysis of ^{14}C and OSL ages, we found that the OSL dating can produce reliable ages and has good potential for lacustrine sediments dating. By contrast, even though ^{14}C dating is a mature dating method with high accuracy for dating lacustrine sediments, ^{14}C ages of both aquatic plants remnants and BOM are negatively impacted by LRE, which can lead to apparent ^{14}C ages being older than their actual ages. During warm-humid periods/cold-arid periods, RAs decrease/increase in response to higher/lower water levels, indicating that fluctuating that RA values are clearly associated with variations in the overarching hydrological regime. Due to the multitude of factors affecting LRE, it can be difficult to obtain reliable ages from APR and BOM, especially as the timing of both the death and ultimate deposition of terrestrial plants is often impossible to establish. In summary, OSL ages were more reliable than ^{14}C ages in this study. Accordingly, we suggest that radiocarbon dating alone may be inappropriate for dating lacustrine sediments and that OSL dating could be applied when evaluating the reliability of ^{14}C ages. Only by exploring areas of agreement and disagreement between multiple dating methods can we work toward building an accurate chronological framework for lacustrine sediments within the TP.

DATA AVAILABILITY STATEMENT

The original contributions presented in the study are included in the article/**Supplementary Material**, further inquiries can be directed to the corresponding author/s.

AUTHOR CONTRIBUTIONS

LC designed the research. LC, YW, XZ, TC, DG, and FA performed the research. LC and YW analyzed the data and wrote the manuscript. All authors contributed to the article and approved the submitted version.

FUNDING

This work was funded by the Second Tibetan Plateau Scientific Expedition and Research Program (2019QZKK0202) and the National Natural Science Foundation of China (41671006) to X.-J. Liu, the Science and Technology foundation Platform Project of Qinghai Province (2018-ZJ-T10), and the Science and Technology program of Qinghai Province (2018-ZJ-723).

ACKNOWLEDGMENTS

We thank two reviewers for their valuable suggestions and comments on the manuscript. Furthermore, we thank X.-J. Liu who firstly designed and guided the performance of this study; Aijun Sun and Jun Zhou for their help in the field; and Guoqiang Li, Jun Peng, and He Yang for help with analysis of the data.

SUPPLEMENTARY MATERIAL

The Supplementary Material for this article can be found online at: https://www.frontiersin.org/articles/10.3389/feart.2021.640172/full#supplementary-material

Supplementary Figure 1 | Characteristics of quartz luminescence growth curves and decay curves of samples CQ1-A and CQ2–60.

Supplementary Figure 2 | Preheat plateau test results for 90–125 μm quartz in samples CQ1-A and CQ1-B.

Supplementary Figure 3 | Radial plots showing distributions of equivalent dose (D_e) and uncertainties of the OSL samples.

Supplementary Table 1 | The raw data for equivalent dose (D_e) determination; the red numbers indicate abnormal data, which were removed before further analysis.

REFERENCES

Aitken, M. J. (1998). *An Introduction to Optical Dating*. Oxford: Oxford University Press.

An, F. Y., Liu, X. J., Zhang, Q. X., Wang, Y. X., Chen, T. Y., Yu, L. P., et al. (2018). Drainage geomorphic evolution in response to paleoclimatic changes since 12.8 ka in the eastern Kunlun Mountains, NE Qinghai-Tibetan Plateau. *Geomorphology* 319, 117–132. doi: 10.1016/j.geomorph.2018.07.016

Arnold, L. J., Bailey, R. M., and Tucker, G. E. (2007). Statistical treatment of fluvial dose distributions from southern Colorado arroyo deposits. *Quat. Geochronol.* 2, 162–167. doi: 10.1016/j.quageo.2006.05.003

Ascough, P., Cook, G. T., Kinch, H., Dunbar, E., Church, M. J., Einarsson, A., et al. (2011). An Icelandic fresh-water radiocarbon reservoir effect: implications for lacustrine 14C chronologies. *Holocene* 21, 1073–1080. doi: 10.1177/0959683611400466

Batanero, G. L., León-Palmero, E., Li, L. L., Green, A. G., Rendón-Martos, M., Suttle, C. A., et al. (2017). Flamingos and drought as drivers of nutrients and microbial dynamics in a saline lake. *Sci. Rep.* 7:12173. doi: 10.1038/s41598-017-12462-9

Blaauw, M., and Christen, J. (2011). Flexible paleoclimate age-depth models using an autoregressive gamma process. *Bayesian Anal.* 6, 457–474. doi: 10.1214/ba/1339616472

Chen, F. H., Huang, X. Z., Zhang, J. W., Holmes, J. A., and Chen, J. H. (2006). Humid Little Ice age in arid central Asia documented by Bosten Lake, Xinjiang, China. *Sci. China Ser. D Earth Sci.* 49, 1280–1290.

Chen, H., Zhu, L. P., Ju, J. T., Wang, J. B., and Ma, Q. F. (2019). Temporal variability of 14C reservoir effects and sedimentological chronology analysis in lake sediments from Chibuzhang Co, North Tibet (China). *Quat. Geochronol.* 52, 88–102. doi: 10.1016/j.quageo.2019.02.009

Chen, T. Y., Lai, Z. P., Liu, S. W., Wang, Y. X., Wang, Z. T., Miao, X. D., et al. (2019). Luminescence chronology and palaeoenvironmental significance of limnic relics from the Badain Jaran Desert, northern China. *J. Asian Earth Sci.* 177, 240–249. doi: 10.1016/j.jseaes.2019.03.024

Chen, T. Y., Liu, S. W., Lai, Z. P., Wang, Z. T., Han, F. Q., and Wang, Y. X. (2017). A preliminary study of AMS 14C dating of young lacustrine sediments in the Badain Jaran Desert. *J. Salt Lake Res.* 25, 60–66.

Chen, Y. W., Zhong, Y. Q., Li, B., Li, S. H., and Aitchison, J. C. (2013). Shrinking lakes in Tibet linked to the weakening Asian monsoon in the past 8.2ka. *Quat. Res.* 80, 189–198. doi: 10.1016/j.yqres.2013.06.008

Cheng, P., Burr, G., Zhou, W. J., Chen, N., Hou, Y. Y., Du, H., et al. (2019). The deficiency of organic matter 14C dating in Chinese Loess-paleosol sample. *Quat. Geochronol.* 56:101051. doi: 10.1016/j.quageo.2019.101051

Chongyi, E., Sun, Y. J., Liu, X. J., Hou, G. L., Lv, S. C., Yuan, J., et al. (2018). A comparative study of radiocarbon dating on terrestrial organisms and fish from Qinghai Lake in the northeastern Tibetan Plateau, China. *Holocene* 28, 1712–1719. doi: 10.1177/0959683618788671

Cupper, M. L. (2006). Luminescence and radiocarbon chronologies of playa sedimentation in the Murray Basin, Southeastern Australia. *Quat. Sci. Rev.* 25, 2594–2607. doi: 10.1016/j.quascirev.2005.09.011

Duller, G. A. T. (2003). Distinguishing quartz and feldspar in single grain luminescence measurements. *Radiat. Meas.* 37, 161–165. doi: 10.1016/S1350-4487(02)00170-1

Fontes, J. C., Gasse, F., and Gibert, E. (1996). Holocene environmental changes in Lake Bangong basin (Western Tibet). Part 1: chronology and stable isotopes of carbonates of a Holocene lacustrine core. *Palaeogeogr. Palaeoclimatol. Palaeoecol.* 120, 25–47. doi: 10.1016/0031-0182(95)00032-1

Gilet-Blein, N., Marien, G., and Evin, J. (1980). Unreliability of 14C dates from organicmatter of soils. *Radiocarbon* 22, 919–929. doi: 10.1017/S0033822200010328

Harkness, D. (1975). "The role of the archaeologist in C-14 measurement," in *Radiocarbon: Calibration and Prehistory*, ed. T. Watkins (Edinburgh: Edinburgh University Press), 128–135.

Hou, J. Z., D'Andrea, W. J., and Liu, Z. H. (2012). The influence of 14C reservoir age on interpretation of paleolimnological records from the Tibetan Plateau. *Quat. Sci. Rev.* 48, 67–79. doi: 10.1016/j.quascirev.2012.06.008

Hou, J. Z., Huang, Y. S., Brodsky, C., Alexandre, M. R., Mcnichol, A. P., King, J. W., et al. (2010). Radiocarbon dating of individual lignin phenols: a new approach for establishing chronology of late quaternary lake sediments. *Anal. Chem.* 82, 7119–7126. doi: 10.1021/ac100494m

Hu, G., Yi, C. L., Zhang, J. F., Cao, G. R., Pan, B. L., Liu, J. H., et al. (2017). Chronology of a lacustrine core from Lake Linggo Co using a combination of OSL, 14C and 210Pb dating: implications for the dating of lacustrine sediments from the Tibetan Plateau. *Boreas* 47, 656–670. doi: 10.1111/bor.12291

Jonell, T. N., Aitchison, J. C., Li, G. Q., Shulmeister, J., Zhou, R. J., and Zhang, H. X. (2020). Revisiting growth and decline of late Quaternary mega-lakes across the south-central Tibetan Plateau. *Quat. Sci. Rev.* 248:106475. doi: 10.1016/j.quascirev.2020.106475

Kang, S. G., Wang, X. L., Roberts, M. H., Duller, G. A. T., Song, Y. G., Liu, W. G., et al. (2020). Increasing effective moisture during the Holocene in the semiarid regions of the Yili Basin, Central Asia: evidence from loess sections. *Quat. Sci. Res.* 246:106553. doi: 10.1016/j.quascirev.2020.106553

Lai, Z. P., and Brückner, H. (2008). Effects of feldspar contamination on equivalent dose and the shape of growth curve for OSL of silt-sized quartz extracted from Chinese loess. *Geochronometria* 30, 49–53. doi: 10.2478/v10003-008-0010-0

Lai, Z. P., Zöllerr, L., Fuchs, M., and Brückner, H. (2008). Alpha efficiency determination for OSL of quartz extracted from Chinese loess. *Radiat. Meas.* 43, 767–770. doi: 10.1016/j.radmeas.2008.01.022

Lee, J., Li, S. H., and Aitchison, J. C. (2009). OSL dating of paleoshorelines at Lagkor Tso, western Tibet. *Quat. Geochronol.* 4, 335–343. doi: 10.1016/j.quageo.2009.02.003

Lei, Y. B., Zhang, H. C., Li, S. J., Yang, L. Q., Yao, S. C., Li, C. H., et al. (2010). Variation of 13C value in authigenic carbonates from Zigetang Co, Tibetan Plateau since 1950 AD. *J. Lake Sci.* 1, 143–150. doi: 10.18307/2010.0120

Li, C. G., Zheng, Y., Wang, M. D., Sun, Z., and Jin, C. S. (2021). Refined dating using palaeomagnetic secular variations on a lake sediment core from Guozha Co, northwestern Tibetan Plateau. *Quat. Geochronol.* 62:101146. doi: 10.1016/j.quageo.2020.101146

Li, G. Q., Zhang, H. X., Liu, X. J., Yang, H., Wang, X. Y., Zhang, X. J., et al. (2020). Paleoclimatic changes and modulation of East Asian summer monsoon by high-latitude forcing over the last 130,000 years as revealed by independently dated loess-paleosol sequences on the NE Tibetan Plateau. *Quat. Sci. Rev.* 237:106283. doi: 10.1016/j.quascirev.2020.106283

Li, X. Z., and Liu, W. G. (2012). The stable oxygen isotopic composition of ostracoda Limnocythere inopinata Bird and its possible response to water salinity in Lake Qinghai. *J. Lake Sci.* 24, 623–628. doi: 10.18307/2012.0417

Li, X. Z., and Liu, W. G. (2014). Water salinity and productivity recorded by ostracod assemblages and their carbon isotopes since the early Holocene at Lake Qinghai on the northeastern Qinghai-Tibet Plateau, China. *Palaeogeogr. Palaeoclimatol. Palaeoecol.* 407, 25–33. doi: 10.1016/j.palaeo.2014.04.017

Li, X. Z., Liu, W. G., Zhou, X., Xu, L. M., and Cheng, P. (2015). A 700-year macrophyte productivity record inferred from isotopes of macrophyte remains and bulk carbonates in Lake Koucha, northeast Qinghai–Tibetan Plateau. *Quat. Int.* 430, 32–40. doi: 10.1016/j.quaint.2015.11.053

Liu, W. M., Hu, K. H., Carling, P. A., Lai, Z. P., Cheng, T., and Xu, Y. L. (2018). The establishment and influence of Baimakou paleo-dam in an upstream reach of the Yangtze River, southeastern margin of the Tibetan Plateau. *Geomorphology* 321, 167–173. doi: 10.1016/j.geomorph.2018.08.028

Liu, X. J., and Lai, Z. P. (2013). Optical dating of sand wedges and ice-wedge casts from Qinghai Lake area on the northeastern Qinghai-Tibetan Plateau and its palaeoenvironmental implications. *Boreas* 42, 333–341. doi: 10.1111/j.1502-3885.2012.00288.x

Liu, X. J., Lai, Z. P., Fan, Q. S., Long, H., and Sun, Y. J. (2010). Timing for high lake levels of Qinghai Lake in the Qinghai-Tibetan Plateau since the Last Interglaciation based on quartz OSL dating. *Quat. Geochronol.* 5, 218–222. doi: 10.1016/j.quageo.2009.03.010

Liu, X. J., Lai, Z. P., Madsen, D., Yu, L. P., Liu, K., and Zhang, J. R. (2011). Lake level variations of Qinghai Lake in northeastern Qinghai-Tibetan Plateau since 3.7 ka based on OSL dating. *Quat. Int.* 236, 57–64. doi: 10.1016/j.quaint.2010.08.009

Liu, X. J., Lai, Z. P., Madsen, D., and Zeng, F. M. (2015). Last Deglacial and Holocene lake level variations of Lake Qinghai, northeastern Qinghai-Tibetan Plateau. *J. Quat. Sci.* 30, 245–257. doi: 10.1002/jqs.2777

Liu, X. J., Lai, Z. P., Yu, L. P., Sun, Y. J., and Madsen, D. B. (2012). Luminescence chronology of aeolian deposits from the Qinghai Lake area in the Northeastern Qinghai-Tibetan Plateau and its palaeoenvironmental implications. *Quat. Geochronol.* 10, 37–43. doi: 10.1016/j.quageo.2012.01.016

Liu, X. J., Xiao, G. Q., Chongyi, E., Li, X. Z., Lai, Z. P., Yu, L. P., et al. (2017). Accumulation and erosion of aeolian sediments in the northeastern Qinghai-Tibetan Plateau and implications for provenance to the Chinese Loess Plateau. *J. Asian Earth Sci.* 135, 166–174. doi: 10.1016/j.jseaes.2016.12.034

Liu, X. J., Zhang, X. J., Lin, Y. L., Jin, L. Y., and Chen, F. H. (2019). Strengthened Indian summer monsoon brought more rainfall to the western Tibetan Plateau during the early Holocene. *Sci. Bulletin.* 64, 1482–1485. doi: 10.1016/j.scib.2019.07.022

Liu, X. Q., Dong, H. L., Rech, J. A., Matsumoto, R., Yang, B., and Wang, Y. B. (2008). Evolution of Chaka Salt Lake in NW China in response to climatic change during the Latest Pleistocene–Holocene. *Quat. Sci. Rev.* 27, 867–879. doi: 10.1016/j.quascirev.2007.12.006

Long, H., Haberzettl, T., Tsukamoto, S., Shen, J., Kasper, T., Daut, G., et al. (2014). Luminescence dating of lacustrine sediments from Tangra Yumco (southern Tibetan Plateau) using post-IR IRSL signals from polymineral grains. *Boreas* 44, 139–152. doi: 10.1111/bor.12096

Long, H., Lai, Z. P., Frenzel, P., Fuchs, M., and Haberzettl, T.(2012). Holocene moist period recorded by the chronostratigraphy of a lake sedimentary sequence from Lake Tangra Yumco on the south Tibetan Plateau. *Quat. Geochronol.* 10, 136–142. doi: 10.1016/j.quageo.2011.11.005

Long, H., Lai, Z. P., Wang, N. A., and Li, Y. (2010). Holocene climate variations from Zhuyeze terminal lake records in East Asian monsoon margin in arid northern China. *Quat. Res.* 74, 46–56. doi: 10.1016/j.yqres.2010.03.009

Long, H., Lai, Z. P., Wang, N. A., and Zhang, J. R. (2011). A combined luminescence and radiocarbon dating study of Holocene lacustrine sediments from arid northern China. *Quat. Geochronol.* 6, 1–9. doi: 10.1016/j.quageo.2010.06.001

Long, H., Shen, J., Wang, Y., Gao, L., and Frechen, M. (2015). High-resolution OSL dating of a late Quaternary sequence from Lake Xingkai (NE Asia): chronological challenge of the "MIS 3a Mega-palaeolake"hypothesis in China. *Earth Planet. Sci. Lett.* 428, 281–292. doi: 10.1016/j.epsl.2015.07.003

Meng, B. W., Zhou, A. F., Zhang, Y. C., Song, M., Liu, W. G., Xie, Z. Q., et al. (2020). Downcore variations of carbon reservoir ages linked to lake level changes in northwest China. *Quat. Geochronol.* 60, 101–105. doi: 10.1016/j.quageo.2020.101105

Meyers, P. A., and Ishiwatari, R. (1993). Lacustrine organic geochemistry: anoverview of indicators of organic matter sources and diagensis in lakesediments. *Organ. Geochem.* 20, 867–900. doi: 10.1016/0146-6380(93)90100-P

Mischke, S., Aichner, B., Diekmann, B., Herzschuh, U., Plessen, B., Wünnemann, B., et al. (2010). Ostracods and stable isotopes of a late glacial and Holocene lake record from the NE Tibetan Plateau. *Chem. Geol.* 276, 95–103. doi: 10.1016/j.chemgeo.2010.06.003

Mischke, S., Weynell, M., Zhang, C., and Wiechert, U. (2013). Spatial variability of 14C reservoir effects in Tibetan Plateau lakes. *Quat. Int.* 313-314, 147–155. doi: 10.1016/j.quaint.2013.01.030

Morrill, C., Overpeck, J. T., Cole, J. E., Liu, K., Shen, C., and Tang, L. (2006). Holocene variations in the Asian monsoon inferred from the geochemistry of lake sediments in central Tibet. *Quat. Res.* 65, 232–243. doi: 10.1016/j.yqres.2005.02.014

Murray, A. S., and Wintle, A. G. (2000). Luminescence dating of quartz using and improved single-aliquot regenerative protocol. *Radiat. Meas.* 32, 571–577. doi: 10.1016/S1350-4487(99)00253-X

Murray, A. S., and Wintle, A. G. (2003). The single aliquot regenerative dose protocol: potential for improvements in reliability. *Radiat. Meas.* 37, 377–381. doi: 10.1016/S1350-4487(03)00053-2

Olsson, I. U. (2009). Radiocarbon dating history: early days, questions, and problems met. *Radiocarbon* 51, 1–43. doi: 10.2458/azu_js_rc.51.3477

Peng, J., Dong, Z. B., Han, F. Q., Long, H., and Liu, X. J. (2013). R package numOSL: numeric routines for optically stimulated luminescence dating. *Ancient TL* 31, 41–48.

Prescott, J. R., and Hutton, J. T. (1994). Cosmic ray contributions to dose rates for luminescence and ESR dating: large depths and long-term time variations. *Radiat. Meas.* 23, 497–500. doi: 10.1016/1350-4487(94)90086-8

Reimer, P. J., Austin, W. E. N., Bard, E., Bayliss, A., Blackwell, P. G., Ramsey, C. B., et al. (2020). The IntCal20 Northern hemisphere radiocarbon age calibration curve (0–55 cal kBP). *Radiocarbon* 62, 725–757. doi: 10.1017/RDC.2020.41

Roberts, H. M. (2007). Assessing the effectiveness of the double-SAR protocol in isolating a luminescence signal dominated by quartz. *Radiat. Meas.* 42, 1627–1636. doi: 10.1016/j.radmeas.2007.09.010

Shen, J., Liu, X. Q., Wang, S. M., and Matsumoto, R. (2005). Palaeoclimatic changes in the Qinghai lake area during the last 18,000 years. *Quat. Int* 136, 131–140. doi: 10.1016/j.quaint.2004.11.014

Shen, Z. X., Bloemendal, J., Mauz, B., Chiverrell, R. C., Dearing, J. A., Lang, A., et al. (2008). Holocene environmental reconstruction of sediment-source linkages at Crummock Water, English Lake District, based on magnetic measurements. *Holocene* 18, 129–140. doi: 10.1177/0959683607085604

Shi, X. H., Kirby, E., Furlong, K. P., Meng, K., Robinson, R., Lu, H. J., et al. (2017). Rapid and punctuated Late Holocene recession of Siling Co, central Tibet. *Quat. Sci. Rev.* 172, 15–31. doi: 10.1016/j.quascirev.2017.07.017

Singarayer, J. S., and Bailey, R. M. (2003). Further investigations of the quartz optically stimulated luminescence components using linear modulation. *Radiat. Meas.* 37, 451–458. doi: 10.1016/S1350-4487(03)00062-3

Song, Y. G., Lai, Z. P., Li, Y., Chen, T., and Wang, Y. X. (2015). Comparison between luminescence and radiocarbon dating of late Quaternary loess from the Ili Basin in Central Asia. *Quat. Geochronol.* 30, 405–410. doi: 10.1016/j.quageo.2015.01.012

Song, Y. G., Luo, D., Du, J. H., Kang, S. G., Cheng, P., Fu, C. F., et al. (2017). Radiometric dating of late Quaternary loess in the northern piedmont of South Tianshan Mountains: implications for reliable dating. *Geol. J.* 53:8. doi: 10.1002/gj.3129

Stuiver, M., and Braziunas, T. F. (1993). Modeling atmospheric 14C influences and 14C ages of marine samples to 10,000 BC. *Radiocarbon* 35, 137–189. doi: 10.1017/S0033822200013874

Stuiver, M., Reimer, P. J., and Reimer, R. W. (2021). *CALIB 8.1.0 [WWW program]*. Available online at: http://calib.org (accessed 01 January 2021).

Wang, H., Cui, P., Liu, D. Z., Liu, W. M., Bazai, N. A., Wang, J., et al. (2019). Evolution of a landslide-dammed lake on the southeastern Tibetan Plateau and its influence on river longitudinal profiles. *Geomorphology* 343, 15–32. doi: 10.1016/j.geomorph.2019.06.023

Wang, S. M., and Dou, H. S. (1998). *Chinese Lake Records*. Beijing: Science Press.

Wang, Y., Shen, J., Wu, J., Liu, X. Q., Zhang, E. L., and Liu, E. F. (2007). Hard-water effect correction of lacustrine sediment ages using the relationship between 14C levels in lake waters and in the atmosphere: the case of Lake Qinghai. *J. Lake Sci.* 19, 504–508. doi: 10.18307/2007.0502

Wang, Y. X., Chen, T. Y., Chongyi, E., An, F. Y., Lai, Z. P., Zhao, L., et al. (2018). Quartz OSL and K-feldspar post-IR IRSL dating of loess in the Huangshui river valley, northeastern Tibetan plateau. *Aeolian Res.* 33, 23–32. doi: 10.1016/j.aeolia.2018.04.002

Wang, Y. X., Chen, T. Y., Wu, C., Lai, Z. P., Guo, S. D., and Cong, L. (2019). Formation and evolution of the Xitaijinair Salt Lake in Qaidam Basin revealed by chronology. *Arid Land Geogr.* 42, 876–884. doi: 10.12118/j.issn.1000-6060.2019.04.19

Wang, Z. L., Zhao, H., Dong, G. H., Zhou, A. F., Liu, J. B., and Zhang, D. J. (2014). Reliability of radiocarbon dating on various fractions of loess-soil sequence for Dadiwan section in the western Chinese Loess Plateau. *Front. Earth Sci.* 8, 540–560. doi: 10.1007/s11707-014-0431-1

Wu, Y. H., Wang, S. M., Zhou, L. P., and Sun, Z. B. (2007). Modern reservoir age for 14C dating in DaiHai Lake. *Qua. Sci.* 4, 507–510. doi: 10.3321/j.issn:1001-7410.2007.04.005

Xu, H., Ai, L., Tan, L. C., and An, Z. S. (2006). Stable isotopes in bulk carbonates and organic matter in recent sediments of Lake Qinghai and their climatic implications. *Chem. Geol.* 235, 262–275. doi: 10.1016/j.chemgeo.2006.07.005

Yao, T. D., Thompson, L., Yang, W., Yu, W. S., Gao, Y., Guo, X. J., et al. (2012). Different glacier status with atmospheric circulations in Tibetan Plateau and surroundings. *Nat. Clim. Change* 2, 663–667. doi: 10.1038/nclimate1580

Yu, J. J., Zheng, M. P., Wu, Q., Wang, Y. S., Nie, Z., and Bu, L. Z. (2016). Natural evaporation and crystallization of Bangor salt lake water in Tibet. *Sci. Technol. Rev.* 34, 60–66. doi: 10.3981/j.issn.1000-7857.2016.05.006

Yu, S. Y., Shen, J., and Colman, S. M. (2007). Modeling the radiocarbon reservoir effect in lacustrine systems. *Radiocarbon* 49, 1241–1254. doi: 10.2458/azu_js_rc.49.3016

Zhang, J. F., Zhou, L. P., Yao, S. C., Xue, B., and Wang, X. L. (2007). Radiocarbon and optical dating of lacustrine sediments—a case study in Lake Gucheng. *Quat. Sci.* 4, 522–528. doi: 10.1016/S1872-5791(07)60044-X

Zhang, S., Zhang, J. F., Zhao, H., Liu, X. J., and Chen, F. H. (2020). Spatiotemporal complexity of the "Greatest lake Period" in the Tibetan Plateau. *Sci. Bull.* 65:16. doi: 10.1016/j.scib.2020.05.004

Zhong, Q., Fang, H., Liu, C. W., Li, X. C., Lu, J. Q., and Gao, B. T. (2010). The Paleozoic carbonate rocks depression of Coqen basin: evidence from geophysics on the Qinghai-Tibet Plateau, China. *Geol. Bull. China* 29, 870–879. doi: 10.3969/j.issn.1671-2552.2010.06.009

Zhou, A. F., Chen, F. H., Wang, Z. L., Yang, M. L., Qiang, M. R., and Zhang, J. W. (2011). Temporal change of radiocarbon reservoir effect in Sugan Lake, Northwest China during the Late-Holocene. *Radiocarbon* 51, 529–535. doi: 10.2458/azu_js_rc.51.3514

Zhou, K. E., Xu, H., Lan, J. H., Tan, D. N., Shen, E. G., Yu, K. K., et al. (2020). Variable Late Holocene 14C Reservoir Ages in Lake Bosten, Northwestern China. *Front. Earth Sci.* 7:601503. doi: 10.3389/feart.2020.601503

Zhu, D. G., Meng, X. G., Zhao, X. T., Shao, Z. G., Xu, Z. F., Yang, C. B., et al. (2004). Evolution of ancient large Lake in the Southeast of the Northern Tibetan Plateau. *Acta Geol. Sin.* 78, 982–992. doi: 10.1111/j.1755-6724.2004.tb00220.x

Zhu, L. P., Wu, Y. H., Wang, J. B., Lin, X., Ju, J. T., Xie, M. P., et al. (2008). Environmental changes since 8.4 ka reflected in the lacustrine core sediments from Nam Co, central Tibetan Plateau, China. *Holocene* 18, 831–839. doi: 10.1177/0959683608091801

Conflict of Interest: The authors declare that the research was conducted in the absence of any commercial or financial relationships that could be construed as a potential conflict of interest.

frontiers in Earth Science

ORIGINAL RESEARCH
published: 31 May 2021
doi: 10.3389/feart.2021.682875

Provenance and Climatic Implications of the Middle-Pleistocene Loess Deposit, Southern China

Qingbin Fan[1,2], Jie Liao[1]*, Yan Li[3], Wei Ye[4], Tao Wang[1] and Xiao Feng[1,2]

[1]Key Laboratory of Desert and Desertification, Northwest Institute of Eco-Environment and Resources, Chinese Academy of Sciences, Lanzhou, China, [2]University of Chinese Academy of Sciences, Beijing, China, [3]College of Forestry, Nanjing Forestry University, Nanjing, China, [4]College of Geography and Environmental Sciences, Zhejiang Normal University, Jinhua, China

The middle-Pleistocene Xiashu loess deposit in the lower reaches of the Yangtze River (LRYR), southern China, may yield evidence with significant climatic and environmental significance. However, its provenance remains controversial. In this study, grain size analysis, and quartz grain surface microtextural and morphological observations, enabled comparison of the provenance of loess in the LRYR with those on the Loess Plateau in northern China. The results show that the grain size characteristics of the Xiashu loess do not follow the coarse-fine NW-SE trend in northern China, and the surface microtextures of the quartz grains in the Xiashu loess are distinctly different from those on the Loess Plateau in northern China, indicating that the loess deposits in the two regions have different provenances. The Gobi Desert in inland northwestern China are not considered as the primary provenance of the Xiashu loess. Instead, the adjacent floodplains in the LRYR, the alluvial plains of the Huai River and the Yellow River to the north during glacial periods are suggested as the dominant source materials for the Xiashu loess. Under the background of middle-Pleistocene climate transition (MPT), regional aridity and a strengthened east Asian winter monsoon (driven by global cooling and the rapid uplift of the Tibetan Plateau) were considered as the primary drivers for the development of the Xiashu loess. The sustained eolian loess accumulation represent a regional response of the northern subtropical area of southern China to the MPT global cooling event at around 0.9 Ma.

Keywords: Xiashu loess, eolian, provenance, east Asian winter monsoon, global cooling

Edited by:
Xiangjun Liu,
Northwest Normal University, China

Reviewed by:
Ruijie Lu,
Beijing Normal University, China
Zhiyong Ling,
Chinese Academy of Sciences, China

Correspondence:
Jie Liao
liaojie@lzb.ac.cn

Specialty section:
This article was submitted to Quaternary Science, Geomorphology and Paleoenvironment, a section of the journal Frontiers in Earth Science

Received: *19 March 2021*
Accepted: *07 May 2021*
Published: *31 May 2021*

Citation:
Fan Q, Liao J, Li Y, Ye W, Wang T and Feng X (2021) Provenance and Climatic Implications of the Middle-Pleistocene Loess Deposit, Southern China.
Front. Earth Sci. 9:682875.
doi: 10.3389/feart.2021.682875

INTRODUCTION

Global climate changes and their regional responses are receiving considerable research attention, with Quaternary climate evolution providing an important focus (Liu, 1985; Pye, 1987; Li et al., 2001a; Li et al., 2018a; Purtill et al., 2019; Westerhold et al., 2020). China is a typical monsoon-influenced country, the summer monsoon brings abundant water vapor to the continent, and the winter monsoon entrains and transports large volumes of dust, carrying it to the middle, east and south of China (Ding et al., 2019; Li et al., 2021a; Li et al., 2021b). The eolian dust deposited on the continent thus provides a basis for the reconstruction of environment in China. Such as the thick eolian loess deposit on the Chinese Loess Plateau (CLP) in northern China, which is regarded as a valuable sedimentary archive for Quaternary climate and environment changes. Systematic studies have revealed its sedimentation chronology, provenance, the process causing aridification in

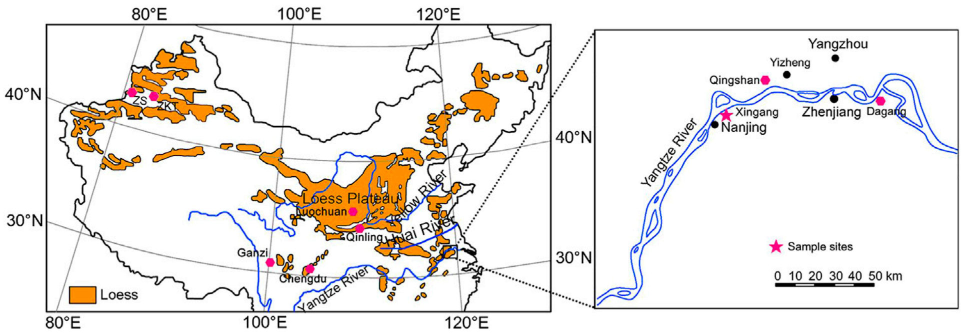

FIGURE 1 | Loess distribution in China (Liu, 1985; Li et al., 2018b) and sampling locations.

northern China and the evolution of the east Asian monsoon climate (Liu, 1985; An et al., 1990; Guo, 2010; Ding et al., 2019). However, Quaternary loess deposits in China are not only distributed on the CLP, but also distributed in the northwest and northeast China, as well as the areas of Nanjing, Zhenjiang and Yangzhou in the lower reaches of the Yangtze River (LRYR) (**Figure 1**). In 1932, Siguang Li and Sen Zhu named the loess in the LRYR as Xiashu Loess according to the loess strata in Xiashu Town, Jiangsu Province (Hao et al., 2010). The Xiashu loess is located at the boundary of northern and southern China, in the north subtropics and at the southeast edge of the loess distribution area in China, a region that is sensitive to climate changes. The occurrence of dust deposition usually indicates an important climatic or environmental change in the source and/or deposition regions (Pye, 1995). Therefore, The development of the eolian Xiashu loess deposit in the LRYR of southern China may yield evidence with significant environmental implications.

Previous studies have focused on grain-size characteristics (Li et al., 1997, Li et al., 2001b; Qiao et al., 2003), environmental magnetism (Zhang et al., 2007, Zhang et al., 2009), clay mineral assemblage (Shi et al., 2005), sedimentary chronology (Qiao et al., 2003; Zhang et al., 2009; Hao et al., 2010; Li et al., 2018b) and chemical weathering (Yang et al., 2004; Chen et al., 2008) in order to study the sedimentary chronology, provenance and environmental significance of the Xiashu loess. In terms of its chronology, due to the limitations in the employed dating methods, dated materials and stratigraphic profiles, this issue has been debated for decades. Firstly some researchers suggested that the Xiashu loess was deposited in the late Pleistocene (Li et al., 1978; Wu, 1985; Zheng, 1999), whereas others suggested that the loess deposit began in the mid Pleistocene (Liu, 1985; Lai et al., 2001; Wu et al., 2006; Zhang et al., 2009). In recent years, new advances in magnetostratigraphy and optically stimulated luminescence (OSL) dating have constrained the age of the lower boundary of the Xiashu loess to approximately 0.9 Ma, representing the oldest age reported to date and is widely accepted (Qiao et al., 2003; Hao et al., 2010; Li et al., 2018b).

With regard to its origin, there are mainly two viewpoints: although eolian origin is becoming increasingly accepted, the material source area of the Xiashu loess remains controversial. A "distant-source" theory believes that the Xiashu loess originated from the Gobi Desert in inland northwestern China, analogous to the loess deposit on the CLP; on the contrary, the "near-source" theory suggests that the loess materials were derived from the adjacent floodplains to the north of the Yangtze River and the Huai River system during glacial periods (Hao et al., 2010; Yang et al., 2017; Li et al., 2018b; Jiang et al., 2020; Wu et al., 2020). Different views on the origin of the Xiashu loess lead to contrasting environmental interpretations. The former interpretation implies that the development of the Xiashu loess was a consequence of increasing aridification in the northwest inland of China, coupled with the intensified east Asian winter monsoon linked to global cooling, uplift of the Tibetan Plateau and the consequent enhancement of the Siberian high pressure (Liu, 1985). The latter view considers the occurrence of the Xiashu loess to be an indicator of aridification in nearby north subtropical regions during glacial periods (Hao et al., 2010; Li et al., 2018b; Jiang et al., 2020). Therefore, identification the provenance of the Xiashu loess could provide new insights into the environmental implications of this valuable sedimentary archive and the driving factors of climate changes in the north subtropics area of southern China.

Aiming at the most controversial problem in study of the Xiashu loess, this paper reports field investigations of the Xingang (XG) profile, a typical Xiashu loess profile in Nanjing on south bank of the Yangtze River. After systematic sampling, the grain-size characteristics and quartz grain surface microtextures were analyzed, interpreted and compared with those on the CLP in northern China in order to find valid evidence for identifying its provenance. Our results may provide further data to support paleoenvironmental reconstruction for the LRYR in southern China.

MATERIALS AND METHODS

The Study Area and Sampling

The Xiashu loess deposit is widespread in the lower reaches of the Yangtze River (LRYR). This area is now situated in a warm-humid north subtropics monsoon climatic zone, with a mean annual precipitation of 1,000–1,200 mm, and a mean annual temperature of 15–17°C (Yang et al., 2017). In most cases, the Xiashu loess covers on the terraces along the Yangtze River and its tributaries.

TABLE 1 | Stratigraphic description of the Xiashu loess profile in XG, Nanjing.

Layer	Depth(m)	color of the loess		description
1	0–3.6	Paleosol	Reddish-brown	Granular structure, loose, contains many plant roots
2	3.6–4.0	Loess	Pale brown	Contains black iron-manganese films, and is more strongly weathered than other loess layers
3	4.0–5.8	Paleosol	Reddish-brown	Granular structure, the upper texture is sticky and the lower texture is loose
4	5.8–9.0	Loess	Pale yellow	The texture is uniform, loose and porous, with vertical joints. Brown films are visible in the lower part
5	9.0–11	Loess	Brownish yellow	The texture is uniform, porous, and denser than the upper layer, with many iron manganese nodules in the lower part
6	11–13	Paleosol	Reddish-brown	Prismatic structure with dense texture, contains many black films
7	13–13.45	Paleosol	Reddish-brown	Prismatic structure with compact texture and plant roots
8	13.45–14.20	Loess	Brownish yellow	Large prismatic block structure, porous, with few films
9	14.20–15.30	Paleosol	Summer tan	Granular and compact in texture, with many films in the lower part, and large iron-manganese nodules
10	15.3-bottom not observed	Semi-weathered sandstone	Summer tan	Weathered bedrock materials, with iron-manganese nodules, gradually transiting downward to the bedrock

The Xiashu loess deposit accounts for 35–50% in the LRYR (**Figure 1**), especially prevalent on the hills, highlands, terraces, and other geomorphic units along the Yangtze River and its tributaries. In addition, loess also occurs on the Yangtze River Delta, the continental shelf and islands of the East China Sea. The elevation of the Xiashu loess exposures varies significantly, from over 60 m above sea level to 20 m below sea level. The thickness of the Xiashu loess reaches a maximum of over 50 m in Qingshan, Dagang and Zhenjiang. In Nanjing, the Xiashu loess deposit is distributed as platforms on the river terraces of the Yangtze River, with surface elevations of 30–40 m and thicknesses of approximately 20 m. The outcropping landforms of the Xiashu loess are mostly characterized by highlands and river terraces, and the underlying strata are mainly composed of gravel layers or Cretaceous sandstones. The loess strata are generally horizontal, slightly inclined, inconsistent with the bedrock inclination.

The Xingang (XG) profile (32° 08′ 45.5″N, 118° 50′ 51.6″E) (**Figure 1**) is located in the Xingang Development Zone on south bank of the Yangtze River, approximately 20 km northeast of Nanjing City, Jiangsu Province. The XG profile is a typical Xiashu loess profile exposed by engineering excavation. The profile is about 15.7 m in thickness, with interbedded loess and paleosol (**Table 1**), and has three steps dividing the profile into three distinct sections: from bottom to top, these are XG-1, XG-2 and XG-3, respectively. The complete profile has four paleosol layers and three loess layers (**Table 1**). A weathering crust and Cretaceous sandstone are visible in the lower part. A total of 81 samples were collected from bottom to top at equal intervals of 20 cm for grain-size analysis and quartz grain surface microtextural and morphological observations.

Methods

Grain Size

Grain size characteristics are mainly controlled by transportation mode and sedimentary environment. Therefore, grain size analysis is often used to identify provenance and the sedimentary environment (Vandenberghe, 2013; Vandenberghe et al., 2018; Yang et al., 2019; Van Buuren et al., 2020). For the convenience of comparison with previous studies, the classification scheme used in this study is: sand (> 50 μm), silt (50–5 μm), coarse silt (50–10 μm), fine silt (10–5 μm), clay (< 5 μm) (Lei, 1998; Li et al., 2001b). The commonly used grain size parameter indexes include average grain size (Mz), standard deviation (Sd), skewness (Sk) and kurtosis (Kg). The mathematical calculation formula of particle size parameters are as follows (Folk and Ward, 1957; Yang et al., 2014):

$$Mz = \frac{\sum_{i=1}^{n} x_i f_i}{100},$$

$$Sd = \sqrt{\frac{\sum_{i=1}^{n} (x_i - Mz)^2 f_i}{100}},$$

$$Sk = \sqrt[3]{\frac{\sum_{i=1}^{n} (x_i - Mz)^3 f_i}{100Sd^3}},$$

$$Kg = \sqrt[4]{\frac{\sum_{i=1}^{n} (x_i - Mz)^4 f_i}{100Sd^4}}$$

The grain size analysis experiment was carried out in the geographic process laboratory, Zhejiang Normal University, using a Mastersizer 2000 laser grain size analyzer (Malvern, United Kingdom) with a measurement range of 0.01–2000 μm and an error of <2%. Samples for grain size analysis were pre-treated as follows. Samples were first boiled with 10% H_2O_2 and 10% HCl to remove the organic matter and carbonate, respectively. Next, 0.5 mol/L $(NaPO_3)_6$ was added as a dispersant, then the pretreated samples were ultrasonicated for 15 min before being analyzed.

Fisher Linear Discriminant Analysis

Fisher linear discriminant analysis (FLDA) is a common classification method for multivariate statistical analysis, and is

TABLE 2 | Equality test of group means.

Parameters	Wilks' lambda	F	Significance probability
Mz	0.262	286.586	0
Sd	0.02	5,079.284	0
Sk	0.042	2,334.562	0
Kg	0.203	401.401	0

widely used to identify various sedimentary environment. In this paper, we use FLDA to identify sedimentary environment based on statistical analysis of fluvial deposit (FD) and eolian deposit (ED) grain size parameters. The function we create is as follows. $y = -1.138*Mz + 1.58*Sd - 0.781*Sk + 0.805*Kg$, the threshold level is -4.5744 (if $y > -4.5744$, they belong to ED; if $y < -4.5744$, they belong to FD).

In this study, we select a typical eolian loess profiles Zeketai (ZKT) profile in Xinjiang province, which is considered as a provenance for the loess on the CLP (Liu, 1985; Yang et al., 2014), and also selected Luochuan (LC) loess profile located on the central CLP, as well as Nantong (NT) profile (floodplain deposit) in the LRYR, which is considered to have played an important role in the accumulation of the Xiashu loess. To test the linear discriminant function created above, 215 typical eolian loess samples from ZKT profile and 33 typical floodplain deposit samples from NT profile were inputted into statistical software (SPSS) as ED and FD training sets respectively. All the significance probability values of the variable group mean are less than 0.001 (**Table 2**). Therefore, the four variables included in this discriminant analysis are all effective.

The Box's M test assesses the assumption of homogeneity of covariance matrices. This test is very sensitive to meet the assumption of multivariate normality. The statistical value of Box's M is 738.71 (**Table 3**), far greater than 0.05. Therefore, each of the covariance matrices can be considered equal. The significance probability of the F-test is 0.000, less than 0.05, indicating that the error judgment rate is minimal.

In order to verify the reliability of this model, sediment grain size parameters (Mz, Sd, Sk, and Kg) of eolian loess samples from ZKT profile, floodplain deposit samples from NT profile, and 57 eolian loess samples from LC profile were computed using the function. As shown in **Table 3**, all the eolian loess samples from ZKT profile and LC profile were identified as ED, resulting in an accuracy of 100% (**Table 4**). All the floodplain deposit samples from NT profile were identified as FD. Hence, the discriminant model is reliable.

End-Member Modeling Analysis

End-member analysis is one of the most effective methods to study the transportation dynamics and sedimentary environment (Vandenberghe, 2013; Ding et al. 2021), the grain size of the Xiashu loess was primarily controlled by source materials as well as transport dynamics and post-depositional weathering and pedogenesis (Liu, 1985). In this study, either we selected three or four endmembers, $R^2 > 99\%$, when we selected three endmembers, the correlation between endmembers >0.4, while when we selected four endmembers, the correlation <0.2. Therefore, it is reasonable to select four endmembers in this study (**Figure 2**).

TABLE 3 | Box's M test results of equality covariance matrixes.

Boxe's M	F	
	Approx	Sig
738.71	70.049	0

Quartz Grain Microtextures

Quartz minerals have high hardness, stable chemical properties and strong weathering resistance, leading to a variety of microtextures that can be well preserved on the surface of quartz grains. These microtextures are considered to reflect sedimentary history of the quartz grains, and can indicate the parent rock, transportation process, and depositional environment. Many researchers have therefore stated that quartz grain surface microtextures can be used to identify different sedimentary environments (Liu 1985; Pye K 1995; Helland et al. 1997; Mahaney &Kalm, 2000; Mahaney 2002; Guo et al. 2002; Qiao et al. 2003; Costa et al. 2012, Costa et al. 2013; Mahaney et al. 2014; Smith et al. 2018; Chen et al. 2019). On one hand, dish-shaped depressions, crescentic marks, upturned plates, meandering ridges and pockmarked surfaces are regarded as typical features of eolian quartz grains (Wang and Deonarine, 1985; Mahaney, 2002; Krinsley and Doornkamp, 2011; Costa et al., 2012, Costa et al., 2013). For example, dish-shaped depressions often occur in high-energy eolian environments where grains collide with each other. Pockmarks are typical characteristics of markings for eolian quartz grains, crowded pits result from collision with other grains during wind transportation, forming pockmarked surfaces. Upturned plates, which commonly occurred on edges of the grains that had good roundness, resulted from abrasion between grains in eolian environments. Meandering ridges are associated with eolian environments too (Wang and Deonarine, 1985; Mahaney, 2002). On the other hand, conchoidal fractures, V-shaped cracks, polished surfaces, triangular cracks, parallel striations, and grooves (straight and curved) are considered to be typical features for quartz grains from subaqueous environments (Wang and Deonarine, 1985; Mahaney et al., 2001; Mahaney, 2002; Sweet and soreghanm, 2010; Vos et al., 2014; Smith et al., 2018). V-shaped cracks are considered to be developed by "grain-to-grain collisions" in subaqueous environments, where grains are triangular in shape and are non-oriented. Parallel striations result from "grain-to-grain scratches" in fluvial environments (Wang and Deonarine, 1985; Mahaney, 2002; Vos et al., 2014). Mahaney (2002) concluded that V-shaped cracks are the most common feature associated with fluvial environment.

In this study, quartz grain microtextures were observed under an S-4800 high-resolution field emission scanning electron microscope (SEM) produced by Hitachi (Japan) at the Institute of Physical Chemistry, Zhejiang Normal University. The extraction method for quartz grain before SEM observation was as follows:

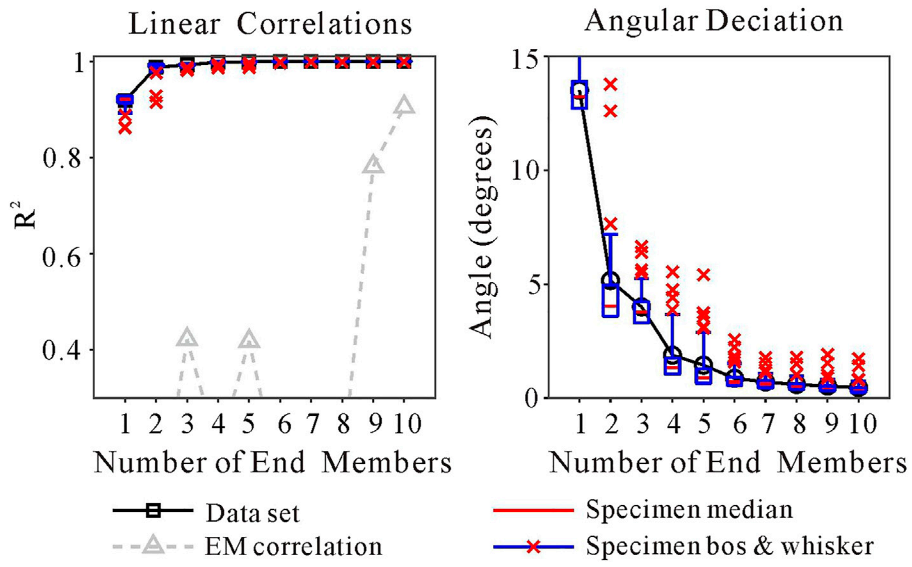

FIGURE 2 | End-member analysis results of XG profile.

(1) To remove free iron, the dried sample was placed in centrifuge tube with sodium dithionite, sodium citrate (0.3 mol/L) and sodium bicarbonate solution (1 mol/L) and heated in a water bath. The solution was then separated by centrifuge until clear.

(2) The quartz minerals were separated and purified by the potassium pyrosulfate melting-fluorosilicic acid immersion method. After removing the free iron, the samples were mixed with potassium pyrosulfate powder and heated in a muffle furnace for 1 h (initial temperature 350°C, then 650°C from 20 min to the end). The heated samples were transferred to a beaker, and HCL solution (l:3) was added to the heating plate to dissolve the frit. After separation by centrifuge, the samples were dried in the oven. The samples were then soaked in fluorosilicic acid for 3 days. The solution was centrifuged and the clear liquid was removed three days later. The residue was dried, and the quartz grains with highest purity were extracted.

According to Tsoar and Pye (1987), dust particles <20 μm can be transported over wide altitudinal ranges and long distances by long-term suspension. Therefore, we observed grains that were large than 20 μm and finer than 20 μm under the Scanning Electron Microscope (SEM), and 20 quartz grains (including 10 grains >20 μm and 10 grains <20 μm) in each sample were selected in XG profile, and a total of 1,620 quartz grains were observed and counted.

RESULTS

Grain Size Characteristics of XG Profile

The grain-size analysis results show that the Xiashu loess in XG, Nanjing mainly consists of fine components <50 μm. No particles >250 μm were found in any samples. The content of sand grains (>50 μm) is low (range 5.5–8%, average 6.84%) (**Table 5**). The silt (50–5 μm) content varies from 62.41 to 75.02% (mean 68.82%). The average content of coarse silt (50–10 μm) is 53.57%; this is the dominant grain size both in XG profile and for the loess on the CLP, and is regarded as a characteristic grain size in eolian loess deposit (Liu, 1985; Guo et al., 2002; Qiao et al., 2003). The average fine silt (10–5 μm) content is 15.25%. Finally, clay (< 5 μm) is the sub-dominant grain size (average 24.34%), second only to the coarse silt in XG profile (**Table 5**).

The average grain size (Mz) of samples from XG profile varied from 6.23φ to 6.68φ (mean 6.47φ) (**Table 5**). The sorting coefficient (Sd) ranges from 1.52 to 1.79, with a mean value of 1.65, indicating a poor sorting; skewness (Sk) varies from 0.54 to 0.84 (mean 0.67), indicating positive skewness; kurtosis (Kg) ranges from 2.53 to 3.13 (mean 2.80), showing that most samples are sharply peaked.

The grain-size frequency curve (**Figure 3**) of XG profile is characterized by a major peak and other three small peaks. The major peak is located near 5.5φ, with other three small peaks near 2φ, 8φ, and 10.5φ respectively. The small peak near 2φ indicates that the XG profile contains a certain amount of coarse-grained materials, namely sand content. The two small peaks near 8φ and 10.5φ suggest that the Xiashu loess contains more fine-grained materials in the two places. On the whole, the frequency curve is characterized by a striking high content of sand, fine silt and clay component, which is unusual for pure windblown loess, the small peak near 8φ probably indicate a small amount of far - distant component, and the small peak near 10.5φ may indicate the existence of a large amount of clay component in XG profile. The frequency curve of XG profile suggests that the Xiashu loess is probably a admixture composed of near - source materials and long - transport materials. On one hand, it is likely that the Xiashu loess is primarily a near - source deposit, so the sand, silt and clay were mixed together during transportation, resulting in more sand materials in XG profile, and these materials have undergone a strong

TABLE 4 | The verification of the discriminant function.

Profile codes	No. of samples	Actual category	Discriminant results		Accuracy (%)
			ED	FD	
ZKT	215	ED	215	0	100
NT	33	FD	0	33	100
LC	57	ED	57	0	100

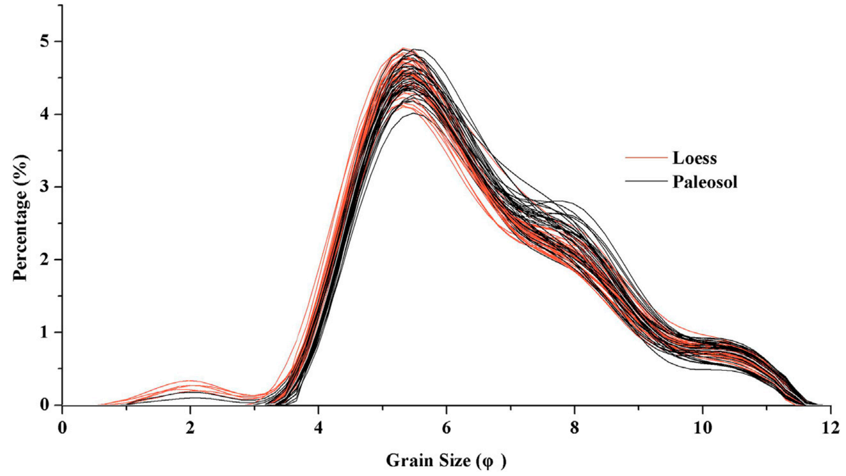

FIGURE 3 | The grain-size frequency curve of XG profile.

TABLE 5 | Grain size composition and Grain size parameters of XG profile.

Profile		Grain size composition/% grain size parameters										
		<5	5–10	10–50	>10	>20	>50	>250	Mz	Sd	Sk	kg
XG	Min	21.45	12.85	44.65	52.75	34.54	5.5	0.00	6.23	1.52	0.54	2.53
	Max	27.24	17.46	57.84	65.59	46.69	8.00	0.00	6.68	1.79	0.84	3.13
	Mean value	24.34	15.25	53.57	60.51	38.92	6.84	0.00	6.47	1.65	0.67	2.80

weathering and pedogenesis process in the warm-humid north subtropical monsoon climate after deposition, causing a obviously high content of clay component. On the other hand, the join up of a small amount of far - distant fine materials caused a small peak near 8φ and a poor sorting in XG profile.

Origin Identification by FLDA for XG Xiashu Loess

81 samples from XG profile were computed using the function, as shown in **Table 6**, all the samples from XG profile and ZKT profile are identified as ED, and all the floodplain deposit samples from NT profile are identified as FD. Therefore, the Xiashu loess in XG profile is considered as a eolian deposit.

Genetic Interpretation of End-Members for XG Xiashu Loess

By end-member modeling analysis, the XG Xiashu loess profile was divided into four end-members (EM) (**Figures 4**, **5**), from EM1 to EM4, they account for 11.97, 23.06, 57.64, and 7.33% on average respectively (**Figure 5**). EM1 (modal size 1.0 um) should be the product of weathering and pedogenesis after deposition. According to Tsoar and Pye (1987), dust particles >20 μm are unlikely to be transported in long-term suspension across a large height range, and the >10 μm components were regarded as nearby-source materials for Xiashu loess, whereas <5 μm components were regarded as far-distant materials that was mainly derived from the arid regions of northwestern China by long-range transport (Wu et al., 2020). Therefore, we suggest that EM2 (modal size 4.5 μm, accounting for 23.06%) represent the far-source materials that were mainly originated from the arid regions of NW China. EM3 (modal size 22.4 μm, accounting for 57.64%) and EM4 (modal size 44.8 μm, accounting for 7.33%) represent nearby-source materials that were mainly derived from local sources, which account for at least 64.97% in total and were presumed probably originated from the floodplains in the lower reaches of the Yangtze River, the Huai River, and the Yellow River to the north during glacial periods.

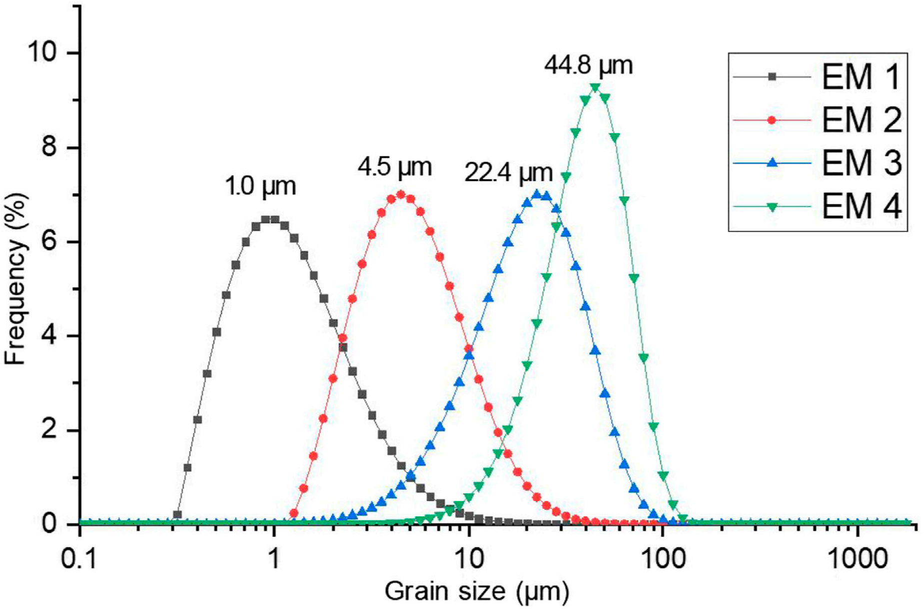

FIGURE 4 | End-member analysis results of the grain size of XG profile.

Quartz Grain Surface Microtextural and Morphological Observations

SEM observations of quartz grains from XG profile show that 55% grains observed are characterized by subangular outlines (**Figures 6A,B**, **7**, **8**), with a certain number of angular particles (29%) and round particles (5%) (**Figure 8**). The XG profile quartz grains show various shapes, such as plates, strips, triangles, cubes, pointed, slightly rounded, irregular, etc (**Figures 6A,B**). Mechanically produced features are abundant and varied, indicating that the quartz grains have experienced a range of external forces. Characteristics typical of eolian quartz grains in XG profile are common (**Figures 6C–F**), e.g. dish-shaped depressions (**Figures 6C–F**) and crescentic marks (**Figure 6F**) have occurrence rates 61% (**Figure 8**) and 48% (**Figure 8**), respectively. Other eolian features like upturned plates and meandering ridges (**Figure 6D**) also occurred on the grains, as well as pockmarks, formed pockmarked surfaces (**Figures 6D,F**), indicating quartz grain surface erosion during wind transportation. These features are similar to the microtextures characteristics in quartz grains from the loess on the CLP (**Figure 9**), reflecting transportation process by wind power. Meanwhile, many subaqueous features are also observed on the quartz grains: for example, V-shaped cracks (**Figures 6G,I**), grooves (**Figure 6I**), conchoidal fractures (**Figure 6H**), parallel striations caused by scratch (**Figures 7C–E**), triangular cracks (**Figure 6H**), underwater polished surfaces (**Figures 7A,B,F**), as well as bulbous edges and smooth edges (**Figures 7F,G**) caused by abrasion in subaqueous environments. V-shaped cracks, the most representative feature produced by grain-to-grain collisions in subaqueous environments (Mahaney, 2002; Krinsley and Doornkamp, 2011), reach an occurrence rate of 63% in XG profile (**Figure 8**), suggesting a fluvial environment. A majority of quartz grains with high relief and abundant mechanical V-shaped cracks (**Figures 6G–I**), as well as parallel striations (**Figures 7C–E**) caused by scratch demonstrated that the quartz grains underwent a high-energy subaqueous transport. Some grains have surface microtextures that are typical of a subaqueous fluvial environment, with dish-shaped depressions or small impact pocks superimposed. This suggests the quartz grains were abraded in a fluvial environment before undergoing eolian transportation. In addition, 13% of the quartz grains (<20 μm) in XG profile have aeolian features and sharp edges on their surfaces, but without subaqueous characteristics, it is presumed that these grains were originated from far-distant materials. The grains in XG profile also exhibit silica dissolution and silica precipitation textures indicative of chemical weathering. Silica dissolution mainly comprise oriented etch pits (**Figure 7H**), solution pits and crevasses. Oriented etch pits are oriented and aligned, which are likely to be developed in rivers, lakes or marine environments, where the water affects the grains by dissolution (Mahaney, 2002; Krinsley and Doornkamp, 2011). 18% of the grains show oriented etch pits in XG profile, indicating a fluvial environment. Silica precipitation has produced silica globules (**Figure 7I**), silica pellicles and silica flowers, indicating that the quartz grains have undergone post-depositional weathering and pedogenesis.

DISCUSSION

Evidence of Aeolian Deposition

The XG profile and other reported Xiashu loess profiles present typical characteristics of eolian origin, including a uniform loose

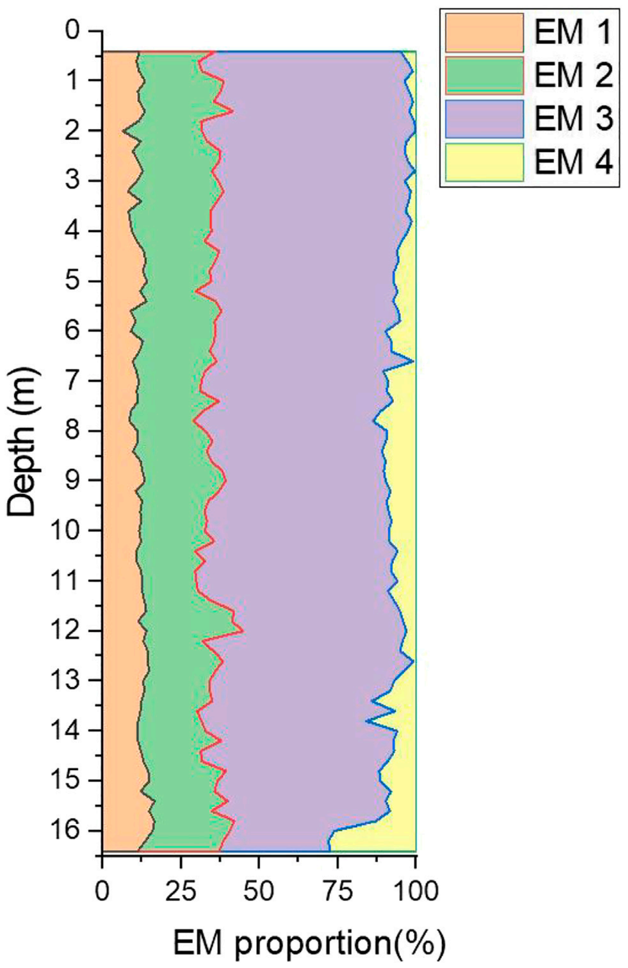

FIGURE 5 | Variations of End-members corresponding to sampling depth of XG profile.

and porous texture, massive structure, significant vertical joints, and disseminated iron-manganese films. The Xiashu loess covers hills, highlands, terraces, and other geomorphic units at varying elevations, and shows a range of origins and characteristics. In addition, the Xiashu loess strata are composed of alternating dark-colored (paleosol) and light-colored (loess) layers, resembling the typical loess-paleosol sequence on the CLP of northern China (Liu, 1985). Furthermore, although in some cases, the underlying strata of the Xiashu loess are composed of gravel layers, both of reported results and this study show that there are no sand layers or gravel layers in Xiashu loess profiles (Hao et al., 2010; Li et al., 2018b; Jiang et al., 2020), These depositional features distinguish aeolian deposits from fluvial deposits.

Grain Size Evidence for the Provenance of XG Profile

The grain size composition of XG profile shows obvious aeolian characteristics, most notably the fine grain size and high clayey silt fraction. Silt is the dominant component in all layers, with an average content of 68.82%, followed by clay and sand. The components with grain size < 50 μm in XG profile account for 93.16% on average. This clear dominance of the fine fraction (<50 μm) is considered to be a typical feature for eolian loess deposit (Liu, 1985; An et al. 1990; Guo et al. 2002). Coarse silt (50–10 μm), which is the primary grain size group (average content 53.57%) (**Table 5**) in XG profile, is regarded as a key characteristic of aeolian loess on the CLP (Liu, 1985). The grain size compositions and grain size parameters of the loess are highly uniform between different layers of XG profile, suggesting that the Xiashu loess was likely to have been transported by a single external force. In addition, the grain size characteristics of loess in XG profile, Zhenjiang profile and Nanjing Zhoujiashan profile are strongly consistent, indicating a shared provenance (Li et al., 1997, Li et al., 2001b, Qiao et al., 2003, Hao et al., 2010; Jiang et al., 2020).

Due to the wind-sorting effect, prevailing northwesterly wind direction, and the decreasing carrying capacity with increasing distance from the source area, the grain size of loess on the CLP decreases from coarse to fine from northwest to southeast. Here, we choose two classical loess profiles on the CLP, one is Luochuan profile in the middle of the CLP, the other is Qinling profile in the southernmost part of the CLP. They are two representative profiles on the CLP. For example, the average grain size (Mz) of the loess layers in Luochuan profile is 6.01φ, the mean value of that in other six loess profiles in the interior of the CLP is 6.00φ (Lei, 1998; Lei, 1999), indicating that the Luochuan profile is very representative. Here, we take Luochuan profile and Qinling profile in northern China as examples, the respective contents of sand (>50 μm) and clay (<5 μm) in Luochuan profile are 6.8 and 27.4% on average, the average grain size (Mz) of Luochuan profile is 6.01φ (Liu, 1985; Lei, 1998; Lei, 1999). The respective values for the Qinling loess are 4.3%, 30.5%, and 6.59φ respectively, demonstrating the NW-SE trend toward finer grain sizes. The Xiashu loess is located far from northwest China; In addition, the warm-humid climate in the LRYR is highly conducive to post-depositional weathering and pedogenesis. Therefore, the sand content in the Xiashu loess should be lower than that of the loess on the CLP in northern China, while the contents of silt and clay materials should be higher. However, results show that sand (>50 μm) contents of the Xiashu loess in the LRYR, including XG (6.84%), Zhoujiashan of Nanjing (8.6%) and Zhenjiang (10.1%) are higher than those of the Luochuan profile (6.8%) and the Qinling profile (4.3%), while clay content in XG (24.3%), Zhoujiashan of Nanjing (21.3%) and Zhenjiang (19.1%) are lower than those in Luochuan (27.4%) and the Qinling loess (30.5%), so is the LGS Xiashu loess profile (24.9%) in East China Sea (**Table 7**). The average grain size of the loess layers in XG (6.42φ, Paleosol layers not included) is coarser than that in Qinling loess (6.58φ) (Liu, 1985; Lei, 1998, Lei, 1999; Xu et al., 2016). All the characteristics above suggest that the grain size of the Xiashu loess in the LRYR does not follow the NW-SE trend of decreasing grain size. On the other hand, grains larger than 20 μm are unlikely to be transported for long distances by wind. The components larger than 20 μm in XG profile account for 38.92%, and sand content (>50 μm) accounts for 6.84%,

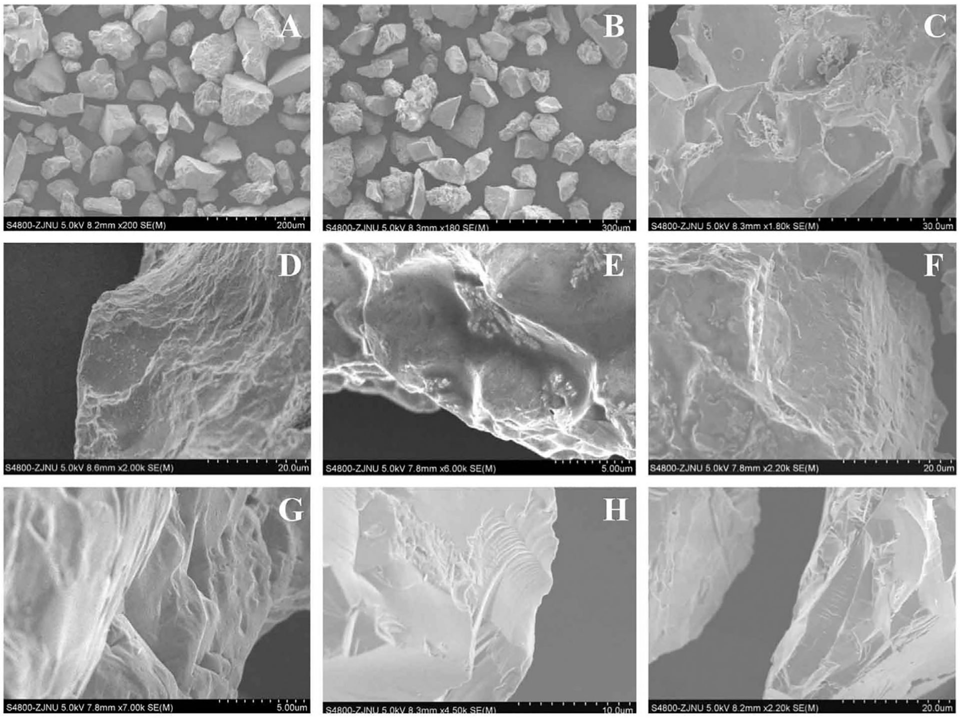

FIGURE 6 | (A–B). Quartz grains in XG profile. **(C)**. Collision dish-shaped depressions are common on the surface. **(D)**. Elongated dish-shaped depressions, meandering ridges, upturned plates and pockmarked surfaces. **(E)** Elongated dish-shaped depressions and crescentic marks. **(F)**. Crescentic marks, dish-shaped depressions and pockmarked surfaces. **(G)**. V-shaped cracks. **(H)**. Conchoidal fractures, triangular cracks and underwater polished surfaces. **(I)**. Grooves and V-shaped cracks.

especially the >10 μm components, which were considered as nearby-source materials for the Xiashu loess (Wu et al., 2020), account for 60.51% in XG profile. In addition, end-member modeling analysis show that EM3 (modal size 22.4 um, accounting for 57.64%) and EM4 (modal size 44.8 μm, accounting for 7.33%) represent nearby-source materials that were mainly derived from local sources, account for at least 64.97% in total. The relatively high content of grains >10 μm and >20 μm in XG profile is hard to explain using the distant source theory. In other words, nearby-source materials dominate the accumulation of the Xiashu loess. Finally, the poor sorting of XG and other reported Xiashu loess profiles in the LRYR is unusual (Li et al., 1997, Li et al., 2001b, Li et al., 2018b; Qiao et al., 2003; Xu et al., 2016), if the Xiashu loess was originated from the remote Gobi Desert of northwestern China or originated from the adjacent floodplains, it should have been well sorted. Therefore, multiple characteristics suggest that the Gobi Desert in inland NW China were not the primary source materials for the Xiashu loess, the Xiashu loess is probably a admixture composed of nearby-source materials and long-transport materials. Previous studies show that dust from inland NW China can be transported to the sea of Japan (Xiao et al., 1999), and the grain-size frequency curve of XG profile has also proved this point, so we suggest that a small amount of dust from the remote Gobi Desert in areas of northwestern China was likely to be transported to the LRYR during glacial periods, and the poor sorting of XG profile and other reported Xiashu loess profiles is not difficult to understand.

Quartz Grain Surface Microtextural Evidence for the Provenance of XG Profile

The loess on the CLP were originated from the remote Gobi Desert in inland northwestern China. The quartz grains in the loess are mostly subangular and angular, and with characteristic shapes (e.g. water drops, spears, diamonds, spindles or spirals) (Wang et al, 1985; Liu, 1985). These forms are mostly streamlined with a long primary axis, especially the twisted spiral shape representing the typical eolian loess on the CLP (**Figure 9**). This is because the quartz grains were carried by airflow for a long distance, and the grains themselves also rotated around their long axis, gradually being shaped by wind friction (Wang et al, 1985; Sun and An, 2000). Previous studies show that the quartz grains from the loess on the CLP are dominated by eolian features, subaqueous environmental characteristics are rare or absent (Liu, 1985; An et al., 1990; Ding et al., 1995; Guo et al., 2000). Our results show that most of the quartz grains of XG profile not only have typical features of wind transportation (such as dish-shaped depressions, crescentic marks and pockmarked surfaces), but also display a range of subaqueous environment characteristics (e.g. V-shaped cracks, subaqueous polished surfaces, grooves, etc) with high frequencies indicating that the grains have undergone

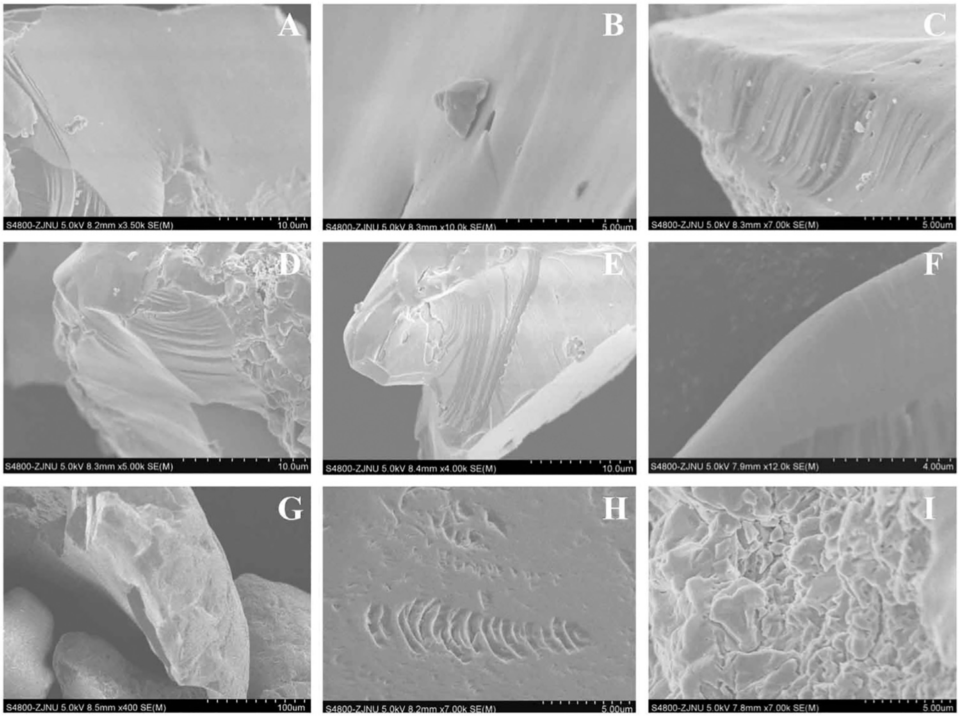

FIGURE 7 | (A–B). Underwater polished surfaces formed in subaqueous environment. **(C–E)**. Parallel striations resulted from “grain-to-grain scratches” in subaqueous environment. **(F)**. Polished surfaces and smooth edges caused by abrasion in subaqueous environment. **(G)**. Smooth edges and V-shaped cracks. **(H)**. Oriented etch pits. **(I)**. Silica globules caused by precipitation.

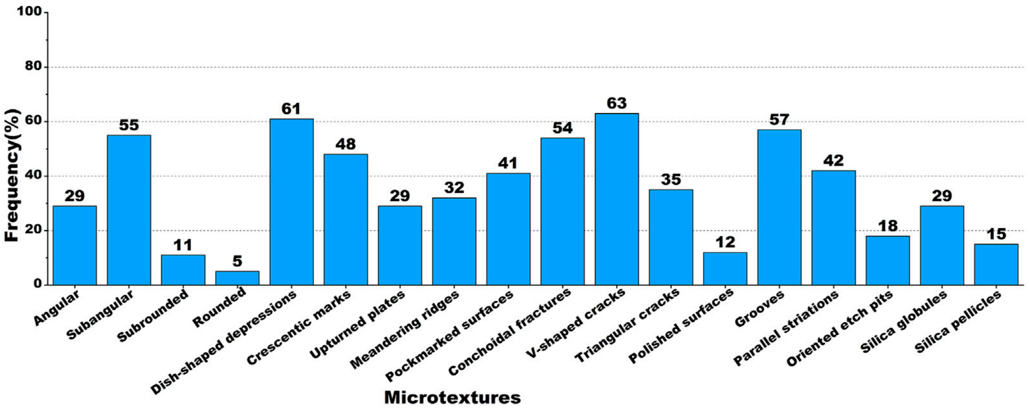

FIGURE 8 | Frequencies of different microtextures identified in XG profile.

subaqueous transport. Some grains with surface features of fluvial environments have aeolian characteristics superimposed on them, suggesting that the quartz grains were firstly abraded in a fluvial environment, and then transported and deposited by wind action. These features are distinctly different from those of the quartz grains on the CLP, and are also significantly different from those of the quartz grains derive from underlying parent rocks that are almost without any transportation and typically irregularly shaped with sharp edges and extremely irregular shapes. In addition, if the Xiashu loess were originated from the remote Gobi Desert in inland of NW China, its quartz grains would have developed the same streamlined or spiral shapes as those of the loess on the CLP. However, SEM observations show that the quartz grains of XG profile present various shapes (such as plates, strips, triangles, cubes, points, and slightly rounded; and no screw - like grain occurs in the quartz grains observed), which were clearly distinct from the quartz grains on the

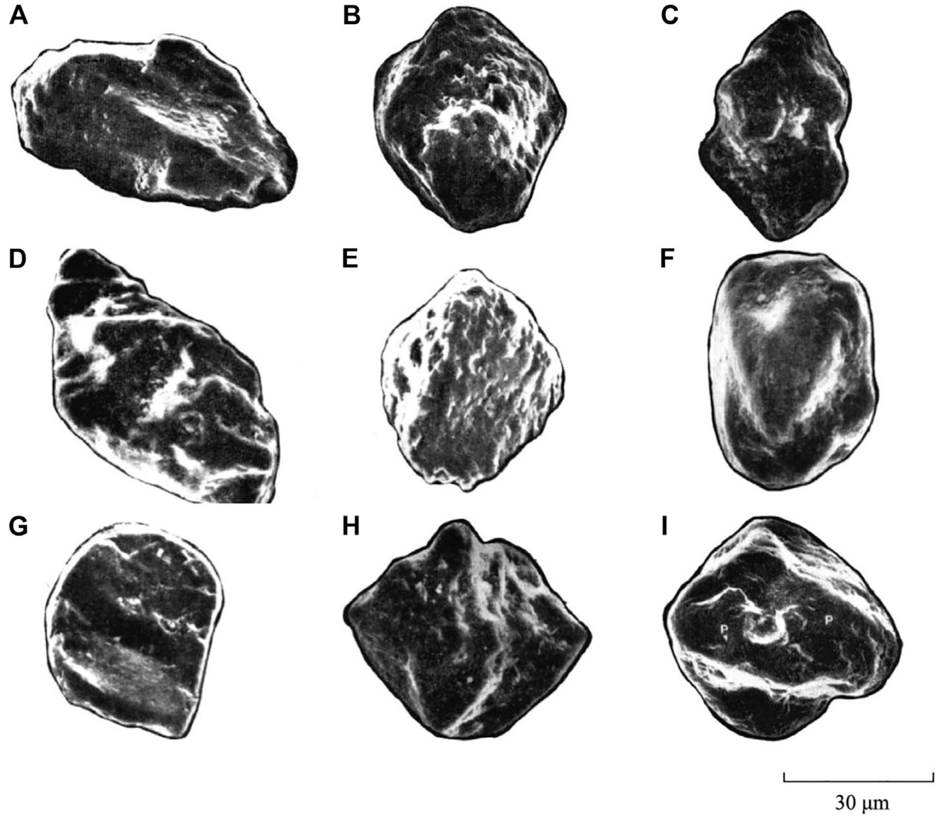

FIGURE 9 | Quartz grains of the loess on the CLP. **(A)**. Streamlined grain with precipitated silica. **(B)**. Spear-shaped grain with a thick layer of silica precipitates and pockmarked surfaces, small collision pocks are visible on the original surface. **(C)**. Fusiform grain with silica precipitation. **(D)**. A fusiform - twisted grain with a thick precipitated silica cover. The streamlined grain is characteristic of the aeolian quartz grain of loess on the CLP. The screw-like shape of this grain is typical of aeolian loess that has been transported by air currents in suspension for a long distance. **(E)**. Lenticular grain with solution - precipitation features covering the surface. **(F)**. Ellipsoidal grain with chipped depressions and smooth outline. **(G)**. A typical water - drop-shaped grain, smooth edges with one edge along the long axis. The grain surface carries chipped depressions, collision pocks and silica fragments. **(H)**. Lenticular-shaped grain with solution-precipitation of silica. **(I)**. Equant grain with subrounded edges, chipped depressions and collision pocks are common on the surface (Wang et al., 1985).

CLP. In addition, subaqueous environmental characteristics such as conchoidal fractures and V-shaped depressions are rare in typical eolian quartz grains, only can be seen in quartz grains that have just entered the eolian environment. The subaqueous environmental features in XG profile are abundant and clearly visible, indicating that the grains have been changed little by the eolian environment and have not been transported by wind for a long distance. Quartz grains >20 μm are unlikely to be transported by wind over long distance and therefore are regarded as regional materials, SEM observations show that >20 μm quartz grain (including sand grains) in XG profile are with obvious eolian features and subaqueous characteristics, indicating a near-source deposition. 13% of the quartz grains (<20 μm) observed have eolian features on their surfaces, but without subaqueous characteristics, it is presumed that these grains were originated from far-distant materials. These characteristics suggest that the Xiashu loess should be eolian deposit that was mainly originated from near-source materials. Previous studies show that dust from inland of NW China can be transported to the sea of Japan (Xiao et al., 1999), the grain-size frequency curve and the quartz grain microtextures, as well as end-member modeling analysis indicate that the Xiashu loess may contain a certain amount of far-distant materials, so we suggest that nearby-source materials dominate the accumulation of the Xiashu loess, and the dust from the Gobi Desert in inland NW China have played a small role in the accumulation of the Xiashu loess. The surface microtextures and morphologies of the quartz grains provide a evidence for identifying the provenance of the Xiashu loess.

Onset of Dust Accumulation in the LRYR and Its Environmental Significance

The accumulation of the Xiashu loess in the LRYR of southern China have significant environmental implications. In terms of sedimentary chronology, new advances in magnetostratigraphy and optically stimulated luminescence (OSL) dating have constrained the age of the lower boundary of the Xiashu loess to approximately 0.9 Ma, and the uppermost loess layer formed in the last glacial period (Qiao et al., 2003; Hao et al., 2010; Li et al., 2018b). The development of aeolian loess deposit in Asian

TABLE 6 | The verification of the discriminant function.

Profile codes	No. of samples	Actual category	Discriminant results	
			ED	FD
ZKT	215	ED	215	0
NT	33	FD	0	33
XG	81	ED	81	0

subtropical regions since 0.9 Ma against a backdrop of global climate change. In the late Cenozoic, the overall climate trend was characterized by a global cooling, as evidenced by the expansion of continental ice sheets. This was accompanied by continental stepwise aridification, which led to the formation and development of the eolian loess deposit on the CLP (Liu, 1985; Guo et al. 1998; Sun and An, 2000; Guo 2010; Hao et al., 2010; Li et al., 2018b; Westerhold et al., 2020).

Great changes have taken place in global climate and environment in the middle of the Quaternary (Hao et al., 2010; Westerhold et al., 2020). The Mid-Pleistocene Transition (MPT) at about 1.25–0.7 Ma marked a shift in the primary climatic cyclicity from a 41 ka cycle to a 100 ka cycle, caused a significant increase in global ice volume and global cooling (Ruddiman et al., 1989; Clarket al., 2006; Hao et al., 2010; Elderfield et al., 2012; Westerhold et al., 2020). On the other hand, a significant tectonic movement (the “Kunlun-Yellow River movement”) on the Tibetan Plateau at about 1.2–0.6 Ma resulted in a period of rapid uplift. The "Kunlun-Yellow River Movement" raised the plateau and many surrounding mountains to a critical height of 3,500 m by around 0.9 Ma, causing widespread growth of glaciers which brought the Tibetan Plateau into the cryosphere and induced the first ice age in China since the Quaternary (Fang et al., 1996; Cui et al., 1998, Cui et al., 2011; Li et al., 2001a). The uplifted Tibetan Plateau serves as a cold source in winter and a heat source in summer, thereby intensifying both the winter monsoon and the summer monsoon, and also split the westerly jet into two streams. Thus resulted in the intensification and northward displacement of the Siberian high-pressure system. Global cooling and the uplifted Tibetan Plateau led to the enhancement of the Siberian high pressure, and caused a severe aridification in Asian interior and the intensification of the east Asian winter monsoon (Ruddiman et al., 1989; Kutzbach et al., 1997). Hence, the dust deposition rate in northern China accelerated during 1.2–0.9 Ma, created extensive areas of eolian loess. The development of the exceptionally thick and coarse loess layers L15 (deposited at about 1.2 Ma) and L9 (deposited at about 0.9 Ma) on the CLP is a strong evidence for the cold-dry event in this period: L15 and L9 correspond to marine oxygen isotope stages 38 and 22, representing two periods of severe global cooling (Liu, 1985; Ding et al., 2002; Guo et al., 2000; Lu et al., 2000, Lu et al., 2008; Sun and Guo, 2017). Global cooling and the uplifted Tibetan Plateau also strongly influenced the LRYR region in southern China, resulting in a severe regional cooling and aridification. In addition, retreat of the coastline of the western Pacific Ocean increased the area of the continental land mass: for example, during the LGM, the coastlines of the East China Sea and the Yellow Sea had retreated eastwards by 6–7° of longitude (about 600 km), and the sea level had dropped by 150 m (Wang, 1999, Xu et al., 2012). The area of the LRYR, the Huai River and the Yellow River to the north is low, flat, and densely covered with rivers and lakes. In glacial periods, with declining of the sea level, the reduced river and lake levels yielded large areas of desiccated rivers, floodplains and lake beds, promoted these areas as a dust source for the accumulation of the Xiashu loess. The intensified winter monsoon produced strong wind erosion capacity and provided enough power to transport these regional fine materials, the river valleys and multistage river terraces of the Yangtze River and its tributaries provide good geomorphological conditions for loess deposition. The far-distant dust from the Gobi Desert of northwestern China may have played a small role in the accumulation of the Xiashu loess as well.

Sporopollen analysis of a typical loess stratum in Nanjing shows that herbaceous pollen dominated the total pollen assemblage, the sporopollen are mainly comprised of Compositae and Gramineae (subordinately artemisia and Chenopodiaceae), while arboreal pollen was mainly composed of Pinus, indicating a relatively arid and cold climate (Hao et al., 2010). The Ganzi loess in western Sichuan and the red earth in Chengdu plain (**Figure 1**) in the upper reaches of the Yangtze River have been confirmed as near-source eolian deposits formed in this period (Zhao et al., 2007; Qiao et al., 2007; Wang et al., 2018). The occurrence of sustained dust deposit reflects an important climate and environment change in the source and/or deposition regions (Pye, 1995). This means that the

TABLE 7 | Comparison of grain size composition of loess in the LRYR and on the CLP (Li, 1998; Liu, 2006; Xu et al., 2016; Chen et al., 2017).

Sample sites	Clay (<5 μm) %	Fine silt (5–10 μm) %	Coarse silt (10–50 μm) %	Sand (> 50 μm) %
XG, nanjing	24.3	15.3	53.6	6.8
ZJS, nanjing	21.3	15.6	54.5	8.6
CS, zhenjiang	19.1	14.8	56	10.1
DG, zhenjiang	28.4	18	49.4	4.2
LGS island	24.9	12.9	48.3	13.9
Qinling	30.5	16.9	48.3	4.3
Luochuan	27.4	12.5	53.3	6.8

environment of the whole Yangtze River Basin generally deteriorated at around 0.9 Ma. Therefore, we suggest that under the background of MPT, the strengthened east Asian winter monsoon and regional aridification driven by global cooling and the rapid uplift of the Tibetan Plateau are suggested as the primary drivers for the Xiashu loess. The development of the Xiashu loess was a regional response of the northern subtropical region in southern China to the MPT global cooling event.

CONCLUSION

The grain size of the Xiashu loess in the LRYR do not follow the coarse-fine NW-SE trend of the loess deposit on the CLP, and the surface microtextures of the quartz grains in the Xiashu loess are mostly different from those on the CLP, indicating that the loess deposits in the two regions have different provenances. The Gobi Desert in inland NW China are not considered as the primary provenance for the Xiashu loess. Instead, the adjacent floodplains in the LRYR, the alluvial plains of the Huai River and the Yellow River to the north during glacial periods are suggested as the dominant source materials for the Xiashu loess. Regional aridification and a strengthened east Asian winter monsoon (driven by global cooling and the rapid uplift of the Tibetan Plateau) are considered as the primary drivers for the accumulation of the Xiashu loess.

DATA AVAILABILITY STATEMENT

The raw data supporting the conclusion of this article will be made available by the authors, without undue reservation.

AUTHOR CONTRIBUTIONS

Investigation, QBF and LJ.; methodology, QBF and YL; data curation, QBF and XF.; writing original draft, QBF; review and editing, LJ and WY; funding acquisition, TW.

FUNDING

This research was funded by the National Key and Program Of China (2016YFC0500909)" Key Techniques and Demonstration of Desertification Control in Semiarid Area in North China", and the National Key Research and Development Program of China (Grant No. 2017YFC0504804).

REFERENCES

An, Z. S., Liu, T. S., Lou, Y C, Porter, S. C., kukla, G., Xihao, W., et al. (1990). The long-termpaleomonsoon variation recorded by the loess-paleosol sequence in Central China. *Quaternary international* 7-8, 91–95. doi:10.1016/1040-6182(90)90042-3

Chen, Y., Li, X., Han, Z., Yang, S., Wang, Y., and Yang, D. (2008). Chemical weathering intensity and element migration features of the Xiashu loess profile in Zhenjiang, Jiangsu Province. *J. Geogr. Sci.* 18, 341–352. doi:10.1007/s11442-008-0341-9

Chen, P J, Zheng, X M, and Zhou, L M, (2017). Grain Size Distribution and Its Significance of the Xiashu Loess in Nanjing-Zhenjiang Area. *Geological Science and Technology Information* 34 (5), 8–13.

Chen, R., Chen, J., Ma, J., and Cui, Z. (2019). Quartz Grain Surface Microtextures of Dam-Break Flood Deposits from a Landslide-dammed Lake: A case study. *Sedimentary Geology* 383, 238–247. doi:10.1016/j.sedgeo.2019.02.010

Clark, P. U., Archer, D., Pollard, D., Blum, J. D., Rial, J. A., Brovkin, V., et al. (2006). The middle Pleistocene transition: Characteristics, mechanisms, and implications for long-term changes in atmospheric pCO2. *Quaternary Science Reviews* 25, 3150–3184. doi:10.1016/j.quascirev.2006.07.008

Costa, P. J. M., Andrade, C., Dawson, A. G., Mahaney, W. C., Freitas, M. C., Paris, R., et al. (2012). Microtextural characteristics of quartz grains transported and deposited by tsunamis and storms. *sedimentary geology* 275-276, 55–69. doi:10.1016/j.sedgeo.2012.07.013

Costa, P. J. M., Andrade, C., Mahaney, W. C., Marques da Silva, F., Freire, P., Freitas, M. C., et al. (2013). Aeolian microtextures in silica spheres induced in a wind tunnel experiment: Comparison with aeolian quartz. *Geomorphology* 180-181, 120–129. doi:10.1016/j.geomorph.2012.09.011

Cui, Z., Wu, Y., Liu, G., Ge, D., Pang, Q., and Xu, Q. (1998). On Kunlun-Yellow River tectonic movement. *Sci. China Ser. D-Earth Sci.* 41, 592–600. doi:10.1007/bf02878741

Cui, Z J, Chen, Y X, Zhang, W, et al. (2011). Glacial chronology and origins of Quaternary glaciations in China. *Quaternary sciences* 31, 749–764.

Ding, Z., Liu, T., Rutter, N. W., Yu, Z., Guo, Z., and Zhu, R. (1995). Ice-Volume Forcing of East Asian Winter Monsoon Variations in the Past 800,000 Years. *Quat. res.* 44, 149–159. doi:10.1006/qres.1995.1059

Ding, Z. L., Derbyshire, E., Yang, S. L., Yu, Z. W., Xiong, S. F., and Liu, T. S. (2002). Stacked 2.6-Ma grain size record from the Chinese loess based on five sections and correlation with the deep-sea δ18O record. *Paleoceanography* 17, 5–1. doi:10.1029/2001pa000725

Ding, Z, Lu, R, and Wang, Y (2019). Spatiotemporal variations in extreme precipitation and their potential driving factors in non-monsoon regions of China during 1961-2017. *Environmental Research Letters* 14, 024005. doi:10.1088/1748-9326/aaf2ec

Ding, Z., Lu, R., Wang, L., Yu, L., Liu, X., Liu, Y., et al. (2021). Early-Mid Holocene climatic changes inferred from colors of eolian deposits in the Mu Us Desert. *Geoderma* 401, 115172. doi:10.1016/j.geoderma.2021.115172

Elderfield, H., Ferretti, P., Greaves, M., Crowhurst, S., McCave, I. N., Hodell, D., et al. (2012). Evolution of ocean temperature and ice volume through the mid-pleistocene climate transition. *Science* 337, 704–709. doi:10.1126/science.1221294

Fang, X. M., Chen, F. B., Shi, Y. F., and Li, J. J. (1996). Garze Loess and the Evolution of the Cryosphere on the Tibetan Plateau. *Journal of Glaciology and Geocryology* 18 (3), 193–200.

Folk, R. L., and Ward, W. C. (1957). Brazos River bar [Texas]; a study in the significance of grain size parameters. *Journal of Sedimentary Research* 27 (1), 3–26. doi:10.1306/74d70646-2b21-11d7-8648000102c1865d

Guo, Z. T. (2010). "22–8 Ma Monsoon evolution history recorded by eolian deposits (in Chinese)," in *Integrated Research on Environmental Evolution in Western China*. Editor Z. L. Ding (Beijing, China: China Meteorological Press), 1–19.

Guo, Z., Liu, T., Fedoroff, N., Wei, L., Ding, Z., Wu, N., et al. (1998). Climate extremes in Loess of China coupled with the strength of deep-water formation in the North Atlantic. *Global and Planetary Change* 18, 113–128. doi:10.1016/s0921-8181(98)00010-1

Guo, Z., Biscaye, P., Wei, L., Chen, X., Peng, S., and Liu, T. (2000). Summer monsoon variations over the last 1.2 Ma from the weathering of loess-soil sequences in China. *Geophys. Res. Lett.* 27, 1751–1754. doi:10.1029/1999gl008419

Guo, Z. T., Ruddiman, W. F., Hao, Q. Z., Wu, H. B., Qiao, Y. S., Zhu, R. X., et al. (2002). Onset of Asian desertification by 22 Myr ago inferred from loess deposits in China. *Nature* 416, 159–163. doi:10.1038/416159a

Hao, Q., Guo, Z., Qiao, Y., Xu, B., and Oldfield, F. (2010). Geochemical evidence for the provenance of middle Pleistocene loess deposits in southern China. *Quaternary Science Reviews* 29, 3317–3326. doi:10.1016/j.quascirev.2010.08.004

Helland, P. E., Huang, P.-H., and Diffendal, R. F. (1997). SEM Analysis of Quartz Sand Grain Surface Textures Indicates Alluvial/Colluvial Origin of the Quaternary "Glacial" Boulder Clays at Huangshan (Yellow Mountain), East-Central China. *Quat. res.* 48, 177–186. doi:10.1006/qres.1997.1916

Jiang, Q., Hao, Q., Peng, S., et al. (2020). Grain-size evidence for the transport pathway of the Xiashu oess in northern subtropical China and the linkage with fluvial systems. *Aeolian Research* 46, 1006–1013. doi:10.1016/j.aeolia.2020.100613

Krinsley, D H, and Doornkamp, J C (2011). *Atlas of quartz sand surface textures*. Cambridge, United Kingdom: Cambridge University Press.

Kutzbach, J. E., Ruddiman, W. F., and Prell, W. L. (1997). "Possible effects of Cenozoic uplift and CO2 lowering on global and regional hydrology," in *Tectonic Uplift and Climate Change*. Editor WF Ruddiman (New York, NY: Plenum Press), 149–170. doi:10.1007/978-1-4615-5935-1_7

Lai, Z. P., Zhou, J., and Xia, Y. F., (2001). Luminescence geochronology of Xiashu Loess near Nanjing. *Journal of Desert Research* 21, 116–121.

Lei, X. Y. (1998). Research for the loss in Fengzhou, Qinling mountain. *Geology of Shanxi* 16 (2), 45–57.

Lei, X. Y. (1999). Paleoenvironmental changes recorded by Shangzhou loess paleosol sequences on the eastern Qinling MTS. during the 0.6Ma. *Marine Geology & Quaternary Geology* 19 (1), 63–73.

Li, L. W., Fang, Y. S., and Qiu, S. Z. (1978). Discovery and significance of the deer and cattle fossils in calcareous concretion of XiaShu formation in Laohushan, 1. Nanjing, China: J Nanjing Norm Univ-Nat Sci Ed, 22–26.

Li, J. J., Fang, X. M., Pan, B., Zhao, Z., and Song, Y. (2001a). Late Cenozoic intensive uplift of Qinghai-Xizang Plateau and its imp-acts on environments in surrounding area. *Quaternary sciences* 21, 381–391.

Liu, T. (1985). *Loess and the Environment*. Beijing, China: China Ocean Press.

Li, C. Y., Peng, F., Xue, X., You, Q., Lai, C., Zhang, W., et al. (2018a). Productivity and Quality of Alpine Grassland Vary With Soil Water Availability Under Experimental Warming. *Frontiers in plant science* 9, 1790. doi:10.3389/fpls.2018.01790

Li, C.-Y., Peng, F., Xue, X., Lai, C.-M., Zhang, W.-J., You, Q.-G., et al. (2021a). Degradation stage effects on vegetation and soil properties interactions in alpine steppe. *J. Mt. Sci.* 18, 646–657. doi:10.1007/s11629-020-6192-2

Li, C., Peng, F., Lai, C., Xue, X., You, Q., Chen, X., et al. (2021b). Plant community changes determine the vegetation and soil δ 13 C and δ 15 N enrichment in degraded alpine grassland, *Land Degrad Dev* 32, 2371–2382. doi:10.1002/ldr.3912

Li, X. S., Yang, D. Y., Lu, H. Y., and Han, H., (1997). The grain-size features of Quaternary aeolian-dust deposition sequence in south Anhui and their significance. *Marine Geology and Quaternary Geology* 17, 73–81.

Li, X. S., Yang, D. Y., and Lu, H. Y. (2001b). Grain-size features and genesis of the Xiashu loess in Zhenjiang. *Marine Geology and Quaternary Geology* 21, 25–32.

Li, X. S., Han, Z. Y., Lu, H. Y., Chen, Y., Yang, L., Xiaokong, Y., et al. (2018b). Onset of Xiashu loess deposition in southern China by 0.9 Ma and its implications for regional aridification. *Science in China* 48 (2), 210–223.

Liu, F (2006). *Paleo-Environmental Information study of Loess on Islands in East China Sea and Xiashu Loess[D]*. Shanghai, China: East China normal University.

Lu, H., van Huissteden, K., Zhou, J., Vandenberghe, J., Liu, X., and An, Z. (2000). Variability of East Asian winter monsoon in Quaternary climatic extremes in North China. *Quat. res.* 54, 321–327. doi:10.1006/qres.2000.2173

Lu, H. Y., Wang, X. Y., and Li, L. P. (2008). Aeolian dust records indicate the linkage of global cooling and Asian drying in late Cenozoic (in Chinese). *Quat Sci* 28, 949–956.

Mahaney, W. (2002). *Atlas of Sand Grain Surface Textures and Applications*. Oxford, United Kingdom: Oxford University Press.

Mahaney, W., and Kalm, V. (2000). Comparative scanning electron microscopy study of oriented till blocks, glacial grains and Devonian sands in Estonia and Latvia. *Boreas* 29, 35–51. doi:10.1111/j.1502-3885.2000.tb01199.x

Mahaney, W. C., Stewart, A., and Kalm, V. (2001). Quantification of SEM microtextures useful in sedimentary environmental discrimination. *Boreas* 30, 165–171. doi:10.1080/030094801750203170

Mahaney, W. C., Hancock, R. G. V., Milan, A., Pulleyblank, C., Costa, P. J. M., and Milner, M. W. (2014). Reconstruction of Wisconsinan-age ice dynamics and compositions of southern Ontario glacial diamictons, glaciofluvial/lacustrine, and deltaic sediment. *Geomorphology* 206, 421–439. doi:10.1016/j.geomorph.2013.10.014

Purtill, M. P., Kite, J. S., and Forman, S. L. (2019). Geochronology and Depositional History of the Sandy Springs Aeolian Landscape in the Unglaciated Upper Ohio River Valley, United States. *Front. Earth Sci.* 7, 322 doi:10.3389/feart.2019.00322

Pye, K. (1987). *Aeolian Dust And Dust Deposits*. London, United Kingdom: Academic Press, 1–165.

Pye, K. (1995). The nature, origin and accumulation of loess. *Quaternary Science Reviews* 14, 653–667. doi:10.1016/0277-3791(95)00047-x

Qiao, Y., Guo, Z. T., Hao, Q. Z., Wu, W., Jiang, W., Yuan, B., et al. (2003). Loess-soil sequences in southern Anhui Province: magnetostratigraphy and paleoclimatic significance. *Chinese Sci Bull* 48, 2088–2093. doi:10.1360/03wd0183

Qiao, Y. S., Zhao, Z. Z., and Li, Z. Y., (2007). Aeolian origin of The red earth formation in the Cheng Du Plain. *Quaternary Sciences* 27, 286–294.

Ruddiman, W. F., Raymo, M., and McIntyre, A. (1989). Matuyama 41000-year: cycles: North Atlantic Ocean and northern hemisphere ice sheets. *Earth and Planetary Science Letters* 80, 117–129. doi:10.1016/0012–821X(86)90024-5

Shi, Y., Zhang, W., and Dai, X., (2005). Characteristics of clay mineral assemblage of Xiashu Loess and their paleoenvironmental significance. *Marine Geology and Quaternary Geology* 25, 99–105.

Smith, C., Soreghan, G. S., and Ohta, T. (2018). Scanning electron microscope (SEM) microtextural analysis as a paleoclimate tool for fluvial deposits: a modern test. *Geological Society of America Bulletin* 130, 1256–1272. doi:10.1130/b31692.1

Sun, Y. B., and Guo, F. (2017). Rapid monsoon changes recorded by Chinese loess deposits. *Journal of Quaternary Science* 37 (5), 963–973. doi:10.11928/j.issn.1001-7410.2017.05.04

Sun, Y B, and An, Z S (2000). Sedimentary interpretation of surface textures of quartz grains from the eolian deposits. *Acta Sedimentologica Sinica* 18 (4), 506–510.

Sweet, D. E., and Soreghan, G. S. (2010). Application of Quartz Sand Microtextural Analysis to Infer Cold-Climate Weathering for the Equatorial Fountain Formation (Pennsylvanian-Permian, Colorado, U.S.A). *Journal of Sedimentary Research* 80, 666–677. doi:10.2110/jsr.2010.061

Westerhold, T., Marwan, N., Drury, A. J., Liebrand, D., Agnini, C., Anagnostou, E., et al. (2020). An astronomically dated record of Earth's climate and its predictability over the last 66 million years. *Science* 369, 1383–1387. doi:10.1126/science.aba6853

Tsoar, H., and Pye, K. (1987). Dust transport and the question of desert loess formation. *Sedimentology* 34, 139–153. doi:10.1111/j.1365-3091.1987.tb00566.x

Vandenberghe, J. (2013). Grain size of fine-grained windblown sediment: A powerful proxy for process identification. *Earth-Science Reviews* 121, 18–30. doi:10.1016/j.earscirev.2013.03.001

Vandenberghe, J., Sun, Y., Wang, X., Abels, H. A., and Liu, X. (2018). Grain-size characterization of reworked fine-grained aeolian deposits. *Earth-Science Reviews* 177, 43–52. doi:10.1016/j.earscirev.2017.11.005

Van Buuren, U., Prins, M. A., Wang, X. Y., Stange, M., Yang, X., and van Balen, R. T. (2020). Fluvial or aeolian? Unravelling the origin of the silty clayey sediment cover of terraces in the Hanzhong Basin (Qinling Mountains, central China). *Geomorphology* 367, 1–18. doi:10.1016/j.geomorph.2020.107294

Vos, K., Vandenberghe, N., and Elsen, J. (2014). Surface textural analysis of quartz grains by scanning electron microscopy (SEM): from sample preparation to environmental interpretation. *Earth-Science Reviews* 128, 93–104. doi:10.1016/j.earscirev.2013.10.013

Wang, Y., and Deonarine, B. (1985). *Model Atlas of Surface Textures of Quartz Sand[M]*. Beijing, China: Science Press.

Wang, P. (1999). Response of Western Pacific marginal seas to glacial cycles: paleoceanographic and sedimentological features. *Marine Geology* 156, 5–39. doi:10.1016/s0025-3227(98)00172-8

Wang, X., Lu, H., Zhang, H., Wu, J., Hou, X., Fu, Y., et al. (2018). Distribution, provenance, and onset of the Xiashu Loess in Southeast China with paleoclimatic implications. *Journal of Asian Earth Sciences* 155, 180–187. doi:10.1016/j.jseaes.2017.11.022

Wu, B Y. (1985). On depositional characteristic of Xiashu loess from Nanjing. *Marine Geology & Quaternary Geology* 5, 113–121.

Wu, C., Zheng, X., Zhou, L., Ren, S., and Qian, P. (2020). Quantitative Estimation of Provenance Contributions to Loess Deposits in Eastern China and Implication for Paleo-dust Storm Activity. *Geomorphology* 373, 107489. doi:10.1016/j.geomorph.2020.107489

Wu, C L, Zhu, C, and Lu, H Y, (2006). Magnetostratigraphic dating of the Xiashu loess in Nanjing area and its paleoenvironmental interpretation. *Journal of Stratigraphy* 30, 116–123.

Xiao, J., and An, Z., (1999). Three large shifts in East Asian monsoon circulation indicated by loess -paleosol sequences in China and late Cenozoic deposits in Japan. *Palaeogeography, Palaeoclimatology, Palaeoecology,* 154(3), 179–189. doi:10.1016/s0031-0182(99)00110-8

Xu, D., Lu, H., Wu, N., and Liu, Z., (2012). 30000-Year vegetation and climate change around the East China Sea shelf inferred from a high-resolution pollen record. *Quaternary International* 279-280, 543. doi:10.1016/j.quaint.2012.08.1908

Xu, H. Y., Zheng, X. M., and Zhou, L. M., (2016). Characteristics of Quartz Grains of the Xiashu Loess in Zhoujiashan Nanjing and Its Provenance Significance. *Acta Sedimentologica Sinica* 34 (6), 1176–1186.

Yang, L. H., Ye, W., and Zheng, X. M., (2014). The Discriminant Function with Grain Size of Floodplain and Aeolian Sediments and Its Application in the Quaternary Red Clay. *Geographical Research* 33 (10), 1848–1856. doi:10.11821/dlyj201410006

Yang, L.-H., Zheng, X.-M., Ye, W., et al. (2017). Sedimentary environment of vermicular red clay in South China. *J. Mt. Sci.* 14 (3), 513–526. doi:10.1007/s11629-016-3973-8

Yang, S. Y., Li, C. X., Yang, D. Y., and Li, X. S. (2004). Chemical weathering of the loess deposits in the lower Changjiang Valley, China, and paleoclimatic implications. *Quaternary International* 117, 27–34. doi:10.1016/s1040-6182(03)00113-7

Yang, X., Wang, X., Van Balen, R. T., Prins, M. A., Wang, S., van Buuren, U., et al. (2019). Fluvial terrace formation and its impacts on early human settlement in the Hanzhong basin, Qinling Mountains, central China. *Global and Planetary Change* 178, 1–14. doi:10.1016/j.gloplacha.2019.04.007

Zhang, W., Yu, L., Lu, M., Zheng, X., and Shi, Y. (2007). Magnetic properties and geochemistry of the Xiashu Loess in the present subtropical area of China, and their implications for pedogenic intensity. *Earth and Planetary Science Letters* 260, 86–97. doi:10.1016/j.epsl.2007.05.018

Zhang, W., Yu, L., Lu, M., Zheng, X., Ji, J., Zhou, L., et al. (2009). East Asian summer monsoon intensity inferred from iron oxide mineralogy in the Xiashu Loess in southern China. *Quaternary Science Reviews* 28, 345–353. doi:10.1016/j.quascirev.2008.10.002

Zhao, Z Z, Qiao, Y S, Wang, Y, Fu, J., Wang, S., Li, C., et al. (2007). Magnetostratigraphy and its Paleoclimatic Significance Of The Red Earth Formation In The Cheng Du Plain. *Science in China, Series D* 37, 370–377.

Zheng, X M. (1999). *Aeolian Deposition and Environment in Changjiang Delta and Extending Sea Areas*. Shanghai, China: East China Normal University Press.

Conflict of Interest: The authors declare that the research was conducted in the absence of any commercial or financial relationships that could be construed as a potential conflict of interest.

frontiers in Earth Science

ORIGINAL RESEARCH
published: 15 June 2021
doi: 10.3389/feart.2021.698229

Halogenases of Qarhan Salt Lake in the Qaidam Basin: Evidence From Halite Fluid Inclusions

Jun Li[1,2,3], Xiying Zhang[1,2]*, Mingyue Hu[4]*, Wenxia Li[1,2,3], Weiliang Miao[1,2], Xiaolong Yuan[1,2], Yongshou Li[1,2], Qiliang Tang[1,2], Wenxia Han[5] and Haizhou Ma[1,2]

[1]Key Laboratory of Comprehensive and Highly Efficient Utilization of Salt Lake Resources, Qinghai Institute of Salt Lakes, Chinese Academy of Sciences, Xining, China, [2]Qinghai Provincial Key Laboratory of Geology and Environment of Salt Lakes, Qinghai Institute of Salt Lakes, Chinese Academy of Sciences, Xining, China, [3]University of Chinese Academy of Sciences, Beijing, China, [4]National Research Center for Geoanalysis, Beijing, China, [5]College of Resources and Environment, Linyi University, Linyi, China

The fluid inclusion composition of halite can help track chemical composition of ancient fluids and, thus, serves as a reliable index to analyze ancient brine in salt lakes. Qarhan Salt Lake (QSL) is the largest potash brine deposit in China. Although the mixing of modern river water and Ca-Cl deep water is widely accepted as potassium formation, the mixing characteristics in the time domain and driving factors of deep water are still unclear. Here, the chemical composition of fluid inclusions in primary halite samples collected from the ISL1A borehole in QSL was measured by LA-ICP-MS technology. The analysis results show that, during the formation stage of the S_4 salt layer in QSL, the main potassium salt layer, the contents of Ca^{2+} and Sr^{2+} in brine increased significantly. There is evidence confirming that Ca-Cl deep water is beneficial to the enrichment of potassium and the surrounding rivers generally develop terraces. It suggests that, during the formation stage of the QSL potassium salt layer, more Ca-Cl inflow water of the northern margin supplies the salt lake, inferring that it was driven by tectonic activities. In addition, the chemical composition of halite fluid inclusions shows that there is an anomaly in geochemistry at the early stage of salt formation in QSL. By combining the time of tectonic activities, it is inferred that the anomaly is not caused by tectonic activities but maybe caused by a salt-forming event. This work indicates that deep water and tectonic movement have a huge impact on the evolution of salt lakes. Therefore, it is necessary to consider the influence of deep water and tectonic activities on the salt-forming evolution stage of salt lakes when studying the salt-forming evolution stage of salt lakes and paleoclimate by using salt lake deposition.

Keywords: Qaidam Basin, Qarhan Salt Lake, Ca-Cl brines, halogenases, halite fluid inclusions, tectonic activities

Edited by:
Xiangzhong Li,
Yunnan University, China

Reviewed by:
Yangtong Cao,
Chinese Academy of Geological Sciences, China
Yuan-Yuan Lü,
Chinese Academy of Geological Sciences, China

***Correspondence:**
Xiying Zhang
xyzhchina@isl.ac.cn
Mingyue Hu
luna010_w@163.com

Specialty section:
This article was submitted to Quaternary Science, Geomorphology and Paleoenvironment, a section of the journal Frontiers in Earth Science

Received: *21 April 2021*
Accepted: *25 May 2021*
Published: *15 June 2021*

Citation:
Li J, Zhang X, Hu M, Li W, Miao W, Yuan X, Li Y, Tang Q, Han W and Ma H (2021) Halogenases of Qarhan Salt Lake in the Qaidam Basin: Evidence From Halite Fluid Inclusions. Front. Earth Sci. 9:698229. doi: 10.3389/feart.2021.698229

INTRODUCTION

As an important part of the Tibetan Plateau (TP), the Qaidam Basin (QB) is located in the north of the TP and occupied by a large number of salt lakes having potassium, lithium, and boron salt resources. Qarhan Salt Lake (QSL) is the largest salt lake in the QB and has always been the hot and typical spot for studying the evolution and environmental changes of modern salt lakes (Yang et al., 1995; Yu, 2000; Fan et al., 2018; Li et al., 2020; He et al., 2020).

The beginning of salt formation in QSL was about 50 ka ago, and the whole process is divided into three stages during which the main salts were deposited (Zhang et al., 1990; Zhang et al., 1993; Fan et al., 2015). Except for the impact of the climate changes on the evolution of QSL, the mixing of different brines also played an important role during the evolution of the salt lake (Yuan and Duan, 1989). It is found that the formation of potassium-bearing brine in QSL is the result of the mixing of river water and Ca-Cl deep water (Lowenstein et al., 1989; Zhang et al., 1993), which is confirmed by Pitzer model simulation (Liu et al., 2002). The study of mineral assemblage in different sections of the QSL surface also indicated the existence of the mixing phenomenon in different water bodies (Yi et al., 2017). A recent study argues that mixing probably continued the whole process of salt formation (Fan et al., 2018) and exerted important influence on the formation of salts (Li et al., 2020). In a word, the mixing process of magnesium sulfate subtype water and calcium chloride–type water controls the enrichment of QSL. However, although many studies on mixing existing in the modern QSL have been carried out, only few studies focus on ancient salts. Therefore, it is not so clear whether mixing happened in the evolution history of QSL. Determining the driving mechanism of mixing is even more interesting.

The analysis of fluid inclusion in halite is a direct and effective method to indicate the evolution of saline fluid/paleo-brine in ancient and modern evaporite basins (Goldstein and Reynolds, 1994; Meng et al., 2011, 2012; Weldgehebriel et al., 2020). In this paper, the chemical composition of primary fluid inclusion in halite from the ISL1A borehole drilled in the north QSL is studied. Based on the information from fluid inclusion in halite, we will make an attempt to identify the mixing of brines and discuss its influence on halogenases of QSL.

Geological Setting

The QB is a large intermontane basin on the northeastern Tibetan Plateau. The formation and evolution of the QB are influenced by the Altyn Tagh left strike-slip fault system, Kunlun thrust fault system, and Qilian Mountain south thrust system. Its active tectonic activity and developed faults provide a channel and power for a Ca-Cl–type deep hydrothermal brine to deposit in lakes (Zhang, 1987; Ren et al., 2006; Lowenstein and Risacher, 2009). There is a thrust fault extending for hundreds of kilometers from northwest to southeast in the basin, and the Ca-Cl deep hydrothermal brine in the Huobuxun section of QSL is upwelling along this fault (Zhang, 1987; Lowenstein et al., 1989). The distribution of salt lakes in the QB is mainly controlled by geological structural factors. According to its relationship with structural units, it can be divided into three salt lake areas: Mangya fault depression, central strong depression, and Qilian Mountain front block fault zone (Yuan, 1959; Zhang, 1987) (**Figure 1A**). The combined presence of ambient high mountains with altitudes >4000 m and a low basin with altitudes ranging from 2600 to 3200 m in the QB, as well as the secular drying of the climate and environment within the basin during the Cenozoic, favors the formation of salt deposits (Yuan et al., 1983; Zhang, 1987). Thus, more than 30 salt lakes with rich thick salt beds and brines are distributed in the basin (Zhang, 1987). QSL lies in the eastern part of the QB and covers an area of 5856 km^2. Nowadays, QSL is almost a “dry lake,” with only some brine lakes remaining in the eastern, western, and southern margins (Zhang, 1987; Zheng et al., 2002; Huang and Han, 2007) (**Figure 1B**).

The Sanhu depression, the eastern depression of the QB, is abundant in biogenic gas and brine–salt resources (Li et al., 2020). QSL is located in the Sanhu depression and southeast of the QB. Both the north and south sides of the lake are compressional and torsional deep faults, and the salt accumulation area is located in this graben depression. Geological development is dominated by subsidence, and thousands of meters of sediments have accumulated in the lake area. There are nine surface brine lakes distributed within the margin of the playa, including North Huobuxun Lake, South Huobuxun Lake, Xiezuo Lake, Senie Lake, Tuanjie Lake, Dabuxun Lake, Dongling Lake, Dabiele Lake, and Xiaobiele Lake (**Figure 1B**). These marginal brine lakes are not residual lakes but formed through river and spring water inflows following the formation of the salt playa (Chen et al., 1981). Accompanied by the change in climate, the sediments also appeared alternately as salt layers and clastic layers (Zhang et al., 2003) and ultimately formed a super-large salt deposit mainly composed of salt intercrystalline brine.

Salt-bearing strata in the mining area are mainly lacustrine fine clastic and chemical sedimentary formations since Quaternary. Fine clastic formations are mainly silt and clay, while chemical sedimentary formations are mainly halite formations (Hu, 1990). The salt deposits in QSL can be divided into four layers from bottom to top (**Figure 2**), namely, S_1, S_2, S_3, and S_4. The potassium deposit mainly exists in the upper S_4 layer (Yang, 1982; Huang and Cai, 1987).

MATERIALS AND METHODS

The borehole ISL1A (37°3′50″N, 94°43′41″E) is located in the Bieletan section of QSL (**Figure 1B**), and the lithology and sedimentary characteristics of the borehole have been described in previous studies (An et al., 2013; Fan et al., 2014; Wei et al., 2015; Miao et al., 2016). Totally, the upper part of ISL1A (0–51.0 m) consists of halite, silty sand, and clay. The lower part of ISL1A (51.0–102.0 m) consists of silty sand and clay with organic matter and no evaporites. Here, the halite from the upper evaporite section was sampled for further study. The ISL1A borehole core profile shows that salt suddenly begins to form at 51 m (An, 2012; Zhang, 2020), but there is no formed halite crystal until about 45 m, so the sample is selected from 43.46 m.

Samples and Observation

According to the sedimentary characteristics, 12 halite samples were selected for petrographic observation to test composition. The processing method refers to the method of Benison and Goldstein, 1999. In order to avoid damaging the fluid inclusions of halite, firstly, the halites selected with better crystal form are peeled off along the cleavage plane with a knife and made into 0.5–1 mm slices (**Figure 3**). After that, they are observed under a microscope with single polarized light. The identification of primary halite, which has the characteristics of the chevron and cumulate inclusion zone, refers to previous works (Haride et al., 1983; Lowenstein and Haride, 1985; Zhang et al., 1990). The

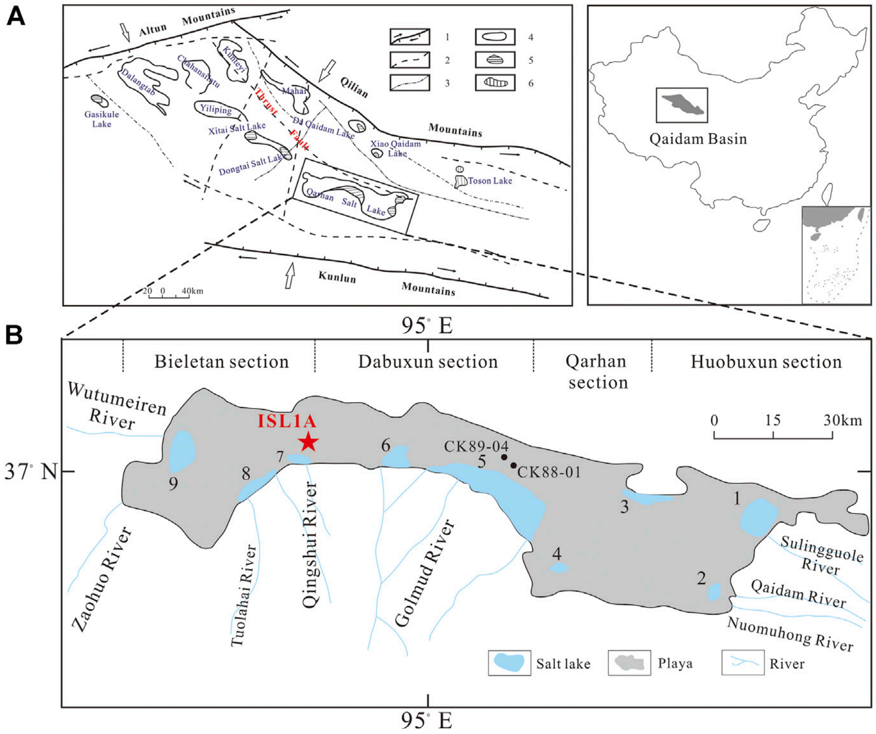

FIGURE 1 | Tectonic outline and salt lakes in the QB (Li et al., 2020). **(A)** Map showing the tectonic divisions of the QB and the location of Qarhan Salt Lake (QSL). 1: grade I structural line controlling the boundary of the Qaidam ancient block; 2: grade II structural line controlling the Qaidam Basin; 3: grade III structural line controlling the salt lake belt; 4: salt playa; 5: brine lake; 6: brackish water lake. **(B)** Location of drillholes ISL1A, CK89-04, and CK88-01 in QSL.

samples were observed and screened with reference to the standards above. The result of observation shows that the inclusions are mainly single liquid phase, more than 90% of which are regular cubes. The size is within 10–30 μm and occasionally larger more than 100 μm (**Figure 4**).

Analytical Methods

The chemical composition of halite fluid inclusions was measured at the National Research Center for Geoanalysis of the Chinese Academy of Geological Sciences, by the LA-ICP-MS method, using an Element 2 plasma mass spectrometer (Finnigan Company, Germany) and UP 213 laser (New Wave Company). The halite slice was fixed on the glass slide, and the glass slide was placed in the laser ablation chamber. The laser beam with a wavelength of 193 nm and beam spot of 50 μm was focused on the surface of the sample for single-point ablation, with a pulse frequency of 8 Hz, pulse energy of 0.26 mJ, output energy of 80%, and energy density of about 16 J/cm^2. The background collection time of ICP-MS is 20 s, and the denudation time is 160 s. Because this method cannot know the volume of inclusions and needs the comparison of elements with known concentrations, the calibration method adopts the combination of internal and external standards (Hu et al., 2008; Sun et al., 2013). In the external standard method, the prepared standard solution was drawn into a pure quartz capillary tube and quickly sealed with epoxy resin. During the test and analysis, manufactured artificial fluid inclusions were attached to a glass sheet with double-sided adhesive and put into a laser ablation sample chamber together with test samples. In the internal standard method, Na was selected as the internal standard element for halite fluid inclusion samples, and the Na content was calculated to be 141.62 g/L based on the theoretical value. It is assumed that the relative sensitivity between the standard calibration instrument and elements in the unknown sample remained unchanged; that is, calibration was carried out according to the consistency of changes in the internal standard element and elements to be measured (Longerich et al., 1996; Hu et al., 2008).

RESULTS

Age of Samples

Fan et al. (2014) established the chronological linear regression equation of the ISL1A borehole, which is y = 1.2091 x −10.266; here, the ordinate is the sampling depth, and the horizontal ordinate represents age. By the interpolation method, the age of the samples in this study is obtained (**Figure 5** and **Table 1**).

Chemical Composition of Fluid Inclusion in Halite

In this study, the chemical composition of 171 halite fluid inclusions in 12 halite samples was determined by LA-ICP-MS

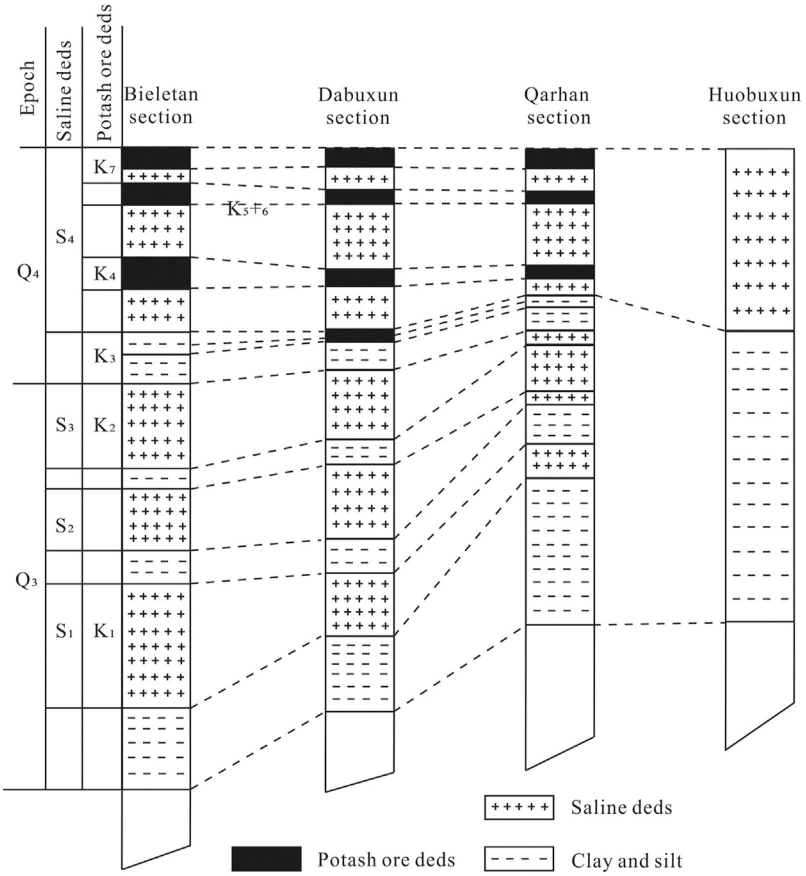

FIGURE 2 | Comparison sketch of the potash ore beds with saline beds in different sectors in Qarhan saline lake from Yang (1982).

technology. Due to the large number of halite fluid inclusions we measured, here we only list the average concentration of ions in each halite sample after data processing (**Table 1**). There are two significant inflection points in the longitudinal variation tendency of Mg^{2+}, K^+, Ca^{2+}, Br^-, Sr^{2+}, Li^+, B^{3+}, and Rb^+ contents in the evaporation salt layer in the upper part of the ISL1A borehole. From the beginning of salt formation to 25.32 m, the ion content decreased at the same time and then increased significantly at 11.10 m, which divided the variation tendency of data into three parts (**Table 1** and **Figure 6**). The study of δD and $\delta^{18}O$ shows that the evolution of QSL can be divided into three stages (Lowenstein et al., 1994; Yang et al., 1995; Zhang et al., 1995). Meanwhile according to the sedimentary characteristics of the evaporation salt layer in the upper part of ISL1A, we share its three salt-bearing layers (Fan et al., 2015; Du et al., 2019). In this study, the variation tendency of the ion content can also be divided into three stages (**Figure 6**), which is confirmed by the three stages of salt formation in QSL. It reflects the evolution process of QSL from concentration to desalination and concentration again. But there are two anomalies that deserve attention. The one is that Mg^{2+}, Br^-, K^+, and B^{3+} contents, which reflect the concentration degree of the salt lake, are higher at an early stage of salt formation, especially Mg^{2+} and Br^- reaching 64.62 g/L and 19.58 mg/L, respectively. Another abnormal phenomenon is that, during the middle and late evolution of QSL, the enrichment stage of potassium and magnesium, the contents of Ca^{2+} and Sr^{2+} increased suddenly at the same time, and the peak values reached 11.22 g/L and 244.25 mg/L, respectively.

DISCUSSION

Ca-Cl Deep Water During Halogenases in QSL

A previous study argues that the Ca-Cl deep water supply and mixing probably continued the whole process of salt formation in QSL (Fan et al., 2018), but the specific change in supply quantity is not clear. According to the δD and $\delta^{18}O$ characteristics of the fluid inclusions in the primary halite of ZK88-01 and ZK89-04 in QSL, we share the salt-forming environment of the salt lake's three stages: I, II, and III partitions represent three ranges of variation from bottom to top (Zhang et al., 1990; Zhang et al., 1995) (**Figure 6**). In the first stage (depth > 23 m), δD and $\delta^{18}O$ values are large and very close (**Figure 6** I), indicating that the salt lake is in a stable drying stage. In addition, because δD vs. $\delta^{18}O$ is located in the upper right of the evaporation line in the study area, it does not completely fall on the evaporation line (**Figure 6** I),

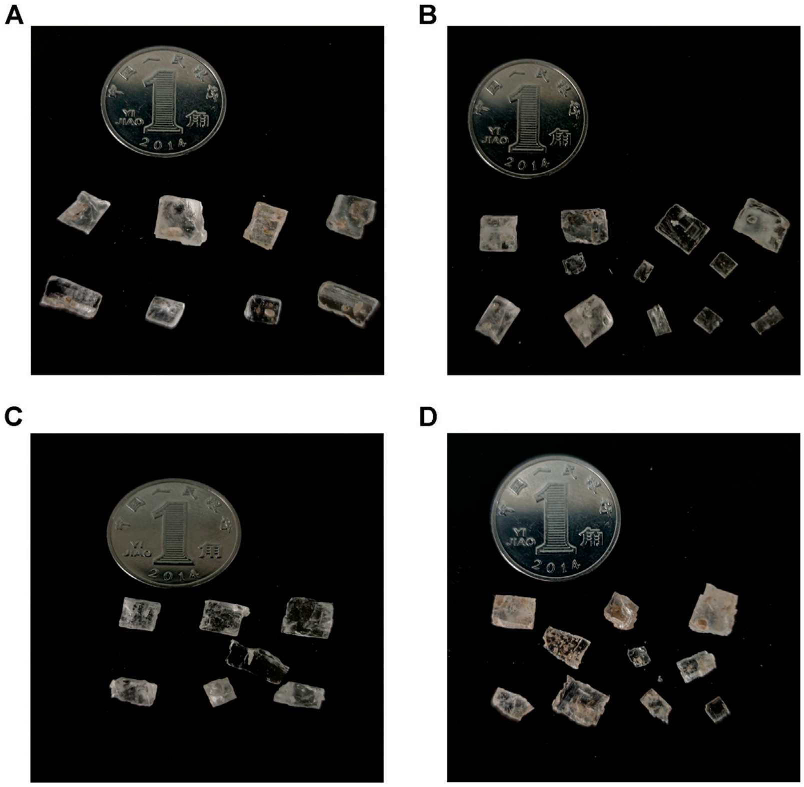

FIGURE 3 | Halite debris particles from the ISL1A drillhole. **(A,D)** Halite crystals and chips mixed with clay and silt that were prepared by cleaving 0.5–1 mm thickness with a razor blade. **(B,C)** Typical halite idiomorphic crystals and chips without clay and silt.

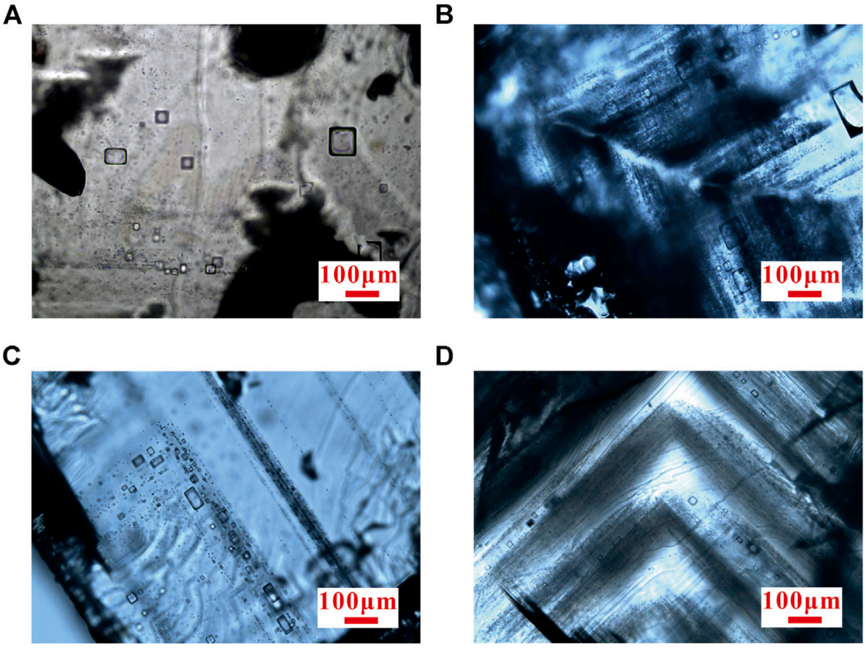

FIGURE 4 | Petrologic characteristics of halite fluid inclusions. **(A)** Irregular dispersion of primary halite fluid inclusions. **(B,D)** Parallel fluid inclusion bands in hopper primary crystals that form bright and dark bands with host minerals, with dark ones being fluid inclusion groups. **(C)** Primary halite fluid inclusions regularly distributed along the crystal growth.

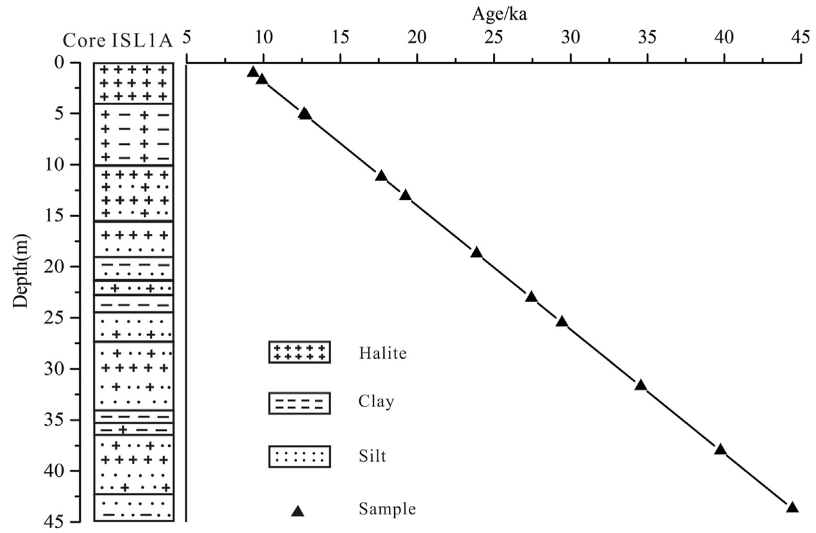

FIGURE 5 | Age and depth of halite samples in this study.

TABLE 1 | Chemical components of fluid inclusions in halites from the ISL1A drillhole.

Content	Depth (m)	Age (ka)	n	Avg. ρ(B) (g/L)			Avg. ρ(B) (mg/L)				
				Mg	K	Ca	Br	Sr	Li	B	Rb
Q-1	1.00	9.32	59	101.71	46.36	1.92	0.00	33.21	118.47	107.70	3.91
Q-2	1.70	9.89	9	49.37	10.52	0.19	19.62	7.26	60.07	134.19	2.61
Q-3	5.00	12.64	9	214.73	43.33	4.58	0.00	54.68	94.57	44.13	19.93
Q-4	5.15	12.75	17	194.89	25.14	0.98	16.58	14.81	196.28	197.11	7.35
Q-5	11.10	17.67	4	137.23	46.89	11.22	18.93	244.25	183.38	62.47	11.77
Q-6	13.00	19.24	11	190.38	41.57	9.02	0.00	180.45	119.83	53.76	11.49
Q-7	18.60	23.87	10	16.91	5.28	0.62	3.80	11.51	8.89	8.94	0.89
Q-8	22.91	27.44	13	19.38	5.64	1.31	5.46	28.98	15.50	21.49	1.75
Q-9	25.32	29.43	8	5.07	1.62	0.33	3.90	7.31	8.69	7.47	0.68
Q-10	31.52	34.56	13	9.45	2.25	0.22	4.86	4.22	25.21	22.70	0.68
Q-11	37.79	39.75	13	27.72	5.91	0.66	8.88	33.40	60.90	50.40	2.44
Q-12	43.46	44.43	5	64.62	13.04	0.43	19.58	10.33	68.01	140.17	1.80

which proves that the hydrological characteristics of the ancient lake at this time are not controlled by evaporation factors alone, and there may be a situation of high salt brine replenishment. In the second stage (8–23 m), δD vs. δ^{18}O deviates significantly from the evaporation line in the study area (**Figure 6** II), which indicates that there should be a large amount of δD- and δ^{18}O-poor water supply in the lake area at this time. In the third stage (depth < 8 m), δD vs. δ^{18}O is all distributed on the evaporation line in the study area (**Figure 6** III), indicating that the hydrological characteristics of the lake at this time are mainly controlled by temperature rise and evaporation (Zhang et al., 1990).

In view of the characteristics of rich Sr^{2+} and Ca^{2+} in deep water, $\rho(Ca^{2+})$ and $\rho(Sr^{2+})$ of halite fluid inclusions in the ISL1A borehole are compared with the δD contents of CK89-04 and CK88-01, and there is an obvious negative correlation near 10 m (**Figure 9**). The normal salt precipitation sequence shows that the deposition of potassium and magnesium salts, expressed by enrichment of potassium and magnesium ions, will not be accompanied by the abnormal enrichment of Ca^{2+} ions (Hu, 1991). However, the deposition of potassium and magnesium salts in QSL was accompanied by abnormally enriched Ca^{2+} in the ISL1A borehole (**Figure 7**). Meanwhile, unpublished data show that polyhalite ($K_2Ca_2Mg\,[SO_4]_4.2H_2O$) appears in the stage of abnormal Ca^{2+} enrichment. The polyhalite found in the salt-bearing strata of QSL is considered to be a primary mineral formed by fluid mixing (Sun and Lock, 1988). Not only Ca^{2+} but also Sr^{2+} is abnormally enriched (**Figure 7**), and Ca-Cl deep waters and brines are enriched with Sr^{2+} and Ca^{2+} in QSL (Fan et al., 2018). However, the Br^{-} content, which reflects the salt lake concentration, did not increase abnormally but increased gradually (**Figure 9**). The formation of $MgSO_4$-deficient evaporites in QSL (Zhang et al., 1991; Li et al., 2020) also indicates that the lake has been replenished by Ca-Cl deep

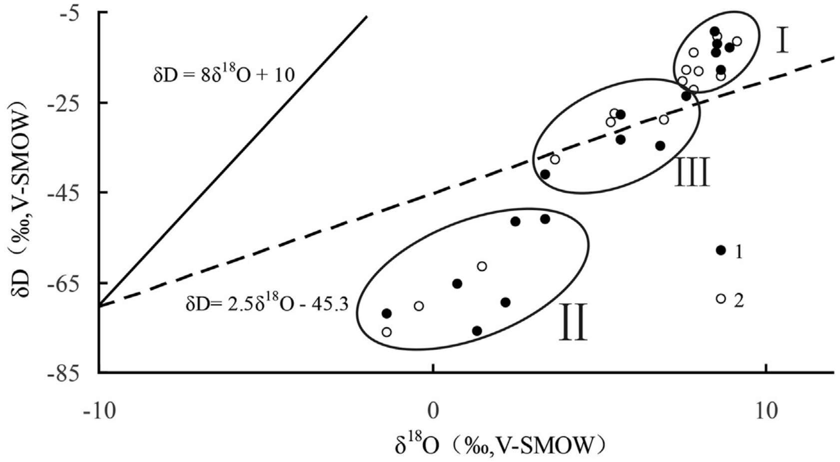

FIGURE 6 | $\delta^{18}O$ vs. δD graph of primary halite fluid inclusions in QSL. 1: ZK88-01; 2: ZK89-04; I, II, III: partitions. The full line is the Global Meteoricwater Line of Craig, and the dotted line is the evaporation line in the QSL area from Zhang et al. (1995).

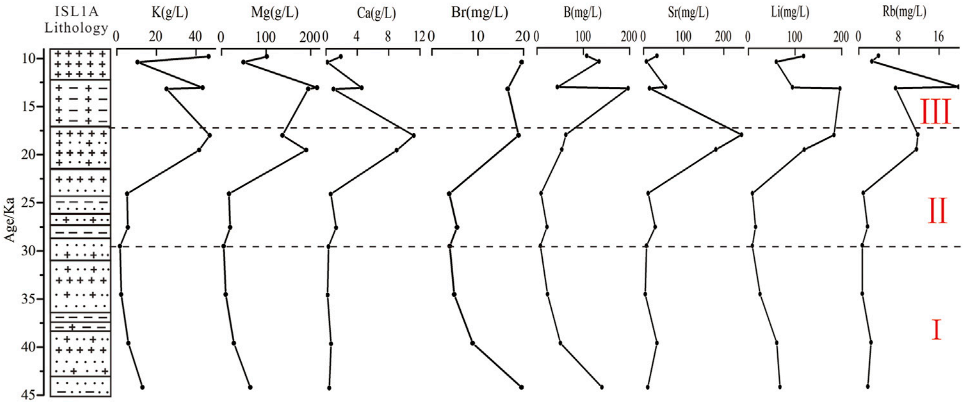

FIGURE 7 | Change characteristics about chemical composition of halite fluid inclusions.

waters after entering the salt precipitation stage, and their hydrochemical types have been reformed. Based on these, it is speculated that the sudden enrichment of Sr^{2+} and Ca^{2+}, the second stage of salt formation in QSL, may be caused by the greatly enhanced activity of Ca-Cl deep water, and more deep water supplies to the normally evolving salt lakes for mixing, resulting in the anomaly of ancient brine and minerals. In addition, combined with the characteristics of high concentration of chemical composition of halite fluid inclusions in the ISL1A core at the initial stage of salt formation, and the characteristics of high $\delta^{18}O$ and δD values of ZK88-01 and ZK89-04 at the first stage and deviating from the evaporation line, it is speculated that Ca-Cl deep water replenishment also has influence on the initial stage of salt formation in QSL. However, Ca-Cl deep water is weak in the third salt-forming stage and modern salt-forming process of QSL.

The comprehensive analysis of chemical composition, variation characteristics, and stable isotopes of ancient brine shows that the evolution of QSL is not a simple cycle of evaporation concentration–dilution desalination affected by climate fluctuations. The replenishment and mixing of Ca-Cl deep water play an important role in the evolution of ancient brine and the formation of evaporation salt.

Geochemical Anomalies at the Initial Stage of Salt Formation in QSL

Br^- in saline minerals/waters is an important indicator to reflect the degree and stage of the evaporation condition of the brine, and a higher content of Br^- usually indicates a stronger evaporation of the salt lake and thus a higher concentration of brine (Sanders, 1991; Warren, 2006; Cheng et al., 2008; Farid et al., 2013; Zarei et al., 2013; Biehl et al., 2014; Zhao et al., 2020). However, the Br^- content in the ISL1A core was abnormally high in the early stage of salt formation (**Figure 7**); it then decreased since 37.79 m, re-increased in the late stage of salt formation,

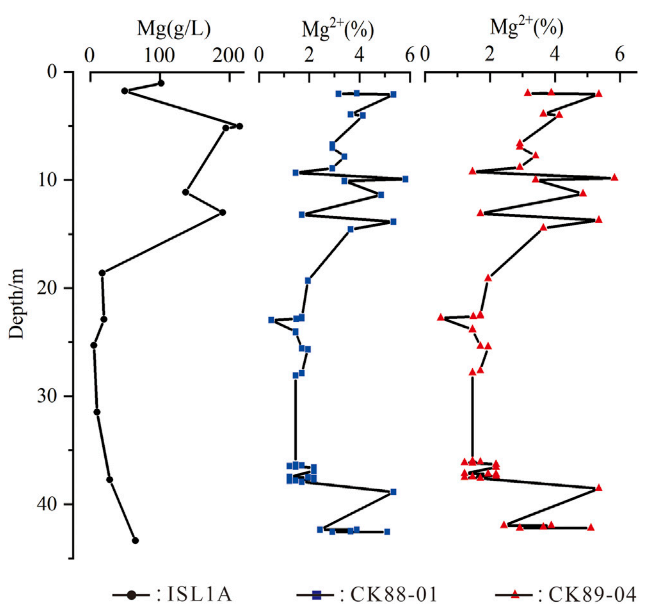

FIGURE 8 | Comparison of the Mg^{2+} concentration variation trend of halite fluid inclusions in boreholes ISL1A, CK88-01, and CK89-04 (the Mg^{2+} data in CK88-01 and CK89-04 from Zhang et al. (1993)).

began to rise again in the late stage of salt formation, and reached its peak at the location of potassium formation. The Mg^{2+} and B^{3+} contents are also good indicators to track the concentration of salt lake brine. Studies on different types of lakes in the Tibetan Plateau show that Mg^{2+} concentration in chloride lakes can well indicate the salinity of salt lakes (Wang and Wang, 2010). The study of $\delta^{11}B$ and $\rho(B^{3+})$ in salt lakes of the QB shows that there is a significant positive correlation between them, indicating B^{3+} contents can be used as an index to reconstruct the salinity of ancient lakes in arid areas (Liu et al., 2000; Du et al., 2019; Zhang et al., 2019). The variations of $\rho(Br^{-})$, $\rho(Mg^{2+})$, and $\rho(B^{3+})$ are therefore used to reflect the variation of salinity in QSL and the characteristics of high brine concentration in the initial stage of salt formation. The B^{3+} and Mg^{2+} variations in halite of the ISL1A borehole were analyzed by Fan et al. (2015), and they proposed that the contents of B^{3+} and Mg^{2+} stem primarily from halite fluid inclusions, rather than salt minerals. According to the characteristics of high concentration of halite fluid inclusions $\rho(Mg^{2+})$, $\rho(B^{3+})$, $\rho(Br^{-})$, and $\rho(K^{+})$ in the early stage of salt formation in the ISL1A borehole (**Figure 7**), the salinity of lake water in QSL is relatively high during this interval.

In the CK6 borehole located in the Bieletan section, the transition between the halite layer at the bottom and the underlying clastic layer is also abrupt, accompanied by a sudden appearance of salt minerals (Huang and Han, 2007). The cores CK89-04 and CK88-01 are located in the northern edge of Dabuxun Lake, close to the studied ISL1A (**Figure 1B**). The evaluation and comparison of lake sediment ages in QSL show that the salt-forming periods of ISL1A, CK89-04, and CK88-01 cores are almost the same (Fan et al., 2014). Therefore, we compared the Mg^{2+} results in halite fluid inclusions of the three boreholes and found that the variation tendency of Mg^{2+} in the upper evaporation strata in the ISL1A borehole is almost consistent with that of Mg^{2+} in the other two boreholes (**Figure 8**). The change in Mg^{2+} content can indicate the evolution degree of salt lake brine (Zhang et al., 1993). It also reflects the characteristics of high brine concentration at the initial stage of salt formation in QSL and the general evolution trend of the salt lake. As far as the evolution law of salt lakes is concerned, the salinity of water is generally a process from low to high, but the chemical characteristics of ancient lake water represented by halite fluid inclusions and the actual deposition of boreholes are not the case. However, these high-concentration elements, other than Na^{+} and Cl^{-}, did not appear in the diffraction results of borehole minerals; these elements did not form salt minerals but were dispersed in brine and wrapped in halite inclusions, which confirmed the existence of high-salinity brine in this period. At least the existence of water rich in Na^{+}, Cl^{-}, Mg^{2+}, B^{3+}, K^{+}, and Br^{-} led to geochemical anomalies in the early stage of salt formation in QSL.

There are two explanations for this abrupt salt formation in QSL provided by previous studies. Firstly, the neotectonic activity in the late Pleistocene facilitates the uplift of the Kunlun Mountain, leading to the transfer of sulfate-type ancient lake water in the East Kunlun Mountain by rivers to Qarhan, making it enter suddenly into the salt-forming stage (Zhu et al., 1990). Secondly, the tectonic activity caused the uplift in the west and the decline in the east of the QB, forcing the supersaturated NaCl brine in the west to migrate eastward, promoting Qarhan to enter suddenly into the salt-forming stage (Huang and Han, 2007). All the above conclusions are indirect speculations, and there is no direct evidence to prove that the migration of ancient water bodies caused the sudden salt formation in QSL. Especially in the East Kunlun area, the water supply is diverse and the environment is humid, so it is debatable whether the ancient lake evolved to the salt lake stage. Furthermore, these studies suggest the tectonic activity as the key driving factor for the sudden formation of salt layers in QSL, but they did not further reveal this important tectonic activity. Chen et al. (2011) divided the terrace of the Golmud River into two stages: the filling period of the Sancha River in 82–16 ka and the cutting period of the Golmud River since 16 ka, and considered that structural stability is the basis of filling in 82–16 ka, while the cutting period since 16 ka is driven by tectonic uplift. The research on sediments and alluvial fans in the Xidatan–Golmud drainage shows that the river terraces lasting before 30 ka are in the stage of filling and alluvial fan formation (Owen et al., 2006). The stable tectonic environment of the Sancha River in the Golmud River during the filling period is further explained. The study of tectonic stages of the Qilian Mountain in the adjacent area since Quaternary shows that there are at least five tectonic uplift activities, and the most recent one is about 80 ka (Guo et al., 2016). It suggests that the structure of QSL is not active at the initial stage of salt formation, and the suddenness of its initial salt formation should not be driven by tectonic activities. It suggests that the tectonic uplift drove the supersaturated NaCl brine in the west to migrate to QSL and caused it suddenly to form salt, which needs further demonstration.

Halite deposition suddenly started at 52 m in the ISL1A borehole, the semi-quantitative content of halite suddenly increased from 5% in the clastic layer to 30%, and the average value of the semi-quantitative content of halite reached 60% at 45 m, which started the first salt-forming period (An, 2012). In addition, the boron isotope results of carbonate in the ISL1A borehole show that the boron isotope content suddenly increases at about 52 m, which is thought to be caused by the sudden increase in lake salinity (Zhang., 2020). Paleoclimate was reconstructed by clay minerals and fossil pollen from the ISL1A borehole; the climate in the study area began to become dry and cold at about 53 ka, which led to the evolution of lake to salt lake (Wei et al., 2015; Miao et al., 2016). The results suggest that the abnormally high ρ(Mg^{2+}), ρ(B^{3+}), ρ(Br^-), and ρ(K^+) in fluid inclusions of halite in the first stage of this study reflect the late stage of the first normal salt-forming period in QSL. This salt-forming event resulted in the high concentration of ancient brine in the early stage of salt formation. The study of $\delta^{18}O$ and δD in QSL shows that although the isotopic composition in the first salt formation stage of the salt lake is stable, it deviates slightly from the evaporation line in the study area (**Figure 6**), reflecting that the hydrological characteristics of the lake are not completely controlled by evaporation factors. This study holds that the high concentration in the early stage of salt formation in QSL is caused by a normal salt formation event, so there is no sudden large-scale supply of other water to the salt lake. Meanwhile, one study has confirmed that the $\delta^{18}O$ and δD values of lake water lie on the evaporation line of the study area (Zhang et al., 1991), and its supply will not cause $\delta^{18}O$ and δD of lake water to deviate from the evaporation line. Therefore, it is speculated that the replenishment of Ca-Cl deep water with high salt content has impact on the hydrological characteristics of lakes. However, the replenishment amount is not as significant as that in the second stage, and the contents of ρ(Ca^{2+}), ρ(Sr^{2+}), ρ(Li^+), and ρ(Rb^+) in halite fluid inclusions do not increase significantly (**Figure 7**). This is the reason why $\delta^{18}O$ vs. δD deviates from the evaporation line in the study area for a small distance.

Ca^{2+} and Sr^{2+} Anomalous Enrichment in the Late Stage of Halogenases in QSL

The average value of δD of primary halite fluid inclusions in boreholes CK89-04 and CK88-01 is -35.2‰, which is considered to be due to the deuterium-poor external water mixed in the whole process of primary halite precipitation in QSL, and it is considered that water may be the deuterium-poor water in the deep fault zone about the northern margin of the lake area (Zhang et al., 1990; Zhang et al., 1993). The peak value of ρ(Ca^{2+}) and ρ(Sr^{2+}) in ISL1A is in the No. 5 sample at 11.5 m, which is basically in the same stratum as δD of CK89-04 and CK88-01. Deuterium deficiency is the characteristic of deep water; the smaller the δD value, the larger the proportion of deep water (Zhang et al., 1993), and the corresponding contents of ρ(Ca^{2+}) and ρ(Sr^{2+}) are higher. According to the characteristics of δD and $\delta^{18}O$ of boreholes, the evolution of QSL can be divided into three stages; the sedimentary stage of 8–24 m spans 15–21 ka, which is in the great ice age of the last glacial stage (Lowenstein et al., 1994; Yang et al., 1995; Zhang et al., 1995). Combining the low δD interval of CK89-04 and CK88-01 with the high ρ(Mg^{2+}), ρ(K^+), ρ(Ca^{2+}), and ρ(Sr^{2+}) intervals of ISL1A (**Figure 7**), the geological time is limited to 12–19 ka (**Figure 9**). As mentioned earlier, the potassium salt in QSL mainly occurs in the S_4 layer in the late stage of salt formation. In view of the high enrichment characteristics of 12–19 ka ions, it is inferred that this period should reflect the S_4 potassium salt layer in QSL. Compared with the deep sea oxygen isotope, it is found that the great ice age of the last glacial stage appeared in the northern margin of the Qinghai–Tibet Plateau in 21–15 ka (Zhang et al., 1995). Major elements and stable isotopes in primary halite fluid inclusions show that QB climate is extremely dry and cold during 20–11 ka (Lowenstein et al., 1994; Yang et al., 1995). As far as paleoclimate is concerned, during the period of 12–19 ka, the study area is dry and has low temperature, which is suitable for salt formation. However, the negative correlation between ρ(Ca^{2+}), ρ(Sr^{2+}), and δD in ancient brine of QSL during the period of 12–19 ka (**Figure 9**) also indicates a sudden increase in the recharge of Ca-Cl deep water during this interval. Moreover, the abrupt increase in ρ(Ca^{2+}) and ρ(Sr^{2+}) was also accompanied by a sharp increase in ρ(Mg^{2+}), ρ(K^+), ρ(Li^+), and ρ(Rb^+). This abrupt increase in multi-ions during 12–19 ka cannot be solely explained by climate change, and we suggest that the increased supply of Ca-Cl deep water should also play an important role. The reason for the increase of Ca-Cl deep water supply in the potassium-magnesium salt deposition stage is still unclear.

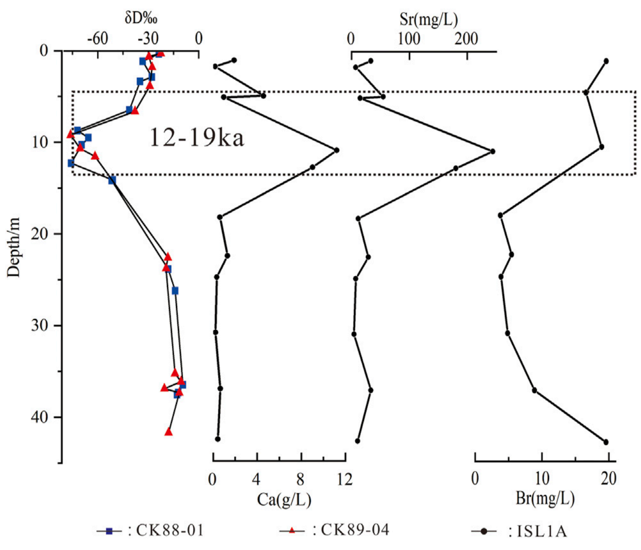

FIGURE 9 | Comparison of the Ca^{2+}, Sr^{2+}, and Br^- change trend of halite fluid inclusions in the ISL1A borehole and δD change trend of halite fluid inclusions in CK88-01 and CK89-04 boreholes (the δD data from Zhang et al. (1993)).

Based on the variations characteristics of fluid inclusion composition in halite and related evidence, we consider that the abrupt increase in the ion content from 19 to 12 ka in QSL and more Ca-Cl–type deep water supply to the salt lake are driven by tectonic activities. The study on river terraces developed in the northeastern margin of the Tibetan Plateau relates river terraces to the combined effects of climate change and tectonic uplift (Gao et al., 2008). The Golmud River, as an important regional water system, preserves the tectonic activity and climate change information in this area. The stream trenching of the Golmud River since 16 ka was suggested to be driven by the regional tectonic activity (Chen et al., 2011). A systematic study on the chronology of river terraces of the Kunlun River, Hongshui River, and Halaguole River developed in the East Kunlun Mountains (Wang et al., 2009) indicates that these rivers have developed river terraces during the period of 21.9–12.9 ka, and the characteristics of terraces are consistent with the characteristics of intermittent tectonic uplift with strong frequency but small amplitude. A study on the lake surface change in Great Qaidam shows that the last replenishment time of the Yuka River to Great Qaidam Lake is about 23–17 ka, without further replenishment (Madsen et al., 2013). They also speculated that the river diverted from the Great Qaidam Lake system due to the sharp downcutting of the river. According to the development time of river terraces in the surrounding water systems of the study area, terraces were developed in all major rivers during this period (19–12 ka) and were significantly uplifted by tectonic activity. In view of this, we speculate that the reason for the enhancement of Ca-Cl deep water activity is the neotectonic activity during this period, which leads to the ion content increase of Ca^{2+}, Sr^{2+}, etc., during 12–19 ka.

Re-Recognition of Halogenases in QSL

It is known that there exist three salt-forming periods in past 50 ka in QSL (Zhang et al., 1990; Yang et al., 1995; Zhang et al., 1995; Fan et al., 2018; Du et al., 2019; Zhang, 2020). However, as the most direct index of ancient brine research, in terms of the evolution process of QSL revealed by the chemical composition of halite fluid inclusions, it directly reveals the unique advantages of the chemical composition of ancient brine, which contributes to a comprehensive understanding of the salt formation process of QSL. Firstly, there is a geochemical anomaly in the early stage of salt formation in QSL, which is considered to be caused by a normal salt formation event. Secondly, the direct evidence shows that, in the late stage of salt formation and potassium formation in QSL, there is a phenomenon of increase in deep Ca-Cl water supply, which is speculated to be driven by tectonic activities.

The river water and Ca-Cl deep water are currently two main sources supplying waters to QSL. Although the mixed of two kinds of water runs through the whole process of salt formation in QSL, the solid potassium did not appear in the whole salt formation process, only forms in S_4 salt layer. Although Ca-Cl deep water in the northern margin of QSL is rich in Ca^{2+} and Sr^{2+}, the content of K^+ is not enriched (Lowenstein and Risacher, 2009; Fan et al., 2018) due to the mixing process of Ca-Cl deep water and magnesium sulfate subtype river water, which is beneficial to the enrichment of potassium (Yuan, 1995). In addition to the evolution of salt lakes to salt playas and frequent climate fluctuations under the general trend of drought, the mixing process is necessary for potassium salt formation in QSL (Zhang et al., 1993). Based on the study of chemical composition of ancient brine, combined with geological age and tectonic activities, the most direct evidence indicates that the activity of Ca-Cl deep water increased and the recharge increased in the formation stage of potassium salt in QSL. It suggests that the increase in Ca-Cl deep water supply driven by tectonic activities plays an important role in the formation of potassium salt in QSL.

In order to study the salt-forming evolution process of salt lakes in the QB, a basin with active tectonic activities and complex hydrogeological conditions (deep oilfield brine development), we must consider the specific influence of deep water on salt lake evolution and the connection between deep water and tectonic activities. In addition, while using the core profile of the evaporite basin to study paleoclimate, it is also necessary to consider the specific influence of deep water and tectonic activities on the sedimentary evolution of salt lakes and eliminate their influence on the salt formation process. In this way, we will get the salt-forming process and paleoclimate results that are closest to the truth.

CONCLUSIONS

(1) The formation of the main potassium salt layer in QSL and the massive replenishment and mixing process of Ca-Cl deep water are the key factors, and it is speculated that the increase in replenishment is due to tectonic activities.
(2) The geochemical anomaly characteristics in the early stage of salt formation in QSL are analyzed and speculated to be caused by a salt-forming event besides Ca-Cl deep water that may also have some influence, which is hardly irrelevant to tectonic activities.
(3) Re-recognition of halogenases in QSL shows that there are many factors affecting the evolution of salt formation in the salt lake, which need to be explored continuously. Among them, deep water has an important impact; the salt lake as a carrier to carry out research must take into account its factors.

DATA AVAILABILITY STATEMENT

The original contributions presented in the study are included in the article/Supplementary Material, and further inquiries can be directed to the corresponding authors.

AUTHOR CONTRIBUTIONS

JL involved in data analysis and article writing. XZ provided ideas for writing the article and paid for testing. MH tested and corrected data. JL and WL pretreated the sample. WL tested the sample. WM analyzed core sedimentation characteristics and gave sampling guidance. XZ and WM revised the article. XY, YL and QT performed field core sedimentation edits and sample selection. WH gave a lot of suggestions on the logic and language expression of the article. HM selected the area for drilling construction and paid the drilling construction cost.

FUNDING

This research was supported by the National Natural Science Foundation of China (Grant Nos. 41672087, 41402082 and 42071111) and Foundation of Qinghai Science & Technology Department (Grant No. 2014-ZJ-704).

ACKNOWLEDGMENTS

We thank two reviewers for their valuable suggestions and comments on the manuscript. We are also grateful to Special Issues convener, editors and typesetters.

REFERENCES

An, F., Ma, H., Wei, H., Fan, Q., and Han, W. (2013). Grain-size Distribution Patterns of Lacustrine Sediments of Qarhan Area and its Environmental Significance. *Arid Geogr.* 36 (2), 212–220. doi:10.13826/j.cnki.cn65-1103/x.2013.02.009

An, F. (2012). *Paleoenvironmental and Paleolake Evolution, Aeolian Component Record in Lacustrine Sediments and its Atmospheric Circulation Signifificance since 93 Ka in Qarhan Area, Qaidam Basin*. [Beijing: Graduate University of Chinese Academy of Sciences. [dissertation thesis] [in Chinese]

Benison, K. C., and Goldstein, R. H. (1999). Permian Paleoclimate Data from Fluid Inclusions in Halite. *Chem. Geology.* 154, 113–132. doi:10.1016/S0009-2541(98)00127-2

Biehl, B. C., Reuning, L., Strozyk, F., Kukla, P. A., Reuning, L., and Strozyk, F. (2014). Origin and Deformation of Intra-salt Sulphate Layers: an Example from the Dutch Zechstein (Late Permian). *Interational J. Earth Sciceces* 103 (3), 697–712. doi:10.1007/s00531-014-0999-4

Chen, K., Yang, S., and Zheng, X. (1981). The Salt Lakes on the Qinghai-Xizang Plateau. *Acta Geogr. Sin.* 36, 13–21. [in Chinese]

Chen, Y., Li, Y., Zhang, Y., Zhang, M., Zhang, J., Yi, C., et al. (2011). Late Quaternary Deposition and Incision Sequences of the Golmud River and Their Environmental Implication. *Quat. Sci.* 31 (02), 347–359. doi:10.3969/1001-7410.2011.02.17[in Chinese]

Cheng, H., Ma, H., Tan, H., Xu, J., and Zhang, X. (2008). Geochemical Characteristics of Bromide in Potassium Deposits: Review and Research Perspectives. *Bull. Mineralogy, Pet. Geochem.* 27 (4), 399–408. doi:10.1016/S1872-5791(08)60056-1[in Chinese]

Du, Y., Fan, Q., Gao, D., Wei, H., Shan, F., Li, B., et al. (2019). Evaluation of boron Isotopes in Halite as an Indicator of the Salinity of Qarhan Paleolake Water in the Eastern Qaidam Basin, Western China. *Geosci. Front.* 10, 253–262. doi:10.1016/j.gsf.2018.02.016

Fan, Q., Lowenstein, T., Wei, H., Yuan, Q., Qin, Z., Shan, F., et al. (2018). Sr Isotope and Major Ion Compositional Evidence for Formation of Qarhan Salt Lake, Western China. *Chem. Geology.* 497, 128–145. doi:10.1016/09.001

Fan, Q., Ma, H., Ma, Z., Wei, H., and Han, F. (2014). An Assessment and Comparison of ^{230}Th and AMS ^{14}C Ages for Lacustrine Sediments from Qarhan Salt Lake Area in Arid Western China. *Environ. Earth Sci.* 71, 1227–1237. doi:10.1007/s12665-013-2526-5

Fan, Q., Ma, Y., Cheng, H., Wei, H., Yuan, Q., Qin, Z., et al. (2015). Boron Occurrence in Halite and boron Isotope Geochemistry of Halite in the Qarhan Salt Lake, Western China. *Sediment. Geology.* 322, 34–42. doi:10.1016/j.sedgeo.2015.03.012

Farid, I., Trabelsi, R., Zouari, K., Abid, K., and Ayachi, M. (2013). Hydrogeochemical Processes Afecting Groundwater in an Irrigated Land in Central Tunisia. *Environ. Earth Sci.* 68 (5), 1215–1231. doi:10.1016/j.jafrearsci.2012.10.001

Gao, H., Liu, X., Pan, B., Wang, Y., Yu, Y., and Li, J. (2008). Stream Response to Quaternary Tectonic and Climatic Change: Evidence from the Upper Weihe River, central China. *Quat. Int.* 186 (1), 123–131. doi:10.1016/j.quaint.2007.08.046

Goldstein, R. H., and Reynolds, T. J. (1994). *Systematics of Fluid Inclusions in Diagenetic Minerals: SEPM Short Course 31*. Oklahoma: Society for Sedimentary Geology press.

Guo, H., Yang, L., Zhu, X., Zhu, T., Yue, L., Wu, H., et al. (2016). River Terrace and Quaternary Tectonic Uplift in the Qilian Mountain. *Geol. Bull. China* 35 (12), 2033–2044. doi:10.3969/j.issn.1671-2552.2016.12.011

He, M., Luo, C., Yang, H., Kong, F., Li, Y., and Deng, L. (2020). Sources and a proposal for comprehensive exploitation of lithium brine deposits in the Qaidam Basin on the northern Tibetan Plateau, China: Evidence from Li isotopes. *Geol. Rev.* 117, 1–7. doi:10.1016/j.oregeorev.2019.103277

Hardie, L. A., Lowenstein, T. K ., and Spencer, R. J. (1983). The Problem of Distinguishing between Primary and Secondary Features in Evaporites. *Sixth Int. Symp. Salt* 1, 11–39.

Hu, D. (1991). Metamorphism and Deformation Regularity of Modern Sediments in the Qarhan Salt Lake, Qinghai, China. *Geotectonica et Metallogenia* 15 (3), 243–254. doi:10.16539/j.ddgzyckx.1991.03.009 [in Chinese]

Hu, D. (1990). *Rediscussion on the Tectonic Evolution of Qarhan Salt Lake Deposit*. Hunan: Hunan Normal University press [in Chinese]

Hu, M., He, H., Zhan, X., Fan, X., Wang, G., and Jia, Z. (2008). Matrix Normalization for Insitumulti-Element Quantitative Analysis of Zircon in Laser Ablation Inductively Coupled Plasma Mass Spectrometry. *Chin. J. Anal. Chem.* 36 (7), 947–953. doi:10.3321/j.issn:0253-3820.2008.07.016

Huang, Q., and Cai, B. (1987). *Geochronological Study on the Sediments in Qarhan lake. China-Australia Conference on Quaternary Cooperation*, 106–114. [in Chinese]

Huang, Q., and Han, F. (2007). *Evolution of Salt Lakes and Palaeoclimate Fluctuation in Qaidam Basin*. Beijing: Science Press [in Chinese]

Li, Q., Fan, Q., Wei, H., Qin, Z., Zhang, X., Du, Y., et al. (2020). Sulfur Isotope Constraints on the Formation of $MgSO_4$-Deficient Evaporites in the Qarhan Salt Lake, Western China. *J. Asian Earth Sci.* 189, 1–11. doi:10.1016/j.jseaes.2019.104160

Li, R., Liu, C., Jiao, P., Liu, W., Tang, D., and Wang, S. (2020). The Effect of Solvent Chemistry on Potassium Dissolution Extraction from Low-Grade Solid Potash Ore in Qarhan Salt Lake, China. *Appl. Geochem.* 115, 1–11. doi:10.1016/j.104550

Liu, W., Xiao, Y., Peng, Z., An, Z., and He, X. (2000). Boron Concentration and Isotopic Composition of Halite from Experiments and Salt Lakes in the Qaidam Basin. *Geochimica et Cosmochimica Acta* 64 (13), 2177–2183. doi:10.1016/S0016-7037(00)00363-X

Liu, X., Cai, K., and Yu, S. (2002). Geochemical Simulation of Formation and Evolution of Salt Lakes and Their Water Sources in Qardam Basin: Application of Pitzers Model. *Geochimica* 31 (05), 501–507. doi:10.19700/j.0379-1726.2002.05.012

Longerich, H. P., Jackson, S. E., and Gunther, D. (1996). Inter-laboratory Note Laser Ablation Inductively Coupled Plasma Mass Spectrometric Transient Signal Data Acquisition and Analyte Concentration Calculation. *J. Anal. At. Spectrom.* 11 (09), 899–904. doi:10.1039/JA9961100899

Lowenstein, T. K., and Hardie, L. A. (1985). Criteria for the Recognition of Salt-pan Evaporites. *Sedimentology* 32, 627–644. doi:10.1111/j.1365-3091.1985.tb00478.x

Lowenstein, T. K., and Risacher, F. (2009). Closed basin brine evolution and the influence of Ca-Cl inflow waters: death Valley and Bristol Dry Lake California, Qaidam Basin, China, and Salar de Atacama, Chile. *Aquetic Geochem.* 15, 71–94. doi:10.1007/s10498-008-9046-z

Lowenstein, T. K., Spencer, R. J., Yang, W., Casas, E., Zhang, P., Zhang, B., et al. (1994). Major-element and Stable-Isotope Geochemistry of Fluid Inclusionsin Halite, Qaidam Basin, Western China: Implications for Late Pleistocene/

Holocene Brine Evolution and Paleoclimates. *Geol. Soc. America Spec. Pap.* 289, 19–32. doi:10.1130/SPE289-p19

Lowenstein, T. K., Spencer, R. J., and Zhang, P. (1989). Origin of Ancient Potash Evaporites: Clues from the Modern Nonmarine Qaidam Basin of Western China. *Science* 245, 1090–1092.

Madsen, D. B., Lai, Z., Sun, Y., Rhode, D., Liu, X., and Brantingham, P. J. (2013). Late Quaternary Qaidam lake Histories and Implications for an MIS3 "Greatest Lakes" Period in Northwest China. *J. Paleolimnology* 51, 161–177. doi:10.1007/s10933-012-9662-x

Meng, F., Liu, C., and Ni, P. (2012). To Forecast Sylvite Deposits Using the Chemistry of Fluid Inclusions in Halite. *Acta Micropalaeontogica Sinica* 29 (1), 62–69. [in Chinese]

Meng, F., Ni, P., Yan, X., Wang, T., Yan, K., Wang, G., et al. (2011). Chemical Composition of the Ancient lake at JinTan Salt Mine: Evidence from Fluid Inclusions in Halite. *Acta Micropalaeontogica Sinica* 28 (3), 324–328. doi:10.1631/jzus.B1000197[in Chinese]

Miao, W., Fan, Q., Wei, H., Zhang, X., and Ma, H. (2016). Clay Mineralogical and Geochemical Constraints on Late Pleistocene Weathering Processes of the Qaidam Basin, Northern Tibetan Plateau. *J. Asian Earth Sci.* 127, 267–280. doi:10.1016/j.jseaes.2016.06.013

Owen, L. A., Finkel, R. C., Ma, H., and Barnard, P. (2006). Late Quaternary Landscape Evolution in the Kunlun Mountains and Qaidam Basin, Northern Tibet: A Framework for Examining the Links between Glaciation, lake Level Changes and Alluvial Fan Formation. *Quat. Int.* 154-155, 73–86. doi:10.1016/02.008

Ren, S., Ge, X., Yan, Z., Lin, Y., Hu, Y., Liu, Y., et al. (2006). Application of ^{36}Cl-Dating to the Last Rapid Uplift of the Tibet Plateau. *Acta Geologica sinica* 80 (8), 1110–1117. doi:10.3321/j.issn:0001-5717.2006.08.003[in Chinese]

Sanders, L. L. (1991). Geochemistry of Formation Waters from the Lower Silurian Clinton Formation (Albion Sandstone), Eastern Ohio. *AAPG Bull.* 75 (10), 1593–1608. doi:10.1061/(ASCE)0733-9410(1991)117:11(1831.2)

Sun, D., and Lock, D. (1988). Formation of Potash Deposits in Qaidam Basin. *Sci. China* 18 (12), 1323–1333. Available at: http://ir.isl.ac.cn/handle/363002/1420 [in Chinese]

Sun, X., Hu, M., Liu, C., Jiao, P., Ma, L., Wang, X., et al. (2013). Composition Determination of Single Fluid Inclusions in Salt Minerals by Laser Ablation ICP-MS. *Chin. J. Anal. Chem.* 41 (02), 235–241. doi:10.1016/S1872-2040(13)60631-3

Wang, A., Smith, J. A., Wang, G., Zhang, K., Xiang, S., and Liu, D. (2009). Late Quaternary River Terrace Sequences in the Eastern Kunlun Range, Northern Tibet: A Combined Record of Climatic Change and Surface Uplift. *J. Asian Earth Sci.* 34, 532–543. doi:10.1016/j.jseaes.2008.09.003

Wang, H., and Wang, Y. (2010). Preliminary Analysis on Mg^{2+}, Ca^{2+} and Mg/Ca as Salinity Indicators of Lakes in the Qinghai-Tibetan Plateau. *J. Lake Sci.* 22 (6), 849–900. doi:10.1080/09500340.2010.529951[in Chinese]

Warren, J. K. (2006). *Evaporites: Sediments, Resources and Hydrocarbons*. Berlin: Springer-Verlag Berlin Heidelberg.

Wei, H., Fan, Q., Zhao, Y., An, F., Shan, F., Ma, H., et al. (2016). Chemical Elements in Core Sediments of the Qarhan Salt Lake and Palaeoclimate Evolution during 94-9 Ka. *Acta Geoscientica Sinica* 37 (2), 193–203. doi:10.3975/cagsb.2016.02.07 [in Chinese]

Wei, H., Fan, Q., Zhao, Y., Ma, H., Shan, F., An, F., et al. (2015). A 94-10 Ka Pollen Record of Vegetation Change in Qaidam Basin, Northeastern Tibetan Plateau. *Palaeogeogr. Palaeoclimatol. Palaeoecol.* 431, 43–52. doi:10.1016/j.palaeo.2015.04.025

Weldgehebriel, M. F., Lowenstein, T. K., Veigas, J. G., Collins, D., Sendula, E., Bodnar, R. J., et al. (2020). Combined LA-ICP-MS and Cryo-SEM-EDS: an Improved Technique for Quantitative Analysis of Major, Minor, and Trace Elements in Fluid Inclusions in Halite. *Chem. Geology.* 20, 1–46. doi:10.1016/j.chemgeo.2020.119762

Yang, Q. (1982). The Sedimentation Mechanism of Potash Deposits in the Qarhan Inland Salt lake. *Acta Geologica Sinica* 03, 281–292. doi:10.1007/BF01093415

Yang, W., Spencer, R. J., Krouse, H. R., Lowenstein, T. K., and Casas, E. (1995). Stable Isotopes of lake and Fluid Inclusion Brines, Dabusun Lake, Qaidam Basin, Western China: Hydrology and Paleoclimatology in Arid Environments. *Palaeogeogr. Palaeoclimatology,Palaeoecology.* 117, 279–290. doi:10.1016/0031-0182(94)00126-S

Yi, J., Fan, Q., Wei, H., Wang, M., Qin, Z., Yuan, Q., et al. (2017). The Characteristics of the Mineral Assemblage and the Forming Clue in Qarhan Salt Lake. *J. Salt Lake Res.* 25 (02), 47–54. [in Chinese]

Yu, S. (2000). *Potassium Brine Dynamics and Prediction in the First Mining Area of Qarhan Salt Lake*. Beijing, China: Science Press.

Yuan, J., and Duan, Z. (1989). Mixation of Natural Waters and the Application of HW-Model to the Study of Mixation. *Earth Science-Journal China Univ. Geosciences* 14 (5), 553–561. [in Chinese]

Yuan, J. (1995). *Formation Conditions of Potassium Salt deposit in Qarhan Salt Lake*. Beijing, China: Science Press.

Yuan, J., Huo, C., and Cai, K. (1983). The High Mountain-Deep basin saline Environment-A New Genetic Model of Salt Deposits. *Geol. Rev.* 29 (02), 159–165. [in Chinese]

Yuan, J. (1959). Types of Salt Lakes in the Qaidam Basin. *Acta Geol. Sinica* 39 (3), 318–323. [in Chinese]

Zarei, M., Raeisi, E., Merkel, B. J., and Kummer, N. A. (2013). Identifying Sources of Salinization Using Hydrochemical and Isotopic Techniques, Konarsiah, Iran. *Environ. Earth Sci.* 70 (2), 587–604. doi:10.1007/s12665-012-2143-8

Zhang, B., Fan, H., Zhang, P., Lowenstein, T. K., and Spencer, R. J. (1990). Hydrogen and Oxygen Stable Isotope Analyses of Fluid Inclusions in Halite in Qarhan Salt lake with Geochemical Implications. *Acta Sedimentologica Sinica* 8 (1), 3–17. doi:10.1016/0925-8388(94)01490-6 [in Chinese]

Zhang, B., Zhang, P., Lowenstein, T. K., and Spencer, R. J. (1995). Time Range of the Great Ice Age of the Last Glacial Stage and its Related Geological Event of Playa in the Qinghai-Xizang (Tibet) Plateau. *Quat. Sci.* 3, 193–201. [in Chinese]

Zhang, P. (1987). *Salt Lake in Qaidam Basin*. Beijing, China: Science Press.

Zhang, P., Zhang, B., Lowenstein, T. K., and Spencer, R. J. (1991). On the Origin of Ancient Anomalous Evaporites: Evidence from Qaidam Basin. *Geochimica* 2, 134–143. doi:10.19700/j.0379-1726.1991.02.005[in Chinese]

Zhang, P., Zhang, B., Lowenstein, T. K., and Spencer, R. J. (1993). *Origin of Ancient Potash Evaporites: Examples from the Formation of Potash of Qarhan Salt Lake in Qaidam Basin*. Beijing, China: Science Press

Zhang, X. (2020). *Boron Isotope Fractionation of Carbonates in Salt Lakes and its Tracer to the Evolution of the Qarhan Salt lake*. [Beijing: University of Chinese Academy of Sciences. [dissertation thesis] [in Chinese]

Zhang, X., Li, Q., Qin, Z., Fan, Q., Du, Y., Wei, H., et al. (2019). Boron Isotope Geochemistry of a Brine Carbonate System in the Qaidam Basin, Western China. *Sediment. Geol.* 383, 293–302. doi:10.1016/j.sedgeo.2019.02.011

Zhang, X., Xu, Z., Duan, Y., Ma, L., Meng, Z., Zhou, S., et al. (2003). Metabolic Pathway of the Quaternary Biogenetic Gases and Their Migration and Accumulation in the Qaidam Basin, China. *Geol. Rev.* 49 (2), 168–174. doi:10.1007/BF02873153[in Chinese]

Zhao, Y., Liu, C., Ding, T., Gonzalez, L., Li, Z., Wang, M., et al. (2020). Origin and depositional paleoenvironment of Triassic polyhalite in the Jialingjiang Formation, Sichuan Basin. Carbonates and Evaporites. *Sediment. Geol.* 35 (64), 1–17. doi:10.1007/s13146-020-00596-3

Zheng, X., Zhang, M., Xu, C., and Li, B. (2002). *China Salt Lake Annals*. Beijing: Science Press [in Chinese]

Zhu, Y., Li, Z., Wu, B., and Wang, M. (1990). The Formation of the Qarhan Salt Lakes as Viewed from the Neotectionic Movement. *Acta Geol. Sinica* 01, 13–21. [in Chinese]

Conflict of Interest: The authors declare that the research was conducted in the absence of any commercial or financial relationships that could be construed as a potential conflict of interest.

frontiers
in Earth Science

ORIGINAL RESEARCH
published: 23 June 2021
doi: 10.3389/feart.2021.700194

Application of a Diatom Transfer Function to Quantitative Paleoclimatic Reconstruction — A Case Study of Yunlong Lake, Southwest China

Yafei Zou[1]*, Luo Wang[2], Haibo He[1], Guangxin Liu[1], Jiaoyang Zhang[3], Yao Yan[3], Zhaoyan Gu[2] and Hongbo Zheng[1,4]

[1]Yunnan Key Laboratory of Earth System Science, Yunnan University, Kunming, China, [2]Key Laboratory of Cenozoic Geology and Environment, Institute of Geology and Geophysics, Chinese Academy of Sciences, Beijing, China, [3]School of Geosciences and Resources, China University of Geosciences, Beijing, China, [4]School of Earth and Environmental Sciences, The University of Queensland, Brisbane, QLD, Australia

Edited by:
Xiangjun Liu,
Northwest Normal University, China

Reviewed by:
Xuhui Dong,
Guangzhou University, China
Rong Wang,
Nanjing Institute of Geography and
Limnology (CAS), China

***Correspondence:**
Yafei Zou
zouyafei123@ynu.edu.cn

Specialty section:
This article was submitted to
Quaternary Science, Geomorphology
and Paleoenvironment,
a section of the journal
Frontiers in Earth Science

Received: 25 April 2021
Accepted: 10 June 2021
Published: 23 June 2021

Citation:
Zou Y, Wang L, He H, Liu G, Zhang J,
Yan Y, Gu Z and Zheng H (2021)
Application of a Diatom Transfer
Function to Quantitative Paleoclimatic
Reconstruction — A Case Study of
Yunlong Lake, Southwest China.
Front. Earth Sci. 9:700194.
doi: 10.3389/feart.2021.700194

Although diatom records from lake sediments have been used for quantitative paleoclimatic reconstruction, their validity and sensitivity have rarely been tested rigorously. At Yunlong Lake, an alpine lake in Southwest China, we studied the seasonal succession of diatom assemblages to produce a mean surface water temperature (MSWT) transfer function. In addition, based on the spatial distribution of surface diatom assemblages with water depth, we produced a diatom-water depth (WD) transfer function. Combined with the analysis of diatom assemblages in a sediment core (YL2013-A), changes in surface water temperature and water level over the last ~100 years were quantitatively reconstructed using the diatom-based transfer functions. Comparison with records of regional meteorology and reservoir water capacity revealed that the diatom-based lake water level reconstruction is a sensitive indicator of short-term fluctuations in precipitation, and it also reflects a long-term stepwise rise in water level caused by the impounding and large-scale extension of the reservoir. In addition, the diatom-inferred MSWT is consistent with the changes in air temperature prior to large-scale human disturbance of the site. However, after the extension of the reservoir, although the regional air temperature continued to increase, the water temperature decreased substantially. This suggests that the large increase in lake water volume in the short term led to a decrease in the average water temperature, which in turn led to the occurrence of a diatom bloom in the cold season. The results demonstrate that diatom transfer functions based on modern observations of the same lake has a high environmental sensitivity and can be used for the quantitative reconstruction of regional climate change. Overall, our findings provide a foundation for the use of lake diatom records for quantitative paleoclimatic reconstruction on various timescales.

Keywords: diatoms, transfer function, quantitative reconstruction, climate change, Yunlong Lake

INTRODUCTION

Diatom records from lake sediments are important in paleoclimatic reconstruction, for the following three major reasons. First, diatoms are widely distributed in lakes, and they have a high diversity and can be clearly classified (Battarbee et al., 2001). Second, diatoms have a relatively short reproductive cycle and are very sensitive to climate changes (temperature, precipitation, snowfall, wind speed, etc.) (Smol and Douglas, 2007; Wang et al., 2011; Wang et al., 2012; Wang et al., 2018; Rühland et al., 2015). Third, the siliceous valves of diatoms are well preserved in lake sediments, and compared with other algal indicators this makes them uniquely advantageous for paleoclimatic reconstruction on various timescales (Smol and Cumming, 2000; Dong et al., 2016).

Different diatom species in lakes respond differently to climate changes, such as temperature and precipitation. Diatoms in lakes, especially planktonic diatoms, are very sensitive to temperature changes (Smol and Douglas, 2007; Rühland et al., 2015), including direct and indirect responses (Zou et al., 2018). For example, recent global warming has led to the predominance of the warm-preference planktonic diatom *Aulacoseira granulata* in Douhu Lake in China (Li et al., 2021), and this preference was also evidenced by an investigation on the seasonal diatom succession of Yunlong Lake in China (Zou et al., 2018), which indicated a direct response of diatoms to temperature. Meanwhile, global warming has greatly reduced the length of the ice-cover period of high-latitude lakes, and intensified the thermal stratification of temperate lakes, which has led to blooming of the cyclotelloid diatom taxa (Wang et al., 2012; Rühland et al., 2015), this is an indirect climatic response.

The spatial distribution of planktonic and benthic diatoms within a lake basin, especially of benthic diatoms, is controlled mainly by light penetration and is closely linked to water depth. Therefore, different benthic diatom assemblages and the ratio of planktonic to benthic diatoms are sensitive indicators of past lake water level (Stone and Fritz, 2004; Laird et al., 2010; Laird et al., 2011; Kingsbury et al., 2012). For lakes supplied mainly by atmospheric precipitation, water level is a valuable index of changes in precipitation within the lake catchment (Yang et al., 2003; Magny, 2004), enabling lake diatom assemblages to be used to reconstruct past changes in precipitation.

A major prerequisite of climatic reconstruction using diatoms is a clear understanding of their ecological preferences (Zou et al., 2018). However, because diatom species are numerous, in many cases we still lack a comprehensive understanding of their ecological preferences; moreover, due to site-specific factors, diatom assemblages can vary substantially between lakes. Therefore, arguably the best way of interpreting paleolimnological diatom records is to investigate modern diatom assemblages in specific lakes in order to determine their ecological response to environmental factors.

Determining the quantitative relationship between diatom assemblages and the environmental factors of temperature and water level requires two steps. First, investigating the seasonal succession of modern lake diatom species is an effective means of understanding their response to temperature changes. Seasonality is a major characteristic of diatoms in freshwater ecosystems (Köster and Pienitz, 2006; Winder and Cloern, 2010; Zou et al., 2018). Pronounced changes in physical and chemical conditions within a lake can occur on a seasonal basis, resulting in major changes in diatom assemblages (Winder and Cloern, 2010). Therefore, the seasonal succession of diatom assemblages in lakes is often a rich source of information on the response of diatoms to environmental changes. Additionally, large environmental gradients typically accompany seasonal changes, such as in the temperature contrast between summer and winter, which is important for diatom-based temperature reconstruction on various timescales (Zou et al., 2018).

Second, investigating the spatial pattern of diatom assemblages in surface lake sediments can be used to obtain a quantitative relationship between diatom assemblages and water depth, which can then be used to reconstruct past changes in lake water level (Stone and Fritz, 2004; Laird et al., 2010; Laird et al., 2011). This is because diatoms are photosynthetic algae, which requite light for growth, and different diatom species have different requirements for light conditions. Since lakes are seldom entirely translucent, benthic diatoms can often only grow within the shallow-water photic zone, while planktonic diatoms can remain suspended in the upper photic zone of the entire lake. Therefore, the relative abundance of different benthic diatom species, as well as the ratio between planktonic and benthic diatoms, is significantly correlated with water depth (Kingsbury et al., 2012; Zou et al., 2020).

Transfer functions are widely used for diatom-based quantitative paleoclimatic reconstruction. The methodology can be summarized as follows: A dataset of modern diatom samples and environmental variables is collected, which is used to establish a quantitative relationship between diatom assemblages and the main controlling environmental variables (e.g., water temperature and water depth). This enables a transfer function to be constructed which can then applied to fossil diatom assemblages to quantitatively reconstruct the corresponding climatic variable(s) (Lotter and Bigler, 2000; Yang et al., 2003; Laird et al., 2010; Laird et al., 2011). Many advanced data processing methods are available for constructing transfer functions, such as weighted average partial least squares regression (WAPLS) (Birks, 2012), which is statistically robust and simple to calculate, and hence is widely used. Several paleoclimatic reconstructions have been produced using diatom transfer functions (Lotter and Bigler, 2000; Köster and Pienitz, 2006); however, the sensitivity and validity of these reconstruction need to be further examined (Juggins, 2013), based for example on comparisons with meteorological observations.

Yunlong Lake, a subtropical alpine lake in Yunnan Province of China which is very sensitive to the regional climate change (Wang et al., 2018; Zou et al., 2018; Zou et al., 2020; Jiang et al., 2019) was selected to produce diatom-based environmental transfer functions. Through a two-year investigation of the modern diatom seasonal succession at the lake (Zou et al., 2018), a diatom-water temperature transfer function was constructed. By investigating spatial pattern of surface diatom assemblages with water depth (Zou et al., 2020), a diatom-water

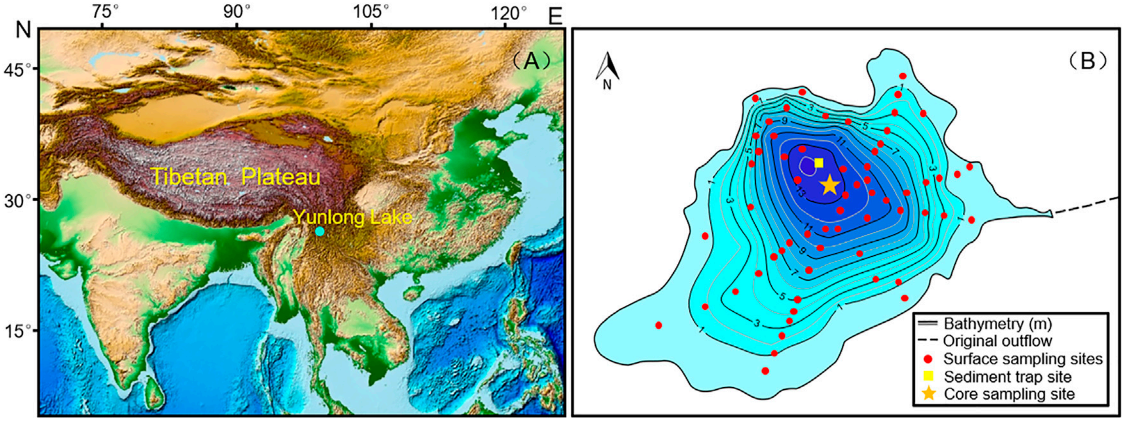

FIGURE 1 | Location of Yunlong Lake and sampling sites. **(A)** Schematic diagram of the geographical location of Yunlong Lake. **(B)** Bathymetry of Yunlong Lake and the locations of the surface samples, sediment core, and sediment trap.

depth transfer function was also constructed. Combined with the analysis of diatom assemblage changes in a sediment core over the last ~100 years, the two diatom transfer functions were used to quantitatively reconstruct changes in mean surface water temperature and water level at the site. Finally, the sensitivity and validity of the diatom-inferred climate reconstruction were examined by comparing the results with meteorological and reservoir capacity records over the last 60 years.

Overview of the Study Site

Yunlong Lake is located in the Tianchi National Nature Reserve in Yunnan Province, Southwest China, in the core area of the longitudinal ridge valley of the Hengduan Mountains (**Figure 1A**). The climate of the region is influenced mainly by the Indian Summer Monsoon, and there is a very strong positive relationship between temperature and rainfall (Zou et al., 2018). According to meteorological records for Yunlong Station (25°32′24″ N, 99°13′12″ E; 1,659 m.a.s.l.) for 1981–2010, the average annual air temperature was 16.2°C, and the average monthly air temperature was generally high from april to October (>15°C). The average annual rainfall was 780.5 mm and the rainy season was from May to October (Zou et al., 2018).

Yunlong Lake (25°52′12.89″ N, 99°16′49.75″ E, **Figure 1B**) is at an altitude of 2,551 m.a.s.l.; it has a surface area of ~1.5 km^2, a watershed area of ~11.25 km^2, and a maximum water depth of ~14.1 m. Yunlong Lake is a typical tectonic faulted lake with no natural inflows, and the lake water is charged mainly by atmospheric precipitation (Zou et al., 2018; Zou et al., 2020). In the past, there was a natural outflow in the east (**Figure 1B**), which flowed into a branch of the Lantsang River. Prior to the 1950s, the lake was largely unaffected by human activity due to its remoteness and relatively high altitude. However, to alleviate the local scarcity of water, from the 1950s onwards, it was gradually transformed into an artificial reservoir. A dam with a total height of ~12.74 m was constructed between 1953 and 1985 on the eastern outflow. Later, in October 2003, in response to increasing demand for water for domestic consumption and irrigation, a water input project to increase the reservoir capacity was initiated and completed in July 2009. Subsequently, the lake was enlarged to form a medium-sized reservoir (Zou et al., 2020).

MATERIALS AND METHODS

Construction of Diatom Transfer Functions

We chose the WAPLS method (Component 1 and Component 2) to construct diatom transfer functions (Birks, 2012). The diatom percentage data were square root transformed, and the error of the climate reconstruction was estimated by the bootstrapping method (conducted 100 times). The transfer function was constructed using C2 software. To construct a diatom-water temperature transfer function, we used the results of a two-year diatom study of the seasonal diatom succession in Yunlong Lake (Zou et al., 2018). Details of the deployment of the sediment trap (**Figure 1B**), sample collection and diatom analysis are given in Zou et al. (2018). The results showed that water temperature is the most important environmental variable controlling the seasonal succession of diatom assemblages in Yunlong Lake (**Figure 2**). However, the diatom assemblages postdating November 2014 were significantly influenced by an increase in lake trophic status (Zou et al., 2018), and therefore we only used the 12 samples collected before November 2014 to construct the transfer function. Based on the high correlation between seasonal diatom assemblages and the MSWT (mean surface water temperature at depths of 1, 5, and 7 m), we constructed a diatom-MSWT transfer function for Yunlong Lake in order to quantitatively reconstruct the past changes in surface water temperature.

To construct a diatom-water depth transfer function, we used the results of an investigation of the spatial distribution of lake sediment surface diatom assemblages according to water depth (Zou et al., 2020). The results showed that the surface diatom assemblages are highly correlated with water depth: epiphytic and benthic diatoms are dominant in the littoral and shallow water zones, and the percentage of planktonic diatoms increases significantly in the deep profundal zone (**Figure 3**). Based on

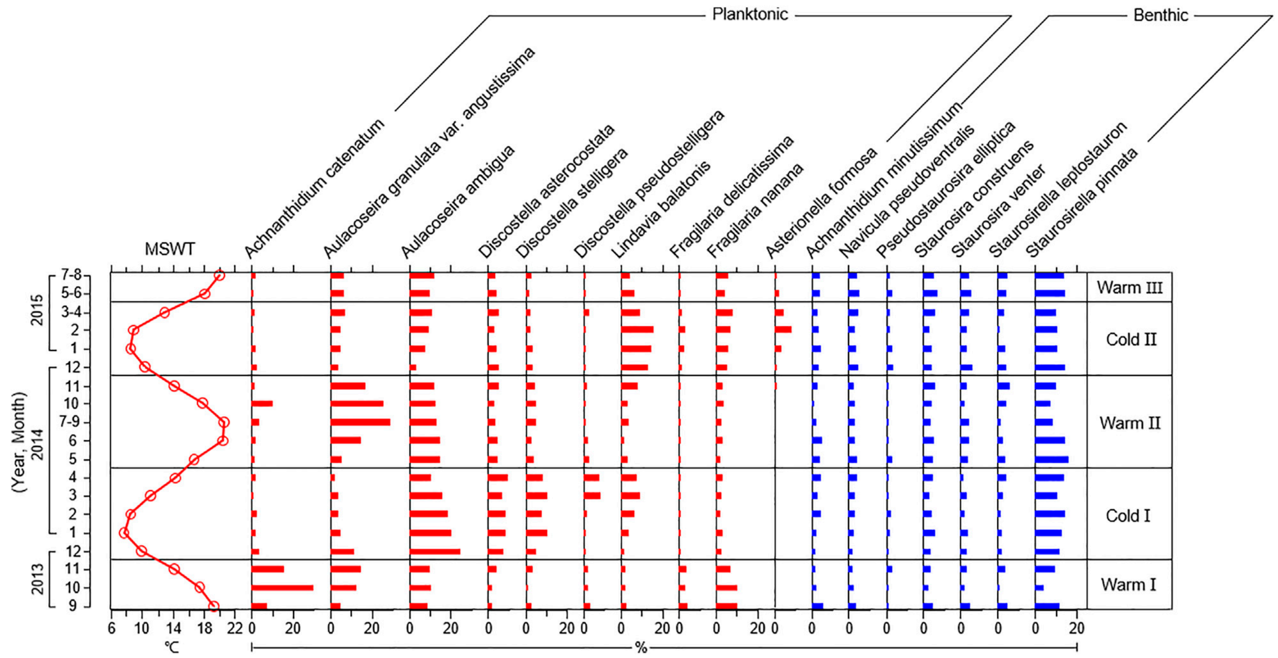

FIGURE 2 | Changes in the mean relative abundance of the main diatom species from diatom seasonal investigation of Yunlong Lake. MSWT represents the mean surface water temperature at depths of 1, 5 and 7 m. Three warm and two cold seasons are defined by changes in monthly average water temperature at the four depths within the water column (Zou et al., 2018).

this relationship, we constructed a diatom-water depth transfer function, which can be used to quantitatively reconstruct past changes in lake water level and hence regional precipitation.

Meteorological Monitoring and Reservoir Capacity Records

To evaluate the sensitivity and validity of the diatom-based transfer functions for temperature and precipitation in the lake catchment, we collected meteorological observations (including mean annual air temperature and mean annual precipitation data) from the nearby Dali Station (covering 1951–2013, ~ 150 km away from Yunlong Lake) and Yunlong Station (1977–2013, just surrounding Yunlong Lake), and measured changes in the water capacity of the reservoir from engineering records which were used to determine long-term changes in water level.

Chronology and Diatom Analysis :

In July 2013, we retrieved a short sediment core (YL2013-A, **Figure 1B**) from near the lake center using a UWITEC gravity corer. The chronology of the uppermost 39 cm of the core was determined using the ^{210}Pb distribution calculated using the CRS (Constant Rate of Supply) model, together with the location of peaks in the distribution of ^{137}Cs (Zou et al., 2020). Diatom analysis of all sediment samples was carried out according to standard methods (Battarbee et al., 2001). Diatoms were identified to species level mainly using the taxonomic references of Krammer and Lange-Bertalot (1986-1991), and with reference to algaebase (https://www.algaebase.org/) for the identification of rare species. For all sediment samples, at least 600 diatom valves were counted, and the diatom data were expressed as percentage relative abundance of the total number of valves counted.

RESULTS

The final diatom-mean surface water temperature (MSWT) transfer function was constructed using the screened 12 sediment trap samples. The results of a test of the performance and prediction ability of the transfer function constructed using Component 1 and Component 2 with the WAPLS method are listed in **Table 1**. It can be seen that predictive ability of the transfer function constructed using Component 2 has a better fit to the observations ($R^2 = 0.97$) and a smaller residual (RMSE = 0.53) (**Figure 4**). However, it did not pass the random *t*-test, likely due to the small number of samples involved in the training set.

The diatom-water depth (WD) transfer function was constructed using the 62 surface samples. Transfer functions constructed using Component 1 and Component 2 using the WAPLS method were both effective in predicting water depth, with $R^2 > 0.9$ (**Table 2**); however, the predicted water depth of the transfer function constructed using Component 2 had the better fit to the observations ($R^2 = 0.95$) and a smaller residual (RMSE = 0.96) (**Figure 5**), which also passed the random *t*-test ($p = 0.04 < 0.05$) (**Table 2**).

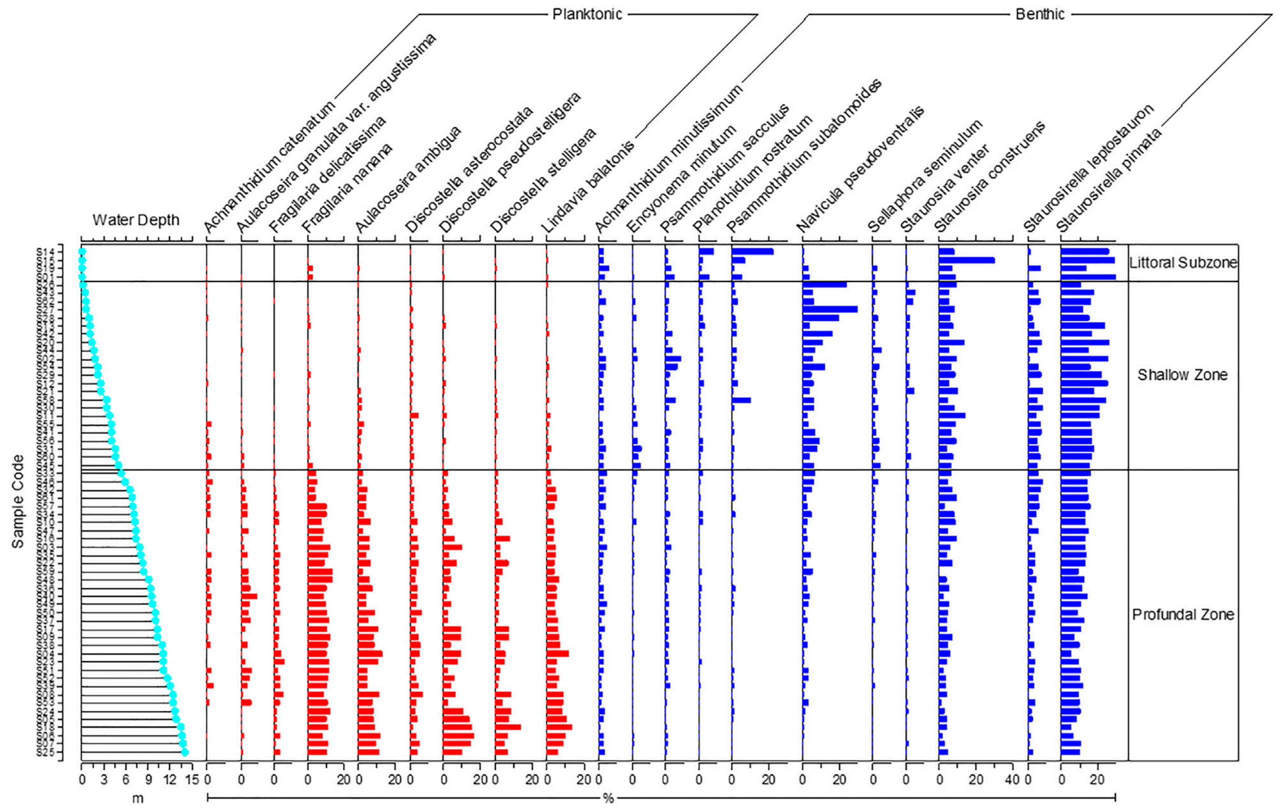

FIGURE 3 | Changes in diatom assemblages vs. water depth for the 62 surface samples from Yunlong Lake. Only diatom species with a total relative abundance >1% are shown.

TABLE 1 | Comparison of the performance of diatom mean surface water temperature (MSWT) transfer function constructed using WAPLS-Component 1 and Component 2 in predicting changes in surface water temperature.

Trap samples	Method	Component	RMSE	R^2	Ave_Bias	Max_Bias	RMSEP	Rand. *t*-test *p*
19 (Unscreened)	WAPLS	Component 1	1.532	0.732	-0.046	1.493	2.6	…
		Component 2	0.946	0.897	-0.005	0.772	2.676	0.628
12 (Screened)	WAPLS	Component 1	1.326	0.807	-0.042	1.304	2.87	…
		Component 2	**0.53**	**0.969**	**-0.005**	**0.346**	**2.888**	**0.471**

The age range of the upper 39 cm of sediment core YL2013-A is 1919–2013, nearly 100 years (Zou et al., 2020). Using the constructed diatom-MSWT and diatom-WD transfer functions, combined with the diatom assemblage succession in the core (Zou et al., 2020), we reconstructed the changes in the annual average surface water temperature and the annual average water level of Yunlong Lake over the last ~100 years using the WAPLS method (Component 1 and Component 2) (**Figure 6**). The trend of variation of water temperature and water level reconstructed by Component 1 and Component 2 is very similar, with the difference being the range of the reconstructed variables and the estimated errors (**Figure 6**). The reconstructed MSWT using Component 1 ranges from 9.21 to 13.03°C, with an average of 10.6°C, and the estimated error range is from 0.6 to 1.33°C. The reconstructed MSWT using Component 2 ranges from 8.97 to 12.18°C, with an average of 10.58°C, and the estimated error range is from 0.7 to 1.67°C. The annual average water level of Yunlong Lake over the last ~100 years reconstructed by Component 1 ranges from 6.23 to 13.51 m, with an average of 9.5 m, and an estimated error ranging from 0.23 to 0.39 m. While the annual average water level reconstructed by Component 2 ranges from 5.47 to 12.52 m, with an average of 8.98 m, and an estimated error ranging from 0.37 to 0.69 m. Because both transfer functions constructed using Component 2 have a better performance (a higher R^2 value and a smaller residual), we selected the results reconstructed by Component 2 and compared them with the meteorological and reservoir capacity records (**Figure 7**) in order to evaluate their sensitivity and validity for reconstructing climate changes.

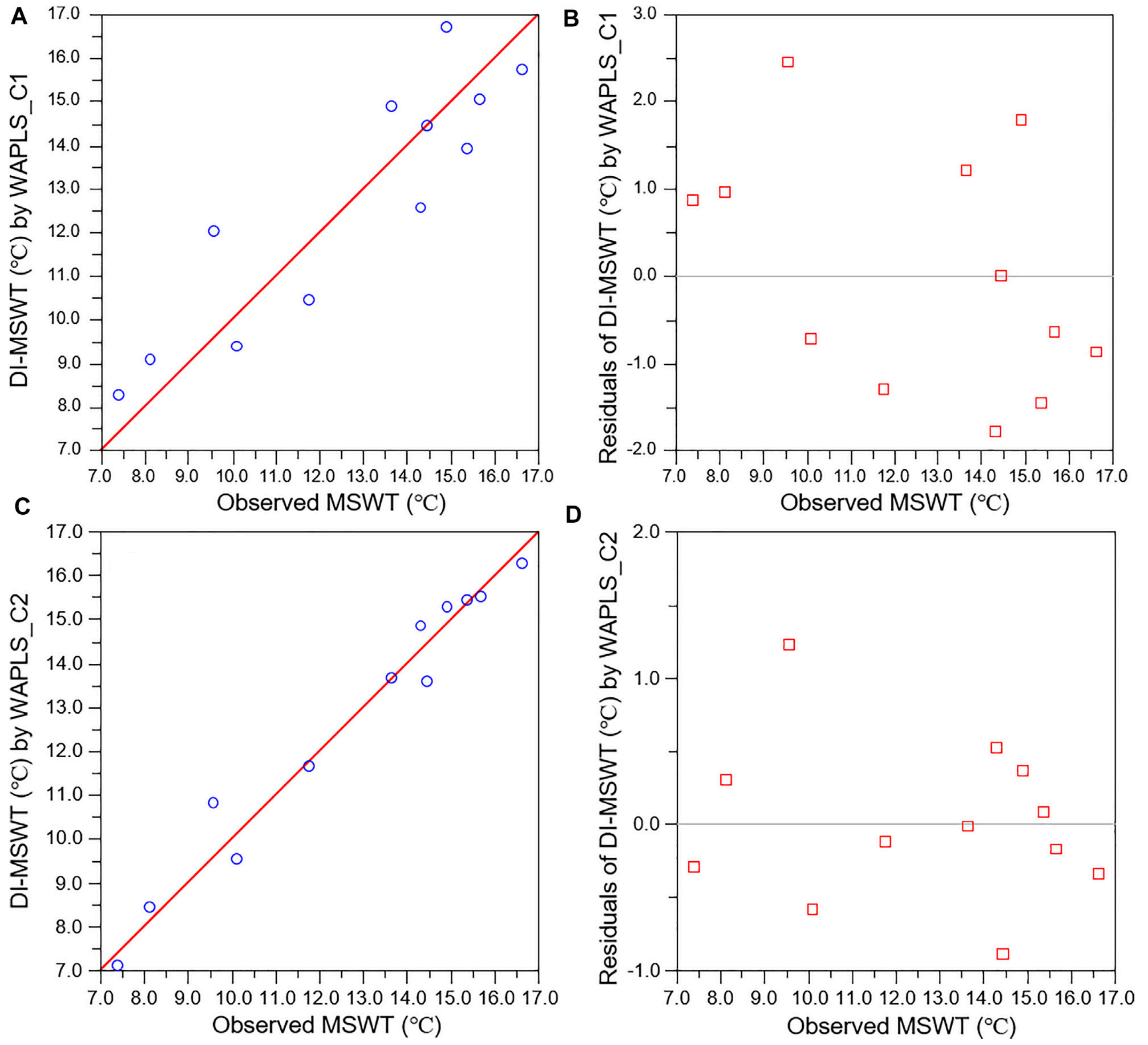

FIGURE 4 | Performance of the diatom-inferred mean surface water temperature (DI-MSWT) transfer function for Yunlong Lake, constructed by WAPLS (Components 1, 2) method. **(A)** Regression analysis results of the DI-MSWT using Component 1 and the measured dataset. **(B)** Residuals of the DI-MSWT using Component 1. **(C)** Regression analysis results of the DI-MSWT based on Component 2 and the measured dataset. **(D)** Residuals of the DI-MSWT using Component 2.

TABLE 2 | Comparison of the performance of diatom water depth (WD) transfer function constructed using WAPLS-Component 1 and Component 2 in predicting changes in water depth.

Surface samples	Method	Component	RMSE	R^2	Ave_Bias	Max_Bias	RMSEP	Rand. *t*-test *p*
62	WAPLS	Component 1	1.161	0.931	-0.027	1.279	1.33	. . .
(Unscreened)		**Component 2**	**0.964**	**0.952**	**-0.001**	**1.286**	**1.205**	**0.04**

Because the monitoring interval of Yunlong Station is relatively short (since 1977), we conducted Pearson correlation analysis of the mean annual air temperature (MAAT) and the mean annual precipitation (MAP) obtained from Dali and Yunlong Station since 1977. The resulting correlation coefficients for MAAT and MAP are 0.94 and 0.71,

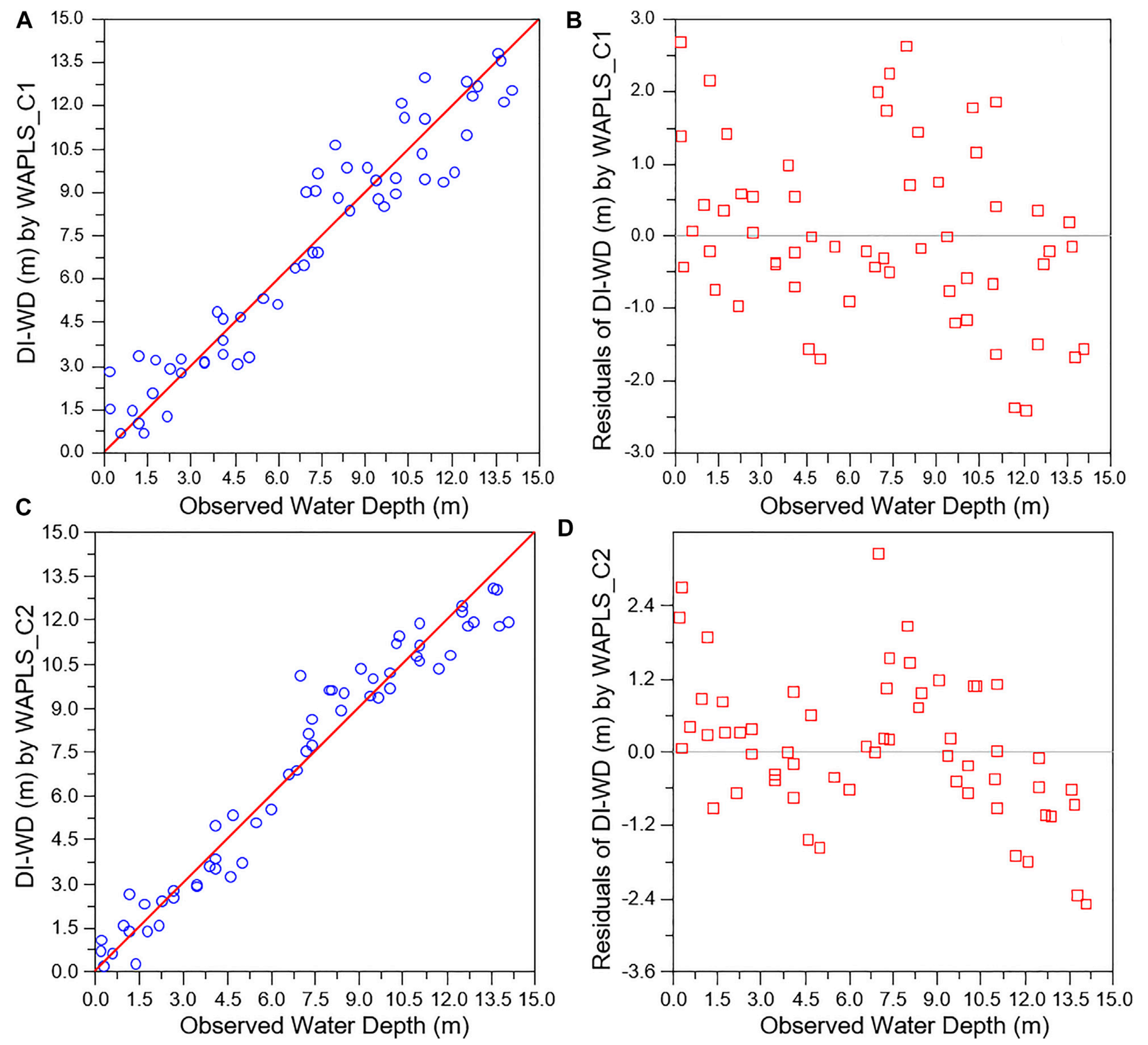

FIGURE 5 | Performance of the diatom-inferred water depth (DI-WD) transfer function for Yunlong Lake, constructed by WAPLS (Components 1, 2). **(A)** Regression analysis results of the DI-WD using Component 1 and the measured dataset. **(B)** Residuals of the DI-WD using Component 1. **(C)** Results of regression analysis of the DI-WD using Component 2 and the measured dataset. **(D)** Residuals of the DI-WD using Component 2.

respectively, indicating that the patterns of climate change recorded at the two locations are essentially the same, and both reliably reflect the climatic conditions of the Yunlong Lake area (**Figure 7**).

We estimated the approximate water level during four phases (described below) based on the water capacity of the reservoir recorded by the dam construction project and the measured water level in 2013 (Zou et al., 2020). The results show that since the beginning of dam construction in 1953, the water level of Yunlong Lake exhibited a stepwise increase due to the dam construction and the reservoir extension project: the water level rose from 7 m (the reservoir water capacity was 7.26 × 10^6 m^3) in 1953 to 7.79 m (7.9 × 10^6 m^3) when dam construction was completed in 1985. When the reservoir extension project was completed in 2009, the water level increased to 11.45 m (1.09 × 10^7 m^3), and the final water level measured during field work in 2013 was 13.3 m (**Figure 7A**).

By comparison, we found that the water temperature and water level change of Yunlong Lake over the last ~100 years reconstructed by the diatom transfer function correspond well to the meteorological observations of air temperature and precipitation and the long-term stepwise increasing trend of water level estimated by the reservoir capacity record (**Figure 7A**). Based on these records, the pattern of climate change of the Yunlong region over the last ~100 years can be divided into four phases, as follows.

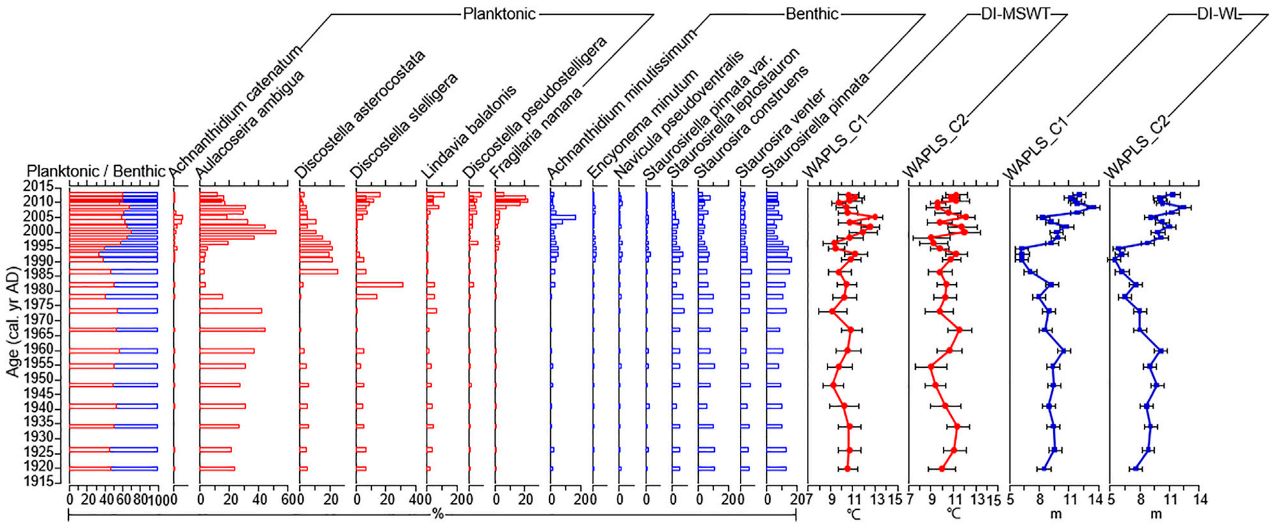

FIGURE 6 | The succession of dominant diatom assemblages over the last ~ 100 years in sediment core YL2013-A from Yunlong Lake and diatom-inferred MSWT and water level (WL) obtained using a transfer function using WAPLS (Components 1, 2).

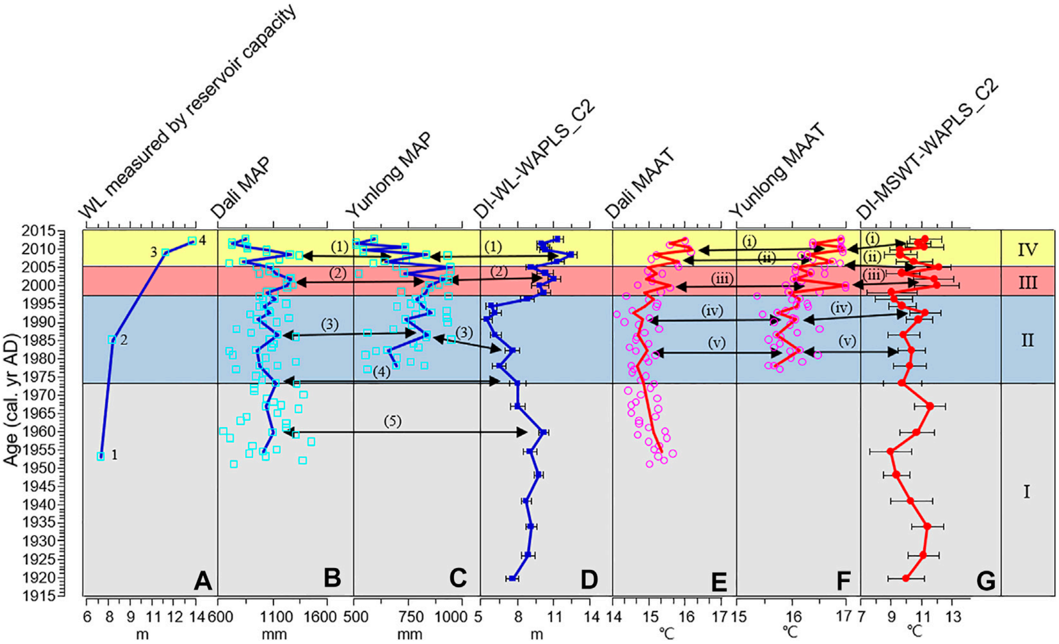

FIGURE 7 | Comparison of diatom-inferred lake water level, mean surface water temperature and meteorological and reservoir capacity records over the last ~100 years in the Yunlong Lake area. **(A)** Long-term change in lake water level estimated by the reservoir capacity records and the measured water level in 2013. **(B)** Mean annual precipitation (MAP) during 1950–2013 recorded by Dali Station. The squares represent the measured data points, and the solid line represents the fitted trend of the precipitation corresponding to the diatom sampling points based on sediment dating, and the same below. **(C)** Mean annual precipitation (MAP) during 1977–2013 recorded at Yunlong Station. **(D)** Diatom-inferred lake water level obtained using WAPLS-Component 2 and the estimated reconstruction errors. **(E)** Mean annual air temperature (MAAT) during 1950–2013 recorded at Dali Station. The circles represent the measured data points, and the solid line represents the fitted trend of the air temperature corresponding to the diatom sampling points based on sediment dating, and the same below. **(F)** Mean annual air temperature (MAAT) during 1977–2013 recorded at Yunlong Station. **(G)** Diatom-inferred MSWT obtained using WAPLS-Component 2 and the estimated reconstruction errors. 1–4 represents four damming and reservoir extension time interval. (1)–(5) represents five interannual interval of increased precipitation. (i)–(v) represents five interannual interval of increased temperature.

Phase I (~1919–1973): relatively stable temperature and precipitation. Overall, the temperature was relatively high, and the diatom-inferred MSWT ranges from 8.97 to 11.6°C, with an average of 10.36°C. The MAAT recorded by Dali Station for 1951–1973 varied from 14.46 to 15.68°C, with an average 15.05°C. The climate was generally humid during this interval. The MAP recorded by Dali

Station during 1951–1973 is 1,080 mm, and the diatom-inferred lake water level ranges from 7.61 to 10.17 m, with an average of 8.84 m.

Phase II (~1973–1997): decreasing temperature, precipitation and lake water level. The MAAT recorded by Dali Station ranges from 14.12 to 15.3°C, with an average of 14.79°C; and the MAAT recorded by Yunlong Station for 1977–1997 ranges from 15.38 to 16.52°C, with an average of 15.93°C. The diatom-inferred MSWT ranges from 9.04 to 11.27°C, with an average of 10.07°C. All of these values are lower than during Phase I. Precipitation also decreased during this phase. The averaged MAP recorded by Dali Station was 1,024 mm, and the MAP recorded by Yunlong Station is 559–951 mm with an average of 772 mm; thus the climate was relatively dry. The diatom-inferred lake water level has the range of 5.47–10.21 m, with an average of 7.11 m, which is much lower than during Phase I.

Phase III (~1997–2005): increasing temperature, precipitation and lake water level. The temperature records show that temperatures in the region began to increase, with averaged MAAT recorded by Dali and Yunlong Stations of 15.25 and 16.37°C, respectively. The diatom-inferred MSWT ranges from 9.75 to 12.18°C, with an average of 11.45°C. Regional precipitation also increased. The averaged MAP recorded by Dali and Yunlong Stations during this interval was 1,148 and 814 mm, respectively, which is much higher than during Phase II. The diatom-inferred lake water level ranges from 9.16 to 11.04 m, with an average of 10.09 m, which is much higher than during Phase II.

Phase IV (~2005–2012): increasing air temperature, decreasing water temperature and rainfall, and increasing lake water level. The records of air temperature and water temperature show opposing trends during this interval. The averaged MAAT recorded by Dali and Yunlong Stations was 15.71 and 16.66°C, respectively; this is higher than during Phase III and indicates the regional air temperature continued to increase. However, the diatom-inferred MSWT ranges from 9.59 to 11.29°C, with an average of 10.51°C, which is much lower than during the preceding phase. The averaged MAP recorded by Dali and Yunlong Stations was 963 and 667 mm, respectively, which is much lower than during Phase III. However, in response to the completion of the reservoir extension project, the lake water level increased, with the diatom-inferred water level ranging from 10.04 to 12.52 m, with an average of 10.96 m.

A total of five intervals of relatively high diatom-inferred water level occurred, which match the interannual pattern of increased precipitation, within the range of the dating error (**Figure 7**). Additionally, there are five intervals of relatively high diatom-inferred water temperature which correspond to the intervals of observed increases in air temperature (**Figure 7**).

DISCUSSION

Much research work has been conducted on quantitative paleoclimatic reconstruction using diatom transfer functions, which is a generally accepted method of paleoclimatic reconstruction. For example, the seasonal diatom succession in lakes has been used to reconstruct temperature changes (Lotter and Bigler, 2000; Köster and Pienitz, 2006), and the spatial pattern of surface diatom assemblages with water depth has been used to reconstruct changes in lake water level (Moos et al., 2005; Laird et al., 2010; Laird et al., 2011). However, Juggins (2013) suggested that the observed correlation between diatom assemblages and temperature and water depth may be an artifact, and that temperature and water depth may not be the primary environmental variables controlling changes in diatom assemblages. Moreover, the lack of reliable evidence has meant that the validity of these climatic reconstructions is still questioned.

The results from Yunlong Lake demonstrate that a surface sediment diatom-water depth transfer function established within a single lake can effectively be used to reconstruct water level changes. The investigation of the spatial pattern of surface diatom assemblages with water depth at Yunlong Lake shows that water depth is the most important environmental variable determining the pattern of surface diatom assemblages. This is because water depth exerts a strong control on the ratio of planktonic to benthic diatoms and of the relative abundances of different benthic diatoms (Zou et al., 2020). Although this spatial pattern of surface diatom assemblages is in fact controlled by the degree of light penetration, it is directly linked with water depth, which leads to the observed high correlations between surface diatom assemblages and water depth (Kingsbury et al., 2012). Although the spatial pattern of diatom assemblages in a lake may also be affected by factors such as the nutrient content and pH of the lake water, many studies have shown that water depth is the most important environmental factor (Moos et al., 2005; Laird et al., 2010; Laird et al., 2011; Kingsbury et al., 2012; Zou et al., 2020). We have used the observed high correlation between water depth and surface diatom assemblages at Yunlong Lake to construct a diatom-water depth transfer function, which was then used to reconstruct the history of lake water level changes over the last ~100 years.

Comparison with the meteorological rainfall records and the long-term trend of water level estimated by the record of reservoir water capacity, the diatom-inferred record of lake water level is shown to accurately track changes in precipitation. For example, within the dating error, the diatom-inferred lake level tracks the five interannual-scale intervals of heavy precipitation (**Figure 7**). Moreover, the diatom-inferred water level is also coupled with the long-term stepwise rise in water level caused by the human activities, which is especially pronounced in Phase IV (**Figure 7**). The diatom-inferred water level of the lake was generally high, mainly due to the implementation of the reservoir extension project, while the meteorological records show that the MAP during this interval decreased substantially (**Figure 7**).

In addition, the changes in diatom-inferred MSWT reliably reflect the water temperature fluctuations at Yunlong Lake over the last ~100 years, which include the signal of natural climate change prior to human disturbance (Phases I, II and III) and the ecological response signal of the lake under strong human disturbance (Phase IV). During Phases I, II and III, the diatom-inferred surface water temperature changes are largely consistent with changes in air temperature. For example, during Phase II both the air temperature and water temperature were relatively low overall; and during Phase III, both the regional air temperature and the water temperature increased substantially (**Figure 7**). In addition, the diatom-inferred MSWT captured five interannual-scale warming events (**Figure 7**), which indicates that diatoms respond sensitively and rapidly to regional temperature changes, and that the diatom-inferred water temperature changes are reliable.

During Phase IV, the diatom-inferred MSWT decreased substantially, but the MAAT in the study area continued to increase (**Figure 7**). The opposing trends of air temperature and water temperature during this period were mainly the result of human disturbance. From October 2003 to July 2009, the local government implemented a large-scale reservoir extension project for Yunlong Lake, which led to a short-term large increase in the reservoir water capacity which may have triggered an immediate response of the lake ecology. When the external heat source (i.e, solar radiation) for the lake remained essentially unchanged or increased slightly (as a result of regional warming), the increased heating of the lake water may not have been sufficient to offset the greatly increased thermal capacity of the reservoir within a short interval, resulting in the observed pronounced decrease in lake water temperature (Zou et al., 2020). Because diatoms respond directly to changing water temperature, the decrease in water temperature finally led to the dominance of diatom assemblages that bloomed in the cold season (Zou et al., 2018), while the relative abundance of warm-preference diatom species, such as *Achnanthidium catenatum*, did not increase with the further warming of the study area (**Figure 6**). As a result, the diatom-inferred MSWT decreased substantially during this interval, but the air temperature continued to increase (**Figure 7**).

CONCLUSIONS

1) Diatom-climate reconstruction and the meteorological records aiming at Yunlong Lake over the last ~100 years show that climatic and environmental change of the Yunlong Lake region experienced four phases. Phase I (~1919–1973), relatively stable temperature and precipitation; Phase II (~1973–1997), decreasing temperature, precipitation and lake water level; Phase III (~1997–2005), increasing temperature, precipitation and lake water level; Phase IV (~2005–2012), increasing air temperature, decreasing water temperature and rainfall, and increasing lake water level.
2) At a lake site where temperature and water depth are the dominant environmental variables determining the seasonal succession and spatial pattern of diatom assemblages, a diatom-based transfer function was constructed and is shown to provide a reliable quantitative reconstruction of past changes in temperature and precipitation of different timescales in the study area.
3) When using lake diatoms to reconstruct past water temperature changes, the impact of substantial changes in lake water volume on thermal properties and the resulting ecological response should be considered.

DATA AVAILABILITY STATEMENT

The original contributions presented in the study are included in the article/Supplementary Material, further inquiries can be directed to the corresponding author.

AUTHOR CONTRIBUTIONS

YZ and LW designed research. YZ, LW, JZ, and YY collected samples. YZ and ZG analyzed data. YZ, LW, HH, and GL wrote and revised the article, and HZ provided suggestions. All authors read and approved the final manuscript.

FUNDING

This study was supported by the National Natural Science Foundation of China (42001077, 41772379, 41991323), China Postdoctoral Science Foundation (2021T140582), and the National Key R&D Program of China (2017YFA0603400).

ACKNOWLEDGMENTS

We thank Jan Bloemendal for polishing the manuscript.

REFERENCES

Battarbee, R. W., Jones, V. J., Flower, B. P., Cameron, N. G., Bennion, H., Carvalho, L., et al. (2001). "Diatoms," in *Tracking Environmental Change Using Lake Sediments*. Editors JP Smol, HJB Birks, and W M Last (Dordrecht: Kluwer Academic Publishers), 155–202. doi:10.1007/978-94-007-2745-8

Birks, H. H. (2012). Ecological Responses to Late-Glacial Climate Changes in Northern and Western Norway. *Quat. Int.* 279-280, 52. doi:10.1016/j.quaint.2012.07.227

Dong, X., Yang, X., Chen, X., Liu, Q., Yao, M., Wang, R., et al. (2016). Using Sedimentary Diatoms to Identify Reference Conditions and Historical Variability in Shallow lake Ecosystems in the Yangtze Floodplain. *Mar. Freshw. Res.* 67, 803–815. doi:10.1071/mf14262

Jiang, W., Leroy, S. A. G., Yang, S., Zhang, E., Wang, L., Yang, X., et al. (2019). Synchronous Strengthening of the Indian and East Asian Monsoons in Response to Global Warming since the Last Deglaciation. *Geophys. Res. Lett.* 46, 3944–3952. doi:10.1029/2019GL082084

Juggins, S. (2013). Quantitative Reconstructions in Palaeolimnology: New Paradigm or Sick Science?. *Quat. Sci. Rev.* 64, 20–32. doi:10.1016/j.quascirev.2012.12.014

Kingsbury, M. V., Laird, K. R., and Cumming, B. F. (2012). Consistent Patterns in Diatom Assemblages and Diversity Measures across Water-Depth Gradients from Eight Boreal Lakes from north-western Ontario (Canada). *Freshw. Bio.* 57, 1151–1165. doi:10.1111/j.1365-2427.2012.02781.x

Krammer, K., and Lange-Bertalot, H. (1986-1991). *Bacillariophyceae. Süsswasserflora von Mitteleuropa, Band 2*. Berlin: Spektrum Akademischer Verlag Heidelberg.

Köster, D., and Pienitz, R. (2006). Seasonal Diatom Variability and Paleolimnological Inferences-A Case Study. *J. Paleolimnol.* 35, 395–416. doi:10.1007/s10933-005-1334-7

Laird, K. R., Kingsbury, M. V., and Cumming, B. F. (2010). Diatom Habitats, Species Diversity and Water-Depth Inference Models across Surface-Sediment

Transects in Worth Lake, Northwest Ontario, Canada. *J. Paleolimnol.* 44, 1009–1024. doi:10.1007/s10933-010-9470-0

Laird, K. R., Kingsbury, M. V., Lewis, C. F. M., and Cumming, B. F. (2011). Diatom-inferred Depth Models in 8 Canadian Boreal Lakes: Inferred Changes in the Benthic:planktonic Depth Boundary and Implications for Assessment of Past Droughts. *Quat. Sci. Rev.* 30, 1201–1217. doi:10.1016/j.quascirev.2011.02.009

Li, J., Wang, L., Cao, Q., Rioual, P., Lei, G., Cai, B., et al. (2021). Diatom Response to Global Warming in Douhu Lake, Southeast China. *Acta Geologica Sinica - English Edition*. 95, 638–647. doi:10.1111/1755-6724.14294

Lotter, A. F., and Bigler, C. (2000). Do diatoms in the Swiss Alps Reflect the Length of Ice-Cover?. *Aquat. Sci.* 62, 125–141. doi:10.1007/s000270050002

Magny, M. (2004). Holocene Climate Variability as Reflected by Mid-European lake-level Fluctuations and its Probable Impact on Prehistoric Human Settlements. *Quat. Int.* 113, 65–79. doi:10.1016/s1040-6182(03)00080-6

Moos, M. T., Laird, K. R., and Cumming, B. F. (2005). Diatom Assemblages and Water Depth in Lake 239 (Experimental Lakes Area, Ontario): Implications for Paleoclimatic Studies. *J. Paleolimnol.* 34, 217–227. doi:10.1007/s10933-005-2382-8

Rühland, K. M., Paterson, A. M., and Smol, J. P. (2015). Lake Diatom Responses to Warming: Reviewing the Evidence. *J. Paleolimnol.* 54, 1–35. doi:10.1007/s10933-015-9837-3

Smol, J. P., and Cumming, B. F. (2000). Tracking Long-term Changes in Climate Using Algal Indicators in Lake Sediments. *J. Phycology*. 36, 986–1011. doi:10.1046/j.1529-8817.2000.00049.x

Smol, J. P., and Douglas, M. S. (2007). From Controversy to Consensus: Making the Case for Recent Climate Change in the Arctic Using lake Sediments. *Front. Ecol. Environ.* 5, 466–474. doi:10.1890/060162

Stone, J. R., and Fritz, S. C. (2004). Three-dimensional Modeling of Lacustrine Diatom Habitat Areas: Improving Paleolimnological Interpretation of Planktic: Benthic Ratios. *Limnol. Oceanogr.* 49, 1540–1548. doi:10.4319/lo.2004.49.5.1540

Wang, L., Jiang, W. Y., Jiang, D. B., Zou, Y. F., Liu, Y. Y., Zhang, E. L., et al. (2018). Prolonged Heavy Snowfall during the Younger Dryas. *J. Geophys. Res. Atmos.* 123, 13748–13762. doi:10.1029/2018JD029271

Wang, L., Li, J., Lu, H., Gu, Z., Rioual, P., Hao, Q., et al. (2012). The East Asian winter Monsoon over the Last 15,000 Years: its Links to High-Latitudes and Tropical Climate Systems and Complex Correlation to the Summer Monsoon. *Quat. Sci. Rev.* 32, 131–142. doi:10.1016/j.quascirev.2011.11.003

Wang, R., Yang, X., Langdon, P., and Zhang, E. (2011). Limnological Responses to Warming on the Xizang Plateau, Tibet, over the Past 200 Years. *J. Paleolimnol.* 45, 257–271. doi:10.1007/s10933-011-9496-y

Winder, M., and Cloern, J. E. (2010). The Annual Cycles of Phytoplankton Biomass. *Phil. Trans. R. Soc. B*. 365, 3215–3226. doi:10.1098/rstb.2010.0125

Yang, X., Kamenik, C., Schmidt, R., and Wang, S. (2003). Diatom-based Conductivity and Water-Level Inference Models from Eastern Tibetan (Qinghai-Xizang) Plateau Lakes. *J. Paleolimnol.* 30, 1–19. doi:10.1023/A:1024703012475

Zou, Y., Wang, L., Xu, H., Yan, Y., Zhang, J., Liu, Y., et al. (2020). Do changes in Water Depth and Water Level Influence the Diatom Diversity of Yunlong Lake, in Yunnan Province, Southwest China?. *J. Paleolimnol.* 64, 273–291. doi:10.1007/s10933-020-00137-x

Zou, Y., Wang, L., Zhang, L., Liu, Y., Li, P., Peng, Z., et al. (2018). Seasonal Diatom Variability of Yunlong Lake, Southwest China - a Case Study Based on Sediment Trap Records. *Diatom Res.* 33, 381–396. doi:10.1080/0269249X.2018.1541823

Conflict of Interest: The authors declare that the research was conducted in the absence of any commercial or financial relationships that could be construed as a potential conflict of interest.

frontiers
in Earth Science

ORIGINAL RESEARCH
published: 02 July 2021
doi: 10.3389/feart.2021.685928

The Driving Forces Underlying Spatiotemporal Lake Extent Changes in the Inner Tibetan Plateau During the Holocene

Xiangjun Liu[1,2]*, *David Madsen*[2,3] *and Xiaojian Zhang*[4]

[1]College of Geography and Environmental Science, Northwest Normal University, Lanzhou, China, [2]Salt Lake Institute of Qinghai, Chinese Academy of Sciences, Xining, China, [3]Department of Anthropology, University of Nevada-Reno, Reno, NV, United States, [4]School of Geography and Ocean Science, Nanjing University, Nanjing, China

OPEN ACCESS

Edited by:
Shiyong Yu,
Jiangsu Normal University, China

Reviewed by:
Mingrui Qiang,
South China Normal University, China
Ulrike Herzschuh,
Alfred Wegener Institute Helmholtz Centre for Polar and Marine Research, Germany
Jianhui Chen,
Lanzhou University, China

***Correspondence:**
Xiangjun Liu
xiangjunliu@126.com

Specialty section:
This article was submitted to Quaternary Science, Geomorphology and Paleoenvironment, a section of the journal Frontiers in Earth Science

Received: *26 March 2021*
Accepted: *21 June 2021*
Published: *02 July 2021*

Citation:
Liu X, Madsen D and Zhang X (2021) The Driving Forces Underlying Spatiotemporal Lake Extent Changes in the Inner Tibetan Plateau During the Holocene.
Front. Earth Sci. 9:685928.
doi: 10.3389/feart.2021.685928

The Inner Tibetan Plateau (ITP), the central and western part of the Tibetan Plateau (TP), covers about one-fourth of the entire TP and contains more than 800 endorheic lakes larger than 1 km^2. These lakes are important water reservoirs and sensitive to TP climate changes. They regulate regional water circulations, and further influence local ecosystems. Many lakes in ITP are surrounded by conspicuous paleoshorelines indicating much higher past lake levels. Previous studies found that lakes in the western ITP (west of ~86°E) apparently expanded to higher levels than those to the east during the Holocene high lake level stage, however, there is no in-depth study on the reasons for the spatial differences of high lake levels within the ITP. In this study, we first identify Holocene lake level (or lake extent) changes over the ITP by combining published lake level variation data with our reconstruction of Dagze Co lake level variations. We then investigate spatial differences in the magnitude of lake expansions and explore the underlying forces driving these differences using the transient climate evolution of the last 21 ka (TraCE-21ka) and Kiel Climate Model (KCM) simulation results. We find that lakes in the ITP expanded to their highest levels during the early Holocene when the Indian summer monsoon (ISM) greatly intensified. After the mid-Holocene, lake levels fell as a result of the weakening of the ISM. The early Holocene northward shift of the westerly jet and a positive phase of the Atlantic multidecadal oscillation (AMO) resulted in the intensification of southwesterly winds on the southwest TP flank. Concurrently, westerly winds over the TP weakened, causing a differential increase in water vapor transport to the ITP with higher precipitation levels in the southwestern ITP and lower levels to the northeast. These wind-driven differential precipitation levels caused lakes in the southwestern ITP to expand to higher levels than those in the central, northern and northeastern ITP. During the early Holocene, expansion of lakes in the northwestern ITP was enhanced by an increase in glacier melt water besides the increased summer rainfall associated with the intensified ISM.

Keywords: inner Tibetan plateau, holocene, lake extent changes, lake level variations, paleoshoreline

INTRODUCTION

The Tibetan Plateau (TP) is the largest elevated landform on Earth, occupying an area of ~300 × 10^4 km^2 (Zhang et al., 2020). More than ten large Asian rivers originate from the TP, supplying living water for more than one billion people within and surrounding the TP. The TP is rightly regarded as "the water tower of Asia" (Barnett et al., 2005; Immerzeel et al., 2010). Long-term climate changes have reshaped the environment of the TP *via* interactions among the atmosphere, hydrosphere, cryosphere and biosphere (Chen et al., 2020). The variations of environment influenced water budgets over the TP by modulating precipitation and evaporation, which then regulated the size of lakes in the TP and the amount of river discharge flowing out of the TP.

The TP as a whole is situated within the region influenced by the Indo-China monsoons (Conroy and Overpeck, 2011). Using an empirical orthogonal function based regionalization of gridded precipitation values, Conroy and Overpeck (2011) reported that most precipitation in the southwestern TP (region ③ in **Figure 1B**) is related to the Indian summer monsoon (ISM). They also reported that most precipitation in the eastern TP (region ① in **Figure 1B**) is correlated with the East Asian summer monsoon (EASM) which has a significant negative correlation with the western North Pacific summer monsoon (Conroy and Overpeck, 2011). Lai et al. (2021) using a self-organizing map algorithm, analyzed the Global Precipitation Measurement satellite product and ERA5, and determined that the western TP gets most precipitation during the winter and spring seasons that are associated with the westerly jet (blue areas in **Figure 2**). The southwestern TP gains more precipitation during late summer associated with intensity changes in the South Asian High (SAH) and ISM (green areas in **Figure 2**). Eastern TP precipitation is largely related to ISM and anticyclonic circulation over the western North Pacific which peaks during the early summer (yellow areas in **Figure 2**). There are more than 1,000 lakes scattered over the TP, with a total area of ~5 × 10^4 km^2 (Zhang et al., 2019a; Qiao et al., 2019). These lakes are not only sensitive to large scale climate changes, but also have knock-on effects on regional water balances and water vapor circulation (Chen et al., 2020). The changes of lake areas in the TP are considered as direct proxy to illustrate the variations in precipitation (Liu et al., 2021).

The Inner Tibetan Plateau (ITP) locates at the central-western part of the TP (**Figure 1**), it composed of hundreds of endorheic

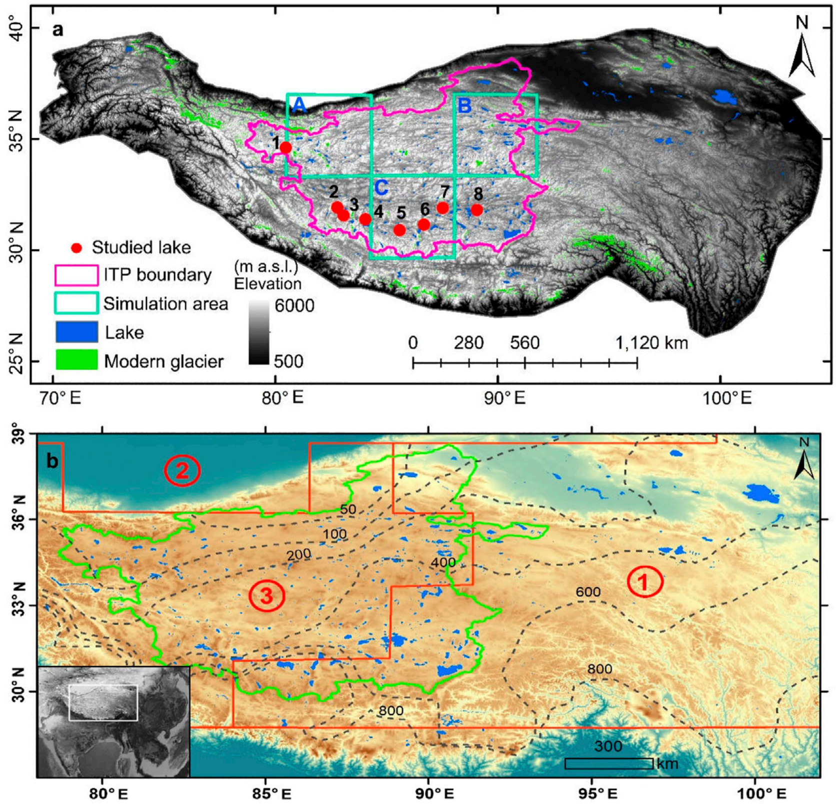

FIGURE 1 | Location of the Inner Tibetan Plateau (ITP) within the Tibetan Plateau (TP). Modern closed-basin lakes on the Tibetan Plateau (blue patches). Pink and green lines in **(A)** and **(B)** outline the scope of ITP. The ITP boundary follows Zhang et al. (2013). Red dots in **(A)** are lakes that have reported Holocene lake level variation curves, 1-Longmu Co, 2-Baqan Co, 3-Ngangla Ring Co, 4-Zhari Nam Co, 5-Zabuye Lake, 6-Tangra Yumco, 7-Dagze Co, 8-Seling Co. The cyan squares (marked with A, B and C) in **(A)** are unit-pixels of TraCE-21ka model we used for modeled Holocene precipitation and temperature changes. Red lines in **(B)** outline regional TP precipitation zones proposed by Conroy and Overpeck (2011). Dashed black lines in **(B)** are modern annual total precipitation (mm) contours obtained from a monthly 1900–2014 global gridded precipitation data set (Hudson and Quade, 2013).

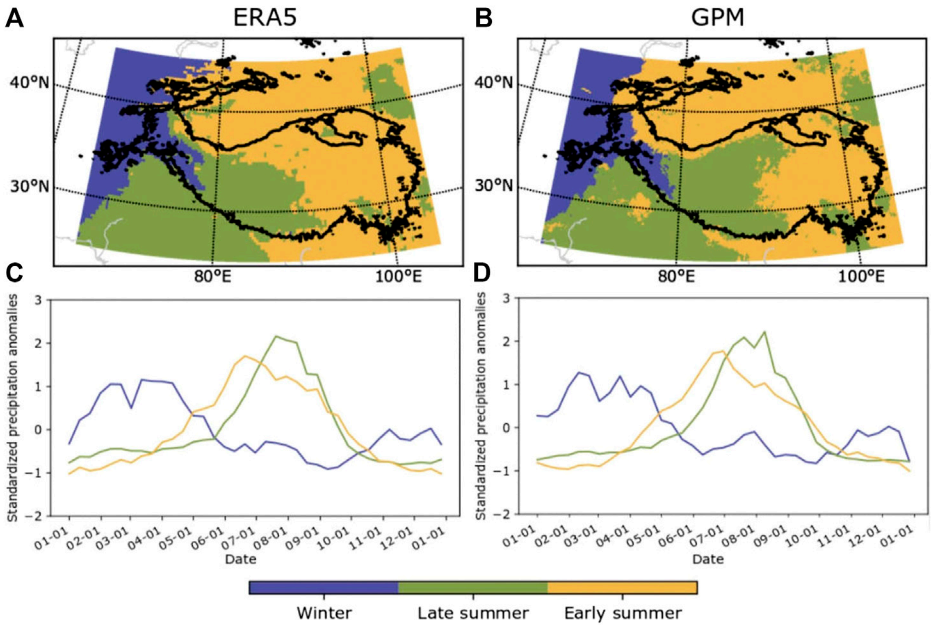

FIGURE 2 | Precipitation classification maps of 19-year averaged (2000–2019) seasonal cycles of standardized precipitation from ERA5 **(A)** and Global Precipitation Measurement product **(B)**. Three precipitation regimes of winter precipitation dominant, early summer precipitation dominant, and late summer precipitation dominant are showed with blue, yellow and green colors. **(C)** and **(D)** show the standardized precipitation anomalies of the spatially averaged precipitation for each precipitation regime (modified from Lai et al. (2021); **Figure 3**).

basins that have average elevations of ~4,960 m above sea level (a.s.l.). A map of the spatial extent of the ITP, when laid over spatial TP precipitation classification maps (**Figures 1**, **2**), indicates that the ITP is located primarily within the region influenced by the ISM. At present, the ITP contains about 55% of lakes in the TP, accounting for 66% of the total TP lake area (Li et al., 2019). Lakes in ITP expand and contract in response to dynamic water balance changes between the input water (precipitation, river runoff, and melt water) and evaporation. The recent history of most lakes in the ITP indicates they contracted from 1976–1995, then expanded rapidly after 1996, closely responding to water balance changes related to differences in precipitation, glacier melt water, and evaporation (Zhang et al., 2020). Lakes in the ITP expanded synchronously with an increase in precipitation during the past 30 years (Chen et al., 2020; **Figure 3**). Increased growing season precipitation was the main reason (contributing ~74% of water inflow) causing ITP lakes to expand rapidly during the past 2 decades (Lei et al., 2014; Zhang et al., 2020). Since the mid-1990s, a warm phase of the Atlantic multidecadal oscillation (AMO) induced a wave train of cyclonic and anticyclonic storms during the summer, enhancing the meandering of the westerly jet. This further modulated precipitation over the ITP by changing its position and strength, causing precipitation over the ITP to steadily increase, with ITP lakes expanding in response (Sun et al., 2020). This expansion of lakes in the ITP caused both ecological and social problems, as vast areas of grasslands surrounding the lakes were submerged, the houses of herdsmen were flooded and important infrastructure, such as the Qinghai-Tibetan railway, were threatened by the rising lake waters (Liu et al., 2016a; Yao et al., 2016). As a result of these threats, recent research has focused on lake variations and on predicting future changes (Lei et al., 2014; Yang et al., 2018; Qiao et al., 2019; Zhang et al., 2020), with some studies predicting lakes

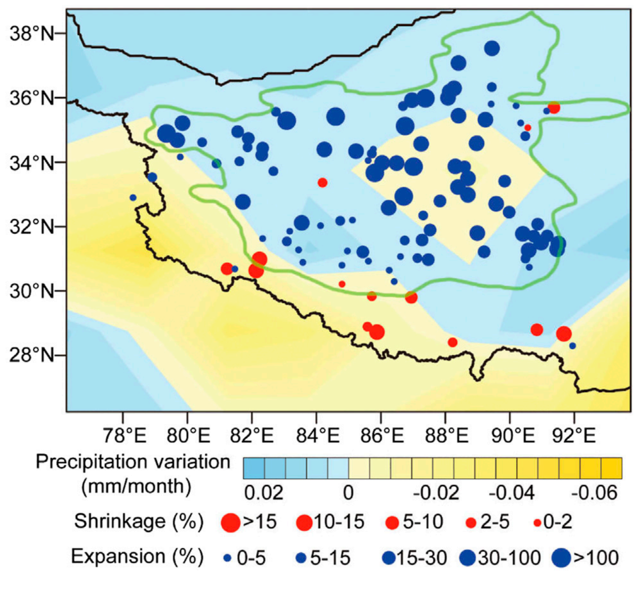

FIGURE 3 | Changes in lake area (1976–2010 CE) (solid dots) and precipitation (yellow [–], blue [+]) (1979–2010 CE) on the TP. The green closed line outlines the extent of ITP (modified from Chen et al., 2020; **Figure 5**).

in the TP will continue to expand until at least 2035 (Yang et al., 2018; Zhang et al., 2020).

Most lakes in the ITP have drastically expanded during the past as evidenced by conspicuous regressive shorelines (Hudson and Quade, 2013; Liu et al., 2013). Paleoshoreline dating has been widely used to reconstruct past lake extent changes and paleohumidity, and to quantify paleorainfall on the TP based on paleohydrological modeling (Chen et al., 2020 and references therein). Both paleoshoreline dating results and paleoenvironmental proxies suggest that during the early Holocene (10–8 ka) rainfall substantially increased and lakes in TP significantly expanded in response to intensification of the ISM (Fleitmann et al., 2007; Cai et al., 2012; Chen et al., 2013; Hudson and Quade, 2013; Liu et al., 2013, Liu et al., 2016b; Bird et al., 2014; Hudson et al., 2015; Huth et al., 2015; Shi et al., 2017). However, lakes located in the western TP (west of 86° N) reached higher lake levels than lakes in the eastern TP (east of 86° N), and the magnitude of lake expansion also decreased from west to east (Hudson and Quade, 2013; Liu et al., 2013). This west/east TP lake history asymmetry during the Holocene high lake level stage is thought to have been caused by differential enhancement of the ISM and the EASM (Hudson and Quade, 2013). As the ISM weakened after the mid-Holocene (~6 ka), precipitation decreased and lakes in the central and western TP regressed, most of these lakes are located in the ITP (Bird et al., 2014; Liu et al., 2016b).

In the ITP, the spatial pattern of lake expansions during the Holocene is different from the relatively homogeneous pattern reflected in modern lake expansions (**Figure 3**). Since the relatively even expansion of lakes in ITP in recent decades does not provide a simple analogy for their Holocene expansions, understanding spatial differences during the Holocene high lake level stage and the underlying driving forces can help us better predict future changes. To more comprehensively understand the Holocene lake extent (or lake level) changes in the ITP and to explore the underlying causes, seasonal precipitation changes need to be considered because the ISM and the Westerlies alternatively influenced the ITP during the summer and winter seasons across the Holocene (Zhu et al., 2015). Such needed research has not been conducted. Moreover, the influence of glacier melt water on the lakes in the ITP and their variations during the Holocene is as yet poorly estimated, both qualitatively and quantitatively.

Here, we combine lake extent variation data, lake level variation curves, and modeled glacier coverage map of the last glacial maximum (LGM) with the modeled transient climate evolution of the last 21 ka (referred to as TraCE-21ka) and with the Kiel Climate Model (KCM) simulation. We use this combined data set to summarize the spatial and temporal changes of lake extents (or lake levels) in the ITP during the Holocene and to explore the underlying causes. TraCE-21ka model results have coarse spatial resolution (3.75° × 3.75°), and its simulated data were used to analyze Holocene precipitation and temperature changes over the ITP. The KCM model was used to simulate spatial precipitation and temperature changes over the TP during the early, mid and late Holocene. Although some environmental proxies can reflect moisture or precipitation changes in ITP during the Holocene, they are less useful in describing spatial differences in moisture or precipitation changes in the ITP. Moreover, some proxy-based precipitation reconstructions may be related to climate factors other than precipitation, such as temperature, atmospheric circulation changes, and lake water salinity (Chen et al., 2020). Hence, in this study, we only include pollen-based precipitation reconstruction results within the TP as a reference.

HOLOCENE LAKE LEVEL VARIATIONS AND HETEROGENOUS EXPANSION OF LAKES IN THE INNER TIBETAN PLATEAU

Inner Tibetan Plateau Setting and Modern Conditions

The ITP locates at central-western TP with an area of ~70 × 10^4 km^2 (**Figure 1**), it covers more than one fourth of the entire TP with an average elevation of ~4,960 m a.s.l., and it is surrounded by the Tanggula, Gangdise, Kunlun, and Karakorams mountains. Average annual temperature is less than 0°C over the ITP, annual evaporation over lake surfaces is >1,000 mm (Li et al., 2019). Annual precipitation is 500–600 mm in the southern and southeastern ITP, and decreases to less than 100 mm in the northwestern ITP (**Figure 1B**). At present, there are about 820 endorheic lakes larger than 1 km^2 lie in the ITP (Zhang et al., 2019a). The ITP lies in the transition zone between the Westerlies and the Indian monsoon, hence lakes in ITP are sensitive to climate changes associated with Westerlies and the ISM interactions (Yao et al., 2012; Li et al., 2019).

Previous Research on Inner Tibetan Plateau Holocene Lake Level Variations

Paleoshorelines provide evidence of past lake levels and can be dated to reconstruct lake level variation histories and to investigate past moisture changes over lake drainage basins (Quade and Broecker, 2009). Paleoshorelines surrounding lakes in the ITP are distinct and well preserved due to limited human modifications (**Supplementary Figure S1**). During the past 20 years, increasing numbers of paleoshorelines in the ITP have been dated as improvements in dating precision and reductions in age uncertainties of non-radiocarbon dating methods have progressed. These new age estimates, derived primarily from Optically Stimulated Luminescence (OSL) methods, have been used in combination with ^{14}C ages to define lake level fluctuation histories (Lee et al., 2009; Li et al., 2009; Chen et al., 2013; Rades et al., 2013; Ahlborn et al., 2015; Huth et al., 2015; Hudson et al., 2015; Liu et al., 2016b; Shi et al., 2017; Alivernini et al., 2018; Hou et al., 2020; Jonell et al., 2020). Although high-stand paleoshoreline ages for many lakes have been reported, Holocene lake level variations for only a few have been described, including Seling Co (Shi et al., 2017; Hou et al., 2021), Baqan Co (Huth et al., 2015), Tangra Yumco

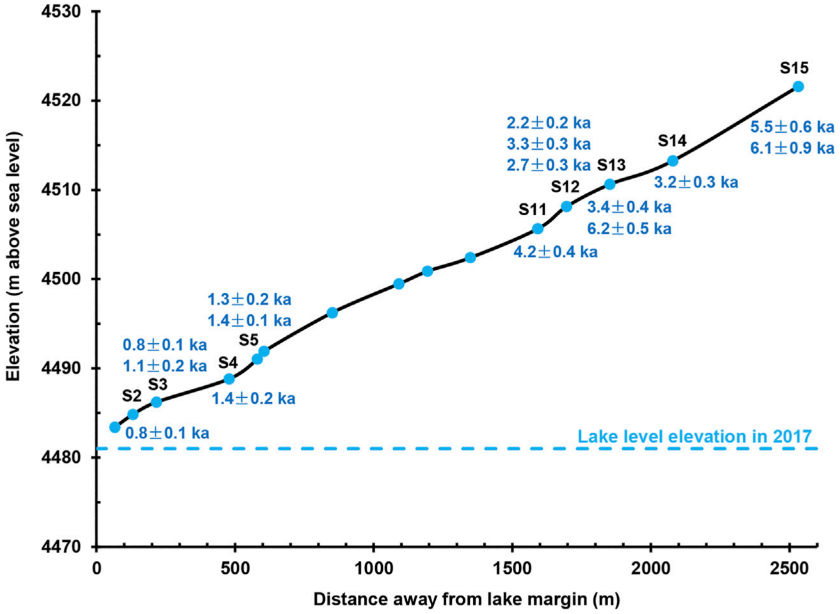

FIGURE 4 | Elevations plotted against the distances from the lake margin for corresponding paleoshorelines in Dagze Co. The associated OSL ages are shown above or below the corresponding paleoshorelines. The locations of OSL dating samples were marked in **Supplementary Figure S2**, and the details of OSL ages were shown in **Table S1**.

(Ahlborn et al., 2015), Zhari Nam Co (Chen et al., 2013), Ngangla Ring Co (Hudson et al., 2015), Longmu Co (Liu et al., 2016b), Zabye Lake (Alivernini et al., 2018), and Dagze Co (reported below). Seven out of these eight lakes are located in the southern ITP, with only Longmu Co being located in the western ITP (**Figure 1A**). Several other lakes in the central and northern ITP also have reported paleoshorelines or lacustrine sediment ages, but these ages are very limited in numbers (only very few highstand lacustrine sediments or paleoshorelines were dated) and/or only indicate a highstand stage, and not enough to be used to reconstruct lake level variation histories (Long et al., 2012; Ma et al., 2012; Pan et al., 2012; Hou et al., 2020).

Dagze Co Holocene Lake Level Variations

We previously reported OSL ages of ~22.7 and 6.1–5.5 ka for the late glacial and Holocene highstands of Dagze Co, respectively (Liu et al., 2020). Here, we add to these other lake records by presenting a newly reconstructed Holocene lake level fluctuation curve for Dagze Co, based on OSL dating of paleoshorelines (**Supplementary Figure S2**).

Dagze Co, with a modern lake surface elevation of 4,480 m a.s.l., is located in the southern ITP (31.82°–31.98°N, 87.36°–87.65°E) (see Liu et al. (2020) for setting and modern climate descriptions). We identified and mapped 15 paleoshorelines surrounding the now brackish lake. The highest paleoshoreline we identified, S15, is ~41.6 m above the modern lake level, and was formed during the mid-Holocene (**Figure 4**). We obtained OSL age estimates for eight other paleoshorlines which appear to have formed during brief stillstands as the lake regressed from this Holocene high (see Liu et al. (2020) for field and laboratory methods). Dagze Co would have overflowed to the west into lower basins when it reached the highest level at S15 as evidenced by a remnant channel connecting Dagze Co with the western basins (Liu et al., 2020). The dividing crest between Dagze Co and the western basins is approximately the same elevation as paleoshoreline S15. Hence, the lake level would maintain approximately the same height as paleoshoreline S15 or slightly higher during the early Holocene ISM intensification stage when several other lakes in ITP experienced their highest Holocene lake levels (Liu et al., 2016b; Liu et al., 2020). The Holocene lake level variation curve for Dagze Co was then reconstructed based on the OSL ages of these nine paleoshorelines (**Figure 4**).

Holocene Lake Level Variations in the Inner Tibetan Plateau

Longmu Co lake levels started to rise following the last deglacial, with the lake reaching its peak during the earliest Holocene (**Figure 5**). The lake level was dropped abruptly during the Young Dryas (YD) cold interval, and then maintained in a secondary high level during the early Holocene (10–8 ka), but lake levels dropped abruptly again at ~7.2 ka (**Figure 5**). At the seven other ITP lakes the highest lake levels all occurred between 10 and 8 ka (**Figure 5**), consistent with lacustrine and stalagmite records indicating summer season rainfall substantially increased during the early Holocene in the region influenced by the ISM (Fleitmann et al., 2007; Bird et al., 2014). The levels of Baqan Co, Tangra Yumco, Zhari Nam Co, and Zabye Lake initially began to decline between 8and 7 ka, while the lake levels of Dagze Co and Ngangla Ring Co began to decline at 5.5–6 ka (**Figure 5**),

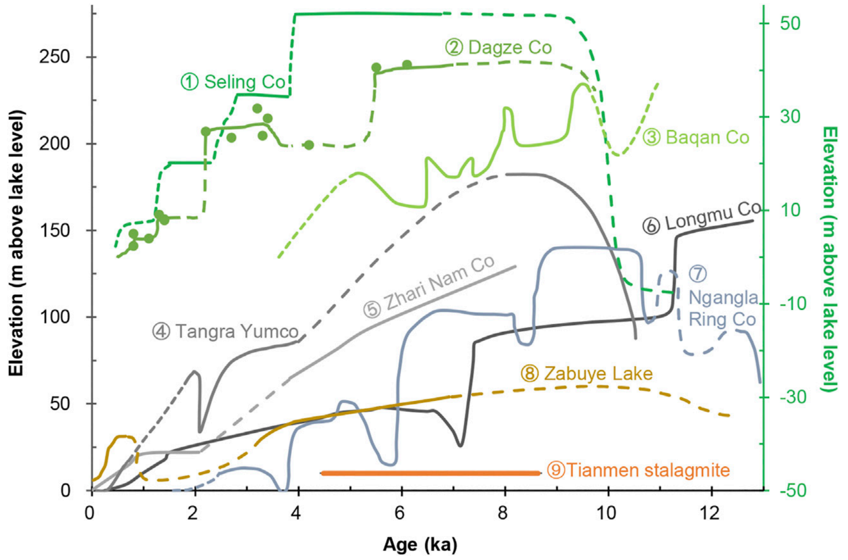

FIGURE 5 | Holocene lake level variations in the ITP. ① Seling Co (Shi et al., 2017), ② Dagze Co (our study), ③ Baqan Co (Huth et al., 2015), ④ Tangra Yumco (Ahlborn et al., 2015); ⑤ Zhari Nam Co (Chen et al., 2013); ⑥ Longmu Co (Liu et al., 2016b); ⑦ Ngangla Ring Co (Hudson et al., 2015); ⑧ Zabuye Lake (Alivernini et al., 2018). ⑨ is the growth period of the Tianmen stalagmite (Cai et al., 2012), near Nam Co in the eastern ITP. Note: the three green lines correspond to the right ordinate axis marked with green color.

corresponding to the initial weakening of the ISM during the mid-Holocene (Fleitmann et al., 2007; Bird et al., 2014; Cai et al., 2012). In contrast, the lake levels of Seling Co and Zabuye Lake remained steady or declined only slightly before 4 ka, regressing rapidly in a stepwise fashion after 4 ka (**Figure 5**). A stalagmite adjacent to Nam Co also stopped growing after ~4.2 ka when the ISM weakened and the climate became more arid (**Figure 5**; Cai et al., 2012). As we discuss below, the reasons for these divergent initial lake regression times are complex, but may include differences in precipitation in each lake basin, differences in glacier melt water supply, and difference in precipitation related to local water vapor recirculation. In addition, a recent study proposed that the abrupt lake level drops may related to the disintegration of ancient mega-lakes that were formed when the available water over the TP was plenty during the early Holocene (Jonell et al., 2020).

Spatial Lake Expansions in Inner Tibetan Plateau During the Holocene Highest Lake-Level Stage

While paleoshorelines are a useful indicator of past climate changes, they can be difficult to interpret since their formation can be influenced by terrain differences in individual watersheds and thus their association with paleo-precipitation changes may not be sufficiently direct. To address this issue, we use lake area ratios (*Aw*), the ratio of summed lake or paleolake areas to the total basin area for each basin system, to make climatic inferences from grouped lake histories. *Aw* reduces the influence of watershed differences on lake histories and is more directly related to annual precipitation (Hudson and Quade, 2013). The analysis showed that differing evaporation rates in different lake and differing lake area to lake volume ratios were not the main parameters that determine the paleolake expansion patterns during the Holocene high lake level stage (Hudson and Quade, 2013). Melt water was also not a dominant factor that caused lakes in the TP expanded synchronously during the Holocene high lake level stage because glacier melting is more related to local climate conditions and lakes with and without glaciers in their catchments expanded in a similar pattern (Hudson and Quade, 2013). Hence, the ratio of paleo-*Aw* to modern *Aw* mainly represents the expansion of a lake in response to past increased precipitation (Liu et al., 2019). Here we use modern lake areas, largest Holocene lake areas and watershed areas reported by Hudson and Quade (2013) for lakes in the ITP. We then calculate paleo-*Aw*s, modern *Aw*s and their ratios for each lake to investigate spatial differences in lake transgression/regression patterns.

We investigated the spatial distributions of modern *Aw* in response to modern precipitation, which decreases from the southern and southeastern ITP to the northwestern ITP, to explore if lakes in more arid regions require larger basins to maintain lakes as the same size as those in relatively wet regions. That is, do lakes in arid regions have smaller *Aw*s when compared with those located in wet regions? Result demonstrates that lakes in the ITP have relative uniform *Aw* values (**Figure 6**), with no significant spatial variations. This suggests that the basin sizes of lakes in different precipitation zones do not dictate how the lakes respond to the varied precipitation amount. This may be because lakes in different precipitation zones have salinity differences which influence surface evaporation. Lakes in arid regions have relative high salinity which reduces lake surface evaporation because salts absorb atmospheric water vapors (Li et al., 1992),

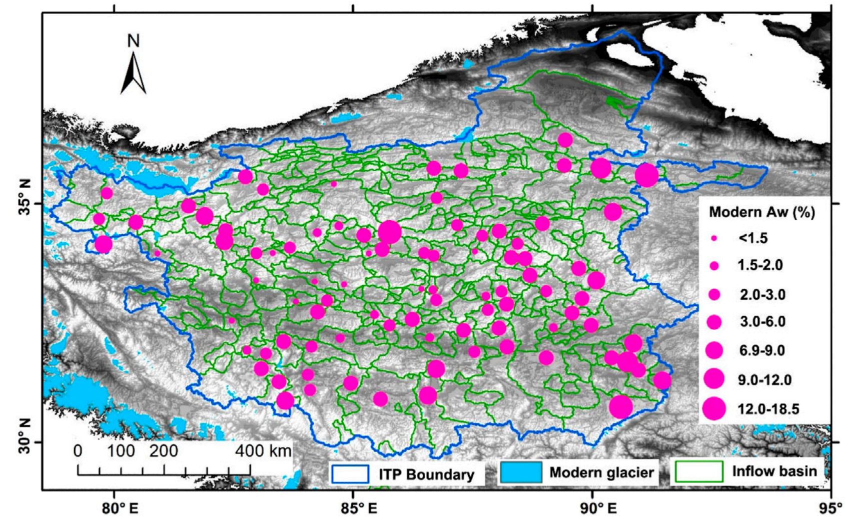

FIGURE 6 | Modern *Aw* (ratios) of lake areas to catchment areas. The blue line is the boundary of the ITP. The blue patches are modern glaciers. The green lines are lake catchment boundaries for ITP lakes. Pink dots represent the modern *Aw*.

while lakes in wet regions have relatively low salinity which enhances evaporation.

We also compared the size and distribution of modern ITP lakes to lakes at their highest Holocene levels (**Figure 7**). At present, large lakes (>500 km^2) are primarily distributed along the southern and eastern margins of the ITP, while lakes in the central and northwestern ITP are mostly smaller than 400 km^2 (**Figure 7A**). Large modern lakes are distributed in the regions where annual precipitation is relatively high (**Figure 1B**). During the early Holocene highstands, large lakes (>500 km^2) were found along the western, southern, and eastern margin of ITP, while those smaller than 500 km^2 were mostly distributed in the central and northern ITP (**Figure 7B**). The spatial lake size distribution pattern during the early Holocene highstand was generally similar to the modern lake size distribution pattern except for several lakes in the western ITP. This suggests large lakes expanded more in terms of surface areas. While small lakes also expanded, their surface areas remained smaller, in relative terms, than the large lakes (**Figure 7B**). From **Figures 6**, **7**, we deduce that precipitation instead of lake basin size was an important factor influencing the magnitude of lake expansion during the Holocene highstands. Hudson and Quade (2013) also indicate that glacial melt water differences, varied evaporation rates and differing lake area/volume relationships were not the dominant forces which controlled Holocene lake expansions in the TP. They concluded that the patterns of lake expansions in different parts of the ITP is best explained by regional precipitation differences.

We also explored spatial variations in lake level heights and *Paleo-Aw* to modern *Aw* ratios in the ITP during the highest Holocene lake level stage. **Figure 8A** shows that many lakes in the western and southwestern ITP had lake levels more than 80 m higher than at present. Lake levels were 15–40 m higher than present in the central ITP and less than 15 m higher in the northeastern ITP (**Figure 8A**). The ratios of paleo-*Aw* to modern *Aw* have the same spatial trend, with the ratios of paleo-*Aw* to modern *Aw* gradually decreasing in a southwest-northeast direction (**Figure 8B**). Using the concept Hudson and Quade (2013) proposed, this spatial pattern in paleo-*Aw* to modern *Aw* ratios suggests that the increase in precipitation associated with the enhanced ISM may have extended into the ITP from the southwestern TP, with the southwestern ITP getting more rainfall because the atmospheric water vapors first reached there and formed precipitation. Additionally, glaciers over the TP advanced during the LGM (Yan et al., 2018), might providing increased glacier melt water supplies to lower elevation lakes during the last deglacial and Holocene, contributing to rising lake levels. Glaciers expanded markedly in the western ITP and along the southern boundary of the ITP during the LGM (**Figure 8**), supplying additional melt water to lakes in the western and southern ITP. In the western ITP, Longmu Co obtained plenty of melt water supply since last deglacial, its lake level reached the peak at the end of the Bølling warm period and the onset of Holocene (Liu et al., 2016b). Lake levels then dropped abruptly during the Younger Dryas and at ~7.2 ka (**Figure 5**). Li et al. (2021) investigated the authigenic carbonate δ^{18}O of a glacier fed lake in the western ITP and quantitatively estimated glacier melt water variations during the Holocene based on a hydrological balance model incorporating δ^{18}O. They found that glaciers in the western Kunlun Mountain melted substantially during the early Holocene, but melted only slightly during the late Holocene. Hou (2019) proposed that the Chongce glacier (western TP) may have completely melted during the early Holocene high temperature stage, but redeveloped during the mid and late Holocene. This all suggests that lake level variations in the western ITP were substantially influenced by glacier melt water during the deglacial and early Holocene. Lakes in the southern ITP, on the other hand, rose steadily following the earliest Holocene, reaching their highest levels between 10 and 8 ka (**Figure 5**), as they were synchronized with the

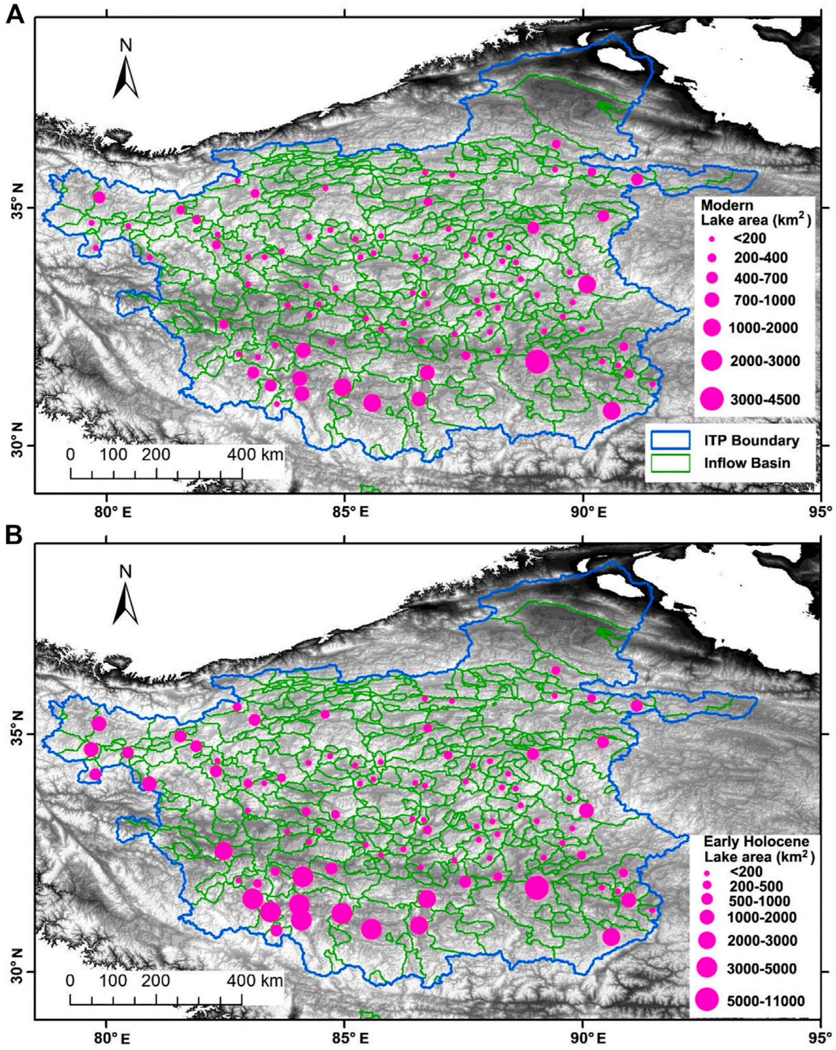

FIGURE 7 | Lakes and their sizes at **(A)** modern and **(B)** early Holocene for lakes in ITP. Blue line outlines the boundary of ITP. Green lines outline lake catchment boundary for lakes in ITP. Pink dots show lake sizes.

intensification of the ISM (Fleitmann et al., 2007). In addition, lakes located at the southern ITP west of 86° E expanded substantially more than lakes to the east (**Figure 8B**). Because the Holocene lake level variations in southern ITP are synchronous with the ISM variations, we then speculate that lakes in the southern ITP are primarily controlled by the ISM, and that glacier melt water only plays a secondary role in lake level variations.

CLIMATE MODEL SIMULATIONS

Seasonal Precipitation and Temperature Changes Based on the TraCE-21ka Model

The TraCE-21ka climate model provides estimates of seasonal precipitation and temperature changes for the past 21 ka. The TraCE-21ka simulation employs realistic external forcing, including orbital insolation, greenhouse gases, ice sheets, and freshwater fluxes (Liu et al., 2009). The model consists of four coupled components (atmospheric-model, oceanic-model, land-model, and sea ice-model) (Yan et al., 2020). The spatial resolution of the TraCE-21ka simulation is 3.75° × 3.75° in the ITP. We use these simulated seasonal precipitation and temperature changes to explore why lakes in the ITP expanded during the early Holocene, but regressed asynchronously following the mid-Holocene. We select three units that cover the northwest, northeast, and south parts of ITP, and then average the precipitation and temperature data of these three units to obtain the corresponding data for the ITP as a whole (**Figure 1A**).

The TraCE-21ka simulated seasonal precipitation and temperature changes in the ITP are shown in **Figure 9**. Spring (from March to May, MAM) precipitation is relatively stable, with no long-term trend in variation, but fluctuates frequently throughout the Holocene (**Figure 9A**). Summer precipitation (from June to August, JJA) is relatively high between 12 and 9 ka,

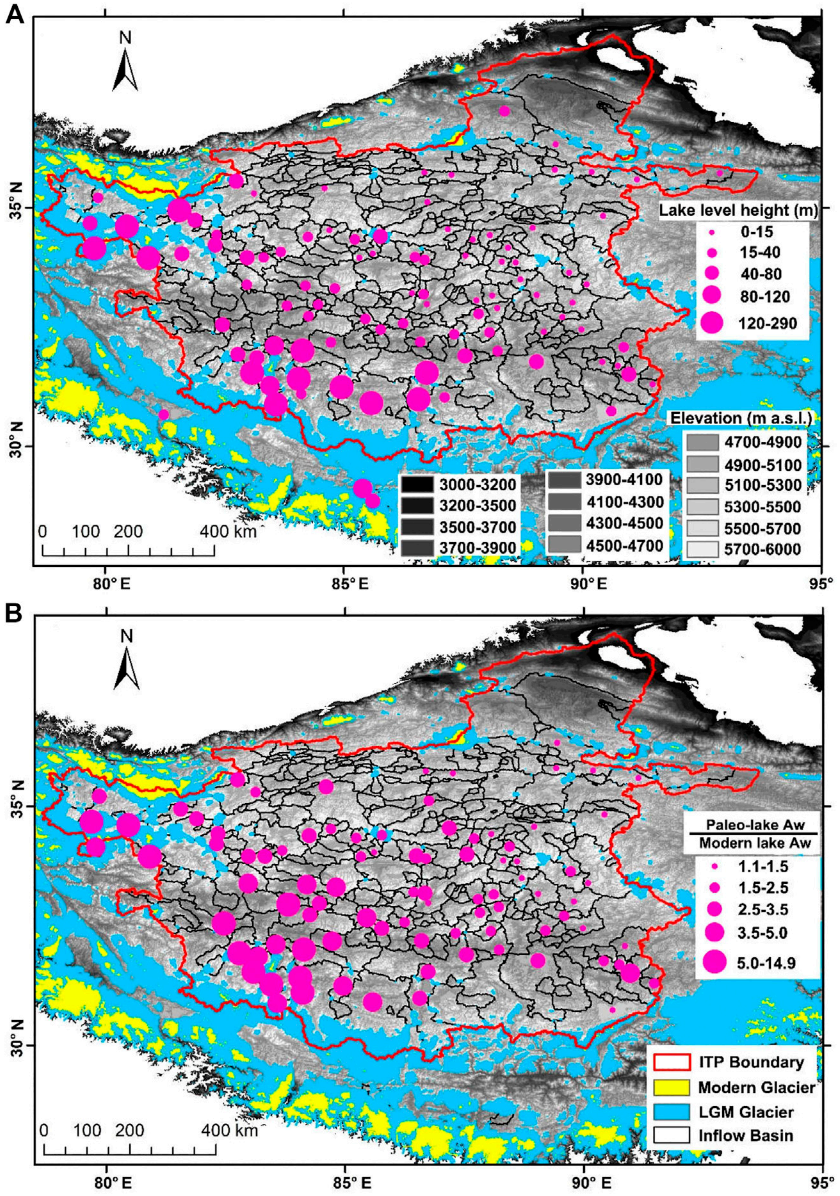

FIGURE 8 | Highest early Holocene lake levels above present lake surfaces **(A)** and Paleolake *Aw* versus modern *Aw* ratios of the highest Holocene lake level stage **(B)** for lakes in the ITP. The red line is the ITP boundary. The black lines are lake catchment boundaries. The colored patches show glacier extents during the LGM (blue) and at present (yellow) (Yan et al., 2018). The pink dots in **(A)** show lake level heights, and in **(B)** show the ratios of Paleolake *Aw* to modern *Aw*.

slightly decreases from 8–6 ka, substantially declines from 6–4 ka, and is maintained at lower values, but with substantial fluctuations during the past 4 ka (**Figure 9A**). Autumn precipitation (from September to November, SON) increases from 12–10 ka, stays relatively high with substantial fluctuations between 10 and 6 ka, then decreases after 6 ka (**Figure 9A**). Winter precipitation (from December to February, DJF) continuously increases across the Holocene (**Figure 9A**). Annual precipitation and net annual precipitation (precipitation minus evaporation, abbreviated as P-E) co-varies across the Holocene, they increase from 12–10 ka, are maintained at high values between 10 and 6 ka, decline from 6–4 ka, and slightly decrease during the last 4 ka (**Figure 9A**). Net annual precipitation change represents effective moisture changes, and further reflects basin-wide water balance variations. Lake level variations in the ITP across the Holocene are similar to net annual precipitation changes (**Figures 5**, **9A**). They also co-vary with annual precipitation, JJA precipitation and SON precipitation, suggesting that summer and autumn precipitation were important for annual precipitation changes and were the dominant influence on Holocene lake level variations in the ITP.

During the Holocene, modeled winter, spring, and autumn average temperatures are below zero centigrade and only summer

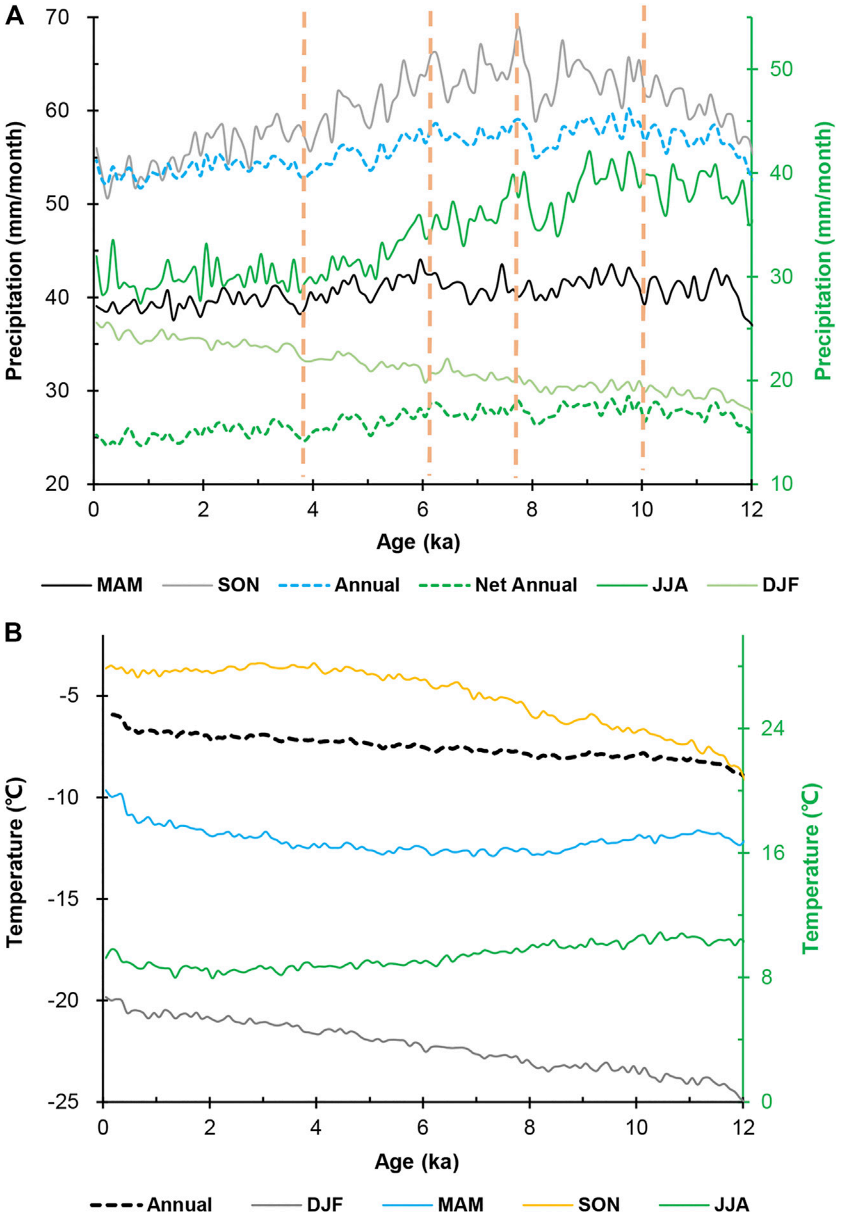

FIGURE 9 | (A) TraCE-21ka modeled annual precipitation, seasonal precipitation (MAM, JJA, SON, DJF) and net annual precipitation (P-E) over the ITP, **(B)** TraCE-21ka modeled annual and seasonal temperature (MAM, JJA, SON, DJF) over the ITP. Note: three green lines in **(A)** and one in **(B)** correspond to the right ordinate axis marked with green color.

temperatures are above zero (**Figure 9B**). However, modeled summer temperatures decline following the early Holocene (**Figure 9B**). Since high summer temperatures may enhance lake surface evaporation and inhibit lake expansion on the one hand, on the other hand, high summer temperatures may enhance regional water vapor recirculation over the ITP. At present, the precipitation recycle ratio over the TP during the summer is ~23% (Zhao and Zhou, 2021), and large lakes in the TP reshape regional precipitation patterns and also influence precipitation amounts adjacent and downwind of them (Dai et al., 2020a; Dai et al., 2020b). During the early Holocene, enlarged lakes, and elevated summer temperatures would conducive to precipitation recycling within the ITP that helped to maintain lakes in high lake levels.

Holocene Spatial Precipitation Changes in the Inner Tibetan Plateau Based on the Kiel Climate Model

In order to more comprehensively understand why lakes in the southwestern ITP expanded more than lakes in the northern and northeastern ITP during the Holocene highstand, we simulated

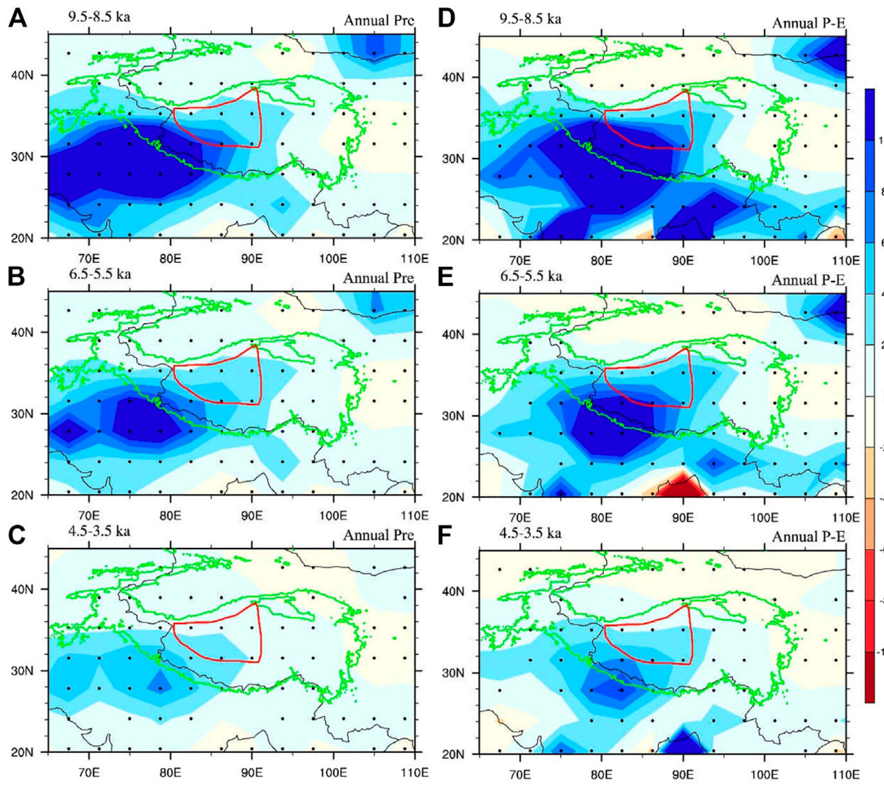

FIGURE 10 | Percentage changes of annual precipitation during the early Holocene **(A)**, mid-Holocene **(B)**, and late Holocene **(C)** relative to the past 1 ka over the TP and surrounding areas based on Kiel Climate Model (KCM) simulations. Corresponding percentage changes of annual P-E are shows in **(D–F)**. The red closed line outlines approximate extent of the ITP.

seasonal, annual, and net precipitation (P-E) changes for the early Holocene (9.5–8.5 ka), mid-Holocene (6.5–5.5 ka), and late Holocene (4.5–3.5 ka) relative to the last 1 ka over the TP and its adjacent areas using the KCM. The KCM model is a non-flux-corrected coupled general circulation model. This Holocene climate simulation holds Greenhouse Gas concentrations constant at pre-industrial levels, but adjusts orbital precession from 9.5–0 ka with a ten-fold acceleration scheme (Jin et al., 2014; see Park et al. (2009) for a detailed description of the KCM model).

KCM simulation results show that annual precipitation significantly increases over the southwestern TP during the early Holocene (9.5–8.5 ka), and that the relative amount of precipitation increase lessens along a southwest-northeast route toward the inner TP (**Figure 10A**). Annual P-E has the same modeled trends in variation as that of annual precipitation (**Figure 10D**), suggesting that the increase in precipitation is the dominant controlling factor for water balance changes in the ITP. KCM modeled spatial percentage changes in annual precipitation and annual P-E can explain why lakes in southwestern ITP expanded more dramatically, with a decreasing magnitude of expansion towards the northern and northeastern ITP (**Figure 8**). Modeled precipitation and P-E over the ITP decrease throughout the mid- and late Holocene (**Figure 10**), consistent with the shrinkage of lakes after the mid-Holocene. Regions with significant precipitation increases in TP generally overlap with regions influenced by the ISM as Lai et al. (2021) outlined using a self-organizing map algorithm to analyze the Global Precipitation Measurement satellite product and ERA5 (**Figure 2**). This confirms a proposal by Conroy and Overpeck (2011) that the early Holocene amplified ISM resulted in a monsoon precipitation increase rather than a northward shift in the monsoon boundary. Hudson and Quade (2013) also suggested that the areas influenced by the modern ISM and EASM persisted throughout the Holocene, with the ISM-influenced western TP gaining more rainfall than the EASM controlled eastern TP during the early Holocene high lake level stage.

We also investigated seasonal precipitation and P-E changes over the ITP during the Holocene and their potential contributions to lake level variations. Modeled spring (MAM) precipitation substantially increases during the early Holocene, but this increase lessens from the southwestern to northeastern ITP (**Supplementary Figure S3A**). Modeled spring P-E suggests early Holocene effective moisture mainly increases across the southern ITP, while the P-E over the northern ITP increases only slightly (**Supplementary Figure S3D**). Spring precipitation and P-E decline during the mid-Holocene, with no evident changes

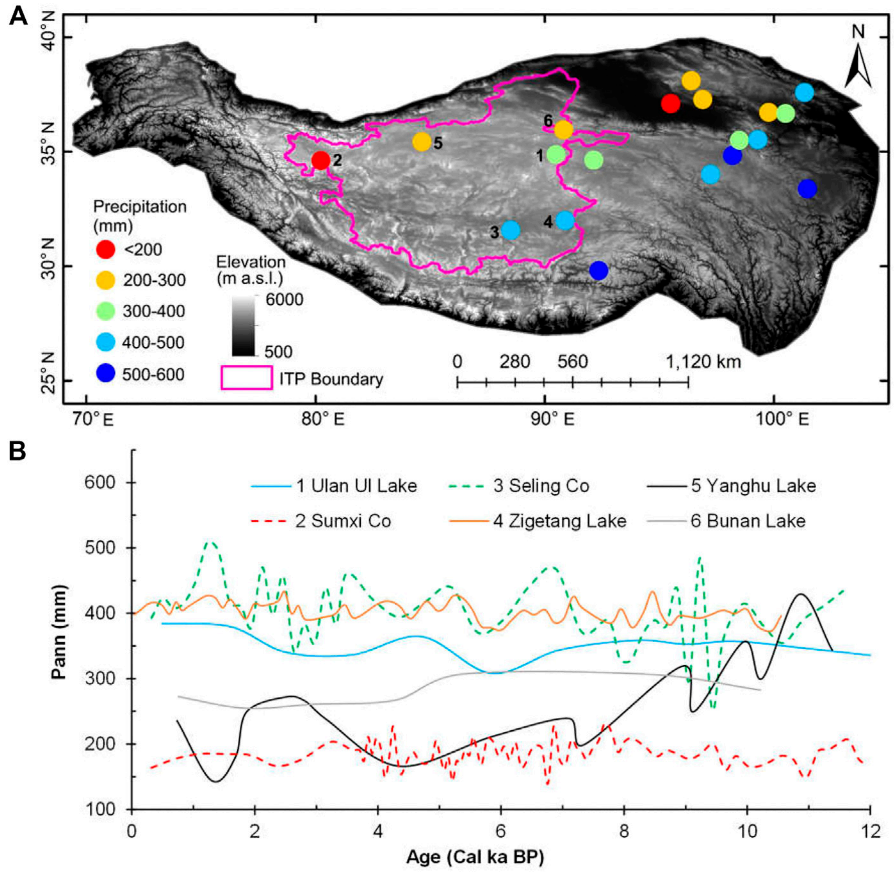

FIGURE 11 | (A) Pollen-based reconstruction of annual precipitation in TP during the last 2 ka, the pink line outlines the area of ITP. **(B)** Pollen-based reconstruction of Holocene annual precipitation for six lakes in ITP. The data was obtained from Herzschuh et al. (2019).

from the mid- to late Holocene (**Supplementary Figure S3**). Summer (JJA) precipitation significantly increases over the western TP during the early Holocene, and decreases after the mid-Holocene (**Supplementary Figures S4A–C**). Summer P-E over the ITP substantially increases during the early Holocene, slightly decreases during the mid-Holocene, and then rapidly declines during the early stages of the late Holocene (**Supplementary Figures S4D–F**). Modeled autumn (SON) precipitation increases in the southwestern TP throughout the Holocene, but the percentage increases are highest during the early Holocene, decreasing slightly after the mid-Holocene (**Supplementary Figures S5A–C**). Modeled autumn P-E indicates that effective moisture in the ITP increases during the early and mid-Holocene, but the western and northern ITP becomes dry following the early stage of the late Holocene (**Supplementary Figures S5D–F**). Winter (DJF) precipitation and P-E change only a little in the ITP through the Holocene (**Supplementary Figure S6**). A synthesis of the seasonal precipitation and P-E changes in the ITP during early, mid and late Holocene, suggests that the increased precipitation during the spring, summer, and autumn seasons contributed to the marked early Holocene lake expansions in the ITP. According to the modern observations, the increased spring precipitation was due mainly to moisture input from the Eurasian continent (Zhang et al., 2019b; Li et al., 2019). Increased rainfall during the summer season was mostly correlated with intensification of the ISM, while increased autumn precipitation came partially from the prolonged seasonal influence of the ISM and partially from enhanced water vapor recycling over the ITP (Li et al., 2019; Zhao and Zhou, 2021). After the mid-Holocene, the summer and autumn percentage of annual precipitation declined, causing lakes in the ITP to regress as a consequence (**Supplementary Figures S4, S5**). **Figure 8** illustrates that the expansion of lakes in the southwestern ITP was much greater than lakes located in the central, northern, and northeastern ITP. This spatial contrast in lake expansion is consistent with spatial differences in annual precipitation and net annual P-E changes during the early Holocene (**Figure 10**), suggesting that an increasing spatial differentiation in annual precipitation may have been an important driver of differential lake transgressions in the ITP. The nearly synchronous variations of percentage changes in annual

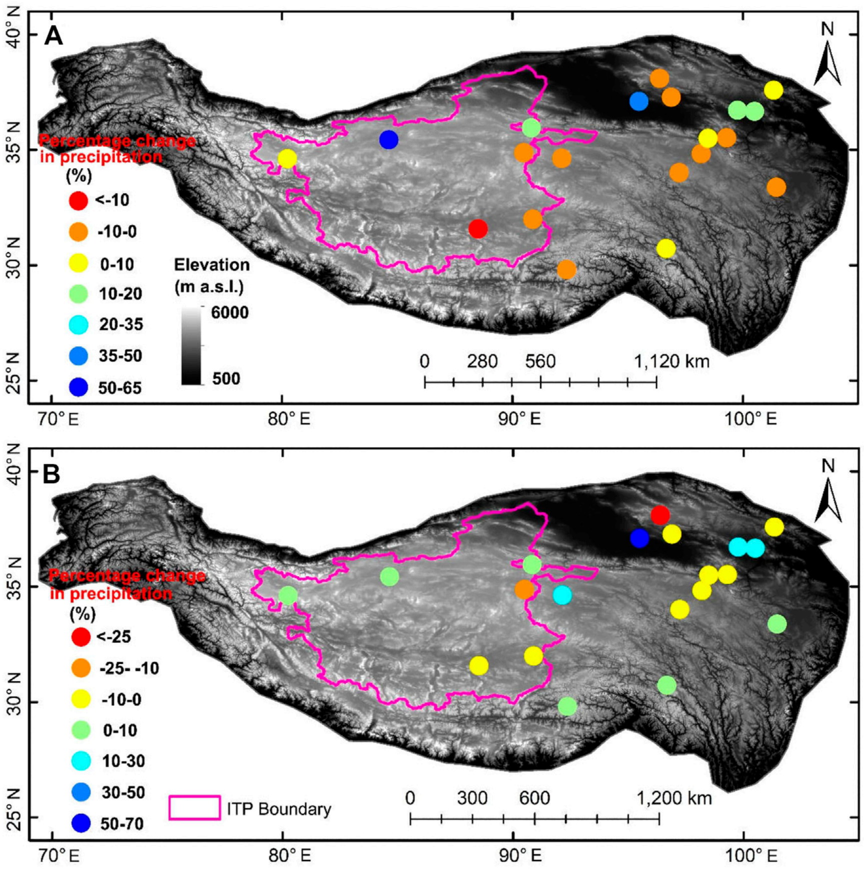

FIGURE 12 | Pollen-based reconstruction of percentage precipitation changes in TP during the early Holocene [12–8 ka] **(A)** and mid-Holocene [7–4 ka] **(B)** relative to the past 2 ka, respectively. The pink line outlines the area of ITP. The data was obtained from Herzschuh et al. (2019).

precipitation and net annual P-E suggest that precipitation was the dominant component influencing effective moisture changes in the ITP during the Holocene (**Figure 10**).

POLLEN-BASED HOLOCENE PRECIPITATION RECONSTRUCTIONS IN INNER TIBETAN PLATEAU

Several researches reported that the climate in southern and western TP were wettest during the early Holocene (from 10–7.5 ka), but became dry since ~7.5 ka (Gasse et al., 1991; Bird et al., 2014; Chen et al., 2020; Zhang et al., 2021). These researches are consistent with paleoshoreline dating results that the highest lake level for most lakes in central, southern, and western TP occurred during the early Holocene. However, these proxies cannot provide valuable information about changes in precipitation amount and its spatial variations during the Holocene over the TP.

Recently, Herzschuh et al. (2019) quantitatively reconstructed changes of annual precipitation in China during the Holocene by using fossil pollen datasets. They assume that vegetation types and pollen composition are mainly determined by precipitation. We extract the relevant data covering the TP from their datasets to compare the results with our own. There are six lakes within the ITP (**Figure 11A**). Pollen-based result shows precipitation of the last 2 ka in the southeastern ITP was 400–500 mm, and decreased to 200–300 mm in northern ITP and to <200 mm in northwestern ITP (**Figure 11A**). The magnitude and spatial distribution of the pollen constructed precipitation are consistent with modern precipitation changes across the ITP (**Figure 1B**). The pollen reconstructed precipitation in Yanghu Lake and Bunan Lake in northern ITP were high during the early Holocene, but decreased since mid-Holocene (**Figure 11B**). However, temporal trends in the reconstructed precipitation of the Ulan Ul Lake, Seling Co, Sumxi Co, and Zigetang Lake are not obvious, but with centennial to millennial fluctuations (**Figure 11B**). We further analyzed percentage precipitation changes in the early (12–8 ka) and mid-Holocene (7–4 ka) relative to the last 2 ka for lakes over TP. During the early Holocene (12–8 ka), precipitation in the Yanghu Lake and Bunan Lake in northern ITP increased, while over the other four lakes decreased (**Figure 12A**). During the mid-Holocene (7–4 ka), three lakes in northern ITP show slight increase in precipitation, while the other three lakes in central and southern

ITP show slight decrease in precipitation (**Figure 12B**). Generally, precipitation over TP is higher during the mid-Holocene than the early Holocene (**Figure 12**).

Pollen-based precipitation in southeastern ITP during the early and mid-Holocene was lower than the late Holocene (last 2 ka) (**Figure 12**). However, the KCM simulated results show the precipitation in southeastern ITP was higher during the early and mid-Holocene than the late Holocene (**Figure 10**). Furthermore, lakes in southeastern ITP also expanded to some extent during the early Holocene (**Figure 8**). Pollen-based precipitation in northwestern ITP during the early Holocene was also lower than the late Holocene (**Figure 12**), in contrast to KCM simulated increase in precipitation and drastic expansions of lakes (Longmu Co and Sumxi Co). Lacks of reconstructed precipitation record in central and southwestern ITP where lakes expanded more drastic during the early Holocene, which limit our ability to estimate the contributions of precipitation and melt water to the expansions of lakes in these regions. The discrepancy between pollen-based precipitation changes and KCM model results in ITP, and the expansion of lakes may in one hand due to the amounts of glacier melt water are hard to be estimated that supply the lakes, and in another hand to that pollen assemblages may contain certain portions of long distance transported pollens which introduce uncertainties in the precipitation reconstructions (Zhao et al., 2021). In addition, the response of ecosystem (soil moisture and tree cover) to precipitation variations can lag for several thousand years due to the impacts of winter warming (Cheng et al., 2021).

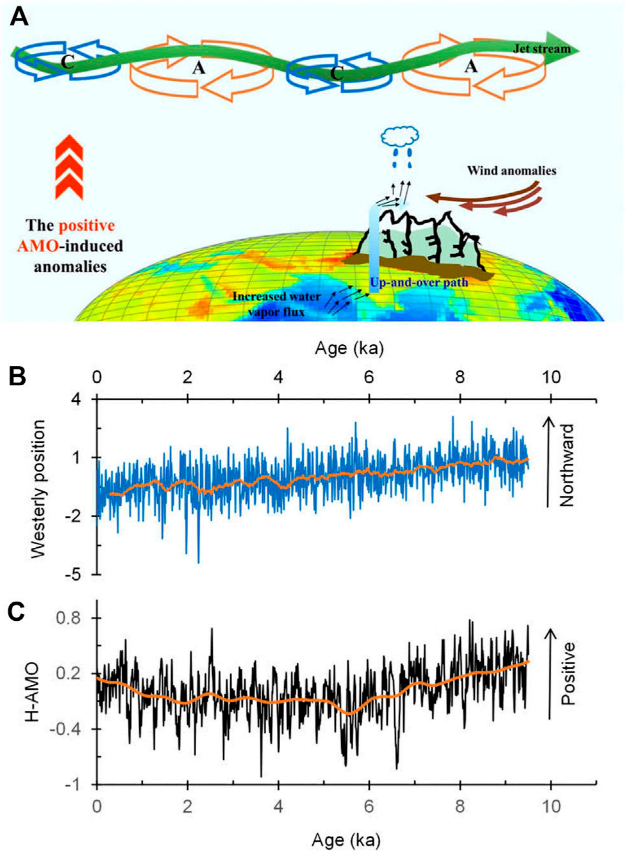

FIGURE 13 | (A) Schematic cartoon diagram of Atlantic multidecadal oscillation (AMO) influence on variability in summer precipitation over the ITP (Sun et al., 2020, **Figure 11**). **(B)** Northern Hemisphere westerly jet position changes during the Holocene (Zhang and Jin, 2018). **(C)** Holocene evolution of the Atlantic multidecadal oscillation estimated from a KCM simulation (Zhang et al., 2016).

THE REASONS FOR SPATIAL DIFFERENCES OF PRECIPITATION IN INNER TIBETAN PLATEAU DURING THE EARLY AND MID HOLOCENE

A number of recent studies indicate the ITP lies in an area where precipitation is most closely linked to the ISM (Conroy and Overpeck, 2011; Lai et al., 2021). An increase in modern ITP precipitation is correlated with interdecadal time scale changes of the AMO and related changes in the strength of the subtropical westerly jet stream near and over the TP (Sun et al., 2020). Liu et al. (2021) reported that intimate correlation existed between the moisture budget in the TP and the AMO as well as interdecadal Pacific oscillation (IPO). The IPO can exert impact on the TP moisture budget by affecting the westerly jet stream (Liu et al., 2021). The AMO has been regarded as the key factor influencing summer rainfall over the ITP (Sun et al., 2020). First, the AMO warm phase induces an anomalous summer cyclonic and anticyclonic wave train over Eurasia, causing the westerly jet to weaken and shift northward (Sun et al., 2020). Second, while the westerly jet over the TP weakens, the westerly jet to its west remains strong, causing enhanced air convergence over the TP (Sun et al., 2020; Liu et al., 2021). Water vapor then intrudes into the ITP through an “up-and-over” moisture transport pattern (Dong et al., 2016). Third, the weaker westerly winds over the TP in turn weakens water vapor transport at increasing distances from its eastern boundary (Liu et al., 2021). A strong cyclone west of the ITP concurrently enhances southwestern winds and convection over the India subcontinent, promoting water vapor transport from the Arabian Sea (**Figure 13A**). During the past 3 decades, lake expansions over the ITP are, as a result, attributed to a positive phase of the AMO (Sun et al., 2020).

The AMO was persistent across the Holocene with a 55–80 years cycle, and it is highly associated with the multidecadal variability of the Atlantic meridional overturning circulation (Knudsen et al., 2011; Wei and Lohmann, 2012). During the early Holocene, the intertropical convergence zone shifted northward (Jin et al., 2014; Zhang and Jin, 2018), the ISM substantially intensified (Fleitmann et al., 2007; Bird et al., 2014), the north hemisphere subtropical westerly jet shifted northward (**Figure 13B**), and the AMO was in a positive state (**Figure 13C**). Together these driving forces induced a wave train of cyclonic and anticyclonic anomalies during the growing season, enhancing the meandering of the westerly jet (Mölg et al., 2017; Sun et al., 2020). Due to this enhancement, the cyclonic circulation on the west side of TP enhanced that further caused southwesterly winds on the southwestern flank of the TP intensified, but westerly winds over the TP weakened as the subtropical westerly jet shifted northward. As with modern precipitation shifts, this "up-and-over" moisture transport pattern resulted in a substantial increase in precipitation in the southwestern ITP since water vapor crossing the high mountains initially arrives in that part of the ITP, producing more rainfall than further to the north and northeast (Liu et al., 2019).

Since the early mid-Holocene, the northern hemisphere subtropical westerly jet shifted southward (**Figure 13B**), and the AMO became increasingly negative between 8 and 6 ka, before rising slightly again during the past 2 ka (**Figure 13C**). As the position of the westerly jet shifted southward and the AMO changed to a negative phase, the ISM also weakened after the mid-Holocene. Water vapor introduced into the ITP was reduced, but water vapor transport across its east boundary increased, causing lakes in the ITP to shrink in response to a net loss of precipitation.

It is noteworthy that while increased precipitation over the western ITP was not as great as in the southwestern ITP during the early Holocene (**Figure 10A**), lakes in this area also expanded markedly (**Figure 8**). It has been suggested that glacier melt water from an ice cap in the western TP was at maximum during the early Holocene (Li et al., 2021), and as a result we propose that lakes in western ITP may have expanded due to increased glacier melt water supply as well as to increased rainfall related to the intensified ISM.

CONCLUSION

In this study we investigate Holocene lake level variations in ITP and their driving forces by combining reported lake level variation curves and spatial lake expansion patterns, with TraCE-21ka and KCM simulated precipitation and P-E changes over the ITP. We draw the following conclusions: 1) The highest lake levels appeared during the early Holocene (10–8 ka), and lake levels started to decline after the mid-Holocene. 2) This early Holocene expansion was greatest in the southwestern and western ITP, but the magnitude of lake transgressions decreased toward the northern and northeastern ITP. 3) TraCE-21ka and KCM simulation results show that a summer and autumn precipitation increase may be the main reason for Holocene lake expansions in the southern, central, and northern ITP, while increased glacier melt water accompanied by an increase in summer rainfall caused lakes in the western ITP to dramatically expand. 4) During the early Holocene the ISM intensified in response to a northward shift of the tropical convergence zone, with the northern hemisphere westerly jet also shifting northward and with the AMO in a positive phase. As a result, southwesterly winds on the southwestern flank of the TP were enhanced, while westerly winds over the TP decreased, causing more water vapor to be transported to the ITP through the "up-and-over" moisture transport route and stuck in there. The amount of enhanced precipitation decreased from the southwestern to northeastern ITP, causing lakes in the southwestern ITP to expand to higher levels than those in the central, northern, and northeastern ITP.

DATA AVAILABILITY STATEMENT

The original contributions presented in the study are included in the article/**Supplementary Material**, further inquiries can be directed to the corresponding author.

AUTHOR CONTRIBUTIONS

LX designed the research. LX and MD wrote the manuscript. ZX performed the KCM climate modelling.

FUNDING

This work was funded by the Second TP Scientific Expedition and Research Program (2019QZKK0202) and the National Natural Science Foundation of China (41671006).

ACKNOWLEDGMENTS

We thank Professor Chen Fahu for help LX joins the Second Tibetan Plateau Scientific Expedition and Research Program. Thanks Professor Yang Kun for his shares of the figure we used in **Figure 13**. We also thank three reviewers for their constructive comments that help improve the quality of this paper. The TraCE-21ka model simulation data were downloaded from http://202.195.239.65:8888/.

SUPPLEMENTARY MATERIAL

The Supplementary Material for this article can be found online at: https://www.frontiersin.org/articles/10.3389/feart.2021.685928/full#supplementary-material

REFERENCES

Ahlborn, M., Haberzettl, T., Wang, J., Fürstenberg, S., Mäusbacher, R., Mazzocco, J., et al. (2015). Holocene lake Level History of the Tangra Yumco lake System, Southern-central Tibetan Plateau. *The Holocene* 26, 176–187. doi:10.1177/0959683615596840

Alivernini, M., Lai, Z., Frenzel, P., Fürstenberg, S., Wang, J., Guo, Y., et al. (2018). Late Quaternary lake Level Changes of Taro Co and Neighbouring Lakes, Southwestern Tibetan Plateau, Based on OSL Dating and Ostracod

Analysis. *Glob. Planet. Change* 166, 1–18. doi:10.1016/j.gloplacha.2018.03.016

Barnett, T. P., Adam, J. C., and Lettenmaier, D. P. (2005). Potential Impacts of a Warming Climate on Water Availability in Snow-Dominated Regions. *Nature* 438, 303–309. doi:10.1038/nature04141

Bird, B. W., Polisar, P. J., Lei, Y., Thompson, L. G., Yao, T., Finney, B. P., et al. (2014). A Tibetan lake Sediment Record of Holocene Indian Summer Monsoon Variability. *Earth Planet. Sci. Lett.* 399, 92–102. doi:10.1016/j.epsl.2014.05.017

Cai, Y., Zhang, H., Cheng, H., An, Z., Lawrence Edwards, R., Wang, X., et al. (2012). The Holocene Indian Monsoon Variability over the Southern Tibetan Plateau and its Teleconnections. *Earth Planet. Sci. Lett.* 335-336, 135–144. doi:10.1016/j.epsl.2012.04.035

Chen, F., Zhang, J., Liu, J., Cao, X., Hou, J., Zhu, L., et al. (2020). Climate Change, Vegetation History, and Landscape Responses on the Tibetan Plateau during the Holocene: a Comprehensive Review. *Quat. Sci. Rev.* 243, 106444. doi:10.1016/j.quascirev.2020.106444

Chen, Y., Zong, Y., Li, B., Li, S., and Aitchison, J. C. (2013). Shrinking Lakes in Tibet Linked to the Weakening Asian Monsoon in the Past 8.2 Ka. *Quat. Res.* 80, 189–198. doi:10.1016/j.yqres.2013.06.008

Cheng, J., Wu, H., Liu, Z., Gu, P., Wang, J., Zhao, C., et al. (2021). Vegetation Feedback Causes Delayed Ecosystem Response to East Asian Summer Monsoon Rainfall during the Holocene. *Nat. Commun.* 12, 1843. doi:10.1038/s41467-021-22087-2

Conroy, J. L., and Overpeck, J. T. (2011). Regionalization of Present-Day Precipitation in the Greater Monsoon Region of Asia*. *J. Clim.* 24, 4073–4095. doi:10.1175/2011JCLI4033.1

Dai, Y., Chen, D., Yao, T., and Wang, L. (2020b). Large Lakes over the Tibetan Plateau May Boost Snow Downwind: Implications for Snow Disaster. *Sci. Bull.* 65, 1713–1717. doi:10.1016/j.scib.2020.06.012

Dai, Y., Yao, T., Wang, L., Li, X., and Zhang, X. (2020a). Contrasting Roles of a Large Alpine Lake on Tibetan Plateau in Shaping Regional Precipitation during Summer and Autumn. *Front. Earth Sci.* 8, 358. doi:10.3389/feart.2020.00358

Dong, W., Lin, Y., Wright, J. S., Ming, Y., Xie, Y., Wang, B., et al. (2016). Summer Rainfall over the Southwestern Tibetan Plateau Controlled by Deep Convection Over the Indian Subcontinent. *Nat. Commun.* 7, 10925. doi:10.1038/ncomms10925

Fleitmann, D., Burns, S. J., Mangini, A., Mudelsee, M., Kramers, J., Villa, I., et al. (2007). Holocene ITCZ and Indian Monsoon Dynamics Recorded in Stalagmites from Oman and Yemen (Socotra). *Quat. Sci. Rev.* 26, 170–188. doi:10.1016/j.quascirev.2006.04.012

Gasse, F., Arnold, M., Fontes, J.C., Gibert, E., Fort, M., Huc, A., et al. (1991). A 13000-year climate record from western Tibet. *Nature* 353, 742–745.

Herzschuh, U., Cao, X., Laepple, T., Dallmeyer, A., Telford, R. J., Ni, J., et al. (2019). Position and Orientation of the westerly Jet Determined Holocene Rainfall Patterns in China. *Nat. Commun.* 10, 2376. doi:10.1038/s41467-019-09866-8

Hou, S. (2019). How Old Are the Tibetan Ice Cores? *Chin. Sci. Bull.* 64, 2425–2429. [in Chinese]. doi:10.1360/N972019-00189

Hou, Y., Long, H., Gao, L., and Shen, J. (2020). Luminescence Dating of Lacustrine Sediments from CuoE lake on the central Tibetan Plateau. *Geochronometria*. in press. doi:10.2478/geochr-2020-0002

Hou, Y., Long, H., Shen, J., and Gao, L. (2021). Holocene lake-level Fluctuations of Selin Co on the central Tibetan Plateau: Regulated by Monsoonal Precipitation or Meltwater? *Quat. Sci. Rev.* 261, 106919. doi:10.1016/j.quascirev.2021.106919

Hudson, A. M., Quade, J., Huth, T. E., Lei, G., Cheng, H., Edwards, L. R., et al. (2015). Lake Level Reconstruction for 12.8-2.3 Ka of the Ngangla Ring Tso Closed-Basin Lake System, Southwest Tibetan Plateau. *Quat. Res.* 83, 66–79. doi:10.1016/j.yqres.2014.07.012

Hudson, A. M., and Quade, J. (2013). Long-term East-West Asymmetry in Monsoon Rainfall on the Tibetan Plateau. *Geology* 41, 351–354. doi:10.1130/G33837.1

Huth, T., Hudson, A. M., Quade, J., Guoliang, L., and Hucai, Z. (2015). Constraints on Paleoclimate from 11.5 to 5.0 Ka from Shoreline Dating and Hydrologic Budget Modeling of Baqan Tso, Southwestern Tibetan Plateau. *Quat. Res.* 83, 80–93. doi:10.1016/j.yqres.2014.07.011

Immerzeel, W. W., van Beek, L. P. H., and Bierkens, M. F. P. (2010). Climate Change Will Affect the Asian Water Towers. *Science* 328, 1382–1385. doi:10.1126/science.1183188

Jin, L., Schneider, B., Park, W., Latif, M., Khon, V., and Zhang, X. (2014). The Spatial-Temporal Patterns of Asian Summer Monsoon Precipitation in Response to Holocene Insolation Change: a Model-Data Synthesis. *Quat. Sci. Rev.* 85, 47–62. doi:10.1016/j.quascirev.2013.11.004

Jonell, T. N., Aitchison, J. C., Li, G., Shulmeister, J., Zhou, R., and Zhang, H. (2020). Revisiting Growth and Decline of Late Quaternary Mega-Lakes across the South-central Tibetan Plateau. *Quat. Sci. Rev.* 248, 106475. doi:10.1016/j.quascirev.2020.106475

Knudsen, M. F., Seidenkrantz, M.-S., Jacobsen, B. H., and Kuijpers, A. (2011). Tracking the Atlantic Multidecadal Oscillation through the Last 8,000 Years. *Nat. Commun.* 2, 178. doi:10.1038/ncomms1186

Lai, H.-W., Chen, H. W., Kukulies, J., Ou, T., and Chen, D. (2021). Regionalization of Seasonal Precipitation over the Tibetan Plateau and Associated Large-Scale Atmospheric Systems. *J. Clim.* 34, 2635–2651. doi:10.1175/JCLI-D-20-0521.1

Lee, J., Li, S.-H., and Aitchison, J. C. (2009). OSL Dating of Paleoshorelines at Lagkor Tso, Western Tibet. *Quat. Geochronol.* 4, 335–343. doi:10.1177/095968361140523210.1016/j.quageo.2009.02.003

Lei, Y., Yang, K., Wang, B., Sheng, Y., Bird, B. W., Zhang, G., et al. (2014). Response of Inland lake Dynamics over the Tibetan Plateau to Climate Change. *Climatic Change* 125, 281–290. doi:10.1007/s10584-014-1175-3

Li, C.-G., Wang, M., Liu, W., Lee, S.-Y., Chen, F., and Hou, J. (2021). Quantitative Estimates of Holocene Glacier Meltwater Variations on the Western Tibetan Plateau. *Earth Planet. Sci. Lett.* 559, 116766. doi:10.1016/j.epsl.2021.116766

Li, D., Li, Y., Ma, B., Dong, G., Wang, L., and Zhao, J. (2009). Lake-level Fluctuations since the Last Glaciation in Selin Co (lake), Central Tibet, Investigated Using Optically Stimulated Luminescence Dating of beach Ridges. *Environ. Res. Lett.* 4, 045204. doi:10.1088/1748-9326/4/4/045204

Li, G., Xue, S., Yao, Z., and Gao, S. (1992). Evaporation of Brine at Different Concentrations in the Sun Farm Area of Lake Da-Qaidam. *Saltlake salt Chem. industry* 2, 13–17. [in Chinese].

Li, Y., Su, F., Chen, D., and Tang, Q. (2019). Atmospheric Water Transport to the Endorheic Tibetan Plateau and its Effect on the Hydrological Status in the Region. *J. Geophys. Res. Atmos.* 124, 12864–12881. doi:10.1029/2019JD031297

Liu, B., Du, Y. e., Li, L., Feng, Q., Xie, H., Liang, T., et al. (2016a). Outburst Flooding of the Moraine-Dammed Zhuonai Lake on Tibetan Plateau: Causes and Impacts. *IEEE Geosci. Remote Sensing Lett.Remote Sens. Lett.* 13, 570–574. doi:10.1109/LGRS.2016.2525778

Liu, X.-J., Lai, Z.-P., Zeng, F.-M., Madsen, D. B., and E, C.-Y. (2013). Holocene lake Level Variations on the Qinghai-Tibetan Plateau. *Int. J. Earth Sci. (Geol Rundsch)* 102, 2007–2016. doi:10.1007/s00531-013-0896-2

Liu, X.-J., Madsen, D. B., Liu, R., Sun, Y., and Wang, Y. (2016b). Holocene lake Level Variations of Longmu Co, Western Qinghai-Tibetan Plateau. *Environ. Earth Sci.* 75, 301. doi:10.1007/s12665-015-5188-7

Liu, X., Cong, L., Li, X., Madsen, D., Wang, Y., Liu, Y., et al. (2020). Climate Conditions on the Tibetan Plateau during the Last Glacial Maximum and Implications for the Survival of Paleolithic Foragers. *Front. Earth Sci.* 8, 606051. doi:10.3389/feart.2020.606051

Liu, X., Zhang, X., Lin, Y., Jin, L., and Chen, F. (2019). Strengthened Indian Summer Monsoon Brought More Rainfall to the Western Tibetan Plateau during the Early Holocene. *Sci. Bull.* 64, 1482–1485. doi:10.1016/j.scib.2019.07.022

Liu, Y., Chen, H., Li, H., Zhang, G., and Wang, H. (2021). What Induces the Interdecadal Shift of the Dipole Patterns of Summer Precipitation Trends over the Tibetan Plateau? *Int. J. Climatol.*, 1–19. doi:10.1002/joc.7122

Liu, Z., Otto-Bliesner, B. L., He, F., Brady, E. C., Tomas, R., Clark, P. U., et al. (2009). Transient Simulation of Last Deglaciation with a New Mechanism for Bolling-Allerod Warming. *Science* 325, 310–314. doi:10.1126/science.1171041

Long, H., Lai, Z., Frenzel, P., Fuchs, M., and Haberzettl, T. (2012). Holocene Moist Period Recorded by the Chronostratigraphy of a lake Sedimentary Sequence from Lake Tangra Yumco on the South Tibetan Plateau. *Quat. Geochronol.* 10, 136–142. doi:10.1016/j.quageo.2011.11.005

Ma, N., Ma, Z., Zheng, M., and Wang, H. (2012). 230Th Dating of Stem Carbonate Deposits from Tai Cuo lake, Western Tibetan Plateau, China. *Quat. Int.* 250, 55–62. doi:10.1016/j.quaint.2011.09.012

Mölg, T., Maussion, F., Collier, E., Chiang, J. C. H., and Scherer, D. (2017). Prominent Midlatitude Circulation Signature in High Asia's Surface Climate during Monsoon. *J. Geophys. Res. Atmos.* 122, 12702–12712. doi:10.1002/2017JD027414

Pan, B., Yi, C., Jiang, T., Dong, G., Hu, G., and Jin, Y. (2012). Holocene lake-level Changes of Linggo Co in central Tibet. *Quat. Geochronol.* 10, 117–122. doi:10.1016/j.quageo.2012.03.009

Park, W., Keenlyside, N., Latif, M., Ströh, A., Redler, R., Roeckner, E., et al. (2009). Tropical Pacific Climate and its Response to Global Warming in the Kiel Climate Model. *J. Clim.* 22, 71–92. doi:10.1175/2008JCLI2261.1

Qiao, B., Zhu, L., and Yang, R. (2019). Temporal-spatial Differences in lake Water Storage Changes and Their Links to Climate Change throughout the Tibetan Plateau. *Remote Sensing Environ.* 222, 232–243. doi:10.1016/j.rse.2018.12.037

Quade, J., and Broecker, W. S. (2009). Dryland Hydrology in a Warmer World: Lessons From the Last Glacial Period. *Eur. Phys. J. Spec. Top.* 176, 21–36. doi:10.1140/epjst/e2009-01146-y

Rades, E. F., Hetzel, R., Xu, Q., and Ding, L. (2013). Constraining Holocene lake-level Highstands on the Tibetan Plateau by 10Be Exposure Dating: a Case Study at Tangra Yumco, Southern Tibet. *Quat. Sci. Rev.* 82, 68–77. doi:10.1016/j.quascirev.2013.09.016

Shi, X., Kirby, E., Furlong, K. P., Meng, K., Robinson, R., Lu, H., et al. (2017). Rapid and Punctuated Late Holocene Recession of Siling Co, central Tibet. *Quat. Sci. Rev.* 172, 15–31. doi:10.1016/j.quascirev.2017.07.017

Sun, J., Yang, K., Guo, W., Wang, Y., He, J., and Lu, H. (2020). Why Has the Inner Tibetan Plateau Become Wetter since the Mid-1990s? *J. Clim.* 33, 8507–8522. doi:10.1175/JCLI-D-19-0471.1

Wei, W., and Lohmann, G. (2012). Simulated Atlantic Multidecadal Oscillation during the Holocene. *J. Clim.* 25, 6989–7002. doi:10.1175/JCLI-D-11-00667.1

Yan, Q., Owen, L. A., Wang, H., and Zhang, Z. (2018). Climate Constraints on Glaciation over High-Mountain Asia during the Last Glacial Maximum. *Geophys. Res. Lett.* 45, 9024–9033. doi:10.1029/2018GL079168

Yan, Q., Owen, L. A., Zhang, Z., Jiang, N., and Zhang, R. (2020). Deciphering the Evolution and Forcing Mechanisms of Glaciation over the Himalayan-Tibetan Orogen during the Past 20,000 Years. *Earth Planet. Sci. Lett.* 541, 116295. doi:10.1016/j.epsl.2020.116295

Yang, K., Lu, H., Yue, S., Zhang, G., Lei, Y., La, Z., et al. (2018). Quantifying Recent Precipitation Change and Predicting lake Expansion in the Inner Tibetan Plateau. *Climatic Change* 147, 149–163. doi:10.1007/s10584-017-2127-5

Yao, T., Thompson, L., Yang, W., Yu, W., Gao, Y., Guo, X., et al. (2012). Different Glacier Status with Atmospheric Circulations in Tibetan Plateau and Surroundings. *Nat. Clim Change* 2, 663–667. doi:10.1038/nclimate1580

Yao, X., Sun, M., Gong, P., Liu, B., Li, X., An, L., et al. (2016). Overflow Probability of the Salt Lake in Hoh Xil Region. *Acta Geographica Sinica* 71 (9), 1520–1527. [in Chinese, with English Abstract]. doi:10.11821/dlxb201609005

Zhang, C., Tang, Q., Chen, D., Van Der Ent, R. J., Liu, X., Li, W., et al. (2019b). Moisture Source Changes Contributed to Different Precipitation Changes over the Northern and Southern Tibetan Plateau. *J. Hydrometeorol.* 20, 217–229. doi:10.1175/JHM-D-18-0094.1

Zhang, G., Chen, W., and Xie, H. (2019a). Tibetan Plateau's Lake Level and Volume Changes from NASA's ICESat/ICESat-2 and Landsat Missions. *Geophys. Res. Lett.* 46 (13), 13107–13118. doi:10.1029/2019GL085032

Zhang, G., Yao, T., Xie, H., Kang, S., and Lei, Y. (2013). Increased Mass over the Tibetan Plateau: From Lakes or Glaciers? *Geophys. Res. Lett.* 40, 2125–2130. doi:10.1002/grl.50462

Zhang, G., Yao, T., Xie, H., Yang, K., Zhu, L., Shum, C. K., et al. (2020). Response of Tibetan Plateau Lakes to Climate Change: Trends, Patterns, and Mechanisms. *Earth-Science Rev.* 208, 103269. doi:10.1016/j.earscirev.2020.103269

Zhang, X., Jin, L., and Jia, W. (2016). Centennial-scale Teleconnection between North Atlantic Sea Surface Temperatures and the Indian Summer Monsoon during the Holocene. *Clim. Dyn.* 46, 3323–3336. doi:10.1007/s00382-015-2771-2

Zhang, X., and Jin, L. (2018). Meridional Migration of the South Asian High and its Association With Asian Summer Monsoon Precipitation during the Holocene. *Quat. Sci.* 38, 1244–1254. [in Chinese, with English Abstract]. doi:10.11928/j.issn.1001-7410.2018.05.18

Zhang, Y., Zhang, J., McGowan, S., Metcalfe, S., Jones, M., Leng, M. J. M., et al. (2021). Climatic and Environmental Change in the Western Tibetan Plateau during the Holocene, Recorded by lake Sediments from Aweng Co. *Quat. Sci. Rev.* 259, 106889. doi:10.1016/j.quascirev.2021.106889

Zhao, K., Zhou, X., Ji, M., and Li, X. (2019). Palynological Evidence of Late Holocene Paleo-Monsoon in Eastern Pamir. *Geophys. Res. Lett.* 46, 10015–10023. doi:10.1029/2019GL082941

Zhao, Y., and Zhou, T. (2021). Interannual Variability of Precipitation Recycle Ratio over the Tibetan Plateau. *J. Geophys. Res.-Atmos.* 126, e2020JD033733. doi:10.1029/2020jd033733

Zhu, L., Lü, X., Wang, J., Peng, P., Kasper, T., Daut, G., et al. (2015). Climate Change on the Tibetan Plateau in Response to Shifting Atmospheric Circulation since the LGM. *Sci. Rep.* 5, 13318. doi:10.1038/srep13318

Conflict of Interest: The authors declare that the research was conducted in the absence of any commercial or financial relationships that could be construed as a potential conflict of interest.

frontiers
in Earth Science

ORIGINAL RESEARCH
published: 12 July 2021
doi: 10.3389/feart.2021.702223

The Forming Age and the Evolution Process of the Brine Lithium Deposits in the Qaidam Basin Based on Geochronology and Mineral Composition

Zhe Ma[1,2,3], **Fengqing Han**[1,2]*, **Tianyuan Chen**[1,2]*, **Lei Yi**[1,2], **Xiaohang Lu**[1,2,3], **Fuhong Chen**[1,2,3], **Xiaobao Liu**[1,2,3] and **Wenhu Yuan**[4,5]

[1]Key Laboratory of Comprehensive and Highly Efficient Utilization of Salt Lake Resources, Qinghai Institute of Salt Lakes, Chinese Academy of Sciences, Xining, China, [2]Key Laboratory of Salt Lake Geology and Environment of Qinghai Province, Xining, China, [3]University of Chinese Academy of Sciences, Beijing, China, [4]Qaidam Integrated Geological Exploration Institute of Qinghai Province, Golmud, China, [5]Key Laboratory of Salt Lake Resources Exploration in Qaidam Basin, Golmud, China

Edited by:
Xiangzhong Li,
Yunnan University, China

Reviewed by:
Shugang Kang,
State Key Laboratory of Loess and Quaternary Geology, Institute of Earth Environment (CAS), China
Guoqiang Li,
Lanzhou University, China

***Correspondence:**
Fengqing Han
hanfq@isl.ac.cn
Tianyuan Chen
chen.tianyuan@foxmail.com

Specialty section:
This article was submitted to Quaternary Science, Geomorphology and Paleoenvironment, a section of the journal Frontiers in Earth Science

Received: 29 April 2021
Accepted: 21 June 2021
Published: 12 July 2021

Citation:
Ma Z, Han F, Chen T, Yi L, Lu X, Chen F, Liu X and Yuan W (2021) The Forming Age and the Evolution Process of the Brine Lithium Deposits in the Qaidam Basin Based on Geochronology and Mineral Composition. Front. Earth Sci. 9:702223. doi: 10.3389/feart.2021.702223

Lithium ore deposits are divided into pegmatite and brine deposits. The Puna Plateau and the Qinghai–Tibetan Plateau (QTP) are home to the most abundant brine lithium deposits worldwide. Very few studies have investigated the chronology of brine lithium deposits. This paper reports the Optically Stimulated Luminescence (OSL) dating measurements for typical brine lithium deposits at QTP, including East Taijnar Salt Lake, West Taijnar Salt Lake, and Yiliping Salt Lake in the central Qaidam Basin. Combining the results of OSL dating with previous studies and mineral composition obtained by X-ray diffraction analysis (XRD), this study summarizes the age and characteristics of the climatic environment during the formation of brine lithium deposits in the Qaidam Basin. The main results are: 1) Brine lithium deposits in the Qaidam Basin began to form since 40 ka. Brine lithium deposits in South America formed during the middle Pleistocene and late Pleistocene, and are older than the deposits in the Qaidam Basin. The lithium deposits of Tibet formed around 4 ka, are the youngest. 2) The climate in East Taijnar Salt Lake and West Taijnar Salt Lake was extremely cold and dry during 27–4.6 ka, with a relatively humid climatic condition at ~10 ka. After 4.6 ka, the environment was comparatively more humid around both lakes. Yiliping Salt Lake had a dry climate since 38.09 ka, and the climate in the Three Lakes area is mainly controlled by the westerlies in the Holocene; and 3) East Taijnar Salt Lake, West Taijnar Salt Lake and Yiliping Salt Lake were located in the same secondary basin during the late Pleistocene. However, tectonic activity around 40 ka led to the evolution of Yiliping Salt Lake into an independent basin. East Taijnar Salt Lake and West Taijnar Salt Lake separated around 27 ka, and then deposited the lower salt layers until the Holocene. The substantial amount of detrital minerals that the Nalinggele River brought during the Holocene led to a brief desalination of East Taijnar Salt Lake. The upper salt layer was deposited in East Taijnar Salt Lake and West Taijnar Salt Lake during this period due to the extremely dry climate.

Keywords: qaidam basin, optically stimulated luminescence, lithium deposits, evolution of lake, paleoclimate

INTRODUCTION

Lithium, a scarce strategic resource, is widely used in ceramics and glass industries, batteries, lubricating greases, air treatment, and primary aluminum production. Global lithium deposits are estimated at over 17 Mt (million tons) (Yang et al., 2019). There are three main types of lithium deposits: 1) brine deposits in lacustrine evaporite deposits. The most abundant lithium brine deposits are found in South America (Salar de Uyuni and Salar de Atacama) and China (West Taijnar Salt Lake, East Taijnar Salt Lake, and Yiliping Salt Lake); 2) pegmatite deposits in the vein of pegmatite. For example, the Greenbushes lithium deposit in Australia; and 3) sedimentary rock deposits in Cainozoic clay, such as Jadar lithium deposits in Serbia and La Ventana lithium deposits in Mexico (Wang et al., 2015; Zhang et al., 2020). Brines containing lithium account for 66% of the world's lithium resources (Gruber et al., 2011), primarily in the central Andes and China, with smaller deposits in the western United States and northern Africa (Kesler et al., 2012).

Several existing studies have conducted Quaternary geochronological studies on the Salar de Atacama and the Salar de Uyuni, the two largest brine-producing deposits. However, most studies focus on alluvial fans, deserts, or ice cores nearby these two Salars (Abbott et al., 1997; Klein et al., 1999; Rodbell et al., 1999; Thompson et al., 1999; Baker et al., 2001a; Pfeiffer et al., 2018; Diederich et al., 2020; Walk et al., 2020). Limited research has concentrated on Quaternary geochronology in the Salar de Atacama and the Salar de Uyuni (Baker et al., 2001b; Bobst et al., 2001; Fornari et al., 2001). Additionally, the above-mentioned studies mainly investigated the paleoclimate and evolution of the Salar de Atacama and the Salar de Uyuni. However, the age of formation of lithium deposits remains unconfirmed. The age of brine lithium deposits can help a deeper and broader understanding of the mechanism of mineralization.

Other lithium-rich lacustrine evaporites and brines are found on the Qinghai–Tibet plateau, most of which are distributed in the Qaidam Basin. The Qaidam Basin, at an elevation of 2,800 m a.s.l, is the largest basin on the northeastern Tibetan plateau, covering an area of 2.4 × 10^5 km^2. Thanks to the "higher mountain and lower basin" circumstances and hyper-arid climate (Yuan et al., 1983; An et al., 2012; Yu et al., 2013), the basin has developed a vast area of dry playa capped with salt crust, leading to the deposition of abundant brine resources (Zhang, 1987). Previous research suggests the preservation of a mega–paleolake in the Qaidam Basin before the late Pleistocene (Zhang, 1987; Zhu et al., 1989). Several recent studies (Yu and Lai, 2012; Lai et al., 2014; Yu and Lai 2014) have confirmed the fragmentation of the mega-paleolake to the western (East Tijinaier Salt Lake, West Taijnar Salt Lake, and Yiliping Salt Lake) and eastern parts (Qarhan Salt Lake) (Zhang, 1987; Owen et al., 2006; Zhang et al., 2007) as a result of tectonic evolution and climate change.

Most previous Quaternary chronological studies in the Qaidam Basin primarily used U-series disequilibrium dating methods and radiocarbon dating (^{14}C) (**Figure 1** and **Supplementary Table S1**). Chronological data of salt lakes in the Qaidam Basin over the past 250 ka and 10 ka are shown in **Figure 1** (Shen et al., 1993; Liang and Huang, 1995; Huang and Han, 2007; Fan et al., 2010; Sun et al., 2010; Ma et al., 2011; Fan et al., 2013; Liang and Han, 2013; Han et al., 2014; Chen et al., 2017; Zeng and Xiang, 2017; Wang et al., 2019; Wang, 2020;

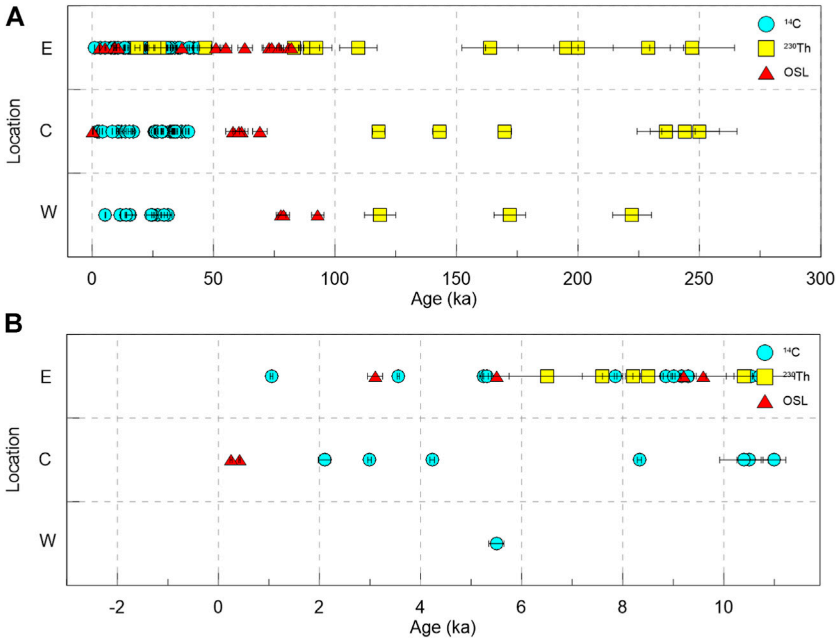

FIGURE 1 | Summary of published chronological data of the salt lakes in the Qaidam Basin over the past 250 ka **(A)** and 10 ka **(B)**. The records are mainly from the east (E), center (C), and west (W) of the Qaidam Basin. For more detailed information, see **Supplementary Table S1** in the supplementary material.

Zhang and Liu, 2020). On the one hand, previous chronological works have focused especially on the east Qaidam Basin, while the central and western Qaidam Basins are still insufficiently studied. On the other hand, most previous chronological analyses mainly used ^{14}C dating and ^{230}Th dating. Chronological studies generally use different types of methods to verify each other, thereby infer the geological evolution accurately. There are 24 OSL ages for the salt lakes in the Qaidam Basin, in which there are only 6 ages for the central Qaidam Basin. The limited ages data has hiatus the understanding of the formation and evolution of salt lakes at the Qaidam Basin. In this study, we excavated three sections in the center of the Qaidam Basin. The sections were suitable for OSL dating due to the thick deposition of detrital minerals, including quartz. Our study demonstrates the applicability of OSL dating in salt lakes and complements data on the age of salt lakes in the central Qaidam Basin, providing key information on the origin and evolution of lakes.

The lithium content in brines in the Qaidam basin is concentrated and has the highest values in West Taijnar Salt Lake, East Taijnar Salt Lake and Yiliping Salt Lake, collectively called “The Three Lakes”. Studies on the origin and formation of brine lithium deposits in the Qaidam Basin are scarce. Three different hypotheses can be drawn from previous research. The first hypothesis suggests a multi-source lithium contribution to the resource with two possibilities: 1) the residual brines formed during the most recent Pliocene in the saline lakes located in the western Qaidam Basin and substantially contributed to the lithium deposits; and 2) the residual brine interacted with Li-rich waters from deep underground connate brines, facilitating lithium enrichment in the salt lakes since the late Pleistocene (Zhang, 1987). The second hypothesis emphasizes the important contribution of lithium from two ancient lakes, Nalinggele Lake and Kunlun Lake. These lakes possibly existed as large intermontane lakes in the Kunlun Mountains until 30 kaBP. The former was in the Nalinggele River valley, while the latter was south of Nalinggele Lake, receiving hot spring water rich in Li, B, and K (Zhu et al., 1989). The tectonic activity induced drainage of these two ancient saline lakes and several others in the eastern Kunlun Mountains in the Qaidam Basin probably led to evaporite deposition, eventually becoming the source of Li, B, and K. The third view from Yu et al. (2013) reported that the hydrothermal fields where the two active faults converged in the upper reach of the Hongshui River are a source of lithium in the Qaidam Basin. Overall, regardless of the source of lithium, it was enriched simultaneously with the evaporite formation, which implies that both were of identical age.

There are few other Quaternary chronological studies for the Three Lakes area. Zhang et al. (2001) indicated that the salt was formed in East Taijnar Salt Lake during one of the driest periods of the Holocene. However, the sampling sites were not in the center of East Taijnar Salt Lake, which led to limitations in the evolution of the lake proposed in the study. Chen et al. (2017) discussed salt deposits and their relationship to the Quaternary glacial period and tectonic movement in Yiliping Salt Lake. However, the time scale was more than a million years, which is not suitable for researching the evolution and age of lithium in the lake since the late Pleistocene. Wang et al. (2019) dated two cores in West Taijnar Salt Lake using OSL and radiocarbon dating (AMS ^{14}C). The condition experiments of OSL dating were conducted, and the feasibility of two methods was also discussed. However, the dating results are not enough to conclude the lake evolution. Zeng and Xiang (2017) studied the chronology of West Taijnar Salt Lake using OSL and AMS ^{14}C. However, the analyzed part was located in the northeastern West Taijnar Salt Lake, near the Bayanwuer anticline, which might have perturbed the stratum sequence. Therefore, the dating results from this study are also not suitable for an accurate illustration of the lake evolution. Chang et al. (2017) dated the terraces of the Nalinggele River, where is the provenance of the Three Lakes. In general, very few studies have analyzed the Three Lakes, especially during the formation of the lithium deposits since the Holocene. The Three Lakes could provide significant insights into the formation and evolution of the central Qaidam Basin due to their location. This study aims to combine the dating results (OSL dating method), mineral compositions (using XRD), and previous studies to conclude the age of lithium deposits and geomorphic processes in the central Qaidam Basin.

GEOLOGICAL AND GEOGRAPHIC SETTING

The Qaidam Basin is the largest closed basin on the northeastern Tibetan Plateau. This hyperarid inland basin, with an area of 2.4×10^5 km^2, is surrounded by the Altun-Qilian Shan Mountains (Mts) in the north, the Ela Shan Mts in the east, and the Kunlun Shan Mts in the south. In the basin, mean annual temperatures range from 0 to 5°C and mean annual precipitation (MAP) ranges from 100 mm in the east to less than 20 mm in the west. The potential mean annual evaporation is over 20 times higher than the MAP. Gravel desert, playa and salt crust, saline lakes and salt marshes and various yardang landforms are widespread in the basin, forming a striking desert landscape (**Figure 2**).

East Taijinar Salt lake, West Taijinair Salt lake and Yiliping Salt Lake lie in sub-depressions of low-lying land along the middle of the central Qaidam Basin in hyperarid conditions with precipitation limited to 15–35 mm/y and potential evaporation to precipitation ratio greater than 100:1. The Three Lakes in the Qaidam Basin, which is fed by the Nalinggele River, are significantly enriched with lithium and boron that are key resources for the regional economy (Zhang, 1987; Zhu et al., 1989; Yu et al., 2013). Before the late Pleistocene, the Three Lakes and the Qrahan salt lake were consolidated freshwater shallow lakes. Neotectonics led to the separation of the Three Lakes from Qarhan salt lake and the subsequent formation of the terminal lake at the end of the Nalinggele River. Quaternary sediments, extending several hundreds of kilometers, are the main deposits in the Three Lakes. The Taijnar tectonic belt and the Bayanwuer tectonic belt, including faults and anticlines, are located north of East Taijnar Salt Lake and

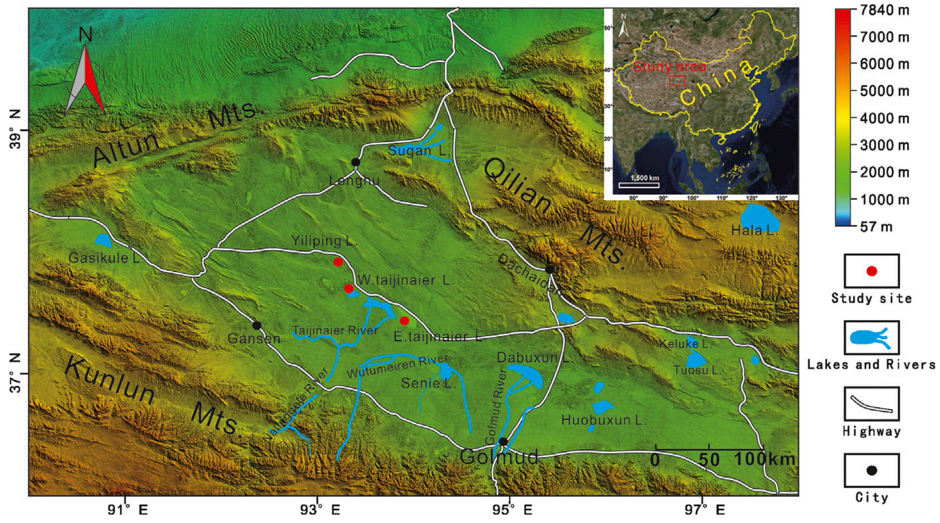

FIGURE 2 | Location of study sites in the western Qaidam Basin (DT, XTW, and YLP sections).

West Taijnar Salt Lake. Few tectonic zones surround Yiliping Salt Lake, while some minor faults are in the south (**Figure 3**).

SAMPLE COLLECTION

Fieldwork was conducted in 2017, and three sections were explored, including DT (in East Taijnar Salt Lake), XTW (in West Taijnar Salt Lake), and YLP (in Yiliping Salt Lake). The East Taijnar Salt Lake section, named the DT section (37°27'47.11" N, 93°57'09.71" E; 2,686 m a.s.l.), lies in the central part of the lake (**Figure 1**). The section was excavated to a depth of 13.4 m (**Figure 2**). The lithology of the DT section from top to bottom is as follows: salt crust from 0 to 0.2 m, with one XRD sample in this layer (0.1 m) and 45 other XRD samples taken for X-ray diffraction analysis (XRD) from 0.3 to 13.4 m, at a distance of 0.3 m; clay-silt from 0.2 to 8.4 m, with 16 optical dating samples collected at intervals of 0.5 m from 0.45 to 7.95 m

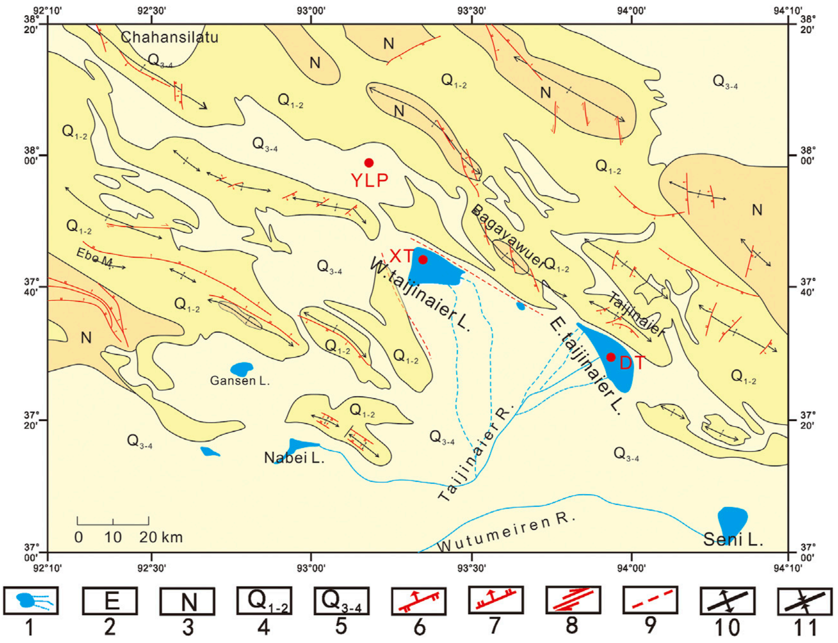

FIGURE 3 | Map of major tectonic and sedimentologic features. Legend: 1. Lakes and rivers; 2. Neogene; 3. Palaeogene; 4. Early Pleistocene-Middle Pleistocene; 5. Epipleistocene–Holocene; 6. Reverse fault; 7. Normal fault; 8. Trike-slip fault; 9. Fault observed by remote sensing; 10. Anticline; and 11. Syncline. Study sites are marked with red dots.

(**Figure 4A**); clay-silt with white halite from 8.4 to 8.7 m; and white halite from 8.7 to 13.4 m.

The XTW section (37°43'54.98" N, 93°20'33.10" E; 2,686 m a.s.l.) lies west of West Taijnar Salt Lake. The section was excavated to a depth of 1.7 m. The XTW section is divided into 5 strata, which are: salt crust from 0 to 0.1 m; clay from 0.1 to 0.3 m; silt from 0.3 to 0.7 m, one sample was taken at 0.5 m and another at 0.6 m for OSL dating; white halite with silt from 0.7 to 1.6 m; and silt with halite from 1.6 to 1.7 m. Another sample for dating was taken at 1.65 m (**Figure 4B**).

West of Yiliping Salt Lake, a 2.7 m long section was discovered and named the YLP section (37°58'3.83" N, 93°13'7.80" E; 2,685 m a.s.l.). The YLP section lies in the western Yiliping Salt Lake. It consists, from top to bottom, of a salt crust layer, halite with silt layer, halite layer, halite with silt layer, and halite layer. We obtained a dating sample at 2.5 m (**Figure 4D**).

All OSL samples were collected by driving iron tubes (diameter 5 cm, length 25 cm) in newly cleaned vertical sections. The tubes were covered with a black cloth and sealed in black plastic bags, then wrapped with tape to avoid exposure to light. Each XRD sample, weighing about 50 g, was taken in clean bags.

MATERIALS AND METHODS

Optically Stimulated Luminescence Dating

Sample preparation and OSL measurements were performed in the Luminescence Dating Laboratory of the Qinghai Institute of Salt Lakes, Chinese Academy of Sciences. First, two sides of each luminescence dating sample tube were removed to measure the concentration of the radioactive element and the water content. The unexposed middle part of the tube was used to extract minerals to determine the equivalent dose (D_e). All samples were treated with 10% HCl and 30% H_2O_2 to remove carbonates and organic matter. Thereafter, the samples were passed through a wet sieve to obtain a grain fraction of 38–63 μm. Polymineral grains of 4–11 μm were separated according to the Stokes' Law settling. Then, the quartz fraction of 38–63 μm was treated with 35% hydrofluorosilicic acid (H_2SiF_6) for about two weeks, while the quartz fraction of 4–11 μm was treated with 35% H_2SiF_6 for 3–5 days. Both fractions were then treated with 10% HCl to remove any fluorides. The purity of the extracted quartz was checked by IR stimulation. In case of obvious IR signals, quartz grains were retreated with H_2SiF_6 to avoid underestimation of age (Duller, 2003; Lai and Brückner, 2008). Samples of pure quartz were then mounted on stainless steel disks (diameter ~0.97 cm), using silicone oil, with an area of about 0.7 cm in diameter.

The OSL signal was measured using an automated Risø TL/OSL-DA-20 reader. The reader was equipped with blue diodes (λ = 470 ± 20 nm) and IR laser diodes (λ = 830 nm). Laboratory irradiation was performed using 90Sr/Y90 sources mounted in the reader, with a dose rate of 0.089 Gy/s. Luminescence, stimulated by blue LEDs at 130°C for 40 s, was detected using a photomultiplier tube with an OSL signal passing through 7.5 mm thick U-340 filters. Equivalent D_e was measured using a

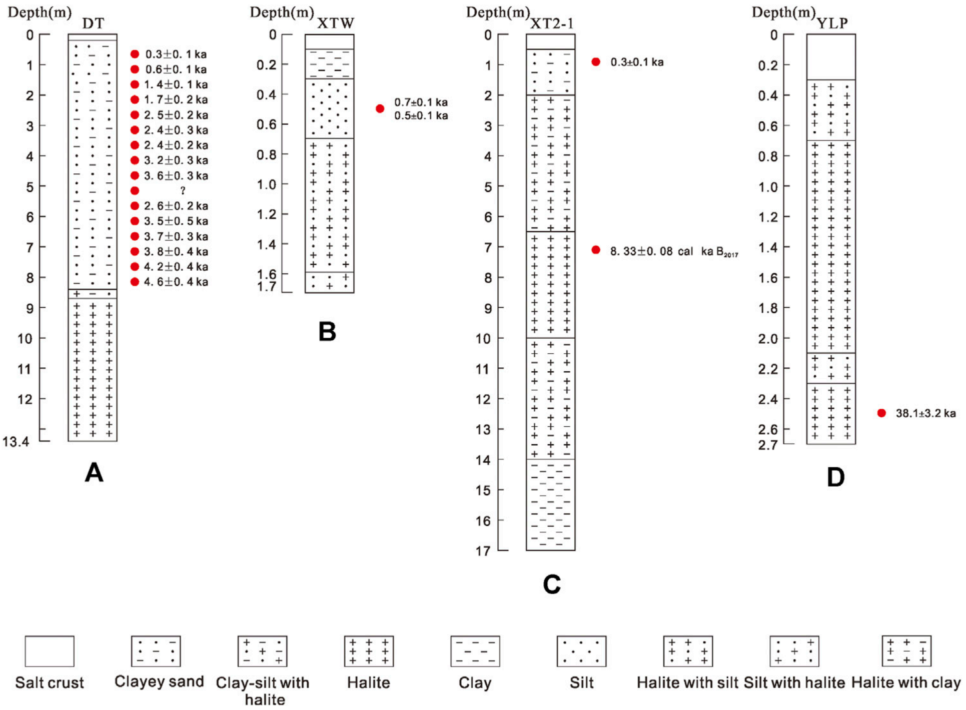

FIGURE 4 | Stratigraphy, OSL sample site, and dating results for the Three Lakes: **(A)** Section DT in East Taijnar Salt Lake; **(B)** Section XTW in West Taijnar Salt Lake; **(C)** Section XT2-1 in West Taijnar Salt Lake (Wang et al., 2019); and **(D)** Section YLP in Yiliping Salt Lake.

TABLE 1 | | Results of the OSL dating of sections DT, XTW and YLP in the Three Lakes. The OSL age of the DT10 sample could not be analyzed due to quartz deficiency.

Sample id	Depth(m)	Grain size (μm)	K (%)	Th (ppm)	U (ppm)	Water content (%)	Dose rate (Gy/ka)	De (Gy)	OSL age (ka)
DT 01	0.45	38–63	2.04 ± 0.04	10.61 ± 0.70	3.37 ± 0.40	16 ± 5	3.49 ± 0.25	1.18 ± 0.14	0.34 ± 0.05
DT 02	0.95	4–11	2.70 ± 0.04	11.95 ± 0.70	5.73 ± 0.50	12 ± 5	5.24 ± 0.38	3.18 ± 0.41	0.61 ± 0.09
DT 03	1.45	4–11	2.89 ± 0.04	11.26 ± 0.70	3.07 ± 0.40	15 ± 5	4.43 ± 0.31	6.09 ± 0.37	1.37 ± 0.13
DT 04	1.95	38–63	2.05 ± 0.04	9.07 ± 0.60	3.35 ± 0.40	14 ± 5	3.43 ± 0.25	5.66 ± 0.43	1.65 ± 0.17
DT 05	2.45	4–11	2.88 ± 0.04	10.87 ± 0.70	2.91 ± 0.40	18 ± 5	4.13 ± 0.29	10.17 ± 0.44	2.46 ± 0.21
DT 06	2.95	4–11	2.53 ± 0.04	11.36 ± 0.70	3.02 ± 0.40	16 ± 5	3.98 ± 0.29	9.65 ± 0.29	2.43 ± 0.19
DT 07	3.45	4–11	2.73 ± 0.04	10.37 ± 0.70	3.24 ± 0.40	17 ± 5	4.10 ± 0.30	9.93 ± 0.56	2.42 ± 0.22
DT 08	3.95	4–11	2.49 ± 0.04	10.55 ± 0.70	3.72 ± 0.40	14 ± 5	4.16 ± 0.30	13.13 ± 0.64	3.15 ± 0.28
DT 09	4.45	4–11	3.08 ± 0.04	12.21 ± 0.70	3.11 ± 0.40	18 ± 5	4.40 ± 0.31	15.86 ± 0.59	3.60 ± 0.29
DT 11	5.45	38–63	2.08 ± 0.04	9.81 ± 0.60	5.25 ± 0.50	13 ± 5	3.93 ± 0.30	10.08 ± 0.32	2.57 ± 0.21
DT 12	5.95	4–11	3.16 ± 0.04	14.76 ± 0.70	3.31 ± 0.40	17 ± 5	4.71 ± 0.33	16.37 ± 1.92	3.47 ± 0.48
DT 13	6.45	38–63	2.63 ± 0.04	12.58 ± 0.70	2.94 ± 0.40	15 ± 5	3.92 ± 0.29	14.32 ± 0.50	3.65 ± 0.30
DT 14	6.95	4–11	2.92 ± 0.04	12.65 ± 0.70	4.21 ± 0.40	9 ± 5	5.11 ± 0.37	19.23 ± 1.21	3.77 ± 0.36
DT 15	7.45	4–11	2.83 ± 0.04	12.60 ± 0.70	5.18 ± 0.50	19 ± 5	4.61 ± 0.34	19.18 ± 1.21	4.16 ± 0.40
DT 16	7.95	38–63	1.92 ± 0.04	9.19 ± 0.60	2.17 ± 0.40	14 ± 5	2.93 ± 0.23	13.35 ± 0.41	4.56 ± 0.38
YLP 01	2.5	38–63	2.00 ± 0.04	11.15 ± 0.70	4.06 ± 0.40	12 ± 5	3.81 ± 0.28	145.01 ± 5.68	38.09 ± 3.16
XTW-01A	0.5	38–63	1.69 ± 0.04	5.86 ± 0.50	3.98 ± 0.40	11 ± 5	3.24 ± 0.24	2.18 ± 0.15	0.67 ± 0.07
XTW-01B	0.5	38–63	2.41 ± 0.04	9.62 ± 0.60	9.28 ± 0.60	18 ± 5	5.02 ± 0.36	2.29 ± 0.15	0.46 ± 0.04
XTW-02	1.6	38–63	1.72 ± 0.04	3.88 ± 0.40	4.03 ± 0.40	4 ± 5	3.37 ± 0.25	5.52 ± 0.41	1.64 ± 0.17

single-aliquot regenerative-dose (SAR) (Murray and Wintle, 2000) and the standardized growth curve (SGC) method (Roberts and Duller, 2004; Lai, 2006). The sample was preheated to 260°C for 10 s and cut-heat to 220°C for 10 s. The signals of the first 0.64 s stimulation are integrated to build a growth curve after background subtraction (last 8 s).

The concentration of U and Th in all samples was measured by ICP-MS, while the K content was measured by ICP-OES. For grains of 38–63 μm, the alpha efficiency value was taken as 0.035 ± 0.003 (Lai et al., 2008). For grains of 4–11 μm, the alpha efficiency value was assumed to be 0.04 (Ree-Jones, 1995). The calcuation of the cosmic dose rate is based on Prescott and Hutton (1994). The water content (%) was determined by the ratio of the weight of water in the sediment to the weight of dry sediments. A 5% error was added to the water content when calculating the dose rate for each sample.

X-ray Diffraction Analysis

Mineral compositions of 45 samples, grounded into powder (<75 μm) using ball mill, were analyzed using a Panalytical X-pert Pro diffractometer at the Qinghai Institute of Salt Lakes, Chinese Academy of Sciences. The relative volume percentage of minerals was calculated using the formula from Chung (1974) based on the diffraction intensity of the sample.

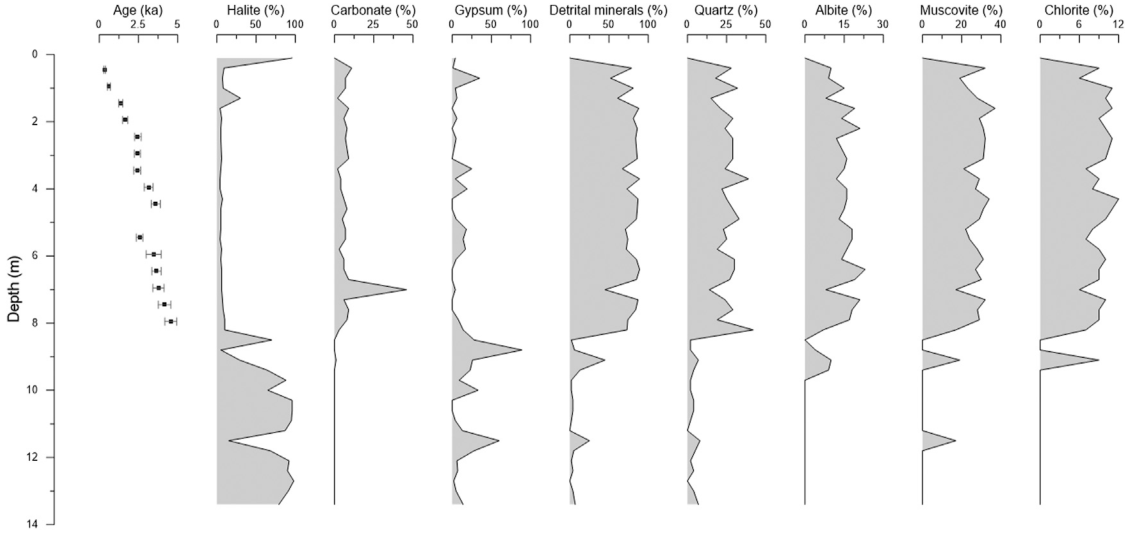

FIGURE 5 | Mineral composition and dating results in the Section DT in East Taijnar Salt Lake.

RESULTS AND DISCUSSION

The results of the OSL dating with their Equivalent dose (De) values are given in **Table 1** and **Figure 4**. The obtained ages are generally in line with their geomorphic sequences (**Figure 4**). The OSL decay curves and the regenerative-dose growth curves fitted by a single saturation exponential plus linear function are presented in **Figure 5**. Mineral composition of section DT is summarized in **Figure 6**. Quartz, alite, muscovite, and chlorite were identified as detrital minerals in the DT section. The average content of these detrital minerals was approximately 49.71%. The average carbonate content was 9%, and consisted mainly of calcite and dolomite, while aragonite occurred in limited horizons. The evaporite salt minerals in section DT were mainly halite and gypsum, with a small amount of sylvine (10–13.4 m). Detrital minerals, carbonates and gypsum were generally abundant between 0.4 and 9.1 m. For comparison, halite appeared mainly at 9.4–13.4 m and its content exceeded 70% (**Figure 6** and **Supplementary Table S2**).

Salt Crust Formation in Central Western Qaidam

The salt crust of the DT section, located in East Taijnar Salt Lake, was 0.2 m thick. The result of OSL dating of DT01 (0.45 m at the DT section) revealed that the age of the salt crust in East Taijnar Salt Lake is about 0.35 ka (**Figure 4A**). The thickness of the salt crust in West Taijnar Salt Lake was recorded as 0.1 m in the section XTW. Dating samples (XTW01A and XTW01B) collected at a depth of 0.5 m were dated to about 0.7 ± 0.1 ka and 0.5 ± 0.1 ka, respectively (**Figure 4B**). These ages indicate that the salt crust in West Taijnar Salt Lake developed after 0.67 ka. The dating results of several sections analyzed by Wang et al. (2019) showed that the age of the salt crust in West Taijnar Salt Lake is younger than at least 0.4 ka, and the age of the crust is even younger than 0.3 ka in some sections. Combining these observations with our results, it can be concluded that the salt crust in West Taijnar Salt Lake developed for several years and is younger than hundreds of years. The results of Zeng and Xiang (2017) show that the age of the surface crust of West Taijnar Salt Lake is approximately 57.9 ka, which does not agree with the results of our study and with the results of Wang et al. (2019). This disagreement could be the result of the fact that the lake section analyzed by Zeng and Xiang (2017) was not in West Taijnar Salt Lake, but in the north of West Taijnar Salt Lake, near the Bayanwuer anticline (**Figure 3**). The YLP section, which lies at Yiliping Salt Lake, has developed a 0.2 m thick salt crust. A limited number of quartz grains resulted in a lack of dating samples, which prevented the assessment of the age of the salt crust. However, the age of the salt crust in Yiliping Salt Lake was obtained by analysis of Huang and Han (2007). This study analyzed the age of borehole 82CK1 in the center of Yiliping Salt Lake by radiocarbon dating and reported the age of the surface salt crust younger than 2.10 ± 0.25 ka.

The salt crust in Chahansilatu playa was explored by Han et al. (2014). Their work shows that the depth of the salt crust in Chahansilatu is about 2.0 m. The age of the three samples with depths of 0.5, 1.0, and 1.9 m was reported as 77.8 ± 4.0 ka, 78.9 ± 4.8 ka and 92.9 ± 5.1 ka, respectively, which confirms the formation of the salt crust in Chahansilatu at 90 ka. The salt crust is 0.21 m thick in Dalangtan salt lake. Ma et al. (2011) analyzed section D26 in Dalangtan salt lake. Their results showed that the salt crust in Dalangtan salt lake is 0.21 m thick. From the sample's age at a depth of 0.47 m it can be concluded that the salt crust in Dalangtan salt lake developed by 118 ka at most. The thickness of the salt crust in Kunteyi salt lake was recorded as 0.1 m, while the age is between 14.1 ka and 24.4 ka (Huang and Han, 2007). Previous studies definitely reveal the variability of salt crust thickness in the Qaidam Basin. The salt crust thickness is less than 0.2 m in the Three Lakes, which is thinner than the salt crust in the western Qaidam Basin, such as Chahansilatu and Dalangtan salt lake. In addition, the salt crust in Chahansilatu, Dalangtan, and Kunteyi salt lakes formed earlier than the salt crust in the Three Lakes.

Age of Lithium Deposits Formation

The brine lithium deposits are distributed in the Three Lakes in the Qaidam Basin. The formation of lithium from evaporites indicates that the age of formation of the lithium deposits is the same as the age of salt formation. Stratigraphy of boreholes from

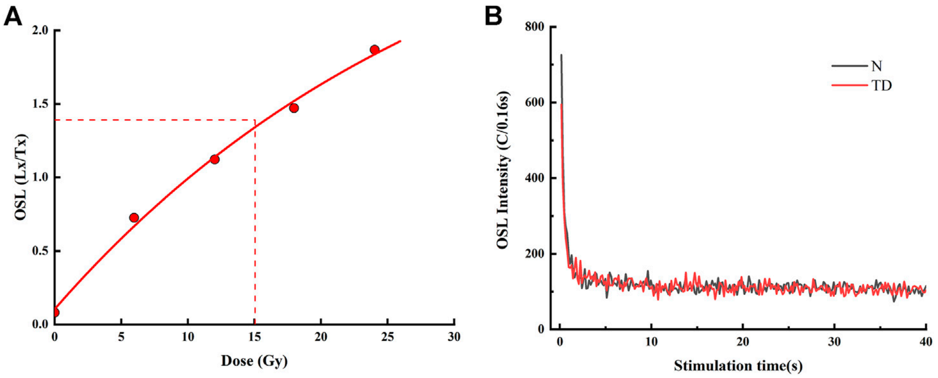

FIGURE 6 | OSL regenerative-dose growth curves **(A)** and decay curves **(B)** for samples DT14.

south to north and from east to west in East Taijnar Salt Lake shows that lithium deposits can be classified into two types: 1) phreatic brine lithium deposits in the upper halite layer, and 2) confined brine lithium deposits in the lower halite layer.

Furthermore, **Figure 7** reveals that the deposition center of the lake is close to the CK264 core, which is also the deposition center of the confined brine lithium deposits. The DT section is close to CK264, which implies that the dating results from the DT section can reflect the age of formation of the confined brine lithium deposits. The confined lithium brine deposits are found in the lower halite layer below 8.4 m in the DT section. The dating results of the clayey sand located above the lower halite layer reveal that the confined brine lithium deposits formed before 4.6 ka (**Figure 4A**). Liang and Han (2013) indicated that the age of the Upper Pleistocene sediments is 27 ka. Therefore, we infer that the age of the confined brine lithium deposits is between 27 and 4.6 ka. Since the depositional center of the phreatic lithium deposits is in the northwestern East Taijnar Salt Lake (**Figure 7A**), we can only conclude that it was formed after 4.6 ka at the most. According to the similarity of the evolution of West Taijnar Salt Lake and East Taijnar Salt Lake from the Late Pleistocene (Zhu et al., 1989), the age of formation of the brine lithium deposits of the two lakes is the same. Lithium deposits in Yiliping Salt Lake are found in surface halite above 2.3 m (**Figure 4D**). Wang (2020) revealed that the upper halite layer began to deposit at 40 ka, which is in line with our conclusions. This not only confirms the accuracy of our dating results, but also suggests that the lithium deposits formed after 40 ka.

The most classic and abundant lithium brine deposits are distributed in South America and the Qaidam Basin, so we compare their age of lithium deposits. Previous chronological studies in South America can help us estimate the age of lithium deposits formation. The current lithium production comes from the Salar de Atacama in Chile, with an area of about 3,000 km^2. The lithium-bearing brine fills the upper part of the salt layer at a depth of about 35 m (Garrett, 2004). From a chronological study of a 100 m long salt core in the central part of the Salar de Atacama (Bobst et al., 2001), it is assumed that the age of formation of lithium deposits in halite above 35 m is about 60.7 ka (**Figure 8A**). Another well-known brine lithium deposit in South America is located in the Salar de Uyuni. The Salar de Uyuni contained 11 lacustrine layers (L1-L11) and 12 salt layers (S1-S12) (**Figure 8B**). Ericksen et al. (1978) indicated that lithium deposit is located in the halite layer at depths of 0–10 m. Lithium levels at depths below 10 m have not been analyzed, which limited the analysis to salt layers above 10 m. Fornari et al. (2001) showed that the salt layers above 10 m formed since 16.1 ka (**Figure 8B**). In contrast, Baker et al. (2001b) indicated the age of the salt layer above 10 m is 18.92 ka BP, implying that the age of formation of lithium is at least 18.92 ka. Lithium deposits below a depth of 10 m may be older than 18.92 ka.

Zabuye Lake is located in the southwestern region of the Tibetan Plateau, which is another region with the brine lithium deposits in the surface lakes. Liu and Zheng (1999) hypothesized that Zhabuye Lake became a salt lake at 8.9 ka. Therefore, strong evaporation around 4 ka led to the deposition of brine lithium.

In summary, the brine lithium deposits in South America formed during the Middle Pleistocene. In contrast, the lithium deposits in the Qaidam Basin are younger as they formed between

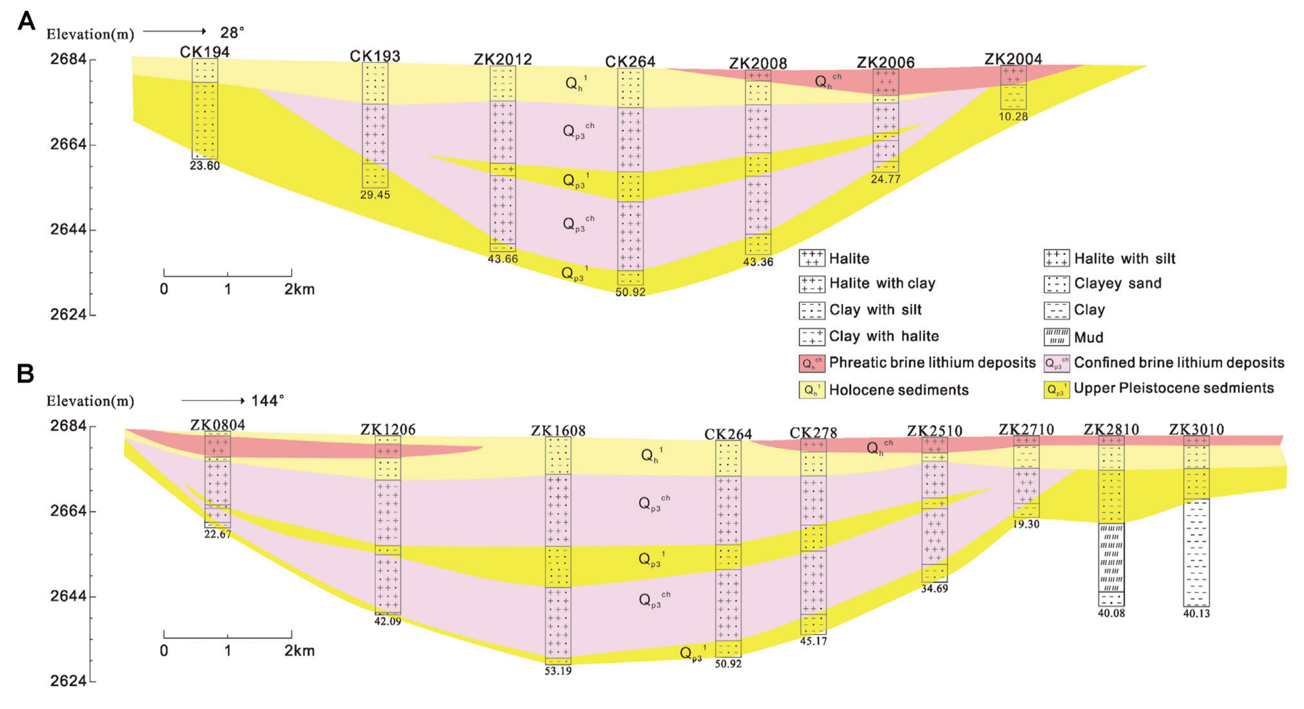

FIGURE 7 | Stratigraphy and distribution of lithium deposits in East Taijnar Salt Lake: **(A)** from south to north, and **(B)** from west to east.

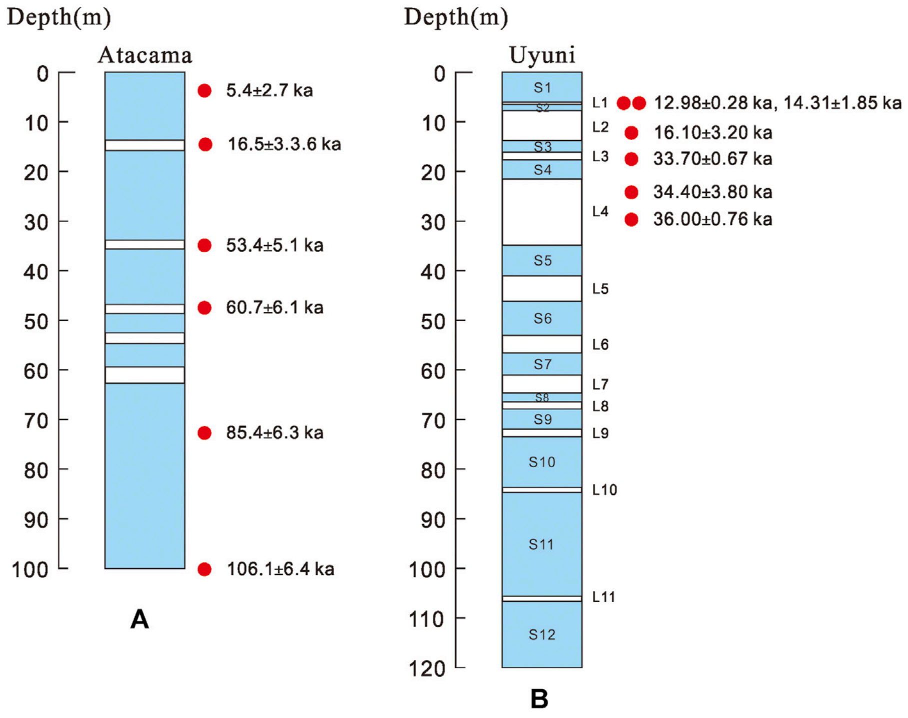

FIGURE 8 | Stratigraphy, sample site, and dating results for salt lakes in South America: **(A)** core in the Salar de Atacama, the dating results being analyzed by the radiocarbon dating method Bobst et al. (2001); and **(B)** core in the Salar de Uyuni, for which the U-series disequilibrium dating method is used. The blue squares represent the salt layers and the white squares represent the lacustrine layers Fornari et al. (2001).

the Late Pleistocene and Holocene. The youngest lithium deposits in Tibet are 4 ka old.

Formation of Salt Deposits and Climate Change

There are two periods of salt formation in the Qaidam basin: 1) the first period is in the Late Tertiary Pliocene, and 2) the second period is in the Late Quaternary Pleistocene (Zhang, 1987). The Three Lakes evolved into salt lakes in the second salt-forming period (Zhu et al., 1989).

A previous investigation by the Qaidam Integrated Geological Exploration Institute of Qinghai Province reported two periods of salt formation in East Taijnar Salt Lake, during which two thick layers of halite were deposited due to dry climate. The climate briefly changed to relatively humid during the first period of salt formation, leading to the deposition of a thin layer of clay in the middle of the lower halite layer (**Figure 7**). Liang and Han (2013) reported that the age of the Upper Pleistocene clay below the lower halite layer is 27 ka, indicating that the lower halite layer formed after 27 ka in East Taijnar Salt Lake. Hence, the dry climate facilitated the deposition of halite since 27 ka. The halite layer below 8.4 m in the DT section represents the top of the lower halite layer. Abundant halite deposition below 8.4 m shows that this was a period of salt formation in East Taijnar Salt Lake. Analysis of OSL dating shows that this period of salt formation lasted from 27 to 4.6 ka, during which East Taijnar Salt Lake witnessed intensely dry conditions that led to significant deposition of halite and gypsum (**Figure 4A** and **Figure 6**). Liang and Han (2013) and Zhang et al. (2001) pointed out that the salt deposits in East Taijnar Salt Lake formed about ten thousand years ago. Since the samples of this study were from the east of East Taijnar Salt Lake, it can be concluded that the age obtained by the study was from a layer of clay in the middle of the lower halite.

The assimilation of the above discussions shows the prevalence of extremely dry climate during 27–4.6 ka, which is the period of salt formation in East Taijnar Salt Lake. However, the climate briefly changed around 10 ka. An increase in relative humidity around 10 ka led to the deposition of a thin layer of clay due to increased runoff. As lithology shows, a clast layer with an average detrital mineral content of 85.1% is deposited in the DT section since 4.6 ka. This layer was deposited by the Nalinggele River. It shows that the climate was relatively humid since 4.6 ka, and the hydrodynamic conditions in the Nalingele River became stronger, which led to the transport of abundant clastic minerals. Yang (2015) reported frequent catastrophic palaeofloods by the Nalinggele River during 4.7–3.5 ka, confirming our conclusion. Although the climate became relatively humid since 4.6 ka, dry conditions still existed, which is also shown by the existence of halite (average content 6.9%) and gypsum (average content 6.7%). The progress of salt formation did not stop since 4.6 ka. From 0.3 ka, the runoff volume of the Nalinggele River decreased and East Taijnar Salt Lake evolved into a landscape as it is today.

The XTW section in West Taijnar Salt Lake is 1.7 m thick. We extracted quartz from the bottom of the section for dating

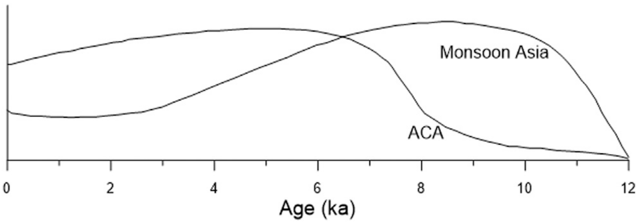

FIGURE 9 | The synthesized Holocene effective-moisture evolution in arid Central Asia (ACA) and monsoon Asia (Chen et al., 2008).

(**Figure 4B**). Dating results and frequent cases of halite deposition show that the climate was dry during 1.64–0.67 ka. Section XT2-1 in West Taijnar Salt Lake is dated using OSL and radiocarbon dating (AMS ^{14}C) (Wang et al., 2019). As the results of their study show, West Taijnar Salt Lake deposited a large quantity of halite during 8.33–0.25 ka (**Figure 4C**), which is similar to the deposition in East Taijnar Salt Lake. However, West Taijnar Salt Lake has fewer clast minerals. East Taijnar Salt Lake receives a larger inflow from the Nalinggele River than West Taijnar Salt Lake, reducing the transport of clast to the latter. The depth of the section YLP in Yilingping Lake is approximately 2.7 m. Data on dating and large halite deposition show that Yiliping Salt Lake is dry since 38.09 ka.

To summarize, the period of salt formation in East Taijnar Salt Lake and West Taijnar Salt Lake began 27 ka ago. During this period, the climate was extremely dry. At the beginning of the period (27–4.6 ka), cold and dry climatic conditions were maintained. The humid climate occurred around 10 ka. In the later stages of the salt formation period (after 4.6 ka ago), the climate was relatively humid, but remained dry. The salt-forming age of Yiliping Salt Lake is 38.09 ka, which testifies to a dry climate since 38.09 ka.

Comparison With Climate in Arid Central Asia and Monsoon Asia

The Qaidam Basin lies close to the border between the Asian Summer Monsoon (ASM) and the mid-latitude westerlies (Chen et al., 2008). Sediments from the Three Lakes in the transition zone between arid Central Asia and monsoon Asia provide insight into the controlling influence of the summer monsoon and the westerlies on the climate in the central Qaidam Basin.

Figure 9 shows the synthesized Holocene effective-moisture evolution in arid central Asia (ACA) and monsoon Asia. ACA as a whole experienced synchronous and coherent changes in moisture during the Holocene, namely the dry early Holocene, the wetter (less dry) early to mid-Holocene, and the moderately wet late Holocene (Chen et al., 2008). As discussed in *Comparison With Climate in Arid Central Asia and Monsoon Asia* Section the dry climate in the early Holocene and relatively humid climate in the late Holocene in the Three Lakes area is similar to the effective moisture history in ACA. The effective-moisture history in monsoonal Asia is out-of-phase with that of the ACA, as shown in **Figure 9**. Thus, we can conclude that the Three Lakes area is mainly controlled by the westerlies in the Holocene.

Geomorphic Processes since the Late Pleistocene

In the early Late Pleistocene, the Three Lakes were located in the same secondary basin, as evidenced by the consistency of the bottom sediments of the late Pleistocene and the continuity of the stratigraphic distribution (Rong, 2002). Due to the uplift of the Bayanwuer anticline and the Taijnar anticline, as well as other anticlines after that, Yiliping Salt Lake changed into an independent basin and deposited the upper salt layer since the middle-late Pleistocene. This separation explains the differences in depositions between Yiliping Salt Lake, West Taijnar Salt Lake and East Taijnar Salt Lake since the late Pleistocene. Wang (2020) indicated the age of formation of the upper halite at 40 ka. Combining this with our dating results from the YLP section, we conclude that the upper halite began to form at 40 ka. Yiliping Salt Lake evolved into an independent basin at 40 ka. In contrast, East Taijnar Salt Lake and Wset Taijnar Salt Lake were a unitive basin fed by the Nalinggele River. Unitive deposition of East Taijnar Salt Lake and West Taijnar Salt Lake was halted by tectonic activity between the late Pleistocene and Holocene, leading to the division of the unitive basin into two lakes in the Holocene (Zhang, 1987; Zhu et al., 1989). The top layer of the late Pleistocene sediments is exposed to the east of East Taijnar Salt Lake (**Figure 7B**). This means that the central and thickest part of the late Pleistocene deposits is between East Taijnar Salt Lake and West Taijnar Salt Lake, which shows that these two lakes were not divided before the late Pleistocene. Liang and Han (2013) reported that the age of the top layer of the late Pleistocene sediments is 27 ka. Therefore, East Taijnar Salt Lake and West Taijnar Salt Lake partitioned at 27 ka, and the lower layer of salt was deposited until the Holocene. The climate in the Holocene evolved from dry to relatively humid, facilitating the transport and deposition of clastic sediments in East Taijnar Salt Lake and West Taijnar Salt Lake (**Figure 4**). Since 4 ka, East Taijnar Salt Lake and West Taijnar Salt Lake deposited the upper salt layer due to dry climate.

CONCLUSION

By combining the results of OSL dating of sections in the Three Lakes with previous studies related to other salt lakes, we conclude that salt crusts in the Qaidam basin have different thicknesses. The thickness of the salt crust in the Three Lakes is less than 0.2 m, which is thinner than the salt crust in the western Qaidam basins, such as Chahansilatu and Dalangtan salt lake. The salt crust in the salt lakes Chahansilatu, Dalangtan and Kunteyi was formed earlier than the salt crust of the Three Lakes.

The confined lithium deposits in East Taijnar Salt Lake were formed before 27–4.6 ka. In comparison, the age of the phreatic lithium deposits in East Taijnar Salt Lake is at most 4.6 ka. Given that the evolutionary processes of West Taijnar Salt Lake and East Taijnar Salt Lake were identical, it could be assumed that the age of the lithium deposits in the former could be 27 ka. The age of the lithium deposit in Yiliping Salt Lake is 40 ka. The brine lithium deposits in South America are older than the corresponding deposits in the Qaidam Basina and probably formed between the middle Pleistocene and late Pleistocene. The youngest lithium deposits in Tibet formed around 4 ka.

According to the OSL dating and the mineral composition analysis of the Three Lakes, the period of salt formation in East Taijnar Salt Lake and West Taijnar Salt Lake began 27 ka ago. The climate was extremely dry during this period. The climatic conditions in the beginning (27–4 ka) could be characterized as cold and dry. A brief, relatively humid event occurred around 10 ka. During the later stages in the period of salt formation (after 4 ka ago), the conditions were relatively humid in the two lakes. However, the climate was predominantly dry as suggested by the crystallization of halite and gypsum. The salt-forming age of Yiliping Salt Lake is 38.09 ka, which has had a dry climate since 38.09 ka. A comparison of the climate with the synthesized Holocene effective-moisture evolution in arid Central Asia and monsoon Asia shows that the Three Lakes area is mainly controlled by the westerlies in the Holocene.

East Taijnar Salt Lake, West Taijnar Salt Lake, and Yiliping Salt Lake were situated in the same secondary basin during the late Pleistocene. By 40 ka, Yiliping Salt Lake evolved into an independent basin due to tectonic activity. The unitive deposition of East Taijnar Salt Lake and West Taijnar Salt Lake was completed gradually from the later period of the late Pleistocene. These two lakes partitioned completely at 27 ka, and then they deposited the lower layers of salt until the Holocene. The Nalinggele River brought abundant detrital minerals during the Holocene, especially in East Taijnar Salt Lake, which led to a brief desalination of the lake. The upper salt layer was deposited in East Taijnar Salt Lake and West Taijnar Salt Lake due to the extremely dry climate during the Holocene.

DATA AVAILABILITY STATEMENT

The original contributions presented in the study are included in the article/**Supplementary Material**, further inquiries can be directed to the corresponding author.

AUTHOR CONTRIBUTIONS

ZM designed the research. ZM, FH, TC, LY, XL, FC, XL, and WY performed the research. ZM and TC analyzed the data. ZM, FH, and TC wrote the manuscript.

FUNDING

This study was supported by the Natural Science Foundation of Qinghai Province (2019-ZJ-911) and the Natural Science Foundation of Qinghai Province (2020-ZJ-939Q).

ACKNOWLEDGMENTS

We thank reviewers for valuable suggestions and comments related to the manuscript. We also thank Li Han for help in the XRD analysis and Yixuan Wang for help in analyzing the OSL data.

SUPPLEMENTARY MATERIAL

The Supplementary Material for this article can be found online at: https://www.frontiersin.org/articles/10.3389/feart.2021.702223/full#supplementary-material

REFERENCES

Abbott, M. B., Seltzer, G. O., Kelts, K. R., and Southon, J. (1997). Holocene Paleohydrology of the Tropical Andes from Lake Records. *Quat. Res.* 47 (1), 70–80. doi:10.1006/qres.1996.1874

An, F., Ma, H., Wei, H., and Lai, Z. (2012). Distinguishing Aeolian Signature from Lacustrine Sediments of the Qaidam Basin in Northeastern Qinghai-Tibetan Plateau and its Palaeoclimatic Implications. *Aeolian Res.* 4, 17–30. doi:10.1016/j.aeolia.2011.12.004

Baker, P. A., Rigsby, C. A., Seltzer, G. O., Fritz, S. C., Lowenstein, T. K., Bacher, N. P., et al. (2001a). Tropical Climate Changes at Millennial and Orbital Timescales on the Bolivian Altiplano. *Nature* 409 (6821), 698–701. doi:10.1038/35055524

Baker, P. A., Seltzer, P. G., Fritz, S. C., Dunbar, R. B., Grove, M., Tapia, P., et al. (2001b). The History of South American Tropical Precipitation for the Past 25,000 Years. *Science* 291 (5504), 640–643. doi:10.1126/science.291.5504.640

Bobst, A., Lowenstein, T. K., Jordan, T. E., Godfrey, L. V., Ku, T. L., and Luo, S. D. (2001). A 106 kapaleoclimate record from the Salar de Atacama, northern Chile. *Palaeogeogr. Palaeoclimatol. Palaeoecol.* 173 (1-2), 21–42. doi:10.1016/S0031-0182(01)00308-X

Chang, Q., Lai, Z., An, F., Wang, H., Lei, Y., and Han, F. (2017). Chronology for Terraces of the Nalinggele River in the north Qinghai-Tibet Plateau and Implications for Salt lake Resource Formation in the Qaidam Basin. *Quat. Int.* 430 (PT.B), 12–20. doi:10.1016/j.quaint.2016.02.022

Chen, A. D., Zheng, M. P., Shi, L. F., Wang, H. L., Xu, J. M., and Yuan, W. H. (2017). Gypsum 230Th Dating of the 15YZK01 Drilling Core in the Qaidam Basin: Salt Deposits and Their Link to Quaternary Glaciation and Tectonic Movement. *Acta Geosci. Sin.* 38 (4), 494–504. (in Chinese with English abstract). doi:10.3975/cagsb.2017.04.06

Chen, F., Yu, Z., Yang, M., Ito, E., Wang, S., Madsen, D. B., et al. (2008). Holocene Moisture Evolution in Arid central Asia and its Out-of-phase Relationship with Asian Monsoon History. *Quat. Sci. Rev.* 27 (3-4), 351–364. doi:10.1016/j.quascirev.2007.10.017

Chung, F. H. (1974). Quantitative Interpretation of X-ray Diffraction Patterns of Mixtures. II. Adiabatic Principle of X-ray Diffraction Analysis of Mixtures. *J. Appl. Cryst.* 7 (6), 526–531. doi:10.1107/S0021889874010387

Diederich, J. L., Wennrich, V., Bao, R., Büttner, C., Bolten, A., Brill, D., et al. (2020). A 68 Ka Precipitation Record from the Hyperarid Core of the Atacama Desert in Northern Chile. *Glob. Planet. Change* 184, 103054. doi:10.1016/j.gloplacha.2019.103054

Duller, G. A. T. (2003). Distinguishing Quartz and Feldspar in Single Grain Luminescence Measurements. *Radiat. Measurements* 37 (2), 161–165. doi:10.1016/S1350-4487(02)00170-1

Ericksen, G. E., Vine, J. D., and Raul Ballón, A. (1978). Chemical composition and distribution of lithium-rich brines in salar de Uyuni and nearby salars in southwestern Bolivia. *Energy* 3 (3), 355–363. doi:10.1016/0360-5442(78)90032-4

Fan, Q., Lai, Z., Long, H., Sun, Y., and Liu, X. (2010). OSL Chronology for Lacustrine Sediments Recording High Stands of Gahai Lake in Qaidam Basin, Northeastern Qinghai-Tibetan Plateau. *Quat. Geochronol.* 5 (2-3), 223–227. doi:10.1016/j.quageo.2009.02.012

Fan, Q., Ma, H., Ma, Z., Wei, H., and Han, F. (2013). An Assessment and Comparison of 230Th and AMS 14C Ages for Lacustrine Sediments from Qarhan Salt Lake Area in Arid Western China. *Environ. Earth Sci.* 71, 1227–1237. doi:10.1007/s12665-013-2526-5

Fornari, M., Risacher, F., and Féraud, G. (2001). Dating of Paleolakes in the central Altiplano of Bolivia. *Palaeogeogr. Palaeoclimatol. Palaeoecol.* 172 (3-4), 269–282. doi:10.1016/S0031-0182(01)00301-7

Garrett, D. E. (2004). *Handbook of Lithium and Natural Calcium Chloride: Their Deposits, Processing, Uses and Properties*. Oxford, England: Elsevier Academic Press. doi:10.1016/B978-0-12-276152-2.X5035-X

Gruber, P. W., Medina, P. A., Keoleian, G. A., Kesler, S. E., Everson, M. P., and Wallington, T. J. (2011). Global Lithium Availability. *J. Ind. Ecol.* 15, 760–775. doi:10.1111/j.1530-9290.2011.00359.x

Han, W., Ma, Z., Lai, Z., Appel, E., Fang, X., and Yu, L. (2014). Wind Erosion on the north-eastern Tibetan Plateau: Constraints from OSL and U-Th Dating of Playa Salt Crust in the Qaidam Basin. *Earth Surf. Process. Landforms* 39, 779–789. doi:10.1002/esp.3483

Huang, Q., and Han, F. Q. (2007). *Evolution of Salt Lakes and Palaeoclimate Fluctuation in Qaidam Basin*. Beijing: Science Press. in Chinese with English abstract

Kesler, S. E., Gruber, P. W., Medina, P. A., Keoleian, G. A., Everson, M. P., and Wallington, T. J. (2012). Global Lithium Resources: Relative Importance of Pegmatite, Brine and Other Deposits. *Ore Geology. Rev.* 48, 55–69. doi:10.1016/j.oregeorev.2012.05.006

Klein, A. G., Seltzer, G. O., and Isacks, B. L. (1999). Modern and Last Local Glacial Maximum Snowlines in the Central Andes of Peru, Bolivia, and Northern Chile. *Quat. Sci. Rev.* 18 (1), 63–84. doi:10.1016/S0277-3791(98)00095-X

Lai, Z., and Brückner, H. (2008). Effects of Feldspar Contamination on Equivalent Dose and the Shape of Growth Curve for OSL of Silt-Sized Quartz Extracted from Chinese Loess. *Geochronometria* 30 (1), 49–53. doi:10.2478/v10003-008-0010-0

Lai, Z., Mischke, S., and Madsen, D. (2014). Paleoenvironmental Implications of New OSL Dates on the Formation of the "Shell Bar" in the Qaidam Basin, Northeastern Qinghai-Tibetan Plateau. *J. Paleolimnol.* 51 (2), 197–210. doi:10.1007/s10933-013-9710-1

Lai, Z. P., Zöller, L., Fuchs, M., and Brückner, H. (2008). Alpha Efficiency Determination for OSL of Quartz Extracted from Chinese Loess. *Radiat. Measurements* 43, 767–770. doi:10.1016/j.radmeas.2008.01.022

Lai, Z. (2006). Testing the Use of an OSL Standardised Growth Curve (SGC) for Determination on Quartz from the Chinese Loess Plateau. *Radiat. Measurements* 41, 9–16. doi:10.1016/j.radmeas.2005.06.031

Liang, Q. S., and Han, F. Q. (2013). Geological Characteristics and Lithium Distribution of East Taijinar Salt Lake in Qaidam Basin. *J. Salt Lake Res.* 21 (3), 1–9. (in Chinese with English abstract)

Liang, Q. S., and Huang, Q. (1995). Salt-forming Ages of the Dabusun and Bieletan Regions in Qarhan Playa, Qinghai. *Acta Sedimentol. Sin.* 13 (3), 126–131. (in Chinese with English abstract). doi:10.14027/j.cnki.cjxb.1995.03.015

Liu, X. F., and Zheng, M. P. (1999). Geological Setting and Mineralizing Evolution of Super Large Li, B deposit, Zabuye, Tibet. *Geol. Chem. Miner.* 21 (2), 65–68. (in Chinese with English abstract)

Ma, N. N., Zheng, M. P., Ma, Z. B., Chen, W. X., Kong, F., and Shi, L. F. (2011). Forming Age of Surface Mirabilite in Dalangtan, Qaidam Basin and its Environmental Significance. *Acta Geol. Sin.* 85 (3), 433–444. (in Chinese with English abstract). doi:10.3724/SP.J.1011.2011.00415

Murray, A. S., and Wintle, A. G. (2000). Luminescence Dating of Quartz Using an Improved Single-Aliquot Regenerative-Dose Protocol. *Radiat. Measurements* 32 (1), 57–73. doi:10.1016/S1350-4487(99)00253-X

Owen, L. A., Finkel, R. C., Haizhou, M., and Barnard, P. L. (2006). Late Quaternary Landscape Evolution in the Kunlun Mountains and Qaidam Basin, Northern Tibet: A Framework for Examining the Links between Glaciation, lake Level Changes and Alluvial Fan Formation. *Quat. Int.* 154-155, 73–86. doi:10.1016/j.quaint.2006.02.008

Pfeiffer, M., Latorre, C., Santoro, C. M., Gayó, E. M., Rojas, R., Carrevedo, M. L., et al. (2018). Chronology, Stratigraphy and Hydrological Modelling of Extensive Wetlands and Paleolakes in the Hyperarid Core of the Atacama Desert during the Late Quaternary. *Quat. Sci. Rev.* 197, 224–245. doi:10.1016/j.quascirev.2018.08.001

Prescott, J. R., and Hutton, J. T. (1994). Cosmic ray Contributions to Dose Rates for Luminescence and ESR Dating: Large Depths and Long-Term Time Variations. *Radiat. Measurements* 23, 497–500. doi:10.1016/1350-4487(94)90086-8

Ree-Jones, J. (1995). Optical Dating of Young Sediments Using Fine-Grain Quartz. *Anc.TL.* 13, 9–13. doi:10.1108/02632779510104021

Roberts, H. M., and Duller, G. A. T. (2004). Standardised Growth Curves for Optical Dating of Sediment Using Multiple-Grain Aliquots. *Radiat. Measurements* 38 (2), 241–252. doi:10.1016/j.radmeas.2003.10.001

Rodbell, D. T., Seltzer, G. O., Anderson, D. M., Abbott, M. B., Enfield, D. B., and Newman, J. H. (1999). An 15,000-Year Record of El Niño-Driven Alluviation in Southwestern Ecuador. *Science* 283 (5401), 516–520. doi:10.1126/science.283.5401.516

Shen, Z. S., Cheng, G., Yue, C. S., Liu, S. Q., Zhang, F. S., Wang, Q., et al. (1993). *The Division and Sedimentary Environment of Quaternary Salt-Bearing Strata in Qaidam Basin*. Beijing: Geological Publishing House. in Chinese with English abstract

Sun, Y., Lai, Z., Long, H., Liu, X., and Fan, Q. (2010). Quartz OSL Dating of Archaeological Sites in Xiao Qaidam Lake of the NE Qinghai-Tibetan Plateau and its Implications for Palaeoenvironmental Changes. *Quat. Geochronol.* 5 (2-3), 360–364. doi:10.1016/j.quageo.2009.02.013

Thompson, L. G., Davis, M. E., Mosley-Thompson, E., Sowers, T. A., Henderson, K. A., Zagorodnov, V., et al. (1998). A 25,000-Year Tropical Climate History from Bolivian Ice Cores. *Science* 282 (5398), 1858–1864. doi:10.1126/science.282.5395.1858

Walk, J., Stauch, G., Reyers, M., Vásquez, P., Sepúlveda, F. A., Bartz, M., et al. (2020). Gradients in Climate, Geology, and Topography Affecting Coastal Alluvial Fan Morphodynamics in Hyperarid Regions - the Atacama Perspective. *Glob. Planet. Change* 185, 102994. doi:10.1016/j.gloplacha.2019.102994

Wang, M. Q. (2020). Origin of Lithium-Rich Brine in Yiliping Salt lake, Qaidam Basin. PhD Thesis ((Beijing: China University of Geosciences). in Chinese with English abstract

Wang, Q. S., Qiu, J. Z., Shao, H. N., and Xu, H. (2015). Analysis on Metallogenic Characteristic and Resource Potential of Salt lake Brine Lithium Deposits in the Global. *China Mining Mag.* 24 (11), 82–88. (in Chinese with English abstract). doi:10.3969/j.issn.1004-4051.2015.11.018

Wang, Y. X., Chen, T. Y., Wu, C., Lai, Z. P., Guo, S. D., and Cong, L. (2019). Formation and Evolution of the Xitaijinair Salt Lake in Qaidam Basin Revealed by Chronology. *Arid land Geogr.* 42 (4), 876–884. (in Chinese with English abstract)

Yang, H. P., Liu, L., and Ding, G. F. (2019). Present Situation and Development Trend of Lithium Resources in the World. *Conservation Utilization Mineral. Resour.* 5, 26–40. (in Chinese with English abstract). doi:10.13779/j.cnki.issn1001-0076.2019.05.004

Yang, X. Y. (2015). Modern Flood Process and the OSL Dating and Grain-Size Characteristic on Palaeoflood Deposits of Nalinggele Watershed, Northern of the Qinghai-Tibet Plateau. Master thesis. (Xining (China): Qinghai Normal University. in Chinese with English abstract

Yu, J., Gao, C., Cheng, A., Liu, Y., Zhang, L., and He, X. (2013). Geomorphic, Hydroclimatic and Hydrothermal Controls on the Formation of Lithium Brine Deposits in the Qaidam Basin, Northern Tibetan Plateau, China. *Ore Geology. Rev.* 50, 171–183. doi:10.1016/j.oregeorev.2012.11.001

Yu, L., and Lai, Z. (2012). OSL Chronology and Palaeoclimatic Implications of Aeolian Sediments in the Eastern Qaidam Basin of the Northeastern Qinghai-Tibetan Plateau. *Palaeogeogr. Palaeoclimatol. Palaeoecol.* 337-338, 120–129. doi:10.1016/j.palaeo.2012.04.004

Yu, L. P., and Lai, Z. P. (2014). Holocene Climate Change Inferred from Stratigraphy and OSL Chronology of Aeolian Sediments in the Qaidam Basin, Northeastern Qinghai–Tibetan Plateau. *Quat. Res.* 81 (3), 488–499. doi:10.1016/j.yqres.2013.09.006

Yuan, J. Q., Huo, C. Y., and Cai, K. Q. (1983). The High Mountain-Deep basin saline Environment – A New Cenetic Model of Salt Deposits. *Geol. Rev* 29 (2), 159–165. (in Chinese with English abstract).

Zeng, F., and Xiang, S. (2017). Geochronology and mineral Composition of the Pleistocene Sediments in Xitaijinair Salt Lake Region, Qaidam Basin: Preliminary Results. *J. Earth Sci.* 28 (4), 622–627. doi:10.1007/s12583-016-0712-6

Zhang, H. C., Lei, G. L., and Chang, F. Q. (2007). Age Determination of Shell Bar Section in Salt Lake Qarhan, Qaidam Basin. *Quat. Sci.* 27 (4), 511–521. (in Chinese with English abstract). doi:10.3321/j.issn:1001-7410.2007.04.006

Zhang, H., Han, F. Q., and Liang, Q. S. (2001). Preliminary Studies on Deposition Characteristics and Ages of the Salt Sediments of Dongtai Salt Lake in Qinghai Province. *Geol. Chem. Miner.* 23 (2), 83–85. (in Chinese with English abstract). doi:10.3969/j.issn.1006-5296.2001.02.003

Zhang, M., and Liu, X. (2020). Climate Changes in the Qaidam Basin in NW China over the Past 40 Kyr. *Palaeogeogr. Palaeoclimatol. Palaeoecol.* 551, 109679. doi:10.1016/j.palaeo.2020.109679

Zhang, P. X. (1987). *The Salt Lakes of the Qaidam Basin*. Beijing: Science Press. in Chinese with English abstract

Zhang, S. J., Cui, L. W., Kong, L. H., Jiang, A. L., and Li, J. B. (2020). Summarize on the mineral Resources and Their Distribution at home and Abroad. *Noferrous Met. Eng.* 10 (10), 95–104. (in Chinese with English abstract). doi:10.3390/met10060767

Zhu, Y. Z., Li, W. S., Wu, B. H., and Liu, C. L. (1989). New Recognition on the Geology of the Yiliping Salt Lake and the East and West Taijnar Lakes in the Qaidam Basin, Qinghai Province. *Geol. Rev* 35 (6), 558–565. (in Chinese with English abstract)

Conflict of Interest: The authors declare that the research was conducted in the absence of any commercial or financial relationships that could be construed as a potential conflict of interest.

frontiers in Earth Science

ORIGINAL RESEARCH
published: 19 July 2021
doi: 10.3389/feart.2021.689087

Strain Transformation Adjacent to the West Qinling Orogen: Implications for the Growth of the Northeastern Tibetan Plateau

Zhangjun Li[1,2]*, *Feng Cheng*[3,4], *Ming Hao*[1]*, *Zachary M. Young*[5], *Shangwu Song*[1], *Fan Yang*[1] and *Wenquan Zhuang*[1]

[1]*The Second Monitoring and Application Center, China Earthquake Administration, Xi'an, China,* [2]*State Key Laboratory of Earthquake Dynamics, Institute of Geology, China Earthquake Administration, Beijing, China,* [3]*Key Laboratory of Orogenic Belts and Crustal Evolution, School of Earth and Space Sciences, Ministry of Education, Peking University, Beijing, China,* [4]*Nevada Bureau of Mines and Geology, University of Nevada, Reno, NV, United States,* [5]*Nevada Geodetic Laboratory, University of Nevada, Reno, NV, United States*

OPEN ACCESS

Edited by:
David K. Wright,
University of Oslo, Norway

Reviewed by:
Xiaoyu Guo,
Sun Yat-Sen University, China
Lupeng Zhang,
The Ohio State University,
United States

***Correspondence:**
Zhangjun Li
george_jun@hotmail.com
Ming Hao
ha_mg@163.com

Specialty section:
This article was submitted to
Quaternary Science, Geomorphology
and Paleoenvironment,
a section of the journal
Frontiers in Earth Science

Received: *31 March 2021*
Accepted: *02 July 2021*
Published: *19 July 2021*

Citation:
Li Z, Cheng F, Hao M, Young ZM,
Song S, Yang F and Zhuang W (2021)
Strain Transformation Adjacent to the
West Qinling Orogen: Implications for
the Growth of the Northeastern
Tibetan Plateau.
Front. Earth Sci. 9:689087.
doi: 10.3389/feart.2021.689087

The West Qinling orogen has played an important role in accommodating the deformation in the northeastern Tibetan Plateau induced by the India-Eurasia convergence. Here we construct a vertical land motion (VLM) model based on the latest leveling observations adjacent to the West Qinling orogen. Combined with the horizontal deformation field, the crustal deformation pattern in this area is investigated. Additionally, slip rate and coupling coefficients of the West Qinling fault, the longest fault separating the West Qinling orogen from the Lanzhou (Longxi) block, are inverted and constrained with GPS and VLM observations. Results show that the West Qinling fault slips slowly at a rate of 1–2 mm/yr and is strongly coupled with a moment magnitude deficit of *Mw*7.4. The crustal uplift rates adjacent to the West Qinling orogen are 0–3 mm/yr; which combined with 0–12.5 × 10^{-9}/yr contraction rates, suggests that strain transformation plays a key role in controlling the tectonic uplift in the West Qinling orogen, and furthers our understanding of the contemporary geomorphic and topographic features. We identify a significant deformation transition belt at longitudes of 105°–106°E, which indicates that crustal deformation, induced from the northeastern expansion of the Tibetan Plateau, is mainly constrained to the plateau, rather than accommodated by crustal materials escaping eastward along the Qinling Mountains.

Keywords: the west qinling orogen, strain transformation, vertical land motion, leveling observations, moment deficit

HIGHLIGHTS

1. A vertical land motion model adjacent to the West Qinling orogen is constructed based on leveling observations.
2. Strain transformation plays an important role in controlling the tectonic uplift in the West Qinling orogen.
3. The West Qinling fault has a moment magnitude accumulation of *Mw*7.4, and thus exhibits high seismic risk.

INTRODUCTION

Strain patterns adjacent to convergent plate boundaries, especially along continent-continent collision zones such as the Tibetan Plateau and Anatolian Plateau, remains a source of active investigation (England et al., 1985; Tapponnier, 2001; Reilinger et al., 2006). Known as the “roof of the world,” the Tibetan Plateau is famous for its high average elevation of 4,000 m, as well as complex tectonics and deformation patterns those are driven by the India-Eurasia convergence (Molnar & Tapponnier, 1975; Tapponnier et al., 1982; Tapponnier, 2001). Horizontal contraction and vertical uplift/ thickening of the crust have been shown to be the primary method to accommodate deformation between the late Cretaceous and Miocene in the Tibetan Plateau (Chung et al., 1998; Ruddiman, 1998; Royden et al., 2008). Since the middle Miocene, the Tibetan Plateau has exhibited expansion and outward growth (Molnar & Tapponnier, 1975; Royden, 1997, 2008). Contemporary GPS observations identify two significant expansion passages blocked by the Sichuan Basin: 1) the southeastward extrusion around the eastern Himalaya Syntaxis (EHS) despite its dynamic mechanisms and 2) the north-/east-/ northeast-ward growth (Zhang et al., 2004; Gan et al., 2007; Wang & Shen, 2020). Unlike the clear extrusion in the southeastern Tibetan Plateau (Bai et al., 2010; Bao et al., 2015; Li et al., 2020; Wang & Shen, 2020), the expansion passage and strain pattern are still under debate within the northeastern Tibetan Plateau.

There are two leading models to explain the expansion and deformation pattern of the northeastern Tibetan Plateau. One model highlights the significance of the eastward extrusion of the crustal materials, which considers the Qinling orogen as the channel for the eastward escape of the plateau materials (Tapponnier, 2001; Ma et al., 2013; Yu & Chen, 2016). The other model suggests bookshelf faulting, governed by the large-scale sinistral Haiyuan and Kunlun faults and the dextral Riyueshan and Elashan faults, in which the deformation induced from the northeast-ward/eastward extrusion of Tibetan Plateau is confined to the plateau and accommodated by complex crustal deformation (i.e., block rotation and tectonic uplift), adjacent to the West Qinling, Qilian, and Liupanshan regions (Cheng et al., 2015; England & Molnar, 1990; Hao et al., 2021; Kirby et al., 2007; Kirby & Harkins, 2013; Li Y. et al., 2018; Zheng et al., 2016; Zuza and Yin, 2016).

Therefore, the West Qinling orogen is pivotal to understand the strain pattern in the northeastern Tibetan Plateau. Previous studies, based on dense horizontal GPS velocities and active tectonics, suggest that the crustal deformation in West Qinling orogen is characterized by crustal contraction, mountain uplift, diffuse deformation, and basin formation (Hao et al., 2021; Kirby et al., 2007; Li Y. et al., 2018; Zheng et al., 2016). However, vertical crustal motions have not been thoroughly investigated, hindering further understanding of the deformation pattern in this region. Hao et al. (2016) proposed a vertical velocity field around the Ordos block, which is inferred from precise leveling observations with a lack of concentration on the contemporary deformation in the West Qinling regions. Additionally, the direct explanation of leveling vertical velocities might be misleading due to the influence of local non-tectonic factors (Hammond et al., 2016; Hao et al., 2016; Hammond et al., 2019).

In this study, a vertical land motion (VLM) model is constructed using a robust imaging method (Hammond et al., 2016; Kreemer et al., 2020) and leveling observations from Hao et al. (2016) with new observations from recent field work. The slip rate and locking coefficients of the West Qinling fault, the longest active fault in West Qinling orogen, are calculated with the GPS velocity field from Hao et al. (2021), and our VLM model. Additionally, the deformation pattern is analyzed based on the 3-D deformation model. This study provides new evidence of strain transformation between horizontal contraction and vertical uplift, which furthers our understanding of the strain pattern in the northeastern Tibetan Plateau.

TECTONIC SETTING

The West Qinling orogen separates the North China block and Lanzhou block from the South China block and Songpan-Ganzi Terrane (**Figures 1A**,**B**; Zheng et al., 2010), and is also recognized as the step-over of the large-scale sinistral Haiyuan and Kunlun faults (**Figure 1**; Yuan et al., 2004), which control the deformation pattern in the northeastern Tibetan Plateau (Kirby et al., 2007; Duvall & Clark, 2010; Yuan et al., 2013; Cheng et al., 2014; Zuza and Yin, 2016). Two small-scale active fault zones, exhibiting low levels of slip, are found along the West Qinling orogen, including the NWW-trending sinistral and NEE-trending dextral fault systems, which signal the diffuse deformation and slip transference along the east end of the Kunlun fault (i.e., Zheng et al., 2016; Zheng et al., 2013).

As the northern boundary of the West Qinling orogen, the nearly W-E striking sinistral West Qinling fault, with a length of ~600 km, separates the Lanzhou (Longxi) block from the West Qinling orogen (**Figure 1B**). The West Qinling fault has experienced a long evolutionary history since the Paleogene. It was initiated as a frontal thrust fault (Clark et al., 2010), and reactivated in the late Quaternary (Li et al., 2007). Field investigations and structural geological data, identify slip rates of ~2.5–2.9 mm/yr (Chen & Lin, 2019), 0.71 ± 0.18 mm/yr (Zheng et al., 2016), and −2.3 ± 0.2 mm/yr (Li et al., 2007) since the Pleistocene. However, contemporary geodetic data indicates slip rates of <1 mm/yr (Hao et al., 2021; Li Y. et al., 2018). Seismic records show that no major earthquakes occurred along the West Qinling fault in the past ~300 years since the 1718 M7.5 Tongwei earthquake.

DATA AND METHODS

GPS horizontal velocities were collected from Hao et al. (2021). The data were obtained from the Crustal Movement Observation Network of China (CMONOC), the National GPS Geodetic Control Network of China (NGGCNC), and the Gansu Bureau of Surveying Mapping and Geoinformation (GBSMG). Parts of the NGGCNC stations were resurveyed by the China Earthquake Administration (CEA) and the Second Monitoring

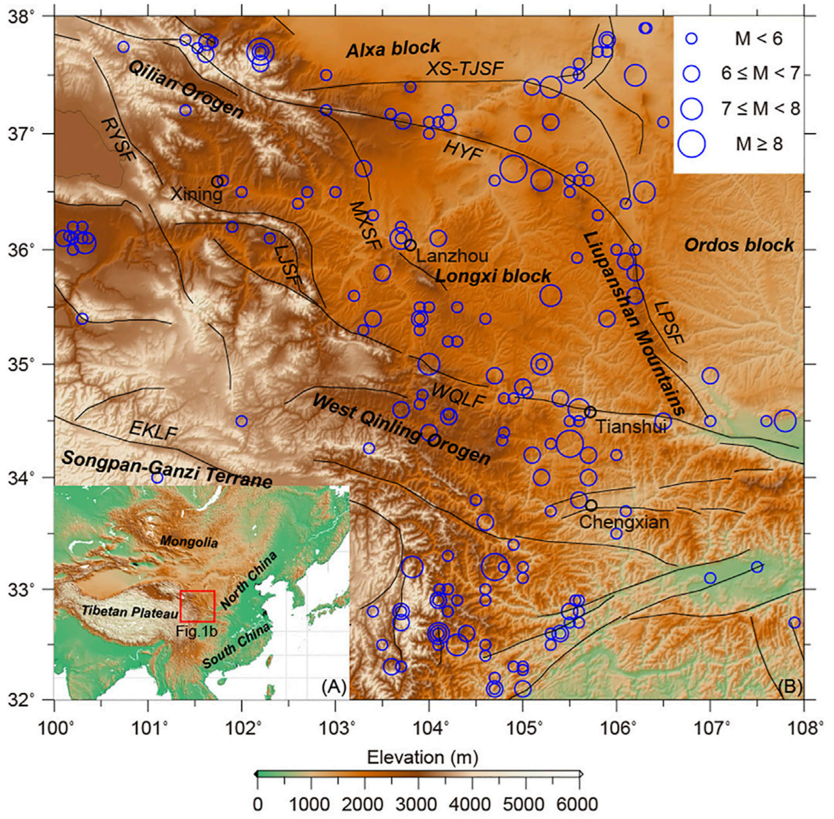

FIGURE 1 | Main tectonic units, active faults, and historic earthquakes with M ≥ 5 since 730 AD from the China Earthquake Datacenter (CEDC) adjacent to the West Qinling Orogen. RYSF: Riyueshan fault; LJSF: Lajishan fault; EKLF: Kunlun fault; MXSF: Maxianshan fault; LPSF: Liupanshan fault; HYF: Haiyuan fault; XS-TJSF: Xiangshan-Tianjingshan fault; WQLF: West Qinling fault.

and Application Center (SMAC). First, the GAMIT package (Herring et al., 2015a) was utilized to process all raw GPS data, containing ~70 International Terrestrial Reference Frame (ITRF) core stations, to obtain loosely daily solutions of satellite orbits, station coordinates, tropospheric zenith delays, and their co-/variances. The geophysical models and parameters used in data processing are shown in Table S1. Second, the GLOBK software (Herring et al., 2015b) was utilized to combine the regional and global daily solutions to estimate station positions and uncertainties, and to convert the loosely daily solutions into the ITRF 2014 (Altamimi et al., 2017). Third, GPS position time series were contaminated by the 2008 *Ms* 8.0 Wenchuan and 2011 *Ms* 9.0 Tohoku-Oki earthquakes (Wang & Shen, 2020). The coseismic displacements from Shen et al. (2009) and Hao and Zhuang, (2020) were therefore interpolated onto GPS sites by utilizing the Kriging method and were used to correct the position time series. Considering the postseismic deformation of the 2008 *Ms* 8.0 Wenchuan earthquake, GPS data measured before 2008 are used for those stations within the postseismic deformation region determined by Wang & Shen (2020). The postseismic deformation of the 2011 Tohoku-Oki earthquake is not significant within our study area, and is thus disregarded. Finally, GPS velocities with respect to ITRF2014 were fitted from the corrected GPS position time series using a linear function (**Equation 1**) and weighted least squares. Here $x(t)$ is the site position time series; x_0 is the initial position at time t_0; v represents station velocity, and D_i is the coseismic (or equipment changes) step at time t_i; $H(t-t_i)$ is the Heaviside function; n_c is the number of earthquakes and equipment changes. Data are then transformed into a regional reference frame with respect to the stable Ordos block using the rotation pole of (75.083°N ± 0.850°, 139.692°W ± 3.701°, 0.352 ± 0.006°/Ma) (**Figure 2A**) provided by Hao et al. (2021).

$$x(t) = x_0 + v(t - t_0) + \sum D_i \mathrm{H}(t - t_i) \tag{1}$$

Parts of the leveling data in Hao et al. (2016) are included. First-order leveling observations were also collected from the National Administration of Surveying, Mapping and Geoinformation (NASMG) resurveyed in 2013, and 500 km leveling routes in the west of the Ordos block observed in 1985/1986/1994 and resurveyed in 2017 and 2018. Vertical velocities (**Figure 2B**) were calculated following Hao et al. (2016), with 37 stable continuous GPS vertical velocities utilized during leveling adjustment to define the reference frame and to reduce systematic errors accumulated during leveling routes (see Hao et al. (2016) for more details). Since the leveling data are sensitive to local environmental effects, such

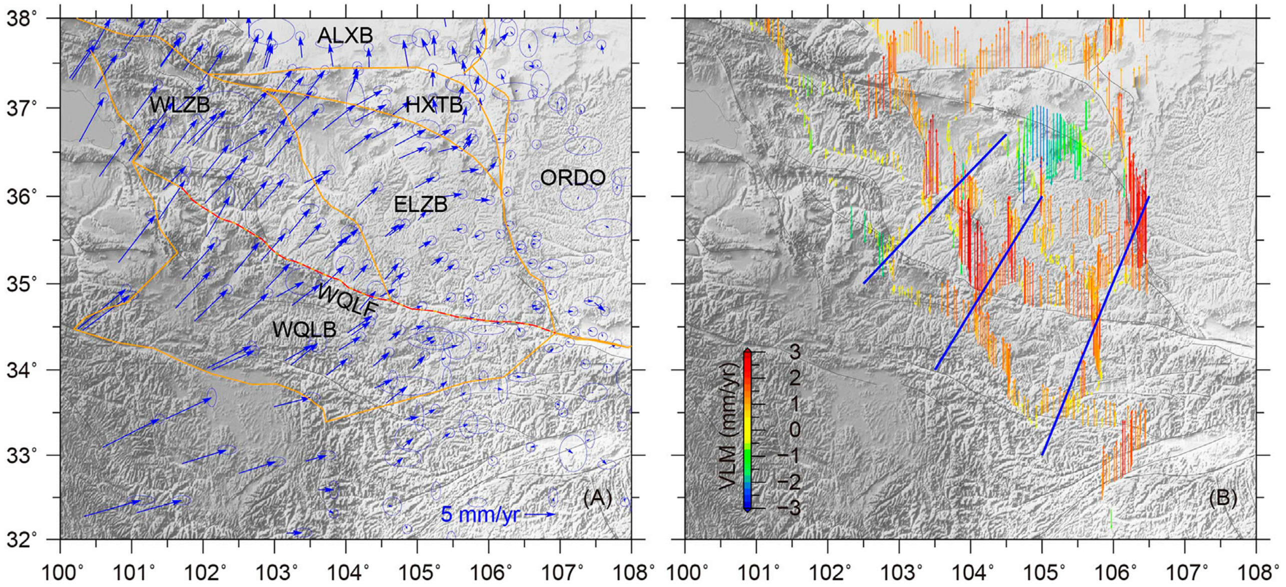

FIGURE 2 | (A) GPS velocity field, relative to the Ordos block, and block models used in this study's inversion. Orange lines indicate block boundaries and the red dashed line denotes the west Qinling active fault. **(B)** Vertical velocities derived from leveling observations. Three blue lines correspond to the profiles presented in **Figure 5**. WLZB: the west Lanzhou (Longxi) block, ELZB: the east Lanzhou (Longxi) block; ORDO: the Ordos block; WQLB: the west Qinling block; ALXB: the Alxa block; HXTB: the block between the Haiyuan and Xiangshan-Tianjingshan faults; WQLF: the west Qinling fault.

as groundwater changes and human activities (Hammond et al., 2016; Hao et al., 2016), we therefore despeckle the velocities with GPS-Imaging, which is robust against outliers, to construct a spatially smoothed VLM model (Hammond et al., 2016; Kreemer et al., 2020; **Figures 3B**, **Supplementary Figure S1**).

RESULTS

Horizontal Deformation From GPS Observations

The GPS horizontal velocity field, with respect to the Ordos block, identifies NNE-directed crustal movement, with significant velocity gradients adjacent to the sinistral Haiyuan and Kunlun faults but not along the West Qinling fault (**Figure 2A**), which suggests large horizontal differential motions along the former faults. Moreover, the velocity vectors decrease significantly to the east of 105°–106°E. To investigate these large velocity gradient belts, the strain rate field is calculated utilizing the Median Estimation of Local Deformation (MELD) algorithm, which is robust against outliers and provides realistic uncertainties (Kreemer et al., 2018, 2020). MELD requires two parameters to calculate the strain rates at grid points from the multivariate median of a set of strain rates from a number of station-based local triangles. The first parameter is the minimum number of the triangles (N_{min}), which we set here to be $N_{min} = 56$, meaning as few as 6 stations can be used to calculate strain rates. The second parameter is the maximum allowed value of σ_{max}, which is based on the theoretical standard deviation in the strain rate for a triangle of stations, based on the triangle's geometry and size. This parameter is used to exclude triangles that are too small and skinny and would be detrimental to the results (Kreemer et al., 2018, 2020). We use $\sigma_{max} = 15 \times 10^{-9}$/yr, which is chosen to calculate the strain rates with a minimum theoretical spatial resolution of ~40 km (**Figure 3D**).

The maximum shear strain rates are 0–30 × 10^{-9}/yr with the largest value existing along the Haiyuan and Kunlun faults (background in **Figure 3A**). These results are consistent with those of Hao and Zhuang, (2020) and Wang & Shen (2020). The dilatation strain rates are −15–15 × 10^{-9}/yr and are dominantly characterized by contraction, with the peak values appearing along the West Qinling and the Qilian orogens (**Figure 3B**). The principal strain rates are oriented with E-/NE-directed contraction and N-/NW-directed extension (**Figure 3A**). In addition, strain rates significantly decrease to the east of 105°–106°E (similar with the GPS velocity field, background in **Figures 3A**,**B**), which may identify the significant deformation regions accommodating the outward expansion of the northeastern Tibetan Plateau (at least in the upper crust) resulting from India-Eurasia convergence being blocked by the rigid Ordos block. The rotation rates in **Figure 3C** (background color) show the clockwise rotation of the West Qinling orogen and the Lanzhou (Longxi) sub-blocks and the anticlockwise rotation of the sub-blocks adjacent to the Haiyuan and Kunlun faults, which are required by the book-shelf kinematic model (i.e., Zuza and Yin, 2016; Cheng et al., 2021).

Vertical Land Motion

The proposed VLM model in **Figure 3B**, **Supplementary Figure S1** shows that the northeastern Tibetan Plateau uplifts at a rate of 0–3 mm/yr, except for the northeastern portion of the east

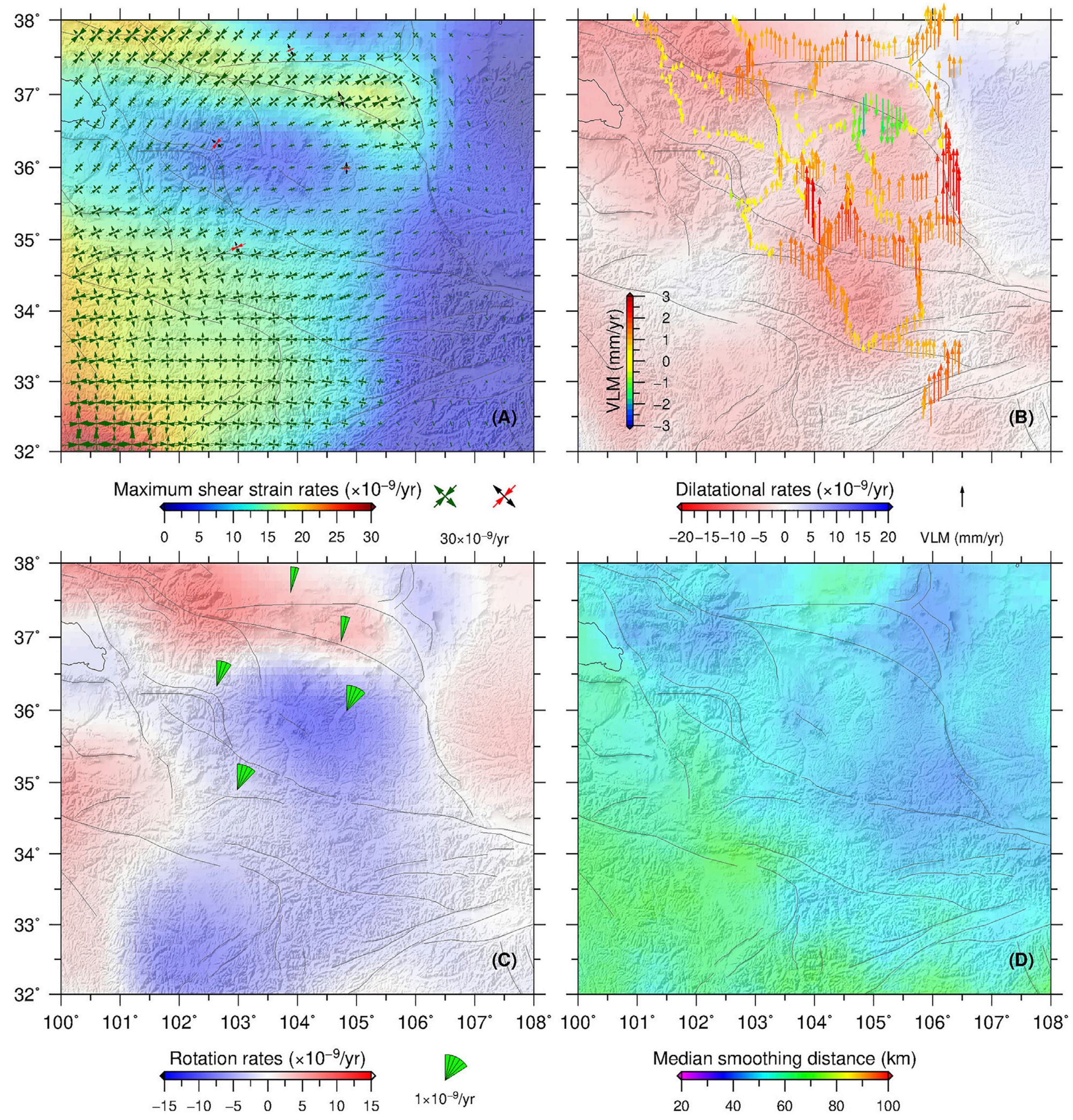

FIGURE 3 | (A) Principal strain rates (darkgreen arrows) and the maximum shear strain rates (background color). Black and red arrows correspond to the block internal principal strain rates determined from TDEFNODE. **(B)** Dilatational strain rates (background color, with the warm color indicating contraction and the cold color denoting dilatation) and vertical land motion model (arrows). **(C)** Rotation rates. Red denotes an anticlockwise rotation, and blue indicates a clockwise rotation. The green fan denotes the rotation rate determined from block models. **(D)** Median smoothing distance.

Lanzhou sub-block (ELZB), where a series of Cenozoic pull-apart basins are present (e.g., the Tianzhu and Ganyanchi basins) due to the sinistral strike-slip of the Haiyuan fault (Tian et al., 2002). The largest uplift rates appear along the Liupanshan fault, which is regarded as the northeastern margin of the outward expansion of the Tibetan Plateau (Li et al., 2017; Du et al., 2018), and the transpressional structure of the Haiyuan active fault to accommodate its sinistral motions (Zheng et al., 2013). Meanwhile, substantial uplift is observed between the central and eastern segments of the West Qinling orogen and the ELZB block, accompanied by large horizontal compression (**Figure 3B**). In the western Lanzhou block (WLZB), the uplift rate is much smaller than that in the ELZB block, which indicates that the strong contraction along the Lajishan fault (LJSF) is transmitted to the Maxianshan fault (MXSF) and/or even further east. The uplift rates along the northern side of the Haiyuan fault are 1–2 mm/yr.

Rigid Block Rotation, Fault Coupling, and Block Internal Deformation

We simultaneously estimate the angular velocities and permanent strain rates within the (sub-) blocks and fault locking parameters of the West Qinling fault using the TDEFNODE program (McCaffrey et al. (2007)). To accomplish this, the study area is divided into seven small (sub-) blocks according to the distribution of active faults and seismicity (**Figures 1**, **2A**): 1) the Ordos block (ORDB, regarded as the reference frame in our inversion), 2) the WLZB, 3) the ELZB, 4) the Alxa block (ALXB), 5) the West Qinling block (WQLB), and 6) the smallest block between the Haiyuan and Xiangshan-Tianjingshan faults (HXTB). Slip vectors (***V)*** of the active fault can be calculated from the angular velocities of adjacent blocks.

In TDENODE, the interseismic elastic deformation adjacent to the fault is denoted by φ (the locking coefficient), which is a purely kinematic, unitless quantity, that represents the instantaneous, spatially averaged creep fraction. $\varphi = 0$ signifies a fully creeping fault, while $\varphi = 1$ indicates a completely locked fault. A φ value between 0 and 1 suggests that the fault is partially locked. Faults are represented in 3-D by nodes distributed on the surface, which is parameterized by longitude, latitude, and depth. The values of φ and slip deficit, defined as $\varphi \boldsymbol{V}$, are calculated at each node.

Block angular velocities, average strain rates, and fault coupling coefficients (φ) are determined using the non-linear simulated annealing and grid search approaches constrained with geodetic observations (McCaffrey et al., 2007). The goodness of fit of a particular set of parameters is based on the reduced χ^2 statistics (**Eq. 2**):

$$\chi_n^2 = (N-P)^{-1}\sum_{1}^{N} p_i, \qquad (2)$$

where N is the number of observations, P is the number of free parameters, and p_i is the misfit penalty function defined by the ratio between the data fitting residuals and data uncertainties. In the inversion, 279 horizontal GPS vectors and 514 vertical rates, derived from leveling observations, are used.

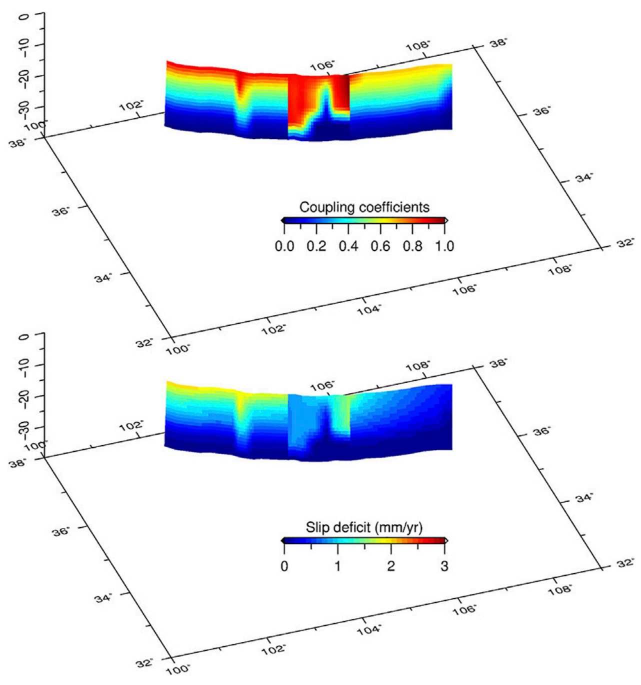

FIGURE 4 | (A) Locking coefficients and **(B)** slip deficit of the WQLF (west Qinling fault) calculated from TDEFNODE and constrained with GPS and VLM observations.

The χ^2 values are 1.03 and 2.1 for the horizontal GPS and vertical velocities respectively, with residuals of horizontal GPS and vertical leveling velocities smaller than 2 mm/yr (**Supplementary Figure S2**). These values are similar to the observed data standard deviations and suggest reliable inversion results. TDEFNODE can only remove an average regional uplift and model uplift due to the locking on the faults (McCaffrey, 2005), resulting in a poor fit to the vertical velocities. **Figures 3A,C** present the rotation rates and internal deformation of the (sub-) blocks. The internal permanent strain rates of each (sub-) block (red arrows in **Figure 3A**) are pretty similar to the strain rates calculated from MELD (dark green arrows in **Figure 3A**). Our results identify clockwise rotations of the ELZB, WLZB, and WQLB relative to the ORDO block with rotation rates of −0.028°/Myr, −0.063°/Myr, −0.040°/Myr (green fans in **Figure 3C**, with negative value indicating clockwise rotation), with the exception of the ALXA block. **Figures 4A,B** show the locking coefficients and slip deficit of the West Qinling fault. Average locking depths of the West Qinling fault are 6.6, 6.8, and 6.1 km from west to east with slip deficits of 1.2 mm/yr, 1.1 mm/yr, and 1.1 mm/yr respectively. In **Figures 4**, the regions of strongest coupling are located within the central and the western segments of the West Qinling fault, suggesting high seismic risks (Ma et al., 2017).

DISCUSSION

Slip Rates and Seismicity of the West Qinling Fault

Slip rates of 1.5 ± 0.4 mm/yr to 1.7 ± 0.3 mm/yr are identified for the West Qinling fault, which are larger than previous geodetic and geologic evidence-based estimates of 0.4 ± 0.3 mm/yr (Hao and Zhuang, 2020), 0.71 ± 0.18 mm/yr (Zheng et al., 2016), and 0.8 mm/yr (Li Y. et al., 2018). However, these values are smaller than the geologically derived slip rates of 2–3 mm/yr (Li et al., 2007; Chen & Lin, 2019). Slip rates of the West Qinling fault are far smaller than other NWW-directed sinistral active faults within the region, such as the Kunlun fault, which exhibits slip of 2.0 ± 0.4 mm/yr along its eastern segment to

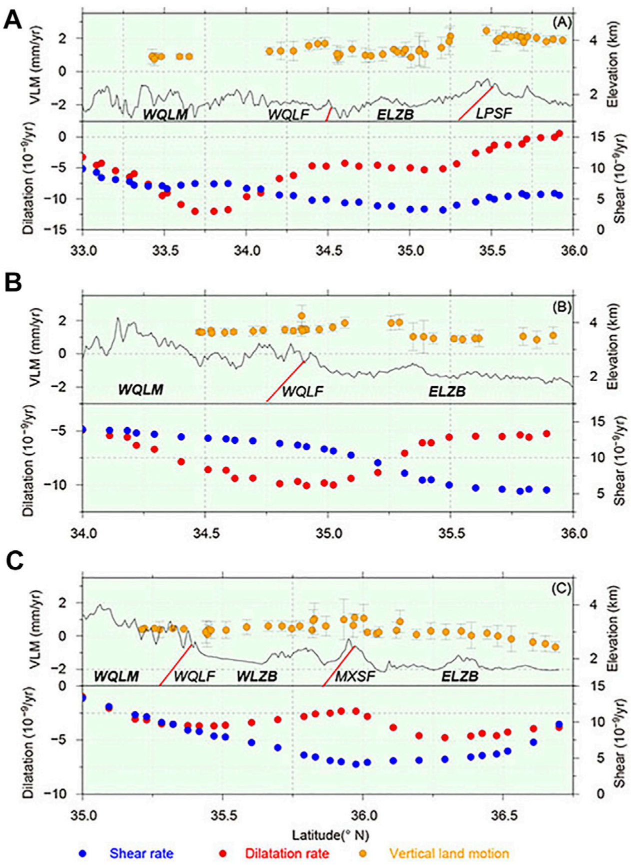

FIGURE 5 | Strain rate (dilatation and shear) and VLM (Vertical Land Motion) profiles perpendicular to the west Qinling fault. **(A,B,C)** represent the east, central, and west profiles in **Figure 2B**, respectively. Blue, red, and orange dots denote the shear strain rate, dilatation strain rate, and uplift rates. The red bold lines represent the active faults. The gray bold line denotes the topography. WQLM: west Qinling Mountains, WQLF: the west Qinling fault; ELZB: the east Lanzhou block; LPSF: the Liupanshan fault; WLZB: the west Lanzhou fault; MXSF: the Maxianshan fault.

~16 mm/yr along its western segment (Kirby et al., 2007; Harkins & Kirby, 2008; Harkins et al., 2010; Loveless & Meade, 2011), and the Haiyuan fault with 1–3 mm/yr along the western segment to 8–10 mm/yr along the eastern segment (Hao and Zhuang, 2020; Li Y. et al., 2018; Loveless & Meade, 2011; Yao et al., 2019; Yuan et al., 2013). The slow slip of the West Qinling fault can be related to limited convergence transfer and that a majority of the strain has likely been absorbed and partitioned by crustal shortening, block rotation, and east-west stretching along the West Qinling orogen (Chen & Lin, 2019; Cheng et al., 2021; Zheng et al., 2016).

Due to the lack of major earthquakes in the last 300 years, the seismic risk of the West Qinling fault has drawn much attention in recent decades. Wang et al. (2011) suggested that there is an *Mw*7.7 moment magnitude deficit in the last 400 years. However, this study might overestimate the slip rate of the West Qinling fault with a value of 2–3 mm/yr, which is 3.7 ± 1.8 mm/yr, compared to results in these few years based on modern dense GPS observations (i.e., Hao and Zhuang, 2020; Li Y. et al., 2018). In this study, the moment deficit of the West Qinling fault is recalculated according to the equation, $M_0 = \mu DA$, based on the determined average locking depth and slip deficit (**Figure 4**), where the shear modulus is assumed to be 30 GPa. This yields an accumulated seismic moment of 1.8×10^{20} N·m (or 1.35×10^{20} N·m) for the past 400 (or 300) years, corresponding to an earthquake with a moment magnitude of *Mw*7.4 (or *Mw*7.35), which is smaller than estimated by Wang et al. (2011).

Strain Transformation and Tectonic Uplift Adjacent to the West Qinling Orogen

Three coexisting end-member models exist to explain the uplift mechanism of the northeastern Tibetan Plateau, where the West Qinling orogen and Liupanshan Mountains are included: 1) strain transformation from horizontal contraction to vertical uplift induced from India-Eurasia oblique convergence (e.g., Tapponnier, 2001; Allen et al., 2017), 2) eastward flow of middle-to-lower crustal materials (Royden, 1997; Royden et al., 2008; Wang et al., 2018), and 3) changes in the balance between stress gradients and body forces, resulting from the removal of lithospheric materials due to asthenospheric flow, and have produced significant topographic relief (England & Houseman, 1989; Molnar et al., 1993; Ye et al., 2017). The latest, dense 3-D geodetic observations provide a new opportunity to reanalyze these models. To identify contemporary crustal deformation features in this region, three vertical velocity and horizontal strain rate profiles are produced, together with the topography along the West Qinling Mountains normal to the West Qinling fault (**Figures 2B**, **5**).

The profiles identify contraction strain rates (red dots in **Figure 5**) ranging between 0 and -12.5×10^{-9}/yr combined with 1–2 mm/yr of uplift (orange dots with gray bars in **Figure 5**), suggesting transformation of strain from crustal contraction to vertical uplift. Assuming that the volume is conserved, the sum of the three principal strain rates should be zero, and contraction should be equal to, or at least proportional to, uplift (Lease et al., 2012; Ge et al., 2015). Considering a crustal thickness of ~50 km in the northeastern Tibetan Plateau (Guo & Chen, 2017; Ye et al., 2017), the observed contraction can produce maximum uplift of 0.625 mm/yr, consistent with the <1 mm/yr from continuous GPS observations (Su et al., 2018), but smaller than 1–2 mm/yr from our VLM model.

Volumetric conservation requires consistency between the crustal contraction and uplift, however, the opposite relationship is observed in **Figure 5**, where the largest contraction occurs along with the smallest uplift (at the lowest elevations) and vice versa, especially adjacent to the West Qinling and Liupanshan Mountains, which are also presented in GPS vertical velocities (Su et al., 2018). A possible explanation may come from the different origins of vertical lithospheric stress. To analyze the lithospheric flexure mechanism in the northeastern Tibetan Plateau, Wang et al. (2018) and She et al. (2016) estimated the effective elastic thickness (Te) and loading ratios based on Gravity and GPS hybrid measurements. Their results show that loading ratios of the West Qinling orogen (F1 = 0.19, F2 = 0.42 and F3 = 0.39), with F1, F2 and F3 implying initial loading resulting from the Earth's surface, the interface between the upper and lower crust, and the Moho, suggesting that the initial loading is primarily attributed to the lower crust (i.e., lower crustal materials flow); however, loading ratio of the Liupanshan Mountains (F1 = 0.95; F2 = 0.05; F3 = 0) indicates that initial loading is primarily attributed to the surface (i.e., strain transformation from crustal contraction to uplift/thickening). Although the existence of middle-to-lower crustal material flow and its contributions to tectonic uplift remain contested (e.g., Lease et al., 2012), seismic tomography identifies complex deep structures beneath the West Qinling orogen and Liupanshan Mountains, i.e., low S-wave velocity underneath the West Qinling orogen at depths of 15–30 km (Yang et al., 2012), low shear-wave velocity in the middle-lower crust but high seismic velocity in the upper crust beneath the West Qinling orogen (Bao et al., 2013), a broad low-velocity zone in the middle-to-lower crust beneath the northeastern Tibetan Plateau (Guo & Chen, 2017; Li S. et al., 2018; Ye et al., 2017), and a complex double Moho structure exists induced from the superposition of the rigid Ordos and the relatively soft northeastern Tibet crust (Li et al., 2017). Therefore, despite quantifying relative contributions from different mechanisms of lithospheric flexure, which still require further investigation (i.e., She et al., 2017; Wang et al., 2018), this study suggests that the strain transformation in the upper crust and complex middle-to-lower crustal structures underneath, control the complex tectonic uplift and geomorphologic/topographic features adjacent to the West Qinling Orogen; i.e., generation of two sets of small-scale active faults, development of several Cenozoic basins (e.g., the Guide, Tongren, Wushan basins; Zheng et al., 2016), and the uplift of the West Qinling Mountains.

Implications for the Outward Growth of the Northeastern Tibetan Plateau

The expansion direction and passage of the northeastern Tibetan Plateau have been contested for decades. In one aspect, some studies suggest that the crustal materials in the northeastern Tibetan Plateau are escaping eastward along the Qinling Mountains and/or beneath the Ordos block (Li S. et al., 2018; Royden et al., 2008; Royden, 1997; Yu & Chen, 2016). Meanwhile, others highlight that the deformation is mainly limited within the plateau and is accommodated by crustal shortening, block rotation, fault movements, and mountain building (Cheng et al., 2015, 2021; Hao et al., 2021; Kirby et al., 2007; Li Y. et al., 2018; Zheng et al., 2016; Zuza and Yin, 2016).

The 3-D crustal deformation model presented in this study indicates that crustal deformation in the northeastern Tibetan plateau is primarily characterized by horizontal contraction, as large as 15×10^{-9}/yr, as well as vertical uplift/thickening, with the magnitude of 0–3 mm/yr. GPS velocities, with respect to the Ordos block, show significant NNE-ward crustal movement instead of eastward materials escape. These observations support the latter and highlight the importance of strain transformation between horizontal crustal shortening and vertical uplift to accommodate crustal deformation induced from outward growth of the northeastern Tibetan Plateau. Additionally, middle-to-lower crustal material expansion (e.g., middle-to-lower crustal flow) may also have some contributions, especially underneath the West Qinling orogen, which requires further investigations to confirm. Both strain rates and GPS velocities identify a deformation gradient belt at longitudes 105°–106°E, which distinguish significant deformation regions accommodating outward expansion of the northeastern Tibetan Plateau. While we are unable to exclude potential contributions of eastward materials escape, it appears to be inconsequential to our 3-D crustal deformation model (**Figures 2A**, **3A,B**).

CONCLUSION

This study constructed a VLM model based on leveling observations adjacent to the West Qinling orogen, identifying uplift rates of 0–3 mm/yr within this region. Combined with the horizontal strain rate field, this study suggests that strain transformation has played an important role in controlling the tectonic uplift of the West Qinling orogen. Moreover, slip rate and locking coefficients were inverted and the moment deficit of the West Qinling fault was calculated. The West Qinling fault slips slowly at a rate of 1–2 mm/yr and is strongly locked with average locking depths of 6.6, 6.8, and 6.1 km in its western, central, and eastern segments. This equates to a moment magnitude deficit of *Mw*7.4. Additionally, results identify a significant deformation transition belt at the longitude of 105°–106°E, which indicates that the deformation of the northeastern Tibetan Plateau is primarily limited to within the plateau, rather than being accommodated by crustal materials that are escaping eastward along the Qinling orogen.

DATA AVAILABILITY STATEMENT

The raw data supporting the conclusions of this article will be made available by the authors, without undue reservation.

AUTHOR CONTRIBUTIONS

ZL designed the study and did all the calculations in the paper. ZL wrote the paper, with contributions of FC and ZY. MH and WZ processed the GPS data. SS and FY processed the leveling data.

FUNDING

This work got funded by the National Key Research and Development Program of China (2017YFC1500102) and National Natural Science Foundation of China (42002234, 41874017, 41474090, and 41874024).

ACKNOWLEDGMENTS

We sincerely thank Associate Editor David K. Wright and two reviewers for their help improving the manuscript. We thank all the staff of Crustal Movement Observation Network of China (CMONOC), the National GPS Geodetic Control Network of China (NGGCNC), the Gansu Bureau of Surveying Mapping and Geoinformation (GBSMG), and the National Administration of Surveying, Mapping and Geoinformation (NASMG) for their hardworking to get the data. All figures were created using Generic Mapping Tools (Wessel and Smith, 1998). The Earthquake catalogs are from China Earthquake Datacenter (http://data.earthquake.cn/) and GCMT (https://www.globalcmt.org/).

SUPPLEMENTARY MATERIAL

The Supplementary Material for this article can be found online at: https://www.frontiersin.org/articles/10.3389/feart.2021.689087/full#supplementary-material

REFERENCES

Allen, M. B., Walters, R. J., Song, S., Saville, C., De Paola, N., Ford, J., et al. (2017). Partitioning of Oblique Convergence Coupled to the Fault Locking Behavior of Fold-And-Thrust Belts: Evidence from the Qilian Shan, Northeastern Tibetan Plateau. *Tectonics* 36 (9), 1679–1698. doi:10.1002/2017TC004476

Altamimi, Z., Métivier, L., Rebischung, P., Rouby, H., and Collilieux, X. (2017). ITRF2014 Plate Motion Model. *Geophys. J. Int.* 209, 1906–1912. doi:10.1093/gji/ggx136

Bai, D., Unsworth, M. J., Meju, M. A., Ma, X., Teng, J., Kong, X., et al. (2010). Crustal Deformation of the Eastern Tibetan Plateau Revealed by Magnetotelluric Imaging. *Nat. Geosci.* 3 (5), 358–362. doi:10.1038/ngeo830

Bao, X., Song, X., Xu, M., Wang, L., Sun, X., Mi, N., et al. (2013). Crust and Upper Mantle Structure of the North China Craton and the NE Tibetan Plateau and its Tectonic Implications. *Earth Planet. Sci. Lett.* 369-370, 129–137. doi:10.1016/j.epsl.2013.03.015

Bao, X., Sun, X., Xu, M., Eaton, D. W., Song, X., Wang, L., et al. (2015). Two Crustal Low-Velocity Channels beneath SE Tibet Revealed by Joint Inversion of Rayleigh Wave Dispersion and Receiver Functions. *Earth Planet. Sci. Lett.* 415, 16–24. doi:10.1016/j.epsl.2015.01.020

Chen, P., and Lin, A. (2019). Tectonic Topography and Late Pleistocene Activity of the West Qinling Fault, Northeastern Tibetan Plateau. *J. Asian Earth Sci.* 176, 68–78. doi:10.1016/j.jseaes.2019.02.007

Cheng, F., Jolivet, M., Dupont-Nivet, G., Wang, L., Yu, X., and Guo, Z. (2015). Lateral Extrusion along the Altyn Tagh Fault, Qilian Shan (NE Tibet): Insight from a 3D Crustal Budget. *Terra Nova* 27 (6), 416–425. doi:10.1111/ter.12173

Cheng, F., Jolivet, M., Fu, S., Zhang, Q., Guan, S., Yu, X., et al. (2014). Northward Growth of the Qimen Tagh Range: A New Model Accounting for the Late Neogene Strike-Slip Deformation of the SW Qaidam Basin. *Tectonophysics* 632, 32–47. doi:10.1016/j.tecto.2014.05.034

Cheng, F., Zuza, A. V., Haproff, P. J., Wu, C., Neudorf, C., Chang, H., et al. (2021). Accommodation of India-Asia Convergence via Strike-Slip Faulting and Block Rotation in the Qilian Shan Fold-Thrust belt, Northern Margin of the Tibetan Plateau. *J. Geol. Soc.* 178, jgs2020–207. doi:10.1144/jgs2020-207

Chung, S.-L., Lo, C.-H., Lee, T.-Y., Zhang, Y., Xie, Y., Li, X., et al. (1998). Diachronous Uplift of the Tibetan Plateau Starting 40?Myr Ago. *Nature* 394 (6695), 769–773. doi:10.1038/29511

Clark, M. K., Farley, K. A., Zheng, D., Wang, Z., and Duvall, A. R. (2010). Early Cenozoic Faulting of the Northern Tibetan Plateau Margin from Apatite (U-Th)/He Ages. *Earth Planet. Sci. Lett.* 296 (1), 78–88. doi:10.1016/j.epsl.2010.04.051

Du, F., Wen, X., Feng, J., Liang, M., Long, F., and Wu, J. (2018). Seismo-tectonics and Seismic Potential of the Liupanshan Fault Zone (LPSFZ), China. *Chin. J. Geophys.* 61 (2), 545–559. (in Chinese with English abstract). doi:10.6038/cjg2018L0181

Duvall, A. R., and Clark, M. K. (2010). Dissipation of Fast Strike-Slip Faulting within and beyond Northeastern Tibet. *Geology* 38 (3), 223–226. doi:10.1130/G30711.1

England, P., and Houseman, G. (1989). Extension during continental Convergence, with Application to the Tibetan Plateau. *J. Geophys. Res.* 94 (B12), 17561. doi:10.1029/JB094iB12p17561

England, P., Houseman, G., and Sonder, L. (1985). Length Scales for continental Deformation in Convergent, Divergent, and Strike-Slip Environments: Analytical and Approximate Solutions for a Thin Viscous Sheet Model. *J. Geophys. Res.* 90 (B5), 3551. doi:10.1029/JB090iB05p03551

England, P., and Molnar, P. (1990). Right-lateral Shear and Rotation as the Explanation for Strike-Slip Faulting in Eastern Tibet. *Nature* 344 (6262), 140–142. doi:10.1038/344140a0

Gan, W., Zhang, P., Shen, Z.-K., Niu, Z., Wang, M., Wan, Y., et al. (2007). Present-day Crustal Motion within the Tibetan Plateau Inferred from GPS Measurements. *J. Geophys. Res.* 112 (B8), B08416. doi:10.1029/2005JB004120

Ge, W.-P., Molnar, P., Shen, Z.-K., and Li, Q. (2015). Present-day Crustal Thinning in the Southern and Northern Tibetan Plateau Revealed by GPS Measurements. *Geophys. Res. Lett.* 42 (13), 5227–5235. doi:10.1002/2015GL064347

Guo, Z., and Chen, Y. J. (2017). Mountain Building at Northeastern Boundary of Tibetan Plateau and Craton Reworking at Ordos Block from Joint Inversion of Ambient Noise Tomography and Receiver Functions. *Earth Planet. Sci. Lett.* 463, 232–242. doi:10.1016/j.epsl.2017.01.026

Hammond, W. C., Blewitt, G., and Kreemer, C. (2016). GPS Imaging of Vertical Land Motion in California and Nevada: Implications for Sierra Nevada Uplift. *J. Geophys. Res. Solid Earth* 121 (10), 7681–7703. doi:10.1002/2016JB013458

Hammond, W. C., Kreemer, C., Zaliapin, I., and Blewitt, G. (2019). Drought-Triggered Magmatic Inflation, Crustal Strain, and Seismicity Near the Long Valley Caldera, Central Walker Lane. *J. Geophys. Res. Solid Earth* 124 (6), 6072–6091. doi:10.1029/2019JB017354

Hao, M., Li, Y., Wang, Q., Zhuang, W., and Qu, W. (2021). Present-Day Crustal Deformation within the Western Qinling Mountains and its Kinematic Implications. *Surv. Geophys.* 42 (1), 1–19. doi:10.1007/s10712-020-09621-5

Hao, M., Wang, Q., Cui, D., Liu, L., and Zhou, L. (2016). Present-Day Crustal Vertical Motion Around the Ordos Block Constrained by Precise Leveling and GPS Data. *Surv. Geophys.* 37 (5), 923–936. doi:10.1007/s10712-016-9375-1

Hao, M., and Zhuang, W. Q. (2020). The Impact of the Great 2011 Tohoku-Oki Earthquake on Crustal Deformation in Eastern China. *Geodesy and Geodynamics* 40 (6), 138–142. (in Chinese with English Abstract). doi:10.14075/j.jgg.2020.06.002

Harkins, N., and Kirby, E. (2008). Fluvial Terrace Riser Degradation and Determination of Slip Rates on Strike-Slip Faults: An Example from the Kunlun Fault, China. *Geophys. Res. Lett.* 35 (5), L05406. doi:10.1029/2007GL033073

Harkins, N., Kirby, E., Shi, X., Wang, E., Burbank, D., and Chun, F. (2010). Millennial Slip Rates along the Eastern Kunlun Fault: Implications for the Dynamics of Intracontinental Deformation in Asia. *Lithosphere* 2 (4), 247–266. doi:10.1130/L85.1

Herring, T. A., King, R. W., and McClusky, S. C. (2015b). *GAMIT Reference Manual, Global Kalman Filter VLBI and GPS Analysis Program*. Cambridge: Massachusetts Institute of Technology. Release 10.6.

Herring, T. A., King, R. W., and McClusky, S. C. (2015a). *GAMIT Reference Manual, GPS Analysis at MIT*. Cambridge: Massachusetts Institute of Technology. Release10.6.

Kirby, E., and Harkins, N. (2013). Distributed Deformation Around the Eastern Tip of the Kunlun Fault. *Int. J. Earth Sci.* 102, 1759–1772. doi:10.1007/s00531-013-0872-x

Kirby, E., Harkins, N., Wang, E., Shi, X., Fan, C., and Burbank, D. (2007). Slip Rate Gradients along the Eastern Kunlun Fault: KUNLUN FAULT, SLIP RATE, TIBET. *Tectonics* 26 (2), na. doi:10.1029/2006TC002033

Kreemer, C., Blewitt, G., and Davis, P. M. (2020). Geodetic Evidence for a Buoyant Mantle Plume beneath the Eifel Volcanic Area, NW Europe. *Geophys. J. Int.* 222 (2), 1316–1332. doi:10.1093/gji/ggaa227

Kreemer, C., Hammond, W. C., and Blewitt, G. (2018). A Robust Estimation of the 3-D Intraplate Deformation of the North American Plate from GPS. *J. Geophys. Res. Solid Earth* 123 (5), 4388–4412. doi:10.1029/2017JB015257

Lease, R. O., Burbank, D. W., Zhang, H., Liu, J., and Yuan, D. (2012). Cenozoic Shortening Budget for the Northeastern Edge of the Tibetan Plateau: Is Lower

Crustal Flow Necessary?: NE Tibetan PLATEAU CRUSTAL SHORTENING. *Tectonics* 31 (3), na. doi:10.1029/2011TC003066

Li, C. Y., Zhang, P. Z., Zhang, J. X., Yuan, D. Y., and Wang, Z. C. (2007). Late-Quaternary Activity and Slip Rate of the Western Qinling Fault Zone at Huangxianggou Segment. *Qua. Sci.* 27, 54–63. (in Chinese with English abstract). doi:10.1016/S1872-5791(07)60044-X

Li, S., Guo, Z., Chen, Y. J., Yang, Y., and Huang, Q. (2018a). Lithospheric Structure of the Northern Ordos from Ambient Noise and Teleseismic Surface Wave Tomography. *J. Geophys. Res. Solid Earth* 123, 6940–6957. doi:10.1029/2017JB015256

Li, W., Gao, R., Wang, H., Li, Y., Li, H., Hou, H., et al. (2017). Crustal Structure beneath the Liupanshan Fault Zone and Adjacent Regions. *Chin. J. Geophys.* 60 (6), 2265–2278. (in Chinese with English abstract). doi:10.6038/cjg20170619

Li, Y., Liu, M., Wang, Q., and Cui, D. (2018b). Present-day Crustal Deformation and Strain Transfer in Northeastern Tibetan Plateau. *Earth Planet. Sci. Lett.* 487, 179–189. doi:10.1016/j.epsl.2018.01.024

Li, Z., Wang, Y., Gan, W., Fang, L., Zhou, R., Seagren, E. G., et al. (2020). Diffuse Deformation in the SE Tibetan Plateau: New Insights from Geodetic Observations. *J. Geophys. Res. Solid Earth* 125 (10). doi:10.1029/2020JB019383

Loveless, J. P., and Meade, B. J. (2011). Partitioning of Localized and Diffuse Deformation in the Tibetan Plateau from Joint Inversions of Geologic and Geodetic Observations. *Earth Planet. Sci. Lett.* 303 (1–2), 11–24. doi:10.1016/j.epsl.2010.12.014

Ma, H., Wu, Y., Feng, J. G., Xu, R., Wu, S., and Wang, Q. (2017). Research on Recent GPS Crustal Deformation Characteristics in the Northeastern Edge of Qinghai-Tibet Plateau. *J. Phys. Conf. Ser.* 910, 012028. doi:10.1088/1742-6596/910/1/012028

Ma, S. X., Zhang, Y. Q., Li, H. L., and Li, J. H. (2013). The Tectonic Extrusion of NE Tibet in Late Neogene Time: Evidence from Anhua-Chengxian basin in West Qinling. *Earth Sci. Front.* 20 (4), 58–74. (in Chinese with English abstract).

McCaffrey, R. (2005). Block Kinematics of the Pacific-North America Plate Boundary in the Southwestern United States from Inversion of GPS, Seismological, and Geologic Data. *J. Geophys. Res.* 110 (B7), B07401. doi:10.1029/2004JB003307

McCaffrey, R., Qamar, A. I., King, R. W., Wells, R., Khazaradze, G., Williams, C. A., et al. (2007). Fault Locking, Block Rotation and Crustal Deformation in the Pacific Northwest. *Geophys. J. Int.* 169 (3), 1315–1340. doi:10.1111/j.1365-246X.2007.03371.x

Molnar, P., England, P., and Martinod, J. (1993). Mantle Dynamics, Uplift of the Tibetan Plateau, and the Indian Monsoon. *Rev. Geophys.* 31 (4), 357. doi:10.1029/93RG02030

Molnar, P., and Tapponnier, P. (1975). Cenozoic Tectonics of Asia: Effects of a Continental Collision: Features of Recent continental Tectonics in Asia Can Be Interpreted as Results of the India-Eurasia Collision. *Science* 189 (4201), 419–426. doi:10.1126/science.189.4201.419

Reilinger, R., McClusky, S., Vernant, P., Lawrence, S., Ergintav, S., Cakmak, R., et al. (2006). GPS Constraints on continental Deformation in the Africa-Arabia-Eurasia continental Collision Zone and Implications for the Dynamics of Plate Interactions: EASTERN MEDITERRANEAN ACTIVE TECTONICS. *J. Geophys. Res. Solid Earth* 111 (B5), na. doi:10.1029/2005JB004051

Royden, L. H., Burchfiel, B. C., King, R. W., Wang, E., Chen, Z., Shen, F., et al. (1997). Surface Deformation and Lower Crustal Flow in Eastern Tibet. *Science* 276 (5313), 788–790. doi:10.1126/science.276.5313.788

Royden, L. H., Burchfiel, B. C., and van der Hilst, R. D. (2008). The Geological Evolution of the Tibetan Plateau. *Science* 321 (5892), 1054–1058. doi:10.1126/science.1155371

Ruddiman, W. (1998). Early Uplift in Tibet?. *Nature* 394, 723–725. doi:10.1038/29401

She, Y., Fu, G., Su, X., Meng, G., Zhu, Y., Guo, S., et al. (2016). Crustal Isostasy and Uplifting Mechanism of the Liupanshan Area. *Prog. Geophys.* 31 (4), 1464–1472. (in Chinese with English abstract). doi:10.6038/pg20160408

Shen, Z.-K., Sun, J., Zhang, P., Wan, Y., Wang, M., Bürgmann, R., et al. (2009). Slip Maxima at Fault Junctions and Rupturing of Barriers during the 2008 Wenchuan Earthquake. *Nat. Geosci* 2, 718–724. doi:10.1038/ngeo636

Su, X., Yao, L., Wu, W., Meng, G., Su, L., Xiong, R., et al. (2018). Crustal Deformation on the Northeastern Margin of the Tibetan Plateau from Continuous GPS Observations. *Remote Sensing* 11 (1), 34. doi:10.3390/rs11010034

Tapponnier, P. (2001). Oblique Stepwise Rise and Growth of the Tibet Plateau. *Science* 294 (5547), 1671–1677. doi:10.1126/science.105978

Tapponnier, P., Peltzer, G., Dain, A. Y. L., Armijo, R., and Cobbold, P. (1982). Propagating Extrusion Tectonics in Asia: New Insights from Simple Experiments with Plasticine. *Geology* 10 (12), 611–616. doi:10.1130/0091-7613(1982)10<611:PETIAN>2.0.CO;2

Tian, Q. J., Ding, G. Y., and Shen, X. H. (2002). Pull-apart Basins and the Total Lateral Displacement along the Haiyuan Fault Zone in Cenozoic. *Earth Res. China* 17 (2), 167–175. (in Chinese with English abstract). doi:10.3969/j.issn.1001-4683.2001.02.007

Wang, H., Liu, M., Cao, J., Shen, X., and Zhang, G. (2011). Slip Rates and Seismic Moment Deficits on Major Active Faults in mainland China. *J. Geophys. Res.* 116 (B2), B02405. doi:10.1029/2010JB007821

Wang, M., and Shen, Z. K. (2020). Present-Day Crustal Deformation of Continental China Derived from GPS and its Tectonic Implications. *J. Geophys. Res. Solid Earth* 125 (2), e2019JB018774. doi:10.1029/2019JB018774

Wang, Z., Fu, G., and She, Y. (2018). Crustal Density Structure, Lithosphere Flexure Mechanism, and Isostatic State throughout the Qinling Orogen Revealed by *In Situ* Dense Gravity Observations. *J. Geophys. Res. Solid Earth* 123 (11), 10026–10039. doi:10.1029/2018JB016117

Wessel, P., and Smith, W. F. H (1998). New, improved version of Generic Mapping Tools released, EOS Trans. *AGU* 79 (47), 579. doi:10.1029/98EO00426

Yang, Y., Ritzwoller, M. H., Zheng, Y., Shen, W., Levshin, A. L., and Xie, Z. (2012). A Synoptic View of the Distribution and Connectivity of the Mid-crustal Low Velocity Zone beneath Tibet. *J. Geophys. Res.* 117 (B4), a–n. doi:10.1029/2011jb008810

Yao, W., Liu-Zeng, J., Oskin, M. E., Wang, W., Li, Z., Prush, V., et al. (2019). Reevaluation of the Late Pleistocene Slip Rate of the Haiyuan Fault Near Songshan, Gansu Province, China. *J. Geophys. Res. Solid Earth* 124 (5), 5217–5240. doi:10.1029/2018JB016907

Ye, Z., Li, J., Gao, R., Song, X., Li, Q., Li, Y., et al. (2017). Crustal and Uppermost Mantle Structure across the Tibet-Qinling Transition Zone in NE Tibet: Implications for Material Extrusion beneath the Tibetan Plateau. *Geophys. Res. Lett.* 44 (20), 316–410. doi:10.1002/2017GL075141

Yu, Y., and Chen, Y. J. (2016). Seismic Anisotropy beneath the Southern Ordos Block and the Qinling-Dabie Orogen, China: Eastward Tibetan Asthenospheric Flow Around the Southern Ordos. *Earth Planet. Sci. Lett.* 455, 1–6. doi:10.1016/j.epsl.2016.08.026

Yuan, D. Y., Ge, W. P., Chen, Z. W., Li, C. Y., Wang, Z. C., Zhang, H. P., et al. (2013). The Growth of Northeastern Tibet and its Relevance to Large-scale continental Geodynamics: A Review of Recent Studies. *Tectonics* 32 (5), 1358–1370. doi:10.1002/tect.20081

Yuan, D. Y., Zhang, P. Z., Liu, B. C., Gan, W. J., Mao, F. Y., Wang, Z. C., et al. (2004). Geometrical Imagery and Tectonic Transformation of Late Quaternary Active Tectonics in Northwestern Margin of Qinghai- Xizang Plateau. *Acta Geol. Sin* 78 (2), 270–278. (in Chinese with English abstract).

Zhang, P. Z., Shen, Z., Wang, M., Gan, W., Bürgmann, R., Molnar, P., et al. (2004). Continuous Deformation of the Tibetan Plateau from Global Positioning System Data. *Geol.* 32 (9), 809. doi:10.1130/G20554.1

Zheng, J. P., Griffin, W. L., Sun, M., O'Reilly, S. Y., Zhang, H. F., Zhou, H. W., et al. (2010). Tectonic Affinity of the West Qinling Terrane (central China): North China or Yangtze?: TECTONIC AFFINITY of the WEST QINLING TERRANE. *Tectonics* 29 (2), na. doi:10.1029/2008TC002428

Zheng, W. J., Zhang, P. Z., He, W. G., Yuan, D. Y., Shao, Y. X., Zheng, D. W., et al. (2013). Transformation of Displacement between Strike-Slip and Crustal Shortening in the Northern Margin of the Tibetan Plateau: Evidence from Decadal GPS Measurements and Late Quaternary Slip Rates on Faults. *Tectonophysics* 584, 267–280. doi:10.1016/j.tecto.2012.01.006

Zheng, W. J., Liu, X. W., Yu, J. X., Yuan, D. Y., Zhang, P. Z., Ge, W. P., et al. (2016). Geometry and Late Pleistocene Slip Rates of the Liangdang-Jiangluo Fault in the Western Qinling Mountains, NW China. *Tectonophysics* 687, 1–13. doi:10.1016/j.tecto.2016.08.021

Zuza, A. V., and Yin, A. (2016). Continental Deformation Accommodated by Non-rigid Passive Bookshelf Faulting: An Example from the Cenozoic Tectonic Development of Northern Tibet. *Tectonophysics* 677-678, 227–240. doi:10.1016/j.tecto.2016.04.007

frontiers in Earth Science

ORIGINAL RESEARCH
published: 26 July 2021
doi: 10.3389/feart.2021.684365

Analysis of Hillslope Erosion Based on Excess Topography in Southeastern Tibet

Weiming Liu[1,2], Zhen Zhou[3], Liqin Zhou[1,4], Xiaoqing Chen[1,2]*, Brian Yanites[5], Yanlian Zhou[1,4], Xuemei Li[1] and Xiaogang Zhang[1]

[1]Key Laboratory of Mountain Hazards and Surface Process, Institute of Mountain Hazards and Environment, Chinese Academy of Sciences, Chengdu, China, [2]China-Pakistan Joint Research Center on Earth Sciences, CAS-HEC, Islamabad, Pakistan, [3]China Railway Eryuan Engineering Group Co. Ltd., Chengdu, China, [4]University of Chinese Academy of Sciences, Beijing, China, [5]Earth and Atmospheric Sciences, Indiana University, Bloomington, IN, United States

The southeastern Tibetan Plateau has been deeply dissected by major rivers and their tributaries into high-relief topography with deep gorges. In this region, most hillslope gradients in the high-relief areas approach a threshold value, and landslides are the dominant surface erosion process. For this work, we analyzed the hillslope erosion process by determining the excess topography from the threshold hillslope. Slope analysis found a similar normal distribution of slope values for six large drainage basins with different lithology, precipitation, and tectonic settings. Overall, 82% of the slopes in our study area were 30 ± 5°, so this was taken as a reasonable range of threshold hillslope angles. We determined that the excess topography calculated for different threshold values all occur along major fluvial inner gorges. We found a linear relationship between excess topography and the mean erosion rate in drainage basins, which indicates that hillslope erosion, especially landslides, is the main erosion process. In contrast, the correlation between excess topography and the slope is only found for low-relief topography. This suggests that excess topography is a better metric than the slope to reflect the spatial distribution of erosion rates in the southeastern Tibetan Plateau. In addition, for a threshold value of 30°, we collected data from 4,430 landslides and found that 71% of these landslides had occurred in an area of excess topography. This implies that most recent landslides did not reduce the slope below the threshold value. As a result, the potential for future landslides remains high in areas where landslides have recently occurred.

Keywords: excess topography, landslides, hillslope erosion, potential landslides, southeastern Tibet

Edited by:
Xiangjun Liu,
Northwest Normal University, China

Reviewed by:
Zhenbo Hu,
Lanzhou University, China
Shibiao Bai,
Nanjing Normal University, China

****Correspondence:***
Xiaoqing Chen
xqchen@imde.ac.cn

Specialty section:
This article was submitted to Quaternary Science, Geomorphology and Paleoenvironment, a section of the journal Frontiers in Earth Science

Received: *23 March 2021*
Accepted: *28 June 2021*
Published: *26 July 2021*

Citation:
Liu W, Zhou Z, Zhou L, Chen X, Yanites B, Zhou Y, Li X and Zhang X (2021) Analysis of Hillslope Erosion Based on Excess Topography in Southeastern Tibet. Front. Earth Sci. 9:684365. doi: 10.3389/feart.2021.684365

INTRODUCTION

Hillslopes usually occupy the main area of mountain ranges which are formed by the downcutting of rivers and glaciers during uplift (Burbank, 2002; Roering et al., 2005; Korup et al., 2010). When the orogen approaches a topographic steady state, a hillslope will continue to steepen in response to increasing rates of river/glacier incision. This leads to diffusive erosion and shallow landslides and, finally, to bedrock landslides. After these processes have occurred, the hillslope gradient will not increase further, which is known as the threshold hillslope (Montgomery, 2001; Burbank, 2002). Under this condition, slope erosion is dominated by bedrock landslides. This not only maintains a steep slope but also limits relief height (Schmidt and Montgomery, 1995), affects valley morphology

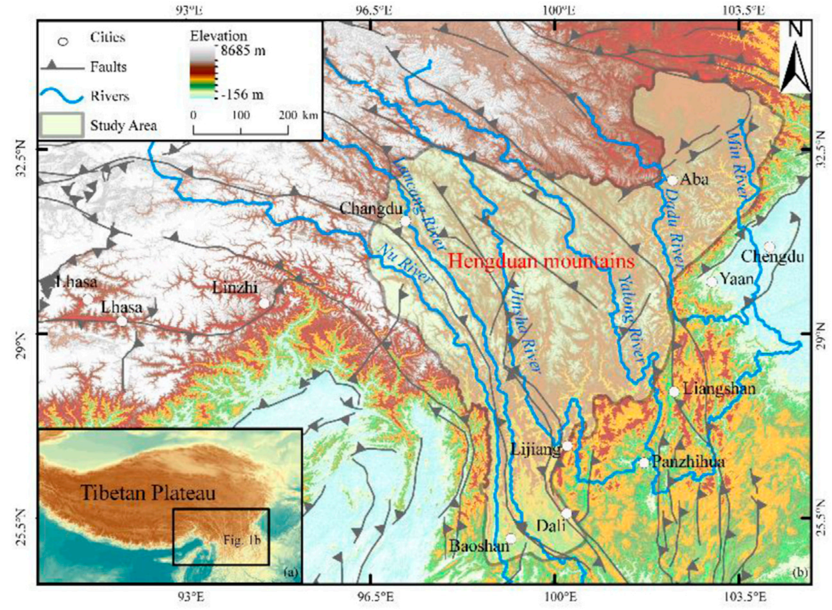

FIGURE 1 | Overview of the southeastern Tibetan Plateau. The fault locations are from the study by Taylor and Yin (2009).

(Densmore et al., 1997), and prevents river incision because of the landslide debris load in the channel (Ouimet et al., 2007; Korup et al., 2010). Landslides also cause the hillslope gradient to decrease over a relatively short timescale (Roering et al., 2005; Korup et al., 2007). Although landslides dominate erosion processes in several mountain ranges (Hovius et al., 1998; Larsen and Montgomery, 2012), more studies are needed to understand the role of landslides in landscape evolution.

The Tibetan Plateau covers an area of 2.6×10^6 km^2. With an average altitude of more than 4,000 m, it is the highest plateau on Earth (Zhang et al., 2002). Overall, the most prominent geomorphic features of the Tibetan Plateau are very flat interiors and steep, abrupt margins (Fielding et al., 1994). The southeastern margin, however, has low topographic gradients and a gradual change in elevation (Clark and Royden, 2000; Clark et al., 2006). This topography allows large amounts of water vapor from monsoons to penetrate deep into the plateau. The precipitation from this is the origin of some famous rivers, including the Yangtze River, the Lancang River, and the Nu River (**Figure 1**). The incision of these rivers and their main tributaries form deep valleys and low-relief landscape dissection (Clark et al., 2006; Yang et al., 2015). The threshold hillslopes, rapid erosion, and frequent landslides of this area (Ouimet et al., 2007; Ouimet et al., 2009; Henck et al., 2011; Zhang et al., in press) make this an ideal area to study the role of landslides in mountain range evolution.

At present, landslide inventories in large regions are mainly performed *via* remote sensing, and some uncertainties remain. For example, estimates of the number of landslides caused by the 2008 Wenchuan earthquake, which, as seismic landslides, are relatively easy to identify, vary from 50,000 to 190,000 (Gorum et al., 2011; Parker et al., 2011; Xu et al., 2014). In addition, there are also large differences in estimates of the volume of these landslides (Li et al., 2014). Excess topography refers to the potentially unstable rock mass that is above the threshold hillslope. This is a quantitative calculation that can approximate landslide erosion (Blöthe et al., 2015; Campforts et al., 2017). In this work, we apply the excess topography model to the southeastern Tibetan Plateau. The distribution of excess topography and its relation with landslides are then used to assess the importance of slope erosion to geomorphic evolution.

STUDY AREA

The study area is limited to the traditionally defined Hengduan Mountain area. There are six mountains and six rivers, from the western Gaoligong Mountains to the eastern Min River (**Figure 1**). The region spans 24°40′–34°00′ N and 96°20′–104°30′ E, and covers 360,000 km^3 (Zhang et al., 1997). The southeastern Tibetan Plateau has been separated into several blocks by a series of large strike-slip and thrust faults formed by the convergence of India and Eurasia (Xu et al., 2003). In the northern region, the Min River, the Dadu River, and the Yalong River, all tributaries of the Yangtze River, incise deep gorges. The Jinsha River (upstream of the Yangtze River), the Lancang River, and the Nu River flow in parallel for thousands of kilometers in the southern region, which is called the "Three Rivers region." Large landslides frequently inundate these river valleys (Liu et al., 2019; Liu et al., 2021).

METHODS

We first calculated the slope values and then systematically analyzed the slope distribution after removing the relatively

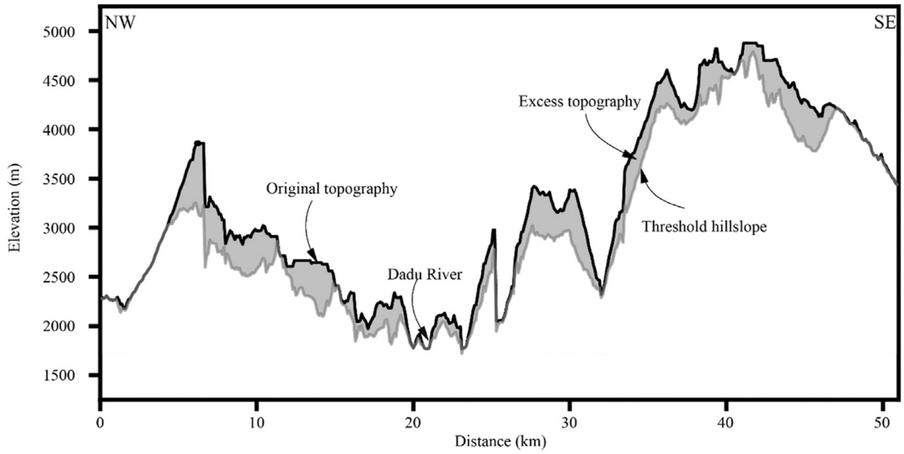

FIGURE 2 | Schematic diagram of excess topography. The black line represents the DEM elevation profile, the gray line represents the threshold hillslope surface under 30°, and the gray shaded part represents excess topography.

flat non-slope component that is far away from the channels. Reasonable threshold hillslopes were obtained using slope distributions over 1° intervals of each river basin (Montgomery, 2001; Korup and Schlunegger, 2007). The excess topography was then calculated following the method of Blöthe et al. (2015). First, the height ($\dot{z}$) of the ideal slope body at a given threshold hillslope angle s_t is obtained as follows:

$$\dot{z}(x,y) = \min_{(s,t)\,\in\,(-\infty,\infty)} \left\{ z(x+s,y+t) + s_t\sqrt{s^2+t^2} \right\}, \tag{1}$$

where z is the real elevation of the topography, x, y are coordinates, and s, t are the filter coefficients, which refer to the distance from the center of the filter to the point (x, y).

The elevation of excess topography z_E can then be obtained by subtracting the elevation of the threshold hillslope surface from the real surface elevation as follows:

$$z_E(x,y) = z(x,y) - \dot{z}(x,y). \tag{2}$$

The calculated excess topography is shown in **Figure 2**.

Among the widely used global digital elevation models (DEMs), only the shuttle radar topography mission (SRTM) and Tan dem-x provide radar data with high elevation accuracy (Rodríguez et al., 2006; Vassilaki and Stamos, 2020). However, after the early free use of Tan dem-x data, it is now difficult to apply for free data (https://tandemx-science.dlr.de/). Therefore, the SRTM is the most widely used in the calculation of geomorphic parameters (Yang et al., 2015; Adams et al., 2020). The geomorphic indexes are analyzed using 30-m SRTM, from the United States Geological Survey (https://earthexplorer.usgs.gov/), and are calculated using TopoToolbox 2 software (Schwanghart and Scherler, 2014).

To analyze the relationship between excess topography and landslides, landslide information was collected from GeoCloud, an online geological database (http://geocloudsso.cgs.gov.cn/) established by the China Geological Survey. Data on 4,430 landslides were collected by local governments in the study area, including the name, type, location, and other disaster information. In addition, 62 erosion rates calculated using *in situ* ^{10}Be in river sand quartz were collected from the OCTOPUS database (Codilean et al., 2018) (**Supplementary Table S1**). For these, the data from the Min River are primarily from the study by Godard et al. (2010), the data from the Dadu River and the Yalong River are from the study by Ouimet et al. (2009), and the remaining data are from the study by Henck et al. (2011).

RESULTS

Slope Values

All slope values are between 0° and 89°, with an average of 25° (**Figure 3**). The slope values in the gorges are generally higher than those of the planation far away from the river valley. If a hillslope reaches the threshold, the real slope is given by a normal distribution because it is randomly distributed around the threshold slope. Previous studies have used the mode value to determine the threshold slope (Montgomery, 2001; Korup and Schlunegger, 2007). From the histogram of slope values for each drainage, the Min River, the Dadu River, and the Lancang River all have normal distributions, and the mode values for them are 32°, 33°, and 26°, respectively.

The slope values of the Yalong River, the Jinsha River, and the Nu River, however, have negative skew distributions because of low planation with low slope values. These have the mode values of 29°, 29°, and 32°, respectively. The slope mode values of the six major river basins are all approximately 30° and between 30 ± 5°. A reasonable range of threshold hillslope angles in this study is thus 30 ± 5°. The ranges of the threshold slope values determined for other mountain ranges, such as the Olympic Mountains, the Southern Alps of New Zealand, and the eastern Himalayas, are all also 30 ± 5°, similar to our study area (Montgomery, 2001; Korup and Schlunegger, 2007; Larsen and Montgomery, 2012).

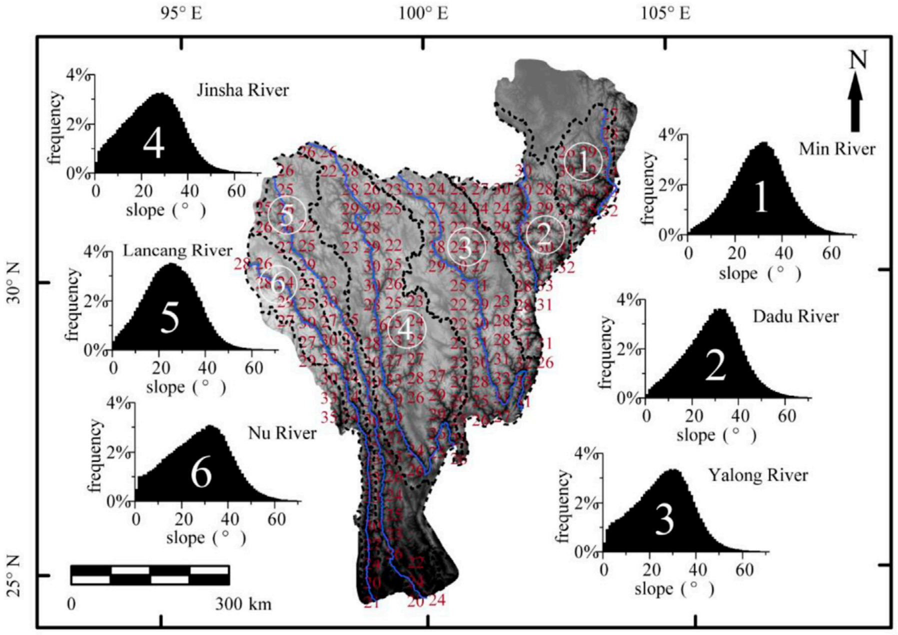

FIGURE 3 | Slope of the study area and the slope frequency distribution of each river drainage.

Distribution of Excess Topography

To determine whether different slope values affect the distribution of excess topography, we calculated the volume of excess topography above slope values of 30°, 35°, 40°, and 45°. With an increase in the slope angle, the excess topography volume decreased substantially; the calculated values were $11.6 \times 10^3\,\text{km}^3$, $5.25 \times 10^3\,\text{km}^3$, $2.19 \times 10^3\,\text{km}^3$, and $0.95 \times 10^3\,\text{km}^3$, respectively, which are inversely proportional to the slope angle. The spatial distribution characteristics of the excess topography are similar. However, most of them are concentrated in high-relief areas and valleys (**Figure 4**). Therefore, slope values do not affect the distribution of excess topography. We focus on excess topography above 30° for this analysis. The thickness of the excess topography differs substantially and ranges from 0 to 2,680 m, with an average of 32.2 m. As with the slope, excess topography is mainly distributed along the channel in the middle and lower reaches of the major rivers.

DISCUSSION

Correlation Between Excess Topography and Erosion Rates

To further analyze the correlation between excess topography and the erosion rate, we took the erosion rate of a ^{10}Be sampling site as the center and calculated the excess topography volume and the average slope value within 5 km. The results are shown in **Supplementary Table S1**. The excess topography volume is widely variable, similar to the erosion rate, and ranges from 0.01 to 18.03 km^3. Moreover, there is a clear positive correlation between excess topography and the erosion rate (the correlation coefficient is 0.83, **Figure 5A**). We have 62 erosion rate values, and the critical value of the correlation coefficient is at a level of 0.001 is 0.41. Therefore, the value 0.83 indicates a linear correlation between excess topography and the erosion rate. This indicates that erosion in the study area is mainly driven by slope erosion. However, the correlation between the slope and the erosion rate is not clear, with a coefficient of only 0.0001 (**Figure 5B**). This demonstrates that excess topography can better reflect the erosion rate than the slope.

Because the erosion rate of the slope is a response to the tectonic uplift, it can quickly adjust. When the uplift rate is high, slope erosion can restrain the increase in topographic relief. This makes the slope values in different regions converge to the threshold hillslope (Burbank, 2002). The excess topography is an extension of the threshold hillslope. When the mountain reaches the threshold hillslope, it should conform to the linear correlation between excess topography and erosion rates.

For example, the slope erosion rate of the eastern Himalayan syntaxis increases more than ten times within 150 km to accommodate the extremely large difference in erosion rates inferred from thermochronometry data, but the slope does not change considerably (Larsen and Montgomery, 2012; Roering, 2012). Continuous tectonic uplift and river undercutting always create topographic relief and provide an opportunity for slope erosion. Excess topography thus continuously exists, and the mountain is in dynamic balance. The formulas for calculating excess topography show that the calculated volume is determined by the slope and the local relief. Both are critical

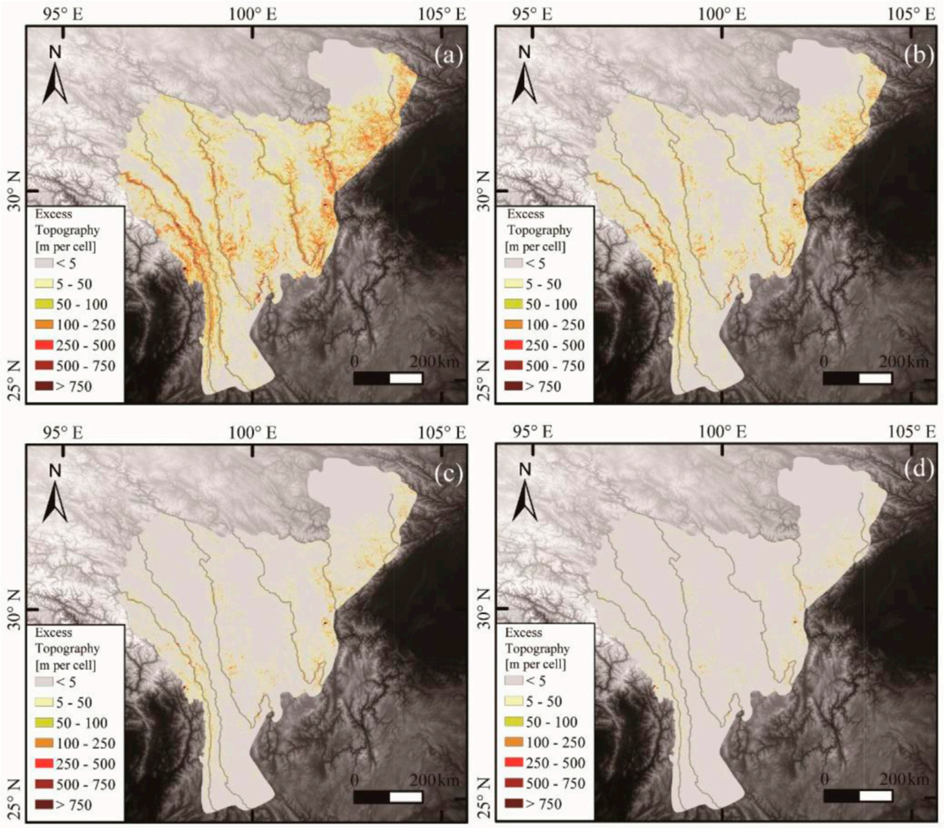

FIGURE 4 | Excess topography under different threshold hillslopes (**(A–D)** are 30°, 35°, 40°, and 45°, respectively).

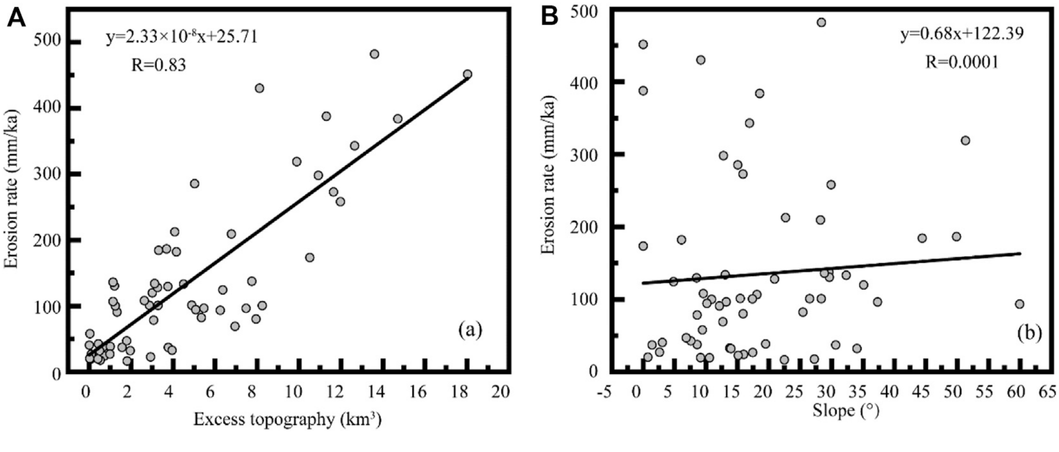

FIGURE 5 | (A) Correlation between the erosion rate and the excess topography volume in the study area. **(B)** Correlation between the erosion rate and the slope in the study area.

factors that determine the erosion rate (Montgomery and Brandon, 2002). A small change in the slope will cause a major difference in the excess topography, and excess topography indicates the volume of potential landslides. Although it is not clear how long the potential landslide represented by the excess topography will erode, the linear relationship with the erosion rate indicates that the excess topography is more indicative of changes in erosion rates than the slope.

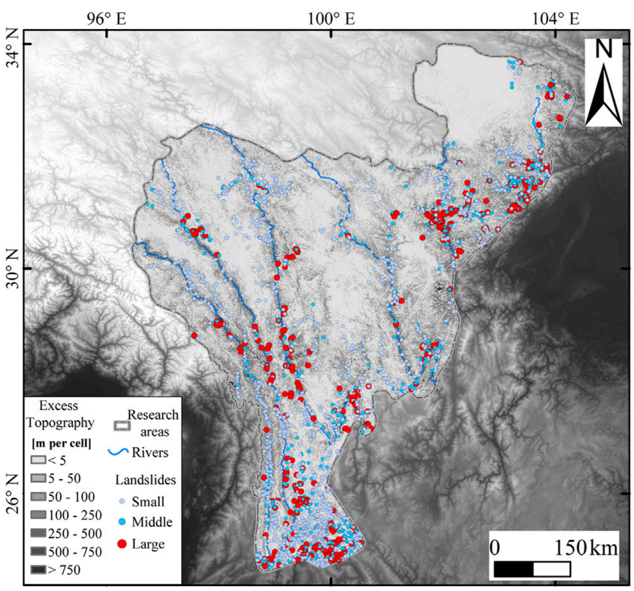

FIGURE 6 | Distribution of landslides in excess topography.

The Relationship Between Excess Topography and Landslides

Among the 4,430 landslides studied, 3,146 landslides occurred in excess topography, which is more than 71%. A total of 1,518 landslides were located within excess topography with a height greater than 50 m. This encompassed an area of only 6.7×10^4 km^2. The area in which the height of the excess topography is less than 5 m is about 1.67×10^5 km^2, and only 554 landslides were recorded. In addition, the landslides that did not occur in an area of excess topography were mostly located in the southeast of the study area (**Figure 6**). We suggest that the rock strength in the southeastern region is substantially lower because of higher rainfall, resulting in a lower threshold slope value.

Although exact occurrence times are not given in the landslide data, they all occurred between 1949 and 2014. The SRTM-DEM data we used were collected in 2000. Therefore, many of the landslides occurred before the DEM data collection. This indicates that although the landslides occurred and caused a decline in the hillslope, most of them did not reduce the slope below the threshold hillslope. This is consistent with the observation that 75% of the landslides in the western margin of the Himalaya–Karakoram ranges occurred in excess topography (Blöthe et al., 2015).

This is because in the formation of a landslide, a potential slip plane forms first, and the weakness plane subsequently penetrates to form a slip plane. The formation of this weakness plane is related to lithology, fracture development, and so on. In addition, when a slope is steeper, it is under a higher degree of shear stress, and a slip plane forms more readily. Therefore, a landslide is usually not able to reduce the slope below the threshold hillslope. A second landslide is thus likely to occur (Ghazvinian et al., 2010). In other words, existing excess topography requires multiple landslides to be eroded away, and an area with excess topography is at high risk of landslides. Theoretically, when the slope is larger, the same mass of rock is subject to a greater sliding force. Therefore, the slope is an important index in landslide susceptibility identification (Reichenbach et al., 2018). The excess topography represents a steep hillslope, which is prone to future landslides.

CONCLUSION

We have calculated the slope and excess topography in the southeastern margin of the Tibetan Plateau and analyzed the relationship between landslides and the erosion rate. From this, we propose the following conclusions:

1) In the study area, the slope value is generally 30 ± 5°, which accounts for about 82% of the total area. The modes of the six river drainage slopes are between 26° and 33°, which are also close to 30°. Therefore, 30 ± 5° can be used as a reasonable value range for the threshold hillslope. The amount of excess topography is inversely proportional to the value of the threshold hillslope, and it is spatially distributed mainly along the river channels. The highest values are inside the gorge. The average thickness of excess topography for a slope above 30° is 32.2 m, with a total volume of 11.6×10^3 km^3.
2) The correlation coefficient between the excess topography and the erosion rates on the millennium scale reaches 0.69, which indicates a clear positive correlation. This relationship suggests that erosion is mainly driven by landslides resulting from excess topography. In addition, more than 71% of the 4,430 landslides observed in the study area occurred in excess topography. This implies that landslides generally cannot decrease the slope below the threshold hillslope, allowing for the occurrence of future landslides.

DATA AVAILABILITY STATEMENT

The raw data supporting the conclusions of this article will be made available by the authors, without undue reservation.

AUTHOR CONTRIBUTIONS

XC and WL designed the research; ZZ, LZ, and YZ performed the research; WL, ZZ, XC, BY, XL, and XZ analyzed data; and WL, LZ, BY, and XC wrote the manuscript.

FUNDING

This work was supported by the National Natural Science Foundation of China (grant nos. 41941017, 42071017, 41771023, and 41807448).

ACKNOWLEDGMENTS

The authors thank Wolfgang Schwanghart for help analyzing parameters and reviewers for constructive comments and suggestions. A special acknowledgment should be expressed to the China–Pakistan Joint Research Center on Earth Sciences that supported the implementation of this study. We thank Katherine Armstrong, PhD, from Liwen Bianji (Edanz) (www.liwenbianji.cn/), for editing the English text of a draft of this manuscript.

REFERENCES

Adams, B. A., Whipple, K. X., Forte, A. M., Heimsath, A. M., and Hodges, K. V. (2020). Climate Controls on Erosion in Tectonically Active Landscapes. *Sci. Adv.* 6, eaaz3166. doi:10.1126/sciadv.aaz3166

Blöthe, J. H., Korup, O., and Schwanghart, W. (2015). Large Landslides Lie Low: Excess Topography in the Himalaya-Karakoram Ranges. *Geology* 43, 523–526. doi:10.1130/g36527.1

Burbank, D. W. (2002). Rates of Erosion and Their Implications for Exhumation. *Mineral. Mag.* 66, 25–52. doi:10.1180/0026461026610014

Campforts, B., Schwanghart, W., and Govers, G. (2017). Accurate Simulation of Transient Landscape Evolution by Eliminating Numerical Diffusion: the TTLEM 1.0 Model. *Earth Surf. Dynam.* 5, 47–66. doi:10.5194/esurf-5-47-2017

Clark, M. K., and Royden, L. H. (2000). Topographic Ooze: Building the Eastern Margin of Tibet by Lower Crustal Flow. *Geol* 28, 703–706. doi:10.1130/0091-7613(2000)28<703:tobtem>2.0.co;2

Clark, M. K., Royden, L. H., Whipple, K. X., Burchfiel, B. C., Zhang, X., and Tang, W. (2006). Use of a Regional, Relict Landscape to Measure Vertical Deformation of the Eastern Tibetan Plateau. *J. Geophys. Res.* 111, a–n. doi:10.1029/2005JF000294

Codilean, A. T., Munack, H., Cohen, T. J., Saktura, W. M., Gray, A., and Mudd, S. M. (2018). OCTOPUS: an Open Cosmogenic Isotope and Luminescence Database. *Earth Syst. Sci. Data* 10, 2123–2139. doi:10.5194/essd-10-2123-2018

Densmore, A. L., Anderson, R. S., McAdoo, B. G., and Ellis, M. A. (1997). Hillslope Evolution by Bedrock Landslides. *Science* 275, 369–372. doi:10.1126/science.275.5298.369

Fielding, E., Isacks, B., Barazangi, M., and Duncan, C. (1994). How Flat Is Tibet? *Geol* 22, 163–167. doi:10.1130/0091-7613(1994)022<0163:hfit>2.3.co;2

Ghazvinian, A. H., Taghichian, A., Hashemi, M., and Mar'ashi, S. A. (2010). The Shear Behavior of Bedding Planes of Weakness between Two Different Rock Types with High Strength Difference. *Rock Mech. Rock Eng.* 43, 69–87. doi:10.1007/s00603-009-0030-8

Godard, V., Lavé, J., Carcaillet, J., Cattin, R., Bourlès, D., and Zhu, J. (2010). Spatial Distribution of Denudation in Eastern Tibet and Regressive Erosion of Plateau Margins. *Tectonophysics* 491, 253–274. doi:10.1016/j.tecto.2009.10.026

Gorum, T., Fan, X., van Westen, C. J., Huang, R. Q., Xu, Q., Tang, C., et al. (2011). Distribution Pattern of Earthquake-Induced Landslides Triggered by the 12 May 2008 Wenchuan Earthquake. *Geomorphology* 133, 152–167. doi:10.1016/j.geomorph.2010.12.030

Henck, A. C., Huntington, K. W., Stone, J. O., Montgomery, D. R., and Hallet, B. (2011). Spatial Controls on Erosion in the Three Rivers Region, southeastern Tibet and Southwestern China. *Earth Planet. Sci. Lett.* 303, 71–83. doi:10.1016/j.epsl.2010.12.038

Hovius, N., Stark, C. P., Tutton, M. A., and Abbott, L. D. (1998). Landslide-driven Drainage Network Evolution in a Pre-steady-state Mountain belt: Finisterre Mountains, Papua New Guinea. *Geol* 26, 1071–1074. doi:10.1130/0091-7613(1998)026<1071:lddnei>2.3.co;2

Korup, O., Clague, J. J., Hermanns, R. L., Hewitt, K., Strom, A. L., and Weidinger, J. T. (2007). Giant Landslides, Topography, and Erosion. *Earth Planet. Sci. Lett.* 261, 578–589. doi:10.1016/j.epsl.2007.07.025

Korup, O., Densmore, A. L., and Schlunegger, F. (2010). The Role of Landslides in Mountain Range Evolution. *Geomorphology* 120, 77–90. doi:10.1016/j.geomorph.2009.09.017

Korup, O., and Schlunegger, F. (2007). Bedrock Landsliding, River Incision, and Transience of Geomorphic Hillslope-Channel Coupling: Evidence from Inner Gorges in the Swiss Alps. *J. Geophys. Res.* 112, F03027. doi:10.1029/2006JF000710

Larsen, I. J., and Montgomery, D. R. (2012). Landslide Erosion Coupled to Tectonics and River Incision. *Nat. Geosci* 5, 468–473. doi:10.1038/ngeo1479

SUPPLEMENTARY MATERIAL

The Supplementary Material for this article can be found online at: https://www.frontiersin.org/articles/10.3389/feart.2021.684365/full#supplementary-material

Li, G., West, A. J., Densmore, A. L., Jin, Z., Parker, R. N., and Hilton, R. G. (2014). Seismic Mountain Building: Landslides Associated with the 2008 Wenchuan Earthquake in the Context of a Generalized Model for Earthquake Volume Balance. *Geochem. Geophys. Geosyst.* 15, 833–844. doi:10.1002/2013gc005067

Liu, W., Zhou, L., Chen, X., Zhou, Z., Wolfgang, S., Hu, X., et al. (2021). The marks of the Dam on the River Elevation Profile of Yalong River basin (In Chinese with English Abstract). *Earth Sci. Front.* 28, 59–70. doi:10.13745/j.esf.sf.2020.9.1

Liu, W., Carling, P. A., Hu, K., Wang, H., Zhou, Z., Zhou, L., et al. (2019). Outburst Floods in China: A Review. *Earth-Science Rev.* 197, 102895. doi:10.1016/j.earscirev.2019.102895

Montgomery, D. R., and Brandon, M. T. (2002). Topographic Controls on Erosion Rates in Tectonically Active Mountain Ranges. *Earth Planet. Sci. Lett.* 201, 481–489. doi:10.1016/s0012-821x(02)00725-2

Montgomery, D. R. (2001). Slope Distributions, Threshold Hillslopes, and Steady-State Topography. *Am. J. Sci.* 301, 432–454. doi:10.2475/ajs.301.4-5.432

Ouimet, W. B., Whipple, K. X., and Granger, D. E. (2009). Beyond Threshold Hillslopes: Channel Adjustment to Base-Level Fall in Tectonically Active Mountain Ranges. *Geology* 37, 579–582. doi:10.1130/g30013a.1

Ouimet, W. B., Whipple, K. X., Royden, L. H., Sun, Z., and Chen, Z. (2007). The Influence of Large Landslides on River Incision in a Transient Landscape: Eastern Margin of the Tibetan Plateau (Sichuan, China). *Geol. Soc. America Bull.* 119, 1462–1476. doi:10.1130/b26136.1

Parker, R. N., Densmore, A. L., Rosser, N. J., de Michele, M., Li, Y., Huang, R., et al. (2011). Mass Wasting Triggered by the 2008 Wenchuan Earthquake Is Greater Than Orogenic Growth. *Nat. Geosci* 4, 449–452. doi:10.1038/ngeo1154

Reichenbach, P., Rossi, M., Malamud, B. D., Mihir, M., and Guzzetti, F. (2018). A Review of Statistically-Based Landslide Susceptibility Models. *Earth-Science Rev.* 180, 60–91. doi:10.1016/j.earscirev.2018.03.001

Rodríguez, E., Morris, C. S., and Belz, J. E. (2006). A Global Assessment of the SRTM Performance. *Photogramm. Eng. Remote Sens.* 72, 249–260. doi:10.14358/PERS.72.3.249

Roering, J. J., Kirchner, J. W., and Dietrich, W. E. (2005). Characterizing Structural and Lithologic Controls on Deep-Seated Landsliding: Implications for Topographic Relief and Landscape Evolution in the Oregon Coast Range, USA. *Geol. Soc. America Bull* 117, 654–668. doi:10.1130/b25567.1

Roering, J. (2012). Landslides Limit Mountain Relief. *Nat. Geosci* 5, 446–447. doi:10.1038/ngeo1511

Schmidt, K. M., and Montgomery, D. R. (1995). Limits to Relief. *Science* 270, 617–620. doi:10.1126/science.270.5236.617

Schwanghart, W., and Scherler, D. (2014). Short Communication: TopoToolbox 2 - MATLAB-Based Software for Topographic Analysis and Modeling in Earth Surface Sciences. *Earth Surf. Dynam.* 2, 1–7. doi:10.5194/esurf-2-1-2014

Taylor, M., and Yin, A. (2009). Active Structures of the Himalayan-Tibetan Orogen and Their Relationships to Earthquake Distribution, Contemporary Strain Field, and Cenozoic Volcanism. *Geosphere* 5, 199–214. doi:10.1130/ges00217.1

Vassilaki, D. I., and Stamos, A. A. (2020). TanDEM-X DEM: Comparative Performance Review Employing LIDAR Data and DSMs. *ISPRS J. Photogramm. Remote Sens.* 160, 33–50. doi:10.1016/j.isprsjprs.2019.11.015

Xu, C., Xu, X., Yao, X., and Dai, F. (2014). Three (Nearly) Complete Inventories of Landslides Triggered by the May 12, 2008 Wenchuan Mw 7.9 Earthquake of China and Their Spatial Distribution Statistical Analysis. *Landslides* 11, 441–461. doi:10.1007/s10346-013-0404-6

Xu, X., Wen, X., Zheng, R., Ma, W., Song, F., and Yu, G. (2003). Pattern of Latest Tectonic Motion and its Dynamics for Active Blocks in Sichuan-Yunnan Region. *China. Sci. China Earth Sci.* 46, 210–226. doi:10.1360/03yd9056

Yang, R., Willett, S. D., and Goren, L. (2015). *In Situ* low-relief Landscape Formation as a Result of River Network Disruption. *Nature* 520, 526–529. doi:10.1038/nature14354

Zhang, R., Zheng, D., Yang, Q., and Liu, Y. (1997). *Physical Geography of Hengduan Mountain Region (in Chinese with English Abstract).* Beijing: Science Press, 151.

Zhang, Y., Li, B., and Zheng, D. (2002). A Discussion on the Boundary and Area of the Tibetan Plateau in China (In Chinese with English Abstract). *Geographical Res.* 21, 1–8. doi:10.3321/j.issn:1000-0585.2002.01.001

Zhang, Y., Liu, X., Wu, R., Guo, C., and Ren, S. (in press). Research on Cognization, Characteristics, Age and advance of Ancient Landslides along the Deep-Cut Valleys on the Eastern Tibetan Plateau, China (In Chinese with English Abstract). *Earth Sci. Front.* 28, 94–105. doi:10.13745/j.esf.sf.2020.9.10

Conflict of Interest: Author ZZ was employed by China Railway Eryuan Engineering Group Co., Ltd.

The remaining authors declare that the research was conducted in the absence of any commercial or financial relationships that could be construed as a potential conflict of interest.

frontiers
in Earth Science

ORIGINAL RESEARCH
published: 27 July 2021
doi: 10.3389/feart.2021.702340

Glacier-Induced Alluvial Fan Development on the Northeast Tibetan Plateau Since the Late Pleistocene

Fuyuan An[1,2,3]*, *BadingQiuying*[1,2,3], *Shanlu Li*[4]*, *Donglin Gao*[5], *Tianyuan Chen*[5], *Lu Cong*[5], *Jinhu Zhang*[1,2,3] *and Xiali Cheng*[1]

[1]Key Laboratory of Physical Geography and Environmental Processes of Qinghai Province, School of Geographical Science, Qinghai Normal University, Xining, China, [2]Key Laboratory of Tibetan Plateau Land Surface Processes and Ecological Conservation (Ministry of Education), Xining, China, [3]Academy of Plateau Science and Sustainability, Qinghai Normal University, Xining, China, [4]Qinghai Branch of China National Geological Exploration Center of Building Materials Industry, Xining, China, [5]Key Laboratory of Comprehensive and Highly Efficient Utilization of Salt Lake Resources, Qinghai Institute of Salt Lakes, Chinese Academy of Sciences, Xining, China

OPEN ACCESS

Edited by:
Feng Cheng,
University of Nevada, United States

Reviewed by:
Xingqi Liu,
Capital Normal University, China
Weiming Liu,
Institute of Mountain Hazards and Environment(CAS), China

***Correspondence:**
Fuyuan An
dongzhu8@sina.com
Shanlu Li
qhnz@163.com

Specialty section:
This article was submitted to Quaternary Science, Geomorphology and Paleoenvironment, a section of the journal Frontiers in Earth Science

Received: *29 April 2021*
Accepted: *23 June 2021*
Published: *27 July 2021*

Citation:
An F, BadingQiuying, Li S, Gao D, Chen T, Cong L, Zhang J and Cheng X (2021) Glacier-Induced Alluvial Fan Development on the Northeast Tibetan Plateau Since the Late Pleistocene. Front. Earth Sci. 9:702340. doi: 10.3389/feart.2021.702340

The origin of alluvial fans at the drainage basin or the margins of the arid sedimentary basin on the northeastern Tibetan Plateau (NETP) has been a focus of debate among scientific communities. Extensive alluvial fans had developed in the mountain-basin systems of this region during the late Pleistocene. Based on geomorphic/stratigraphic studies and the optically stimulated luminescence (OSL) chronology, we investigated numerous alluvial sequences in the drainage basin of the coupled mountain-basin system on the NETP. Sedimentologic analyses showed that these alluvial sediments mainly comprise crudely meter and decimeter beds of fanglomerate and sandy lenticles, which occasionally contain boulders in the thinner layers. OSL dating results showed that the alluvial sediments were mainly developed during the late MIS 5, MIS 3, and Last Glaciation and Deglaciation (maximum aggradations), while little had occurred during the early Holocene. Comparing our ages and their probability density curves with those of glacial advances from the northeastern/eastern TP, the consistency of both records during different stages since the late Pleistocene suggested that the development of alluvial fans was driven by glacier activities, which yielded abundant outwash, feeding alluvial aggradations. Based on this finding, together with results of previous studies, we argued that the dynamics of alluvial geomorphic processes had a paleoclimatic origin rather than surface uplifts. Further studies indicated that the precipitation of glaciations originated from the ISM northward intrusion during the late MIS 5, MIS 3, and Holocene; however, it was mainly influenced by the westerlies during the Last Glaciation and Deglaciation. Therefore, the development of alluvial fans on the NETP represents coupling signals of the ISM and the westerlies on the interglacial–glacial cycle timescales. The coupling evolution of glacier activities and alluvial aggradations in the drainage basins of mountain-basin systems on the NETP provides a model for assessing the linkages between regional geomorphic processes and atmospheric circulations on hemispheric scales.

Keywords: alluvial fans, optically stimulated luminescence dating, glacier activities, moisture source, Northeastern Tibetan Plateau

INTRODUCTION

Geomorphic processes in the drainage basins of river catchments offer insight into the response of mountain-basin surface dynamics to paleoclimate fluctuations (Owen et al., 2006; Chen et al., 2011; An et al., 2018a; Lehmkuhl et al., 2018; Li et al., 2020a; Tao et al., 2020). Using geomorphic processes to reconstruct paleoclimate changes often focuses on specific sedimentary or geomorphological archives such as fluvial terraces, eolian sediments, glacial landforms, lake shorelines, and alluvial fans (An et al., 2021). Geomorphic processes on the Northeastern Tibetan Plateau (NETP) have been intensively studied in recent decades due to its typical location of mountain-basin coupling and the interactional zone of diversiform atmospheric circulations (Owen et al., 2006; Wang et al., 2009; Chang et al., 2017; Stauch et al., 2017; An et al., 2018a, 2018b; Liu et al., 2019; Li et al., 2020b; Tao et al., 2020). For example, Owen et al. (2006) carried out systemic investigations on the alluvial fans, river terraces, and moraines along the eastern Kunlun Mountain slopes that indicated links between climatic amelioration, deglaciation, lake desiccation, and terraced alluvial fan evolution. Wang et al. (2009) likewise carried out an extensive optically stimulated luminescence (OSL) study of alluvial valley fills and associated terraces along the Kunlun Mountains and found synchronous aggradations in different rivers during the last glacial stage.

Similar to geomorphic units in the drainage basin, an alluvial fan is an important dynamic landform process, which commonly develops in areas of high topographic relief, especially in the transition zone between mountain-basin systems (An et al., 2018a). An alluvial fan is a cone-shaped deposit of silt, sand, and gravel that accumulates where a stream flows from an eroding upland catchment and debouches into an adjacent basin (Zhang et al., 2014). Alluvial fans trap sediment delivered from mountain source areas and exert an important control on the delivery of sediment to downstream environments, to axial drainages, and to arid sedimentary basins, and they preserve a sensitive record of environmental fluctuations within the high mountain source area (Ashworth, 2006). Alluvial processes are mainly influenced by tectonic activity, climate changes, and base-level controls. The understanding of such processes has progressed considerably in the past few decades (Owen et al., 2003, 2006; Zhang et al., 2011; An et al., 2018a), whereas effects of climate factors appear to exert an overwhelming control on late Quaternary sequences and sedimentary styles, especially in arid drainage basins (Gao et al., 2018). Alluvial sediments are sensitive to changes in orographic glacial activities and drainage hydrological conditions. They provide valuable information on paleoclimatic fluctuations of upstream areas (Ritter et al., 1995; Vandenberghe, 1995; Bridgland, 2010). Likewise, an alluvial fan is a medium of sediment transportation and groundwater discharge. For instance, high sediment supply to an alluvial fan resulted in the temporary blocking of the river channel and influenced the lake level of the adjacent Heihai Lake. This geomorphic process presumably occurred during or shortly after large glaciations (Stauch et al., 2017). The groundwater in the Qilian Mountains was recharged by high piedmonts, flowed through the alluvial fans from south to north, and was finally discharged several decades later from springs located along the toe of the fan (Guo et al., 2017). Recent studies have found that glacier advance was a key factor for the development of alluvial fans due to the abundant detritus production at the piedmont belt in the eastern Kunlun Mountains (Owen et al., 2006; An et al., 2018b; Cui et al., 2020). These researchers argued that the alluvial Sanchahe Formation filled in the Golmud River valley, described as "a set of periglacial fanglomerates," originated from the piedmont outwash yielded in the high Kunlun Mountains (Van Der Woerd et al., 2002). Therefore, it is important to investigate the association between glacial activities, alluvial fan developments, and atmospheric circulation changes on the orbital timescale of the late Quaternary and the spatial scale of the entire drainage basin of the NETP, through extensive geomorphic investigations and abundant chronology controls. If tectonic uplift were negligible for the formation of alluvial fans since the late Pleistocene, studying the climatic driving mechanism for the geomorphic process from the periglacial zone to the drainage basin would help us come up with a hypothesis that drainage alluvial geomorphic processes respond to climatic systems, moisture transportation, and orographic glacial activity on a hemispheric scale.

In this study, we conducted a geomorphologic and stratigraphic investigation using 59 OSL dating ages from a series of alluvial fans in widespread drainage basins on the NETP. The aims of our study included the following: (i) to establish a chronological framework of these alluvial fans since the last interglaciation, (ii) to establish links between the orographic glacial activity and alluvial geomorphic development, and (iii) to explore their paleoclimatic implication on the atmospheric circulation scale.

SAMPLE COLLECTION AND METHODS

Study Area and Environmental Parameters

The Northeastern TP, with a series of high mountains, basins, alpine steppes, and deep-cutting gorges, covers an area of ~580,000 km^2 (Bureau of Geology and Mineral Resources of Qinghai Province, 1991). The extensively developed basin-mountain systems are the distinguishing topographical feature in this region (Kapp et al., 2011; Liu et al., 2015; An et al., 2018b). The diastrophism in this region shows large-scale crustal shortening and strike-slip faults during the late Cenozoic (Yuan et al., 2011). These faults bring up west-northwest–oriented orogenic belts, such as the Kunlun Mountains, the Qilian Mountains, Ela Mountain, and Riyue Mountain, which separate the several large Cenozoic basins including the Qaidam, Gonghe, Qinghai Lake, and Xining basins (**Figure 1**) (Yuan et al., 2011; Zhang et al., 2014). The alluvial fans associated with strong orographic weathering developed on the piedmonts along both sides of these high mountains. These alluvial fans are almost continuous within the tributary valleys and eventually join with the main valley fill that stretches along the margins of the basins (Owen et al.,

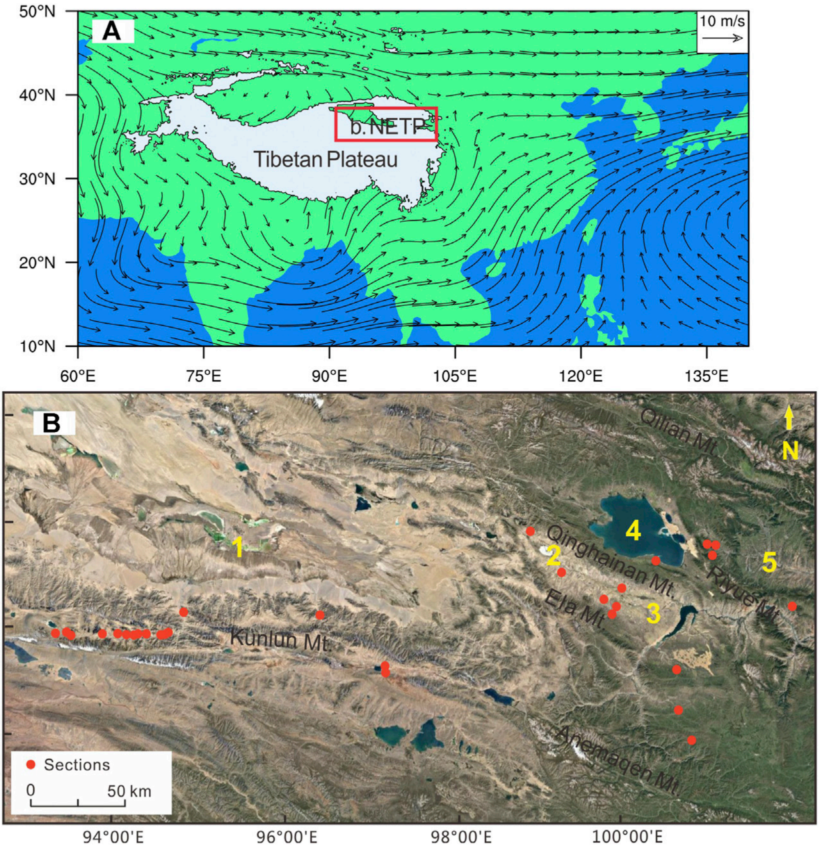

FIGURE 1 | Location map showing the study area and study sections. **(A)** Average atmospheric flow fields at the 700 hPa isobar in summer (modified from Li et al., 2020); the red square denotes the location of the study area. **(B)** Enlargement showing the Northeastern Tibetan Plateau (NETP) and the main mountain-basin systems in this region (1. Qaidam Basin; 2. Chaka Basin; 3. Gonghe Basin; 4. Qinghai Lake Basin; and 5. Xining Basin).

2006; An et al., 2018b; Gao et al., 2018). In the southern margin of the Qaidam Basin, the alluvial landforms contain three sub-geomorphic units: the piedmont alluvial fans along the slopes of the Kunlun Mountains, the main valley fill in the drainages, and the distal alluvial delta fan that cascades into the basin (An et al., 2018b). The highly dissected alluvial fans stretch out to the river valleys, and these are many tens of meters of alluvial fans that form the main valley fill. In the vicinity of the oasis preceding the mountain, a typical valley alluvial fan radiating from a series of large tributary valleys coalesces with the alluvial fill of the main drainage and then drains into the salt lakes in the Qaidam Basin and forms the distal alluvial delta fan (Owen et al., 2006). Five strath terraces have been developed within the alluvial fill (i.e., the Sanchahe Formation) in the middle reaches of the Golmud River, forming the spectacular fluvial landform. The Chaka Basin is part of the Gonghe Basin in the northeastern part of the TP, and it is separated from the Qaidam Basin by Ela Mountain (Liu et al., 2008). The basin is adjacent to the Qinghai Lake basin to the north by the Qinghainan Mountains (Zhang et al., 2012). The alluvial fans in the Chaka–Gonghe–Qinghai Lake regions are divided into three independent landform units, which include the north of the Ela Shan and both sides of the piedmonts of the Qinghainan Mountains. The northern alluvial fans in the Chaka–Gonghe Basin are characterized by bigger area and short lengths, but the southern Qinghai Lake area is relatively small (Zhang et al., 2014). The alluvial fans in the mountains of the eastern Qinghai Lake basin basically cascade from the lateral tributary valleys and stretch out to the main river drainage basin. These fans usually extend 10–20 km to form cliff terraces 30–65 m above the riverbed, and they likewise become detrital aggradations and valley fill (Guo et al., 2017; Liu et al., 2017; Li et al., 2018). Therefore, a large number of alluvial fans constitute the most impressive geomorphic processes in the mountain-basin systems of the NETP. These alluvial fans provide the ideal materials to study paleoclimatic/tectonic history in this region. Although earthquakes occur frequently in the region and the average strike-slip rate of the Kunlun–Qinling Fault in the Quaternary was up to ~10 mm/ y (Van Der Woerd et al., 2002; Li et al., 2005), no indicators of tectonic uplift activity during the late Pleistocene, such as mole tracks, have been observed in the Golmud catchment (Li et al., 2005; Wang et al., 2009; Stauch et al., 2017).

The elevations of the sampling sites range from 2,700 to 4,200 m a.s.l. These elevation gradients present a trend of high in the west and low in the east. The drainage basins of the Kunlun and Qilian Mountains have the average elevations of ~4,000 m

TABLE 1 | OSL sample information and dating results of the alluvial sections.

Sample no.	Coordinate	Profile top elevation (m a.s.l.)	Depth (m)	Grain size range (μm)	K (%)	Th (ppm)	U (ppm)	Water content (%)	Dose rate (Gy/ka)	D_e (Gy)	OSL age (ka)
HF4-1	35°52′57.14"N 93°30′55.91"E	4287	3.10	38–63	2.42 ± 0.10	9.29 ± 0.27	1.73 ± 0.06	15 ± 5	3.12 ± 0.21	50.4 ± 0.84	17.2 ± 1.1
HF8-2	35°51′55.82″N 94°12′26.12″E	3810	11.0	38–63	1.61 ± 0.05	10.5 ± 0.29	2.32 ± 0.09	15 ± 5	2.72 ± 0.19	34.7 ± 0.9	12.8 ± 1.0
HF8-4	36°56′25.82″N 93°12′33.20"E	3946	23.0	38–63	1.60 ± 0.05	9.42 ± 0.27	1.94 ± 0.08	10 ± 5	2.66 ± 0.20	130.4 ± 2.9	49.0 ± 3.8
HF17-1	35°52′11.01"N 94°08′21.23"E	3829	2.0	38–63	1.41 ± 0.05	9.77 ± 0.28	3.03 ± 0.11	10 ± 2	3.05 ± 0.20	29.4 ± 0.7	9.6 ± 0.7
HF17-2	35°52′11.01"N 94°08′21.23"E	3829	5.0	38–63	1.37 ± 0.05	7.34 ± 0.24	1.78 ± 0.08	10 ± 5	2.41 ± 0.17	32.8 ± 1.5	13.6 ± 1.1
HF17-3	35°52′11.01"N 94°08′21.23"E	3829	10.0	38–63	1.36 ± 0.05	7.08 ± 0.23	1.90 ± 0.08	10 ± 5	2.33 ± 0.17	42.3 ± 3.4	17.7 ± 1.9
HHC4-1	35°53′34.60"N 93°29′34.99"E	4300	0.80	38–63	1.99 ± 0.20	5.97 ± 0.22	1.67 ± 0.06	15 ± 5	2.80 ± 0.19	43.5 ± 2.01	16.5 ± 1.3
HR2-1	35°53′08.63"N 93°49′30.17"E	4052	0.70	38–63	2.42 ± 0.10	9.45 ± 0.27	1.52 ± 0.05	15 ± 5	2.91 ± 0.19	60.7 ± 2.74	21.1 ± 1.6
NMH1-1	36°02′39.36"N 96°26′15.36"E	3436	0.4	38–63	1.68 ± 0.06	10.1 ± 0.28	2.05 ± 0.10	10 ± 5	3.09 ± 0.21	70.5 ± 2.9	22.8 ± 1.8
NMH1-4	36°02′39.36"N 96°26′15.36"E	3436	6.0	38–63	1.65 ± 0.05	11.6 ± 0.32	2.73 ± 0.10	10 ± 5	3.39 ± 0.23	85.7 ± 4.8	25.3 ± 2.2
ALK3-1	35°32′23.98"N 97°11′49.70"E	4179	1.2	38–63	1.02 ± 0.04	5.30 ± 0.18	1.40 ± 0.07	10 ± 3	2.01 ± 0.13	32.0 ± 1.2	15.9 ± 1.2
ALK4-1	35°35′03.68"N 97°12′19.11"E	4108	0.4	38–63	1.19 ± 0.05	7.91 ± 0.25	1.95 ± 0.08	15 ± 5	2.41 ± 0.16	46.3 ± 2.5	19.2 ± 1.7
ALK4-2	35°35′03.68"N 97°12′19.11"E	4108	1.1	38–63	1.50 ± 0.05	10.9 ± 0.31	2.68 ± 0.10	20 ± 5	2.82 ± 0.18	50.4 ± 2.3	17.9 ± 1.4
ALK4-3	35°35′03.68"N 97°12′19.11"E	4108	2.4	38–63	1.09 ± 0.05	5.14 ± 0.18	1.34 ± 0.07	20 ± 5	1.76 ± 0.12	50.2 ± 2.6	28.6 ± 2.4
CK2-1	36°51′42.63"N 98°56′03.42"E	3180	9.0	38–63	1.80 ± 0.04	9.61 ± 0.60	2.3 ± 0.4	10 ± 3	3.00 ± 0.24	297.9 ± 31.57	99.2 ± 13.1
GH1-1	36°14′44.95"N 99°49′24.42"E	3036	3.0	90–125	3.19 ± 0.04	15.6 ± 0.80	2.6 ± 0.4	10 ± 3	4.55 ± 0.32	259.9 ± 10.2	57.1 ± 4.5
GH1-2	36°14′44.95"N 99°49′24.42"E	3036	6.0	38–63	3.16 ± 0.04	17.3 ± 0.90	2.7 ± 0.4	10 ± 3	4.94 ± 0.32	409.1 ± 34.0	83.9 ± 9.3
GH2-1	36°13′30.18"N 99°53′15.85"E	2984	1.7	90–125	2.33 ± 0.04	9.8 ± 0.60	2.1 ± 0.3	10 ± 3	3.26 ± 0.23	195.0 ± 13.0	59.9 ± 5.8
GH3-2	36°12′38.94"N 99°52′41.75"E	2991	9.1	90–125	2.26 ± 0.04	13.2 ± 0.80	2.3 ± 0.3	10 ± 3	3.39 ± 0.24	89.8 ± 5.14	26.5 ± 2.4
RYS3-2	36°45′15.32"N 101°00′59.55"E	3112	3.1	38–63	1.85 ± 0.04	8.98 ± 0.60	1.9 ± 0.3	10 ± 3	3.01 ± 0.22	105.2 ± 3.4	35.0 ± 2.8
RYS4-1	36°45′04.80"N 101°03′51.96"E	3117	2.1	38–63	1.85 ± 0.04	10.6 ± 0.70	2.0 ± 0.3	10 ± 3	3.21 ± 0.23	26.2 ± 0.5	8.1 ± 0.6
XS1-1	36°40′47.20"N 101°03′48.87"E	3068	5.0	38–63	2.26 ± 0.04	25.6 ± 1.20	2.2 ± 0.3	15 ± 3	4.35 ± 0.32	126.8 ± 9.8	29.2 ± 3.1
HL1-2	36°13′17.13"N 101°58′54.65"E	2715	16.0	38–63	2.01 ± 0.04	11.3 ± 0.70	2.2 ± 0.3	10 ± 3	3.26 ± 0.25	90.3 ± 2.81	27.7 ± 2.3
TD1-1	35°05′41.52"N 100°45′39.54"E	3447	5.6	90–125	1.92 ± 0.04	11.74 ± 0.70	2.1 ± 0.3	10 ± 3	3.10 ± 0.22	99.7 ± 5.9	32.2 ± 3.0
TD2-3	34°52′15.88"N 100°50′04.48"E	3627	15.0	90–125	1.62 ± 0.04	14.98 ± 0.80	2.8 ± 0.4	10 ± 3	3.02 ± 0.22	170.1 ± 12.6	56.3 ± 5.9
GN1-1	36°56′25.82"N 100°39′29.46"E	3248	16.0	38–63	1.75 ± 0.04	13.5 ± 0.80	3.0 ± 0.4	10 ± 3	4.49 ± 0.33	139.1 ± 4.1	31.0 ± 2.4

a.s.l. But it is approximately ~3,000 m a.s.l. in the Chaka–Gonghe Basin, the Qinghai Lake basin, and even much lower in the further southeast. Many types of glacial landforms and deposits have been developed in the U-shaped valleys, which are etched in the slopes on both sides of the mountains around the basins. The paleo-moraines are preserved at the elevations of 5,000–4,500 m a.s.l. in the western mountains of this region. But these forms are located at lower elevations (3,900–3,600 m a.s.l.) in the east of the mountains (Owen et al., 2006; Wang et al., 2013). The regional climate types are divided into three subzones: the arid feature and lower mean annual temperature in the Kunlun Mountains and the Chaka–Gonghe region, the semi-arid and moderate temperature in the Qilian and Qinghai Lake area, and the relatively humid and warm climate condition in southeastern Qinghai Province. The mean annual precipitation of the regions mentioned above not only depends on the atmospheric moisture but is also related to the topographic relief in the mountains (Yu et al., 2013).

At the present day, annual precipitation in the western region of the NETP is 100–200 mm, with the majority of it occurring during the summer season. The mean annual temperature is 2.0°C; the mean January temperature at the Wudaoliang meteorological station (4,780 m a.s.l.), which is 50 km to the south, is–8.4°C, and the mean July temperature is 12.1°C (Zhang et al., 2013). Owing to the low annual mean temperature, permafrost features are widespread in the study area. Vegetation in the drainage basins consists of dry alpine steppe communities (Stauch et al., 2017). In the eastern regions, the annual mean temperature is–0.3°C, the highest monthly mean temperature is 10.9°C (July), and the lowest monthly mean temperature is -13.5°C (January). The annual mean precipitation is 300–400 mm. The annual mean evaporation is about 1,300 mm (Liu et al., 2011). Alpine steppe and alpine meadow are the main vegetation types in the eastern region.

Sample Collection

The coordinates and elevations of all sampling sections in this study are shown in **Table 1**, and all profile photos are shown in **Figure 2**, in which the sampling sediment layers and dating results are displayed. The sections HF4, HF8, HF17, HHC, and HR are located in the Golmud River drainage basin. The first three sections consist of decimeters-thick alluvial sands to coarse gravels with moderate sorting, sub-rounding, and horizontal bedding traits. The alluvial fans are highly dissected, and several bluffs are developed due to river erosion. The section heights are 3, 24, and 13 m, respectively. The latter two are characterized by weakly sorted fine gravels, with a grain diameter of 2–5 dm, and sand lenticles sandwiched between the gravel layers. The sections NMH1, ALK3, and ALK4 lie on the Nuomuhong River and the Alake Lake catchments in the eastern Kunlun Mountains. The section NMH1 is a ~8-m-high alluvial stack and comprises sub-rounded and poorly sorted alluvial sand and gravel layers, and the upper and middle layers contain sparse boulders. The section ALK3 is 7 m thick and composed of weakly rounded and sorted gravels, which show horizontal layers, sandwiching irregular sand layers. The alluvial deposits are capped by a discontinuous, decimeter-to-meter–thick layer of loess sediment. The section ALK4 comprises a 2.5-m-thick alluvial toe deposit comprising rufous, tawny horizontally bedded clay, and silt layers in the upper half and sand to five gravel layers in the lower part. The sections CK2, GH1, and GH2 are on the piedmont alluvial fan cascades from Ela Mountain and the Qinghainan Mountains. The section CK2 is a 10-m-thick alluvial stock and sandwiches half-meter sand lenticles. Inversely, the sections GH1 and GH2 are predominantly alluvial gravel deposits with 10-dm-thick sand lenticles, and have a thickness of 6.0 and 2.5 m. The sections RYS3, RYS4, and XS1 are situated in the piedmonts of Riyue Mountain. Sections RYS3 and RYS4 mainly comprise crudely stratified meter and decimeter beds of fanglomerates and debris flows (section RYS4 contains abundant boulders), with a section thickness of 3.5 and 3.0 m. Section XS1 is a set of alluvial deposits that contains some boulders, with a thickness of 15 m. In the easternmost segment of the NETP, there are four sections, HL1, TD1, TD2, and GN1, which merge with the distinctive alluvial deposits, with stratification, interbedding, and clear sand and gravels, also containing a few sand lenticles. The four sections have a section thickness of 25, 20, 15, and 18 m, respectively. A total of 26 samples were collected for OSL dating with the stratigraphic order from the alluvial sections mentioned above.

Optically Stimulated Luminescence Dating

The OSL samples were collected by driving iron tubes (25 cm in length and 5 cm in diameter) into newly cleaned vertical sections. Each tube was covered with black plastic bags and was sealed with black packaging tape to avoid light exposure and moisture losses. In the laboratory, 3-cm sections of the sediments at each end of the cylinders were scraped away and were used for water content and dose rate measurements. The unexposed part in the middle of the tube was used for equivalent dose (D_e) determination. We followed the procedures of Lai (2010) to chemically pretreat OSL samples to remove feldspar contamination that might lead to age underestimation (Lai and Brückner, 2008). We checked the purity of the retrieved quartz by infrared light stimulation (830 nm), and no obvious IRSL was observed. The pure quartz samples were mounted on the center (0.7 cm in diameter) of stainless steel discs with a diameter of 0.97 cm with silicone oil.

We used an automated Risø TL/OSL-DA-20 reader for OSL dating, which was equipped with a $^{90}Sr/^{90}Y$ beta source for OSL measurements at the Qinghai Institute of Salt Lakes, Chinese Academy of Sciences. The procedure involved stimulation by blue LEDs at 130°C for 40 s and signal detection using 7.5-mm-thick U-340 filters. We used neutron activation analysis to determine the U, Th, and K concentration at the China Institute of Atomic Energy in Beijing. For grains in the range of 38–63 μm, the α efficiency was taken as 0.035 ± 0.003 (Lai et al., 2008). The cosmic ray dose rate was estimated for each sample as a function of depth, altitude, and geomagnetic latitude (Prescott and Hutton,

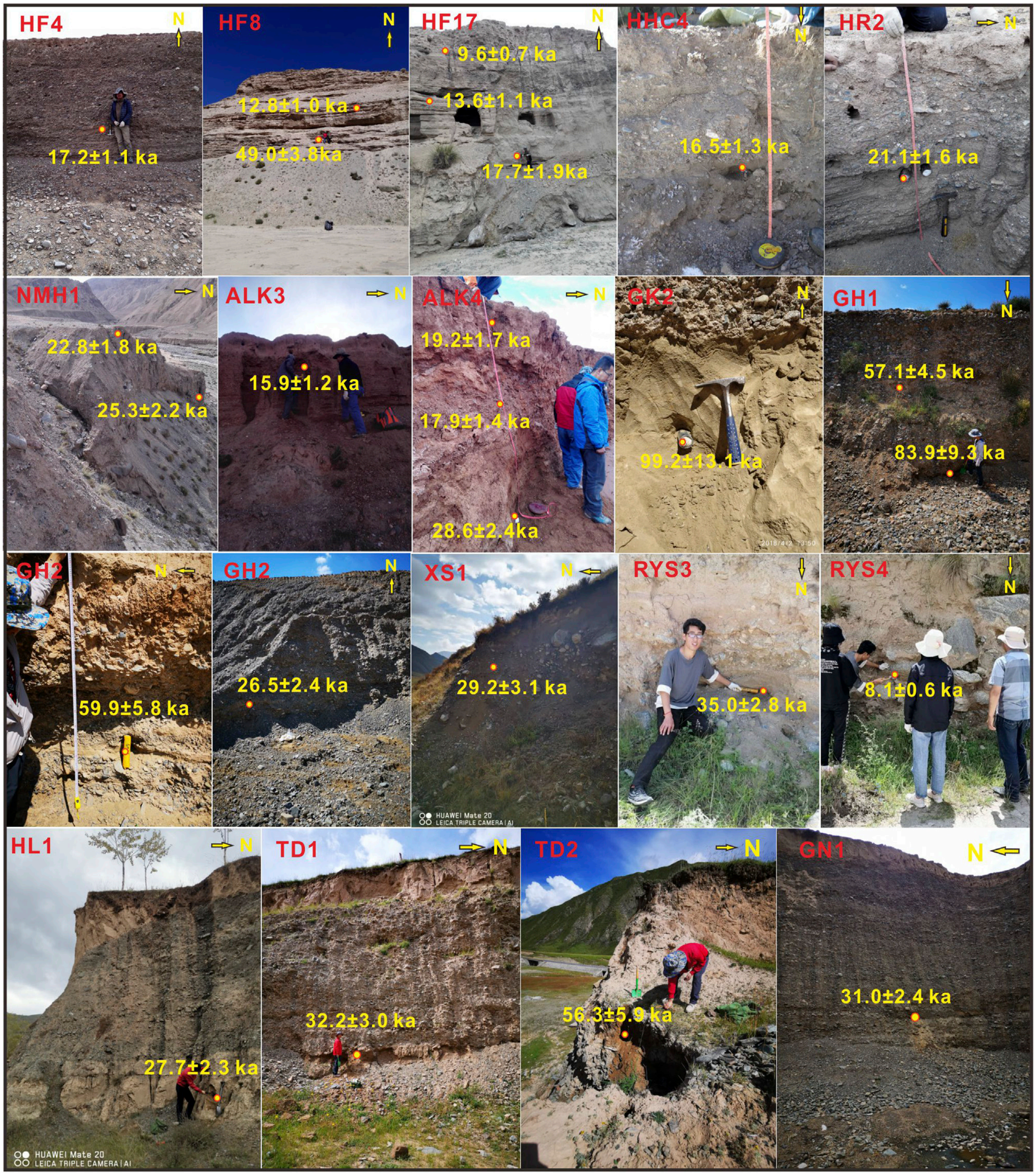

FIGURE 2 | Photos showing profile sedimentary features of all alluvial sections involved in the current study and sampling layers and their corresponding dating results.

1994). Water content was calculated from moisture mass/dry mass (Aitken, 1985), and most of the measured results were near 0%, which is attributed to the arid modern environment. However, considering the uncertainties associated with burial and sediment types, values of 10–15% were estimated for the water content and dose rate calculations (**Table 1**).

The equivalent dose (D_e) was determined using a combination of the single-aliquot regenerative dose (SAR) protocol Murray and Wintle (2000) and a standardized growth curve (SGC) method (Lai and Wintle, 2006), that is, the SAR-SGC method was applied. For each sample, six aliquots were measured using the SAR to construct the SGC, and then twelve aliquots were measured using the SGC. The final D_e for a sample was given by the average of all eighteen D_e values. **Figure 3** shows the typical OSL decay curves and growth curves for ALK4-1 and GH1-1, respectively, suggesting that the OSL signals were from the fast component. Preheat plateau tests were conducted on samples ALK4-3 and RYS3-2, and a preheat plateau was clearly identified from 240 to 280°C in both samples (**Figure 4**). Based on the results, a preheat of 260°C for 10 s and a second heat of 220°C for 10 s were used for D_e measurements. Signals of the first 0.64 s of stimulation were integrated for growth curve construction after back ground subtraction.

Dose recovery tests (Murray and Wintle, 2003), which can validate the SAR procedure, were performed on samples ALK4-3 and RYS3-2, and six aliquots of each sample were tested. The ratios of the average measured dose (54.4 and 106.6 Gy) to the given dose (50 and 105 Gy), which fall into the acceptable range of 0.9–1.1, suggested that the SAR protocol was suitable for D_e determination in this study (**Figure 4**). Recuperation was calculated by comparing the sensitivity-corrected OSL signal of 0 Gy to the sensitivity-corrected natural signal to check the thermo-transferred signals. In this study, recuperations for different preheat temperatures were less than 5% of the natural signal, which was negligible (**Figure 4**). The "recycling ratio" was introduced to check for sensitivity change correction Murray and Wintle (2000), and for most aliquots, the recycling ratios fell into the acceptable range of 0.9–1.1 (**Figure 4**).

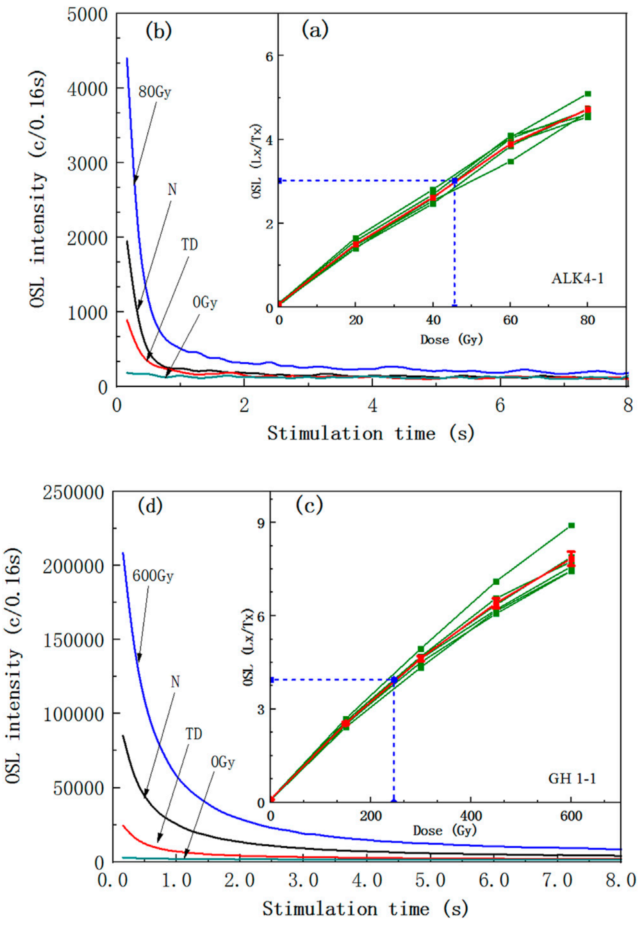

FIGURE 3 | Luminescence characteristics of samples ALK4-1 and GH1-1; **(A)** and **(C)** display the growth curves of six aliquots and the standard growth curve (SGC) (red lines), which is taken as the average of the six growth curves; **(B)** and **(D)** display the decay curves for the natural (N) and regenerative doses of R3, 0 Gy, and test dose (TD), respectively. The points (solid squares) defining each individual growth curve are depicted with error bars. The horizontal and vertical blue dashed lines indicate the projection of the average of the sensitivity-corrected natural signals of the six aliquots onto the SGC.

RESULTS

Considerable success has been obtained from applying OSL dating to dammed fluvial–lacustrine sediments in the central southern TP, with well-bleached samples that yielded accurate age estimates (Liu et al., 2015; Chen et al., 2016; Liu et al., 2018; Wang et al., 2019). Consistent ages of eolian sand lenticels and adjacent alluvial sedimentary layers in the alluvial delta fan supported the reliability of OSL dating of alluvial sediments in the eastern Kunlun Mountains (An et al., 2018a). A modern fluvial sediment sample from the Kunlun River catchment (proximity to the HL3), which produced a D_e of 1.20 ± 0.20 Gy (0.4 ± 0.1 ka) at a depth of 0.3 m, indicated a negligible residual dose in samples from the drainage basin (An et al., 2021).

The OSL ages determined in the current study are presented in **Table 1**, and the quoted chronology data from previous studies are listed in **Supplementary Table S1**. The entire data on alluvial fans cover from the most western part of the eastern Kunlun Mountains to the most eastern end of Qinghai Lake and Riyue Mountain, occupying the main monsoon-dominated region on the NETP. The initiating of the alluvial fans involved in this investigation occurred since the age of 99.2 ± 13.1 ka. Inferences suggested that there are older alluvial sediments than these. However, the older geomorphic processes could have greater odds of tectonic influence, especially the surface uplift; thus, we mainly focused on the alluvial formation since the Last Interglaciation. The youngest ages for a debris flow that is covered by loess have a date of 8.1 ± 0.6 ka. Analysis of the entire forming ages of the alluvial fans on the NETP suggests that the Last Glaciation and Deglaciation were the main developing stages, and the alluvial fans of different scales filled diffusely in the drainage basins of this region. The MIS 3 period is another relative activity stage of alluvial geomorphic processes. From 83.9.1 ± 9.36 to 99.2 ± 13.1 ka, the strong hydrological processes promoted the development of the alluvial fans. This stage corresponded to the late period of the MIS 5. Analyses of these dating results from regionalism showed that the alluvial

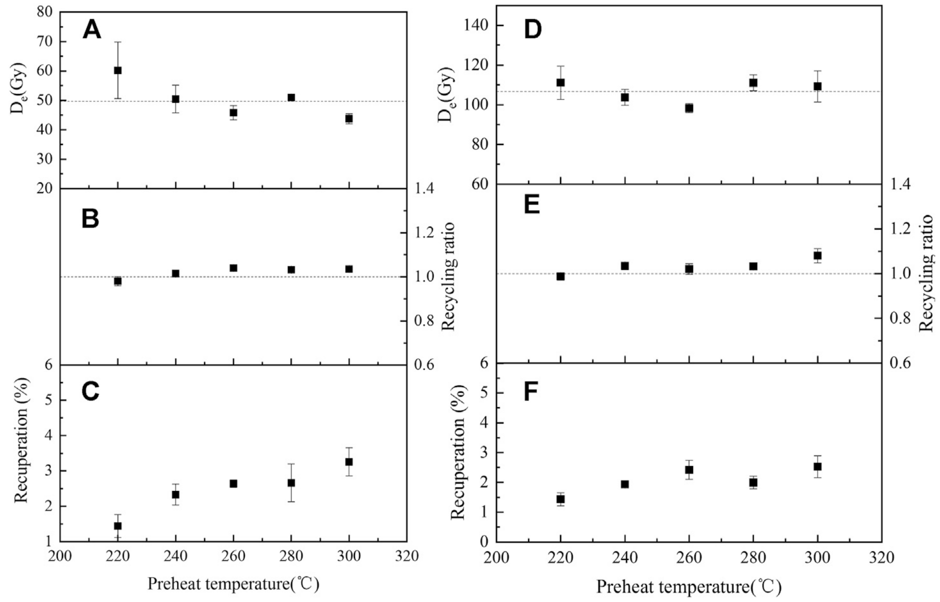

FIGURE 4 | Results of preheat plateau tests **(A)** and **(D)**, recuperation **(C)** and **(F)**, and recycling ratio **(B)** and **(E)** for ALK4-3 **(left)** and RYS3-2 **(right)**. The equivalent dose (*D_e*) of each data point is the mean of four aliquots. The final chosen preheat temperature for quartz OSL dating in this study was 260°C.

fans in the drainage basins of the western high mountains yielded the broad-spectrum ages ranging from the Last Interglaciation to early Holocene periods. Inversely, in the eastern lower mountains, the age data were mainly concentrated in the MIS 3 period, and other climate stage ages were relatively scarce. These results could be ascribed to the high mountain topography (altitude variation from ~4,000 to 6,000 a.s.l), which was more sensitive to the moisture fluctuation dominated by the hemispherical atmospheric circulations.

DISCUSSION

The Climatic/Tectonic Influences on the Alluvial Fans Since 200 Ka

The valley fills or the piedmont cascade of alluvial detritus in the arid and semi-arid drainage basins are commonly ascribed to climate change or tectonic uplift (Chen et al., 2011; Zhang et al., 2014; An et al., 2018a; Tao et al., 2020). In recent decades, various geomorphic units in the northeastern margin of the NETP, such as alluvial fans, fluvial terraces, high-stand lacustrine sediments, sand dunes, and moraines, have been intensively studied. Almost all previous studies have focused on the effect of climate changes for the surface geomorphic dynamics since the penultimate Interglaciation, although the influence of tectonic uplift could not be ruled out in some local places (for the specific statistics of the references, see **Table 2**). As shown in **Table 2**, the paleoclimate change is one of the major factors controlling depositional processes, and it played a prominent role in the formation of various geomorphic units on the NETP. Most landform processes in the Golmud River of the eastern Kunlun Mountains, including impressive piedmont alluvial fans and delta alluvial fans, stretch into the arid basin and are related to climate change rather than surface uplift (Owen et al., 2006; An et al., 2018a, b). The formation of the alluvial fan deposits is related to the hydrological variation in the mountains at the southern border of the Heihai Lake, which is located in the headwater area of the Golmud River, and it influenced the variation of the lake level through blockage of the lake outflow (Stauch et al., 2017). The synthetic wetness index from various geomorphic units in the mountain valleys of the eastern Kunlun Mountains showed a good correspondence to moisture records that were controlled by the ISM, showing their paleoclimatic cause (An et al., 2018a). In a study of the ^{10}Be flux of lacustrine sediments collected at Kunlun Pass, Chen et al. (2021) suggested that there was a shift in the dominant influence in the region from monsoons to westerlies after 4 ka BP. In the Qinghai Lake watershed, alluvial sediments mainly deposited during the middle-to-late MIS 3, and they had a paleoclimatic origin (Liu et al., 2017). A stream-dominated fan in the Xining Basin, which lies on the margin of the NETP, was reported by Gao et al. (2018), Their results indicated that a climate-dominated transition of the sedimentary environment from high- to low-energy fans occurred from the penultimate glacial to the last interglacial. A database of the terrace ages of Quaternary fluvial terraces on the TP and surrounding orogenic belts was integrated by Tao et al. (2020), and they grouped terraces into the three regional climate systems, the ISM, EASM, and westerlies, and found that the formation of terraces younger than 200 ka was mainly controlled by climate changes. However, the incision of fluvial terraces in the Golmud River drainage basin was ascribed to the transitory surface uplift by Chen et al. (2011). They argued that the valley fills occurred during the tectonic stable stage of the Last Glaciation. From the analysis mentioned above, we can draw a

TABLE 2 | Statistics of climatic/tectonic forcing factors for various geomorphic units from previous studies in the Northeastern Tibetan Plateau since 200 ka.

Covered areas	Geomorphic units	Dating methods	Paleoclimatic stage	Forcing factors	Authors
Southern margin of the Qaidam Basin, eastern Kunlun Mountains	Moraines Alluvial fans Pediments and terraces	SED, OSL	Penultimate Glaciation, Last Glaciation, Last Deglaciation, and middle Holocene	Climate	Owen et al. (2006)
Golmud River catchment on the Northeastern Tibetan Plateau	Drainage and lacustrine sediments	ESR U-series	Penultimate Interglaciation Last Interglaciation	Climate	Cui et al. (1999)
Northern margin of the Tibetan Plateau	Valley fills Fluvial terraces	OSL	Last Glaciation Early-to-middle Holocene	Climate	Wang et al. (2009)
Heihai Lake catchment of the eastern Kunlun Mountains	Alluvial fans Eolian sediments Fluvial terraces Drainage and lacustrine sediments	OSL	Last Deglaciation and Holocene	Climate	Stauch et al. (2017)
Nalinggele River catchment of the eastern Kunlun Mountains	Valley fills and fluvial terraces	OSL	Last Glaciation Early-to-middle Holocene	Climate	Chang et al. (2017)
Northeastern Tibetan Plateau	Alluvium, eolian sediments, and sand wedges	OSL	Last Glaciation Last Deglaciation	Climate	Liu et al. (2017)
Huanghui River on the Northeastern Tibetan Plateau	Alluvial fans	OSL	Penultimate Glaciation Last Interglaciation	Climate	Gao et al. (2018)
Heihai Lake catchment of the eastern Kunlun Mountains	Fluvial terraces High-stand lacustrine sediments Lake shoreline	OSL, ^{14}C	Late Holocene	Climate	An et al. (2018a)
Southern margin of the Qaidam Basin, eastern Kunlun Mountains	Alluvial fans Eolian sediments Fluvial terraces Swamp sediments	OSL	Last Deglaciation and Holocene	Climate	An et al. (2018b)
Across the Tibetan Plateau	Fluvial terraces	Integrated age data	Since the Penultimate Interglaciation	Climate	Tao et al. (2020)
Golmud River catchment on the Northeastern Tibetan Plateau	Alluvial fans, dammed lake sediments, and loess	OSL	Last Glaciation Last Deglaciation Early Holocene	Climate	An et al. (2021)
Golmud River catchment on the Northeastern Tibetan Plateau	Valley fills Slope deposits Fluvial terraces	OSL, ^{14}C	Last Glaciation Last Deglaciation Early-to-middle Holocene	Climate and tectonics	Chen et al. (2011)

conclusion that the alluvial fans developed in the studied area responded to the paleoclimatic fluctuations rather than the tectonic uplifts during the late Quaternary.

The Glacial Forcing Mechanism on Alluvial Fans' Development

Enhanced evidence suggested that the dynamic of alluvial fans on the NETP showed a periglacial origin, especially the high relief and elevation regions (Van Der Woerd et al., 2002; Owen et al., 2006; Stauch et al., 2017; An et al., 2018a; Cui et al., 2020). The glacier activities in the high mountains produced abundant glacial debris in the piedmont during glaciation periods (Owen et al., 2006). Subsequently, the glacial debris cascaded onto alluvial fans and was transported into tributary and main valleys by abundant glacier meltwater and finally completed valley filling (An et al., 2018b). The process of aggradations from the piedmont to the alluvial delta fan was probably multistage or leapt forward to the downstream drainage basin, as there are several reservoir segments in the main valley through which detrital materials are transported step by step (Wang et al., 2009; An et al., 2018b). Therefore, the multistage alluvial fans or valley fills in drainage basins and the margin area of arid basins are the main linkage between the orographic glaciers and the distal lower basins. The dating age for the moraine sediments is limited because there are few suitable chronology methods or dating materials (Cui et al., 2020). Thus, the dynamics of the alluvial fans reflect environmental/climatic information of the provenance area, namely, glacial activity processes. Both the geomorphic dynamics showed more consistent feedback to each other on the orbital timescale. In view of the foregoing, we compared the developing ages of alluvial fans in different areas on the NETP with those of the glacial advances from the eastern Kunlun Mountains, the Dalijia Peak of eastern Riyue Mountain, the Queer Shan ranges of the eastern TP, and Yulong Mountain of the southeastern TP (Owen et al., 2006; Wang et al., 2013; Ou et al., 2014; He et al., 2016) (**Figures 5A,B**). There is broad consistency in the timing of both geomorphic dynamics, especially in the early Holocene, Last Deglaciation, and MIS 2. The stages MIS 3 and late MIS 5 were also relatively active periods for the alluvial fans and glaciers. Even in the records of both geomorphic processes, the Younger Dryas (YD) event can be

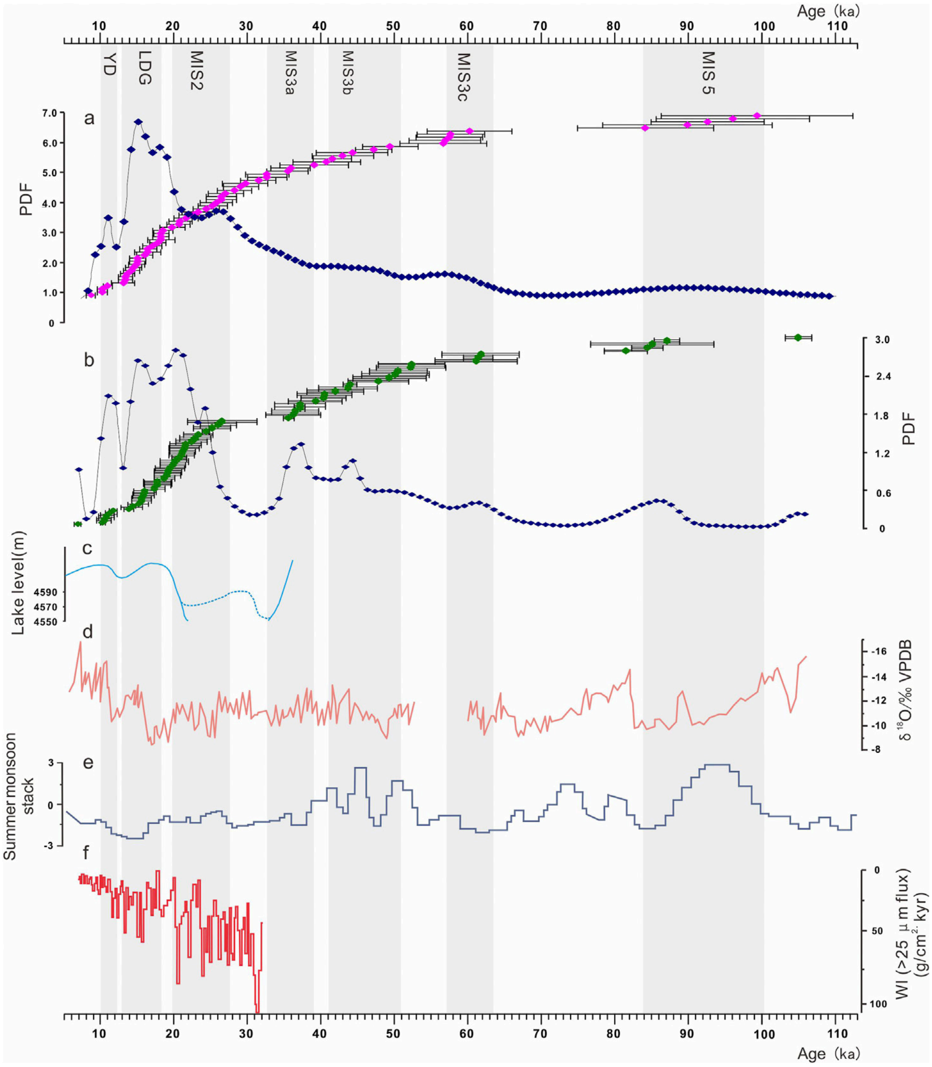

FIGURE 5 | Comparison of alluvial fan and glacial advance OSL ages from the present study with proxy climate indicators. **(A)** Purple rhombuses represent alluvial fan ages with error bars. **(B)** Green rhombuses represent glacial advance ages with error bars. The string of blue rhombus lines in **(A)** and **(B)** are the probability density function (PDF) curves from the ages. **(C)** Reconstructed lake level for the Taro Co lake system, southwestern TP. Dashed line represents the probable maximum lake level (modified by Alivernini et al., 2018). **(D)** δ^{18}O record of the stalagmites from the Xiaobailong cave, southwestern TP (Cai et al., 2015). **(E)** Arabian Sea summer monsoon stack (Caley et al., 2011; Bolton et al., 2013). **(F)** Qinghai Lake westerlies climate index (An et al., 2012). The gray frames represent the prominent increase stages of alluvial aggradations. MIS, Marne Isotope Stage; LDG, Last Deglaciation; YD, Younger Dryas event.

distinguished during ~10.5–12.0 ka (**Figures 5A,B**). The good correspondence between forming ages of alluvial fans and those of glacial advances indicates that the latter controls the former's extension. Meanwhile, strong hydrographic discharge also probably promoted the stretches of alluvial fans and finished most valley fills of drainage basins; the hypothesis can be tested by the mass development of alluvial fans during the Last Deglaciation/Last Interglaciation periods. The melting glaciers yielded abundant high-load runoffs and transported surplus sediments, which boosted the aggradations toward the fan toes (Ou et al., 2014). The strengthened precipitation together with moderate glacier activities during the Late Interglaciation was probably somewhat responsible for the development of the alluvial fans, corresponding to the slight enhancement for the current probability density function (PDF) curves (**Figures 5A,B**). Previous studies provided enhanced evidence that the glacial advances occurred during the penultimate glacial cycle, MIS 3, Last Glacial Maximum (LGM), Late Glacial, and Holocene periods in the northeastern or southeastern mountain regions of the TP (Owen et al., 2003, 2006; Ou et al., 2014; Wang et al., 2014; He et al., 2016; Cui et al., 2021). The expansion of the extent of glaciers was affected by the change in precipitation, and the extent of glaciers during the MIS 3 was more extensive than that during the LGM (Owen et al., 2003; Cui et al., 2021). The alluvial fans originated from orographic outwash formed on the southern side of the Kunlun Mountains prior to 200 ka (Owen et al., 2006) and

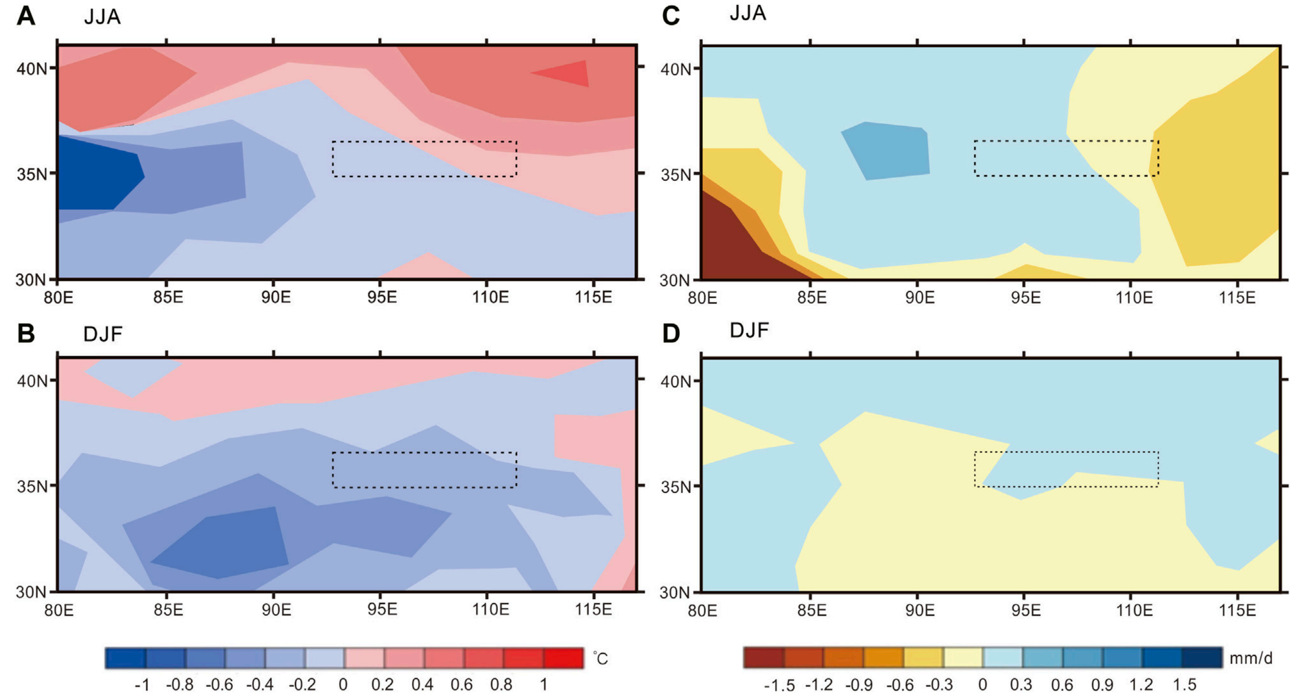

FIGURE 6 | Changes in summer (June–August) and winter (December–February) surface temperatures **(A)** and **(B)** and precipitation rates **(C)** and **(D)** due to the glacier expansions over the northern TP during the LGM (modified from Liu et al., 2020). The dashed rectangle is the covered region of this study.

later frequently occurred in different paleoclimatic stages (Xu et al., 2010). Meanwhile, alluvial sequences in the eastern part of the NETP, such as Riyue Mountain and the Qinghainan Mountains, intensively formed during the MIS 3. This phenomenon is probably ascribed to the lower temperature and more abundant precipitation in this stage, including glacier activities combining the sufficient rainfall that were responsible for the alluvial geomorphic evolutions. Cui et al. (2021) argued that the coupling effect of lower temperature and increased precipitation on the NETP resulted in the expansion of the orographic glaciers during the MIS 3 rather than the LGM. A simulation result of the CAM4 climate model suggests that an expansion of glaciers would lead to a decrease in surface air temperatures during both the summer and winter over most regions of the TP, and coupled with increased summer precipitation and increase in cold glacier meltwater supply, it would be in favor of alluvial advance and high lake levels (Liu et al., 2020).

Paleoclimatic Implications for Glacier-Induced Alluvial Fans

The NETP is situated in a sensitive arid and semi-arid zone between the ISM-controlled and the westerly-influenced regions of Asia, and the dominated atmospheric circulations were commonly altered from the interglacial to glacial periods (An et al., 2012). Thus, construction of the paleoclimate changes from the dynamics of the glacier and alluvial fan geomorphic processes is an intricate procedure. But, this allows us to distinguish the different climatic systems on the interglacial-to-glacial or interstadial-to-stadial cycle timescales. The formation of the alluvial fans involved in the current study began since the late MIS 5 and ended during the early Holocene (**Table 2** and **Figure 5A**). These results referred to various climatic stages, including the MIS 5, MIS 3, MIS 2, Last Deglaciation, and YD periods. Ramisch et al. (2016) suggested that the moisture status of the eastern Kunlun Mountain region is mainly dominated by the ISM and the mountains form the northern boundary of the monsoon system, which triggered orographic rainfall or snowfall. Cui et al. (2020) argued that the temperature drops ranged from –0.5 to 0.1°C with precipitation being 140 ~ 200% during the MIS 3 in the Kunlun Mountains. The lower temperature and high moisture were in favor of glacial advances (Cui et al., 2021), which contributed to abundant outwash supply and alluvial fill in the drainage basin. Recent studies have indicated that the glaciations of most regions of the TP were influenced by the ISM or the Asian monsoon during the MIS 5 and MIS 3, and the increased south Asian monsoon supplied more precipitation as snow at high altitudes (Owen et al., 2003; Xu et al., 2010; Stauch et al., 2017; Cui et al., 2021). However, a remarkable feature of the age distribution for alluvial fans indicates that the periods of Last Glaciation and Deglaciation are the main developing stages for the alluvial aggradations. The results are well consistent with the ages of the glacial advance (**Figures 5A,B**). An et al. (2012) found an antiphase relationship between the westerlies and the ASM for glacial millennial timescales in the Qinghai Lake catchment during the Last Glaciation. Li et al. (2020) argued that the Asian monsoon and the westerlies showed positive correlation on millennial timescales but anticorrelation during suborbital cycles. Therefore, we synthesized a record comparison between our alluvial age data with the proxies for ISM-dominated regions and the westerlies index from Qinghai Lake (**Figures 5C–F**). As shown in the figure, the alluvial age record closely matches that of glacier activities and the record of high lake levels on the southern TP, such as those of the Taro Co lake group (**Figure 5C**). Alluvial aggradations are also consistent with the δ^{18}O record of the stalagmites from the southwestern TP and the summer monsoon stack from the Arabian Sea (**Figures 5D,E**), suggesting the influence of the ISM during the MIS 5, MIS 3, and early Holocene. But the prominent increase in the alluvial ages during the Last Glaciation and Deglaciation showed more consistency with the westerlies index. Thus, we considered that strengthened westerlies combined with slight monsoon dominated the intensive glacial activities and alluvial aggradations in the drainage basin on the NETP during the Last Glaciation. This glacial expansion stage was verified using a simulation. The decrease in surface air temperatures and increase in precipitation rates during both the summer and winter boosted the orographic glacier activities (**Figure 6**), and they also showed inter-feedback to each other, especially the western mountains of the region. Subsequently, massive glaciers melted with the warming climate, finally facilitating a large scale of development for the alluvial fans during the Last Deglaciation.

CONCLUSION

Investigation on the climatically induced alluvial fans that cascaded from mountains in the semi-arid regions provides insight into the geomorphic and hydrographic processes driven by paleoclimatic fluctuations. We investigated a series of alluvial fans on the NETP region using the morphostratigraphic study and OSL dating. These alluvial sequences cascaded from the high piedmonts in the eastern Kunlun Mountains, Ela Mountain, the Qinghainan Mountains, and Riyue Mountain, ultimately filling the drainage basins or stretching into the arid sedimentary basins. Integrated analysis indicated that the alluvial geomorphic processes were related to the paleoclimate changes rather than the surface uplifts. These are basically composed of the coarse-to-fine, weak, and angular gravels and sandy lenticles, which occasionally contained boulders in specific layers. The OSL dating results showed that the alluvial fans had mainly developed during the late MIS 5, MIS3, and Last Glaciation and Deglaciation, little occurring during the early Holocene. The findings are firmly consistent with the orographic glacial advance periods in the northeastern and eastern regions of the TP. Considering that the alluvial fan is a production of downward outwash transportation according to previous studies, we argued that the dynamics of the alluvial fans and alluvial valley fills should be ascribed to the paleo-glacier activities during different climatic stages since the late Pleistocene. The comparisons of wet indexes between our age data and records from the ISM- and westerly-dominated regions showed that both the climatic systems had coupling impacts on the glacial advances and subsequent alluvial aggradations on the supply of moisture in different paleoclimatic stages. The simulation also suggested that lower temperature and enhanced precipitation during the LGM resulted in the glacier expansion. This result matches with our data that indicate that the alluvial aggradations mainly occurred during the MIS 2 and the sequent postglacial stage.

DATA AVAILABILITY STATEMENT

The original contributions presented in the study are included in the article/**Supplementary Material**; further inquiries can be directed to the corresponding authors.

ETHICS STATEMENT

Written informed consent was obtained from the relevant individual(s) for the publication of any potentially identifiable images or data included in this article.

AUTHOR CONTRIBUTIONS

FA and SL designed the research. FA, BN, DG, and JZ performed the research. LC and XC made the figures and analyzed the data. FA and BQ wrote the manuscript. TC analyzed the OSL dating results with age models.

FUNDING

This study was supported by the Natural Science Foundation of Qinghai Province (Grant no. 2020–ZJ–727) and the China NSF (Grant no. 41961014).

ACKNOWLEDGMENTS

We thank Jun Li, Ping, Li, Jingyi Gao, Hongjun, Yu, Fuzhong Zhou, Zhiyong Ling, and Yixuan Wang for field assistance, discussion, and OSL dating. We would also like to thank the editor and the two reviewers who helped to improve the article.

SUPPLEMENTARY MATERIAL

The Supplementary Material for this article can be found online at: https://www.frontiersin.org/articles/10.3389/feart.2021.702340/full#supplementary-material

REFERENCES

Aitken, M. J. (1985). *Thermoluminescence Dating*. London: Academic Press.

Alivernini, M., Lai, Z., Frenzel, P., Fürstenberg, S., Wang, J., Guo, Y., et al. (2018). Late Quaternary lake Level Changes of Taro Co and Neighbouring Lakes, Southwestern Tibetan Plateau, Based on OSL Dating and Ostracod Analysis. *Glob. Planet. Change* 166, 1–18. doi:10.1016/j.gloplacha.2018.03.016

An, F., Lai, Z., Liu, X., Wang, Y., Chang, Q., Lu, B., et al. (2018a). Luminescence Chronology and Radiocarbon Reservoir Age Determination of Lacustrine Sediments from the Heihai Lake, NE Qinghai-Tibetan Plateau and its Paleoclimate Implications. *J. Earth Sci.* 29 (3), 695–706. doi:10.1007/s12583-017-0972-9

An, F., Liu, X., Zhang, Q., Wang, Y., Chen, T., Yu, L., et al. (2018b). Drainage Geomorphic Evolution in Response to Paleoclimatic Changes since 12.8 Ka in the Eastern Kunlun Mountains, NE Qinghai-Tibetan Plateau. *Geomorphology* 319, 117–132. doi:10.1016/j.geomorph.2018.07.016

An, F. Y., Chen, T. Y., Li, X. Z., Liu, X. J., Wang, Y. X., Chen, Z. Y., et al. (2021). Formation, Mechanism and Significance of Alluvial-Dammed Lakes in Golmud River Cathment, NE Qinghai-Tibetan Plateau. *Earth Surf. Proc. Land.*In Press.

An, Z., Colman, S. M., Zhou, W., Li, X., Brown, E. T., Jull, A. J. T., et al. (2012). Interplay between the Westerlies and Asian Monsoon Recorded in Lake Qinghai Sediments since 32 Ka. *Sci. Rep.* 2, 619–625. doi:10.1038/srep00619

Ashworth, P. (2006). Alluvial Fans: Geomorphology, Sedimentology, Dynamics Edited by Adrian Harvey, Anne Mather and Martin Stokes. *Area* 38 (2), 225–226. doi:10.1111/j.1475-4762.2006.690_5.x

Bolton, C. T., Chang, L., Clemens, S. C., Kodama, K., Ikehara, M., Medina-Elizalde, M., et al. (2013). A 500,000 Year Record of Indian Summer Monsoon Dynamics Recorded by Eastern Equatorial Indian Ocean Upper Water-Column Structure. *Quat. Sci. Rev.* 77 (77), 167–180. doi:10.1016/j.quascirev.2013.07.031

Bridgland, D. R. (2010). The Record from British Quaternary River Systems within the Context of Global Fluvial Archives. *J. Quat. Sci.* 25, 433–446. doi:10.1002/jqs.1383

Bureau of geology and mineral resources of Qinghai Province (1991). *Regional Geology of Qinghai Province* (Beijing, China: Geological Publishing House). (in Chinese with English abstract).

Cai, Y., Fung, I. Y., Edwards, R. L., An, Z., Cheng, H., Lee, J.-E., et al. (2015). Variability of Stalagmite-Inferred Indian Monsoon Precipitation over the Past 252,000 Y. *Proc. Natl. Acad. Sci. USA* 112 (112), 2954–2959. doi:10.1073/pnas.1424035112

Caley, T., Malaizé, B., Zaragosi, S., Rossignol, L., Bourget, J., Eynaud, F., et al. (2011). New Arabian Sea Records Help Decipher Orbital Timing of Indo-Asian Monsoon. *Earth Planet. Sci. Lett.* 308 (3-4), 433–444. doi:10.1016/j.epsl.2011.06.019

Chang, Q., Lai, Z., An, F., Wang, H., Lei, Y., and Han, F. (2017). Chronology for Terraces of the Nalinggele River in the north Qinghai-Tibet Plateau and Implications for Salt lake Resource Formation in the Qaidam Basin. *Quat. Int.* 430, 12–20. doi:10.1016/j.quaint.2016.02.022

Chen, P., Yu, Z., Czymzik, M., Aldahan, A., Wang, J., Yi, P., et al. (2021). Holocene Monsoon Dynamics at Kunlun Pass on the Northeastern Qinghai-Tibet Plateau. *Sci. Total Environ.* 771, 145369. doi:10.1016/j.scitotenv.2021.145369

Chen, Y., Aitchison, J. C., Zong, Y., and Li, S.-H. (2016). OSL Dating of Past lake Levels for a Large Dammed lake in Southern Tibet and Determination of Possible Controls on lake Evolution. *Earth Surf. Process. Landforms* 41 (11), 1467–1476. doi:10.1002/esp.3907

Chen, Y., Li, Y., Zhang, Y., Zhang, M., Zhang, J., Yi, C., et al. (2011). Late Quaternary Deposition and Incision Sequences of the Golmud River and Their Environmental Implications. *Quat. Int.* 236, 48–56. doi:10.1016/j.quaint.2010.05.028

Cui, H., Cao, G., Badingquiying, K., Chen, H., and Jiang, G. (2020). Climates since Late Quaternary Glacier Advances: Glacier-Climate Modeling in the Kunlun Pass Area, Burhan Budai Shan, Northeastern Tibetan Plateau. *Quat. Int.* 553, 53–59. doi:10.1016/j.quaint.2020.05.050Chen

Cui, H., Cao, G. C., Chen, K. L., Guo, H., and Jiang, G. (2021). A Review on the Reconstruction of Palaeoclimate by Glacial Landform in the Tibetan Plateau and Adjacent Mountains. *J. Glaciology Geocryology* 43 (1), 254–262.(in Chinese with English abstract).

Cui, Z. J., Wu, Y. Q., Ge, D. K., and Liu, G. N. (1999). Environmental Change of Kunlun Pass Area since Quaternary. *Mar. Geology. Quat. Geology.* 19, 53–62.(in Chinese with English abstract)

Gao, L., Wang, X., Yi, S., Vandenberghe, J., Gibling, M., Lu, H., et al. (2018). Episodic Sedimentary Evolution of an Alluvial Fan (Huangshui Catchment, NE Tibetan Plateau). *Quaternary* 1, 16. doi:10.3390/quat1020016

Guo, Q., Zhou, Z., and Wang, S. (2017). The Source, Flow Rates, and Hydrochemical Evolution of Groundwater in an Alluvial Fan of Qilian Mountain, Northwest China. *Water* 9, 912. doi:10.3390/w9120912

He, Z., He, Y., Zhang, Z., He, L., Qi, C., and Liu, J. (2016). OSL Dating of the Quaternary Glacial Sedimentary Sequences at Mt. Yulong, China. *J. Glaciology Geocryology* 38 (6), 1544–1552 doi:10.7522/j.issn.1000-0240-2016.0180in Chinese with English abstract)

Kapp, P., Pelletier, J. D., Rohrmann, A., Heermance, R., Russell, J., and Ding, L. (2011). Wind Erosion in the Qaidam basin, central Asia: Implications for Tectonics, Paleoclimate, and the Source of the Loess Plateau. *Gsat* 21, 4–10. doi:10.1130/GSATG99A.1

Lai, Z.-P., and Wintle, A. G. (2006). Locating the Boundary between the Pleistocene and the Holocene in Chinese Loess Using Luminescence. *The Holocene* 16 (6), 893–899. doi:10.1191/0959683606hol980rr

Lai, Z., and Brückner, H. (2008). Effects of Feldspar Contamination on Equivalent Dose and the Shape of Growth Curve for OSL of silt-sized Quartz Extracted from Chinese Loess. *Geochronometria* 30 (1), 49–53. doi:10.2478/v10003-008-0010-0

Lai, Z. (2010). Chronology and the Upper Dating Limit for Loess Samples from Luochuan Section in the Chinese Loess Plateau Using Quartz OSL SAR Protocol. *J. Asian Earth Sci.* 37 (2), 176–185. doi:10.1016/j.jseaes.2009.08.003

Lai, Z. P., Zöller, L., Fuchs, M., and Brückner, H. (2008). Alpha Efficiency Determination for OSL of Quartz Extracted from Chinese Loess. *Radiat. Measurements* 43 (2-6), 767–770. doi:10.1016/j.radmeas.2008.01.022

Lehmkuhl, F., Nottebaum, V., and Hülle, D. (2018). Aspects of Late Quaternary Geomorphological Development in the Khangai Mountains and the Gobi Altai Mountains (Mongolia). *Geomorphology* 312, 24–39. doi:10.1016/j.geomorph.2018.03.029

Li, G., Yang, H., Stevens, T., Zhang, X., Zhang, H., Wei, H., et al. (2020a). Differential Ice Volume and Orbital Modulation of Quaternary Moisture Patterns between Central and East Asia. *Earth Planet. Sci. Lett.* 530, 115901. doi:10.1016/j.epsl.2019.115901

Li, G., Zhang, H., Liu, X., Yang, H., Wang, X., Zhang, X., et al. (2020b). Paleoclimatic Changes and Modulation of East Asian Summer Monsoon by High-Latitude Forcing over the Last 130,000 Years as Revealed by Independently Dated Loess-Paleosol Sequences on the NE Tibetan Plateau. *Quat. Sci. Rev.* 237, 106283. doi:10.1016/j.quascirev.2020.106283

Li, H., Van Der Woerd, J., Tapponnier, P., Klinger, Y., Qi, X., Yang, J., et al. (2005). Slip Rate on the Kunlun Fault at Hongshui Gou, and Recurrence Time of Great Events Comparable to 14/11/2001, Mw~7.9 Kokoxili Earthquake. *Earth Planet. Sc. Lett.* 237, 285–299.doi:10.1016/j.epsl.2005.05.041

Li, X., Liu, X., He, Y., Liu, W., Zhou, X., and Wang, Z. (2018). Summer Moisture Changes in the Lake Qinghai Area on the Northeastern Tibetan Plateau Recorded from a Meadow Section over the Past 8400 Yrs. *Glob. Planet. Change* 161, 1–9. doi:10.1016/j.gloplacha.2017.11.016

Li, Y., Han, L., Liu, X., Song, Y., and Wang, Y. (2021). Correlation and Anti-correlation of the Asian Summer Monsoon and Westerlies during the Holocene. *Gondwana Res.* 91, 112–120. doi:10.1016/j.gr.2020.12.013

Liu, B., Jin, H., Sun, L., Su, Z., Zhang, C., and Zhao, S. (2017). History of Moisture Change Derived from Slope Sediments of the Eastern Gonghe Basin (Northeastern Qinghai-Tibetan Plateau) during the Last 17 Ka. *Geol. J.* 52 (4), 583–593. doi:10.1002/gj.2795

Liu, W., Hu, K., Carling, P. A., Lai, Z., Cheng, T., and Xu, Y. (2018). The Establishment and Influence of Baimakou Paleo-Dam in an Upstream Reach of the Yangtze River, southeastern Margin of the Tibetan Plateau. *Geomorphology* 321, 167–173. doi:10.1016/j.geomorph.2018.08.028

Liu, W., Lai, Z., Hu, K., Ge, Y., Cui, P., Zhang, X., et al. (2015). Age and Extent of a Giant Glacial-Dammed lake at Yarlung Tsangpo Gorge in the Tibetan Plateau. *Geomorphology* 246, 370–376. doi:10.1016/j.geomorph.2015.06.034

Liu, X.-J., Lai, Z., Madsen, D., and Zeng, F. (2015). Last Deglacial and Holocene lake Level Variations of Qinghai Lake, north-eastern Qinghai-Tibetan Plateau. *J. Quat. Sci.* 30 (3), 245–257. doi:10.1002/jqs.2777

Liu, X.-J., Xiao, G., E, C., Li, X., Lai, Z., Yu, L., et al. (2017). Accumulation and Erosion of Aeolian Sediments in the Northeastern Qinghai-Tibetan Plateau and Implications for Provenance to the Chinese Loess Plateau. *J. Asian Earth Sci.* 135, 166–174. doi:10.1016/j.jseaes.2016.12.034

Liu, X. J., Cong, L., Li, X. Z., Madsen, D., Wang, Y. X., Liu, Y. G., et al. (2020). Climate Conditions on the Tibetan Plateau during the Last Glacial Maximum and Implications for the Survival of Paleolithic Foragers. *Front. Earth Sc-switz* 8, 606051. doi:10.3389/feart.2020.606051

Liu, X., Lai, Z., Madsen, D., Yu, L., Liu, K., and Zhang, J. (2011). Lake Level Variations of Qinghai Lake in Northeastern Qinghai-Tibetan Plateau since 3.7 Ka Based on OSL Dating. *Quat. Int.* 236 (1), 57–64. doi:10.1016/j.quaint.2010.08.009

Liu, X. Q., Dong, H. L., Rech, J. A., Matsumoto, R., Yang, B., and Wang, Y. B. (2008). Evolution of Chaka Salt Lake in NW China in Response to Climatic Change during the Latest Pleistocene-Holocene. *J. Quat. Sci.* 27, 867–879. doi:10.1016/j.quascirev.2007.12.006

Liu, X., Zhang, X., Lin, Y., Jin, L., and Chen, F. (2019). Strengthened Indian Summer Monsoon Brought More Rainfall to the Western Tibetan Plateau during the Early Holocene. *Sci. Bull.* 64, 1482–1485. doi:10.1016/j.scib.2019.07.022

Murray, A. S., and Wintle, A. G. (2000). Luminescence Dating of Quartz Using an Improved Single-Aliquot Regenerative-Dose Protocol. *Radiat. Meas.* 32 (1), 53–57. doi:10.1016/S1350-4487(99)00253-X

Murray, A. S., and Wintle, A. G. (2003). The Single Aliquot Regenerative Dose Protocol: Potential for Improvements in Reliability. *Radiat. Meas.* 37 (4-5), 377–381. doi:10.1016/S1350-4487(03)00053-2

Ou, X., Lai, Z., Zhou, S., and Zeng, L. (2014). Timing of Glacier Fluctuations and Trigger Mechanisms in Eastern Qinghai-Tibetan Plateau during the Late Quaternary. *Quat. Res.* 81 (3), 464–475. doi:10.1016/j.yqres.2013.09.007

Owen, L. A., Finkel, R. C., Haizhou, M., and Barnard, P. L. (2006). Late Quaternary Landscape Evolution in the Kunlun Mountains and Qaidam Basin, Northern Tibet: A Framework for Examining the Links between Glaciation, lake Level Changes and Alluvial Fan Formation. *Quat. Int.* 154-155, 73–86. doi:10.1016/j.quaint.2006.02.008

Owen, L. A., Finkel, R. C., Haizhou, M., Spencer, J. Q., Derbyshire, E., Barnard, P. L., et al. (2003). Timing and Style of Late Quaternary Glaciation in Northeastern Tibet. *Geo. Soc. Am. Bull.* 115 (11), 1356–1364. doi:10.1130/B25314.1

Prescott, J., and Hutton, J. T. (1994). Cosmic Ray Contributions To Dose Rates For Luminescence and ESR Dating: Large Depths and Long-Term Time Variations. *Radiat Meas* 23, 497–500. doi:10.1016/1350-4487(94)90086-8

Ramisch, A., Lockot, G., Haberzettl, T., Hartmann, K., Kuhn, G., Lehmkuhl, F., et al. (2016). A Persistent Northern Boundary of Indian Summer Monsoon Precipitation over Central Asia during the Holocene. *Sci. Rep.* 6, 25791. doi:10.1038/srep25791

Ritter, J. B., Miller, J. R., Enzel, Y., and Wells, S. G. (1995). Reconciling the Roles of Tectonism and Climate in Quaternary Alluvial Fan Evolution. *Geol* 23, 245–248. doi:10.1130/0091-7613(1995)0232.3.CO10.1130/0091-7613(1995)023<0245:rtrota>2.3.co;22

Stauch, G., Schulte, P., Ramisch, A., Hartmann, K., Hülle, D., Lockot, G., et al. (2017). Landscape and Climate on the Northern Tibetan Plateau during the Late Quaternary. *Geomorphology* 286, 78–92. doi:10.1016/j.geomorph.2017.03.008

Tao, Y., Xiong, J., Zhang, H., Chang, H., and Li, L. (2020). Climate-driven Formation of Fluvial Terraces across the Tibetan Plateau since 200 Ka: A Review. *Quat. Sci. Rev.* 237, 106303. doi:10.1016/j.quascirev.2020.106303

Van Der Woerd, J., Tapponnier, P., Ryerson, F. J., Meriaux, A.-S., Meyer, B., Gaudemer, Y., et al. (2002). Uniform Postglacial Slip-Rate along the central 600 Km of the Kunlun Fault (Tibet), from 26Al, 10Be, and 14C Dating of Riser Offsets, and Climatic Origin of the Regional Morphology. *Geophys.* J. Int. 148, 356–388. doi:10.1046/j.1365-246x.2002.01556.x

Vandenberghe, J. (1995). Timescales, Climate and River Development. *Quat. Sci. Rev.* 14, 631–638. doi:10.1016/0277-3791(95)00043-O

Wang, A., Smith, J. A., Wang, G., Zhang, K., Xiang, S., and Liu, D. (2009). Late Quaternary River Terrace Sequences in the Eastern Kunlun Range, Northern Tibet: a Combined Record of Climatic Change and Surface Uplift. *J. Asian Earth Sci.* 34, 532–543. doi:10.1016/j.jseaes.2008.09.003

Wang, H., Cui, P., Liu, D., Liu, W., Bazai, N. A., Wang, J., et al. (2019). Evolution of a Landslide-Dammed lake on the southeastern Tibetan Plateau and its Influence on River Longitudinal Profiles. *Geomorphology* 343, 15–32. doi:10.1016/j.geomorph.2019.06.023

Wang, J., Kassab, C., Harbor, J. M., Caffee, M. W., Cui, H., and Zhang, G. (2013). Cosmogenic Nuclide Constraints on Late Quaternary Glacial Chronology on the Dalijia Shan, Northeastern Tibetan Plateau. *Quat. Res.* 79, 439–451. doi:10.1016/j.yqres.2013.01.004

Xu, L., Ou, X., Lai, Z., Zhou, S., Wang, J., and Fu, Y. (2010). Timing and Style of Late Pleistocene Glaciation in the Queer Shan, Northern Hengduan Mountains in the Eastern Tibetan Plateau. *J. Quat. Sci.* 25 (6), 957–966. doi:10.1002/jqs.1379

Yu, J., Gao, C., Cheng, A., Liu, Y., Zhang, L., and He, X. (2013). Geomorphic, Hydroclimatic and Hydrothermal Controls on the Formation of Lithium Brine Deposits in the Qaidam Basin, Northern Tibetan Plateau, China. *Ore Geology. Rev.* 50, 171–183. doi:10.1016/j.oregeorev.2012.11.001

Yuan, D.-Y., Champagnac, J.-D., Ge, W.-P., Molnar, P., Zhang, P.-Z., Zheng, W.-J., et al. (2011). Late Quaternary Right-Lateral Slip Rates of Faults Adjacent to the Lake Qinghai, Northeastern Margin of the Tibetan Plateau. *Geol. Soc. America Bull.* 123 (9–10), 2016–2030. doi:10.1130/B30315.1

Zhang, H.-P., Craddock, W. H., Lease, R. O., Wang, W.-t., Yuan, D.-Y., Zhang, P.-Z., et al. (2012). Magnetostratigraphy of the Neogene Chaka Basin and its Implications for Mountain Building Processes in the north-eastern Tibetan Plateau. *Basin Res.* 24 (1), 31–50. doi:10.1111/j.1365-2117.2011.00512.x

Zhang, H.-P., Craddock, W. H., Lease, R. O., Wang, W.-t., Yuan, D.-Y., Zhang, P.-Z., et al. (2011). Magnetostratigraphy of the Neogene Chaka basin and its Implications for Mountain Building Processes in the north-eastern Tibetan Plateau. *Basin Res.* 24, 31–50. doi:10.1111/j.1365-2117.2011.00512.x

Zhang, H., and Lü, Y. (2014). Geomorphometric Features of the Alluvial Fans Around the Chaka-Qinghai Lake in the Northeastern Tibetan Plateau. *J. Earth Sci.* 25 (4), 109–116. doi:10.1007/s12583-014-0404-z

Zhang, W., Mischke, S., Zhang, C., Gao, D., and Fan, R. (2013). Ostracod Distribution and Habitat Relationships in the Kunlun Mountains, Northern Tibetan Plateau. *Quat. Int.* 313-314 (10), 38–46. doi:10.1016/j.quaint.2013.06.020

Conflict of Interest: The authors declare that the research was conducted in the absence of any commercial or financial relationships that could be construed as a potential conflict of interest.

frontiers
in Earth Science

ORIGINAL RESEARCH
published: 27 July 2021
doi: 10.3389/feart.2021.702843

Optical Stimulation Luminescence Dating of Deltas Revealed the Early to Mid-Holocene Lake-level Fluctuations of Daihai, Inner Mongolia, Northern China

Shixin Huang[1,2,3] *and Xi Chun*[1,4]*

[1]Inner Mongolia Restoration Engineering Laboratory of Wetland Eco-Environment System, Inner Mongolia Normal University, Hohhot, China, [2]State Key Laboratory of Lake Science and Environment, Nanjing Institute of Geography and Limnology, Chinese Academy of Sciences, Nanjing, China, [3]University of Chinese Academy of Sciences, Beijing, China, [4]Laboratory of Mongolian Plateau Environment and Global Change, Inner Mongolia Normal University, Hohhot, China

OPEN ACCESS

Edited by:
Xiangjun Liu,
Northwest Normal University, China

Reviewed by:
Yiwei Chen,
Chinese Academy of Sciences (CAS), China
Fuyuan An,
Qinghai Normal University, China

Correspondence:
Xi Chun
chunxi@imnu.edu.cn

Specialty section:
This article was submitted to Quaternary Science, Geomorphology and Paleoenvironment, a section of the journal Frontiers in Earth Science

Received: *30 April 2021*
Accepted: *21 June 2021*
Published: *27 July 2021*

Citation:
Huang S and Chun X (2021) Optical Stimulation Luminescence Dating of Deltas Revealed the Early to Mid-Holocene Lake-level Fluctuations of Daihai, Inner Mongolia, Northern China.
Front. Earth Sci. 9:702843.
doi: 10.3389/feart.2021.702843

Lake-level reconstruction of inland enclosed lakes especially for monsoon-sensitive areas is of great significance to reveal regional climate changes. Daihai, a typical enclosed lake at the marginal of the East Asian summer monsoon (EASM) area in north China, is sensitive to climate changes due to its unique regional characteristics. There were a series of lakeshore terraces, highstand lacustrine sediments, and braided river deltas, providing sufficient geomorphologic and stratigraphic evidence for the reconstruction of lake-level fluctuations of Daihai. Reconstructed lake-level variations during the early and mid-Holocene were constructed based on 22 quartz optical stimulated luminescence (OSL) ages from six well-preserved profiles around Daihai Basin. Our results indicated Daihai showed a relatively low level at 10.2 ka, and a gradually increasing lake level following the enhanced monsoon precipitation during the mid-Holocene. Specifically, the high lake level began to develop at 8.1 ka and reached the maximum at 5.2 ka, with ~40 m higher than present. At this time, the lake area expanded to ~400 km^2, approximately six times as large as that of present, corresponding to the maximum monsoon precipitation and intensity of EASM during the mid-Holocene. However, our stratigraphic records showed a part of the depositional records in the north and east of the Daihai was missed after 5.2 ka, probably indicating a sudden drop of the Daihai lake level. These rapid level fluctuations were likely to be interpreted by some local scenarios and need to be further investigated in the future. Overall, the lake-level fluctuation of Daihai during the early and mid-Holocene was slightly different from that observed in the previously published regional records. Possibly, the interaction of the EASM and regional feedback from topography, and hydrology factors might have contributed to the spatial complexity and distinction.

Keywords: lake-level fluctuation, high lake level, early to mid-Holocene, fluvial delta, optical stimulation luminescence, East Asian summer monsoon, monsoon precipitation

INTRODUCTION

Exploring the evidence of the past global climate change in environment-sensitive regions and obtaining its underlying mechanisms are of great significance for the scientific prediction of future climate change (International Geosphere-Biosphere Programme, IGBP). There are large numbers of inland enclosed lakes near the East Asian monsoon margin of China which are highly sensitive to climate change due to its unique regional characteristics. Thus, their lake-level fluctuations are the most direct indicators of regional precipitation and moisture variability related to the intensity of monsoon activities and climate change (Liu et al., 2015; Li et al., 2020a). However, increasing high-resolution lacustrine deposit records have revealed that the lake-level fluctuations during the early and mid-Holocene in East Asian monsoon marginal regions were quite different; especially, the timing of the high lake level in different lakes was asynchronous, and even the same lake might be distinct based on the different dating methods or different materials and proxies.

Inner Mongolia is at the East Asian summer monsoon (EASM) fringe region, the arid/semiarid climate transition zone, and the ecosystem fragile zone in north China. The unique characteristics of the interlaced nomadic with agricultural civilization make it the most sensitive and typical region responding to global climate change. Daihai is a typical inland enclosed lake in Inner Mongolia, whose lake-level fluctuations are of great significance to indicate the regional climate change. A series of research works have focused on the lake-level fluctuations and climate change based on the deposit of lakeshores and drilling cores in Daihai, presenting many valuable literatures and some representative opinions (Wang et al., 1990; Xiao et al., 2004; Peng et al., 2005; Sun et al., 2006). However, there are still many discrepancies and arguments, even conflicts with regard to climate change patterns among them, especially on the timing of highstand records.

Sedimentary records based on the radiocarbon dating in Daihai revealed the high lake level during the early and mid-Holocene. For instance, core sediments and lacustrine sediments from the surrounding terraces revealed that the Holocene climate optimum in Daihai has already begun at 11.5 Cal ka B.P. (10 ka B.P.) and ended at ca. 5.2 Cal ka B.P. (4.5 ka B.P.), corresponding to the termination of the last high lake level (Wang et al., 1990). Lake terrace records indicated that the lake level has increased since 8.8 Cal ka B.P., followed by the highstands at 8.3–7.8 ka B.P. (Li et al., 1992). Meanwhile, monsoon precipitation in Daihai reached its maximum during the mid-Holocene, with an annual precipitation greater than 550 mm (Peng et al., 2005; Xu et al., 2010; Wang et al., 2013), and the warm and humid climate promoted the development of vegetation in Daihai Basin during the mid-Holocene (Jin et al., 2004; Sun and Xiao, 2006; Du et al., 2013). Whereas there was a cold and wet episode at 7.9–7.2 Cal. ka B.P. (Xiao et al., 2004; Xu et al., 2004), the lake level frequently fluctuated with a decreasing trend during 10.6–10.0, 9.6–9.0, 7.0–6.3, 5.8–5.2, and 4.5–3.7 Cal. ka B.P. inferred from nearshore grain size compositions (Xiao et al., 2013). Moreover, reconstructed lake-level fluctuations based on the ^{14}C dating of lake terraces and sediment cores demonstrated a similar trend that the Daihai lake level expanded temporarily at 10–9 Cal. ka B.P. followed by a decreased lake level; thereafter, the lake expanded again during 7.3–3.2 Cal. ka B.P. with abundant effective precipitation and superior hydrothermal condition (Sun et al., 2009; Sun et al., 2010). The conclusions above based on the different research carriers are slightly distinct, but all of them presented the increased lake level of Daihai during the early Holocene, and then the development of the high lake level during the mid-Holocene or late mid-Holocene, indicating climate optimum. However, Jin et al. (2013) proposed a temporary expansion of Daihai at 7.5–7.0 Cal. ka B.P. and then reached a high lake level at 6.1–2.5 Cal. ka B.P. due to the increasing intensity of the monsoon, with a water depth of ~65 m, 35–40 m higher than the present, revealing the development of highstands in Daihai during the late Holocene.

Similarly, the arguments and discrepancies on the occurrence of the high lake level also exist in other lakes in Inner Mongolia. Huangqihai Lake is also located in the middle-east of Inner Mongolia and only 50 km away from Daihai. Sedimentary records based on the ^{14}C dating revealed the Huangqihai Lake developed the high lake level with >70 m higher than modern lake surface during the mid-Holocene (Li et al., 1992; Shen et al., 2006). However, the geological evidence combined with the high-resolution OSL geochronology indicated that warm and wet climate were prevalent during the early Holocene with a stable high lake level, reaching a peak elevation of ~1,340 m, >77 m higher than that present (Zhang et al., 2011; Zhang et al., 2012; Zhang et al., 2016). Subsequently, the lake surface shrank sharply, and the Great Lakes period ended (Xu et al., 2012). Sedimentary records of Dali Lake in eastern Inner Mongolia showed that the high lake level developed in the early and mid-Holocene, with ~60 m, increased of the lake level in 400 years and the triple annual precipitation, followed by the abrupt termination of Holocene humid conditions at 6.3 Cal ka B.P. (5.5 ka B.P.) with a declined lake level of approximately 35 m (Goldsmith et al., 2017). Another sediment core record also demonstrated Dali Lake developed a high lake level due to temperature rise, and glaciers melt during the early and mid-Holocene (11.5–7.6 Cal. ka B.P.) (Xiao et al., 2008; Xiao et al., 2009). However, reconstructed lake-level fluctuations based on the OSL dating of beach ridges of Dali Lake reflected the lower lake level related to the reduced monsoon precipitation from 12 to 7 ka and the high lake level with a maximum monsoon precipitation during 7–5 ka (Jiang et al., 2020). In addition, lakes in eastern Inner Mongolia also revealed the distinct timing of highstands. Depositional records of Hulun Lake located in northeastern Inner Mongolia demonstrated that Hulun Lake developed a high lake level during the deglacial and early Holocene (Zhang and Wang, 2000), and thereafter, the secondary high lake level developed again during the mid-Holocene (Liu et al., 2016). Reconstructed lake-level fluctuations in Chagan Nur, an enclosed lake located in eastern Inner Mongolia at the fringe of the modern EASM region, showed a lake highstand of 15–12 m higher than that present at 11–5 ka, with a maximum precipitation of 30–50% higher than that present at 8–6 ka (Li et al., 2020a). Similarly, the depositional records of Juyanze and Zhuyeze terminal lakes on the Alashan

Plateau in western Mongolian plateau indicated that the high lake level developed in the early Holocene and gradually disintegrated at 7–5 Cal. ka B.P. (Chen et al., 2003), but on the contrary, based on topographic and geomorphological analyses, combined with OSL dating results, the high lake level of Zhuyeze Lake appeared in the 8–5 ka with 20 m higher than the modern lake level (Long et al., 2012).

Previous studies on lake-level reconstruction and the timing of the high lake level during the Holocene were distinct even with conflict based on the different research materials and carriers, combined with the different dating methods. They mostly emphasized the analysis of lake cores' sediments to reconstruct the lake-level fluctuation, but there was a lack of the most direct geological and geomorphological evidence. Generally, the research of lake-level fluctuations mainly based on the lake drilling cores and the lakeshore deposition records. Core records can provide relatively continuous high-resolution sedimentary records and the details of lake surface fluctuations to a certain extent, but in terms of the high lake level, the lakeshores, spits, river deltas, and highstand lacustrine sediments retained around the lake are usually used as the good geomorphological evidence to directly indicate high lake-level variations (Wang et al., 1990; Yu et al., 2013). High lake level as a symbol of the peak period of lake evolution indicates the regional warm and humid climate environment, which can provide the basic chronological framework and information for climate change. Furthermore, most of the studies of water lake-level fluctuations were based on the limited dating techniques. Recently, optical stimulated luminescence (OSL) dating technology has been widely used in quaternary studies of dating lacustrine sediments (Long et al., 2011; Fan et al., 2012; Fu et al., 2017; Li et al., 2018b), fluvial/alluvial/delta deposits (Zhao et al., 2016; Guo et al., 2017; He et al., 2019; Nian et al., 2019), aeolian dunes (Cao et al., 2012; Costas et al., 2012; Yu and Lai, 2017), loess/paleosol (Roberts, 2008; Stevens et al., 2018; Li et al., 2018a; Wu et al., 2019; Li et al., 2020b), and so on. This technique was extensively used in the dating of lacustrine deposits in arid and semiarid China because of its advantages over radiocarbon dating, which is limited by the so-called reservoir effects. And among those areas with significant reservoir effects, the application of OSL dating also can be used to assess the reservoir effects and calibrate the radiocarbon dating results (Liu and Lai, 2012; Lai et al., 2014).

Consequently, here we investigated the timing of the high lake level during the early-to-mid Holocene based on the OSL dating from Daihai Lake in the margin of EASM in north China. Series of lakeshore terraces, highstand lacustrine deposits, and well-preserved river deltas around the Daihai Basin could provide sufficient sedimentary and geomorphological evidence for the reconstruction of lake-level fluctuations, which is of great significance to reveal the regional climate change. Based on 22 quartz OSL ages, we attempted to reconstruct lake-level fluctuations and figure out the timing of highstands during the early and mid-Holocene, and further discuss the underlying mechanisms of the lake-level fluctuation in Daihai and its response to the variability of EASM intensity during the early and mid-Holocene.

MATERIALS AND METHODS

Study Area

Daihai Basin is located in Liangcheng County of the southeastern Inner Mongolia Plateau, northern China, with complex landforms which are mainly composed of mountains and hilly areas (**Figure 1A**). Daihai Lake (40°29′27″ N–40°37′06″ N, 112°33′31″ E–112°46′40″ E, 1,220 m a.s.l.) is an ellipse-shaped enclosed lake at the lowest point of the basin. The water supply of Daihai mainly depends on atmospheric precipitation, rivers, and surface runoff. Daihai is fed by 22 rivers, most seasonal braided rivers developed on the northern shore, and only those in the western are meandering rivers; among them, five main rivers, Gongba River, Wuhao River, Tiancheng River, Buliang River, and Muhua River, flow into the lake (Shi et al., 2014) (**Figure 1B**). The lake area is 61.5 km^2, with a drainage area of 2364.2 km^2, a maximum depth of 11.5 m, and a mean depth of 6.67 m.

Daihai located in the margin of EASM-influenced regions is mainly dominated by a semiarid moderate temperate continental monsoon climate (**Figure 1A**). Regional precipitation was mainly delivered *via* EASM transportation (Wang et al., 1990). The meteorological data analysis results of Liangcheng Station in Inner Mongolia from 1960 to 2017 AD demonstrate that the annual average temperature in Daihai Basin was approximately 5.6°C; the annual average precipitation was ~410 mm and ca. 70%; annual precipitation decreased in July–September; the mean annual evaporation reached 1860 mm, four times higher than the annual precipitation; the average of the frost-free period was generally 120 days; Daihai Basin in winter is often affected by Mongolian–Siberian cold air and northwest wind with wind scale ranging from 5 to 8. The annual average wind speed was 2.6 m/s, and the maximum wind speed was up to 15 m/s. In recent decades, the semiarid climatic condition makes the precipitation of Daihai Basin a natural shortage, and then the anthropogenic-induced climate warming and agricultural activities make Daihai rapidly shrink (Liu et al., 2019; Chun et al., 2020).

Daihai Basin is an asymmetric closed rift basin. Because of the fault activities, the slope of the lake basin is different from that of the north and the south, which shows the characteristics of steepness in the north and gentle in the south. Since the formation, Daihai has experienced frequent lake-level fluctuations, and thus, there were many ancient relics left behind and well-preserved lake sedimentary profiles due to its long-term hydrologic closure state.

Sample Collection

Lakeshore terraces at different heights, highstand lacustrine deposits, fluvial terraces, and river deltas are widely distributed around the Daihai Basin (Wang et al., 1990; Sun et al., 2009; Yu et al., 2013). There are nine small deltas in the northern steep slope of Daihai Basin due to topographic characteristics, and fluvial and seasonal floods, such as Yuanzigou Delta; only two but big deltas were distributed in the southern gentle slope (Buliang River Delta and Tiancheng River Delta): the largest Muhua River

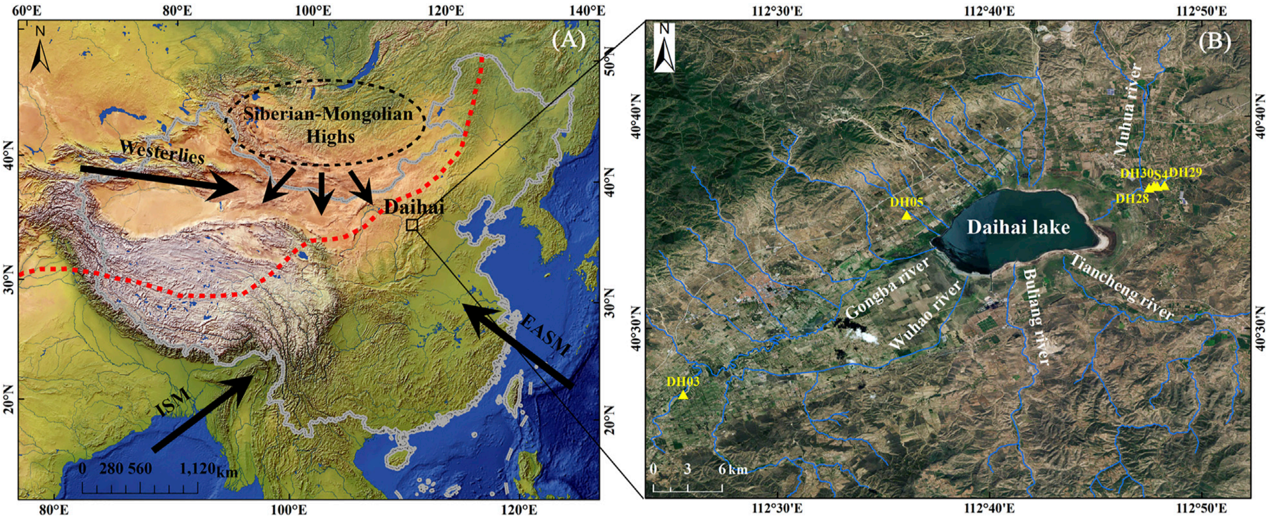

FIGURE 1 | Geographical map of the study area showing **(A)** the location of the Daihai Lake Basin and atmospheric circulation systems of China [i.e., Indian summer monsoon (ISM), East Asian summer monsoon (EASM), Westerlies, and Siberian–Mongolian High winter monsoon], the red dash line represents the modern northern boundary of the EASM according to Chen et al. (2008), and **(B)** sampling sites around the Daihai lake basin based on the Map World (https://www.tianditu.gov.cn/).

(braided river) delta in the eastern Daihai and Gongba River (meandering river) delta in the western area (Yu et al., 2013). Thus, the braided river delta plains were formed on the north, south, and east coast of Daihai, while the meandering river delta plain only developed in the west. The formation of the braided river deltas was determined by the construction of the braided river plain entering the lake and the wave action of the lake. The basin tectonic activity, seasonal flood intensity, and lake-level fluctuations are the main factors to control its development, so braided river deltas can be used as the most intuitive indicator of lake-level fluctuations in Daihai (more details in Supplementary Material and **Supplementary Figure S1**).

By conducting field geomorphic investigations around the Daihai Basin, we collected OSL age samples at six sites from the west to east of Daihai Basin (**Figure 1B**). DH03 section is a fluvial terrace in Gongba River catchment, western Daihai. DH05 section is located in Yuanzigou Delta, northern Daihai. DH28, DH29, and DH30 sections are located in Muhua River Delta, eastern Daihai. The Yuanzigou delta is a braided river delta with the steep slope in a near-source transportation way, while the Muhua River Delta is far away from the source with fine grains of good abrasion. The way they entered the lake mainly depended on the seasonal floods and rainfalls. Differential global positioning system (DGPS) was used to measure elevations during field investigation, and the elevation of each section was further determined by a 1:50,000 topographic map of Liangcheng County combined with Google Earth.

Grain Size Pretreatment

Pretreatment of grain size was performed according to the method proposed in the study by Peng et al. (2005). Samples in beakers were treated with 10 ml of 30% H_2O_2 and 10 ml of 10% HCl to remove the organic matter and carbonate, respectively; the beakers were filled with deionized water, maintained for 24 h, and acidic ions were removed until the solution was nearly neutral (PH = 7); sample residues were deflocculated with 10 ml of 0.05 mol/L $(NaPO_3)_6$ with an ultrasonicator for 15 min to facilitate dispersion and eliminate the sample cementation. The grain size of prepared samples was measured and analyzed by Malvern Mastersizer 3000 analyzer with a measurement range of 0.01–3,500 μm. The repeated measurement error was less than 2%.

Optical Stimulated Luminescence Dating

A total of 22 OSL samples from six sections around Daihai Basin were taken from the freshly prepared vertical profiles by using light-tight steel tubes and were sealed on sites to prevent light exposure and moisture loss for luminescence dating. Sample preparations and measurements were performed in the Laboratory of Mongolian Plateau Environment and Global Change, Inner Mongolia Normal University. Under the subdued red light conditions, the outer materials at the ends of each tube were reserved for the measurement of water content and the environmental dose rate, and the unexposed materials at the middle part of the tubes were treated with 10% HCl and 30% H_2O_2 to remove carbonates and organic material, respectively. Samples were wet-sieved to select medium-grained (MG, 38–63 μm) or coarse-grained (CG, 63–90 μm or 90–125 μm) fractions and then separated using heavy liquids calibrated to the density of 2.72 and 2.62 g cm^{-3} to remove heavy minerals and extract quartz grains, respectively. Afterward, the CG quartz fractions were etched with 40% HF for 40 min to dissolve feldspars and the outer alpha-irradiated surface. The MG quartz fractions were etched with H_2SiF_6 for 1–2 weeks. The etched samples were rinsed with 1 mol/L HCl to remove fluoride precipitates, and then washed with distilled water. The purity of the isolated quartz was checked using the infrared light

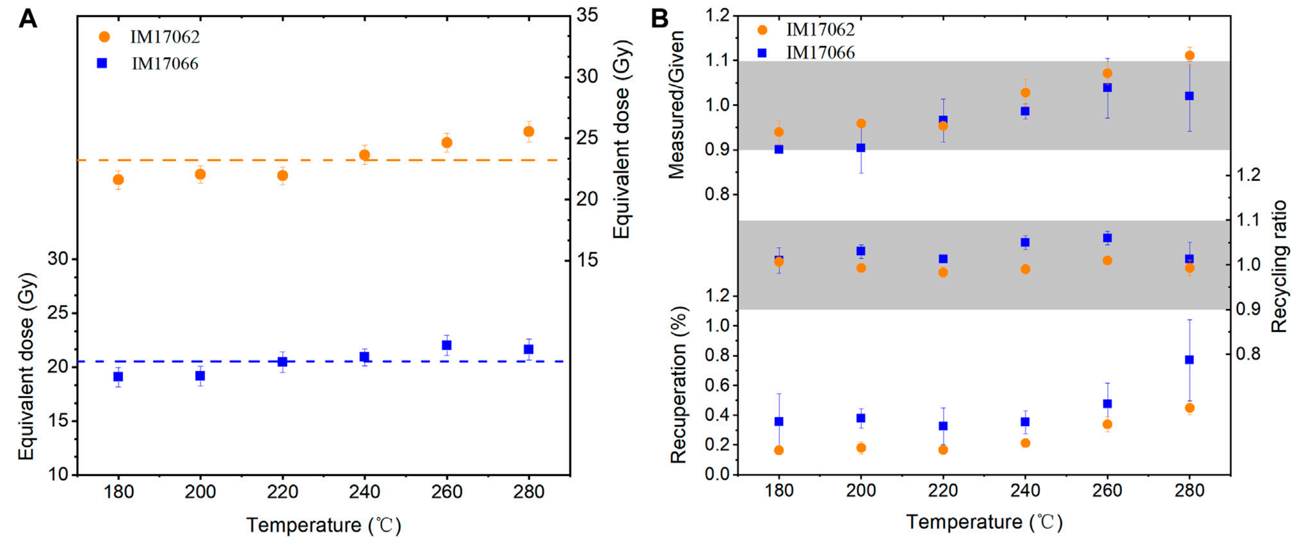

FIGURE 2 | (A): Preheat temperature plateau of equivalent dose for samples IM17062 (medium-grained) and IM17066 (coarse-grained, unpublished in this article); **(B)** dose recovery test results for samples IM17062 and IM17066, respectively.

stimulation (IR checking), and samples with the OSL-IR depletion ratio deviated from 10% of unity were retreated again (Duller, 2003).

OSL measurements were performed using an automated Risø TL/OSL DA-20 reader, equipped with a calibrated ^{90}Sr/^{90}Y beta source (Botter-Jensen et al., 2010) with a dose rate of ~0.115 Gy/s. We used blue light LED ($\lambda = 470 \pm 30$ nm) stimulation for quartz and infrared LED ($\lambda = 830$ nm) stimulation for IR depletion ratio check. Quartz OSL signal was detected through a 7.5-mm Hoya U-340 filter. A standard single aliquot regenerative-dose (SAR) protocol was applied for pretests and equivalent dose (D_e) measurements (**Supplementary Table S1**) (Murray and Wintle, 2000; Wintle and Murray, 2006).

The concentration of radioactive nuclides (U, Th, and Rb) was measured by inductively coupled plasma mass spectrometry (ICP-MS; Thermo iCAP RQ), while the content of K (%) was determined by inductively coupled plasma optical emission spectrometry (ICP-OES; Thermo iCAP 7400). The environment external dose rate determination was based on the U, Th, K, and Rb concentrations from bulk samples. An alpha efficiency factor (α-value) of 0.035 ± 0.003 was used for the aging calculation of 38–63 μm quartz grains (Lai and Brueckner, 2008). The CG quartz fractions were etched to remove the outer alpha-irradiated layer, and thus circumvent the necessity to determine the alpha dose and alpha dose effectiveness. The attenuation factors of Brennan et al. (1991) and Guerin et al. (2012) were used to calculate the alpha and beta dose rates, respectively. The contribution of cosmic ray was calculated using the buried depth of the samples, altitude, and geomagnetic latitude following the reference (Prescott and Hutton, 1994). Based on the local deposited environment, previous research (Li et al., 2020a), and measured and saturated water content of these samples, the water content of 10 ± 5% was assumed in the aging calculation. The total dose rates were finally calculated using the functions defined by Aitken (1985); Aitken (1998).

RESULTS

D_e Determination, Luminescence Characteristics, and Geochronology

All the samples have a thermal luminescence (TL) peak at 110°C, and the IR-depletion ratio ranges between 0.9 and 1.1 (**Supplementary Figures S2, S3**), indicating the prevention of the measured signals of quartz grains from feldspar contamination, which meets test requirements (Thomsen et al., 2008). To select an appropriate thermal treatment, preheat plateau tests were carried out on both MG quartz (IM17062) and CG quartz (IM17066; unpublished in this article, but this sample was taken from the sampling site near the DH05) before the D_e measurement. The preheat plateau test was carried out by dividing the aliquots into six groups, with preheat temperatures ranging from 180 to 280°C with a 20°C increment. The observed D_e plateau from 180 to 280°C indicated that D_e values are rather insensitive to the preheat temperature; both samples present a good D_e plateau (**Figure 2A**). As shown in **Figure 2B**, constrained by acceptable range (0.9–1.1) of the recycling ratio and negligible recuperations (lower than 5%), the dose recovery ratio is consistent with unity within the 1 σ error for all the preheat temperatures (Murray and Olley, 2002). Finally, a preheat temperature of 240°C with a cut-heat of 200°C was chosen for the D_e measurements of all the samples of Daihai.

The decay curves obtained from sample MG quartz (IM17062) and CG quartz (IM18026) are shown in **Figures 3A,C**, with typical dose–response curves inset. The decay curves were

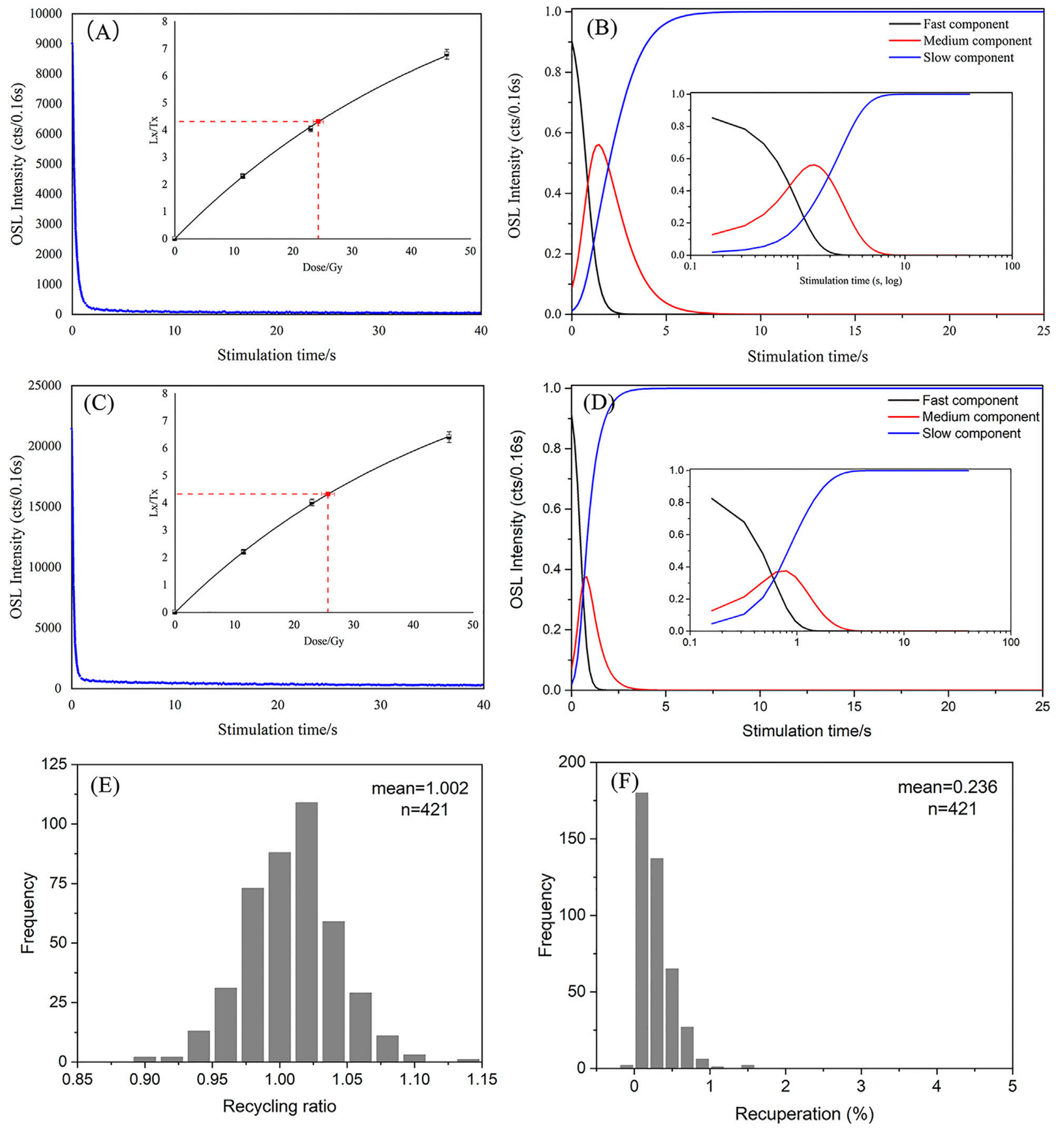

FIGURE 3 | Luminescence characteristics for quartz aliquots. **(A)** OSL decay curve for sample IM17062, and the inset shows the dose–response curve; **(B)** quartz signal decomposition for IM17062, and the inset shows the log for horizontal ordinate; **(C)** OSL decay curve for sample IM18026, and the inset shows the dose–response curve; **(D)** quartz signal decomposition for IM18026 and the inset shows the log for horizontal ordinate; **(E)** statistical distribution histogram of the recycling ratio for 421 aliquots from 22 OSL samples; **(F)** statistical distribution histogram of recuperations for 421 aliquots.

decomposed into three components: fast component, medium component, and slow component by curve fitting (**Figures 3B,D**) (Bailey et al., 1997). As shown in **Figure 3**, the OSL signals rapidly decay to the background, indicating the domination of the fast component in the quartz signal, and the signal can be sufficiently bleached in a very short time, which can be seen in the same characteristics in all samples in this study. The average recycling ratio of 421 aliquots from 22 samples is 1.002 (**Figure 3E**), confirming that the sensitivity corrections work well, and the measurements following the laboratory irradiations are

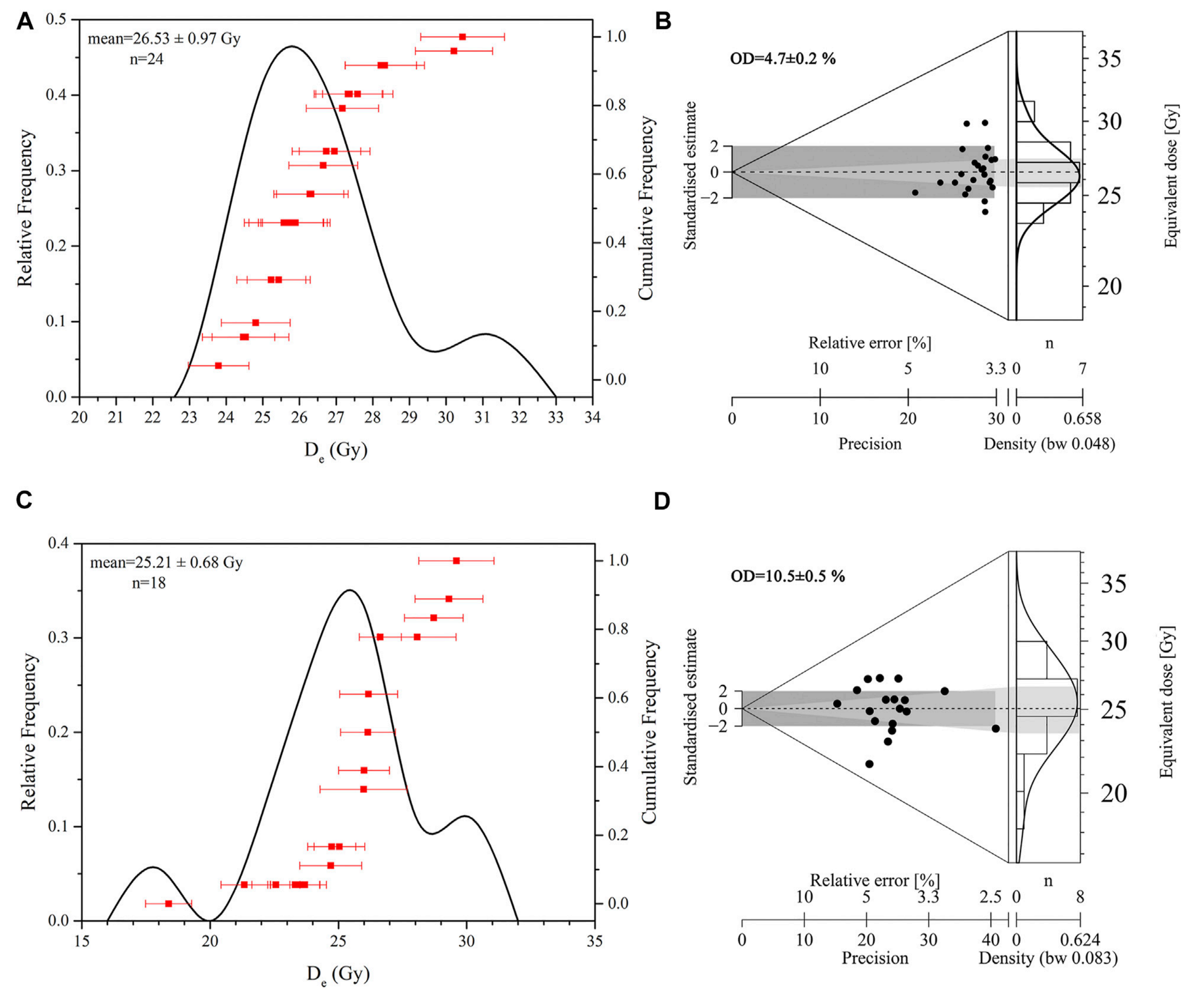

FIGURE 4 | Statistical distribution histogram of De from **(A)** sample IM17062 and **(C)** sample IM18026. Abanico plots of measured doses are shown in **(B)** IM17062 and **(D)** IM18026, in each plot; the shaded region represents the expected burial dose.

reproducible. The recuperations from 421 aliquots are all less than 2% (**Figure 3F**), showing the negligible thermal transfer effects (Wintle and Murray, 2006). The D_e distributions of both MG (IM17062) and CG (IM18026) quartz are quite narrow, with small over-dispersion (OD) values (4.7 ± 0.2 and 10.5 ± 0.5%, respectively) (**Figure 4**), indicating the samples were well bleached before burial (Arnold and Roberts, 2009). Almost all samples showed similar luminescence characteristics and the normal distributions for the D_e values. All above suggest the suitability of the SAR protocol in D_e determination of quartz OSL sedimentary samples in Daihai and the reliability of dating results.

The dating results of 22 OSL samples collected from six sections in this article are listed in **Table 1**. The stratigraphy and OSL sampling sites are illustrated in **Figure 5**. The dating ages are almost consistent with the deposition depth within the error range.

Grain Size Characteristics and Sedimentary Environments of the Sedimentary Sections

Sediment grain size composition and distribution patterns can reflect the hydrodynamic conditions, the sedimentary environment, and depositional processes to some extent (Ding et al., 2001). The ternary diagram of grain size shows (**Supplementary Figure S4**) that sediments were mainly composed of silt (4–63 μm), whereas sand (>63 μm) accounted for a large proportion in some samples of the DH29 and DH30 sections, whose geochronology mainly ranges from 9 to 7 ka. The median size of sediments varied obviously in different deposition periods. At 6.5–5.2 ka, sediment compositions were dominated by fine silt (7.8–15.6 μm). The frequency distribution curves can provide more detailed information on the sedimentary environment. Consequently, combined with the stratigraphic field investigation and the previous research works (Xiao et al.,

TABLE 1 | Summary of quartz OSL dating results from Daihai Basin.

Sample ID	Depth (cm)	Aliquots	Grain size (μm)	De (Gy)	OD (%)	U (ppm)	Th (ppm)	K (%)	Cosmic rate	Dose rate (Gy/ka)	W.C. (%)	Age (ka)
IM17001	1,500	24	63–90	26.51 ± 1.55	19.8 ± 0.6	1.72 ± 0.08	7.56 ± 0.24	1.79 ± 0.06	0.06	2.58 ± 0.14	10 ± 5	10.26 ± 0.83
IM17002	1,300	19	63–90	28.37 ± 0.97	12.9 ± 0.6	0.68 ± 0.04	2.29 ± 0.11	3.26 ± 0.09	0.07	3.42 ± 0.19	10 ± 5	8.29 ± 0.55
IM17003	700	22	63–90	20.58 ± 0.46	8.7 ± 0.4	1.7 ± 0.08	7.44 ± 0.24	1.69 ± 0.06	0.11	2.53 ± 0.14	10 ± 5	8.12 ± 0.48
IM17004	100	22	63–90	15.17 ± 0.76	22.0 ± 0.7	1.18 ± 0.06	8.29 ± 0.26	2.03 ± 0.06	0.22	2.93 ± 0.15	10 ± 5	5.19 ± 0.37
IM17062	395	24	38–63	26.53 ± 0.34	4.7 ± 0.2	4.60 ± 0.50	16.29 ± 0.70	2.06 ± 0.04	0.13	4.37 ± 0.33	10 ± 5	6.06 ± 0.46
IM17063	350	23	38–63	23.55 ± 0.39	6.5 ± 0.3	2.84 ± 0.40	14.00 ± 0.70	2.00 ± 0.04	0.14	3.70 ± 0.28	10 ± 5	6.36 ± 0.49
IM17064	320	24	38–63	15.23 ± 0.20	5.4 ± 0.2	1.82 ± 0.30	8.20 ± 0.60	1.65 ± 0.04	0.15	2.70 ± 0.21	10 ± 5	5.64 ± 0.44
IM17074	200	22	90–125	31.78 ± 1.30	16.1 ± 0.6	1.52 ± 0.30	13.18 ± 0.7	2.21 ± 0.04	0.20	3.43 ± 0.18	10 ± 5	9.26 ± 0.62
IM17075	150	18	63–90	30.10 ± 1.52	19.8 ± 0.8	1.39 ± 0.3	12.94 ± 0.7	2.20 ± 0.04	0.21	3.42 ± 0.18	10 ± 5	8.80 ± 0.64
IM17076	100	18	90–125	26.34 ± 1.38	21.0 ± 0.9	1.36 ± 0.30	12.50 ± 0.70	2.28 ± 0.04	0.22	3.45 ± 0.18	10 ± 5	7.62 ± 0.56
IM18001	90	18	90–125	25.12 ± 1.61	24.2 ± 1.0	1.44 ± 0.30	15.35 ± 0.70	2.35 ± 0.04	0.23	3.73 ± 0.2	10 ± 5	6.73 ± 0.56
IM18017	40	16	90–125	23.20 ± 1.12	17.4 ± 0.8	1.16 ± 0.30	6.87 ± 0.60	2.18 ± 0.04	0.26	2.98 ± 0.15	10 ± 5	7.78 ± 0.55
IM18018	60	18	90–125	25.47 ± 0.84	14.8 ± 0.6	1.11 ± 0.30	12.37 ± 0.70	2.58 ± 0.04	0.24	3.70 ± 0.19	10 ± 5	6.89 ± 0.43
IM18019	90	18	90–125	27.52 ± 0.70	9.2 ± 0.4	0.75 ± 0.30	5.61 ± 0.60	3.07 ± 0.05	0.23	3.62 ± 0.19	10 ± 5	7.61 ± 0.45
IM18020	120	17	90–125	27.07 ± 1.04	14.2 ± 0.6	1.18 ± 0.30	6.89 ± 0.60	2.79 ± 0.04	0.22	3.51 ± 0.18	10 ± 5	7.70 ± 0.50
IM18021	160	18	90–125	24.57 ± 0.64	10.1 ± 0.4	1.91 ± 0.30	10.09 ± 0.70	1.80 ± 0.04	0.21	2.93 ± 0.15	10 ± 5	8.38 ± 0.49
IM18022	210	15	63–90	23.48 ± 0.89	13.7 ± 0.7	2.92 ± 0.40	12.92 ± 0.70	1.85 ± 0.04	0.19	3.37 ± 0.18	10 ± 5	6.96 ± 0.45
IM18023	280	18	63–90	22.23 ± 0.44	7.0±.0.4	1.97 ± 0.30	9.47 ± 0.60	1.71 ± 0.04	0.18	2.81 ± 0.15	10 ± 5	7.93 ± 0.45
IM18024	430	15	90–125	24.35 ± 0.62	8.2 ± 0.5	2.60 ± 0.40	7.86 ± 0.60	1.83 ± 0.04	0.15	2.88 ± 0.16	10 ± 5	8.46 ± 0.51
IM18025	510	18	90–125	27.90 ± 1.15	14.4 ± 0.6	1.99 ± 0.30	10.59 ± 0.70	1.96 ± 0.04	0.14	3.05 ± 0.16	10 ± 5	9.14 ± 0.62
IM18026	590	18	90–125	25.21 ± 0.68	10.5 ± 0.5	2.27 ± 0.40	7.87 ± 0.60	1.89 ± 0.04	0.13	2.85 ± 0.16	10 ± 5	8.84 ± 0.54
IM18031	1,540	16	90–125	32.16 ± 0.73	8.6 ± 0.4	1.86 ± 0.30	11.26 ± 0.70	2.68 ± 0.04	0.05	3.67 ± 0.20	10 ± 5	8.77 ± 0.52

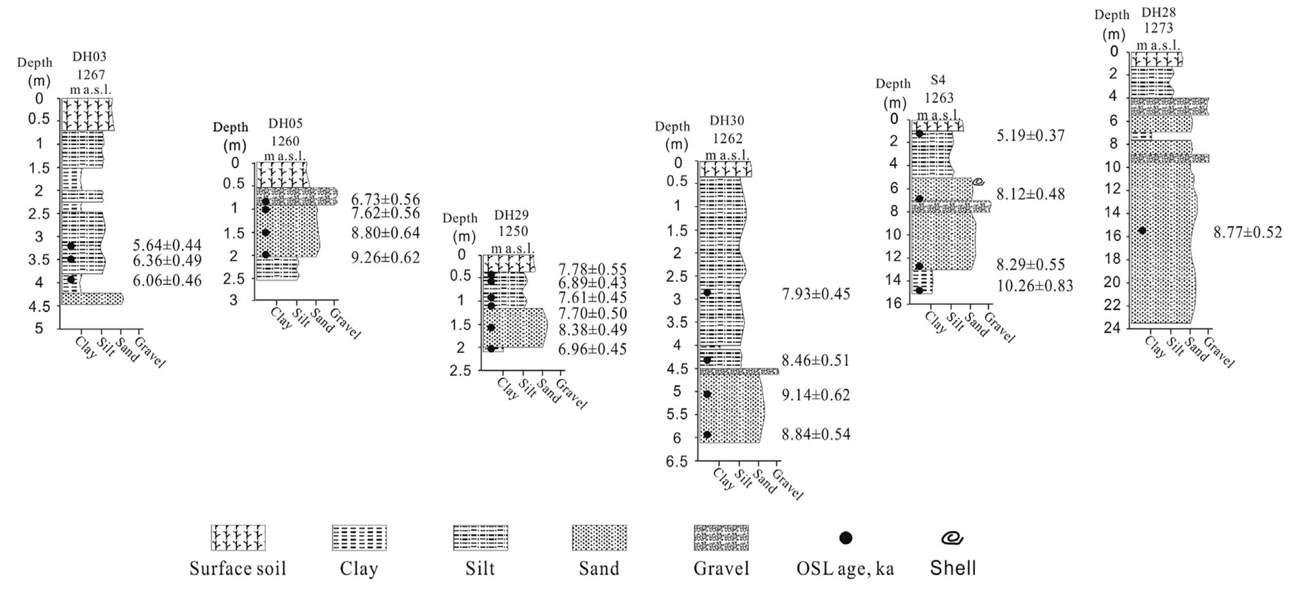

FIGURE 5 | Stratigraphy, lithology, and chronology of sampling sections in Daihai. The log of Gravel represented the sandy bed with fine gravels.

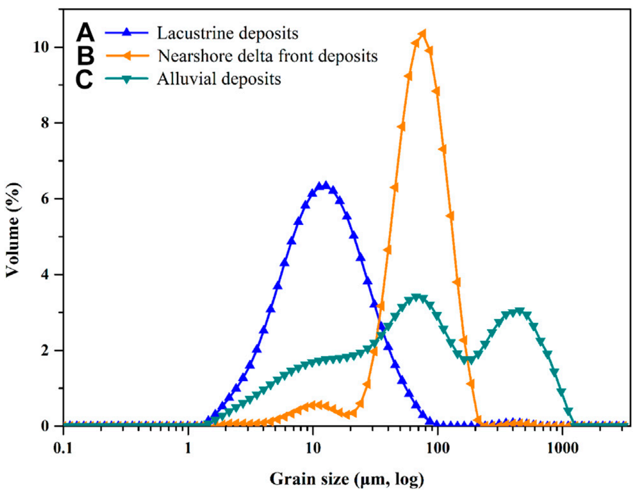

FIGURE 6 | Representative frequency distribution curves of different sedimentary grains.

2013), we designed frequency distribution curves as three types in this article: (A) lacustrine deposits, (B) nearshore delta deposits, and (C) alluvial/fluvial deposits (**Figure 6**).

DH03 section is located in the west of Daihai (1,267 m a.s.l.) and was identified as typical fluvial deposition (**Supplementary Figure S5A**), and it mainly comprised fine silt accounting for 69.8–89.8%, and the frequency distribution curves show a single peak with positive skewness (**Supplementary Figure S6A**). During 6.4–5.6 ka, the Gongba River with stronger hydrodynamic force carried a large number of loess around and then deposited here with a high sedimentation rate, and with frequent alluvial transformations, which indicates humid climate and increased precipitation in the Daihai Basin at 6.4–5.6 ka.

The frequency distribution curves of samples in DH05 section are bimodal distribution with a main peak at the fine sand grains and the secondary peak at 859 µm at 7.62 ± 0.56 ka (**Supplementary Figure S6B**), which indicated the heavy rainfalls with alluvial deposits [Type (C) in **Figure 6**], carrying a massive of coarse grains from lakeshores into the lake. At 9.2–6.7 ka, the frequency curves present a single peak with leptokurtosis [Type (B) in **Figure 6**]. The main components of sediments were silt, and the delta front developed with small sandy mixed bedding (**Supplementary Figure S5B**).

The frequency distribution curves of samples in DH29 section (**Supplementary Figures S5C, S6C**) revealed the depositions of the delta front during 8–7 ka. Meanwhile, wave action with wind transported a large number of coarse grains into the lake. Thereafter, the lake began to expand at 6.96 ± 0.45 ka, and pro-delta developed, indicating a transition to the deep lake phase. The frequency distribution curves of samples in DH30 and **Supplementary Figure S4** section (**Supplementary Figures S6D,E**) also indicated the delta front developed during 9–8 ka. Consequently, sections DH05, DH26, DH29, and DH30 were recognized as the braided river delta depositions to indicate the fluctuations of the lake level.

The frequency distribution curves of samples in DH28 section (**Supplementary Figure S6F**) displayed shallow lacustrine deposits with a secondary peak of coarse grains, which indicated highstand lacustrine deposits here with a relative high lake level at 8.77 ± 0.52 ka.

Lake-Level Reconstruction of Daihai During the Early-to-Mid Holocene

Based on the quartz OSL dating results and elevations of typical lakeshore/fluvial terraces and braided river deltas preserved in the

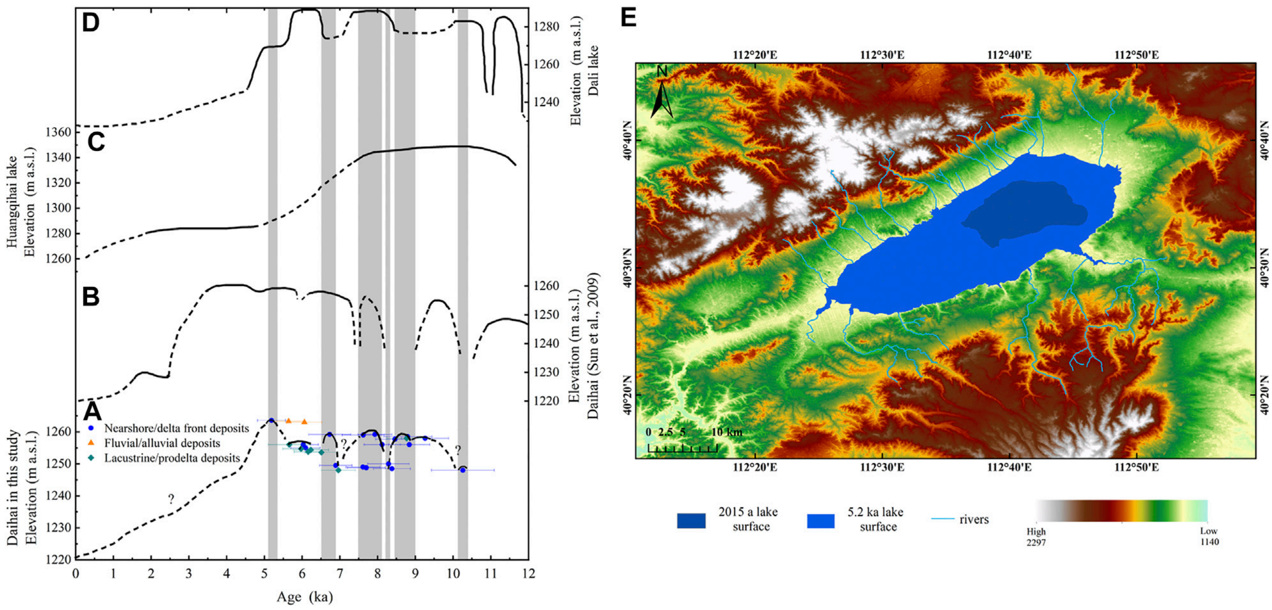

FIGURE 7 | Reconstruction of lake-level fluctuations in Daihai during the early and mid-Holocene and the comparison of lake-level fluctuations with the lakes in the marginal of EASM regions. **(A)** The lake-level fluctuations of Daihai in this study. The error bars represent the OSL ages. **(B)** The reconstructed lake-level fluctuation based on the ^{14}C dating from cores and terraces in Daihai (Sun et al., 2009) **(C)** The reconstructed lake-level variations of Huangqihai Lake (Zhang et al., 2016). **(D)** The lake-level fluctuation in Dali Lake (Goldsmith et al., 2017). **(E)** High lake level and the largest lake area at 5.2 ka in Daihai. The solid lines denote the position of the lake level, while the dashed lines represent the possible lake-level fluctuation processes without a firmly determined the lake level. The shaded gray bars indicate periods of significant lake-level fluctuations in Daihai.

sections around Daihai, we reconstructed the history of lake-level fluctuations during the early and mid-Holocene (**Figure 7A**). It is generally considered that the uppermost lacustrine sediments of the terraces were limited to represent the lower water level during that time (Sun et al., 2009). The uppermost delta front depositions could be used to indicate the highest water level once reached. The delta front is affected by the current lake shoreline and is a part of transforming into the delta plain, which can provide a conservative evidence to indicate lake-level fluctuations. Consequently, for the delta front depositions at the same time on different terraces, the highest elevation of the deposits was used to represent the lake level at that time. The pro-delta is regarded as a part of shallow lake, and thus the pro-delta deposits as same as the lacustrine sediments are also used to constrain the lower lake level.

The reconstructed lake-level fluctuation curve showed a relatively low level at 10.2 ka. Thereafter, the lake level may present an upward trend during 10.2–9.2 ka, and then increased to a higher lake level at 9.2–8.8 ka. However, the lake level temporarily rapidly declined at ca. 9.0 ka. Subsequently, the lake level quickly increased to the former water level and remained at a relatively high lake level during 8.8–8.5 ka. While the lake level dropped significantly at 8.5–8.1 ka again, we assumed it was possibly a response to the 8.2 ka cold events (Matero et al., 2017). After the episode, the Daihai lake level gradually increased and remained at a higher lake level at 8.1–5.2 ka, and then reached the optimum at 5.2 ka with the ~40 m higher than the modern lake level, and the lake area expanded to ~400 km^2, about six times as large as that of present (**Figure 7E**). At that time, Daihai Lake extended west to the Sandao Bay and east to the Wayao village, covering a large area of modern cropland. However, the depositional records showed that the lake-level fluctuations between 8.1 and 5 ka were more frequent, and the heavy rainfall events occurred at ca. 6.2 ka and ca. 7.6 ka when surface runoff and rivers carried massive coarse grains and gravel into the lake and then deposited. Our sedimentary records showed that a part of the depositional records in the northern and eastern Daihai (e.g., DH29 and **Supplementary Figure S4**) was missed after 5.2 ka, and the soil humus layer developed, which may indicate the sudden drop of the Daihai lake level. We inferred that another reason was that the upper lacustrine deposit layer or delta deposits may be eroded after the lake declined, and thus developed into the soil humus layer. Due to the lack of more evidence from the other geomorphic profiles, the specific reasons were largely unknown, but be worthy of further investigation in the future. Thus, here we do not discuss the lake-level fluctuations of Daihai after 5.2 ka.

DISCUSSION

Regional Comparison of Reconstructed Lake-Level Fluctuations at the Fringe of EASM-Influenced Areas

Here, we compared the reconstructed lake-level fluctuations of Daihai in this article with those of Daihai based on the different dating methods and proxies (Sun et al., 2009)

(**Figure 7B**), and further compared with the reconstructed lake levels of Huangqihai Lake (Zhang et al., 2016) (**Figure 7C**), and Dali Lake (Goldsmith et al., 2017) (**Figure 7D**) located in the EASM margin regions during the early-to-mid Holocene. Results demonstrate that Daihai had a relatively lower level at 10.2 ka., which may be a response to Younger Dryas (YD) events. However, it was not recorded in Daihai based on the ^{14}C dating but replaced with an inferred declined lake level. Subsequently, the Daihai lake level was prone to rise at 10.2–9.2 ka, which was also recorded in **Figure 7B**, and then reached a relatively higher lake level until 9.2–8.5 ka. Thereafter, the lake level underwent a decrease as a response to 8.2 ka cooling event, which crossed large parts of the Northern Hemisphere (Matero et al., 2017). After 8.2 ka cooling event, the Daihai lake level began to increase again and was maintained at a persistent and stable high lake level during 8.1–5.2 ka, except an inferred declined lake level at 7.5 ka. At 5.2 ka, the Daihai lake level reached its maximum, about 40 m higher than the modern lake level. Similar records in **Figure 7B** also revealed the high lake level during this time. However, our results showed that the high lake level developed at 5.2 ka, and then a sudden declined level occurred after 5.2 ka, while reconstruction results in **Figure 7B** indicated Daihai expanded on a large scale with the abundant monsoon effective precipitation and humid climate at 8.1 Cal ka B.P (7.3 ka B.P), and this persistent and stable high lake-level stage remained until 3.4 Cal ka B.P (3.2 ka B.P) (Sun et al., 2009). Overall, our reconstruction results filled the knowledge gap of lake-level variations of Daihai based on the ^{14}C dating of cores and lakeshores.

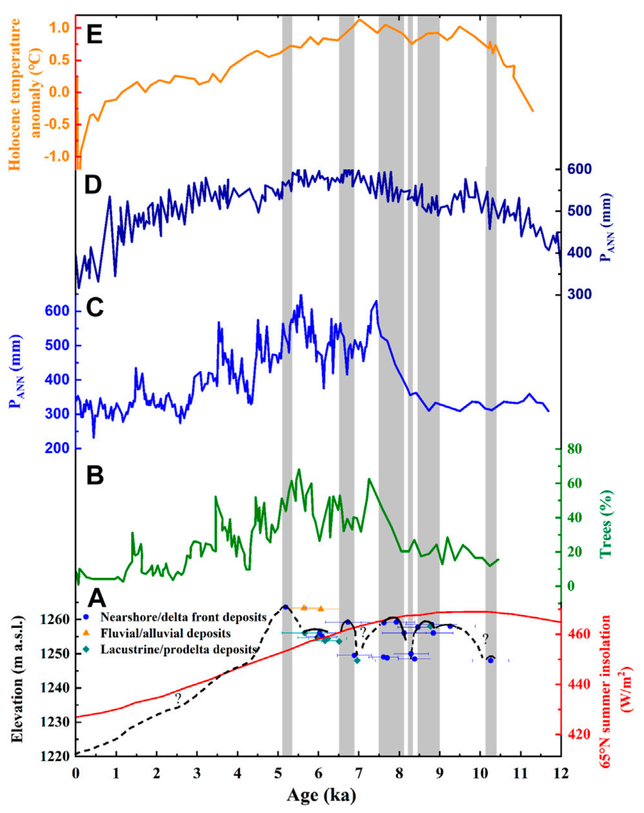

FIGURE 8 | Regional comparison of Daihai lake-level fluctuations with various regional and global environmental signals. **(A)** The lake-level fluctuation curve for Daihai in this study with 65°N summer insolation (red line) (Berger and Loutre, 1991). The error bars represent the OSL ages. The shaded gray bars indicate periods of significant lake-level fluctuations in Daihai. **(B)** The variation of trees pollen percentage from Daihai (Xiao et al., 2004). **(C)** Pollen-based annual precipitation (P_{ANN}) reconstructed from Daihai (Xu et al., 2010). **(D)** Pollen-based annual precipitation (P_{ANN}) reconstructed from Gonghai Lake (Chen et al., 2015). **(E)** Synthesized Northern Hemisphere (30°–90°N) temperature record during the Holocene (Marcott et al., 2013).

Lake-level fluctuations displayed in Huangqihai Lake and Dali Lake were slightly distinct with Daihai (**Figures 7C,D**). Results showed that the Dali lake level was more than 60 m higher than present, with a two-fold increase in annual rainfall during the 8.8–6.3 Cal ka B.P. (8.0–5.5 ka B.P.). At ca. 6.3 Cal ka B.P. (5.5 ka B.P.), the lake level dropped about 35 m, indicating the termination of humid conditions, which triggered a large cultural collapse of Early Neolithic cultures in north China, and possibly promoted the emergence of complex societies of the Late Neolithic (Goldsmith et al., 2017). There were also sub-fluctuations at ca. 10.6–10, 9.6–9, 7–6.3, 5.8–5.2, 4.5–3.7, 3.2–2.7, 2.3–2, 1.7–1.4, and 1.1–0.2 Cal. ka B.P.; the precipitation decreased, and the lake level declined with the decreasing nearshore components of lake sediments (Xiao et al., 2013; Xiao et al., 2015). Lake-level fluctuations of Dali in the Holocene were not only related to the monsoon intensity but also affected by ice and ice melt. Thus, the beginning of the high lake level was slightly earlier than that of Daihai, and the terminal time was also slightly earlier. Lake-level reconstruction of Huangqihai Lake based on OSL dating (**Figure 7C**) revealed a peak elevation of ~1,340 m (>77 m higher than the present) during the early Holocene, which remained such highstand from ~10 to ~8 ka and retreated toward the middle and late Holocene. The beginning and termination of the high lake level from Huangqihai Lake were both much earlier than those of Daihai Lake.

The Underlying Mechanism of lake-level fluctuations of Daihai During the Early and Mid-Holocene

We further compared various regional and global environmental signals to investigate the underlying mechanism of lake-level fluctuations of Daihai Lake or even lakes at the fringe of the EASM regions (**Figures 8, 8A**). The variation of tree pollen percentage from Daihai (**Figure 8B**) indicated woody plants showed an increasing trend during the early-to-mid Holocene, which may suggest the humidity gradually increased during 10.2–7.9 Cal. ka B.P., and then there was a large-scale coverage of mixed coniferous and broadleaved forests at 7.9–4.5 Cal. ka B.P., marking the warm and humid climate environment (Xiao et al., 2004). Precipitation variability in Daihai also indicated that the increasing precipitation at 7.9–3.1 Cal. ka B.P. and reached a higher level at 5.2 ka (Peng et al., 2005). Pollen-based annual precipitation (P_{ANN}) reconstructed from Daihai (**Figure 8C**) demonstrated that the period of 6.2–5.1 Cal ka B.P. was the wettest and warmest interval, with annual precipitation greater than 550 mm (Xu et al., 2010); cold-dry event at 8.2 Cal ka B.P. was also identified. Reconstructed annual precipitations based on the $\delta^{13}C$ of black carbon in Daihai further revealed that the precipitation during the mid-Holocene ranged from less than 170 to 310 mm higher than that at the present. However, the annual precipitation in the early and late Holocene was 70 mm lower than the present (Wang et al., 2013). The content of total organic matter (TOC) also reflected similar results, indicating the high vegetation production and increasing effective precipitations (Sun et al., 2006). All the above records demonstrated the volatility decline after 5 ka. However, our reconstructed results showed that the sediment records missed after 5.2 ka, and the upper layer developed soil humus. We inferred that the upper lacustrine deposit layer may be eroded after the lake declined and the soil humus developed.

Compared with the pollen-based annual precipitation reconstructed from Gonghai Lake located at the fringe of EASM areas controlled by the intensity of EASM (Chen et al., 2015) (**Figure 8D**), the annual precipitation of Gonghai Lake could represent the most areas of North China and be regarded as an ideal region to evaluate the EASM variability. The reconstructed results demonstrated a gradually intensifying monsoon from 14.7 to 7.0 ka, and a maximum monsoon from 7.8 to 5.3 ka with 30% higher monsoon precipitation than the present. These trends were punctuated by two millennial-scale weakening events which synchronously occurred with the YD event and at 9.5–8.5 ka, which further corresponded to the episodes at ca.10.2, 9, and 8.5–8.1 ka with the declined lake level from Daihai in this study. Since 3.3 ka, a sharp decline occurred in the annual precipitation of Gonghai Lake. Maximum annual precipitation at 7–5 ka during the mid-Holocene revealed the maximum intensity of EASM, which was strongly coupled with the development of Neolithic culture in northern China; for example, Yangshao culture during this period was more prosperous than other Neolithic cultures. Therefore, the strengthening of EASM brought high precipitation with a warm and humid climate, which provided a suitable climate environment for the development of human civilization. Lake-level fluctuations of Daihai corresponded to the EASM variability, which further indicated that the high lake level in Daihai during the Holocene was related to the enhancement of EASM. The evolution pattern of lake-level fluctuations in Daihai was also consistent with the 65°N summer solar insolation variation curve (Berger and Loutre, 1991) (**Figure 8A**, red line), which could be inferred that the lake-level fluctuation in Daihai was mainly controlled by the intensity of EASM driven by summer solar insolation. The synthesized Northern Hemisphere (30°–90°N) temperature record during the Holocene (**Figure 8E**) revealed early Holocene (10,000–5,000 years ago) warmth was followed by ~0.7°C cooling through the middle-to-late Holocene (<5,000 years ago), culminating in the coolest temperatures of the Holocene during the Little Ice Age. The high lake level at 5.2 ka was corresponding to the high temperature. However, after 5.2 ka, the lake level declined sharply, while the temperature and annual precipitation variability always displayed a relatively slow descent, which indicated that the lake-level fluctuations nonlinearly responded to the climate change, and thus, stratigraphic boundaries may not always represent climatic boundaries.

Overall, the lake-level fluctuation of Daihai directly indicates climate change during the early and mid-Holocene. Comparing the lake-level fluctuations with different lakes in the margin of EASM areas and other various regional and global climate signals, we concluded the lake-level fluctuation of Daihai was a regional response to global climate change during the early and mid-Holocene when the climate change is mainly controlled by the EASM driven by solar insolation at high-latitude summer in the Northern Hemisphere. Especially, the high lake level with the high precipitation associated with an intense EASM during the mid-Holocene may have provided a suitable and favorable environment for cultural development, for example, the distribution of the Haishengbulang cultural sites around Daihai at 6.6–5.7 Cal ka B.P. (5.8–5 ka B.P.) with the elevation of 1,290–1,300 m a.s.l. from early to late periods, indicating the expanding lake surface. However, there were 200 years of cultural vacancy during 5.7–5.5 Cal ka B.P. (5.0–4.8 ka B.P.) after the termination of Haishengbulang culture, which might indicate the occurrence of a centennial scale dry event, followed by the emergence of the Laohushan culture. Laohushan culture was a developed primitive agricultural culture with local characteristics around the Daihai Basin, which mainly distributed in the ecotone of agriculture and animal husbandry. Its cultivation was mainly extensive with tools of grindstone knives. However, the sudden collapse of Laohushan culture at 4.8 Cal ka B.P. may be related to the cold events caused by monsoon intensity at the end of the Holocene optimum (Xiao et al., 2019). The decrease in temperature resulted in changes in the heat conditions of agricultural production and the inability to meet the needs of crop growth. People will change their original land-use patterns to adapt to changes in the natural environment, from agriculture-based to semi-agricultural and semi-pastoral or pure animal husbandry. Thus, the ecotone of agriculture and animal husbandry in Daihai basin was developed from then on. Correspondingly, this episode was consistent with the sudden drop of the Daihai lake level after 5.2 ka.

The EASM plays a key role in the evolution of the lake level of Daihai, which is largely consistent with the Gonghai Lake and Dali Lake controlled by the intensity of EASM as well. However, on the centennial scale, the lake-level changes were more complex, which is determined by the regional characteristics of the lake, so the response of different lakes to the EASM intensity could be distinct. For example, the high lake level in the early and mid-Holocene of Dali Lake was not only affected by the EASM driven by solar insolation but also depends on the supply of ice melt and snowmelt.

CONCLUSION

In this study, a series of lakeshore terraces with different heights and braided river deltas around Daihai providing direct geomorphic evidence were used to reconstruct the history of lake-level fluctuations based on the OSL dating method during the early and mid-Holocene. We concluded that the Daihai lake level was at a relative low level at 10.2 ka. Thereafter, the lake level began to rise at 10.2–8.1 ka, and stayed at a relatively highstand level at 8.1–5.2 ka. Furthermore, the lake level of Daihai reached optimum at 5.2 ka, with ~40 m higher than the modern lake level, and the lake area expanded to about 400 km^2, approximately six times larger than that of the present. However, the records of the depositional sections revealed that part of the depositional records in the north and east of the Daihai were missed after 5.2 ka, maybe indicating the sudden drop of the lake level of Daihai. The overall climate pattern of Daihai during the early and mid-Holocene shows that the lake level has gradually risen since the early Holocene, and thereafter reached its peak in the mid-Holocene, developing a high lake level, which indicates that the monsoon effective precipitation increased and the humid climate prevailed with the strengthen EASM. The lake-level fluctuations of Daihai during the early and mid-Holocene were mainly controlled by the intensity of EASM. While it is not always synchronous in responding to climate change, which is well confirmed by other lakes at the fringe of ESAM-influenced areas. The local and regional factors are responsible for the fluctuation of the water lake level as well.

DATA AVAILABILITY STATEMENT

The original contributions presented in the study are included in the article/**Supplementary Material**; further inquiries can be directed to the corresponding author.

AUTHOR CONTRIBUTIONS

SH and XC conceived the idea for this article. SH conducted the experiments of Optical Stimulation Luminescence dating and grain size, led the data statistical analyses, and wrote the manuscript. XC was involved in discussions and contributed to the drafting of the article. All authors approved the final version and agreed to be accountable for the content of the work.

FUNDING

This study was supported financially by the National Natural Science Foundation of China (Nos. 41662011, 41967052, and 61661045) and the Natural Science Foundation of Inner Mongolia (Nos. 2019ZD10 and 2019GG020).

ACKNOWLEDGMENTS

We thank Z. W. Wu and Y. L. Zhang for their help in the field. We are grateful to Prof. H. Long (State Key Laboratory of Lake Science and Environment, Nanjing Institute of Geography and Limnology, Chinese Academy of Sciences) for the discussion of stratigraphic characteristics, and appreciate C. Zhang for improving manuscript. We are particularly grateful to J. Wu (School of Geography and Ocean Science, Nanjing University) for his help with data analysis, graphic drawing, and writing. We also thank the discussion of the sedimentary environment to S. Z. Xin and C. C. Leng. We thank two reviewers for their constructive comments and suggestions which improved the quality of this paper.

SUPPLEMENTARY MATERIAL

The Supplementary Material for this article can be found online at: https://www.frontiersin.org/articles/10.3389/feart.2021.702843/full#supplementary-material

REFERENCES

Aitken, M. J. (1998). *An Introduction to Optical Dating: The Dating of Quaternary Sediments by the Use of Photon-Stimulated Luminescence*. Oxford: Oxford University Press, 1–60.

Aitken, M. J. (1985). *Thermo Luminescence Dating*. London: Academic Press, 67.

Arnold, L. J., and Roberts, R. G. (2009). Stochastic Modelling of Multi-Grain Equivalent Dose (De) Distributions: Implications for OSL Dating of Sediment Mixtures. *Quat. Geochronol.* 4, 204–230. doi:10.1016/j.quageo.2008.12.001

Bailey, R. M., Smith, B. W., and Rhodes, E. J. (1997). Partial Bleaching and the Decay Form Characteristics of Quartz OSL. *Radiat. Measurements* 27, 123–136. doi:10.1016/s1350-4487(96)00157-6

Berger, A., and Loutre, M. F. (1991). Insolation Values for the Climate of the Last 10 Million Years. *Quat. Sci. Rev.* 10, 297–317. doi:10.1016/0277-3791(91)90033-q

Bøtter-Jensen, L., Thomsen, K. J., and Jain, M. (2010). Review of Optically Stimulated Luminescence (OSL) Instrumental Developments for Retrospective Dosimetry. *Radiat. Measurements* 45, 253–257. doi:10.1016/j.radmeas.2009.11.030

Brennan, B. J., Lyons, R. G., and Phillips, S. W. (1991). Attenuation of Alpha Particle Track Dose for Spherical Grains. *Int. J. Radiat. Appl. Instrumentation. D. Nucl. Tracks Radiat. Measurements* 18, 249–253. doi:10.1016/1359-0189(91)90119-3

Cao, G., Long, H., Zhang, J., and Lai, Z. (2012). Quartz OSL Dating of Last Glacial Sand Dunes Near Lanzhou on the Western Chinese Loess Plateau: A Comparison between Different Granulometric Fractions. *Quat. Geochronol.* 10, 32–36. doi:10.1016/j.quageo.2011.12.002

Chen, F., Wu, W., Holmes, J. A., Madsen, D. B., Zhu, Y., Jin, M., et al. (2003). A Mid-holocene Drought Interval as Evidenced by lake Desiccation in the Alashan Plateau, Inner Mongolia, China. *Chin. Sci Bull* 48, 1401–1410. doi:10.1360/03wd0245

Chen, F., Xu, Q., Chen, J., Birks, H. J. B., Liu, J., Zhang, S., et al. (2015). East Asian Summer Monsoon Precipitation Variability since the Last Deglaciation. *Sci. Rep.* 5, 11186. doi:10.1038/srep11186

Chen, F., Yu, Z., Yang, M., Ito, E., Wang, S., Madsen, D. B., et al. (2008). Holocene Moisture Evolution in Arid central Asia and its Out-of-phase Relationship with Asian Monsoon History. *Quat. Sci. Rev.* 27, 351–364. doi:10.1016/j.quascirev.2007.10.017

Chun, X., Qin, F.-Y., Zhou, H.-J., Dan, D., Xia, Y.-Y., and Ulambadrakh, K. (2020). Effects of Climate Variability and Land Use/land Cover Change on the Daihai Wetland of central Inner Mongolia over the Past Decades. *J. Mt. Sci.* 17, 3070–3084. doi:10.1007/s11629-020-6108-1

Costas, I., Reimann, T., Tsukamoto, S., Ludwig, J., Lindhorst, S., Frechen, M., et al. (2012). Comparison of OSL Ages from Young Dune Sediments with a High-Resolution Independent Age Model. *Quat. Geochronol.* 10, 16–23. doi:10.1016/j.quageo.2012.03.007

Ding, Z. L., Yu, Z. W., Yang, S. L., Sun, J. M., Xiong, S. F., and Liu, T. S. (2001). Coeval Changes in Grain Size and Sedimentation Rate of Eolian Loess, the Chinese Loess Plateau. *Geophys. Res. Lett.* 28, 2097–2100. doi:10.1029/2000gl006110

Du, Q., Chang, S., Li, Z., Zhang, L., and Zhang, P. (2013). Holocene lake Sediments and Environmental Changes in Daihai. *Northwest. Geology* 46, 140–147.

Duller, G. A. T. (2003). Distinguishing Quartz and Feldspar in Single Grain Luminescence Measurements. *Radiat. Measurements* 37, 161–165. doi:10.1016/s1350-4487(02)00170-1

Fan, A., Li, S.-H., and Chen, Y.-G. (2012). Late Pleistocene Evolution of Lake Manas in Western China with Constraints of OSL Ages of Lacustrine Sediments. *Quat. Geochronol.* 10, 143–149. doi:10.1016/j.quageo.2012.01.007

Fu, X., Cohen, T. J., and Arnold, L. J. (2017). Extending the Record of Lacustrine Phases beyond the Last Interglacial for Lake Eyre in central Australia Using Luminescence Dating. *Quat. Sci. Rev.* 162, 88–110. doi:10.1016/j.quascirev.2017.03.002

Goldsmith, Y., Broecker, W. S., Xu, H., Polissar, P. J., Demenocal, P. B., Porat, N., et al. (2017). Northward Extent of East Asian Monsoon Covaries with Intensity on Orbital and Millennial Timescales. *Proc. Natl. Acad. Sci. USA* 114, 1817–1821. doi:10.1073/pnas.1616708114

Guérin, G., Mercier, N., Nathan, R., Adamiec, G., and Lefrais, Y. (2012). On the Use of the Infinite Matrix assumption and Associated Concepts: A Critical Review. *Radiat. Measurements* 47, 778–785. doi:10.1016/j.radmeas.2012.04.004

Guo, Y., Huang, C. C., Pang, J., Zhou, Y., Zha, X., and Mao, P. (2017). Reconstruction Palaeoflood Hydrology Using Slackwater Flow Depth Method in the Yanhe River valley, Middle Yellow River basin, China. *J. Hydrol.* 544, 156–171. doi:10.1016/j.jhydrol.2016.11.017

He, Z., Long, H., Yang, L., and Zhou, J. (2019). Luminescence Dating of a Fluvial Sequence Using Different Grain Size Fractions and Implications on Holocene Flooding Activities in Weihe Basin, central China. *Quat. Geochronol.* 49, 123–130. doi:10.1016/j.quageo.2018.05.007

Jiang, M., Han, Z., Li, X., Wang, Y., Stevens, T., Cheng, J., et al. (2020). Beach Ridges of Dali Lake in Inner Mongolia Reveal Precipitation Variation during the Holocene. *J. Quat. Sci.* 35, 716–725. doi:10.1002/jqs.3195

Jin, Z., Li, X., Zhang, B., Han, Y., and Zheng, G. (2013). Geochemical Records in Holocene lake Sediments of Northern China: Implication for Natural and Anthropogenic Inputs. *Quat. Int.* 304, 200–208. doi:10.1016/j.quaint.2013.04.019

Jin, Z., Wang, S., Shen, J., and Song, J. (2004). Watershed Chemical Weathering and its Response to Climate Events in Daihai Area during Holocene. *Geochimica* 33, 29–36. doi:10.19700/j.0379-1726.2004.01.00410.1080/03009480410001280

Lai, Z., and Brückner, H. (2008). Effects of Feldspar Contamination on Equivalent Dose and the Shape of Growth Curve for OSL of silt-sized Quartz Extracted from Chinese Loess. *Geochronometria* 30, 49–53. doi:10.2478/v10003-008-0010-0

Lai, Z., Mischke, S., and Madsen, D. (2014). Paleoenvironmental Implications of New OSL Dates on the Formation of the "Shell Bar" in the Qaidam Basin, Northeastern Qinghai-Tibetan Plateau. *J. Paleolimnol* 51, 197–210. doi:10.1007/s10933-013-9710-1

Li, G., Chen, F., Xia, D., Yang, H., Zhang, X., Madsen, D., et al. (2018a). A Tianshan Mountains Loess-Paleosol Sequence Indicates Anti-phase Climatic Variations in Arid central Asia and in East Asia. *Earth Planet. Sci. Lett.* 494, 153–163. doi:10.1016/j.epsl.2018.04.052

Li, G., Madsen, D. B., Jin, M., Stevens, T., Tao, S., She, L., et al. (2018b). Orbital Scale lake Evolution in the Ejina Basin, central Gobi Desert, China Revealed by K-Feldspar Luminescence Dating of Paleolake Shoreline Features. *Quat. Int.* 482, 109–121. doi:10.1016/j.quaint.2018.03.040

Li, G., Wang, Z., Zhao, W., Jin, M., Wang, X., Tao, S., et al. (2020a). Quantitative Precipitation Reconstructions from Chagan Nur Revealed Lag Response of East Asian Summer Monsoon Precipitation to Summer Insolation during the Holocene in Arid Northern China. *Quat. Sci. Rev.* 239, 106365. doi:10.1016/j.quascirev.2020.106365

Li, G., Zhang, H., Liu, X., Yang, H., Wang, X., Zhang, X., et al. (2020b). Paleoclimatic Changes and Modulation of East Asian Summer Monsoon by High-Latitude Forcing over the Last 130,000 Years as Revealed by Independently Dated Loess-Paleosol Sequences on the NE Tibetan Plateau. *Quat. Sci. Rev.* 237, 106283. doi:10.1016/j.quascirev.2020.106283

Li, H., Liu, Q., and Wang, J. (1992). Study of Evolution of Huangqihai and Daihai lake in Holocene in Inner Mongolia Plateau. *J. Lake Sci.* 4, 31–39.

Liu, B., Tan, C., Yu, X., Shan, X., and Li, S. (2019). Evolution Model of a Modern delta Fed by a Seasonal River in Daihai Lake, North China: Determined from Ground-Penetrating Radar and Trenches. *Front. Earth Sci.* 13, 262–276. doi:10.1007/s11707-018-0740-x

Liu, J., Wang, Y., Li, T., Dong, J., Jiang, N., and Tang, W. (2016). Lake Level Fluctuations since 12.5 Cal Ka BP Recorded by Lakeshores of the Dali Lake in Middle-East of Inner Mongolia. *J. Palaeogeogr.* 18, 1044–1052.

Liu, K., and Lai, Z. P. (2012). Chronology of Holocene Sediments from the Archaeological Salawusu Site in the Mu Us Desert in China and its Palaeoenvironmental Implications. *J. Asian Earth Sci.* 45, 247–255. doi:10.1016/j.jseaes.2011.11.002

Liu, X.-J., Lai, Z., Madsen, D., and Zeng, F. (2015). Last Deglacial and Holocene lake Level Variations of Qinghai Lake, north-eastern Qinghai-Tibetan Plateau. *J. Quat. Sci.* 30, 245–257. doi:10.1002/jqs.2777

Long, H., Lai, Z., Fuchs, M., Zhang, J., and Li, Y. (2012). Timing of Late Quaternary Palaeolake Evolution in Tengger Desert of Northern China and its Possible Forcing Mechanisms. *Glob. Planet. Change* 92-93, 119–129. doi:10.1016/j.gloplacha.2012.05.014

Long, H., Lai, Z., Wang, N., and Zhang, J. (2011). A Combined Luminescence and Radiocarbon Dating Study of Holocene Lacustrine Sediments from Arid Northern China. *Quat. Geochronol.* 6, 1–9. doi:10.1016/j.quageo.2010.06.001

Marcott, S. A., Shakun, J. D., Clark, P. U., and Mix, A. C. (2013). A Reconstruction of Regional and Global Temperature for the Past 11,300 Years. *Science* 339, 1198–1201. doi:10.1126/science.1228026

Matero, I. S. O., Gregoire, L. J., Ivanovic, R. F., Tindall, J. C., and Haywood, A. M. (2017). The 8.2 Ka Cooling Event Caused by Laurentide Ice Saddle Collapse. *Earth Planet. Sci. Lett.* 473, 205–214. doi:10.1016/j.epsl.2017.06.011

Murray, A. S., and Olley, J. M. (2002). Precision and Accuracy in the Optically Stimulated Luminescence Dating of Sedimentary Quartz: a Status Review. 21**,** 1–16.

Murray, A. S., and Wintle, A. G. (2000). Luminescence Dating of Quartz Using an Improved Single-Aliquot Regenerative-Dose Protocol. *Radiat. Measurements* 32, 57–73. doi:10.1016/S1350-4487(99)00253-X

Nian, X., Zhang, W., Qiu, F., Qin, J., Wang, Z., Sun, Q., et al. (2019). Luminescence Characteristics of Quartz from Holocene delta Deposits of the Yangtze River and Their Provenance Implications. *Quat. Geochronol.* 49, 131–137. doi:10.1016/j.quageo.2018.04.010

Peng, Y., Xiao, J., Nakamura, T., Liu, B., and Inouchi, Y. (2005). Holocene East Asian Monsoonal Precipitation Pattern Revealed by Grain-Size Distribution of Core Sediments of Daihai Lake in Inner Mongolia of north-central China. *Earth Planet. Sci. Lett.* 233, 467–479. doi:10.1016/j.epsl.2005.02.022

Prescott, J. R., and Hutton, J. T. (1994). Cosmic ray Contributions to Dose Rates for Luminescence and ESR Dating: Large Depths and Long-Term Time Variations. *Radiat. Measurements* 23, 497–500. doi:10.1016/1350-4487(94)90086-8

Roberts, H. M. (2008). The Development and Application of Luminescence Dating to Loess Deposits: a Perspective on the Past, Present and Future. *Boreas* 37, 483–507. doi:10.1111/j.1502-3885.2008.00057.x

Shen, H., Jia, Y., Zhang, H., Wei, L., and Wang, P. (2006). Environmental Change Inferred from Granular Size Character of Lacustrine Sediment in Inner Mongolia Huangqihai, during 8.02.2 Ka BP. *Arid Land Geogr.* 29, 457–462.

Shi, L., Jin, Z., Li, G., Gao, B., and Yan, W. (2014). Depositional Characteristics and Models of the Modern Braided River delta in the Daihai lake, Inner Mongolia. *Nat. Gas Industry* 34, 33–39. doi:10.3781/j.issn.1000-0976.2014.09.005

Stevens, T., Buylaert, J.-P., Thiel, C., Újvári, G., Yi, S., Murray, A. S., et al. (2018). Ice-volume-forced Erosion of the Chinese Loess Plateau Global Quaternary Stratotype Site. *Nat. Commun.* 9, 983. doi:10.1038/s41467-018-03329-2

Sun, Q., Wang, S., Zhou, J., Shen, J., Cheng, P., Xie, X., et al. (2009). Lake Surface Fluctuations since the Late Glaciation at Lake Daihai, North central China: A Direct Indicator of Hydrological Process Response to East Asian Monsoon Climate. *Quat. Int.* 194, 45–54. doi:10.1016/j.quaint.2008.01.006

Sun, Q., and Xiao, J. (2006). Characteristics of the Holocene Optmum in the Monsoon/arid Transition belt Recorded by Core Sediments of Daihai lake, North China. *Quat. Sci.* 26, 781–790.

Sun, Q., Xiao, J., and Liu, T. (2010). Hydrothermal Status in the Monsoon/arid Transition belt of China since the Lase Glaciation Inferred from Geochemical Characteristics of the Sedimenr Cores at Daihai lake. *Quat. Sci.* 30, 1121–1130.

Sun, Q., Zhou, J., Shen, J., Chen, P., Wu, F., and Xie, X. (2006). Environmental Characteristics of Mid-holocene Recorded by Lacustrine Sediments from Lake Daihai, north Environment Sensitive Zone, China. *Sci. China Ser. D* 49, 968–981. doi:10.1007/s11430-006-0968-2

Thomsen, K. J., Jain, M., Murray, A. S., Denby, P. M., Roy, N., and Bøtter-Jensen, L. (2008). Minimizing Feldspar OSL Contamination in Quartz UV-OSL Using

Pulsed Blue Stimulation. *Radiat. Measurements* 43, 752–757. doi:10.1016/j.radmeas.2008.01.020

Wang, S., Wu, R., and Jaing, X. (1990). Environment Evolution and Paleoclimate of Daihai lake, Inner Mongolia since the Last Glaciation. *Quat. Sci.*, 223–232.

Wang, X., Cui, L., Xiao, J., and Ding, Z. (2013). Stable Carbon Isotope of Black Carbon in lake Sediments as an Indicator of Terrestrial Environmental Changes: An Evaluation on Paleorecord from Daihai Lake, Inner Mongolia, China. *Chem. Geology* 347, 123–134. doi:10.1016/j.chemgeo.2013.03.009

Wintle, A. G., and Murray, A. S. (2006). A Review of Quartz Optically Stimulated Luminescence Characteristics and Their Relevance in Single-Aliquot Regeneration Dating Protocols. *Radiat. Measurements* 41, 369–391. doi:10.1016/j.radmeas.2005.11.001

Wu, J., Lu, H., Yi, S., Xu, Z., Gu, Y., Liang, C., et al. (2019). Establishing a High-Resolution Luminescence Chronology for the Zhenbeitai Sand-Loess Section at Yulin, North-Central China. *Quat. Geochronol.* 49, 78–84. doi:10.1016/j.quageo.2018.03.013

Xiao, J., Chang, Z., Si, B., Qin, X., Itoh, S., and Lomtatidze, Z. (2009). Partitioning of the Grain-Size Components of Dali Lake Core Sediments: Evidence for lake-level Changes during the Holocene. *J. Paleolimnol* 42, 249–260. doi:10.1007/s10933-008-9274-7

Xiao, J., Fan, J., Zhai, D., Wen, R., and Qin, X. (2015). Testing the Model for Linking Grain-Size Component to lake Level Status of Modern Clastic Lakes. *Quat. Int.* 355, 34–43. doi:10.1016/j.quaint.2014.04.023

Xiao, J., Fan, J., Zhou, L., Zhai, D., Wen, R., and Qin, X. (2013). A Model for Linking Grain-Size Component to lake Level Status of a Modern Clastic lake. *J. Asian Earth Sci.* 69, 149–158. doi:10.1016/j.jseaes.2012.07.003

Xiao, J., Si, B., Zhai, D., Itoh, S., and Lomtatidze, Z. (2008). Hydrology of Dali Lake in central-eastern Inner Mongolia and Holocene East Asian Monsoon Variability. *J. Paleolimnol* 40, 519–528. doi:10.1007/s10933-007-9179-x

Xiao, J., Xu, Q., Nakamura, T., Yang, X., Liang, W., and Inouchi, Y. (2004). Holocene Vegetation Variation in the Daihai Lake Region of north-central China: a Direct Indication of the Asian Monsoon Climatic History. *Quat. Sci. Rev.* 23, 1669–1679. doi:10.1016/j.quascirev.2004.01.005

Xiao, J., Zhang, S., Fan, J., Wen, R., Xu, Q., Inouchi, Y., et al. (2019). The 4.2 Ka Event and its Resulting Cultural Interruption in the Daihai Lake basin at the East Asian Summer Monsoon Margin. *Quat. Int.* 527, 87–93. doi:10.1016/j.quaint.2018.06.025

Xu, J., Jia, Y., Lai, Z., Wang, P., Xu, M., and Shen, H. (2012). Climate Variations during Early to Mid-holocene in Huangqihai Lake in Northern China Based on the Lake Deposit Analysis. *Acta Sedimentologica Sinica* 30, 731–738. doi:10.14027/j.cnki.cjxb.2012.04.021

Xu, Q., Xiao, J., Li, Y., Tian, F., and Nakagawa, T. (2010). Pollen-Based Quantitative Reconstruction of Holocene Climate Changes in the Daihai Lake Area, Inner Mongolia, China. *J. Clim.* 23, 2856–2868. doi:10.1175/2009jcli3155.1

Xu, Q., Xiao, J., Nakamura, T., Yang, X., Zheng, Z., Liang, W., et al. (2004). Pollen Evidence of Vegetation and Climate Changes in Daihai lake Area during the Holocene. *J. Glaciology Geocryology* 26, 73–80.

Yu, L., and Lai, Z. (2017). Holocene Climate Change Inferred from Stratigraphy and OSL Chronology of Aeolian Sediments in the Qaidam Basin, Northeastern Qinghai-Tibetan Plateau. *Quat. Res.* 81, 488–499. doi:10.1016/j.yqres.2013.09.006

Yu, X., Li, S., Tan, C., Xie, J., Chen, B., and Yang, F. (2013). The Response of Deltaic Systems to Climatic and Hydrological Changes in Daihai Lake Rift basin, Inner Mongolia, Northern China. *J. Palaeogeogr.* 2, 41–45. doi:10.3724/SP.J.1261.2013.00016

Zhang, J., Jia, Y., Lai, Z., Long, H., and Yang, L. (2011). Holocene Evolution of Huangqihai Lake in Semi-arid Northern China Based on Sedimentology and Luminescence Dating. *The Holocene* 21, 1261–1268. doi:10.1177/0959683611405232

Zhang, J., Lai, Z., and Jia, Y. (2012). Luminescence Chronology for Late Quaternary lake Levels of Enclosed Huangqihai lake in East Asian Monsoon Marginal Area in Northern China. *Quat. Geochronol.* 10, 123–128. doi:10.1016/j.quageo.2012.04.015

Zhang, J., Tsukamoto, S., Jia, Y., and Frechen, M. (2016). Lake Level Reconstruction of Huangqihai Lake in Northern China since MIS 3 Based on Pulsed Optically Stimulated Luminescence Dating. *J. Quat. Sci.* 31, 225–238. doi:10.1002/jqs.2861

Zhang, Z., and Wang, S. (2000). Paleoclimate Significance of Lake Level Fluctuation, Oeat Development and Eolian Sand-Paleosoil Series in Hulun Lake. *J. Arid Land Resour. Environ.* 14, 56–59.

Zhao, X., Huang, C. C., Pang, J., Zha, X., Guo, Y., and Hu, G. (2016). Holocene Climatic Events Recorded in Palaeoflood Slackwater Deposits along the Middle Yiluohe River valley, Middle Yellow River basin, China. *J. Asian Earth Sci.* 123, 85–94. doi:10.1016/j.jseaes.2016.04.002

Conflict of Interest: The authors declare that the research was conducted in the absence of any commercial or financial relationships that could be construed as a potential conflict of interest.

frontiers
in Earth Science

ORIGINAL RESEARCH
published: 17 August 2021
doi: 10.3389/feart.2021.728202

Physiochemical Characteristics, Provenance, and Dynamics of Sand Dunes in the Arid Hexi Corridor

Bing-Qi Zhu[1]*, *Jia-Xing Zhang*[1,2] *and Chun Sun*[1,2]

[1]Key Laboratory of Water Cycle and Related Land Surface Processes, Institute of Geographic Sciences and Natural Resources Research, Chinese Academy of Sciences, Beijing, China, [2]University of Chinese Academy of Sciences, Beijing, China

Dynamic changes of aeolian landforms under changing environments in a middle-latitude desert belt is a typical problem of climate change and related landscape response. It need a comprehensive understanding of the formation mechanisms of dune landforms with the supply of material suitable for aeolian transport and favorable conditions of sediment availability and wind regimes in the region. Based on comprehensive evidences from geomorphological, sedimentological, geochemical, and hydrological analysis, this study discussed the dynamical changes of different dune landforms during the past half century and their provenance in the Hexi Corridor, China. The results show that there are two states of sand dunes movement in the Hexi Corridor in the past half century, dynamic migration and basically stable. The crescent-shaped dunes move the fastest, followed by the chains of barchan dunes. Only the top of the pyramid dunes wigwags, while the parabolic dunes and the longitudinal dunes hardly move forward. The moving speed of sand dunes is positively correlated with the wind speed ≥5 m/s at a yearly scale. The grain size of sand dunes in the western Hexi Corridor is coarser than that in the central-eastern part, and also larger than those in other deserts of northern China and of the world. Different motion modes of saltation, suspension, and creeping are identified between aeolian, alluvial/fluvial and gobi sediments. Dune sands are mainly “sediments of *in-situ* rising” that originated from alluvial/fluvial/lacustrine deposits of ancient rivers, lakes, and aeolian deposits in the erosion zone of the forelands of the Qilian and Beishan Mountains and the north-neighboring deserts. This reveals a significance interaction between wind and water dynamics in the formation and evolution of aeolian landforms in the arid study area. Sufficient transport capacity is evidenced for both the western and eastern parts of the Hexi Corridor, sufficient sand supply and sand availability, however, is the favorable factor for dune formation in the east part but is the limiting factor for the west.

Keywords: sand dunes and gobi sediments, geomorphological dynamics, grain size sedimentology, major- and trace-elements geochemistry, sediment provenance, desertification, Hexi Corridor, middle-latitude desert

OPEN ACCESS

Edited by:
Xiangjun Liu,
Northwest Normal University, China

Reviewed by:
Zhiwei Xu,
Nanjing University, China
Mingrui Qiang,
South China Normal University, China

****Correspondence:***
Bing-Qi Zhu
zhubingqi@igsnrr.ac.cn

Specialty section:
This article was submitted to
Quaternary Science, Geomorphology
and Paleoenvironment,
a section of the journal
Frontiers in Earth Science

Received: *21 June 2021*
Accepted: *09 August 2021*
Published: *17 August 2021*

Citation:
Zhu B-Q, Zhang J-X and Sun C (2021)
Physiochemical Characteristics,
Provenance, and Dynamics of Sand
Dunes in the Arid Hexi Corridor.
Front. Earth Sci. 9:728202.
doi: 10.3389/feart.2021.728202

INTRODUCTION

The mid-latitude desert belt refers to the desert zone ranging between 30 and 60 °N latitude outside the control of the subtropical high climate in the Northern Hemisphere, more than 90% of which are distributed in the arid inland of central Asia and northern China. In northern China, about 566,000 square kilometers of land area are covered by aeolian sand, covering a wide range of geomorphological and tectonic backgrounds ranging from 155 m below sea level to 5,000 m above sea level (Yang, 2006). The desert landscapes dominated by active sand dunes are mainly distributed in the arid areas with an average annual precipitation of less than 200 mm, while the sandy-land landscapes dominated by semi-active dunes and vegetated dunes mainly appeared in the semi-arid areas with an average annual precipitation of 200–400 mm (Zhu et al., 1980). The present geomorphology of these sandy deserts is the product of long-term and short-term changes of the interaction between endogenic forces (such as tectonic movement) and external forces (such as climate) of the earth system (Goudie, 2002; Lancaster et al., 2013; Williams, 2014; Lancaster et al., 2016; Yang et al., 2019). In turn, these deserts may have affected the global climate system indirectly through desert sediment circulation such as dust cycles (Goudie, 2002; Yang, 2006). Therefore, the understanding of desert landscape evolution will increase our understanding of the earth system.

The movement of aeolian materials and the dynamics of dune landforms are the results of the transportation and accumulation of sandy sediments under the influence of climate (especially wind and atmospheric circulation), which is the direct cause of landsurface desertification (Zhu et al., 1980; Zhu and Wang, 1992; Yang et al., 2004, Yang et al., 2012, Yang et al., 2019). Thus, in terms of genetic mechanism, formation of aeolian deposits depends on an array of requirements: the supply of material suitable for aeolian transport and favorable conditions of sediment availability and wind strength (Kocurek and Lancaster, 1999; Yang et al., 2012; Nottebaum et al., 2015b; Lv et al., 2018). In brief, the sedimentological environment (such as the supply and availability of source materials), geomorphic conditions (such as the route and distance between a specific sediment and its potential source area), and climatic conditions (such as wind regime and effective moisture controlling dust-trapping vegetation covers) constitute a complex system of dune landform development (Kocurek and Lancaster, 1999). Dune formation and dynamics in China were qualitatively or semi-quantitatively described in most early studies (Yang, 2006). Some pioneer scholars have studied the development and movement of sand dunes in the Taklamakan Desert of China, the second largest active sand desert in the world, and they quantitatively analyzed the moving speed and evolution process of local crescent dunes (Zhu et al., 1964; Zhu et al., 1980, Zhu et al., 1981a). These studies laid a solid foundation for the later development of refined and quantitative researches due to the progress of research methods and technical tools, and until now, they are still a milestone and cornerstone of desert researches in China.

The Hexi Corridor is located in the center of the desert belt in northern China and at the middle-latitudes of Northern Hemisphere (NH). It was once one of the most important trunk sections of the world-famous Silk Road, and a place where several ancient cultures converged. Today the Hexi Corridor is facing severe problems of desertification and climate change under global warming. For nearly half a century, frequent sandstorms in northern China have been considered to be the direct consequence of desertification in the Hexi Corridor, because the Hexi area is regarded as the main source area and the engine area of sandstorms in northern China (Zhang and Ren, 2003; Pu, 2005; Li and Zhang, 2007). Therefore, the problem of desertification in the Hexi Corridor is one of the major problems that have been urgently needed to be resolved in northern China for half a century.

For nearly half a century, desertification in the arid areas of northern China and its origin, causes, processes, impacts on climate change and methods of combating desertification have been studied and discussed in more detail, such as the classification (Zhu et al., 1980; Zhu et al., 1981b), causes (Wu et al., 1997; Wu and Ci, 1998; Sun, 2000; Sun and Li, 2002; Wu and Ci, 2002; Runnstrom, 2003), trends (Zhu, 1985; Ci et al., 2002; Wang et al., 2004; T. Wang et al., 2003, Wang et al., 2004a, Wang et al., 2004b) and environmental effects (Ci and Yang, 2004; Yang et al., 2008) of desertification in China. Although significant progress has been made in the study of desertification in China in recent decades and the understanding of the classification of desertification has reached a basic consensus, its causes are still controversial. Many scientists believe that the desertification in northern China is mainly caused by human activities (Wu, 2001; Wang et al., 2003a; Wang et al., 2004b), while others believe that climate change is the main cause of desertification in northern China (Zhao, 1981; Wang, 2002; Han, 2003; Wang et al., 2005, Wang et al., 2006a, Wang et al., 2008a). But in any case, desertification is a dynamic process, which is potentially affected by surface erodibility and atmospheric erosivity (Thomas et al., 2005; Thomas and Leason, 2005) and may also be affected by geomorphological processes on the geological time scale even greater than the effects of climate change (Nottebaum et al., 2015a), and these dynamics are still not well understood at present, especially at the inter-decadal time scale.

The purpose of this study is, based on the comprehensive evidences from the extensive dune geomorphological survey, the sedimentological and geochemical analysis of dune sediments to understand the provenance and dynamic changes of sand dunes in the Hexi Corridor and their formation mechanism during the past half century.

BACKGROUND AND ANALYTICAL METHODS

Natural Backgrounds of the Hexi Corridor

The Hexi Corridor is geographically located in the central and western parts of Gansu Province in Northwest China (**Figures 1**, **2**), including Wuwei, Jinchang, Zhangye, Jiuquan, Jiayuguan and other cities in the west of the Yellow River, with a total area of approximately 5,100 square kilometers.

In terms of geomorphology, the Hexi Corridor represents the transition zone from high mountain areas towards the lower northwestern Chinese deserts, located in the lowland area between the Qilian Mountains to the south and the Alashan Plateau to the north (**Figure 2**). The Alashan Plateau distributes three large sandy deserts of China, i.e., the Badanjilin Desert, the Tenggeli Desert and the Ulanbuhe Desert. The Qilian Mountains is trending west-northwest-east-southeast (WNW-ESE) and

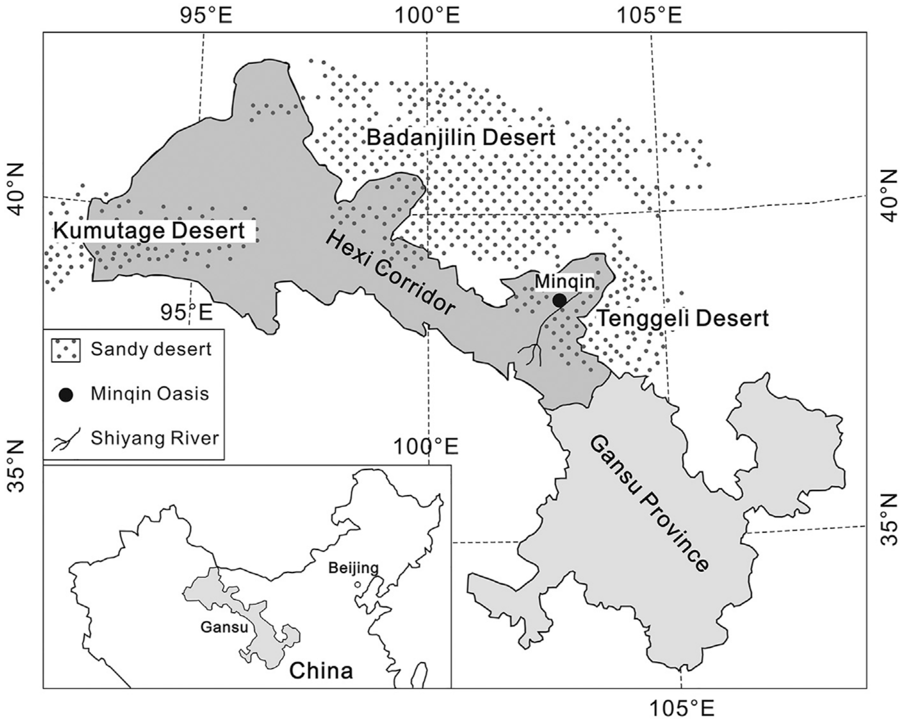

FIGURE 1 | Geographical position of the Hexi Corridor in China (the Hexi Corridor is located in the west of Gansu Province and is a part of Gansu Province).

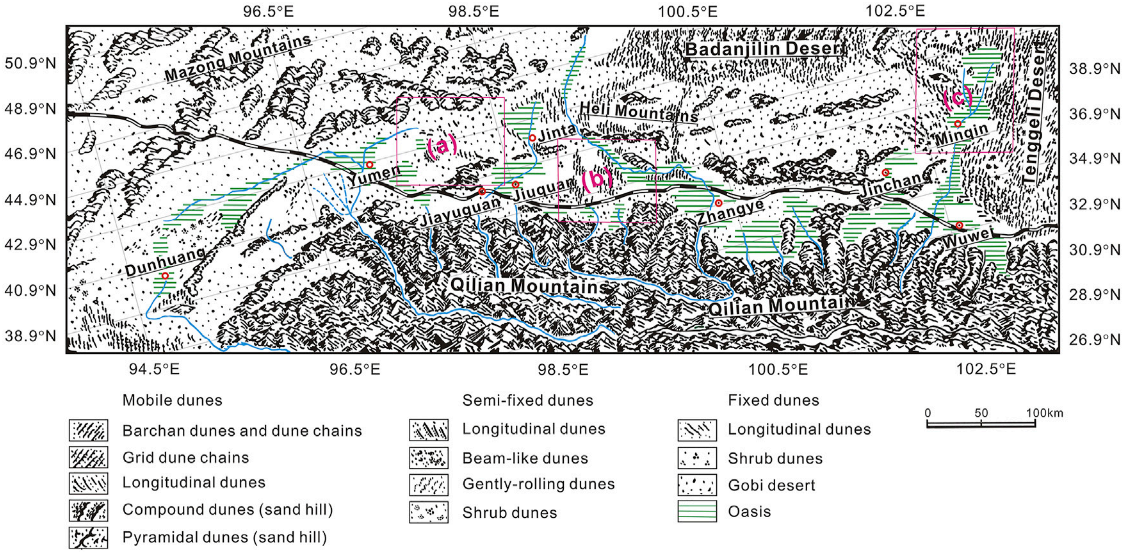

FIGURE 2 | Geomorphological map of the Hexi Corridor (modified after Wang (2003)).

reaches up to 5,700 m above sea level (a.s.l.). It was uplifted during the Caledonian orogenesis and got reactivated by the India-Eurasia collision during Cretaceous and Neogene times (Tapponnier et al., 1990; Meyer et al., 1998). It dominantly consists of metamorphic and sedimentary rocks, i.e., sandstones and conglomerates (Bureau of Geology and Mineralogy Resources of Gansu Province (BGMRGP), 1984).

The geomorphologic landscape appearance is remarkably different in the western part compared to the central and eastern parts of the Hexi Corridor. The west is mainly dominated by gravel gobi surfaces, accompanied by rare sand sheets and dune fields in the surrounding of the Huahai palaeolake (G. Wang et al., 2003, N. Wang et al., 2013), while the central and east exhibit frequent alternation of alluvial and lacustrine deposits, several dune fields, sand sheets, and widespread oases including cropland (Nottebaum et al., 2015a).

In climate, the Hexi Corridor is situated in the center part of the temperate desert belt in the mid-latitudes of Northern Hemisphere. Except for the forest and grasslands distributed in the middle- and high-elevation mountain areas in the south, most of the Hexi Corridor is under a typical arid climate with desert landforms widely developed. The desert types are dominated by gobi desert and sandy desert, which account for 46.64% of the total area of the region.

In hydrology, the melting water of ice and snow in the high Qilian Mountains in the south converges into several large rivers flowing northward into the Hexi Corridor, including the Shule River, the Heihe River, and the Shiyang River from west to eat (**Figure 2**). In the middle and lower reaches of these rivers flowing through the corridor from south to north, diluvial and alluvial fans are well developed, and hydrologically, they are also the main locations of spring overflow zone of each catchment derived from the Qilan Mountains. Oases are widely developed in the toes of these alluvial fans and are the major agricultural exploitation areas and the resident agglomeration areas of northwest China. The ephemeral drainages of the western Hexi Corridor terminate close to the southern edge of the adjacent Beishan Mountains to the north which was the terminal basin hosting Huahai palaeolake (**Figure 2**), whereas the main eastern drainage (Heihe River) flows farther north into the Ejina basin, feeding the Juyanze, Sugunur, and Garshunnur palaeolakes (Hartmann and Wünnemann, 2009).

In sedimentological geology, the Hexi Corridor was affected by widespread Quaternary (glacio-) fluvial sediment accumulation (Hetzel et al., 2004; Kuster et al., 2006), resulting in several generations of alluvial fans. These fans are partly affected by tectonic activity (Hetzel et al., 2002) and subsequently dissected by fluvial incision. Due to the geomorphological differences between the western and central eastern parts of the Hexi Corridor, their surface strata also have two different sedimentary characteristics. One is that the gravel strata are often covered by interbedded sedimentary strata of aeolian and alluvial/proluvial sediments, and the other is that the aeolian strata in sand dunes are often interrupted by flood deposition. Geochronology and paleoenvironment studies from the superficial sedimentary strata indicate that there is also a completely different sedimentary evolution history between the western and central-eastern parts of the Hexi corridor during the Late Quaternary (Nottebaum et al., 2015a). For example, the sedimentary process in the western part of the Hexi Corridor is limited to a short period of the Pleistocene-Holocene transition, while the sedimentary process in the central-eastern of the Corridor occurs throughout the Holocene, reflecting a history of frequent sediment recycling during the Holocene.

Aeolian sediments (loess, loess-like, sand and dust) and dune landforms are widespread in the western, central and eastern parts of the Hexi Corridor (Zhang et al., 2008; Nottebaum et al., 2014, Nottebaum et al., 2015b). In terms of aeolian landforms, sand dunes or dune fields in the Hexi Corridor are mainly distributed in a narrow and long belt between the Qilian Mountains and the Heli mountains from the west of Wushaoling to the east of Palaeo-Yumenguan (**Figure 2**) (Zhu et al., 1980). Compared with dune landforms in the adjacent areas of the Badanjilin and Tenggeli Deserts, in which the sand dunes tend to be convergent in spatial distribution, while the Hexi Corridor is different, where the dunes are almost scattered, mainly distributed in the vicinity of oases along some rivers, in the oasis or gobi desert areas (**Figure 2**). From east to west in the dune belt, sand dunes are mainly distributed around the Minqin Oasis in the lower reaches of the Shiyang River, the Zhangye and Gaotai oases in the middle reaches of Heihe River, the Jiuquan and Jinta oases in the lower reaches of the Beidahe River, and the Dunhuang oasis in the lower reaches of the Danghe River (**Figure 2**) (Zhu et al., 1980).

The total area of dune fields in the Hexi Corridor is about 754 square kilometers, and many big crescent-shaped dunes and chains of crescent-shaped dunes develop on the edges of oases. The Minqin Basin is a typical area with dune landforms development in the Hexi Corridor. It is located at the lower reaches of the Shiyang River and the western edge of the Tenggeli Desert. The annual average precipitation is about 116.4 mm and the annual average wind speed is about 2.25 m/s. A large number of crescent-shaped dunes are distributed on the northwestern edge of the oasis, i.e., the windward of sand-transport winds in the oasis.

Historically, the Hexi Corridor was a necessary place for the famous ancient Silk Road in China. In modern times, however, the expansion of population and socio-economic development of the Hexi Corridor, as well as the human-caused competitive redistribution of water resources, have led to the onset and enhancement of desertification in the Hexi Corridor (Pu, 2005). The expansions of sand dunes and dune fields in the corridor, and even the combination with surrounding sandy desert, have occurred in the past 2 ka (Zhu and Wang, 1992; Ren et al., 2014).

Methods and Analytical Data

Formation and characteristics of dune landforms are considered to be the result of a complex interplay between sediment properties and local preconditions (Nottebaum et al., 2015b). Although wind regime, surface condition, and sediment availability all control sand dune formation (Pye, 1995; Kocurek and Lancaster, 1999), geoscientists have mostly put emphasis on the wind regime. However, researches show that the formation of dune cannot be explained solely on wind because different dune types can form under the same wind regime in a given area (Rubin and Hesp, 2009; Lv et al., 2018). For example, in areas with little or no vegetation, dune formation depends strongly on wind regime and sediment availability (Wasson and Hyde, 1983; Baas and Nield, 2007), and both factors must be considered in studies on the formation and morphology of aeolian dunes; otherwise, modern dune morphology may lead to erroneous interpretations of the evolutionary history of dune environments (Rubin and Hesp, 2009). Therefore, sediment properties and local preconditions must be paid attention to.

In detail, sediment properties are partly inherited from source materials, e.g., grain size and geochemical/mineralogical composition (e.g., Jahn et al., 2001; Prins and Vriend, 2007; Feng et al., 2011; Guan et al., 2013; Vandenberghe, 2013; Nottebaum et al., 2014, Nottebaum et al., 2015b). Important local preconditions comprise surface and topographic properties, e.g., the geomorphologic setting, vegetation cover, and surface roughness on various spatial scales (Mason et al., 1999; Hugenholtz and Wolfe, 2010; Stauch et al., 2012; Stauch et al., 2014; Nottebaum et al., 2014, Nottebaum et al., 2015b) and wind conditions (e.g., Pye, 1995; Lu et al., 2000; Sun et al., 2003; Kimura et al., 2009). Thus, an insight into the potential relationship between dune-forming factors related to the wind regime, surface conditions and the available sediment sources within a dune system is needed.

Based on this idea, in this study, our analysis methods and data mainly focus on the following aspects of dune landform: first, the data of morphological parameters varied with time in different dune types and dune units and the related acquisition method of these data are used to explore the characteristics of dynamic change and evolution of dune landforms in the study area. Secondly, the grain-size sedimentological data of sand dunes and their analytical methods are used to explore the characteristics of particles' mixing, potential transport mode and sedimentary maturity of aeolian sand in the study area, and to provide sedimentological clues about the wind forcing intensity and source area distance of dune sediments. Thirdly, the geochemical data and related analytical methods of dune sediments are used to determine the material sources of these detrital sediments in the study area. Fourthly, the meteorological, hydrological, and climatic data of dune fields and the surrounding areas are used to explore the relationship between the dynamic evolution of dune landforms and environmental factors and its implications on desertification in the study area. These data and related analysis methods are described in detail below.

For the data of dune geomorphology, the first method is to use the sample-quadrate survey procedure to measure the height and shape of typical high dunes in the field with a rangefinder, and the second is to measure the length, angle and width of the windward slope and downwind slope of each dune in the sample quadrate and between different quadrates along the local dominant wind direction by using rangefinder and remote sensing image scales (such as Google Earth scales, etc.), and then the comprehensive geomorphic data of sand dunes in the region is obtained. In addition to the geomorphological data of sand dunes themselves, landscape researchers will also use the sample-quadrate survey method to investigate the ecological parameters of vegetation cover in the selected sampling area. For both geomorphological and ecological surveys, sub-scale sample quadrates will be selected from the upper, middle, and lower parts of the windward and leeward slopes of each dune. Three quadrates can be selected from the dune slope in the windward and downwind directions of each dune along the local prevailing wind direction and the size of each quadrate can be designed as 5 m × 5 m or smaller. In recent years, observation works have been carried out in different parts of the Hexi Corridor to investigate the different landform types of widespread sand dunes at a geomorphic unit scale in the field (Chang et al., 2016, Chang et al., 2017; Lang et al., 2017), including the crescent-shaped (barchan) dunes, chains of barchan dunes, pyramid-shaped dunes, parabolic dunes, and longitudinal dunes belt. Based on time-series satellite remote sensing image data in different periods, the geomorphological parameters of these dunes are also obtained (Zhang and Dong, 2014; Chang et al., 2016, Chang et al., 2017; Lang et al., 2017). In this study, the observation data and digital data were collected and sorted out systematically and corrected uniformly. Parts of these comprehensive data of geomorphological parameters of sand dunes in the Hexi Corridor are shown in **Tables 1**, **2**. In addition to the above-mentioned intuitive survey and measurement of geomorphic parameter of sand dunes, quantifying the structure of wind-blown sand flow and the movement rate of dunes is also the most direct and effective means to explain the dynamic change of dunes and their geomorphological evolution (Dong et al., 1998; Chen and Liu, 2011; He et al., 2012; Dong and Huang, 2013; J. Wang et al., 2013; Hu et al., 2016; Mao et al., 2016). Generally, there are two methods to study the moving velocity of sand dunes, one is early positioning observation (Minqin Desert Control Experiment Station (MDCES), 1975; Dong et al., 1998; He et al., 2012; Shi et al., 2018) and the other is based on remote sensing images (Chen and Liu, 2011; Dong and Huang, 2013; Mao et al., 2016). Research works based on the both methods have been carried out in dune fields of the Hexi Corridor (Minqin Desert Control Experiment Station (MDCES), 1975; Chen and Liu, 2011; Chang et al., 2015, Chang et al., 2016, Chang et al., 2017; Hu et al., 2016; Shi et al., 2018). On this basis, this study integrates and organizes the different observation data of dune movement measurement in the Hexi Corridor. Parts of these data of dune movement measurement are shown in **Table 3**. The specific analysis methods mentioned above are as follows.

Based on comprehensive investigations of the crescent-shaped dunes and the chains of crescent-shaped dunes at the edge of the Minqin oasis in the Hexi Corridor, several typical crescent-shaped dunes were selected for field observation of sand flow, wind erosion and sand deposition. The specific methods of observation are stated here taken two typical dunes as examples. Two tall crescent-shaped dunes (dunes No. 1 and No. 2) were selected in Xishawo (the western edge of the Tengerli Desert) in Minqin and several automatic observation recorders of wind speed and wind direction were set up in key parts of the dunes. For wind speed observation, the observation period for dune No. 1 was from April to September 2014, when the highest point of this dune was separated from the dune ridge line at the beginning of the observation. The observation period of dune No. 2 was from April to September 2015, when the highest point of the dune was coincident with the dune ridge line at the beginning of the observation. While observing the wind speed and wind direction, several wind erosion rods were set up at each key part of the sand dunes to measure the wind erosion depth and the sand deposition thickness of each part. At the same time the vegetation and potential sand source conditions around the

TABLE 1 | The locations, heights, movement directions, and lengths of dunes in the Hexi Corridor.

Dune type	Dune ID	Geographic location		Height of dunes (m)	Movement direction	Length of the slopes (m)		Source
		Longitude (E)	Latitude (N)		(N-W)	Upwind	Downwind	
Barchan dunes	1	102°55′16″	38°37′52″	9.8	48°	438.5	252	Chang et al. (2016), Chang et al. (2017)
	2	102°55′13″	38°38′00″	11.2	48	163.3	492.7	Chang et al. (2016), Chang et al. (2017)
	3	102°55′05″	38°36′06″	9.5	48°	129.2	163.3	Chang et al. (2016), Chang et al. (2017)
	4	102°55′02″	38°37′51″	3.7	48°	304.2	484.1	Chang et al. (2016), Chang et al. (2017)
	5	102°56′34″	38°32′11″	7.9	45°	271.7	229.4	Chang et al. (2016), Chang et al. (2017)
	6	102°56′43″	38°31′59″	7.6	46°	762.3	430.1	Chang et al. (2016), Chang et al. (2017)
	7	102°54′37″	38°25′47″	3.9	45°	295.9	80.8	Chang et al. (2016), Chang et al. (2017)
	8	102°52′56″	38°25′17″	5.9	87°	42.6	52	Chang et al. (2016), Chang et al. (2017)
	9	98°49′44″	39°57′41″	5	51°	350.4	254.5	Chang et al. (2016), Chang et al. (2017)
	10	98°49′59″	39°58′07″	2.6	54°	222.8	437.9	Chang et al. (2016), Chang et al. (2017)
	11	98°49′18″	40°00′41″	7.2	57°	184.6	197.3	Chang et al. (2016), Chang et al. (2017)
Chains of barchans dunes	12	102°54′53″	38°37′46″	6.4	54°	726.9	752.8	Chang et al. (2016), Chang et al. (2017)
	13	102°55′55″	38°37′48″	5.8	54°	443.4	406.7	Chang et al. (2016), Chang et al. (2017)
	14	102°54′46″	38°37′24″	11.1	50°	794.8	658.4	Chang et al. (2016), Chang et al. (2017)
	15	98°51′17″	39°57′59″	13.8	53°	413.6	361.1	Chang et al. (2016), Chang et al. (2017)
	16	98°51′31″	39°57′31″	8.7	54°	501.8	466.2	Chang et al. (2016), Chang et al. (2017)
	17	98°48′04″	39°58′50″	9.6	53°	554	445	Chang et al. (2016), Chang et al. (2017)
Pyramid dunes	18	94°42′23″	40°05′16″	25.8	SW-NE	—	—	Chang et al. (2016), Chang et al. (2017)
	19	94°42′10″	40°05′14″	90.3	SW-NE	—	—	Chang et al. (2016), Chang et al. (2017)
	20	94°41′47″	40°05′11″	76.6	SW-NE	—	—	Chang et al. (2016), Chang et al. (2017)
	21	94°40′53″	40°05′11″	121.8	SW-NE	—	—	Chang et al. (2016), Chang et al. (2017)
	22	94°40′43″	40°05′09″	114.1	SW-NE	—	—	Chang et al. (2016), Chang et al. (2017)
	23	94°40′12″	40°05′24″	88.9	SW-NE	—	—	Chang et al. (2016), Chang et al. (2017)
Parabolic dunes	24	102°57′15″	38°36′27″	4.6	—	286.1	35.3	Chang et al. (2016), Chang et al. (2017)
	25	102°57′42″	38°36′26″	4.4	—	228.9	188	Chang et al. (2016), Chang et al. (2017)
	26	102°58′15″	38°36′10″	3.3	—	133.3	198.5	Chang et al. (2016), Chang et al. (2017)
	27	93°59′40″	38°37′08″	3.7	—	396	302.2	Chang et al. (2016), Chang et al. (2017)
	28	98°41′36″	41°35′64″	4.4	—	59.9	0	Chang et al. (2016), Chang et al. (2017)
	29	98°41′20″	40°08′51″	4.1	—	15.7	17.7	Chang et al. (2016), Chang et al. (2017)

(Continued on following page)

TABLE 1 | (*Continued*) The locations, heights, movement directions, and lengths of dunes in the Hexi Corridor.

Dune type	Dune ID	Geographic location		Height of dunes (m)	Movement direction	Length of the slopes (m)		Source
		Longitude (E)	Latitude (N)		(N-W)	Upwind	Downwind	
Accumulated sand-belts (longitudinal dunes belts)	30	103°12′36″	38°47′57″	15.2	—	70.4	Farmland	Chang et al. (2016), Chang et al. (2017)
	31	103°13′30″	38°48′36″	17.1	—	44	Farmland	Chang et al. (2016), Chang et al. (2017)
	32	103°32′03″	39°02′12″	18.6	—	811.7	Farmland	Chang et al. (2016), Chang et al. (2017)
	33	103°31′29″	39°02′10″	5.6	—	707.7	Farmland	Chang et al. (2016), Chang et al. (2017)
	34	103.29′49″	39°02′34″	12.2	—	1557.6	Farmland	Chang et al. (2016), Chang et al. (2017)
	35	103°26′19″	39°02′20″	9.4	—	207.1	223.4	Chang et al. (2016), Chang et al. (2017)

TABLE 2 | Morphological characteristics of barchans dunes in the Hexi Corridor.

Dune ID	Plots area	Height (m)	Thickness of camponotus (m)	Length (m)	Width (m)	Slope of leeward direction (°)	Forward direction (°)	Length of upwind slope (m)	Length of downwind slope (m)	Source
1	Minqin 3–1	9.8	123.3	214.6	202.5	32.6	N48°W	662.9	378	Chang et al. (2017)
2	Minqin 3–2	11.2	155.7	294.4	227.4	32.2	N48°W	163.3	491.6	Chang et al. (2017)
3	Minqin 3–3	9.5	12.5	197.5	209.8	32.1	N48°W	134.2	176.6	Chang et al. (2017)
4	Minqin L	3.7	78.8	86.5	81.8	31.8	N48°W	251.8	367.8	Chang et al. (2017)
5	Minqin 9	7.9	90.8	112.5	81.5	32.9	N45°W	214.3	253.3	Chang et al. (2017)
6	Minqin 10	7.6	86.7	136.8	64.7	31.5	N46°W	137.9	430.1	Chang et al. (2017)
7	Minqin 11	11.6	104.4	183.6	57.3	31.6	N46°W	179.9	243.1	Chang et al. (2017)
8	Minqin 12	8.6	64.1	131.4	77.9	30.1	N46°W	135.2	697.3	Chang et al. (2017)
9	Jinchang 1	8.4	130.3	197.6	123.2	31.7	N55°W	227.4	372.1	Chang et al. (2017)
10	Jingta 1	6	83.7	125.3	104.8	31.5	N63°W	250.4	129.5	Chang et al. (2017)
11	Jinta 2	5.3	73.5	104.8	76.6	31.7	N63°W	108.2	419.8	Chang et al. (2017)

observed dunes were measured. In the process of wind speed observation, the measured height of wind speed and wind direction was 50 cm from the ground, sampling once every 20 min, and statistics were made with every 2 m/s as a wind speed level. The maximum wind speed observed was 14.9 m/s. During the observation of wind erosion and sand accumulation processes, No. 8 steel wires (level 8 in thickness) were used for the observation of wind erosion depth and sand accumulation depth, with one end of the wire being buried underground and the other end being kept 30 cm above the dune surface. The height (depth) of the ground were measured for each observation. In this study, the forward wind system and the reverse wind system were defined. The forward wind refers to the local main wind direction (the NW wind), and the reverse wind is the SE

TABLE 3 | Annual movement distance and speed of sand dunes in the Hexi Corridor. Data from Shi et al. (2018).

Area or observation site	Duration (a)	Width of dune (m)	Movement distance of dune (m)	Movement speed of dune (m/a)
Gulang	8	277.95	38.4	4.8
Minqin	9	132.87	55.8	6.2
Jinchang	9	156.32	40.5	4.5
Linze	8	240.14	33.6	4.2
Gaotai	8	170.30	11.2	1.4
Jinta	9	290.70	36.0	4.0
Dunhuang	8	225.75	6.4	0.8

wind. Whether it is a forward wind process or a reverse wind process, the windward slope of a sand dune is defined in accordance with the forward wind commonly documented in the previous research practices, that is, if the local main wind direction is NW wind, the NW slope of a sand dune is considered to be the windward slope of the dune in this study. The definition of the leeward slope is the opposite of the above. The vertex of a sand dune refers to the highest point of a dune. The chord length of a dune refers to the distance between the two wing endpoints of the dune. The aspect ratio of a dune refers to the ratio of the total length to the total width of the dune. The bow back thickness of a dune refers to the distance from the bottom of the windward slope to the bottom of the leeward slope of the dune. Meteorological and climatological data were collected from local weather stations and the China Meteorological Science Data Sharing Service Network.

In order to unify the multi-parameter measurement data obtained from different research works, this paper classifies and adjusts the data of geomorphic parameters and dynamic change parameters of sand dunes in the Hexi Corridor from three aspects, taking the crescent-shaped dune at the edge of oasis in the Hexi Corridor as an example: sand dune distribution environment, sand flow in dune field and characteristics of two wings of sand dunes. Furthermore, a unified analysis was made in the aspects of wind speed classification and wind direction characterization. Among them, the forward wind was classified according to 2 m/s as a wind speed level, which was divided into five grades: <2 m/s, ≥2 − <4 m/s, ≥4 − < 6 m/s, ≥ 6–8 m/s and ≥8 m/S. The wind speed of the reverse wind was relatively small, so it was graded as a wind speed level of 1 m/s. The wind speed data analysis was completed using SPSS 13.0. The detailed results can be seen in **Tables 1–3**.

In addition to field surveys and measurements, the data of geomorphic parameters of the large-scale dune types and dune shapes of the study area are also obtained from some remote sensing image data. For example, it can be distinguished and extracted from the combination of Google Earth high-definition images and environmental disaster mitigation satellite (HJ-1A/1B Satellite) images. The environmental disaster mitigation satellite imagery is provided by the China Resources Satellite Application Center, with a resolution of 30 m. The geomorphological map produced by the environmental disaster mitigation satellite images uses colour synthesis of bands 3, 2 and 1. The range of oasis and desert is divided by the normalized vegetation index (NDVI). NDVI > 0.1 is classified as an oasis and NDVI ≤ 0.1 is classified as a desert. NDVI is calculated by using the Band 3 and Band 4 data of environmental disaster mitigation satellite images. The calculation formula is NDVI = (B2 − B1)/(B2 + B1). B1 and B2 are the Band 3 and Band 4 of satellite, respectively. The remote sensing image processing is carried out in ENVI 4.4 and the output map is from ArcMap v9.3 (ESRI).

Erodible clastic sediments as the material sources are the fundamental base for the formation of sedimentary landforms (Pettijohn et al., 1972; Taylor and McLennan, 1985). Therefore, identifying the composition, source, transport, and accumulation of wind-induced materials in an arid environment is a prerequisite for understanding the formation of dune landforms (Zhu et al., 1980; Zhu et al., 1981a; Yang et al., 2012). Although sediment sections are usually used in many studies to observe the variability of sediment accumulation and sources in one location through time, in this study, the investigation approach of surface aeolian sediment samples at a regional scale is applied. The surface sample approach allows identification of distribution pathways by considering the continuous variety of geomorphological settings (Lehmkuhl, 1997; Kuster et al., 2006; Schettler et al., 2009; Nottebaum et al., 2014; Zhu and Yu, 2014; Zhu et al., 2014; Nottebaum et al., 2015b). Therefore, this method offers an opportunity to analyze the spatial distribution and composition of surface aeolian sediments accumulated under variable conditions and from different perspectives (i.e., geomorphological setting, relief, and vegetation).

Grain size composition and distribution of aeolian sediment is an important indicator to understand the formation and development of sand dunes, because grain size distribution (GSD) analysis of sediments is an established tool to analyze the composition of sediments and to distinguish different transport, accumulation and potential remobilization processes (Folk and Ward, 1957; Friedman, 1961; Ashley, 1978; Bagnold and Barndorff-Nielsen, 1980; McLaren and Bowles, 1985; Sun et al., 2002; Qiang et al., 2007; Weltje and Prins, 2007; Qiang et al., 2010; Guan et al., 2013; Vandenberghe, 2013; Nottebaum et al., 2014; Zhu et al., 2014; Zhu and Yu, 2014). The depositional environment (aeolian, fluvial or lacustrine) and the movement types (creep, saltation or suspension) of sediments in the transportation process can be identified and distinguished by using grain size parameters of sand particles (Folk and Ward, 1957; Friedman 1961; Bagnold and Barndorff-Nielsen, 1980; McLaren and Bowles, 1985; Nottebaum et al., 2014; Zhu et al., 2014). At present, grain-size analysis of aeolian sediments and relevant detrital sediments, such as alluvial and proluvial fans, lacustrine deposits, fluvial deposits, has been widely carried out in the Hexi Corridor (Nottebaum et al., 2014, Nottebaum et al., 2015b; Zhu et al., 2014; Zhu and Yu, 2014; Zhang and Dong, 2015; Zhang et al., 2016; Pan et al., 2019; Zhang et al., 2020). On this basis, this study systematically collects and organizes these granular data and records, which makes it possible to further conduct a comprehensive and comparative study on the dunes in the Hexi Corridor from a perspective of sedimentology. The specific analysis methods of grain size are as follows.

The grain-size sedimentological data of dune sediments from different sources used in this paper are almost measured by using the instrument of high-frequency mechanical vibrating screen (shaker), so the grain size data from different sources have good coordination and consistency, and do not need further classification and unification. The sample analysis method and data processing method of the grain size data are as follows. Different dune fields in the Hexi Corridor were widely sampled in the study region. Dune surface sediments were collected from the windward toe, stoss, crest, and leeward toe. At each site, surface materials (0–1 cm layer) from a 20 cm × 20 cm transect area were collected; each sample weighted about 0.5–1 kg. Grain size analyses of all samples were undertaken using standard sieving (on a Retsch AS200 Sieving Shaker, Haan, Germany) for 10 min. Each fraction of the sample was weighed to the nearest 0.001 g. All the granularity analysis data in this paper are uniformly calculated using the method of Folk and Ward (1957). The mass proportion of each fraction in grain size is expressed in phi (φ) unit ($\varphi = -\log2d$, where d is grain size in millimeters), and described using the parameters of mean size (Mz), standard deviation (δ1), skew (Sk1), and kurtosis (KG), as proposed by Folk and Ward (1957). Characterized grain size and sorting parameters were also calculated following the formulae devised by Folk and Ward (1957).

The analysis of major and trace elements, including rare earth elements, has become a reliable technique for detecting the source of desert sediments (Muhs et al., 1995, Muhs et al., 1996; Honda and Shimizu, 1998; Pease et al., 1998; Wolfe et al., 2000; Zimbelman and Williams, 2002; Pease and Tchakerian, 2003; Muhs, 2004; Yang et al., 2007; Zhu and Yang, 2009; Jiang and Yang, 2019). The reason is that for aeolian sediments, the differences in compositions and distributions of rare earth elements and other trace elements in different samples/sub-fractions are largely controlled by the parent-rock compositions, because these elements only exist in specific minerals and are difficult to be lost during transportation (Pettijohn et al., 1972; Taylor and McLennan, 1985). In the Hexi Corridor, preliminary results have been achieved in the case studies of analyzing the elemental compositions of aeolian sediments using major- and trace-element geochemical methods (e.g., Schettler et al., 2009; Wang et al., 2010; Ren et al., 2014; Pan et al., 2019; Zhang et al., 2020), which provide basic data for this study to comprehensively identify the material sources of different dunes in the study area.

The geochemical data of major and trace elements compositions of dune sediments used in this study are almost obtained by using the XRF analysis method, so the data from different sources have good coordination and consistency. The measurement method and processing method of these data are as follows. Bulk samples of dune sands from the Hexi Corridor were taken for laboratory preparation and measurements. Samples were dried at low temperature (43°C) for 72 h and grinded to less than 75 mm. Up to 4 g of sample was weighed and poured into the center of the column apparatus, together with boric acid, and pressurized to 30 t/m2 for 20 s using a YYJ-40 semiautomatic oil hydraulic apparatus. The processed samples, approximately 4 cm in diameter and 8 mm thick, were analyzed by using a Philips Panalytical Magix PW2403 X-ray fluorescence (XRF) spectroscope. Analytical results are reported in oxide compound form apart from trace elements which are given in elemental form. The standard deviations for the major elements were estimated by the repeated analysis of the samples. Standard deviations were <10% for Ce, Co, Cs, Ga, La, Rb, Sc, Y, Hf and Zr, <8% for Ba, Bi, Cr, Mn, Ni, Sr and V, <3% for MgO and Na2O and <0.5% for the other major elements. Our analysis of geochemical data focuses on element abundance and element ratio methods widely used in geochemistry. In addition, we apply hierarchical cluster analysis of the data to group samples based on multi-elements analysis (Zhu et al., 2017). Hierarchical cluster analysis, based on Ward's method (Ward, 1963) and the Euclidean distance, was conducted to classify samples using trace elements as the variables (Wolff and Parsons, 1983; Zhu and Wang, 2016). Trace elements (Ba, Bi, Ce, Co, Cr, Cs, Ga, La, Mn, Rb, Sr, V and Zr) and Ti whose average abundance were larger than 20 ppm were selected for hierarchical cluster analysis in order to avoid errors caused by the detection limit of analytical instrument. To reduce the impact of the large difference in abundance level of the various elements, the data were standardized to z scores, with a mean of 0 and a standard deviation of 1. Hierarchical cluster analysis was performed using the IBM SPSS Statistics 20 program.

The continuous data records of different meteorological parameters of local weather stations in the Hexi Corridor in the past half century, such as temperature, precipitation, relative humidity, wind speed, strong wind days and sandstorms days, will not only be the basis for this study to discuss the regional climate change under the background of global warming, but also the basis for exploring the response of regional landscape to climate change based on the statistical relationship between geomorphic parameters and climate parameters on a multi-decade time scale. Therefore, this study collects and uses the meteorological data of the Hexi Corridor for the past half a century to analyze the regional climate change and its relationship with the dynamic changes of dune landforms.

RESULTS

Geomorphological Characteristics of Sand Dunes in the Hexi Corridor

The comprehensive data on the heights of different types of sand dunes widely developed in different areas of the Hexi Corridor, as well as other geomorphic parameters of these dunes, can be found in **Tables 1**, **2** and **Figure 3**. It can be seen from **Tables 1**, **2** and

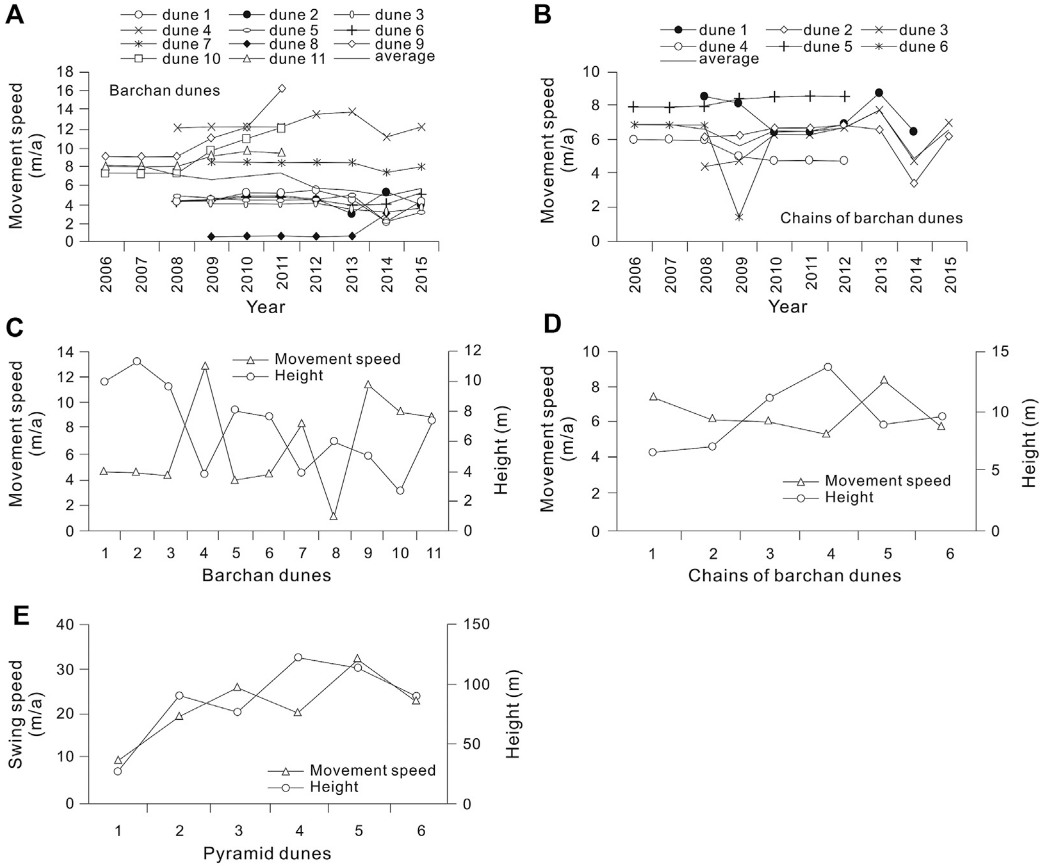

FIGURE 3 | The moving speed and height of sand dunes in the Hexi Corridor (modified after Chang et al. (2016)). **(A)** the moving speed of crescent-shaped (barchan) dunes; **(B)** the moving speed of chains of barchan dunes; **(C)** the moving speed and height of barchans dunes; **(D)** the moving speed and height of chains of barchan dunes; **(E)** the movement speed and height of pyramidal dunes.

Figure 3 that the average height of typical crescent-shape (barchan) dunes in the Hexi Corridor is about 6.75 m, the maximum is about 11.20 m, and the minimum is only about 2.60 m. The average height of typical chains of barchan dunes in the study area is about 9.23 m, the maximum is about 13.80 m, and the minimum is only about 5.80 m. The typical pyramid-shaped dunes in the study area have an average height of about 86.25 m, with a maximum of about 121.80 m and a minimum of about 25.80 m. The average height of typical parabolic dunes in the study area is about 4.08 m, the maximum is about 4.60 m, and the minimum is only about 3.38 m. The average height of typical longitudinal dunes in the study area is about 13.02 m, the maximum is about 18.60 m, and the minimum is only about 5.60 m.

Regarding the dynamic changes of sand dune landforms, as early as 1959–1964, the newly established Minqin Comprehensive Experimental Station of Desertification Control (MCESDC) in China carried out the field positioning observation and research on wind-blown sand flows in the Hexi Corridor (Zhu et al., 1980; Zhu and Chen, 1994; Zhu, 1999; Zhu and Wang, 1992; Wang, 2003). 187 positioning observation points were set up in field along a 20 km long observation line in the Minqin Basin and many observations were made to assess the structure of wind-blown sand flow, the shape of sand dunes, erosion and accumulation of aeolian sand, changes in sand ripples and sand dune movement, etc. Later works continued to carry out relevant researches on different areas of the Hexi Corridor (Minqin Desert Control Experiment Station (MDCES), 1975; Zhu et al., 1980; Wang, 2003; Zhang et al., 2004; Qu et al., 2005; N. Wang et al., 2013; X. Wang et al., 2013; Yin et al., 2014; Yin et al., 2016; Chang et al., 2016, Chang et al., 2017; Zhang et al., 2016; An et al., 2019; Chang, 2019; Hu et al., 2020). In this study, we synthesized and collated these observational data and analytical results. It shows that in the Hexi Corridor, 80% of the sand particles of the wind-blown sand flows are moving in the height of 20–30 cm near the ground surface, of which about half of the sand particles are moving in the height of 0.3–0.5 cm near the surface. At the wind speed of 7 m/s, 75% of the sand particles are within the height of 10 cm, and only 0.035% are within the height of 76–200 cm.

About the dynamic changes of different sand dunes in the Hexi Corridor in the past half century, the crescent-shaped (barchan) dunes, chains of barchan dunes, pyramid-shaped dunes, parabolic dunes, and longitudinal dunes have received

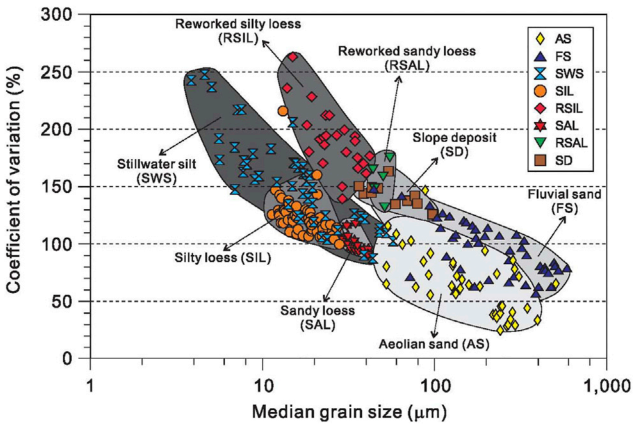

FIGURE 4 | The coefficient of variation (CV) plotted against the median grain size of classified surface sediment types in the Hexi Corridor (modified after Nottebaum et al., 2014). The coefficient of variation (CV) is an indicator of the degree of sorting process reflected by the standard deviation (StD), a discrimination parameter of GSD of sediment types. AS, aeolian sand; FS, fluvial sand; SWS, stillwater silt; SIL, silty loess; RSIL, reworked silty loess; SAL, sandy loess; RSAL, reworked sandy loess; SD, slope deposit.

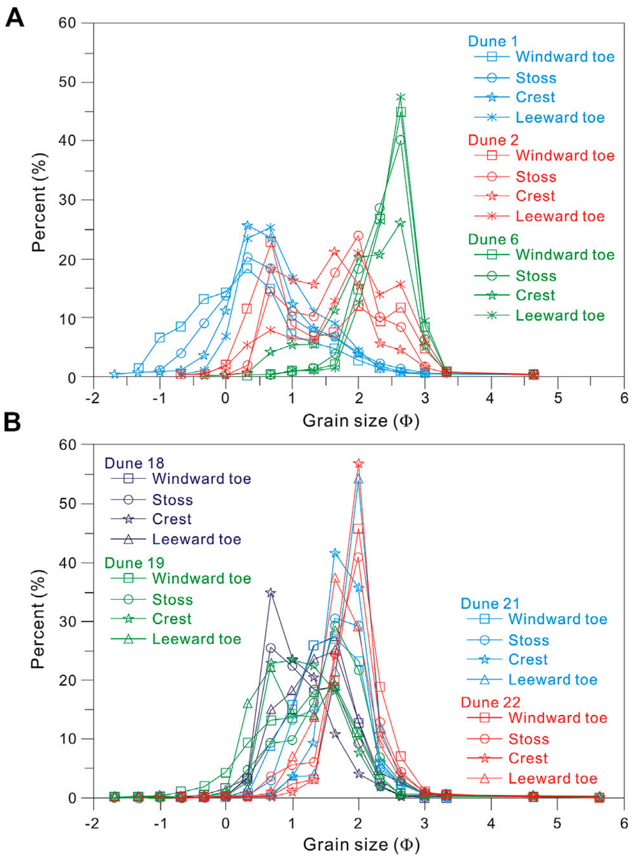

FIGURE 5 | The frequency distribution curves of grain size of dune sediments in the Hexi Corridor (modified from Zhang and Dong (2015)).

the most extensive attention (e.g., Ren et al., 2010; Chang et al., 2016). Based on field surveys/measurements (e.g., measurement of the electronic total station) and digital image data (e.g., Google Earth) of different periods, the geomorphological parameters and moving speeds of these different dunes are obtained, as shown in **Tables 1–3** and **Figure 3**. It can be seen that the average moving speed of the crescent-shaped dunes is about 6.62 m/a in the study area, the maximum is 12.51 m/a, and the minimum is only 1.01 m/a (**Figure 3A**). The average moving speed of the chains of barchan dunes is about 6.54 m/a, the maximum is 8.30 m/a, and the minimum is only 5.34 m/a (**Figure 3B**). Compared with the crescent-shaped dunes, the chains of barchan dunes move relatively slowly and the movement speed changes little. In general, the crescent-shaped dunes and the chains of barchan dunes in the Hexi Corridor move along the NW-SE direction. The direction of movement of the east part of the corridor is about N45°W, while the movement angle of the Jinta area in the western corridor increases (**Table 1** and **Figure 3**). The average swing velocity at the tops of the pyramid dunes is about 6.32 m/a, the maximum is 97.37 m/a, and the minimum is only 1.14 m/a. The direction of movement of the pyramid dunes will also change, but its main direction of motion is SW-NE (**Figure 3**).

Surface Sediment Types and Granular Sedimentology of Sand Dunes in the Hexi Corridor

Analysis of grain size statistical parameters, geomorphological settings, sedimentological structures, and features to surface detrital sediments collected from different areas between the Qilian Mountains and their arid forelands (the Hexi Corridor) (e.g., Wang et al., 2008b; Wang et al., 2010; Wang, 2011; Nottebaum et al., 2014; Zhu et al., 2014; Zhu and Yu, 2014; Zhang and Dong, 2015; Pan et al., 2019) were performed. Parts of these analytical results are comprehensively compared and re-analyzed by us and are shown in **Figures 4**, **5**. In general, six main sediment types can be classified in the Hexi Corridor based on the wide investigations of surface sediment distribution. They are fluvial sand, aeolian sand, sandy loess, silty loess, stillwater silts, and slope deposits (**Figure 4**). The term "stillwater silts" is firstly used by Nottebaum et al. (2014) to comprise altogether lacustrine, alluvial and mainly silty deposits in river channels (among which the latter are therefore neither lacustrine nor alluvial). A tripartite distribution of sedimentological landscape units in the Heix Corridor is evident, namely, the high mountain periglacial zone (from ~5,700 to ~3,800 m a.s.l.), the loess altitudinal zone (from ~3,800 to ~2,000 m a.s.l.), and the foreland zone (<2,000 m a.s.l.) (Nottebaum et al., 2014). Dune fields are limited to areas below 1700 m a.s.l.

At a regional scale of the study area and compared to other types of surface detrital sediments in the Hexi Corridor, the movement modes of aeolian sand particles in the study area include creeping (wriggling/rolling), saltation (jumping/springing) and suspension (floating/levitating), and the movement modes of sand dunes include three ways: straight-forward movement, wigwagging movement, and onward-wigwagging movement (Wang, 2003; Zhu et al., 2014). Aeolian sands collected from dune ridges and sand sheets in surface sediment investigations in the study area are usually best sorted (Nottebaum et al., 2014; Zhu and Yu, 2014). It can be evidenced by low CV values of 24–85 for aeolian sands in the study area and mostly have unimodal grain size distributions (GSDs) (**Figures 4**, **5**). Among this sediment type (aeolian sand), bimodal distributions (**Figure 5**) may be mixtures of loess and aeolian sand or due to mixing of two aeolian sand populations (Nottebaum et al., 2014; Zhu et al., 2014). The general modal values of aeolian sands' GSD typically cluster around ~200 μm in the study area. In contrast, aeolian samples with finer modes occur at small vegetated dunes where wind speeds are reduced due to locally higher surface roughness, and aeolian samples with larger mode values originate, for example, from barchans (mode = 430 μm) or coarse sand ripples (mode = 825 μm) (Nottebaum et al., 2014). This type is mainly formed by saltation and creeping processes, accumulating grain sizes determined by wind speed and source material properties (Zhu et al., 2014). These dunes and sand sheets are restricted to the lowland areas, overlying the foreland alluvial fans, and are interchanging with oases and agricultural areas.

At the local scale, dune sands in different regions also have different sedimentological characteristics, especially between the middle-East and the west of the study area. Basically, the eastern parts of the Hexi Corridor show higher aeolian sand occurrence. In contrast, the western parts are dominated by gravel gobi surfaces. This is possibly attributed to higher sand supply in eastern parts provided by the Badanjilin Desert and fluvial storages as sand sources (Nottebaum et al., 2014).

In the Jiuquan-Gaotai area in the central-eastern Hexi Corridor (area B in **Figure 2**), grain size parameters of sand dunes at different geomorphological positions on the dune surface were determined (**Figure 5**), such as the toes of windward slope, slope surface, dune crest (top), toes of leeward slope, etc. The results show that the grain-size frequency distribution curves of sand dunes in this area are mostly unimodal, and a few are bimodal (**Figure 5**). The dune surface sands are mostly fine sand and very fine sand, with an average grain size of 0.07 mm ± 0.01–0.24 mm ± 0.06, which is similar to the average particle size of sand dunes in the world (Zhu et al., 2014; Zhang and Dong, 2015). The finer the dune particle is, the better the sorting degree is. The mean grain size increases with the increase of the skewness values, but decreases with the increase of the kurtosis values. From upwind to downwind, the dune sediment becomes finer, the medium-sand fraction decreases, and the fine-sand fraction, very-fine-sand fraction, silt-fraction, and clay-fraction increase. It may be the source materials that affect the changes in the average grain size of dune sands from upwind to downwind (Zhang and Dong, 2015). In this dune field, there are three types of grain-size-distribution patterns in a dune-scale unit: the dune crest is coarser (the dune slope and inter-dune area are finer), the dune crest is finer (the dune slope and inter-dune land are coarser), and there is no significant difference between dune crest, windward and leeward slopes. Among them, the coarser-dune-crest model is the most common type, accounting for 69% of all sand dunes, while the finer-dune-crest is the second most common type (accounting for 24%) (Zhang and Dong, 2015).

In the Jinta-Jiayuguan-Huahai area in the western Hexi Corridor (area A in **Figure 2**), granular sedimentology of the crescent-shaped (barchan) dunes developed on gobi deserts and ancient playas have been determined (e.g., Pan et al., 2019). The results show that the grain size of dune surface sediments is mainly the medium sand (21.7–57.4%), followed by the fine sand (23.2–53.0%). The mean grain size of dune sands range between 0.27 and 0.43 mm, while the paleolacustrine sediments range between 0.10 and 0.21 mm. The crescent-shaped dune sediments in this region are mainly medium to good in the sorting level. The frequency cumulative curves of dunes are mostly unimodal and nearly symmetrical, and the kurtosis is medium in level. The granular characteristics of sand dunes in this region are closely linked to their dune morphology and the properties of the underlying gobi surface (Pan et al., 2019).

Geochemical Characteristics of Dune Sediments and Soil Aggregate in the Hexi Corridor

Due to the application of geochemical methods in recent years, it is possible to identify sediment sources more precisely. The geochemical characteristics of aeolian sediments in the Hexi Corridor had been investigated as early as 1959–1964 by the China's Minqin Comprehensive Experimental Station of Desertification Control (MCESDC) (Minqin Desert Control Experiment Station (MDCES), 1975; Zhu et al., 1980; Chang, 2019), and continues to this day (Wang et al., 2010, Wang et al., 2018; Ferrat et al., 2011; Wang, 2011; Ren and Wang, 2010; Wang and Wang, 2013; Ren et al., 2014; Zhang and Dong, 2015; Zhang et al., 2016, Zhang et al., 2020; Chang, 2019; Pan et al., 2019). In this study, based on the integrated geochemical data, we explored the material sources of dune sands in the study area at different regional scales, as shown in **Figures 6**, **7**. We take the Minqin Basin in the eastern Hexi Corridor (area C in **Figure 2**), the Huahai-Jiayuguan-Jinta region of the western Hexi Corridor (area A in **Figure 2**), and the Jinta-Gaotai region of the middle Hexi Corridor (area B in **Figure 2**) as the case examples to discuss in detail.

The Minqin Basin in the eastern Hexi Corridor (area C in **Figure 2**) is dominated by an oasis landscape. It is bordered by the Badanjilin Desert to the northwest and the Tenggeli Desert to the southeast and is located the northern edge of the Loess Plateau (**Figures 1**, **2**). In geomorphology the Minqin Basin is considered a natural obstacle to the convergence of the two deserts (Zhu et al., 1980), thus identifying the origin and transportation of aeolian sediments in the Minqin oasis and its adjacent desert areas will help to better understand the relationship between loess and desert in China (Liu, 1985; Sun, 2002; Yang et al., 2007; Wang et al., 2010; Yang et al., 2011; Ren et al., 2014). Aeolian sediments sampled from sand dunes in the Minqin Oasis and its surrounding desert areas (the Badanjilin and Tenggeli Deserts) have been geochemically studied recently (e.g., Ren, 2010; Ren and Wang, 2010; Ren et al., 2014). In this study, the characteristics of major and trace elements of aeolian samples from the Minqin Oasis and its adjacent deserts, as well as the provenance and transportation pathways of aeolian sediments in these areas, were discussed using these integrated geochemical data, combined with wind data and cluster analysis methods, as shown in **Figure 6**.

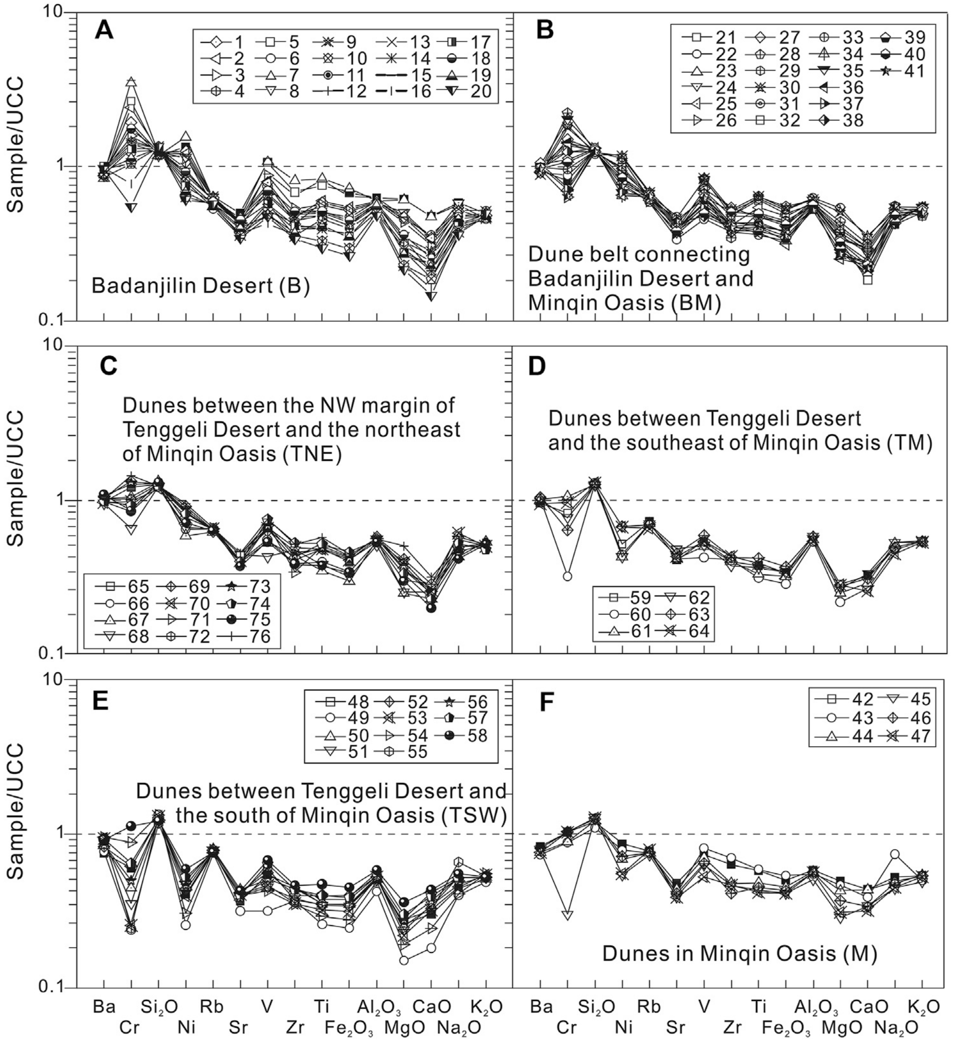

FIGURE 6 | The UCC-standardized distributions and compositions of major and trace elements of sand dunes in the Minqin Basin and its surrounding areas in the western Hexi Corridor (modified after Ren et al. (2014)).

The analytical result shows that in the bulk (whole-rock) samples of dune sands in the Minqin Basin (M) and its surrounding areas, including the Badanjilin Desert (area B), the Badanjilin-Minqin transition zone (area BM), the Tenggeli-Minqin transition zone (area TM), the northeast edge of the Tenggeli Desert (area TNE), and the southwest edge of the Tenggeli Desert (area TSW) in **Figure 6**, the contents of major elements are higher in SiO_2, reaching between 72.2 and 88.9% with an average of about 83.3%. In contrast, the contents of most trace elements are relatively low, and only the contents of Ba, Ce, Co, Mn, and Sr reach > 100 ppm. Compared with the average composition of the upper continental crust (UCC, Taylor and McLennan, 1985), the concentrations of Ba, SiO_2, Rb, Sr, Al_2O_3 and K_2O in the Minqin Basin and its surrounding areas are relatively uniform (**Figure 6**), indicating that the spatial differences of these elements in abundance are small and they are relatively homogeneous in the study area. However, obvious convex and concave shapes are observed for other elements (**Figure 6**), indicating that the spatial differences of these elements in abundances are large and they are relatively heterogeneous in the study area. The homogeneous and heterogeneous characteristics between different elements thus can be used as geochemical indicators to identify different sources of sediments in the study area. For the major elements' compositions, only SiO_2 is enriched relative to UCC, and the others are relatively depleted (**Figure 6**). For the trace elements' abundance, most elements are also depleted, except for Cr and Ni enriched in areas B and BM and Cr enriched in area TNE. The binary and ternary diagrams of some major and trace elements and their ratios (Ren et al., 2014), such as Cr, Ni, Cr/V, Y/Ni, Al, V, Zr, Hf, Zr/Hf, reveal that sand dunes have different material sources between the western part of the Minqin Basin (including sub-areas B, BM and TNE) and the southeast side of the Minqin Basin (TSW), while sand dunes in the Minqin Basin (M) and the Tenggeli-Minqin transition zone (TM) are closely related to the two big deserts, respectively.

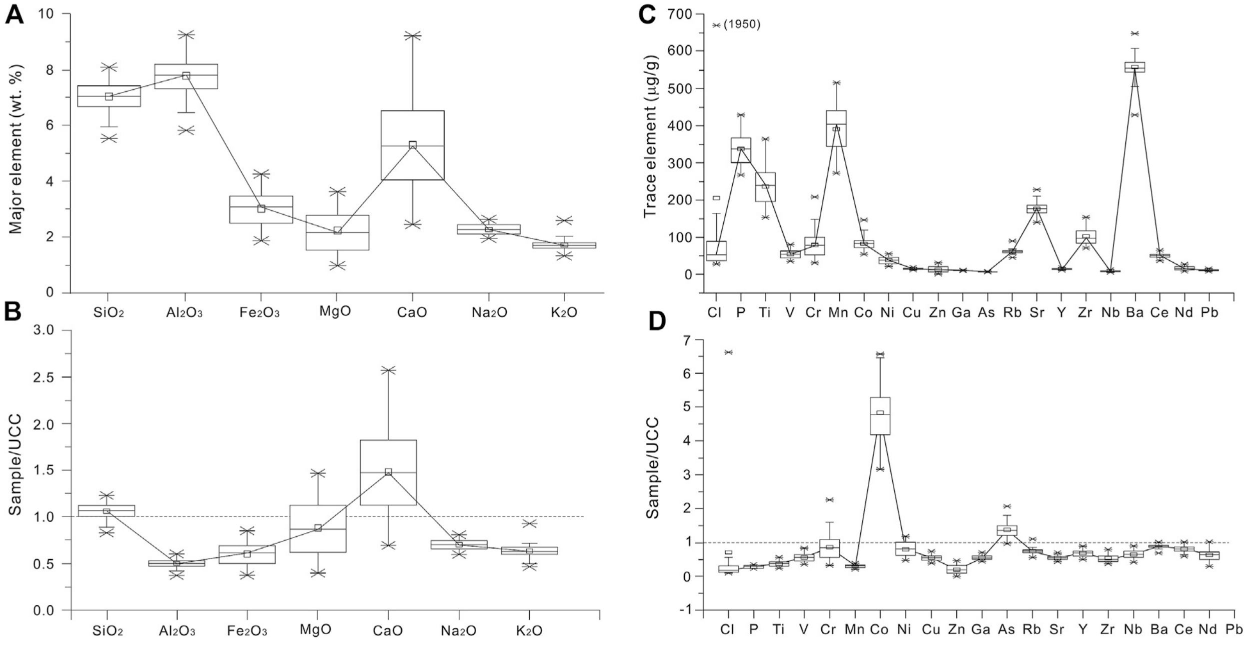

FIGURE 7 | Compositions of the major and trace elements and their UCC-standardized distributions of sand dunes in the Jinta-Gaotai area of the middle Hexi Corridor (modified after Zhang et al. (2020)).

In the western Hexi Corridor, data of major and trace elements of aeolian sediments and other types of sediments sampled in this region are also synthesized and integrated in this study based on previous studies (e.g., Wang et al., 2010; Zhang et al., 2017; Pan et al., 2019). The sand dunes analyzed in this study are mainly located in the gobi areas to the northern and western Jiayuguan (area A in **Figure 2**). The dune types are mainly barchan dunes, chains of barchan dune and asymmetric barchans dunes (Zhang et al., 2017; Pan et al., 2019). The aeolian samples were mainly collected from the surface sediments of barchan dunes and asymmetric barchan dunes, including different geomorphic sites of dunes such as the crest of dune, the bottom of the windward slope, the middle of the windward slope, and the bottom of the leeward slope. The analytical results show that after the standardization of UCC, the barchan dunes on the Gobi surface in the western Hexi Corridor are significantly enriched in the major elements CaO and SiO_2 (accounting for 5.55 and 66.12% of the total rock mass, respectively). In terms of spatial distribution, the element contents of Cao, MgO and Fe_2O_3 are gradually enriched from northwest to Southeast, that is, the enrichment degree increases along the dominant wind direction. The UCC-normalized concentrations of Na_2O and K_2O are both significantly <1, indicating that alkali metal elements are significantly depleted or leached in the study area. The contents of trace elements vary among different dune samples, reflecting a complexity of provenance of these dune sediments. However, the variations of trace elements are similar in different geomorphic positions of the one dune (Pan et al., 2019). Compared with UCC, trace elements Co, As, La, and Nd are significantly enriched in the western Hexi Corridor, while other elements are depleted.

In the middle Hexi Corridor, mineralogical, major- and trace-element data of aeolian sediments and other types of sediments from the Jinta-Gaotai area (area B in **Figure 2**) are also collected and integrated in this study based on previous studies (e.g., Ferrat et al., 2011; Wang and Wang, 2013; Wang et al., 2018; Zhang et al., 2020). Indicators such as the light/heavy mineral assemblages, the ratios of Na_2O/Al_2O_3 to K_2O/Al_2O_3 and SiO_2/Al_2O_3, Ba/Sr to Rb/Sr, Rb/Sr to Ce/Sr, and the composition of CaO and Cl in the sampled aeolian sediments are used to identify the geochemical characteristics of aeolian sediments in the study area, as shown in **Figure 7**. Compared with the composition of the upper continental crust (UCC), dune sediments in the Jinta-Gaotai area are also enriched in CaO and SiO_2 (**Figure 7**). Based on analysis of multi-dimensional scaling (MDS), principal component analysis (PCA) and regional topography analysis (e.g., Zhang et al., 2020), the results suggest that the Hexi Corridor is not only the sediment sink of the Qilian Mountains, but also the sediment sink of the Beishan Mountains.

Compared with the chemical elements in the Tenggeli and Badanjilin Deserts (Li, 2011), the Hexi Corridor has lower SiO_2 content, similar K_2O content, and lower contents of other trace elements. However, in terms of major- and trace-element ratios, the sand dunes from the Hexi Corridor are similar in provenance to those from the Tenggelil, Badanjilin, and Kumtag Deserts (Zhang et al., 2020). Similar mineralogical assemblages (mica, quartz, illite, muscovite and albite) are also found in dune sediments from the Hexi Corridor and adjacent areas such as the Tenggeli and Badanjilin Deserts (Ferrat et al., 2011). This feature is also found by major and trace element analysis in other studies (Wang and Wang, 2013; Zhang et al., 2020). This indicates that the geochemical characteristics and provenance of aeolian sediments in the Hexi Corridor are closely related to its adjacent areas.

Soil aggregate, as the basic unit of farmland soil structure, is widely developed in oasis areas of the Hexi Corridor (Li, 2006; Su, 2007). It plays important role in surface nutrient recycling, resisting soil wind and water erosion, and are closely related to dust emission and land desertification in arid land (Bronick and Lal, 2005). Thus, the mechanisms of formation and stability of soil aggregate are one of the major topics in land degradation/development science in arid environment (Le, 1996; Bronick and Lal, 2005). In order to determine the geochemical characteristics of soil aggregates, soil samples at the 0–10 cm surface layer from different soil types (i.e., Ari-Sandic Primosols, Calci-Orthic Aridosols, Siltigi-Otrthic Anthrosols, and Ustic Cambosols, etc.) in the marginal farmland in the oasis of the middle Hexi Corridor have been studied (e.g., Li, 2000, Li, 2006; Su, 2007; Su et al., 2007). In this study, we briefly review the results of previous studies.

The physiochemical properties of dry- and wet-sieved soil aggregates in the middle Hexi Corridor, including soil particle-size distribution (SPD), soil organic carbon (SOC), calcium carbonate ($CaCO_3$), and oxides of Fe^{3+} and Al^{3+}, were analyzed (e.g., Li, 2000, Li, 2006; Su, 2007; Su et al., 2007). The results show that the SPD is dominated by fine sand fraction in most of soils except Ustic Cambosols. The SOC concentration is 5.88 ± 2.52 g/kg on average, ranging from 4.75 g kg^{-1} in Ari-Sandic Primosols to 10.51 g kg^{-1} in Ustic Cambosols. The soils have high $CaCO_3$ concentration, ranging from 84.7 to 164.8 g/kg, which is increased with fine SPD and SOC content. The percentage of >0.25 mm dry aggregates ranges from 65.2% in Ari-Sandic Primosols to 94.6% in Ustic Cambosols, and large dry blocky aggregates (>5 mm) is dominant in all soils. The mean weight diameter of dry aggregates (DMWD) ranges from 3.2 to 5.5 mm. The percentage of >0.25 mm water-table aggregate is from 23.8 to 45.4%. The percentage of aggregate destruction (PAD) is from 52.4 to 66.8%, which shows a weak aggregate stability. The mass of macro-aggregates and DMWD are positively significantly correlated with the contents of soil clay and silt, SOC, $CaCO_3$, and oxides of Fe^{3+} and Al^{3+}. Soil fine silt and clay, SOC and $CaCO_3$, are important agents of aggregation in this region, and the effect of SOC and $CaCO_3$, on aggregate stability is more significant than that of soil silt and clay.

DISCUSSION

Dynamic Changes of Dune Landforms in the Hexi Corridor

The above analytical results of geomorphological parameters indicate that the dynamic changes of different dunes are different in the Hexi Corridor during the past several decades. Among different dune types, the crescent-shaped dunes move the fastest, followed by the chains of barchan dunes (**Figure 3**). Only the top of the pyramid dunes wigwags (**Figure 3**), while the parabolic dunes and the longitudinal dunes hardly move forward (Chang et al., 2016). We seem to be able to come to this view that the higher the height of the crescent-shaped dune (or the chain of barchan dunes) is, the slower their movement is. On the contrary, the higher the height of the pyramid dunes is, the faster they swing. The above analysis also suggests that the moving speed of sand dunes in the study area is positively correlated with the local wind speed ≥5 m/s of local climate at a yearly scale.

Here, we compare the moving speed of sand dunes in the Hexi Corridor with that in other sandy desert areas in northwestern China. In the Taklamakan Desert, the largest sand desert in China, the observation results of eight crescent-shaped dunes along the oil transportation highway showed that the moving speed of sand dunes was 4.81–10.87 m in October 1991–1992, with an average of 7.29 m, and the moving speed of these sand dunes was 3.33–8.89 m in October 1992–1993, with an average of 5.56 m (Dong et al., 1998). Based on the digital interpretation results of high-resolution remote sensing images during the period 2010–2014, the average speed of dune movement in the Tenggeli Desert was 4.36 m/a in 2010–2013, and was 2.43 m/a in 2013–2014 (Hu et al., 2016). Based on the digital interpretation results of high-resolution Google Earth QuickBird images during the period 2002–2010, the moving speeds of 22 crescent-shaped dunes in the Maowusu Sandy Land are between 3.5 and 9.5 m/a (J. Wang et al., 2013). The width of these dunes is significantly correlated with the horizontal length of the leeward slope of the dunes, and the width of the dunes and the horizontal length of the leeward slopes decrease during the movement of dunes, while the horizontal length of the windward slopes increases. There is a good correlation between the moving speed and the width of dune.

It can be seen from the above that the moving speeds of sand dunes in different desert areas are quite different. Compared with sand dunes in the deserts mentioned above, the moving speed of the widely distributed crescent-shaped dunes in the Hexi Corridor also varies greatly. During the period 2006–2015, sand dunes at the edge of the Minqin Oasis area moved the fastest, with a moving speed of about 6.2 m/a, while sand dunes at the edge of the Dunhuang Oasis moved the slowest, with a moving speed of only about 0.8 m/a (**Figure 3**). The horizontal length of the windward slope of sand dunes in most areas of the Hexi Corridor increased in 2015 compared with that in 2016, while the horizontal length of the leeward slope of sand dunes decreased (**Tables 1**, **2**).

Summarizing the above characteristics of geomorphological parameters of different dunes, it can be concluded that there are two states of sand dunes movement in the Hexi Corridor in the past half century, dynamic migration and basically stable. This kind of geomorphological evolution of dunes is possibly closely related to their material sources and regional environmental conditions.

Depositional Environmental and Transportation Modes of Sand Dunes in the Hexi Corridor

The above analytical results of grain size of aeolian sediments from the Hexi Corridor have shown that sand dunes have different grain size compositions in different regions of the Hexi Corridor (**Figures 4**, **5**). It is obvious that the average grain size of sand dunes in the western Hexi Corridor (such as the Huahai-Jinta-Jiaquan area, average 0.27–0.43 mm) is larger than that in the central-eastern Hexi Corridor (such as the Jiuquan-Gaotai-Minqin area, average 0.07–0.24 mm) and also larger than those in other desert regions of northern China (average 0.17–0.19 mm, Zhu et al., 2014; Zhu and Yu, 2014) and of the world (average 0.11–0.23 mm, Lancaster, 1995).

The spatial differences in grain size compositions may reflect the different depositional environment, the different sources and the different transportation modes in the formation and development of sand dunes in the Hexi Corridor. According to the grain-size discriminant function proposed by Sahu (1964), the major sedimentary environment in the Hexi Corridor includes three types of deposits, i.e., aeolian deposit, lacustrine deposit and alluvial-proluvial deposit (**Figure 4**), of which aeolian deposit is the dominant (about 50%) (Nottebaum et al., 2014; Zhang and Dong, 2015). Compared with the crescent-shaped dunes in the central-eastern Hexi Corridor, the shrub dunes in the western Hexi Corridor are dominated by the medium- to fine-sand fractions, but not the medium-sand fraction. This is possibly because of the wide distribution of gravel around the shrub dune, which reduce the airflow velocity near the ground, making it difficult for the coarser-grained particles to move up to the surface of shrub dunes (Zhu et al., 2014). While for the crescent-shaped dunes, the length of wind flow path on the windward side of the dune is longer. During the movement of the unsaturated aeolian sand flow, the coarser-grained particles collide with the ground surface elastically, resulting in the coarser-grained particles moving to a higher position on the windward slope of crescent-shaped dune, so the crescent-shaped dunes are dominated by the medium-sand-fraction particles. The clay-grain content is less in the surface layer of the crescent-shaped dunes and the shrub dunes, but more (up to 28.2%) in sand dunes developed on dry lake beds (playas) or ancient lake area, which is obviously related to the local source of fine particles.

Generally, the probability cumulative curve of grain size of aeolian sediments in the world is usually shown as two to four independent line segments, indicating that two to four modes of motion occur during their transportation (Visher, 1969). The probability cumulative curve of grain size of sand dunes in the Hexi Corridor basically presents a three-stage pattern truncated at about 1.8φ (coarse group) or 2.5φ (fine group) (**Figure 5**), indicating that sand dunes in the study area are dominated by the motion mode of saltation under the action of wind, and superimposed with a small number of particles transported by the motion modes of suspension and creeping. This feature has been observed in sand dunes in different areas of the Hexi Corridor including the lower reaches of the Heihe River Basin near the Hexi Corridor (Zhu et al., 2014; Zhang and Dong, 2015; Zhang et al., 2016; Pan et al., 2019). But compared with dune sediments, the movement modes of gobi sediments and lacustrine sediments in the Hexi Corridor are mainly creeping-saltation and saltation-suspension, respectively (Zhu and Yu, 2014; Zhang et al., 2016), indicating different motion modes between aeolian, lacustrine and gobi sediments. The differences can also be reflected from the frequency distribution curves of these sediments, as dune sediments are usually unimodal distribution (**Figure 5**), while aqueous and gobi sediments are bimodal or multimodal distribution (Zhu, 2007; Zhu and Yu, 2014).

Sources of Sand Dunes in the Hexi Corridor

The above geochemical analysis provides good evidences for the understanding of the material sources of sand dunes in the Hexi Corridor. The result that sand dunes in the Minqin area have different material sources between the western part (the Badanjilin-Minqin transition zone), the central part, the southeast side, and the eastern part (the Tenggeli-Minqin transition zone) of the Minqin Basin indicate that aeolian sediments from the Badanjilin Desert can be transported to the west side of the Minqin Oasis through mountains (Yabulai) for a long distance by the northwest wind, and aeolian sediments from the Tenggeli Desert provide material source to the east side of the Minqin Oasis. However, the aeolian sands of the two sandy deserts cannot reach or bypass the other side of the oasis to achieve a confluence of the two deserts. This reveals that the Minqin Oasis is real an effective barrier to prevent the migration and convergence of sand dunes between the Badanjilin and Tenggeli Deserts. However, the large number of aeolian dunes developed in and around the Minqin Basin also suggests that the role of oasis in preventing eaolian erosion is limited and should not be overestimated.

Comparing the major element abundances of aeolian sediments in different deserts of China (**Table 4**), the sand dunes in the Hexi Corridor have certain differences and similarities with deserts in northern China. For example, the content of Fe_2O_3 in sand dunes of the Hexi Corridor can reach 3.50%, which is generally higher than any one of other deserts in China, while the contents of other elements in the Hexi Corridor are in a similar range of element abundance to those of other deserts, indicating that the sand dunes in the Hexi Corridor are rich in iron element. Compared with the composition of the upper continental crust (UCC), dune sediments in the middle and eastern Hexi Corridor are enriched in SiO_2 (**Figures 6**, **7**) and CaO (**Figure 6**), which are similar to those in the fluvial and lacustrine sediments near the Taklamakan and Badanjilin Deserts and the aeolian sediments in the surrounding gobi desert, but they are slightly different from those in the Kumtag and Tenggeli Deserts (Zhang et al., 2020).

The analytical results from heavy mineral assemblages and trace element abundances indicate that the provenance of sand dunes in the Hexi Corridor is mainly from "sands of *in-situ* rising," which is also the genetic mechanism of many desert sands in northern China (Zhu et al., 1980; Yang, 2006; Yang et al., 2007, Yang et al., 2012; Chang, 2019). In this study, the structural distribution of wind-drifting sand flow in the Hexi Corridor and its relationship with wind speed also support this point. The above results show that most part of sand particles in the Hexi Corridor are transported near the ground surface (0.3–10 cm) when the wind speed is < 7 m/s. This implies that if there are any small topographical fluctuations (>20 cm) on the surface of the

TABLE 4 | The average element contents (%) of sand dunes in the Hexi Corridor and other deserts and the average composition of the upper continental crust (UCC). CLP, the Loess Plateau in China.

Regions	Fe_2O_3	CaO	MgO	SiO_2	Al_2O_3	Na_2O	K_2O	References
Hexi Corridor	3.5	5.55	2.07	66.12	9.24	2.45	2	Zhang et al. (2017), Pan et al. (2019)
Badanjilin Desert	1.93	2.06	1.19	80.27	7.78	1.9	2	Zhu and Yang, (2009)
Tenggeli Desert	1.96	1.3	1.12	80.94	8026	1.88	2.25	Zhu and Yang, (2009)
Kumutage Desert	2.88	4.64	2.19	70.13	9.59	2.52	1.98	Dong et al. (2011)
Taklamakan Desert	3.1	7.88	2.2	62.05	10.6	2.58	2.11	Zhu and Yang, (2009)
Loess (CLP)	4.56	8.62	2.31	58.65	11.86	1.68	2.44	Dong et al. (2011)
paleosol (CLP)	5.12	0.83	2.21	65.18	14.79	1.41	3.15	Dong et al. (2011)
UCC	5	4.2	2.22	66	15.2	3.9	3.4	Taylor and McLennan, (1985)
Terrestrial shale	7.22	1.3	1.2	62.8	18.9	1.2	3.7	Taylor and McLennan, (1985)

TABLE 5 | Meteorological data of sandstorm and strong wind in the Hexi Corridor (cited from Chang et al. (2015)).

Weahter station	Average wind speed (m/s)	Wind speed ≥ 8 grade/d	Sandstorm days (d)	Maximum wind direction
Gulang	3.5	4.5	4	NW
Wuwei	1.8	9.7	4.8	NW
Minqin	2.7	25.1	27.4	NW
Jinchang	3.3	25.1	27.4	NW
Yongchang	3	24.6	4.2	NW
Zhangye	2	12.2	11.8	NW, SSE
Linze	2.5	21.7	7.7	NW
Gaotai	2	7.8	11.1	NW
Jiuquan	2.2	16.6	10.3	NNW
Jinta	1.9	14.4	6.4	NW, WNW
Yunmen	3.8	40.6	8.1	WNW
Average	2.61	18.39	11.2	—

study area, it is difficult to transport and migrate these aeolian sands for a long distance to be far away from their source areas. Palaeogeographical and geomorphological studies (e.g., Minqin Desert Control Experiment Station (MDCES), 1975; Zhu et al., 1980) believe that sediments from alluvial plains and alluvial deposits of ancient rivers, lacustrine plain and lacustrine deposits of ancient lakes, aeolian deposits in the erosion zone of the forelands of the northern Qilian Mountains and the southern Beishan Mountains, and alluvial and fluvial deposits of modern rivers are the main material sources of sand dunes in the Hexi Corridor. Based on mineralogical analysis, Ferrat et al. (2011) observed that sand dunes in the Hexi corridor have similar concentrations of mica, quartz, illite, muscovite and albite with adjacent areas, such as the Tenggeli Desert and the Badanjilin Desert. This similar mineralogical composition may lead to the similarity in geochemical characteristics of aeolian sediments in these areas. Geochemical and grain-size analysis of detrital sediments collected from alluvial deposits in the Qilian Mountains, paleo-lacustrine deposits in low-level areas, and surface aeolian sediments in gobi desert areas of the southern Beishan Mountains (e.g., Wang and Wang, 2013; Zhang and Dong, 2015; Zhang et al., 2016; Zhang et al., 2020), also suggest that these regions are the main source areas of sand dunes in the Hexi Corridor.

In addition to the above comparisons from geochemical evidences of aeolian sediments at a regional scale, the local landform type and spatial distribution characteristics and their relationship with the dominant wind/river conditions also provide clues to explore the potential source of sand dunes in the Hexi Corridor.

Most active dune fields in the Hexi Corridor are located between the cities of Jinta and Zhangye and at the margin of Badanjilin Desert (**Figure 2**). The desert marginal dune fields can be regarded to be directly linked to the sand deserts (e.g., Badanjilin and Tenggeli). The above geochemical evidences also support this point. From the local dominant wind conditions in different areas of the Hexi Corridor (**Table 5**), these dunes are subjected to strong northerly winds. This suggests sand transport from the desert into the southerly bordering Hexi Corridor. A southward transport can also be indicated by the linear dune field in this region (Nottebaum et al., 2014). Monthly averaged wind directions for Zhangye show a bimodal pattern (dominant wind directions from northwest and south-southeast, **Table 5**) from May to July, which is the transition period of winter monsoon to summer monsoon dominance (Bourque and Mir, 2012). Nevertheless, as wind speeds are higher in spring (Ta et al., 2004) a positive balance of southward sand transport is likely. Therefore, the Badanjilin Desert is probably the dominant source region for the northern dune fields in the Hexi Corridor. In contrast, dune fields between Jinta and Zhangye are located south of the braided Heihe River valley and in vicinity to the Qilian Mountains front (**Figure 2**). As the Heihe River forms a barrier for saltating sand grains moving south from the Badanjilin Desert, the source regions for the southern dune fields in the Hexi Corridor are suspected to be in the braided Hei River valley and the foreland alluvial fans. This is evident as they are directly connected to fluvial channels breaking through the Qilian Mountains front (Nottebaum et al., 2014).

Different transport of aeolian sand in the western Hexi Corridor is evidenced by isolated barchans dunes with coarser grain sizes than dune fields in the eastern part (**Figure 5**). Hence, a sufficient transport capacity is evidenced. However, dune fields are rare in the western part of the Hexi Corridor. This region is not close to sand deserts but bare low mountains, such as the Beishan Mountains to the north (**Figure 2**). Regarding to the distribution of clastic materials, the northerly bordering Beishan Mountain exhibits vast areas of bare primary weathering rock surfaces. However, according to Kocurek and Lancaster (1999), material for "terrigenous dune fields" is rarely a product of primary rock deflation, but rather results from fluvial deposits, therefore, it has only limited potential to serve as a productive source area for large amounts of sand compared to fluvial deposits (Kocurek and Lancaster, 1999). Additionally, fluvial sand supply from Qilian Mountains is limited as contributing rivers are ephemeral. These conditions are in clear contrast to those in the eastern part of the Hexi Corridor: in the latter, the Badanjilin Desert exposes large amounts of well-sorted aeolian sands to northerly winds, and additionally, perennial Heihe River and the mountain proximal alluvial fans can also serve as sand suppliers for the east part. Therefore, sufficient sand supply and sand availability is provided for the formation of sand dunes in the eastern part of the Hexi Corridor, but not for dunes in the west part. Generally speaking, sufficient transport capacity is evidenced for both the western and eastern parts of the Hexi Corridor, sufficient sand supply and sand availability, however, is the limiting factor for dune field formation in the west part of the Hexi Corridor.

Summarizing the above geochemical, geomorphological, and sedimentological characteristics and related environmental evidences of sand dunes, it can be concluded that dried river deposits (playas), alluvial/proluvial deposits, neighboring desert sands are the main sources of sand dunes in the Hexi Corridor. While the initial provenance of these aqueous and aeolian deposits mainly come from the forelands/foothills of the Qilian Mountains in the south and the Beishan Mountains in the north via river transportation. This reveals that the interaction between wind and water dynamics is of great significance in the formation and evolution of aeolian landforms in terms of geomorphic genesis in arid areas.

Formation of Shrub Dunes in Oasis Area of the Hexi Corridor

Compared with sand dunes in desert area, many sand dunes inside the oasis area of the Hexi Corridor are shrub dunes and have more complex material sources. They are closely linked to regional land degradation and desertification issues in the Hexi Corridor.

In the arid and semi-arid areas of northern China, the occurrence of desertification or reverse desertification (restoration) is closely related to the interaction of local aeolian and fluvial processes (Wang et al., 2008b). Studies have shown that in the past 50 years, desertification and restoration in northern China usually occurred in alluvial plains or flood plains caused by changing hydrological conditions, where the sandy sediments derived from floods and rivers are deflated and reworked by wind (Li et al., 2002). Moreover, the soils that are originated from these parent materials, such as aeolian sandy soil, brown soil, cinnamon soil, gray cinnamon soil, chernozem and karst soil, are also vulnerable to wind deflation and water erosion and thus easily degenerated and degraded (Yang, 1985; Liu et al., 1998; Wang et al., 2008b).

In the middle and eastern areas of the Hexi Corridor, the oasis and surrounding desert landscapes exit paradoxically to a certain extent, with a relationship of being independent and interdependent between them. Although sand dunes also exist inside the oasis, the surface clastic materials are mostly soil aggregates. The potential relationship between aeolian sand and soil aggregates is a basis for understanding the formation of sand dunes in the oasis area. The above analysis has shown that in the oasis areas of the middle Hexi Corridor, most surface soils are characterized by high sand content, low SOC level, and were rich in calcium carbonate. These soils are prone to disperse and harden after irrigation. The large blocky aggregate at the size of >5 mm is the dominant fraction in aggregate size distribution in surface soils, which is in favor of resisting soil erosion by wind. After wet sieving, most macro-aggregates broke down and dispersed, indicating a weak stability. The contents of clay, silt, SOC, $CaCO_3$, Fe_2O_3, and Al_2O_3 had significant influence on the formation of aggregates. The total percentage of dry aggregates and DMWD are more correlated with clay and silt content than SOC and $CaCO_3$ content, although the effect of SOC and $CaCO_3$ content on wet-sieving aggregates were more significant than that of clay and silt content. From the above results, it can be concluded that the distribution and characteristics of soil aggregates in oasis areas of the Hexi Corridor are in favor of controlling soil wind erosion. However, the stability of all soil aggregates is weak in the study area after irrigation. That is to say, water erosion or changes in hydrological conditions will change the structure of soil aggregates, turning them into potential aeolian sand. This means that whether it is viewed from the driving mechanism of environmental background or the degradation mechanism of soil texture, the change in hydrological conditions will be an important reason for the formation of dune landforms in oasis area.

Shrub dunes, which are also referred to as coppice dunes or vegetated dunes, form as a result of basic aeolian processes (Tengberg, 1995) and are usually regarded as good indicators of land degradation and the condition of the environment (e.g., Gile, 1975; Zhu et al., 1981b; Tengberg and Chen, 1998; Wang et al., 2006b, Wang et al., 2008b). As is the case for mobile dunes, the development of shrub dune is closely related to vegetation cover, groundwater levels, and the sediment supply (Zhu et al., 1981b; Nickling and Wolfe, 1994; Parsons et al., 2003). However, many shrub dunes only develop in regions with high levels of wind activity and with groundwater maintained within a certain range (Wang et al., 2008b). In the Hexi Corridor and neighboring areas such as the southern Alashan plateau, field investigations show that the shrub dune development can be divided into several stages (**Figure 8**). 1) During the early stage, the amount of water in rivers decreased slowly, but groundwater levels remained high, so no shrub dunes began to develop. 2) During the origin of the shrub

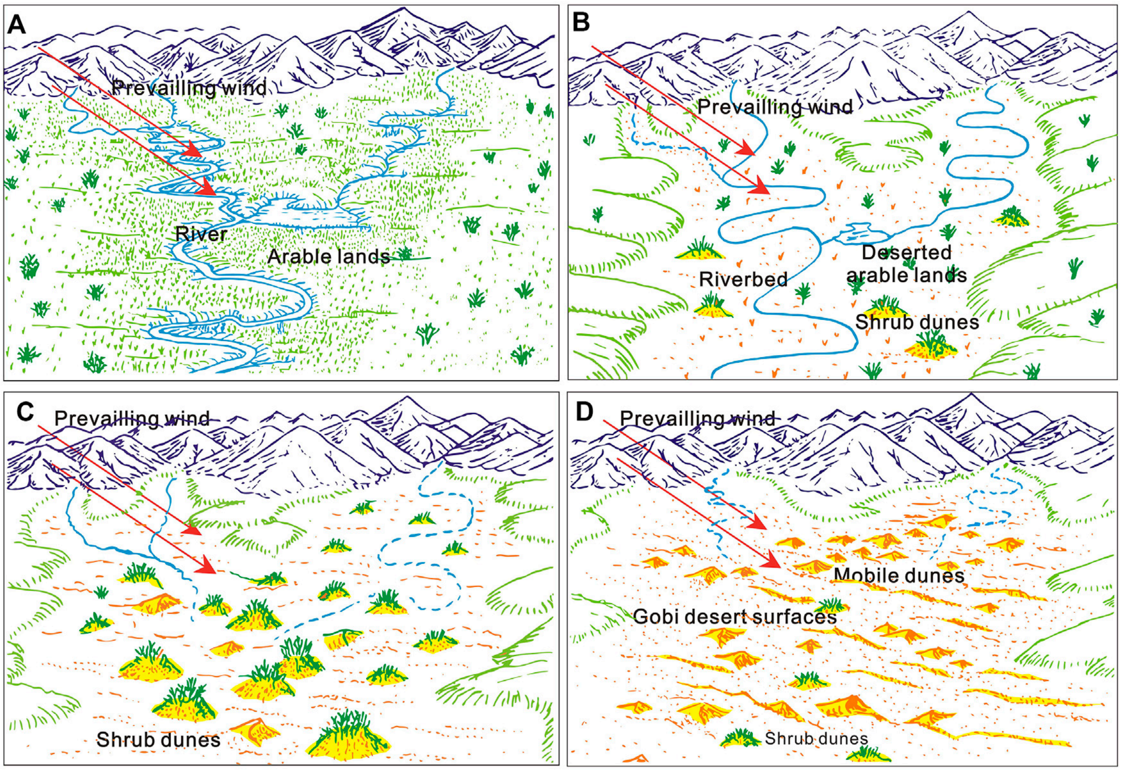

FIGURE 8 | Formation and evolution of shrub dunes in the Hexi Corridor and neighboring areas (modified after Wang et al. (2008b)).

dunes, riverbeds began to emerge due to a decrease in the amount of surface water, and a few shrub dunes began to form on the exposed riverbeds and in deserted arable land. 3) During the developing stage, river beds became thoroughly dry and extensive shrub dune areas began to develop. 4) During the degradation stage, many shrub dunes began to degenerate and evolved into mobile dunes, with only a few distributed in regions with relatively high groundwater levels.

CONCLUSION

Based on comprehensive evidences from geomorphological, aeolian-physical, hydrolgocial, granulometrical and geochemical analysis, this study discussed the dynamical changes of dune landforms and their provenance in the Hexi Corridor. The results show that the dynamic changes of different dunes are different in the Hexi Corridor during the past half century. There are two states of sand dunes movement in the Hexi Corridor in the past half century, dynamic migration and basically stable. This kind of geomorphological evolution of dunes is closely related to their material sources and regional environmental conditions. On the inter-annual and multi-year time scales, the crescent-shaped dunes move the fastest, followed by the chains of barchan dunes. Only the top of the pyramid dunes wigwags, while the parabolic dunes and the longitudinal dunes hardly move forward. The higher the height of the crescent-shaped dune (or the chain of barchan dunes) is, the slower their movement is. On the contrary, the higher the height of the pyramid dunes is, the faster they swing. Dunes at the edge of the Minqin Oasis move the fastest and dunes at the edge of the Dunhuang Oasis move the slowest. The moving speed of sand dunes in the study area is positively correlated with the average wind speed of local climate and there is a good correlation between the moving speed and the width of dune. The average grain size of sand dunes in the western Hexi Corridor (such as the Huahai-Jinta-Jiaquan area, average 0.27–0.43 mm) is larger than that in the central-eastern Hexi Corridor (such as the Jiuquan-Gaotai-Minqin area, average 0.07–0.24 mm) and also larger than those in other desert regions of northern China (average 0.17–0.19 mm) and of the world (average 0.11–0.23 mm). Different motion modes are identified between aeolian, alluvial/fluvial and gobi sediments. The PC curve of grain size of sand dunes in the Hexi Corridor basically presents a three-stage pattern truncated at about 1.8φ (coarse group) or 2.5φ (fine group), indicating that three modes of motion occur during their transportation. only SiO_2 in the major elements' compositions of dune sands is enriched relative to UCC, most trace elements' abundances are also depleted relative to UCC, except for Cr and Ni. The mineralogical and geochemical data indicate that dune sands in the Hexi Corridor are mainly "sediments of *in-situ* rising" that originated from alluvial/fluvial deposits of ancient rivers, lacustrine deposits of ancient lakes, and aeolian deposits in the erosion zone of the forelands of the Qilian and Beishan Mountains and the north-neighboring deserts, which means that dried river deposits (playas), alluvial/proluvial deposits, and neighboring desert sands are the main sources of sand dunes in the Hexi Corridor. This reveals that the interaction between wind and water dynamics is of great significance in the formation and evolution of aeolian landforms in terms of geomorphic genesis in arid areas. Sufficient transport capacity is evidenced for both the western and eastern parts of the Hexi Corridor, sufficient sand supply and sand availability, however, is the favorable factor for dune formation in the east part but is the limiting factor for the west.

DATA AVAILABILITY STATEMENT

The original contributions presented in the study are included in the article/Supplementary Materials, further inquiries can be directed to the corresponding author.

AUTHOR CONTRIBUTIONS

The paper was initiated, prepared, analyzed and written by BZ, JZ, and CS.

FUNDING

The study was financially supported by the National Natural Science Foundation of China (grant nos. 41930640, 41771014) and the Project of the Second Comprehensive Scientific Investigation on the Qinghai Tibet Plateau (2019QZKK1003).

ACKNOWLEDGMENTS

Sincere thanks are extended to Profs. Xiaoping Yang, Xunming Wang, Zhaofeng Chang, Zhibao Dong, Nottebaum V, and Zhengcai Zhang for their help in the author’s research work.

REFERENCES

An, F., Zhang, D., Zhao, J., Chai, C., Zhao, Y., and Sun, T. (2019). Physical and Chemical Properties of Soils in Different Types in the Gobi Areas of the Hexi Corridor. *J. Chin. Soil Water Conserv.* 6, 42–47. doi:10.14123/j.cnki.swcc.2019.0143 in Chinese with English abstract

Ashley, G. M. (1978). Interpretation of Polymodal Sediments. *J. Geol.* 86 (4), 411–421. doi:10.1086/649710

Baas, A. C. W., and Nield, J. M. (2007). Modelling Vegetated Dune Landscapes. *Geophys. Res. Lett.* 34, L06405. doi:10.1029/2006GL029152

Bagnold, R. A., and Barndorff-Nielsen, O. (1980). The Pattern of Natural Size Distributions. *Sedimentology* 27, 199–207. doi:10.1111/j.1365-3091.1980.tb01170.x

Bourque, C. P.-A., and Mir, M. A. (2012). Seasonal Snow Cover in the Qilian Mountains of Northwest China: its Dependence on Oasis Seasonal Evolution and lowland Production of Water Vapour. *J. Hydrol.* 454-455, 141–151. doi:10.1016/j.jhydrol.2012.06.008

Bronick, C. J., and Lal, R. (2005). Soil Structure and Management: a Review. *Geoderma* 124, 3–22. doi:10.1016/j.geoderma.2004.03.005

Bureau of Geology and Mineralogy Resources of Gansu Province (BGMRGP) (1984). *Geological Map of Gansu Province of the People’s Republic of China 1: 1,000,000*. Beijing, China: Geological Publishing House.

Chang, Z., Li, Y., Zhang, J., Wang, Q., Zhang, D., Tang, J., et al. (2017). Stability Mechanisms of Barchan Sand Dunes: a Case Study in the Hexi Desert in Gansu. *Acta Ecol. Sin.* 37 (13), 4375–4383. doi:10.5846/stxb201602120273 in Chinese with English abstract

Chang, Z. (2019). Problems and Solutions to Desertification Combating in the Hexi, Gansu for 60 Years. *J. Arid Land Resour. Environ.* 33 (9), 152–159. doi:10.13448/j.cnki.jalre.2019.250 in Chinese with English Abstract

Chang, Z., Wang, Q., Zhang, J., Xi, J., Wang, Q., Zhang, D., et al. (2015). Environmental Conditions of Barchans Dune and Barchans Chain – a Case Study from the Hexi Desert Area of Gansu. *Anim. Husbanbandry Feed Sci.* 7 (6), 383–388. doi:10.19578/j.cnki.ahfs.2015.06.017

Chang, Z., Zhu, S., Shi, X., Zhang, J., Li, Y., Wang, Q., et al. (2016). Comparisons between Movement Speed of Main Types of Dunes: a Case Study of Desert Areas in Hexi Region of Gansu Province. *J. Landscape Res.* 8 (6), 36–40. doi:10.16785/j.issn1943-989x.2016.6.010

Chen, F., and Liu, Y. (2011). Secular Annual Movement of Sand Dunes in Badain Jaran Desert Based on Geographic Analyses of Remotely Sensed Imagery. *Remote Sensing Tech. Appl.* 26 (4), 501–507. doi:10.11873/j.issn.1004-0323.2011.4.501

Ci, L., Yang, X., and Chen, Z. (2002). The Potential Impacts of Climate Change Scenarios on Desertification in China. *Earth Sci. Front.* 9, 287–294. in Chinese with English abstract

Ci, L., and Yang, X. (2004). Progress in Feedback Mechanism between Desertification and Climate Change. *Acta Ecol. Sin.* 24, 755–760. in Chinese with English abstract.

Dong, Y., and Huang, D. (2013). Preliminary Observation of Movement of Coastal Dunes in Feicui Island in Changli, Hebei Province. *J. Desert Res.* 33 (2), 486–492. doi:10.7522/j.issn.1000-694X.2013.00066

Dong, Z., Chen, G., Yan, C., Han, Z., and Wang, X. (1998). Movement Laws of Dunes along Oiltransportation Highway in the Tarim Desert. *J. Desert Res.* 18 (4), 328–333. in Chinese with English abstract.

Dong, Z., Su, Z., and Qian, G. (2011). *Aeolian Landforms in the Kumtag Desert*. Beijing: Science Press.

Feng, J.-L., Hu, Z.-G., Ju, J.-T., and Zhu, L.-P. (2011). Variations in Trace Element (Including Rare Earth Element) Concentrations with Grain Sizes in Loess and Their Implications for Tracing the Provenance of Eolian Deposits. *Quat. Int.* 236, 116–126. doi:10.1016/j.quaint.2010.04.024

Ferrat, M., Weiss, D. J., Strekopytov, S., Dong, S., Chen, H., Najorka, J., et al. (2011). Improved Provenance Tracing of Asian Dust Sources Using Rare Earth Elements and Selected Trace Elements for Palaeomonsoon Studies on the Eastern Tibetan Plateau. *Geochim. Cosmochim. Acta* 75, 6374–6399. doi:10.1016/j.gca.2011.08.025

Folk, R. L., and Ward, W. C. (1957). Brazos River Bar [Texas]; a Study in the Significance of Grain Size Parameters. *J. Sediment. Res.* 27, 3–26. doi:10.1306/74d70646-2b21-11d7-8648000102c1865d

Friedman, G. M. (1961). Distinction between Dune, beach, and River Sands from Their Textural Characteristics. *J. Sediment. Pet.* 31 (4), 514–529. doi:10.1306/74d70bcd-2b21-11d7-8648000102c1865d

Gile, L. H. (1975). Holocene Soils and Soil-Geomorphic Relations in an Arid Region of Southern New Mexico. *Quat. Res.* 5, 321–360. doi:10.1016/0033-5894(75)90037-x

Goudie, A. (2002). *Great Warm Deserts of the World: Landscapes and Evolution*. New York: Oxford University Press.

Guan, Q., Zhang, J., Wang, L., Pan, B., Gui, H., and Zhang, C. (2013). Discussion of the Relationship between Dustfall Grain Size and the Desert Border, Taking the Southern Border of the Tengger Desert and the Southern Dust deposit Area as an Example. *Palaeogeogr. Palaeoclimatol. Palaeoecol.* 386, 1–7. doi:10.1016/j.palaeo.2013.01.017

Han, Z. (2003). The Evolution of the Mao Wusu Desert and the Reclamation in the Adjacent Areas in the Ming Dynasty. *China Soc. Sci.* 5, 191–204. in Chinese with English abstract.

Hartmann, K., and Wünnemann, B. (2009). Hydrological Changes and Holocene Climate Variations in NW China, Inferred from lake Sediments of Juyanze Palaeolake by Factor Analyses. *Quat. Int.* 194, 28–44. doi:10.1016/j.quaint.2007.06.037

He, J., Guo, J., Xing, E., Cui, W., and Li, J. (2012). Structure of Wind-Sand Flow and Movement Laws of Dunes along the Yellow River in Ulan Buh Desert. *Trans. Chin. Soc. Agric. Eng.* 28 (17), 71–77. in Chinese with English abstract.

Hetzel, R., Niedermann, S., Tao, M., Kubik, P. W., Ivy-Ochs, S., Gao, B., et al. (2002). Low Slip Rates and Long-Term Preservation of Geomorphic Features in central Asia. *Nature* 417 (6887), 428–432. doi:10.1038/417428a

Hetzel, R., Tao, M., Niedermann, S., Strecker, M. R., Ivy-Ochs, S., Kubik, P. W., et al. (2004). Implications of the Fault Scaling Law for the Growth of Topography: Mountain Ranges in the Broken Foreland of north-east Tibet. *Terra Nova* 16 (3), 157–162. doi:10.1111/j.1365-3121.2004.00549.x

Honda, M., and Shimizu, H. (1998). Geochemical, Mineralogical and Sedimentological Studies on the Taklimakan Desert Sands. *Sedimentology* 45, 1125–1143. doi:10.1046/j.1365-3091.1998.00202.x

Hu, F., Zhang, K., An, Z., and Yu, Y. (2020). Composition of Wind Dynamic Environment Among Desert, Oasis and Gobi. *J. Desert Res.* 40 (4), 113–119. doi:10.7522/j.issn.1000-694X.2020.00034 in Chinese with English abstract

Hu, X., Wang, M., and Liu, Y. (2016). Analysis of Movement of Dunes in the Tengger Desert Based on High-Resolution Remote Sensing Images. *China Sci. Tech. Rev.* 2, 337.

Hugenholtz, C. H., and Wolfe, S. A. (2010). Rates and Environmental Controls of Aeolian Dust Accumulation, Athabasca River Valley, Canadian Rocky Mountains. *Geomorphology* 121, 274–282. doi:10.1016/j.geomorph.2010.04.024

Jahn, B.-M., Gallet, S., and Han, J. (2001). Geochemistry of the Xining, Xifeng and Jixian Sections, Loess Plateau of China: Eolian Dust Provenance and Paleosol Evolution during the Last 140 Ka. *Chem. Geol.* 178, 71–94. doi:10.1016/s0009-2541(00)00430-7

Jiang, Q., and Yang, X. (2019). Sedimentological and Geochemical Composition of Aeolian Sediments in the Taklamakan Desert: Implications for Provenance and Sediment Supply Mechanisms. *J. Geophys. Res. Earth Surf.* 124, 1217–1237. doi:10.1029/2018jf004990

Kimura, R., Bai, L., and Wang, J. (2009). Relationships Among Dust Outbreaks, Vegetation Cover, and Surface Soil Water Content on the Loess Plateau of China, 1999-2000. *Catena* 77, 292–296. doi:10.1016/j.catena.2009.02.016

Kocurek, G., and Lancaster, N. (1999). Aeolian System Sediment State: Theory and Mojave Desert Kelso Dune Field Example. *Sedimentology* 46 (3), 505–515. doi:10.1046/j.1365-3091.1999.00227.x

Küster, Y., Hetzel, R., Krbetschek, M., and Tao, M. (2006). Holocene Loess Sedimentation along the Qilian Shan (China): Significance for Understanding the Processes and Timing of Loess Deposition. *Quat. Sci. Rev.* 25, 114–125. doi:10.1016/j.quascirev.2005.03.003

Lancaster, N. (1995). *Geomorphology of Desert Dunes*. London: Routledge.

Lancaster, N., Wolfe, S., Thomas, D., Bristow, C., Bubenzer, O., Burrough, S., et al. (2016). The INQUA Dunes Atlas Chronologic Database. *Quat. Int.* 410, 3–10. doi:10.1016/j.quaint.2015.10.044

Lancaster, N., Yang, X., and Thomas, D. (2013). Spatial and Temporal Complexity in Quaternary Desert Datasets: Implications for Interpreting Past Dryland Dynamics and Understanding Potential Future Changes. *Quat. Sci. Rev.* 78, 301–302. doi:10.1016/j.quascirev.2013.07.018

Lang, L., Wang, X., Zhu, B., Wang, X., Hua, T., Wang, G., et al. (2017). Nebkha Formation and Variations in Sediment Availability and Wind-Energy Regime of the Western Hexi Corridor over the Past Several Dacades. *J. Desert Res.* 37 (4), 611–620. doi:10.7522/j.isnn.1000-694X.2017.00022 in Chinese with English abstract

Le, B. Y. (1996). Aggregate Stability and Assessment of Soil Crusting and Erodibility: I. Theory and Methodology. *Eur. J. Soil Sci.* 47, 425–437.

Lehmkuhl, F. (1997). The Spatial Distribution of Loess and Loess-like Sediments in the Mountain Areas of central and High Asia. *Z. Geomorphol.* 111, 97–116.

Li, E. (2011). Comparative Study on Characteristics of Aeolian Sediments between the Badanjilin and Tengeli Deserts. Ph.D doctoral dissertation. Xi'an: Shaanxi Normal University). in Chinese with English abstract.

Li, X.-G., Li, F.-M., Rengel, Z., Singh, B., and Wang, Z.-F. (2006). Cultivation Effects on Temporal Changes of Organic Carbon and Aggregate Stability in Desert Soils of Hexi Corridor Region in China. *Soil Tillage Res.* 91, 22–29. doi:10.1016/j.still.2005.10.004

Li, X. G. (2000). The Characteristics of Soil Aggregate in Jintai Electricirrigating Area of Gansu. *Acta Pedol. Sin.* 37, 263–269.

Li, Y., and Zhang, S. (2007). Review of the Research on the Relationship between Sand-Dust Storm and Arid in China. *Adv. Earth Sci.* 22 (11), 1169–1176. in Chinese with English abstract.

Li, Z., Zhang, Z., Wang, M., Nie, H., and Yue, L. (2002). Geological Views on the sandy Desertification of the East Part of north China. *Northwest. Geol.* 35, 7–22. in Chinese with English abstract.

Liu, L., Zhou, J., and Liu, D. (1998). Ivanov IV, Gemkin VA, Prikodko VY. Grassland Soil Changes under Different Uses in the Agro-Pastoral Transitional Zones of north China. *Soils* 5, 225–229.

Liu, T. (1985). *Loess and the Environment*. Beijing: China Ocean Press. in Chinese.

Lu, H., van Huissteden, K., Zhou, J., Vandenberghe, J., Liu, X., and An, Z. (2000). Variability of East Asian Winter Monsoon in Quaternary Climatic Extremes in North China. *Quat. Res.* 54, 321–327. doi:10.1006/qres.2000.2173

Lv, P., Dong, Z., and Rozier, O. (2018). The Combined Effect of Sediment Availability and Wind Regime on the Morphology of Aeolian Sand Dunes. *J. Geophys. Res. Earth Surf.* 123, 2878–2886. doi:10.1029/2017jf004361

Mao, D., Lei, J., Zhou, J., Xue, J., wang, C., and Rehemutula, Z. (2016). Movement Rules of Different Shifting Dunes and Semi-shifting Dunes in Cele, Xinjiang Uygur Autonomous Region. *Res. Soil Water Conser.* 23 (3), 278–282.

Mason, J. A., Nater, E. A., Zanner, C. W., and Bell, J. C. (1999). A New Model of Topographic Effects on the Distribution of Loess. *Geomorphology* 28, 223–236. doi:10.1016/s0169-555x(98)00112-3

McLaren, P., and Bowles, D. (1985). The Effect of Sediment Transport on Size Distributions. *J. Sediment. Pet.* 55 (4), 457–470.

Meyer, B., Tapponnier, P., Bourjot, L., Métivier, F., Gaudemer, Y., Peltzer, G., et al. (1998). Crustal Thickening in Gansu-Qinghai, Lithospheric Mantle Subduction, and Oblique, Strike-Slip Controlled Growth of the Tibet Plateau. *Geophys. J. Int.* 135 (1), 1–47. doi:10.1046/j.1365-246x.1998.00567.x

Minqin Desert Control Experiment Station (MDCES) (1975). *Deserts and Control in Gansu*. Lanzhou: Gansu People's Publishing house, 33–38.

Muhs, D., Bush, C., Cowherd, S., and Mahan, S. (1995). "Geomorphic and Geochemical Evidence for the Source of Sand in the Algodones Dunes, Colorado Desert, southeastern California," in *Desert Aeolian Processes*. Editor V. Tchakerian (London: Chapman & Hall), 37–74.

Muhs, D. R. (2004). Mineralogical Maturity in Dunefields of North America, Africa and Australia. *Geomorphology* 59, 247–269. doi:10.1016/j.geomorph.2003.07.020

Muhs, D. R., Stafford, T. W., Cowherd, S. D., Mahan, S. A., Kihl, R., Maat, P. B., et al. (1996). Origin of the Late Quaternary Dune fields of Northeastern Colorado. *Geomorphology* 17, 129–149. doi:10.1016/0169-555x(95)00100-j

Nickling, W. G., and Wolfe, S. A. (1994). The Morphology and Origin of Nabkhas, Region of Mopti, Mali, West Africa. *J. Arid Environ.* 28, 13–30. doi:10.1016/s0140-1963(05)80017-5

Nottebaum, V., Lehmkuhl, F., Stauch, G., Hartmann, K., Wünnemann, B., Schimpf, S., et al. (2014). Regional Grain Size Variations in Aeolian Sediments along the Transition between Tibetan highlands and north-western Chinese Deserts - the Influence of Geomorphological Settings on Aeolian Transport Pathways. *Earth Surf. Process. Landforms* 39, 1960–1978. doi:10.1002/esp.3590

Nottebaum, V., Lehmkuhl, F., Stauch, G., Lu, H., and Yi, S. (2015a). Late Quaternary Aeolian Sand Deposition Sustained by Fluvial Reworking and Sediment Supply in the Hexi Corridor - an Example from Northern Chinese Drylands. *Geomorphology* 250, 113–127. doi:10.1016/j.geomorph.2015.08.014

Nottebaum, V., Stauch, G., Hartmann, K., Zhang, J., and Lehmkuhl, F. (2015b). Unmixed Loess Grain Size Populations along the Northern Qilian Shan (China): Relationships between Geomorphologic, Sedimentologic and Climatic Controls. *Quat. Int.* 372, 151–166. doi:10.1016/j.quaint.2014.12.071

Pan, K., Zhang, Z., Dong, Z., Zhang, C., and Li, X. (2019). Physicochemical Characteristics of Surface Sediments of crescent-shaped Sand Dunes in the Hexi Corridor, Gansu, China. *J. Desert Res.* 39 (1), 44–51. doi:10.7522/j.issn.1000-694X.2018.00150 in Chinese with English abstract

Parsons, A. J., Wainwright, J., Schlesinger, W. H., and Abrahams, A. D. (2003). The Role of Overland Flow in Sediment and Nitrogen Budgets of mesquite Dunefields, Southern New Mexico. *J. Arid Environ.* 53, 61–71. doi:10.1006/jare.2002.1021

Pease, P. P., and Tchakerian, V. P. (2003). Geochemistry of Sediments from Quaternary Sand Ramps in the southeastern Mojave Desert, California. *Quat. Int.* 104, 19–29. doi:10.1016/s1040-6182(02)00132-5

Pease, P. P., Tchakerian, V. P., and Tindale, N. W. (1998). Aerosols over the Arabian Sea: Geochemistry and Source Areas for Aeolian Desert Dust. *J. Arid Environ.* 39, 477–496. doi:10.1006/jare.1997.0368

Pettijohn, F. J., Potter, P. E., and Siever, R. (1972). *Sand and Sandstone*. New York: Springer-Verlag.

Prins, M. A., and Vriend, M. (2007). Glacial and Interglacial Eolian Dust Dispersal Patterns across the Chinese Loess Plateau Inferred from Decomposed Loess Grain-Size Records. *Geochem. Geophys. Geosys.* 8 (7), Q07Q05. doi:10.1029/2006gc001563

Pu, Z. (2005). For the Lost Oasis - a Review of Studies on Desertification in the Hexi Corridor during the Historical Period. *Collections Essays Chin. Hist. Geogr.* 20 (1), 157–158. in Chinese.

Pye, K. (1995). The Nature, Origin and Accumulation of Loess. *Quat. Sci. Rev.* 14, 653–667. doi:10.1016/0277-3791(95)00047-x

Qiang, M., Chen, F., Zhou, A., Xiao, S., Zhang, J., and Wang, Z. (2007). Impacts of Wind Velocity on Sand and Dust Deposition during Dust Storm as Inferred from a Series of Observations in the Northeastern Qinghai-Tibetan Plateau, China. *Powder Tech.* 175 (2), 82–89. doi:10.1016/j.powtec.2006.12.020

Qiang, M., Lang, L., and Wang, Z. (2010). Do fine-grained Components of Loess Indicate Westerlies: Insights from Observations of Dust Storm Deposits at Lenghu (Qaidam Basin, China). *J. Arid Environ.* 74 (10), 1232–1239. doi:10.1016/j.jaridenv.2010.06.002

Qu, J., Huang, N., Ta, W., Lei, J., and Dong, Z. (2005). Structural Characteristics of Gobi Sanddrift and its Significance. *Adv. Earth Sci.* 20 (1), 19–23. in Chinese with English abstract.

Ren, X. (2010). Element Analysis of Surface Sediments from Active Dunes in the Minqin Oasis and its Adjacent Deserts. Ma.D Dissertation. Lanzhou: Lanzhou University. in Chinese with English abstract.

Ren, X., Liu, T., and Wang, Z. (2010). Characters of Geomorphologic Parameter about Barchans Dunes. *Res. Soil Water Conser.* 17 (1), 163–166. in Chinese with English abstract.

Ren, X., and Wang, Z. (2010). The Provenance of Eolian Sediments in Minqin Oasis, Gansu Province. *J. Ningxia Univ. Nat. Sci. Edition* 31 (1), 88–92. in Chinese with English abstract.

Ren, X., Yang, X., Wang, Z., Zhu, B., Zhang, D., and Rioual, P. (2014). Geochemical Evidence of the Sources of Aeolian Sands and Their Transport Pathways in the Minqin Oasis, Northwestern China. *Quat. Int.* 334-335, 165–178. doi:10.1016/j.quaint.2014.04.037

Rubin, D. M., and Hesp, P. A. (2009). Multiple Origins of Linear Dunes on Earth and Titan. *Nat. Geosci.* 2 (9), 653–658. doi:10.1038/ngeo610

Runnström, M. C. (2003). Rangeland Development of the Mu Us sandy Land in Semiarid China: an Analysis Using Landsat and NOAA Remote Sensing Data. *Land Degrad. Dev.* 14, 189–202. doi:10.1002/ldr.545

Sahu, B. K. (1964). Depositional Mechanisms from the Size Analysis of Clastic Sediments. *J. Sediment. Res.* 34 (1), 73–83. doi:10.1306/74d70fce-2b21-11d7-8648000102c1865d

Schettler, G., Romer, R. L., Qiang, M., Plessen, B., and Dulski, P. (2009). Size-dependent Geochemical Signatures of Holocene Loess Deposits from the Hexi Corridor (China). *J. Asian Earth Sci.* 35 (2), 103–136. doi:10.1016/j.jseaes.2009.01.003

Shi, X., Li, G., Liu, S., and Wei, Y. (2018). Dynamic Changes of Barchans Dunes and its Relationship with Meteorological Factors along Oasis Fringe in Hexi Corridor. *J. Gansu Agric. Univ.* 2, 86–93. In Chinese with English Abstract.

Stauch, G., IJmker, J., Pötsch, S., Zhao, H., Hilgers, A., Diekmann, B., et al. (2012). Aeolian Sediments on the north-eastern Tibetan Plateau. *Quat. Sci. Rev.* 57, 71–84. doi:10.1016/j.quascirev.2012.10.001

Stauch, G., Pötsch, S., Zhao, H., and Lehmkuhl, F. (2014). Interaction of Geomorphological Processes on the north-eastern Tibetan Plateau during the Holocene, an Example from a Sub-catchment of Lake Donggi Cona. *Geomorphology* 210, 23–35. doi:10.1016/j.geomorph.2013.12.014

Su, Y.-z., Wang, F., Zhang, Z.-h., and Du, M.-w. (2007). Soil Properties and Characteristics of Soil Aggregate in Marginal Farmlands of Oasis in the Middle of Hexi Corridor Region, Northwest China. *Agric. Sci. China* 6 (6), 706–714. doi:10.1016/s1671-2927(07)60103-5

Su, Y. (2007). Soil Carbon and Nitrogen Sequestration Following the Conversion of Cropland to Alfalfa Forage Land in Northwest China. *Soil Tillage Res.* 92, 181–189. doi:10.1016/j.still.2006.03.001

Sun, D., Bloemendal, J., Rea, D. K., Vandenberghe, J., Jiang, F., An, Z., et al. (2002). Grain Size Distribution Function of Polymodal Sediments in Hydraulic and Aeolian Environments and Numerical Partitioning of the Sedimentary Components. *Sediment. Geol.* 152 (3-4), 263–277. doi:10.1016/s0037-0738(02)00082-9

Sun, D., Chen, F., Bloemendal, J., and Su, R. (2003). Seasonal Variability of Modern Dust over the Loess Plateau of China. *J. Geophys. Res. Atmos.* 108 (D21), 4665. doi:10.1029/2003jd003382

Sun, J. (2002). Provenance of Loess Material and Formation of Loess Deposits on the Chinese Loess Plateau. *Earth Planet. Sci. Lett.* 203, 845–859. doi:10.1016/s0012-821x(02)00921-4

Sun, W., and Li, B. (2002). The Relation between Coupling Among the Principal Components of Desertification Factors and Desertification in Rear hills of Bashang since 1950. *Geogr. Res.* 21, 392–397. in Chinese with English abstract.

Sun, W. (2000). News & Notes. *Seismol. Res. Lett.* 71, 154–158. in Chinese with English abstract. doi:10.1785/gssrl.71.2.154

Ta, W., Xiao, H., Qu, J., Xiao, Z., Yang, G., Wang, T., et al. (2004). Measurements of Dust Deposition in Gansu Province, China, 1986-2000. *Geomorphology* 57, 41–51. doi:10.1016/s0169-555x(03)00082-5

Tapponnier, P., Meyer, B., Avouac, J. P., Peltzer, G., Gaudemer, Y., Guo, S., et al. (1990). Active Thrusting and Folding in the Qilian Shan, and Decoupling between Upper Crust and Mantle in Northeastern Tibet. *Earth Planet. Sci. Lett.* 97, 387–403. doi:10.1016/0012-821x(90)90053-z

Taylor, S. R., and McLennan, S. M. (1985). *The Continental Crust: Its Composition and Evolution*. London: Blackwell Scientific Publications.

Tengberg, A., and Chen, D. (1998). A Comparative Analysis of Nebkhas in central Tunisia and Northern Burkina Faso. *Geomorphology* 22, 181–192. doi:10.1016/s0169-555x(97)00068-8

Tengberg, A. (1995). Nebkha Dunes as Indicators of Wind Erosion and Land Degradation in the Sahel Zone of Burkina Faso. *J. Arid Environ.* 30, 265–282. doi:10.1016/s0140-1963(05)80002-3

Thomas, D. S. G., Knight, M., and Wiggs, G. F. S. (2005). Remobilization of Southern African Desert Dune Systems by Twenty-First century Global Warming. *Nature* 435, 1218–1221. doi:10.1038/nature03717

Thomas, D. S. G., and Leason, H. C. (2005). Dunefield Activity Response to Climate Variability in the Southwest Kalahari. *Geomorphology* 64, 117–132. doi:10.1016/j.geomorph.2004.06.004

Vandenberghe, J. (2013). Grain Size of fine-grained Windblown Sediment: a Powerful Proxy for Process Identification. *Earth Sci. Rev.* 121, 18–30. doi:10.1016/j.earscirev.2013.03.001

Visher, G. (1969). Grain Size Distributions and Depositional Processes. *J. Sediment. Res.* 39 (3), 1074–1106. doi:10.1306/74d71d9d-2b21-11d7-8648000102c1865d

Wang, G., Cheng, G., and Du, M. (2003c). "The Impacts of Human Activity on Hydrological Processes in the Arid Zones of the Hexi Corridor, Northwest China, in the Past 50 Years," in *Water Resources Systems - Water Availability and Global Change*. Editor S. Franks (Oxfordshire Wallingford: IAHS Publisher), 280, 93–103.

Wang, J., Li, W., Song, D., Tang, H., and Dong, G. (2004). The Analysis of Land Desertification Changing of Minqin County in Recent 30 Years. *J. Remote Sensing* 8, 282–288.

Wang, J., Liu, L., and Shen, L. (2013a). Research of Movement Laws of Barchan Dunes in the Mu Us sandy Land Based on Google Earth Software. *Remote Sensing Tech. Appl.* 28 (6), 1094–1100.

Wang, L. (2011). Surface Deposits in the Hexi Corridor and its Adjacent Areas and Implications for Provenance of Asian Dust. Ma.D Dissertation. Lanzhou: Lanzhou University. in Chinese with English abstract.

Wang, L., and Wang, Q. (2013). Elemental Compositions of Surface Deposits in the Hexi Corridor and its Adjacent Areas, Northwestern China. *Northwest. Geol.* 46 (2), 69–80. in Chinese with English abstract.

Wang, N., Zhao, Q., Hu, G., and Chen, Y. (2003a). Climatic and Humanistic Background of Desertification Process in the Recent 2000 Years in Hexi Corridor, China. *J. Desert Res.* 23, 95–100. in Chinese with English abstract.

Wang, N. A., Li, Z., Li, Y., and Cheng, H. (2013b). Millennial-scale Environmental Changes in the Asian Monsoon Margin during the Holocene, Implicated by the lake Evolution of Huahai Lake in the

Hexi Corridor of Northwest China. *Quat. Int.* 313-314, 100–109. doi:10.1016/j.quaint.2013.08.039

Wang, T. (2003). *Desert and Desertification in China*. Shijiazhuang: Hebei Science and Technology Press. in Chinese.

Wang, T., Wu, W., Xue, X., Han, Z., Zhang, W., and Sun, Q. (2004a). Spatial–temporal Changes of sandy Desertified Land during Last 5 Decades in Northern China. *Acta Geogr. Sin.* 59, 203–212. in Chinese with English abstract.

Wang, T., Wu, W., Xue, X., Zhang, W., Han, Z., and Sun, Q. (2003b). Time–space Evolution of Desertification Land in Northern China. *J. Desert Res.* 23, 230–235. in Chinese with English abstract.

Wang, T., Wu, W., Zhao, H., Hu, M., and Zhao, A. (2004b). Analyses on Driving Factors to sandy Desertification Process in Horqin Region, China. *J. Desert Res.* 24, 519–528. in Chinese with English abstract.

Wang, W. (2002). When Maowusu Became a Desert? - View through New Archaeological Finds. *Archaeol. Cult. Relics* 5, 80–85. in Chinese with English abstract.

Wang, X., Lang, L., Hua, T., Zhang, C., and Wang, Z. (2013c). Gravel Cover of Gobi Desert and its Significance for Wind Erosion: an Experimental Study. *J. Desert Res.* 33 (2), 313–319. doi:10.7522/j.issn.1000-694X.2013.00044 in Chinese with English abstract

Wang, X., Chen, F.-H., Dong, Z., and Xia, D. (2005). Evolution of the Southern Mu Us Desert in North China over the Past 50 years: an Analysis Using Proxies of Human Activity and Climate Parameters. *Land Degrad. Dev.* 16, 351–366. doi:10.1002/ldr.663

Wang, X., Chen, F., and Dong, Z. (2006a). The Relative Role of Climatic and Human Factors in Desertification in Semiarid China. *Glob. Environ. Change* 16, 48–57. doi:10.1016/j.gloenvcha.2005.06.006

Wang, X., Chen, F., Hasi, E., and Li, J. (2008a). Desertification in China: an Assessment. *Earth Sci. Rev.* 88, 188–206. doi:10.1016/j.earscirev.2008.02.001

Wang, X., Hua, T., Zhu, B., Lang, L., and Zhang, C. (2018). Geochemical Characteristics of the fine-grained Component of Surficial Deposits from Dust Source Areas in Northwestern China. *Aeolian Res.* 34, 18–26. doi:10.1016/j.aeolia.2018.07.004

Wang, X., Huang, N., Dong, Z., and Zhang, C. (2010). Mineral and Trace Element Analysis in Dustfall Collected in the Hexi Corridor and its Significance as an Indicator of Environmental Changes. *Environ. Earth Sci.* 60, 1–10. doi:10.1007/s12665-009-0164-8

Wang, X., Wang, T., Dong, Z., Liu, X., and Qian, G. (2006b). Nebkha Development and its Significance to Wind Erosion and Land Degradation in Semi-arid Northern China. *J. Arid Environ.* 65, 129–141. doi:10.1016/j.jaridenv.2005.06.030

Wang, X., Xiao, H., Li, J., Qiang, M., and Su, Z. (2008b). Nebkha Development and its Relationship to Environmental Change in the Alaxa Plateau, China. *Environ. Geol.* 56, 359–365. doi:10.1007/s00254-007-1171-2

Ward, J. H. (1963). Hierarchical Grouping to Optimize an Objective Function. *J. Am. Stat. Assoc.* 58, 236–244. doi:10.1080/01621459.1963.10500845

Wasson, R. J., and Hyde, R. (1983). Factors Determining Desert Dune Type. *Nature* 304 (5924), 337–339. doi:10.1038/304337a0

Weltje, G. J., and Prins, M. A. (2007). Genetically Meaningful Decomposition of Grain-Size Distributions. *Sediment. Geol.* 202 (3), 409–424. doi:10.1016/j.sedgeo.2007.03.007

Williams, M. (2014). *Climate Change in Deserts: Past, Present and Future*. New York: Cambridge University Press.

Wolfe, S. A., R. Muhs, D., David, P. P., and McGeehin, J. P. (2000). Chronology and Geochemistry of Late Holocene Eolian Deposits in the Brandon Sand Hills, Manitoba, Canada. *Quat. Int.* 67, 61–74. doi:10.1016/s1040-6182(00)00009-4

Wolff, D. D., and Parsons, M. L. (1983). *Pattern Recognition Approach to Data Interpretation*. New York: Pienum Press.

Wu, B., and Ci, L. (1998). Causes and Development Stages of Desertification in the Mu Us Sandland. *Chin. Sci. Bull.* 43, 2437–2440. in Chinese.

Wu, B., and Ci, L. J. (2002). Landscape Change and Desertification Development in the Mu Us Sandland, Northern China. *J. Arid Environ.* 50, 429–444. doi:10.1006/jare.2001.0847

Wu, W. (2001). Study on Processes of Desertification in Mu Us Sandy Land for Last 50 years, China. *J. Desert Res.* 21, 164–169. in Chinese with English abstract.

Wu, W., Wang, X., and Yao, F. (1997). Applying Remote Sensing Data for Desertification Monitoring in the Mu Us Sandy Land. *J. Desert Res.* 17, 415–420. in Chinese with English abstract.

Yang, T. (1985). Land Desertification on the Fringe Area of Inner Mongolia Plateau Adjacent to Heibei Province and its Rehabilitation. *J. Desert Res.* 5 (4), 25–35. in Chinese with English abstract.

Yang, X., Liang, P., Zhang, D., Li, H., Rioual, P., Wang, X., et al. (2019). Holocene Aeolian Stratigraphic Sequences in the Eastern Portion of the Desert belt (Sand Seas and sandy Lands) in Northern China and Their Palaeoenvironmental Implications. *Sci. China Earth Sci.* 62, 1302–1315. doi:10.1007/s11430-018-9304-y

Yang, X. (2006). Desert Research in Northwestern China. A Brief Review. *Geomorphologie* 12, 275–284. doi:10.4000/geomorphologie.79

Yang, X., Li, H., and Conacher, A. (2012). Large-scale Controls on the Development of Sand Seas in Northern China. *Quat. Int.* 250, 74–83. doi:10.1016/j.quaint.2011.03.052

Yang, X., Rost, K. T., Lehmkuhl, F., Zhenda, Z., and Dodson, J. (2004). The Evolution of Dry Lands in Northern China and in the Republic of Mongolia since the Last Glacial Maximum. *Quat. Int.* 118-119, 69–85. doi:10.1016/s1040-6182(03)00131-9

Yang, X., Scuderi, L., Paillou, P., Liu, Z., Li, H., and Ren, X. (2011). Quaternary Environmental Changes in the Drylands of China - A Critical Review. *Quat. Sci. Rev.* 30, 3219–3233. doi:10.1016/j.quascirev.2011.08.009

Yang, X., Zhu, B., Wang, X., Li, C., Zhou, Z., Chen, J., et al. (2008). Late Quaternary Environmental Changes and Organic Carbon Density in the Hunshandake Sandy Land, Eastern Inner Mongolia, China. *Glob. Planet. Change* 61, 70–78. doi:10.1016/j.gloplacha.2007.08.007

Yang, X., Zhu, B., and White, P. D. (2007). Provenance of Aeolian Sediment in the Taklamakan Desert of Western China, Inferred from REE and Major-Elemental Data. *Quat. Int.* 175, 71–85. doi:10.1016/j.quaint.2007.03.005

Yin, D., Qu, J., Zhao, S., Tan, L., An, Z., and Xiao, J. (2016). Amount Of Wind Erosion To Gravel Gobi Under Different Disturbing Modes. *Arid Land Geo.* 39 (3), 495–503.

Yin, D., Qu, J., Zu, R., Tan, L., and An, Z. (2014). Impact of Disturbing on Amount of Wind Erosion of sandy Gobi. *J. Desert Res.* 34 (1), 1–8. doi:10.7522/j.issn.1000-694X.2013.00279 in Chinese with English abstract

Zhang, K., Qu, J., Zu, R., and Fang, H. (2004). Wind Tunnel Simulation about the Effects of the Different Underlying Surfaces on the Features of Drifting Sand Current. *Arid Land Geogr.* 37 (3), 352–355. in Chinese with English abstract.

Zhang, L., and Ren, G. (2003). Change in Dust Storm Frequency and the Climatic Controls in Northern China. *Acta Meteorol. Sin.* 61 (6), 744–750. in Chinese with English abstract.

Zhang, X., Wang, X., and Yan, P. (2008). Re-evaluating the Impacts of Human Activity and Environmental Change on Desertification in the Minqin Oasis, China. *Environ. Geol.* 55, 705–715. doi:10.1007/s00254-007-1022-1

Zhang, Z., and Dong, Z. (2014). Dune Field Patterns and Wind Environments in the Middle Reaches of the Heihe Basin. *J. Desert Res.* 34 (2), 332–341. doi:10.7522/j.issn.1000-694X.2013.00323 in Chinese with English abstract

Zhang, Z., and Dong, Z. (2015). Grain Size Characteristics in the Hexi Corridor Desert. *Aeolian Res.* 18, 55–67. doi:10.1016/j.aeolia.2015.05.006

Zhang, Z., Dong, Z., Li, J., Qian, G., and Jiang, C. (2016). Implications of Surface Properties for Dust Emission from Gravel Deserts (Gobis) in the Hexi Corridor. *Geoderma* 268, 69–77. doi:10.1016/j.geoderma.2016.01.011

Zhang, Z., Dong, Z., Zhang, C., Qian, G., and Lei, C. (2017). The Geochemical Characteristics of Dust Material and Dust Sources Identification in Northwestern China. *J. Geochem. Explor.* 175, 148–155. doi:10.1016/j.gexplo.2016.11.006

Zhang, Z., Pan, K., Zhang, C., and Liang, A. (2020). Geochemical Characteristics and the Provenance of Aeolian Material in the Hexi Corridor Desert, China. *Catena* 190, 104483. doi:10.1016/j.catena.2020.104483

Zhao, Y. (1981). Mu Us Desert Evolution in Historical Periods. *Hist. Geogr.* 1, 34–47. in Chinese.

Zhu, B. (2007). Geochemistry, Hydrochemistry and Sedimentology of the Taklamakan Desert in Tarim Basin, NW China. Ph.D doctoral dissertation. Beijing: Institute of Geology and Geophysics Chinese Academy of Sciences.

Zhu, B.-Q., and Wang, Y.-L. (2016). Statistical Study to Identify the Key Factors Governing Ground Water Recharge in the Watersheds of the Arid Central Asia. *Environ. Monit. Assess.* 188, 66. doi:10.1007/s10661-015-5075-4

Zhu, B.-Q., Yu, J.-J., Rioual, P., and Ren, X.-Z. (2014). Particle Size Variation of Aeolian Dune Deposits in the Lower Reaches of the Heihe River basin, China. *Sediment. Geol.* 301, 54–69. doi:10.1016/j.sedgeo.2013.12.006

Zhu, B., Wang, X., and Rioual, P. (2017). Multivariate Indications between Environment and Ground Water Recharge in a Sedimentary Drainage basin in Northwestern China. *J. Hydrol.* 549, 92–113. doi:10.1016/j.jhydrol.2017.03.058

Zhu, B., and Yang, X. (2009). Chemical Weathering of Detrital Sediments in the Taklamakan Desert, Northwestern China. *Geogr. Res.* 47 (1), 57–70. doi:10.1111/j.1745-5871.2008.00555.x

Zhu, B., and Yu, J. (2014). Aeolian Sorting Processes in the Ejina Desert basin (China) and Their Response to Depositional Environment. *Aeolian Res.* 12, 111–120. doi:10.1016/j.aeolia.2013.12.004

Zhu, Z., and Chen, G. (1994). *Sandy Desertification in China*. Beijing: Science press. in Chinese.

Zhu, Z., Chen, Z., Wu, Z., Li, J., Li, B., and Wu, G. (1981a). *Study on the Geomorphology of Wind-Drift Sands in the Taklamakan Desert*. Beijing: Science Press. in Chinese.

Zhu, Z. (1999). *Deserts, Desertification, Land Degradation and Strategies for Rehabilitation in China*. Beijing: Environmental Press. in Chinese.

Zhu, Z., Guo, H., and Wu, Q. (1964). Study on the Movement of Dunes Near Oases in the Southwest of the Taklimakan Desert. *Acta Geogr. Sin.* 30 (1), 35–50.

Zhu, Z., Liu, S., and Xiao, L. (1981b). The Characteristics of the Environment Vulnerable to Desertification and the Ways of its Control in Steppe Zone. *J. Desert Res.* 1, 2–12. in Chinese with English abstract.

Zhu, Z. (1985). Status and Trend of Desertification in Northern China. *J. Desert Res.* 5, 3–11. in Chinese with English abstract.

Zhu, Z., and Wang, T. (1992). Theory and Practice on sandy Desertification in China. *Quat. Sci.* 2, 97–106. in Chinese with English abstract.

Zhu, Z., Wu, Z., Liu, S., and Di, X. (1980). *An Outline of Chinese Deserts*. Beijing: Science Press. in Chinese.

Zimbelman, J. R., and Williams, S. H. (2002). Geochemical Indicators of Separate Sources for Eolian Sands in the Eastern Mojave Desert, California, and Western Arizona. *Geol. Soc. Am. Bull.* 114, 490–496. doi:10.1130/0016-7606(2002)114<0490:giossf>2.0.co;2

Conflict of Interest: The authors declare that the research was conducted in the absence of any commercial or financial relationships that could be construed as a potential conflict of interest.

frontiers
in Earth Science

ORIGINAL RESEARCH
published: 23 August 2021
doi: 10.3389/feart.2021.732441

Modern Pollen Rain in the Tibetan Plateau

Caiming Shen[1,2,3]*, Kam-biu Liu[2], Lingyu Tang[3] and Jonathan T. Overpeck[4]

[1]Yunnan Key Laboratory of Plateau Geographical Processes and Environmental Changes, Faculty of Geography, Yunnan Normal University, Kunming, China, [2]Department of Oceanography and Coastal Sciences, College of the Coast and Environment, Louisiana State University, Baton Rouge, LA, United States, [3]Nanjing Institute of Geology and Paleontology, Chinese Academy of Sciences, Nanjing, China, [4]School for Environment and Sustainability, University of Michigan, Ann Arbor, MI, United States

The basis for the interpretation of fossil-pollen assemblages in terms of vegetation and climate is the present-day relationship of vegetation and climate to pollen rain. Detailed modern pollen spectra from the Tibetan Plateau are described here to explore the relationship between modern pollen rain and vegetation. Two hundred and thirty four (234) pollen surface samples were collected from moss polsters, top soil, and lake surface sediments from forests, shrublands, shrub meadows, meadows, steppes, and deserts in the Tibetan Plateau. Pollen assemblages from each vegetation type are detailed described using pollen percentage data, and compared descriptively and numerically using cluster analysis. Pollen spectra from forests are characterized by high percentages of tree pollen types including *Pinus, Abies*, *Picea, Quercus,* and *Betula*. Pollen spectra from shrublands have highest amounts of shrub pollen. The dominants of shrublands, such as *Rhododendron*, *Juniperus*, *Salix*, and shrub *Quercus*, are well-represented in most of these pollen spectra. Pollen spectra from shrub meadows have less shrub pollen than those from shrublands, but more than those from meadows, steppes and deserts. The most frequent shrub pollen in this vegetation type is Rosaceae. Most of pollen spectra from shrub meadows are dominated by Cyperaceae pollen. Pollen spectra from meadows are characterized by the very high percentages of Cyperaceae pollen. The highest amounts of Cyperaceae pollen occur in pollen spectra from alpine-marshy meadows. Pollen spectra from *Stipa* steppes are characterized by the highest percentages of Poaceae pollen, and high Cyperaceae pollen percentages, whereas pollen spectra from *Artemisia* steppes have the highest percentages of *Artemisia* pollen. Pollen spectra from arid deserts are dominated by Chenopodiaceae. Main vegetation types can be distinguished by their modern pollen rain, i.e., modern pollen spectra do reflect the modern vegetation at local and regional scale in the Tibetan Plateau. This modern pollen database can thus be used to explore the pollen/vegetation and pollen/climate relationships by a variety of numerical methods.

Keywords: modern pollen rain, forest, shrubland, shrub meadow, meadow, steppe, desert, the Tibetan plateau

Edited by:
Feng Cheng,
University of Nevada, Reno,
United States

Reviewed by:
Yunfa Miao,
Northwest Institute of Eco-Environment and Resources (CAS),
China
Haicheng Wei,
Qinghai Institute of Salt Lakes (CAS),
China

****Correspondence:***
Caiming Shen
cmshen@hotmail.com

Specialty section:
This article was submitted to Quaternary Science, Geomorphology and Paleoenvironment,
a section of the journal
Frontiers in Earth Science

Received: *29 June 2021*
Accepted: *11 August 2021*
Published: *23 August 2021*

Citation:
Shen C, Liu K, Tang L and Overpeck JT (2021) Modern Pollen Rain in the Tibetan Plateau.
Front. Earth Sci. 9:732441.
doi: 10.3389/feart.2021.732441

INTRODUCTION

The basis for the interpretation of fossil-pollen assemblages in terms of vegetation and climate is the present-day relationship of vegetation and climate to pollen rain (Webb and Bryson, 1972; Liu and Lam, 1985; Bartlein et al., 1986; Delcourt et al., 1987; Gajewski et al., 2002; Schofield et al., 2007; Birks et al., 2010; Seppä et al., 2010; Davis et al., 2013; Ge et al., 2017). In China, modern pollen studies are limited by extensive human impacts on the modern vegetation (Liu, 1988; Xu et al., 2016). Although some studies of surface pollen samples were conducted before this century, most of these earlier studies focused on relation of pollen rain to regional vegetation and climate in some mountainous regions such as Changbaishan and Xiaoxinanling Mountains in northeastern China (Zhou et al., 1983; Shen and Tang, 1992; Li et al., 2000), Zhongtiao Mountain in northern China (Yao, 1989), Shengnongjia Mountain in central China (Li, 1991), the West Kunlun Mountains and Haoniu Mountains in western China (Weng et al., 1989; Jarvis and Clay-Poole, 1992). In this century, Chinese and western palynologists have made great efforts in developing a modern pollen database and applying it into vegetation and climate reconstructions (e.g., Members of China Quaternary Pollen Database, 2001; Yu et al., 2001; Shen et al., 2006, 2008a, b; Zheng et al., 2008, 2014; Herzschuh et al., 2010; Lu et al., 2011; Xu et al., 2016; Chen et al., 2017; Liang et al., 2020).

The Tibetan Plateau (TP), the least anthropologically-disturbed region in China, provides an unusual opportunity to study the relationship between modern pollen rain and vegetation. In the TP, most of the earlier work on pollen surface samples was conducted separately and locally as part of paleoenvironmental studies (e.g., Li and Liu, 1988; Jarvis and Clay-Poole, 1992; Sun et al., 1993; Van Campo and Gasse, 1993; Xiao et al., 1996). In this century, modern pollen studies were extensively conducted in the TP (e.g., Yu et al., 2001; Shen et al., 2006; Herzschuh et al., 2010; Lu et al., 2011; Ma et al., 2017; Liang et al., 2020). These studies examined the spatial distribution of pollen taxa and analyzed the relationship between the modern pollen assemblages and regional vegetation and climate based on modern pollen data sets from moss polsters, top soil, and lake surface sediments. However, none of them gave a detailed description of modern pollen spectra and vegetation at sampling sites involving most of vegetation types in the TP.

This paper describes the modern pollen spectra of the TP as recorded in a network of 234 pollen surface samples. The samples were derived from a variety of vegetation types from monsoonal climate regions to arid and semi-arid regions, including forests, shrublands, shrub meadows, meadows, steppes, and deserts. The relationship between modern pollen rain and vegetation types is examined. This study provides basic information for the quantitative analysis of the relationships among modern pollen rain, vegetation, and climate as well as the quantitative reconstruction of paleovegetation and paleoclimate (Shen et al., 2006, 2008a, b; Lu et al., 2011; Liang et al., 2020).

MATERIAL AND METHODS

Two hundred and thirty four (234) pollen surface samples were collected from moss polsters, top soil, and lake surface sediments in the TP in the summers of 1993–1995, 1999 and 2001 (**Figure 1** and **Supplementary Material**). Pollen sites are located between 29 and 40°N and 90–104°E, and cover an elevation range from 1,100 m to 5,230 m (**Figure 2**). Samples were processed according to the standard procedure described by Faegri and Iversen (1975). The procedure involves treatment with cold 10% HCl, hot 10% KOH, hot 50% HF, and acetolysis solution, staining with safranin, dehydration with tertiary butyl alcohol, and mounting in silicone oil. Prior to chemical treatment, moss polsters and soils were stirred in distilled water and sieved to remove coarse detritus and sand. More than 400 pollen grains were counted for most samples except for some desert samples that contain few pollen grains.

Pollen percentages are calculated from a total pollen sum. ArcGIS and TILIA software are used for mapping, plotting of pollen diagrams, and statistical analysis of modern pollen spectra.

VEGETATION OF THE TP

The TP, known as the “roof of the world”, is a vast highland with an area of nearly 2×10^6 km^2 situated at an average elevation of over 4,000 m above sea level. Its climate shows a marked southeast to northwest precipitation gradient due to the decreasing influence of the Southwest Asian monsoon. Following the steep altitudinal and latitudinal climatic gradient on the TP, the vegetation changes from forests to high-cold alpine meadows and shrublands, and to alpine steppes and desert. Based on a large-scale vegetation map of the whole plateau (Institute of Geography, 1990), ten major vegetation regions are recognized (**Figure 1**).

A. Tropical rainforest-seasonal rainforest: This vegetation type occurs on the south-facing slopes and river valleys of the East Himalayas. The climate is tropical and monsoonal with high annual precipitation (2000–3,000 mm) and a high mean annual temperature (>20°C). Tropical rainforest dominated by *Dipterocarpus, Artocarpus, Canarium, Shorea*, and *Tetrameles* occurs at elevations lower than 600 m. Seasonal rainforest consisting of *Dysoxylum, Chukrasia, Terminalia, Lagerstroemia,* and *Altingia* occurs at elevations of 600–1,000 m. Above 1,000 m are subtropical monsoonal or montane rain forests dominated by a variety of evergreen oaks (*Cyclobalanopsis, Quercus*), *Lithocarpus, Castanopsis*, mixed with subalpine conifers such as *Picea, Abies*, and *Tsuga* (Wu, 1980; Tibetan Investigation Group, 1988).

B. Subalpine conifer forest: It occurs in the southeastern part of the Plateau, which is deeply dissected by several NNW-SSE trending rivers. These river gorges punctuate the Himalayan barrier and permit the SW Indian Monsoon to penetrate deeply into the TP and the western interior parts of China. The annual precipitation ranges from 400 to 1,200 mm and is concentrated in the monsoon season between May and October (Wu, 1980). The mean annual temperature varies from 3°C to 12°C, with a coldest air temperature of −20.7°C and a warmest air temperature of 32.7°C. Coniferous trees are the dominants in this region, which are represented by five genera— *Abies, Picea, Pinus, Tsuga,* and *Juniperus*. The formation also contains an admixture of deciduous hardwood genera such as *Alnus*, *Betula,* and

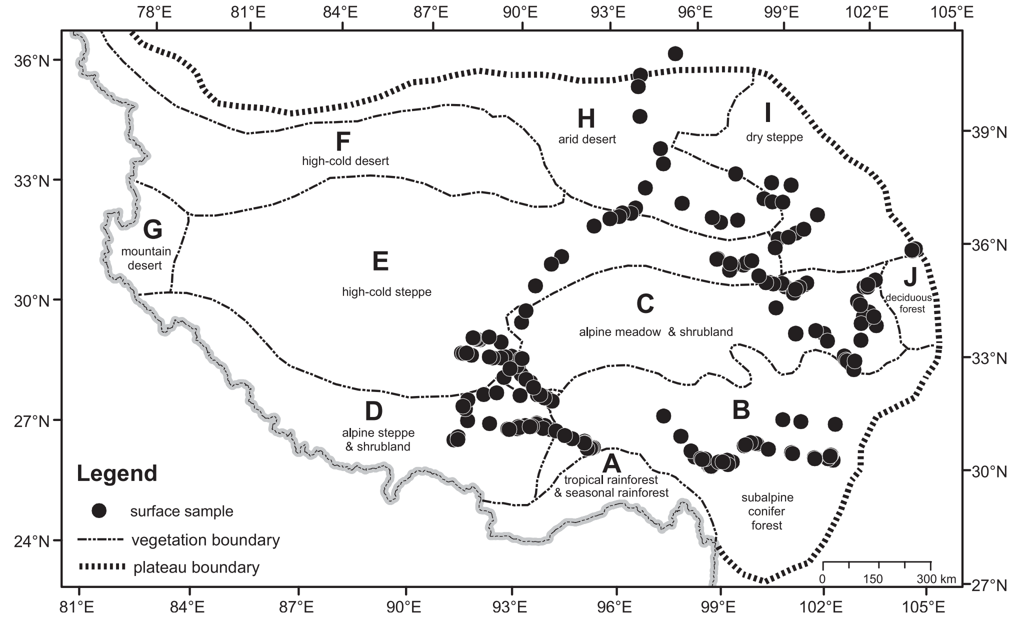

FIGURE 1 | The vegetation of the TP and location of surface samples.

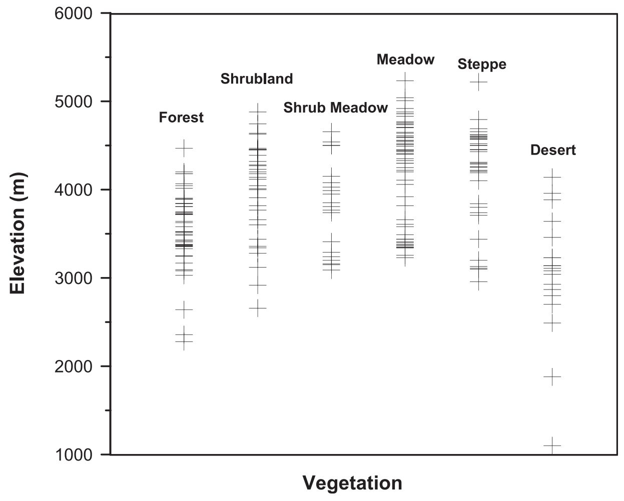

FIGURE 2 | Elevation at which the surface sample sites are located.

Populus; these are successional replacements of the coniferous forest after natural or anthropogenic disturbance. The conifer forest zone, dominated by *Abies*, *Picea*, and *Juniperus*, typically occurs between 3,000 and 4,000 m elevation. With an increase in elevation, the conifer forest zone changes to a shrub zone composed of *Rhododendron* shrubs together with rosaceous genera, and an alpine meadow zone. Evergreen needle-leaved and deciduous broad-leaved mixed forests, consisting of *Pinus, Tsuga, Quercus, Acer, Betula,* and *Corylus*, exists below the conifer forest zone. In addition, arid desert also occurs in hot and dry river valleys. It is mainly composed of *Pertya, Cotoneaster, Androsace, Artemisia, Chenopodium*, and *Miscanthus* (Editorial Broad of Sichuan's Vegetation, 1980).

C. Alpine meadow and shrubland: These vegetation types occur on the relatively open and flat terrains in the eastern part of the Plateau at elevations between 3,500 and 5,000 m. This region is characterized by cold and wet climatic conditions, with a mean annual temperature of −4°C to 3°C, coldest month temperature of −17 to −7°C, and warmest month temperature of 5–13°C. The annual precipitation varies between 350 and 700 mm, which is mostly brought by the summer monsoon penetrating into this region through the river gorges. The shrubland consists of *Dasiphora, Salix, Sibiraea, Rhododendron, Juniperus, Potentilla,* and *Caragana*. Alpine meadow is dominated by *Kobresia* spp, together with *Polygonum, Thalictrum, Anaphalis, Artemisia,* and some species of Poaceae, Asteraceae, and Caryophyllaceae (Editorial Broad of Sichuan's Vegetation, 1980).

D. Alpine steppe and shrubland: These vegetation types occur in southern Tibet under the rain shadow of the Himalayas, where the annual precipitation ranges from 230 to 450 mm. The temperature is relatively high compared with that in alpine meadow, with a mean annual temperature of 0°C to 8°C, coldest month temperature of −12°C to −2°C, and warmest month temperature of 10°C to 16°C. The river valleys and mountains below 4,000 m in elevation are covered by *Sophora moorcroftiana* shrub and *Aristida triseta* steppe. The mountains at elevations of 4,000–4,700 m are occupied by alpine steppe dominated by *Stipa bungeana, S. capillacea, Artemisia wellbyi, A. stracheyii,* and shrubland dominated by *Caragana, Potentilla,* and *Juniperus*. An alpine meadow zone above 4,700 m elevation is composed of *Kobresia* and *Polygonum*.

E. High-cold steppe: This vegetation type occupies a vast region at elevations of 4,400–5,400 m in the interior of the Plateau. The climate is cold and dry, with a mean annual temperature of −6°C to 0°C and an annual precipitation of 150–300 mm. *Stipa purpurea, S. basiplumosa, Carex moorcroftii,* and *Artemisia wellbyi* are dominants of the high-cold steppe. Frequent companion components include *Stipa penicillata, S. glareosa, Carex montis-everestii, Festuca ovina, Poa* spp., *Artemisia minor,* and *Astraglus heydei*. Usually there are some cushion plants (e.g., *Arenaria musciformis, Androsace stapete, Thylacospermum rupifragum*) and mesic herbs such as *Kobresia pygmaea* (Chang, 1981; Wang, 1988).

F. High-cold desert: High-cold desert occurs in the northwestern part of the TP, where the elevation is over 5,000 m. This region experiences the coldest and driest climate of the Plateau. The mean annual temperature is about −8 to −10°C. Mean monthly temperature is lower than 0°C for 9–10 months. The mean annual precipitation is only 20–50 mm (Chang, 1981). The dominants of this vegetation type are cushion minor semi-shrubs adapted to extremely cold and dry climate. The representative community is composed of *Ceratoides compacta,* with few companion species such as *Ajania trilobata, Arenaria monticola, Carex moorcroftii, Hedinia tibetica, Oxytropis densa, Pegaeophyton scapiflorum, Stipa basiplumosa,* and *Thylacospemum caespitosum*. The only woody plant in the region is *Myricaria hedinii*, which grows along rivers (Chang, 1981; Wang, 1988).

G. Mountain desert: This vegetation type occupies the mountains and valleys on the western edge of the Plateau between the northwestern Himalayas and the Karakoram ranges. The center of the summer thermal low of Tibet is located in this region, the driest and hottest region on the Plateau. The July mean temperature is 15°C. The annual precipitation is no more than 50–75 mm (Chang, 1981). The desert community consists of suffrutescent *Ceratoides lateens*, *Ajania fruticulosa,* and the endemic perennial *Christolea crassiflora*. Some feathergrasses (e.g., *Stipa glareso, S. subsessiliflora, S. breviflora*) and xeric shrubs (e.g., *Ephedra gerardiana* and *Caragana versicolor*) are present in the desert community where the climate becomes slightly more humid.

H. Arid desert: In the northern part of the Plateau lies the Qaidam Basin. Its general elevation is 2,600–3,000 m, ca. 2000 m lower than the surrounding mountains. The annual precipitation decreases from 200 mm in the east to 20 mm in the west. The annual mean temperature is 1°C to 5°C, with a coldest monthly temperature of −15°C to −10°C and a warmest monthly temperature of 15°C to 17.5°C. The arid desert is dominated by Chenopodiaceae, *Artemisia, Ephedra, Tamarix (T. laxa, T. ramosissima), Nitraria (N. tangutorum, N. sibirica), Populus, Calligonum,* Poaceae, Asteraceae, Fabaceae, Polygonaceae, and Cyperaceae (Wu, 1980).

I. Dry steppe: This vegetation type occurs in the northeastern part of the Plateau at elevations of 2000–5,000 m, where the annual precipitation ranges from 300 to 500 mm, and the mean annual temperature is −4°C to 4°C. In the south of this region, the vegetation is dry steppe, dominated by *Stipa bugeana, S. breviflora, S. purpurea, Orinus kokonorica, Leymus secalinus, Artemisia scoparia, Achnatherum splendens,* and *Carex ivanova*. The high mountains to the north support alpine meadows dominated by *Kobresia*. *Picea and Juniperus* forests occur between 2,400 and 4,100 m on the northern and wetter southeastern slopes of mountains in the northern and eastern margins of the region.

J. Warm temperate deciduous broadleaved forest: This vegetation type grows in the mountains on the eastern edge of the Plateau. The general elevation of the mountains is above 2,800 m. The climate is warm and wet, with cold winters and cool summers. The annual precipitation is 500–750 mm, of which 70–80% is concentrated in the months of May to September. The mean annual temperature at an elevation of 2,300 m is about 8°C. Below 2,500 m is the coniferous and deciduous broadleaved mixed forest zone, characterized by *Quercus, Tilia, Acer, Pterocarya, Betula, Carpinus, Pinus, Tusga, Abies,* and *Picea*. Between 2,500 and 3,800 m occurs a subalpine conifer forest zone, dominated by *Abies, Picea,* and *Rhododendron.* Above 3,800 m is an alpine meadow zone, consisting of Cyperaceae, Poaceae, and Asteraceae.

MODERN POLLEN RAIN IN THE TP

Although theoretically each modern pollen sample can be assigned to a major vegetation region based on its geographical location, this is difficult and unsound in practice because the vegetation boundaries are transitional and hard to recognize in the field. Moreover, azonal vegetation communities can and often occur locally within a major vegetation region; for example, isolated stands of forest can occur near the ecotone within the alpine meadow region, and shrub meadow or even hot valley deserts can occur within the subalpine conifer forest region. The regional vegetation pattern is further complicated by the altitudinal vegetation zonation. Due to the great variations in elevation, a wide variety of vegetation types can occur within a vegetation region. Therefore, in the field, each pollen sample was classified into a vegetation type (e.g., oak forest, *Rhododendron* shrub, marshy meadow) according to the local vegetation community from which it is derived, and the characteristic or common plant taxa that occur locally were recorded at each site (**Supplementary Material**). These local vegetation communities were then aggregated into six main vegetation groups — forest, shrubland, shrub meadow, meadow, steppe, and desert. Among the 234 pollen surface samples, 50 are derived from forest, 37 from shrubland, 20 from shrub meadow, 66 from meadow, 42 from steppe, and 19 from desert. Based on their palynological signatures, the pollen samples from each major vegetation type are classified into several sub-groups by means of cluster analysis (Grimm, 1987). Here we describe the main features of pollen spectra in each vegetation type.

Forest

The pollen sample sites are located in the subalpine conifer forest and warm temperate deciduous broadleaved forest regions. The

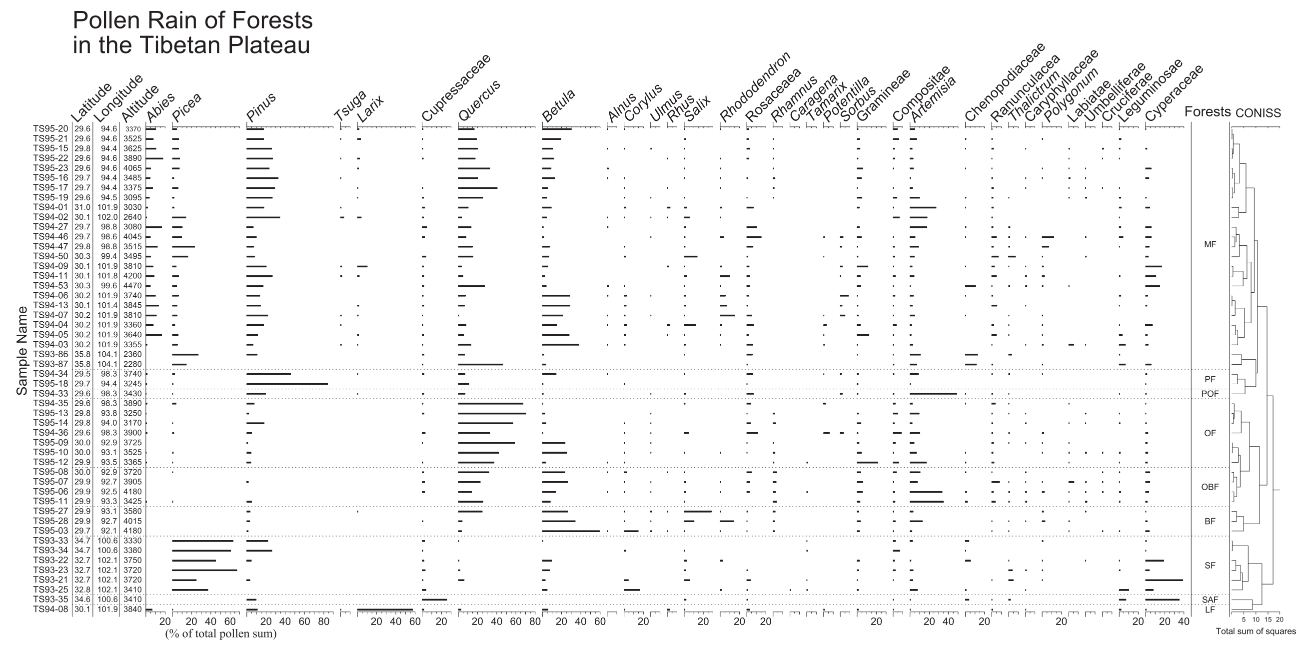

FIGURE 3 | Pollen percentage diagram for surface samples from forests in the Tibetan Plateau. Forest types are: subalpine mixed forest (MF), pine forest (PF), pine and oak forest (POF), oak forest (OF), oak and birch forest (OBF), birch forest (BF), spruce forest (SF), juniper forest (JF), and larch forest (LF).

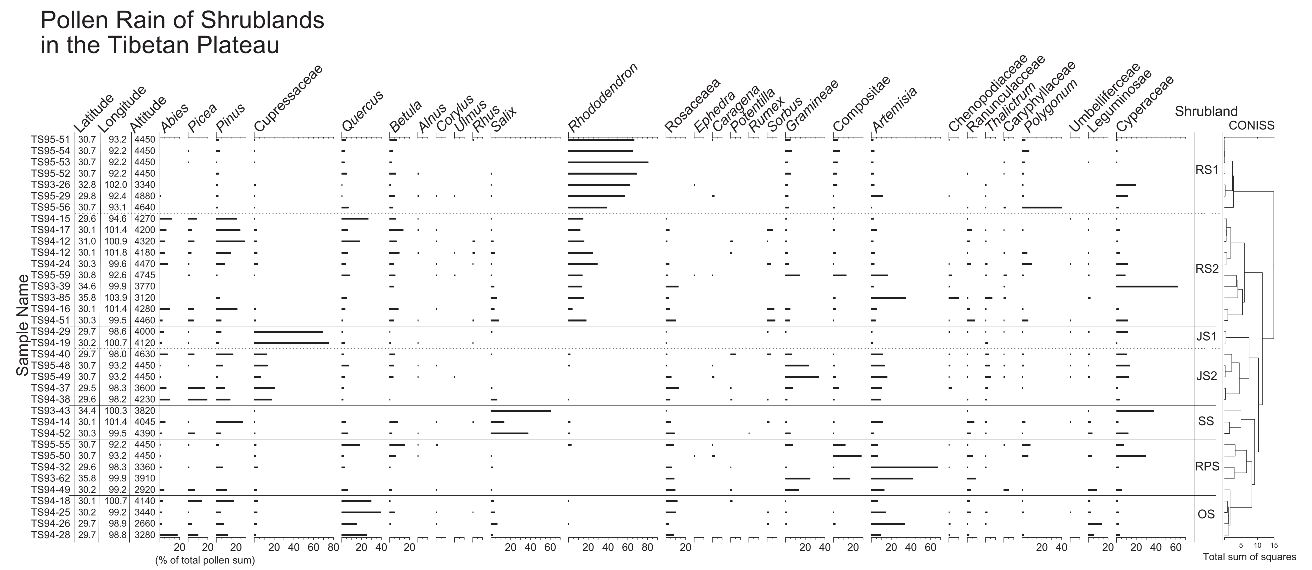

FIGURE 4 | Pollen percentage diagram for surface samples from shrublands in the TP. Shrubland types include rhododendron shrub (RS), juniper shrub (JS), willow shrub (WS), rosaceous shrub (RPS) and alpine oak shrub (OS).

pollen spectra are characterized by high percentages of tree pollen (**Figure 3**). As expected, the main tree pollen types are *Pinus, Abies*, *Picea, Quercus,* and *Betula*. Common herbaceous pollen types are *Artemisia*, Poaceae, Cyperaceae, Asteraceae, *Thalictrum* and Ranunculaceae. Pollen of shrubs such as *Salix, Rhododendron,* and Rosaceae are frequently present. Pollen spectra can be classified into eight groups based on the local vegetation communities from which the surface samples were collected.

Pollen spectra from subalpine mixed forest (MF) are dominated by tree pollen, including *Pinus*, *Picea, Abies*, *Quercus,* and *Betula.* Other tree pollen such as *Tsuga, Larix, Alnus*, and *Corylus* are also present in most of the pollen samples. The highest percentages of *Picea, Pinus, Quercus,* and *Betula*

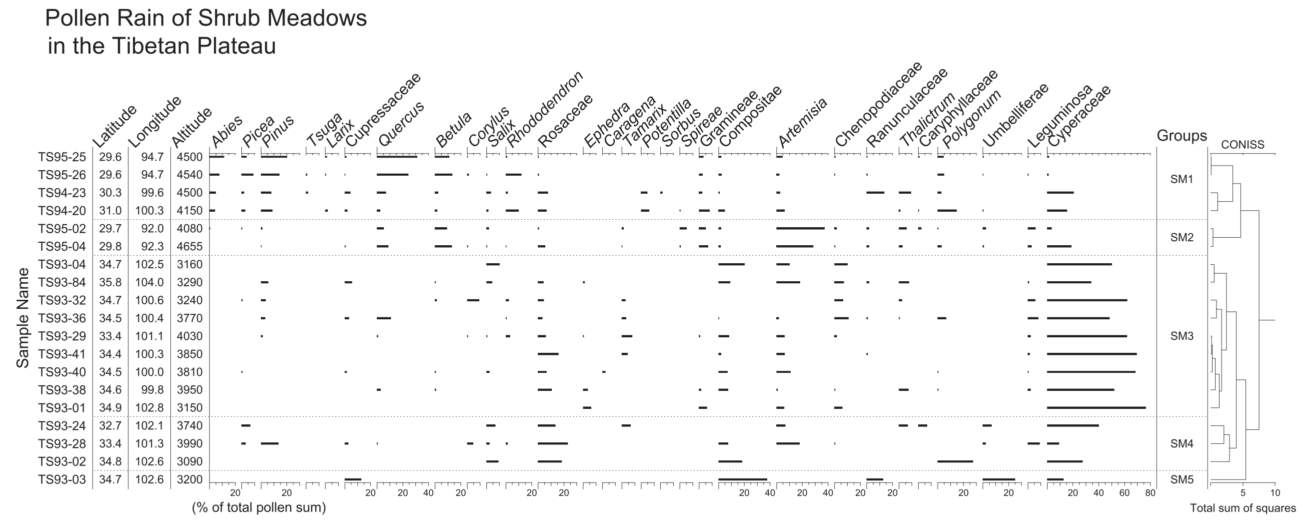

FIGURE 5 | Pollen percentage diagram for surface samples from shrub meadows in the TP. Samples of groups SM1 and SM2 are from the southeast, and the others (SM3, SM4, and SM5) from the northeast.

occur in pollen spectra from spruce forest (SF), pine forest (PF), oak forest (OF), and birch forest (BF), respectively. One sample taken from larch forest (LF) has up to 60% *Larix* pollen, whereas one sample taken from *Juniperus* forest (JF) contains more than 25% Cupressaceae pollen. The pollen spectra from oak-birch forest (OBF) are mainly composed of tree pollen from *Quercus* and *Betula,* but herbaceous pollen like *Artemisia* can be abundant in some samples. In the pollen spectra from pine-oak forest (POF), *Pinus* and *Quercus* are common tree pollen, but the most frequent pollen is *Artemisia.*

Shrubland

Shrublands generally occur in forest regions above the treeline; few can be found in meadow regions. Pollen spectra (**Figure 4**) are characterized by high percentages of shrubs such as *Rhododendron, Salix, Quercus* and Cupressaceae (probably *Juniperus*). According to their local vegetation types observed in field, pollen spectra are classified into five groups.

Two subgroups of pollen spectra from *Rhododendron* shrublands (RS) can be recognized based on pollen percentages. Pollen spectra of subgroup RS1 are dominated by *Rhododendron* pollen, accounting for more than 50% of total pollen sum. Common herbaceous pollen types include Poaceae, Asteraceae, *Artemisia, Polygonum,* and Cyperaceae. Percentages of tree pollen are low, and only *Pinus, Quercus,* and *Betula* pollen are frequently present. Pollen spectra from subgroup RS2 contain somewhat lower percentages of *Rhododendron* pollen, but tree pollen such as *Abies, Picea, Pinus, Quercus,* and *Betula* occur more prominently. Pollen spectra from juniper shrublands (JS) are characterized by high percentages of Cupressaceae pollen. Two pollen spectra (subgroup JS1) are completely dominated by Cupressaceae (>70%). Other pollen spectra (subgroup JS2) have less Cupressaceae pollen (10–30%), but more tree pollen such as *Abies, Picea,* and *Pinus,* and more herbaceous pollen from Poaceae and *Artemisia.* The samples from willow shrublands (WS) have the highest percentages of *Salix* pollen. Relatively low percentages of Rosaceae pollen and high percentages of herbaceous pollen (*Artemisia,* Poaceae, Asteraceae, and Cyperaceae) distinguish the pollen spectra of rosaceous shrublands (RPS) from the others. Pollen spectra from alpine dry oak shrublands (OS) are characterized by the highest *Quercus* pollen percentages among pollen spectra from shrublands, and relatively high percentages of *Abies, Picea, Pinus,* Rosaceae, and *Artemisia.*

Shrub Meadow

Shrub meadows occur in the vegetation regions of alpine meadow and shrubland. The main components of shrubs are similar to those in shrublands, including *Rhododendron, Salix, Juniperus,* and *Potentilla*. Shrubs are scattered amid meadow herbs as accompanying components, thus they cannot be used as indicators to further distinguish meadows. Pollen spectra from shrub meadows can be classified into five distinct groups (**Figure 5**) based on the result of cluster analysis on pollen percentages.

Group SM1 is characterized by its abundance of arboreal pollen, and by moderate amounts of herbaceous pollen such as *Artemisia*, Cyperaceae, Ranunculaceae, *Thalictrum,* and *Polygonum*. The most frequent tree pollen is *Quercus,* followed by *Pinus, Abies, Picea, Betula*, and *Larix.* Common shrub pollen types are Rosaceae, *Salix, Rhododendron*, and *Potentilla.* Group SM2 has the highest amounts of *Artemisia* in shrub meadows, together with moderate amounts of *Quercus, Betula,* Poaceae, and Cyperaceae. Group SM3 is readily distinguished by its highest Cyperaceae pollen (more than 50% for most samples), low amounts of tree pollen, and some shrub pollen such as Rosaceae, *Salix,* and *Tamarix*. Group SM4 is well defined by the highest amounts of Rosaceae pollen (15–25%). The dominants of herbaceous pollen in this group are Cyperaceae, *Polygonum, Artemisia,* and Asteraceae. Group SM5 contains only

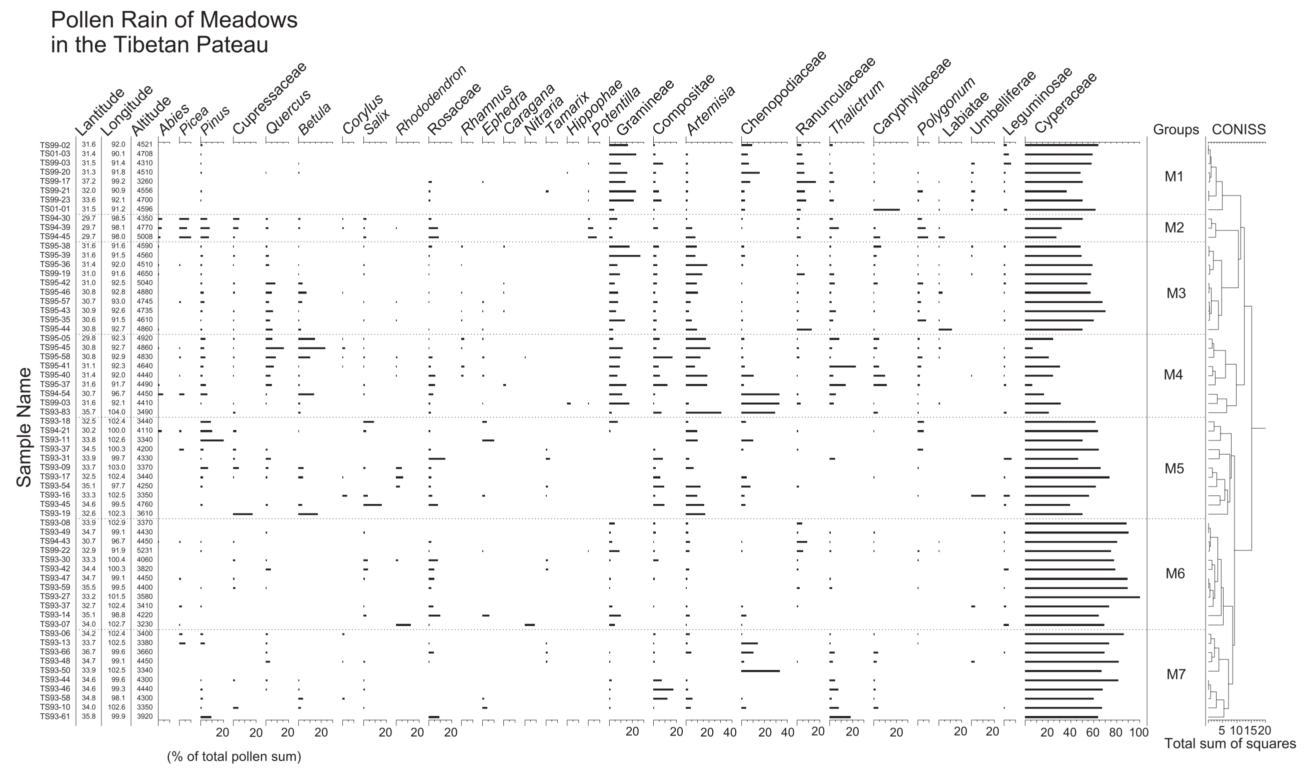

FIGURE 6 | Pollen percentage diagram for surface samples from meadows in the TP. Samples of groups M1-3, M4, M5-7 are mainly from alpine meadows, steppe-meadows, and alpine marshy meadows, respectively.

one sample. This spectrum is dominated by Asteraceae pollen, together with Cupressaceae, Apiaceae, Cyperaceae, and Ranunculaceae pollen.

Meadow

In the TP, alpine meadow communities occur not only in the alpine meadow and shrubland regions, but also in areas above treeline in the tropical rainforest-seasonal rainforest and subalpine conifer forest regions. Except in a few samples, pollen spectra are characterized by high percentage of Cyperaceae (more than 50%) and low percentages of arboreal pollen (**Figure 6**). Seven groups are recognized by cluster analysis of pollen percentages.

Pollen spectra of group M1 are dominated by Cyperaceae pollen, together with Poaceae, Asteraceae, Chenopodiaceae, and Ranunculaceae. Very few arboreal pollen grains are found in pollen spectra of this group. In group M2, pollen percentages of Cyperaceae, Poaceae, Chenopodiaceae, and Ranunculaceae decrease markedly, whereas arboreal pollen such as *Abies, Picea, Pinus,* Rosaceae, and *Potentilla* increase. Cyperaceae dominates the pollen spectra of group M3, with its pollen percentages exceeding 60%. The pollen spectra of group M3 also contain more *Artemisia, Quercus, Betula*, and less Poaceae and Chenopodiaceae than those of group M1. The lowest percentages of Cyperaceae pollen among pollen spectra from meadows distinguish group M4. Some pollen spectra of group M4 also have the highest amounts of Chenopodiaceae, *Artemisia, Thalictrum, Quercus,* and *Betula* pollen. In group M5, 50–75% of the pollen sum are Cyperaceae pollen. *Pinus, Artemisia,* Rosaceae and Asteraceae pollen are present in modest amounts, whereas Poaceae, Ranunculaceae, *Thalictrum,* and Caryophyllaceae pollen are absent in the most samples. Pollen spectra of group M6 are characterized by the highest amounts of Cyperaceae pollen (70–100%) in the meadow samples. Comparing to group M6, pollen spectra of group M7 have slightly less Cyperaceae pollen, but more Chenopodiaceae, Asteraceae, and *Thalictrum* pollen.

Steppe

Steppe is the most widely-distributed vegetation type in the TP. Three types of steppes, i.e., alpine steppe, high-cold steppe, and dry steppe, can be found in the southern, central and northeastern parts of the Plateau. Pollen spectra from different steppe types have completely different characteristics (**Figure 7**). The dominants are herbs, including Poaceae, *Artemisia*, Cyperaceae, Chenopodiaceae and Asteraceae. The samples can be classified into four groups by cluster analysis.

Pollen spectra of group S1 are dominated by Cyperaceae and Poaceae pollen. Chenopodiaceae, *Artemisia*, Asteraceae and Fabaceae are present in modest amounts. In group S2, Chenopodiaceae becomes dominant instead of Poaceae, together with modest amounts of Cyperaceae, *Artemisia,* and Poaceae. Arboreal pollen is present occasionally in both groups S1 and S2. Group S3 is characterized by high pollen percentages of *Artemisia* (30–50%) and Poaceae (10–30%), and low percentages

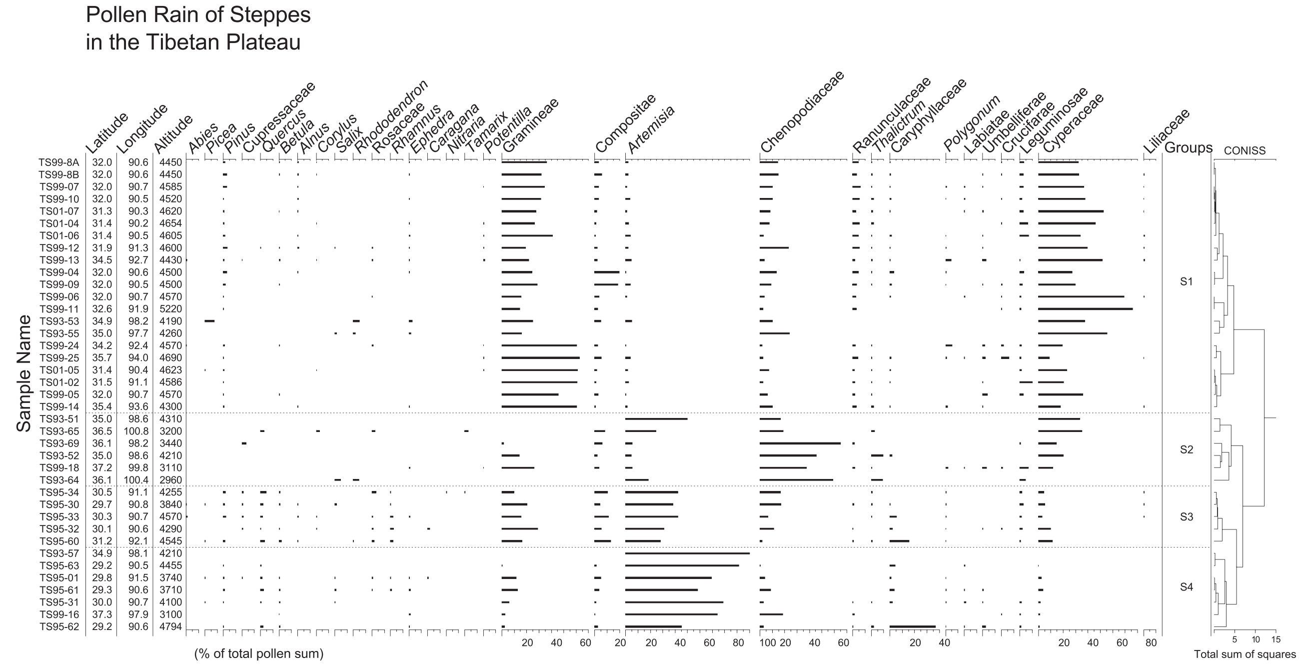

FIGURE 7 | Pollen percentage diagram for surface samples form steppes in the TP. Samples of groups S1, S2, S3, and S4 are from *Stipa* steppe, dry steppe, Poaceae-*Artemisia* steppe, and *Artemisia* steppe, respectively.

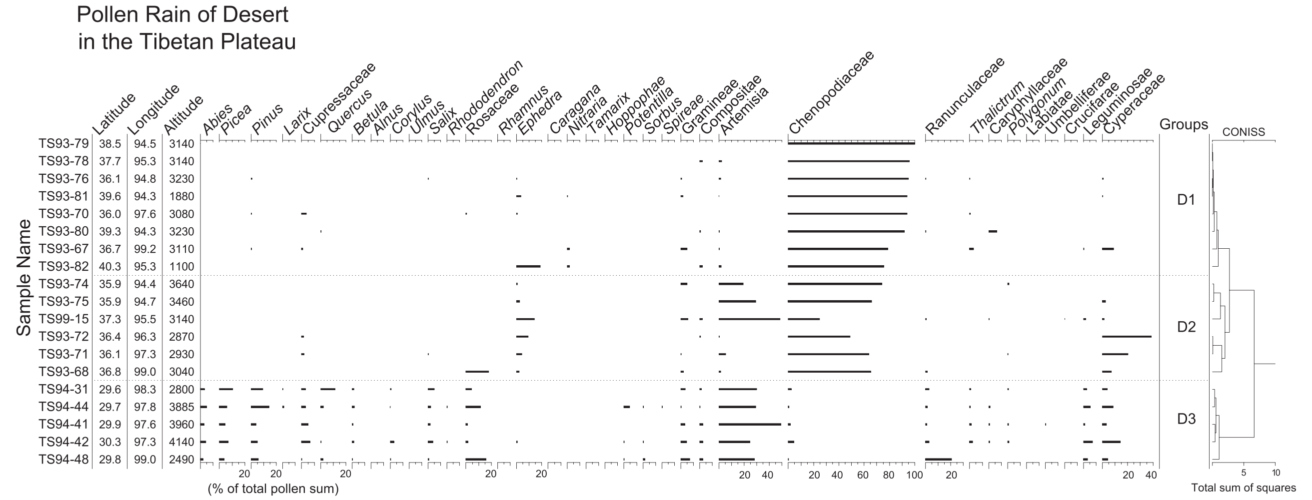

FIGURE 8 | Pollen percentage diagram for surface samples from deserts in the TP. Samples of groups D1 and D2 are from arid desert, and samples of group D3 from hot valley desert.

of arboreal pollen such as *Pinus, Quercus, Betula,* Cupressaceae, Rosaceae, and *Rhamnus*. Pollen spectra of group S4 are distinguished by the highest percentages of *Artemisia* with some Poaceae and Chenopodiaceae pollen.

Desert

Nineteen samples were taken from hot valley desert and arid desert communities. The hot valley deserts are an azonal vegetation type occurring in the subalpine conifer forest region in the southeastern part of the Plateau. The arid desert occurs in the Qaidam Basin and the southern margin of the Tarim Basin. Pollen spectra from deserts (**Figure 8**) are characterized by high pollen percentages of Chenopodiaceae and *Artemisia*. Common herbaceous pollen types include Cyperaceae, Poaceae, and Asteraceae. *Ephedra* and *Nitraria* are the main shrub pollen types. Little tree pollen is found in desert samples except those from hot valley deserts. The pollen samples can be divided into three groups by cluster analysis. Group D1 is distinguished by the

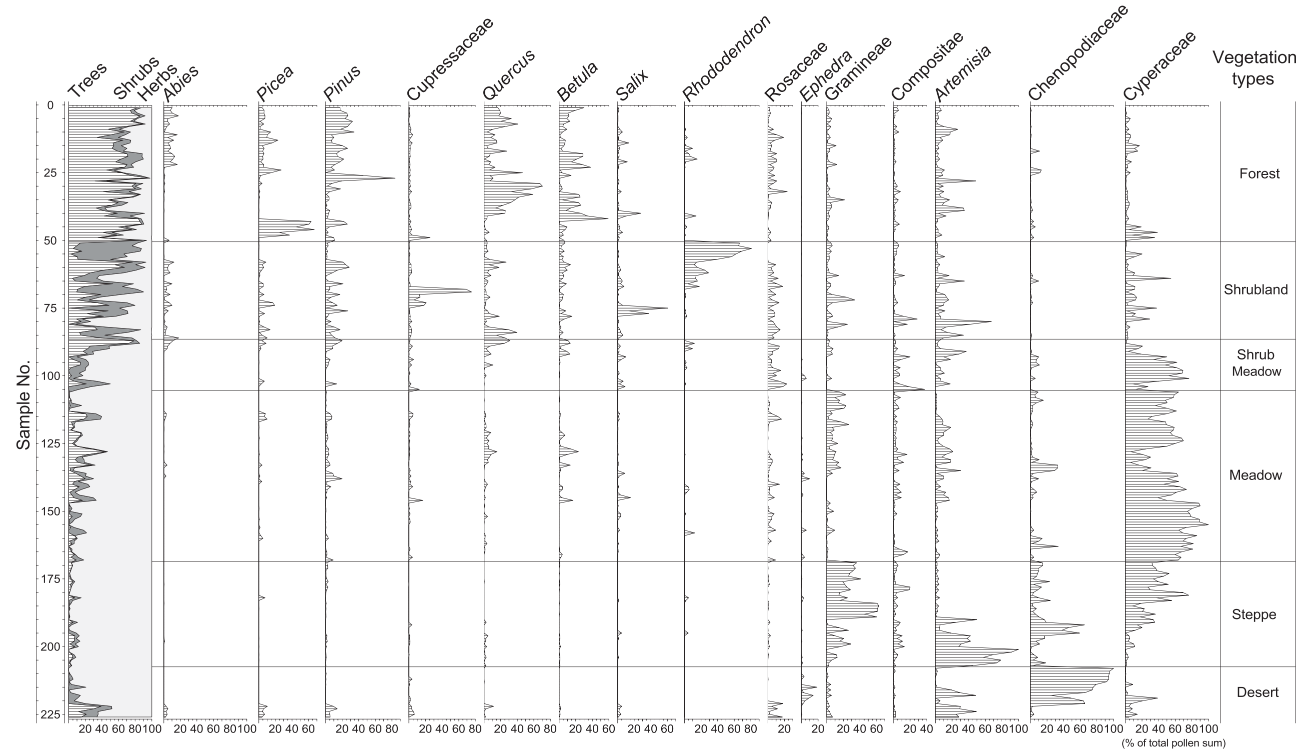

FIGURE 9 | Summary pollen diagram of selected pollen types for surface samples in the TP.

Forest types	Common plant taxa	Mean pollen percentages of common taxa in each forest type
Mixed forest (MF)	*Abies, Picea, Pinus, Larix, Quercus, Betula, Rhododendron*	
Pine forest (PF)	*Pinus, Quercus, Picea, Betula, Populus, Salix,* Rosaceae, *Artemisia*	
Pine-Oak forest (POF)	*Pinus, Rosa, Quercus, Populus, Artemisia*	
Oak forest (OF)	*Quercus, Pinus, Betula,* Rosaceae, *Salix, Rhodo-dendron,* Gramineae	
Oak-birch forest (OBF)	*Quercus, Betula, Salix, Alnus, Juniperus, Potentilla*	
Birch forest (BF)	*Betula, Salix, Quercus, Spiraea, Rhododendron, Potentilla, Carex, Kobresia*	
Spruce forest (SF)	*Picea, Rhododendron, Sabina, Caragana, Salix, Potentilla, Artemisia, Aster, Rubus*	
Sabina forest (SAF)	*Sabina, Salix, Carex, Berberis, Potentilla, Caragana, Polygonum*	
Larch forest (LF)	*Larix, Rhododendron, Abies, Picea, Salix*	

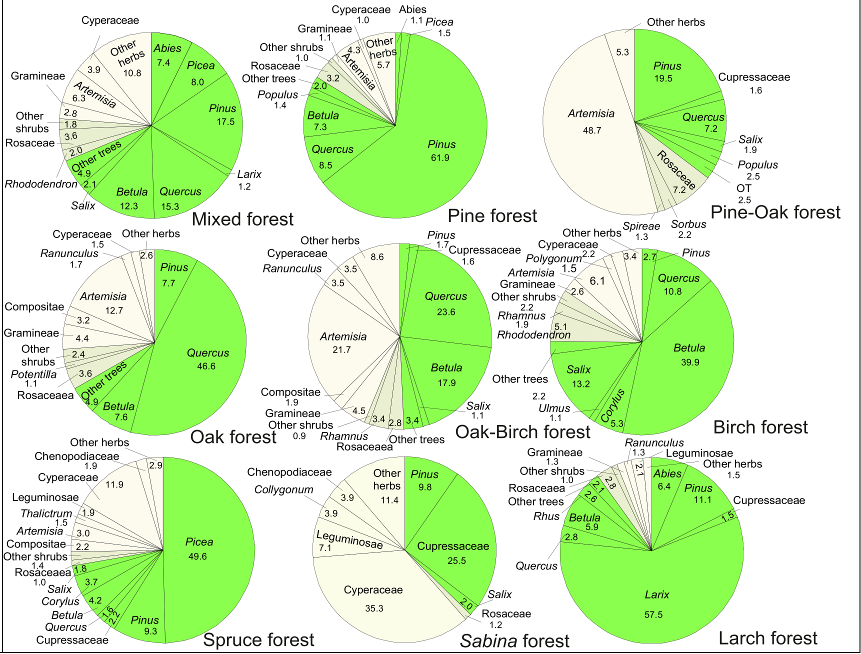

FIGURE 10 | Forest types in the TP and their common plant taxa and representative pollen assemblages. Pie graphs in the right show the mean percentages of the common pollen taxa, calculated by averaging the pollen percentages of the corresponding taxa within each group. For forest type classification, see **Figure 3**.

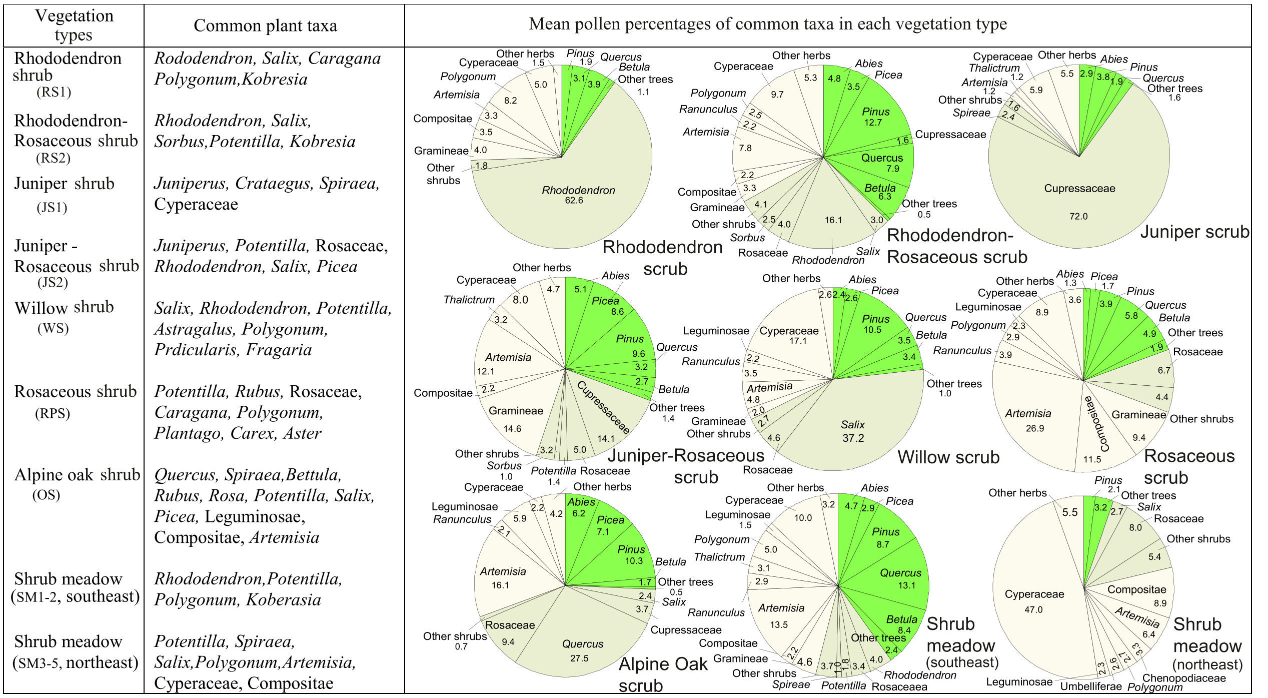

Vegetation types	Common plant taxa
Rhododendron shrub (RS1)	*Rododendron, Salix, Caragana Polygonum,Kobresia*
Rhododendron-Rosaceous shrub (RS2)	*Rhododendron, Salix, Sorbus,Potentilla, Kobresia*
Juniper shrub (JS1)	*Juniperus, Crataegus, Spiraea,* Cyperaceae
Juniper - Rosaceous shrub (JS2)	*Juniperus, Potentilla,* Rosaceae, *Rhododendron, Salix, Picea*
Willow shrub (WS)	*Salix, Rhododendron, Potentilla, Astragalus, Polygonum, Prdicularis, Fragaria*
Rosaceous shrub (RPS)	*Potentilla, Rubus,* Rosaceae, *Caragana, Polygonum, Plantago, Carex, Aster*
Alpine oak shrub (OS)	*Quercus, Spiraea,Bettula, Rubus, Rosa, Potentilla, Salix, Picea,* Leguminosae, Compositae, *Artemisia*
Shrub meadow (SM1-2, southeast)	*Rhododendron,Potentilla, Polygonum, Koberasia*
Shrub meadow (SM3-5, northeast)	*Potentilla, Spiraea, Salix,Polygonum,Artemisia,* Cyperaceae, Compositae

FIGURE 11 | Shrubland and shrub meadow types in the TP and their common plant taxa and representative pollen assemblages. Pie graphs in the right show the mean percentages of the common pollen taxa, calculated by averaging the pollen percentages of the corresponding taxa within each group. For Shrubland and shrub meadow type classification, see **Figures 4**, **5**.

highest Chenopodiaceae pollen percentages (>70%). *Artemisia* and Chenopodiaceae dominate the pollen spectra of group D2, together with some *Ephedra* and Poaceae. The samples of Group D3 were taken from the hot valley deserts. Their pollen spectra contain very little Chenopodiaceae but relatively high percentages of arboreal pollen, including *Abies, Picea, Pinus*, Cupressaceae, *Quercus, Salix*, and Rosaceae. The dominant of herbaceous pollen is *Artemisia* (27–50%). Poaceae, Asteraceae, Ranunculaceae, Fabaceae, and Cyperaceae are present in low or modest amounts.

DISCUSSION AND CONCLUSION

Modern Pollen-Vegetation Relationships

Modern pollen spectra in the TP show a strong relationship with the local vegetation types at the sampling sites. These vegetation types, including forest, shrubland, shrub meadow, meadow, steppe and desert, can be characterized by their pollen spectra.

A summary pollen diagram of all 234 surface samples is plotted in **Figure 9** according to the orders they appear in **Figures 3–8**. Forests are well defined by high amounts of tree pollen. Generally, tree pollen percentages from forests exceed 60%. Pollen spectra from forests not only reflect regional vegetation patterns by their overall composition, but also indicate local forest communities by the relative abundance of their characteristic taxa. Each group of pollen spectra defined by vegetation types corresponds well with the dominant trees in the forests (**Figure 10**). For example, high percentages of *Pinus, Quercus,* and *Picea* clearly indicate the occurrence of pine, oak and spruce forests, respectively. However, some pollen spectra (e.g., TS94-05) from mixed forests also show a complexity in composition, in which some pollen types (e.g., *Betula*) that occur at relatively high pollen percentages are derived from trees that are not found in their local forest communities. This complexity probably reflects a mosaic vegetation pattern largely controlled by slope aspect and elevation. In the southeast of the Plateau pure or mixed forests of pine, oak, birch, spruce, and fir can occur on adjacent slopes with different aspects within a short distance from each other, thus resulting in a mixed pollen assemblage representing different vegetation types.

The samples from shrublands have the highest amounts of shrub pollen (38% on average) among all the samples (**Figure 9**). The dominants of shrublands, such as rhododendron, juniper, willow, and shrub oak, are well-represented in most of these pollen spectra (**Figure 11**). However, some pollen spectra have high percentages of both tree pollen and shrub pollen. It should be pointed out that these shrubland samples are easily distinguished from forest samples according to the local vegetation types in the field (e.g., oak shrub and oak forest), however, it is difficult to distinguish them from pollen composition and percentage. They are generally classified into forest group in the numerical analysis of pollen data (Shen et al., 2008a).

Pollen spectra from shrub meadows have less shrub pollen than those from shrublands, but more than those from meadows, steppes, and deserts. The most frequent shrub pollen in this vegetation type is Rosaceae. Except in a few samples with high amounts of Asteraceae and *Artemisia,* most of the pollen spectra are dominated by Cyperaceae pollen. A major difference in the quantity of tree pollen exists between shrub meadows from the

Vegetation types	Common plant taxa	Mean pollen percentages of common taxa in each vegetation type
Alpine meadow (M1-3)	*Kobresia, Androsace, Carex, Ranunculus, Polygonum, Leguminosae, Aster*	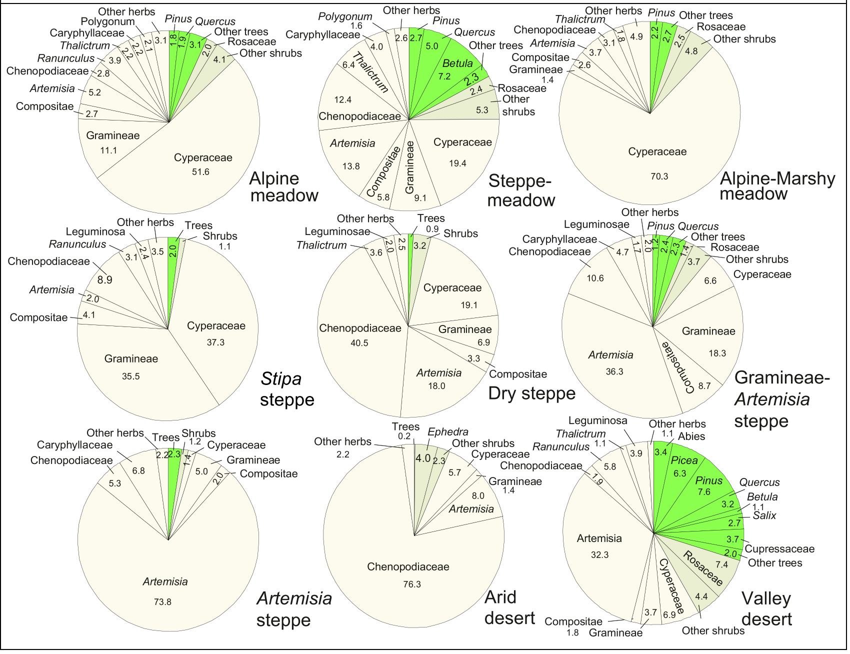
Steppe-meadow (M4)	*Kobresia, Gramineae, Aster, Leguminosae*	
Alpine-marshy meadow (M5-7)	*Kobresia, Carex, Anemone, Polygonum, Andorosace, Ranunculus*	
Stipa steppe (S1)	*Stipa, Kobresia, Polygonum, Poa, Leontopodium, Ranunculus, Artemisia*	
Dry steppe (S2)	*Stipa, Artemisia, Ceratoides, Compositae, Poa*	
Gramineae-*Artemisia*-steppe (S3)	*Artemisia,* Gramineae, Rosaceae, Leguminosae	
Artemisia steppe (S4)	*Artemisia,* Leguminosae, Compositae, Chenopodiaceae, Caryophyllaceae	
Arid desert (D1-2)	*Salsola, Ceratiodes, Artemisia, Ephedra, Natraria*	
Hot valley desert (D1)	*Artemisia, Rumex, Potentilla,* Granineae, Leguminosae	

FIGURE 12 | Meadow, steppe, and desert types in the TP and their common plant taxa and representative pollen assemblages. Pie graphs in the right show the mean percentages of the common pollen taxa, calculated by averaging the pollen percentages of the corresponding taxa within each group. For meadow, steppe, and desert type classification, see **Figures 6–8**.

southeast (groups SM1-2) and the northeast (groups SM3, 4, 5) (**Figure 11**). Pollen spectra from the former region contain more tree pollen than those from the latter region, reflecting a difference in regional vegetation. In the southeast shrub meadows are common vegetation communities near or above treeline, whereas they occur at warmer or more sheltered sites within subalpine or alpine meadows in the northeast where forests are absent or scattered.

In the TP, meadows are dominated by *Kobresia*. As expected, pollen spectra from meadows are characterized by very high percentages of Cyperaceae. The highest amounts of Cyperaceae pollen occur in pollen spectra from alpine-marshy meadows (groups M6 and M7 in **Figure 6**) (**Figure 12**). Pollen spectra from the transitional region between meadows and steppes (referred to as steppe-meadow in **Figure 12**) have much less Cyperaceae pollen than those from alpine meadows (mainly in the south-central parts of the Plateau) and alpine-marshy meadows (mostly in the eastern Plateau). Besides Cyperaceae pollen, common pollen types in the meadows are *Artemisia*, Poaceae, Asteraceae, Caryophyllaceae, *Polygonum,* and *Thalictrum*, whose producer plants are frequently found in meadows.

Pollen spectra from *Stipa* steppes are characterized by the highest percentages of Poaceae pollen, and high Cyperaceae pollen percentages. The general trend is that, the closer the sampling sites are to the steppe/meadow ecotone, the higher the Cyperaceae pollen percentages. Pollen spectra from *Artemisia* steppes have the highest percentages of *Artemisia* pollen, whereas pollen spectra from dry steppes located close to the steppe/desert ecotone have relatively high percentages of Chenopodiaceae (**Figure 12**).

Pollen spectra from the arid desert are dominated by Chenopodiaceae, although *Ephedra, Artemisia*, Poaceae, and Cyperaceae are frequently present. On the other hand, pollen spectra from the hot valley deserts are distinguished by little or no Chenopodiaceae but relatively high frequencies of *Artemisia* and arboreal pollen. It is evident that the tree pollen grains are derived from the forests growing on more humid mountain slopes above the river valley.

Pollen Representation

As expected, tree pollen decreases as the vegetation changes from forests to non-forest vegetation types (**Figure 9**). However, tree pollen percentages are still higher than 20% for some samples from shrublands, shrub meadows, and even meadows, where no trees grow. Some pollen spectra from non-forest vegetation types above treeline in the West Himalayas and Nepal also have high percentages of tree pollen (Bera and Gupta, 1989; Yonebayashi and Minika, 1997). Many researchers have noted the phenomenon of upslope transportation of low-elevation pollen in mountainous region (Maher, 1963; Flenley, 1979; Markgraf, 1980; Solomon and Silkworth, 1986; Spear, 1989). Winds on the mountains are usually up-valley (anabatic) during the day and down-valley (katabatic) at night. Up-valley wind brings pollen uphill during the afternoon, and pollen is deposited in the afternoon or evening by rainfall (Flenley, 1979; Markgraf, 1980). This distortion of the pollen signal has made it difficult to recognize high elevation vegetation types on the basis of their pollen assemblages in many areas. However, a systematic study of both the local and regional pollen rain from mountainous regions can still permit the identification of vegetation patterns from their high-elevation pollen signatures (Minckley and Whitlock, 2000).

In the TP, pollen samples with relatively high tree pollen percentages from non-forest vegetation types were collected from the forest region. Generally, shrublands, shrub meadows, and meadows are located above the treeline, and conifer forests, oak forests and birch forests grow below them. These pollen spectra thus do indeed detect the vegetation patterns at the regional scale. On the other hand, the local pollen signatures such as high percentages of shrub pollen also reflect their vegetation zones at local level. Therefore, these pollen spectra can be used to identify the vegetation and climate patterns.

Abies, Picea, Pinus, Quercus, and *Betula* are dominant tree taxa in a variety of forests. It is difficult to discuss their pollen representation in detail without quantitative data on the abundance of their producers. However, based on our qualitative field observations on common plant taxa near the sampling sites (**Supplementary Material**), we can still make some inference about the pollen representation of these tree taxa. Pollen percentages of *Abies* never exceed 20% although *Abies* is very common in some sites. Previous studies have shown that *Abies* is under-represented in the pollen rain (Jarvis, 1993; Sugita, 1993). Other tree taxa, including *Picea, Pinus, Quercus* and *Betula,* are well-represented or even over-represented in the pollen rain. They usually occur at fairly high pollen percentages where their producers are present, and at low to moderate percentages even where their producers are absent. Comparing pollen spectra and local vegetation types, it can be found that *Picea* is well-represented, whereas *Pinus*, *Quercus*, and *Betula* are over-represented, especially in meadow and desert.

Most of the shrubs are under-represented in the pollen rain. Pollen grains of *Rhododendron, Salix,* and *Juniperus* are rarely found beyond their growing area, and rarely exceed 20%. However, high Cupressaceae pollen percentages occur in some samples (e.g., T94–19 and T94-29). This phenomenon is probably due to the sample materials and local vegetation types. These samples are moss polsters instead of top soil collected from *Juniperus* shrub and *Sabina* scrub, so pollen spectra are multi-year accumulations of pollen rain experiencing less corrosion after their deposition and high Cupressaceae pollen percentages are not unexpected in these pollen spectra. Rosaceae pollen is present in all sites where the vegetation is dominated by rosaceous shrubs, but its pollen percentages never exceed 25%. For Cyperaceae, Poaceae, *Artemisia,* and Chenopodiaceae, their pollen is abundantly produced and wind-transported. These herbaceous taxa seem well represented in the pollen rain.

Summary

Our modern pollen network consisting of 234 surface samples, which were taken in 1993–1995, 1999 and 2001 before the completion of the Qinghai-Tibet Railway, provides a precious modern pollen and vegetation dataset in the least anthropologically-disturbed TP of China. The results of our study show that modern pollen spectra do reflect the contemporary vegetation at local and regional scales. Therefore, we can use this modern pollen dataset as a basis for reconstructing past vegetational and climatic changes by means of a variety of numerical and mapping methods (Shen et al., 2006, 2008a, b; Lu et al., 2011; Liang et al., 2020; Sun et al., 2020; Chevalier et al., 2020). Detailed vegetational and climatic histories from the TP are vital for testing hypotheses concerning the relative importance between solar insulation changes and altered glacial boundary conditions in controlling the timing and changing strengths of the Southwest Asian monsoon and assessing paleoclimate simulations (Chen et al., 2020; Tang et al., 2021). Thus, this modern pollen database will continue to contribute into vegetational and climatic changes in the TP as well as global changes and biome mapping.

DATA AVAILABILITY STATEMENT

The raw data supporting the conclusion of this article will be made available by the authors, without undue reservation.

AUTHOR CONTRIBUTIONS

K-bL, JO, LT and CS designed the study and did fieldwork; CS did lab work, identified pollen and analyzed pollen data; CS and K-bL wrote the paper.

FUNDING

Special Project for Basic Research of Yunnan Province - Key Project (Grant No. 202101AS070006), the Yunnan Project for the Introduction of Advanced Talents (Grant No. 2013HA024), the National Natural Science Foundation of China (Grant Nos. 41372191, 42067061, 49371068 and 49871078), and the U.S. National Science Foundation (NSF grants ATM-9410491, ATM-0081941).

ACKNOWLEDGMENTS

This research was supported by grants from Special Project for Basic Research of Yunnan Province - Key Project (Grant Nos. 202101AS070006), the Yunnan Project for the Introduction of Advanced Talents (Grant Nos. 2013HA024), the National Natural Science Foundation of China (Grant Nos.. 41372191, 42067061, 49371068 and 49871078), and the U.S. National Science Foundation (NSF grants ATM-9410491, ATM-0081941).

SUPPLEMENTARY MATERIAL

The Supplementary Material for this article can be found online at: https://www.frontiersin.org/articles/10.3389/feart.2021.732441/full#supplementary-material

REFERENCES

Bartlein, P. J., Prentice, I. C., and Webb, T., III (1986). Climatic Response Surfaces from Pollen Data for Some Eastern North American Taxa. *J. Biogeogr.* 13, 35–57. doi:10.2307/2844848

Bera, S. K., and Gupta, H. P. (1989). Correlation between Pollen Spectra and Vegetation of Chhora Shigri Glacier in Himachal Pradesh, India. *Palaeobot* 38, 404–410.

Birks, H. J. B., Heiri, O., Seppä, H., and Bjune, A. E. (2010). Strengths and Weaknesses of Quantitative Climate Reconstructions Based on Late-Quaternary Biological Proxies. *Open Ecol. J.* 3, 68–110. doi:10.2174/1874213001003020068

Chang, D. H. S. (1981). The Vegetation Zonation of the Tibetan Plateau. *Mountain Res. Dev.* 1, 29–49. doi:10.2307/3672945

Chen, F., Zhang, J., Liu, J., Cao, X., Hou, J., Zhu, L., et al. (2020). Climate Change, Vegetation History, and Landscape Responses on the Tibetan Plateau during the Holocene: A Comprehensive Review. *Quat. Sci. Rev.* 243, 106444. doi:10.1016/j.quascirev.2020.106444

Chen, J. H., Lv, F. Y., Huang, X. Z., Birks, H. J. B., Telford, R. J., Zhang, S. R., et al. (2017). A Novel Procedure for Pollen-Based Quantitative Paleoclimate Reconstructions and its Application in China. *Sci. Chin. Earth Sci.* 60, 2059–2066. doi:10.1007/s11430-017-9095-1

Chevalier, M., Davis, B. A. S., Heiri, O., Seppä, H., Chase, B. M., Gajewski, K., et al. (2020). Pollen-based Climate Reconstruction Techniques for Late Quaternary Studies. *Earth-Science Rev.* 210, 103384. doi:10.1016/j.earscirev.2020.103384

Davis, B. A. S., Zanon, M., Collins, P., Mauri, A., Bakker, J., Barboni, D.., et al. (2013). The European Modern Pollen Database (EMPD) Project. *Veg Hist. Archaeobot* 22 (6), 521–530.

Delcourt, P. A., Decourt, H. R., and Davidson, J. L. (1987). Mapping and Calibration of Modern Pollen-Vegetation Relationships in the southeastern United States. *Rev. Palaeobot Palynol* 39, 1–45.

Editorial Broad of Sichuan's Vegetation (1980). *The Vegetation of Sichuan*. Chengdu: Sichuan People's Press. (in Chinese).

Edward Schofield, J., Edwards, K. J., and Andy McMullen, J. (2007). Modern Pollen?vegetation Relationships in Subarctic Southern Greenland and the Interpretation of Fossil Pollen Data from the Norse Landnam. *J. Biogeogr.* 34 (3), 473–488. doi:10.1111/j.1365-2699.2006.01607.x

Faegri, K., and Iversen, J. (1975). *Textbook of Pollen Analysis*. New York: Macmillan.

Flenley, J. (1979). *The Equatorial Rain forest: A Geological History*. London: Butterworths.

Gajewski, K., Lezine, A-M., Vincens, A., Delestand, A., and Sawadab, M. (2002). The African Pollen DatabaseModern Climate-Vegetation-Pollen Relations in Africa and Adjacent Areas. *Quat. Sci. Rev.* 21 (14–15), 1611–1631. doi:10.1016/s0277-3791(01)00152-4

Ge, Y., Li, Y., Bunting, M. J., Li, B., Li, Z., and Wang, J. (2017). Relation between Modern Pollen Rain, Vegetation and Climate in Northern China: Implications for Quantitative Vegetation Reconstruction in a Steppe Environment. *Sci. Total Environ.* 586, 25–41. doi:10.1016/j.scitotenv.2017.02.027

Grimm, E. C. (1987). CONISS: A FORTRAN 77 Program for Stratigraphically Constrained Cluster Analysis by the Method of Incremental Sum of Squares. *Comput. Geosciences* 13, 13–35. doi:10.1016/0098-3004(87)90022-7

Herzschuh, U., Birks, H. J. B., Mischke, S., Zhang, C., and Böhner, J. (2010). A Modern Pollen-Climate Calibration Set Based on lake Sediments from the Tibetan Plateau and its Application to a Late Quaternary Pollen Record from the Qilian Mountains. *J. Biogeogr.* 37, 752–766. doi:10.1111/j.1365-2699.2009.02245.x

Institute of Geography (1990). *Map of the Qinghai-Tibet Plateau*. Beijing: Science Press. (in Chinese).

Jarvis, D. I., and Clay-Poole, S. T. (1992). A Comparison of Modern Pollen Rain and Vegetation in Southwestern Sichuan Province, China. *Rev. Palaeobotany Palynology* 75, 239–258. doi:10.1016/0034-6667(92)90018-c

Jarvis, D. I. (1993). Pollen Evidence of Changing Holocene Monsoon Climate in Sichuan Province, China. *Quat. Res.* 39, 325–337. doi:10.1006/qres.1993.1039

Li, W. Y. (1991). Relationships between Pollen and Plant of Abies Fargesii forest and its Succession in the Shennongjia Mountain. *Acta Geogr. Sin* 46, 186–194. (in Chinese).

Li, X., and Liu, J. (1988). Holocene Vegetational and Environmental Changes at Mt. Luoji, Sichuan. *Acta Geogra Sin* 43, 44–51. (in Chinese).

Li, Y., Zhang, X., Zhou, G., and Ni, J. (2000). Quantitative Relationship between Vegetation and Pollen for Several Common Taxa in North China. *Chin. Sci. Bull.* 45, 761–764. doi:10.1007/bf02898901

Liang, C., Zhao, Y., Qin, F., Zheng, Z., Xiao, X., Ma, C., et al. (2020). Pollen-based Holocene Quantitative Temperature Reconstruction on the Eastern Tibetan Plateau Using a Comprehensive Method Framework. *Sci. China Earth Sci.* 63, 1144–1160. doi:10.1007/s11430-019-9599-y

Liu, K.-b., and Lam, N. S.-N. (1985). Paleovegetational Reconstruction Based on Modern and Fossil Pollen Data: an Application of Discriminant Analysis. *Ann. Assoc. Am. Geogr.* 75, 115–130. doi:10.1111/j.1467-8306.1985.tb00062.x

Liu, K.-b. (1988). Quaternary History of the Temperate Forests of China. *Quat. Sci. Rev.* 7, 1–20. doi:10.1016/0277-3791(88)90089-3

Lu, H., Wu, N., Liu, K.-b., Zhu, L., Yang, X., Yao, T., et al. (2011). Modern Pollen Distributions in Qinghai-Tibetan Plateau and the Development of Transfer Functions for Reconstructing Holocene Environmental Changes. *Quat. Sci. Rev.* 30, 947–966. doi:10.1016/j.quascirev.2011.01.008

Ma, Q., Zhu, L., Lu, X., Wang, Y., Guo, Y., Wang, J., et al. (2017). Modern Pollen Assemblages from Surface lake Sediments and Their Environmental Implications on the Southwestern Tibetan Plateau. *Boreas* 46 (2), 242–253. doi:10.1111/bor.12201

Maher, L. J., Jr (1963). Pollen Analyses of Surface Materials from the Southern San Juan Mountains, Colorado. *Geol. Soc. America Bull.* 74, 1485–1504. doi:10.1130/0016-7606(1963)74[1485:paosmf]2.0.co;2

Markgraf, V. (1980). Pollen Dispersal in a Mountain Area. *Grana* 19, 127–146. doi:10.1080/00173138009424995

Members of China Quaternary Pollen Database (2001). Simulation of China Biome Reconstruction Based on Pollen Data from Surface Sediment Samples. *Acta Bot. Sin* 43, 201–209. (in Chinese).

Minckley, T., and Whitlock, C. (2000). Spatial Variation of Modern Pollen in Oregon and Southern Washington, USA. *Rev. Palaeobotany Palynology* 112, 97–123. doi:10.1016/s0034-6667(00)00037-3

Seppä, H., Birks, H. J. B., Odland, A., Poska, A., and Veski, S. (2010). A Modern Pollen-Climate Calibration Set from Northern Europe: Developing and Testing a Tool for Palaeoclimatological Reconstructions. *J. Biogeogr.* 31 (2), 251–267. doi:10.1111/j.1365-2699.2004.00923.x

Shen, C., and Tang, L. (1992). Holocene Climate Based on Pollen Transfer Functions in Changbaishan Mountain and Xiaoxinanling Ranges. In: *Climate and Environment during Holocene Megathermal in China* (eds by Y Shi and Z Kong), pp.34–39. Beijing: China Ocean Press (in Chinese)

Shen, C., Liu, K.-b., Morrill, C., Overpeck, J. T., Peng, J., and Tang, L. (2008b). Ecotone Shift and Major Droughts during the Mid-late Holocene in the Central Tibetan Plateau. *Ecology* 89 (4), 1079–1088. doi:10.1890/06-2016.1

Shen, C., Liu, K.-b., Tang, L., and Overpeck, J. T. (2008a). Numerical Analysis of Modern and Fossil Pollen Data from the Tibetan Plateau. *Ann. Assoc. Am. Geogr.* 98 (4), 755–772. doi:10.1080/00045600802232342

Shen, C., Liu, K.-b., Tang, L., and Overpeck, J. T. (2006). Quantitative Relationships between Modern Pollen Rain and Climate in the Tibetan Plateau. *Rev. Palaeobotany Palynology* 140, 61–77. doi:10.1016/j.revpalbo.2006.03.001

Solomon, A. M., and Silkworth, A. B. (1986). Spatial Patterns of Atmospheric Pollen Transport in a Montane Region,. *Quat. Res.* 25, 150–162. doi:10.1016/0033-5894(86)90053-0

Spear, R. W. (1989). Late-Quaternary History of High-Elevation Vegetation in the White Mountains of New Hampshire. *Ecol. Monogr.* 59, 125–151. doi:10.2307/2937283

Sugita, S. (1993). A Model of Pollen Source Area for an Entire Lake Surface. *Quat. Res.* 39, 239–244. doi:10.1006/qres.1993.1027

Sun, X., Du, N., Chen, Y., Gu, Z., Liu, J., and Yuan, B. (1993). Pollen Analyses of Lacustrine Sediment in Seling Co, Tibet. *Acta Bot. Sin* 35, 943–950. (in Chinese).

Sun, Y., Xu, Q., Zhang, S., Li, Y., Li, M., Li, Y., et al. (2020). A Novel Procedure for Quantitative Regional Paleoclimatic Reconstruction Using Surface Pollen Assemblages. *Quat. Sci. Rev.* 240, 106385. doi:10.1016/j.quascirev.2020.106385

Tang, L., Shen, C., Lu, H., Li, C., and Ma, Q. (2021). 青藏高原第四纪孢粉研究五十年. *Sci. Sin.-Terrae*. (in Chinese). doi:10.1360/SSTe-2020-0361

Tibetan Investigation Group (1988). *Vegetation of Xizang (Tibet)*. Beijing: Science Press. (in Chinese).

Van Campo, E., and Gasse, F. (1993). Pollen- and Diatom-Inferred Climatic and Hydrological Changes in Sumxi Co Basin (Western Tibet) since 13,000 Yr B.P. *Quat. Res.* 39, 300–313. doi:10.1006/qres.1993.1037

Wang, J. T. (1988). The Steppes and Deserts of the Xizang Plateau (Tibet). *Vegetatio* 75, 135–142. doi:10.1007/bf00044634

Webb, T., III, and Bryson, R. A. (1972). Late- and Postglacial Climatic Change in the Northern Midwest, USA: Quantitative Estimates Derived from Fossil Pollen Spectra by Multivariate Statistical Analysis. *Quat. Res.* 2, 70–115. doi:10.1016/0033-5894(72)90005-1

Weng, C. Y., Sun, X., and Chen, Y. (1989). Numerical Characteristics of Pollen Assemblages of Surface Samples from the West Kunlun Mountains. *Acta Bot. Sin* 35, 69–79. (in Chinese).

Wu, Z. (1980). *The Vegetation of China*. Beijing: Science Press. (in Chinese).

Xiao, J., Wu, Y., and Zheng, M. (1996). A Preliminary Study on lake Quaternary flora in Chaby Lake, Xizang (Tibet). *Acta Micropaleontol Sin* 13, 305–400. (in Chinese).

Xu, Q., Zhang, S., Gaillard, M.-j., Li, M., Cao, X., Tian, F., et al. (2016). Studies of Modern Pollen Assemblages for Pollen Dispersal- Deposition- Preservation Process Understanding and for Pollen-Based Reconstructions of Past Vegetation, Climate, and Human Impact: a Review Based on Case Studies in China. *Quat. Sci. Rev.* 149, 151–166. doi:10.1016/j.quascirev.2016.07.017

Yao, Z. (1989). Surface Pollen Analysis in Zhongtiao Mountain, China. *Acta Geogra Sin* 44, 469–477. (in Chinese).

Yonebayashi, C., and Minaki, M. (1997). Late Quaternary Vegetation and Climatic History of Eastern Nepal. *J. Biogeogr.* 24, 837–843.

Yu, G., Tang, L., Yang, X., Ke, X., and Harrison, S. P. (2001). Modern Pollen Samples from alpine Vegetation on the Tibetan Plateau. *Glob. Ecol Biogeogr* 10, 503–519. doi:10.1046/j.1466-822x.2001.00258.x

Zheng, Z., Huang, K., Xu, Q., Lu, H., Cheddadi, R., Luo, Y., et al. (2008). Comparison of Climatic Threshold of Geographical Distribution between Dominant Plants and Surface Pollen in China. *Sci. China Ser. D-earth Sci.* 51 (8), 1107–1120. doi:10.1007/s11430-008-0080-x

Zheng, Z., Wei, J., Huang, K., Xu, Q., Lu, H., Tarasov, P., et al. (2014). East Asian Pollen Database: Modern Pollen Distribution and its Quantitative Relationship with Vegetation and Climate. *J. Biogeogr.* 41, 1819–1832. doi:10.1111/jbi.12361

Zhou, K., Yan, F., Ye, Y., and Liang, X. (1983). Sporo-pollen Assemblages in the Surface Soils of Various Vegetation Zones at Changbaishan Mountains. In: *Sporo-pollen Analyses of the Quaternary and Paleoenvironments* (eds by K Wang and K Zhou), pp.115–122. Beijing: Science Press (in Chinese).

Conflict of Interest: The authors declare that the research was conducted in the absence of any commercial or financial relationships that could be construed as a potential conflict of interest.

frontiers in Earth Science

ORIGINAL RESEARCH
published: 01 September 2021
doi: 10.3389/feart.2021.701037

Luminescence Dating of Relics in Ancient Cities Provides Absolute Dates for Understanding Human-Land Relationships in Qinghai Lake Basin, Northeastern Tibetan Plateau

Manping Sun[1,2], Yongjuan Sun[1,2,3]*, Haicheng Wei[4], Guangliang Hou[1,2,3], Ji Xianba[1,2], Liqian Xie[1,2], Yongxin Zeng[1,2] and Chongyi E[1,2,3]*

[1]Qinghai Provincial Key Laboratory of Physical Geography and Environmental Processes, School of Geographical Science, Qinghai Normal University, Xining, China, [2]MOE Key Laboratory of Tibetan Plateau Land Surface Processes and Ecological Conservation, Qinghai Normal University, Xining, China, [3]Academy of Plateau Science and Sustainability, People's Government of Qinghai Province and Beijing Normal University, Xining, China, [4]Key Laboratory of Comprehensive and Highly Efficient Utilization of Salt Lake Resources, Qinghai Institute of Salt Lakes, Chinese Academy of Sciences, Xining, China

OPEN ACCESS

Edited by:
Feng Cheng,
University of Nevada, Reno,
United States

Reviewed by:
Jintang Qin,
China Earthquake Administration,
China
Xuefeng Sun,
Nanjing University, China

***Correspondence:**
Yongjuan Sun
yongjuansun@163.com
Chongyi E
echongyi@163.com

Specialty section:
This article was submitted to Quaternary Science, Geomorphology and Paleoenvironment, a section of the journal Frontiers in Earth Science

Received: 27 April 2021
Accepted: 05 August 2021
Published: 01 September 2021

Citation:
Sun M, Sun Y, Wei H, Hou G, Xianba J, Xie L, Zeng Y and E C (2021) Luminescence Dating of Relics in Ancient Cities Provides Absolute Dates for Understanding Human-Land Relationships in Qinghai Lake Basin, Northeastern Tibetan Plateau. Front. Earth Sci. 9:701037. doi: 10.3389/feart.2021.701037

The study of ancient city sites provides valuable evidence for understanding human-land relationships. Qinghai Lake Basin, on the northeastern Tibetan Plateau, was a key location for economic and cultural exchanges between East and West in ancient China and archaeological surveys have identified the remains of many ancient cities. Although there are relatively good historical records for some ancient cities, their absolute ages are still unclear due to a lack of systematic chronological dating. In this study, OSL dating of ceramic and tile remains from three ancient cities in Qinghai Lake Basin, Xihaijun (XHJGC), Beixiangyang (BXYGC), and Fuxi (FSC), was combined with documentary and paleoclimate evidence to investigate historical human-land relationships. Relics from XHJGC and BXYGC were dated to 0–220 AD, in the Han Dynasty, while tiles from FSC were dated to 120–520 AD, largely corresponding to the Wei Jin Southern and Northern Dynasties. Luminescence ages were generally consistent with dates recorded in historical documents, indicating that the OSL method can be reliably used to date buried tiles in ancient cities on the northeastern Tibetan Plateau. Comparing the dates with paleoclimatic records suggests that the warm and humid climate at c. 2 ka was an important driver of immigration to the region that led to the construction of cities in the Qinghai Lake area during the late Western Han Dynasty. During the Wei Jin Southern and Northern Dynasties (220–589 AD), communication between East and the West flourished, and human activities in the area were strong with the continuation of the war in Central China and Hexi Corridor. Fuxi was largely abandoned in the later Wei Jin Southern and Northern Dynasties, although it was still used intermittently until the Ming Dynasty. Pollen records confirm that humans were extensively engaged in agricultural production in the Qinghai Lake area during the Wei Jin Southern and Northern Dynasties.

Keywords: optical stimulated luminescence dating, human-land relationship, tiles, ancient cities, Qinghai Lake Basin

INTRODUCTION

It has been argued that cities are the product of a certain stage in the development of human society, marking the end of primitive society and the arrival of civilization (Bureau of National Cultural Relics, 1996). The study of ancient cities can reveal the political, military, economic, and cultural conditions of a region, which is fundamental for understanding the historical development and evolution of human-land relationships (Li, 1995). On the Tibetan Plateau, northeastern Qinghai Province was an important boundary area between nomadic tribes and agricultural regimes during historical periods (Dong et al., 2016). Many wars between ancient agricultural and pastoral regimes in China have been related to climate change, with deterioration of the ecological environment during periods of unfavorable climate conditions leading to social instability (Dong et al., 2016). Frequent wars may have stimulated the construction of a large number of ancient cities on the northeastern Qinghai-Tibet Plateau; Dong et al. (2016) argue that most were initiated for military defense purposes. Documentary evidence and radiocarbon dating suggest that most of the cities were built or repaired during the Han Dynasty (202 BC–220 AD), Tang Dynasty (618–907 AD), the Five Dynasties and Ten Kingdoms period (907–960 AD), the Song Dynasty (960–1279 AD), and the Ming Dynasty (1368–1644 AD) (Dong et al., 2016).

Qinghai Lake is a saline lake in the northeastern Tibetan Plateau; it is the largest water body on the plateau and supports a vast inland wetland ecosystem. Historically, Qinghai Lake Basin was important for cultural interaction and influence between the Yellow River and the Central Asian civilizations (Huo, 2017), and it has been a key research area for studies exploring cultural collision and economic exchange between East and West. Most studies of human activities in the Qinghai Lake area have focused on the prehistoric period (Brantingham and Xing, 2006; Rhode et al., 2007; Sun et al., 2012; Chen et al., 2015; ChongYi et al., 2015; Hou et al., 2015; Sun et al., 2018), with few looking at the relationship between human activities and environmental changes in the historical period. Archaeological investigations have found that ancient cities around Qinghai Lake were first built in the late Western Han Dynasty (c. 4 AD) (Li, 1995; Bureau of National Cultural Relics, 1996). Contact between the agricultural regimes of the Central Plains government and the nomadic tribes of the northeastern Tibetan Plateau also became closer from the Western Han Dynasty period, and the Qinghai Lake area was an important military frontier. As the power of the Central Plains government gradually expanded to the plateau, the number of cities increased and agricultural technology and production tools were also introduced to the Qinghai Lake Basin. Some nomadic tribes in the Qinghai Lake Basin also began to build cities and engage in farming activities. The Qinghai Road, one of the trunk roads of the "Overland Silk Road" (Wang and Zhao, 2013; Huo, 2017), also provided a means for economic and cultural exchange in the region. Thus, military, political, and economic developments all contributed to the formation and development of ancient cities on the northeastern Tibetan Plateau; reconstructing the chronological development of these cities furthers understanding of human activities and provides important evidence relating to the evolution of human-land relationships in the historical period.

The chronological framework for ancient cities in China is mainly based on historical documents, types, and the characteristics of cultural relics, and ^{14}C dating of charcoal and bone. However, the Qinghai Lake area is relatively remote and was under the alternate control of farming and nomadic regimes for a long time, so it lacks historical documents with good records. Moreover, most ancient cities were built with rammed earth, and other buildings had walls of sand, stone, and soil, which are vulnerable to erosion and leave little evidence for the historical record. The development of the thermoluminescence technique in the 1950s offered a means for direct dating ancient pottery(Daniels et al., 1953), and the more recent OSL has widened applications to a range of Quaternary sediments and archaeological materials. Several studies have shown the accuracy and reliability of OSL dating of ceramics from archaeological sites on the Tibetan Plateau (Rhode et al., 2007; Sun, 2019; Sun et al., 2021). Tiles are made in a similar way to ceramics, in which the luminescence signals accumulated by the raw materials over geological periods are completely bleached during firing, so the absolute age can be determined using luminescence dating.

In this study, we applied luminescence dating to tiles and ceramics from three ancient cities in Qinghai Lake Basin, Xihaijun (XHJGC), Beixiangyang (BXYGC), and Fuxi (FSC). The cities were selected due to their good preservation, large area, and suitable dating materials. Historical documents show that the three cities served as royal cities or prefectures in the historical period and played an important role in the ancient Silk Road. Although the ages of the cities can be inferred from historical documents and archaeological studies, their occupation chronology is still controversial due to the relatively long history the lack of direct dating. Dong et al. (2016) determined the ^{14}C age of charred sheep droppings in the cultural layer at Fuxi as the Ming Dynasty. However, the large area of the cities means that they were likely multiphased, so it is necessary to use a variety of methods to systematically date different cultural remains. In this study, the OSL dating of tiles and ceramics gives the direct age of cultural artifacts in the three ancient cities and provides a basis for assessing the age of other ancient cities in the area that have similar relics but lack historical records. Combined with historical documents and paleoclimate records, the dating results indicate the historical evolution of human-land relationships in the Qinghai Lake Basin.

STUDY AREA AND MATERIALS

Study Area

Qinghai Lake is located on the northeastern edge of the Tibetan Plateau and is the largest inland saltwater lake in China. The lake basin is characterized by plateau continental climate and is in the region of interaction between the East Asian monsoon and westerlies, which is sensitive to climate change. Qinghai Lake Basin is a closed inland basin and comprises a flat alluvial plain with multilevel shoreline terraces. Vegetation is mainly alpine meadow and alpine shrub.

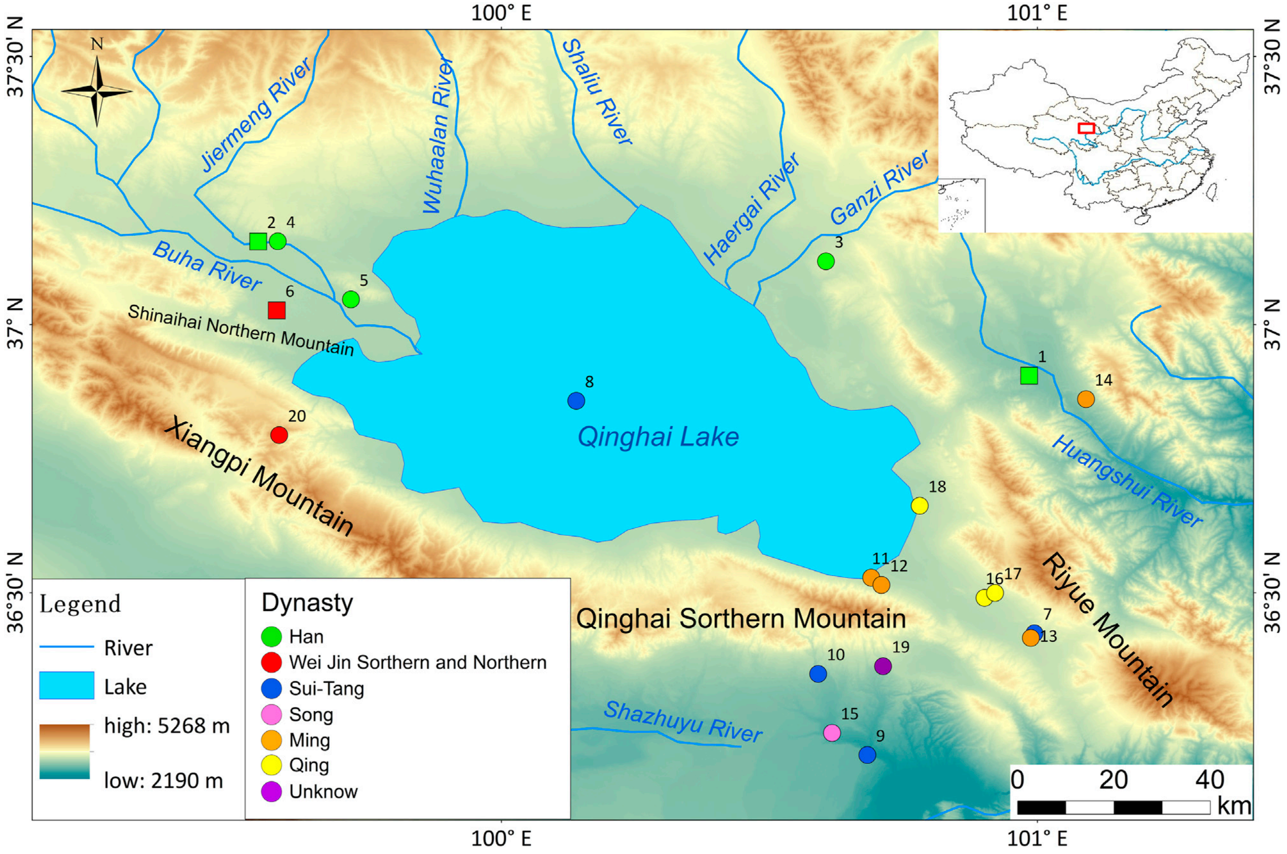

FIGURE 1 | Location of ancient cities around Qinghai Lake, northeastern Tibetan Plateau. Sites are represented by colored circles (already excavated) and squares (investigated in this study): 1) Xihaijun; 2) Beixiangyang; 3) Gahai; 4) Nanxiangyang; 5) Lixin; 6) Fuxi; 7) Heigucheng; 8) Yinglong; 9) Kecai; 10) Jialabei; 11) Qunkejiala; 12) Jiayi; 13) Nahailie; 14) Cangkai; 15) Shangtamai; 16) Jiangjunmiao; 17) Chahan; 18) Hudong; 19) Dongba; 20) Shitoucheng (sources: Bureau of National Cultural Relics, 1996; Cui et al., 1999; Dong et al., 2016). Inset map shows location of Qinghai Lake in China.

TABLE 1 | Area and the dynastic era of ancient cities around Qinghai Lake, northeastern Tibetan Plateau (sources: Bureau of National Cultural Relics, 1996; Li, 1995). See **Figure 1** for locations.

No.	Ancient city	Area (m^2)	Dynasty	No.	Ancient city	Area (m^2)	Dynasty
1	Xihaijun	180,000	Han	11	Jialabei	48,741	Sui-Tang
2	Beixiangyang	120,000	Han	12	Shangtamai	28,500	Song
3	Gahai	189,660	Han	13	Qunkejiala	26,250	Ming
4	Nanxiangyang	10,800	Han	14	Jiayi	-	Ming
5	Lixin	3,000	Han	15	Nahailie	28,224	Ming
6	Fuxi	40,000	Wei Jin Southern and Northern	16	Cangkai	-	Ming
7	Shitou	-	Wei Jin Southern and Northern	17	Jiangjunmiao	27,225	Qing
8	Heigucheng	18,750	Sui-Tang	18	Chahan	123,000	Qing
9	Yinglongcheng	21,210	Sui-Tang	19	Hudong	13,225	Qing
10	Kecaichengzhi	-	Sui-Tang	20	Dongba	49,600	-

Archaeological investigations have shown that the construction of ancient cities in the Qinghai Lake area began in the late Western Han Dynasty (4 AD) (Li, 1995; Bureau of National Cultural Relics, 1996). Many of the ancient cities are not well preserved, due to the length of time since the occupation, strong aeolian activity, and severe trampling by yak and sheep as part of nomadic pastoralism (**Figure 1**). **Table 1** details the area of ancient cities in the Qinghai Lake region, which range in age from the Western Han Dynasty to the Qing Dynasty. It is difficult to collect representative relics from most cities relative to present day pasture cover. For our study, we selected three cities, XHJGC, BXYGC, and FSC, that are relatively well preserved, are large in area, and have numerous tiles exposed on the surface (**Figure 2**). Details of what is known of the age and occupation of the three

FIGURE 2 | Remote sensing images showing an aerial view of the three ancient cities investigated in this study. **(A)** Xihaijun; **(B)** Beixiangyang; **(C)** Fuxi. See **Figure 1** for locations.

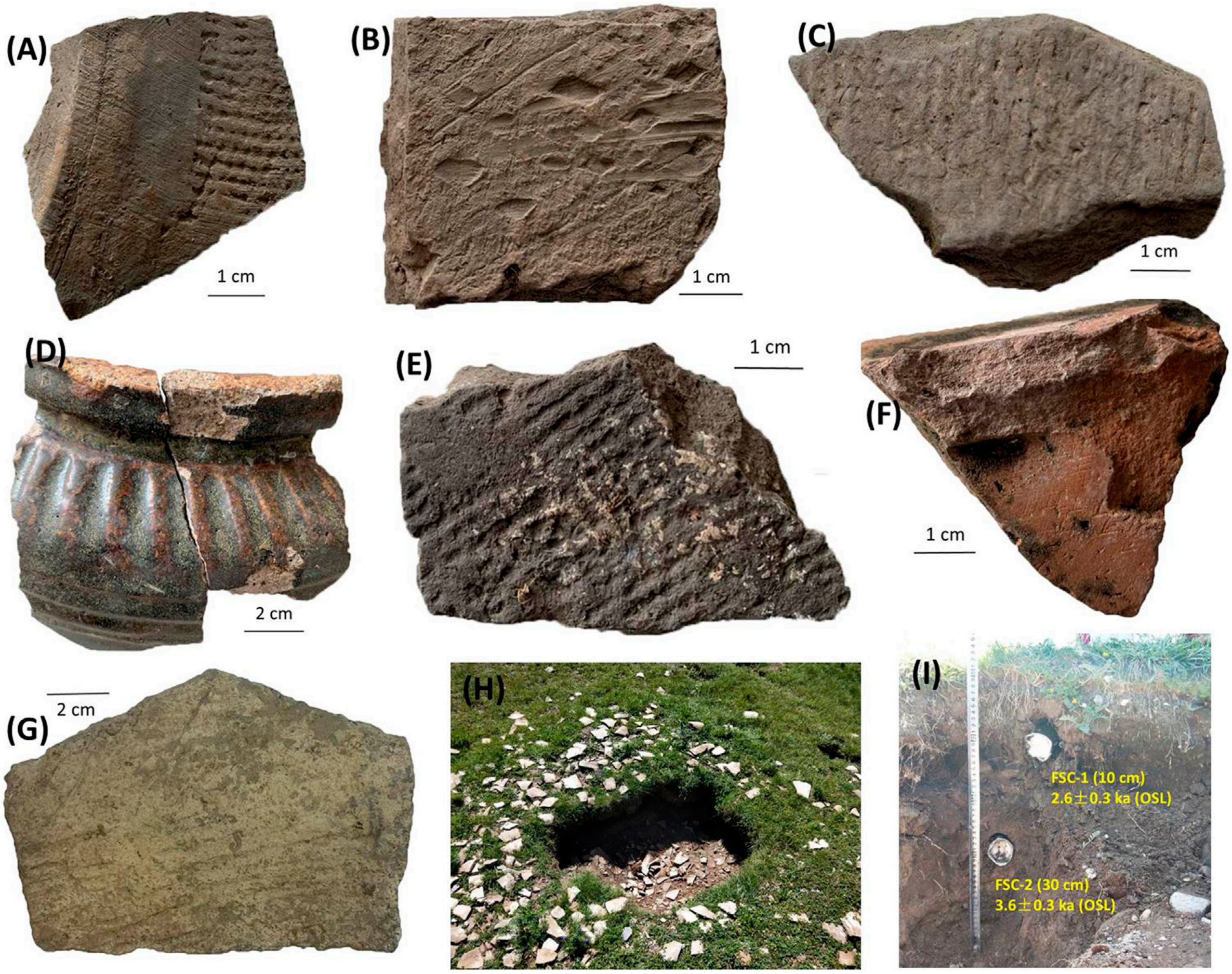

FIGURE 3 | Tiles and ceramics used for OSL dating in this study. **(A–C)** Gray muddy tiles exposed on the ground at Xihaijun. **(D–F)** Tiles and sand-filled red ceramic from Beixiangyang. **(G,H)** Gray-white sand-filled corded tiles found scattered on the ground at Fuxi. **(I)** Subsurface soil samples collected for OSL dating at Fuxi.

cities from the archaeological and documentary record are given below, along with details of samples collected in our fieldwork.

XHJGC (100° 58' 53", 36° 54' 20", 3,022 m) was built by emperor Wang Mang in 4 AD of the Xin Dynasty (9–23 AD), at the end of the Han Dynasty), and was the county capital of Xihai Jun, an administrative district in Chinese history (Cui et al., 1999). The city lies to the east of Qinghai Lake, on the south bank of Huangshui River, and is trapezoidal in shape with sides of 600–650 m. Archaeological finds include a "Xihaijun Tiger Runestone Cabinet," Kayue cultural sandy coarse pottery, tiles, "Wuzhu coins," and other currencies of the Western Han Dynasty and Wang Mang periods, a Wadang (traditional embossed roof tile end) with lotus pattern of the Tang Dynasty, and currencies of the Song Dynasty (Li, 1995). For OSL dating, we collected three gray muddy tiles that were exposed on the ground, approximately 1 cm thick, and decorated with rope patterns (**Figures 3A–C**, samples XHJGC-1, 2, 3).

BXYGC (99° 32' 42", 37° 09' 9", 3,242 m) was one of five county towns of Xihai Jun in the Xin Dynasty, located on the Buha River alluvial plain northwest of Qinghai Lake. The city is rectangular in shape, with east-west walls extending c. 400 m. The southern part of the ancient city was destroyed by a tributary of Buha River, and aeolian deposits have covered much of the area. Remnant walls in the middle and south of the city may be ancient houses, and there is an abandoned modern village on the northwest side. Numerous gray muddy tiles, sand-filled red ceramics, and brown enamel tiles are scattered throughout the city (**Figures 3D–F**) and probably represent more than one period. Two tiles and one ceramic were selected for OSL dating (samples BXYGC-1, 2, 3).

FSC (99° 34' 52", 37° 01' 32", 3,224 m) was the capital of Tuyuhun, a dynastic kingdom of nomadic peoples. Based on historical documents, Huang and Fang (1962) speculated that the city was founded no earlier than 481–491AD. The city is located about 7.5 km west of Qinghai Lake, with Shinaihai Northern Mountain to the south, on the alluvial fan plain of Cheji River (a tributary of Buha River). The main city is roughly within a 200 m square, with a gate about 10 m wide in the middle of the east wall, and an inner city. An outer fortress, located outside the main city, has suffered severe erosion and the northern part has been washed out by the Cheji River; no remains have been found in the outer city. Numerous gray-white sand-filled corded tiles were found on the north side of the main city in an excavated pit and exposed on the surface (**Figures 3G,H**). Four tiles were selected for OSL dating (samples FSC-1, 2, 3, 4), along with two soil samples at 10 and 30 cm depth (**Figure 3I**).

OSL Sample Preparation

Sample preparation was carried out in a dark room under red light. The same pretreatment procedure was used for tiles and ceramics (Sun et al., 2021). The top 2-3 mm was removed from the surface of the sample to eliminate the effect of sunlight exposure. A vice was used to crush the inner part of the sample, which was then gently ground in an agate mortar, and coarse particles of 90–154 μm were screened out. For sediment samples, c. 3 cm was removed from both ends of the sample tube in case of exposure, and the 63–90 μm fraction of the middle section was screened out using the wet screening method. For all samples, the screened coarse particles were soaked with 10% HCl and 30% H_2O_2 to remove carbonate and organic matter, and then 10% HF was added for etching for 40 min to remove impurities such as heavy minerals. Heavy liquid (2.58 g/cm^3) was used to separate feldspar and quartz, and the extracted quartz particles were added to 40% HF for etching for 40 min to remove surface α influence and impurities. Samples were rinsed repeatedly with pure water to neutral after each step. Finally, quartz purity was detected by infrared excitation for 40 s at 125°C followed by blue excitation for 40 s at 125°C. If OSL/IRSL<95%, HF etching was repeated until OSL/IRSL>95%.

OSL Measurement Methods and Instruments

Equivalent doses (D_e) were determined by the single-aliquot regenerative-dose (SAR) protocol (Murray and Wintle, 2000; Wintle and Murray, 2006). For D_e calculations, the initial 0–0.32 s of the OSL signal minus an early background signal of the following 0.32–0.64 s was selected (Ballarini et al., 2007; Cunningham and Wallinga, 2010). We measure 5–18 aliquots for each sample for D_e calculation. The number of aliquots for tile and ceramic samples was relatively low due to the small sample size available.

The dose rate was calculated by measuring the radioactivity of the tile/ceramic and the soil samples. Radioactivity comprises three elements: 1) beta dose from the tile/ceramic; 2) gamma dose from soil surrounding the artifact; and 3) a minor contribution from cosmic rays (Thomas et al., 2008). The concentration of U, Th, and K in tiles and sediments was obtained by inductively coupled plasma mass spectrometry (ICP-MS) and then converted into beta and gamma doses using conversion parameters (Guérin et al., 2012). The range of gamma rays in soil and tile/ceramic is very long (20–40 cm), which is much larger than the thickness of the tile/ceramic, so the internal gamma radiation can be ignored (Wang, 2008). In ceramics, the beta dose provided by the environment is absorbed by 90% at 2 mm depth from the surface; as we removed the top 2-3 mm of our ceramic samples, the beta dose provided by the soil can be ignored (Wang, 1993; 2008). We assumed a homogenous surrounding environment when calculating the dose rate for buried tiles. For those exposed at the surface, we used the gamma dose of the underlying soil to calculate the environmental dose rate. Since the air above the tiles/ceramic does not contribute to the gamma radiation, but we do not know how long the tiles/ceramic is exposed on the surface, half of the gamma dose and the entire gamma dose in the sediment underlying the tiles/ceramic were used to calculate the dose rates, respectively. The cosmic ray dose rate is calculated using the depth, altitude, and geographic coordinates of each sample (Prescott and Hutton, 1994). In this study, a value of 0.95 Gy/ka was used. The depth for estimating the cosmic ray dose rate is the sampling depth (**Table 2**). The altitude and geographic coordinates are based on those of the ancient city. The water content of the two paleosol samples in FSC was estimated with reference to a previous study

TABLE 2 | Characteristics of OSL samples from ancient cities around Qinghai Lake, northeastern Tibetan Plateau, analyzed in this study.

Sample ID	Depth (cm)	Sample type	Thickness (mm)	Size (cm)	Decoration	U (ppm)	Th (ppm)	K (%)	Beta (Gy/ka)	Gamma (Gy/ka)	Gamma[a] (Gy/ka)	Cosmic ray dose rate (Gy/ka)	Water content (%)	Dose rate (Gy/ka)	Dose rate[a] (Gy/ka)	Disc	D_e (Gy)	Age[a] (ka)	Age (ka)	Dynasty
XHJGC-1	0	Tile	14	3 × 4	Rope	5.00 ± 0.50	15.55 ± 0.80	3.19 ± 0.04	3.40 ± 0.05	1.70 ± 0.005		-	5 ± 5	-		-	-		-	-
XHJGC-2	0	Tile	15	3.5 × 4.5	Diamond	2.24 ± 0.30	14.59 ± 0.80	3.25 ± 0.04	3.29 ± 0.04	1.69 ± 0.003		-	5 ± 5	-		-	-		-	-
XHJGC-3	0	Tile	14	3.5 × 5.5	Rope	2.78 ± 0.40	14.51 ± 0.80	2.89 ± 0.04	3.04 ± 0.04	1.60 ± 0.004		-	5 ± 5	4.42 ± 0.18	3.77 ± 0.16	5	9.06 ± 1.22	2.4 ± 0.3	2.1 ± 0.3	Han
XHJGC-DB	0	Sandy loess	-	-	-	3.48 ± 0.40	11.97 ± 0.70	2.15 ± 0.04	2.46 ± 0.04	1.37 ± 0.004	0.69 ± 0.002	0.95	-	-		-	-		-	-
BXYGC-1	0	Tile	12	3.5 × 5	Brown enamel	4.00 ± 0.50	21.15 ± 1.00	1.92 ± 0.04	2.41 ± 0.05	1.48 ± 0.005		-	5 ± 5	-		-	-		-	-
BXYGC-2	0	Tile	14	3.5 × 6	Rope	3.00 ± 0.40	16.55 ± 0.90	3.36 ± 0.04	3.44 ± 0.04	1.76 ± 0.004		-	5 ± 5	4.61 ± 0.19	4.06 ± 0.17	6	7.95 ± 0.14	2.0 ± 0.1	1.7 ± 0.1	Han
BXYGC-3	0	Ceramic	17	4 × 5/2	None	2.59 ± 0.40	12.50 ± 0.70	2.45 ± 0.04	2.66 ± 0.04	1.46 ± 0.004		-	5 ± 5	3.93 ± 0.16	3.38 ± 0.14	6	7.41 ± 0.10	2.2 ± 0.1	1.9 ± 0.1	Han
BXYGC-DB	0	Aeolian sand	-	-	-	1.72 ± 0.30	8.85 ± 0.60	1.52 ± 0.04	1.83 ± 0.04	1.16 ± 0.004	0.58 ± 0.002	0.95	-	-		-	-		-	-
FSC-t-1	0	Tile	18	11 × 9	None	2.91 ± 0.40	14.96 ± 0.80	2.48 ± 0.04	2.55 ± 0.04	1.47 ± 0.004		-	5 ± 5	4.01 ± 0.17		18	7.83 ± 1.58	2.3 ± 0.5	2.0 ± 0.4	Wei Jin Southern and Northern
FSC-sed-1	0	Paleosol	-	-	-	1.93 ± 0.30	9.21 ± 0.60	1.69 ± 0.04	1.99 ± 0.04	1.21 ± 0.003	0.60 ± 0.002	0.95	-	-		-	-		-	-
FSC-t-2	10	Tile	18	12 × 8	None	2.58 ± 0.40	14.08 ± 0.80	2.36 ± 0.04	2.59 ± 0.04	1.46 ± 0.004		-	5 ± 5	3.91 ± 0.16		18	4.89 ± 0.54		1.3 ± 0.2	Wei Jin Southern and Northern
FSC-t-3	10	Tile	18	11 × 8	None	2.76 ± 0.40	16.00 ± 0.90	2.27 ± 0.04	2.55 ± 0.04	1.46 ± 0.004		-	5 ± 5	3.87 ± 0.16		18	7.56 ± 0.31		2.0 ± 0.1	Han
FSC-t-4	20	Tile	18	12 × 8	None	2.75 ± 0.40	14.83 ± 0.80	2.28 ± 0.04	2.72 ± 0.04	1.51 ± 0.004		-	5 ± 5	3.82 ± 0.16		16	6.53 ± 0.47		1.7 ± 0.2	Wei Jin Southern and Northern
FSC-sed-3	10	Paleosol	-	-	-	2.14 ± 0.30	1.41 ± 0.70	1.71 ± 0.04	2.03 ± 0.04	1.25 ± 0.003		0.95	-	-		-	-		-	-
FSC-1	10	Paleosol	-	-	-	1.85 ± 0.40	10.26 ± 0.70	1.61 ± 0.04	1.92 ± 0.04	1.20 ± 0.006		-	7 ± 5	3.00 ± 0.13		18	7.76 ± 0.69		2.6 ± 0.3	-
FSC-2	30	Paleosol	-	-	-	1.84 ± 0.40	11.10 ± 0.70	1.69 ± 0.04	1.99 ± 0.04	1.24 ± 0.006		-	7 ± 5	3.07 ± 0.14		18	10.93 ± 0.75		3.6 ± 0.3	-

[a] *Indicates the results calculated using half of the gamma dose in the sediments on the surface.*

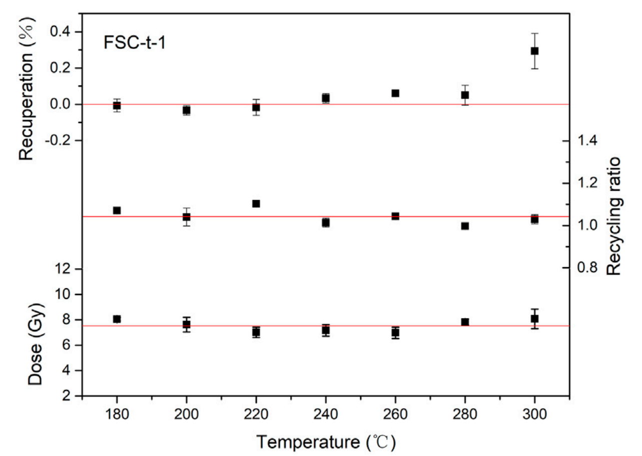

FIGURE 4 | Results of preheat plateau test for tile sample FSC-t-1 showing a plateau between 200 and 280°C.

in Qinghai Lake Basin as 7 ± 5% (Liu et al., 2012), and the tile water content was estimated as 5 ± 5%.

Pretreatment of tiles and stratigraphic samples and determination of D_e were carried out in the Laboratory of Luminescence Chronology at Qinghai Provincial Key Laboratory of Physical Geography and Environmental Processes using a standard Risø TL/OSL DA-20 reader with a ^{90}Sr/^{90}Y β radiation source. The environmental dose rate was measured at Xi'an Geological Survey Center.

RESULTS

Luminescence Characteristics

A preheat plateau test was carried out on tile sample FSC-t-1 to select the appropriate preheating temperature for D_e measurements (**Figure 4**). Three aliquots were measured at each temperature. There was a clear plateau between 200 and 280°C, the recycling ratio was between 0.9 and 1.1, and recuperation was stabilized at 0–1%. Based on this, a routine preheat temperature of 260°C and cut-heat temperature of 220°C were employed for all D_e measurements. Typical growth and decay curves for soil, surface exposed tile, and buried tile samples at FSC are shown in **Figures 5A–C**. The luminescence signal of FSC samples shows characteristics of fast composition, decaying to background levels within 2 s. Decay and growth curves for surface exposed ceramic at BXYGC (**Figure 5D**) show a strong response, with a bright signal that attained 30,000 counts and a perfect growth curve.

Dating Results

Radionuclide concentration and beta and gamma dose rate for tiles, ceramic, and soil samples are given in **Table 2**, along with U, Th, and K concentrations and other characteristics. U, Th, and K concentrations in tiles and ceramics are relatively concentrated, ranging from 2.24 to 5.00 ppm, 12.50–21.15 ppm, and 1.92–3.36%, respectively. The dose rate ranges between 3.00 and 4.58 Gy/ka. For the calculation of the dose rate of all tiles/ceramic, the inner beta dose from tiles/ceramic itself and the outer gamma dose from the sediment surrounding the artifact were used. In XHJGC and BXYGC, the outer gamma doses from XHJGC-DB and BXYGC-DB were used to calculate the dose rate, respectively; in FSC, the gamma dose from FSC-sed-1 was used to calculate the dose rate of FSC-t-1, and the gamma dose from FSC-sed-2 was used to calculate the dose rate of FSC-t-2, 3, and 4. For the sediment samples (FSC-1 and FSC-2), the calculation of dose rate used its own U, Th, and K (**Table 2**). For the tiles/ceramic on the surface, the ages calculated using half of the gamma dose rates are older, and the ages calculated using the entire gamma doses are closer to the ages of the cities recorded in the historical documents (**Table 2**). Since it is not clear how long the tiles/ceramic are exposed on the surface, we assume that the tiles/ceramic are not exposed for a long time. Finally, the entire gamma doses were used to determine the age of the tiles/ceramic on the surface.

The OSL age results (**Table 2**) show dates of 0–220 AD for XHJGC and 20–220 AD for BXYGC, both of which are in the Han Dynasty. Tiles at FSC were dated between 120 and 520 AD, mostly in the Wei Jin Southern and Northern Dynasties. The age of the surface exposed tile at FSC (FSC-t-1) is 20–420 AD, which is within the error range of buried tiles; this suggests that surface tiles at Fuxi are less affected by sun bleaching and may not have been exposed at the surface for a long time. The luminescence ages of paleosol samples at FSC are 2.6 ± 0.3 ka at 10 cm depth and 3.6 ± 0.3 ka at 30 cm depth, which is much earlier than the construction of Fuxi suggested by the tile dates. This indicates the city wall was built on the surface, the ground was not rammed, and the use of the city site did not disturb the soil below 10 cm depth.

DISCUSSION

Age of Construction and Occupation of Ancient Cities in Qinghai Lake Basin

The gray muddy corded tiles we collected at XHJGC and BXYGC have similar typological characteristics, so likely originated from the same period, and this is confirmed by the OSL results that show tiles and ceramics from XHJGC and BXYGC date to 0–220 AD. The dates indicate the cities were built in the Xin Dynasty, which coincides with documentary evidence for the establishment of Xihai Jun (Cui et al., 1999). Based on the similarity of construction systems and artifacts, the three ancient cities identified in archaeological surveys of Qinghai Lake Basin, Gahai, BXYGC, and Nanxiangyang, were considered as three of the five county cities of Xihai Jun (Cui et al., 1999). With the collapse of the Wang Mang regime in 23 AD, Xihai Jun was abandoned, the Qinghai Lake area was reoccupied by the Qiang people, and wars of resistance against the Eastern Han regime erupted many times (Cui et al., 1999). Ancient cities built during the Wang Mang period may have been reused for military defense during these wars. Various finds at XHJGC, including Wadang with the writing of the Eastern Han Dynasty, Lotus pattern tiles of the Tang Dynasty, and coins of the Song Dynasty (Li, 1995), indicate the city was restored and reused in these periods.

Tiles found at FSC, gray-white sand-filled corded types with a rough, thick texture, differ from those of the late Western Han

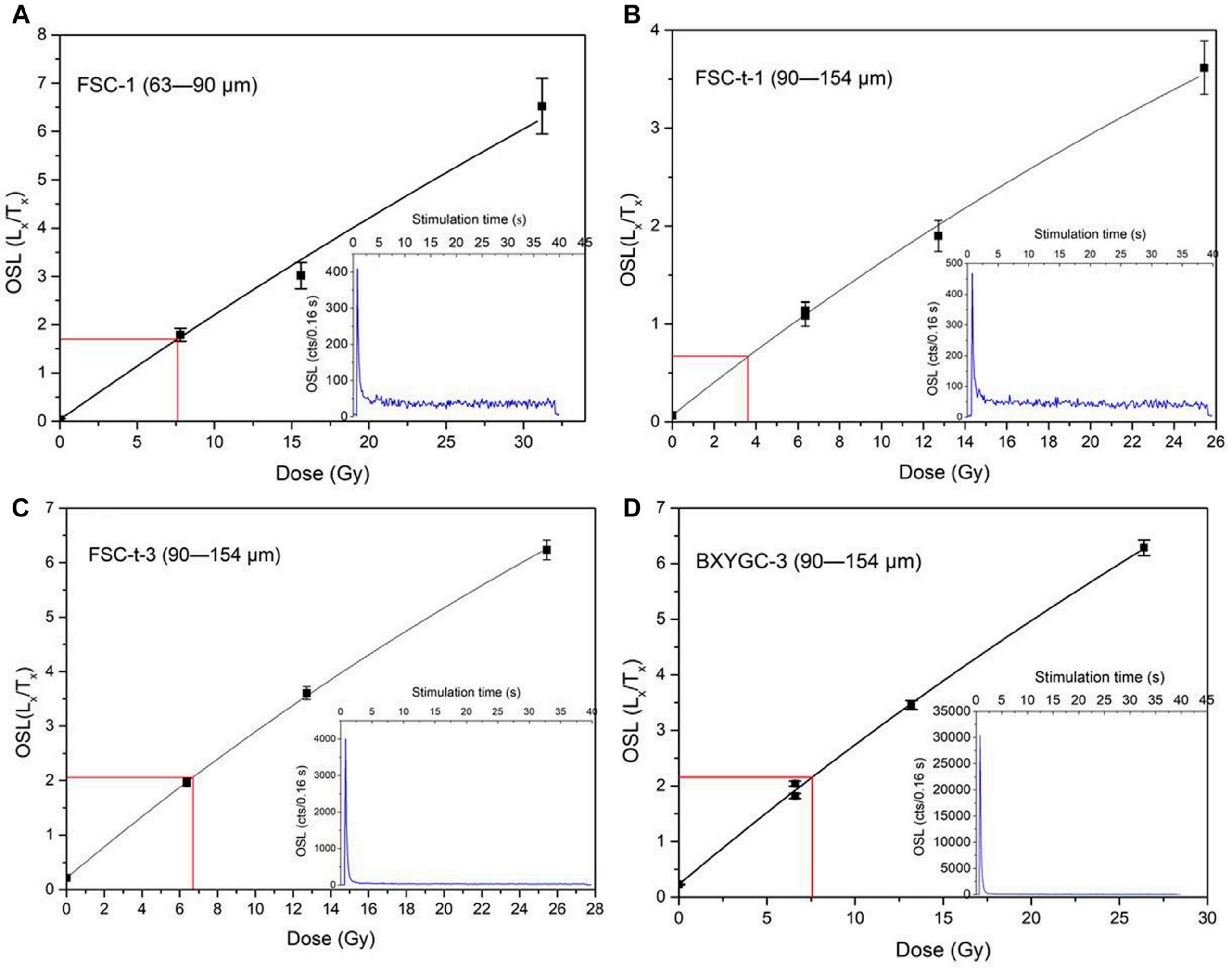

FIGURE 5 | Quartz luminescence characteristics of selected tile and soil samples. **(A)** Growth curve and corresponding decay curve (inset) of soil sample from Fuxi (FSC-1). **(B)** Growth curve and corresponding decay curve of tile sample exposed on the ground at Fuxi (FSC-t-1). **(C)** Growth curve and decay curve of tile sample from the profile at Fuxi (FSC-t-3). **(D)** Growth curve and corresponding decay curve of ceramic exposed on the ground at Beixiangyang (BXYGC-3).

Dynasty found at XHJGC and BXYGC, indicating they belong to a different culture. The luminescence age of the FSC tiles confirms this, dating them to 120–520 AD which mainly corresponds with the Wei Jin Southern and Northern Dynasties. The ancient texts of *Wei Shu, Tuyuhun Zhuan* and *Bei Shi, Tuyuhun Zhuan,* record the construction of Fuxi city during the Wei Jin Southern and Northern Dynasties, and it became the command center for Tuyuhun occupation of the Qinghai Lake area (Huang and Fang, 1962). No traces of earth ramming have been found at Fuxi; it is likely that the nomadic Tuyuhun set up camps, and that the site was only occupied briefly at that time. However, Fuxi was reoccupied for long periods as an imperial city due to its strategic location on the Silk Road and it played an important role in economic and cultural communications between East and West (Cui et al., 1999). Based on the ^{14}C dating of charcoal sheep dung in the cultural layer (Dong et al., 2016), the city was occupied intermittently through to the Ming Dynasty, 1450–1524 AD.

Qinghai Lake Ancient Cities and Human-Land Relationships

In the late Western Han Dynasty, Wang Mang served as the governor of Xihai Jun and established the earliest city in the Qinghai Lake area in c. 4 AD. Tens of thousands of lawbreakers in the Central Plains were forcibly relocated to Xihai Jun and carried out farming activities there (according to the text of *Han Shu, Wangmang Zhuan*). The number and area of cities reflect the high intensity of human activities in the Qinghai Lake area at that time (**Table 1**). Archaeologists have excavated farming tools in the ancient city of Caolongduo (one of the five counties in Xihai Jun, now submerged by the Longyangxia Reservoir) (Chen, 2005), which confirms that residents of Xihai Jun reclaimed farmland in the Qinghai Lake area in the late Western Han Dynasty. Paleoenvironmental records, including alkenone-based water temperature records from Qinghai Lake sediment core QHL3-

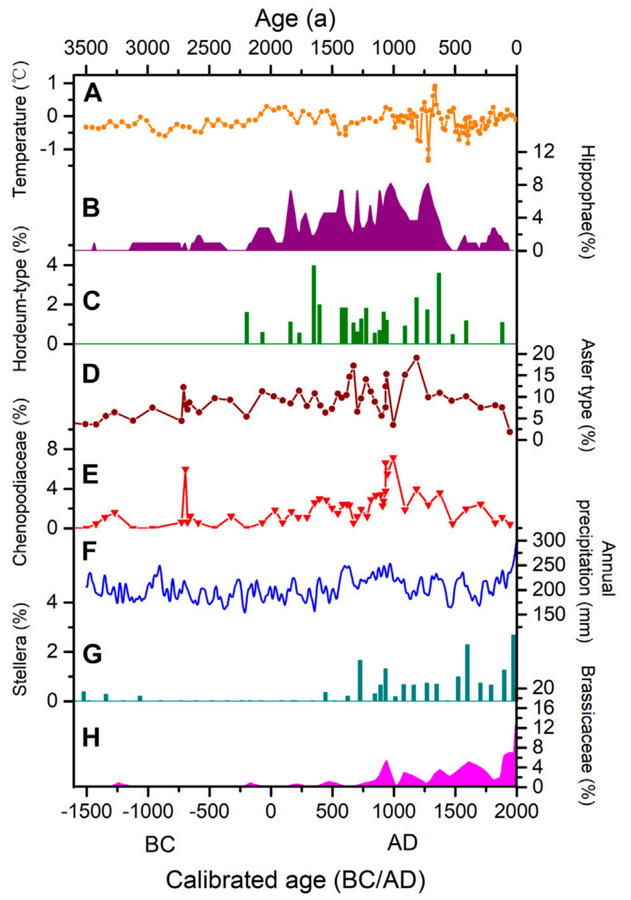

FIGURE 6 | Various paleoenvironmental records for Qinghai Lake area, northeastern Tibetan Plateau. **(A)** Alkenone-based water temperature records from Qinghai Lake (Liu et al., 2006). **(B)** Percentage of Hippophae pollen in the LGR section at the southeastern margin of Qinghai Lake Basin (Wei et al., 2020). **(C–E)** Human-related pollen taxa from the LGR section (Wei et al., 2020). **(F)** Annual precipitation reconstruction for the northeastern Tibetan Plateau based on tree rings (Yang et al., 2014). **(G)** Stellera pollen percentages from core GGHA from Genggahai Lake in the Gonghe Basin (Huang et al., 2017). **(H)** Brassicaceae pollen percentages from Lake Genggahai (Liu et al., 2016).

1 (**Figure 6A**) and Hippophae pollen percentages in the LGR section in eastern Qinghai Lake Basin (**Figure 6B**), indicate this was a relatively warm and humid period (Liu et al., 2006; Wei et al., 2020). Thus, hydrothermal conditions in the late Western Han Dynasty were favorable for the development of agriculture. Pollen taxa associated with human activity, such as Hordeum-type, Aster-type, and Chenopodiaceae, first appeared or increased significantly around 2.2 ka (**Figures 6C–E**), indicating ancient humans were engaged in extensive agricultural production in the Qinghai Lake Basin at that time (Wei et al., 2020). After the fall of the Wang Mang regime in 23 AD, Xihai Jun was abandoned and the Qinghai Lake area came under the control of the nomadic Qiang people, so the intensity of agricultural activities declined.

At the beginning of the 4th century AD, the nomadic Tuyuhun occupied the Qinghai Lake area and after they came into contact with agricultural influences via the Silk Road, they began to engage in grazing activities and plant barley, beans, and vegetables (according to the text of *Bei Shi, Tuyuhun Zhuan).* Chen et al. (2016) reported a period of strong aeolian activity from c. 1.5 to 0 ka in the northeastern Tibetan Plateau; however, precipitation reconstruction from tree rings contradicts this, with an upward trend between 500 and 600 AD (**Figure 6F**) (Chen et al., 2016; Yang et al., 2014). This discrepancy suggests increasing aeolian activity after c. 1.5 ka BP may be related to human activity rather than climate change (Chen et al., 2016). A range of proxy indicators indicate an increased intensity in grazing and cultivation activities in Qinghai Lake region at that time. Magnetic susceptibility results for a section in the southwest of Qinghai Lake show paleosol development at 2–1.5 ka (Zhang et al., 2018). Brassicaceae and Stellera pollen in a sediment core from Genggahai Lake increased significantly after c. 1.5 ka (**Figures 6G,H**) (Liu et al., 2016; Huang et al., 2017).

From the time of the Western Han Dynasty (206 BC to 9 AD) to the end of the Qing Dynasty (1911 AD), a period of more than 1,800 years, there were frequent contacts between the nomadic tribes and the Central Plains regime in the Qinghai Lake region, the number of ancient cities increased, and there were repeated shifts between nomadism and farming. Although the total area of cultivation was limited, it was sufficient to damage the natural alpine meadow and shrub vegetation cover of the Qinghai Lake area. Hence, beginning at least 2,000 years ago, human activities might have started to overtake natural climatic variability as the dominant controls of dust storm activity in eastern China (Chen et al., 2020).

CONCLUSION

OSL dating was undertaken on tiles and ceramics from the ancient Qinghai Lake Basin cities of XHJGC, BXYGC, and FSC. The OSL ages of 0–220 AD for XHJGC and BXYGC and 120–520 AD for FSC are consistent with historical documents. The results provide an absolute chronology for tiles in the late Western Han Dynasty and the Tuyuhun period. Paleoclimate records show that the warm and humid climate at c. 2 ka provided good hydrothermal conditions for human activities in the Qinghai Lake area, including farming. During the Wei Jin Southern and Northern Dynasties, Fuxi became the control center for Tuyuhun. As an important transportation node on the Silk Road, the Qinghai Lake area flourished with east-west communication, so the intensity of human activities increased, and the concentration of sporopollenin related to human activities also increased significantly. Since the late Western Han Dynasty, repeated shifts between nomadic pasture and farmland damaged vegetation cover in the Qinghai Lake area and intensification of human activities has been an important influence on aeolian activity.

DATA AVAILABILITY STATEMENT

The original contributions presented in the study are included in the article/Supplementary Material; further inquiries can be directed to the corresponding authors.

AUTHOR CONTRIBUTIONS

YS, CE, and MS contributed to conception and design of the study. MS and HW organized the database. GH provided a typological study of tiles. YZ and LX participated in field sampling. JX performed the statistical analysis. MS wrote the first draft of the manuscript. All authors contributed to manuscript revision and read and approved the submitted version.

FUNDING

This research was funded by the National Natural Science Foundation of China (Grant nos. 42061016, 41761042, and 2021-ZJ-917).

ACKNOWLEDGMENTS

The authors thank Zhang Jing, Li Ping, and Gao Jingyi for help in the field. Thanks are due to Dr. Barbara Rumsby for editing the manuscript.

REFERENCES

Ballarini, M., Wallinga, J., Wintle, A. G., and Bos, A. J. J. (2007). A Modified SAR Protocol for Optical Dating of Individual Grains from Young Quartz Samples. *Radiat. Measurements* 42, 360–369. doi:10.1016/j.radmeas.2006.12.016

Brantingham, P. J., and Xing, G. (2006). Peopling of the Northern Tibetan Plateau. *World Archaeology* 38, 387–414. doi:10.1080/00438240600813301

Bureau of National Cultural Relics (1996). *Atlas of Chinese Cultural Relics-Fascicule of Qinghai Province*. Beijing: China Cartograghic Publishing House Press. (in Chinese).

Chen, F., Chen, S., Zhang, X., Chen, J., Wang, X., Gowan, E. J., et al. (2020). Asian Dust-Storm Activity Dominated by Chinese Dynasty Changes since 2000 BP. *Nat. Commun.* 11 (1), 992. doi:10.1038/s41467-020-14765-4

Chen, F. H., Dong, G. H., Zhang, D. J., Liu, X. Y., Jia, X., An, C. B., et al. (2015). Agriculture Facilitated Permanent Human Occupation of the Tibetan Plateau after 3600 B.P. *Science* 347, 248–250. doi:10.1126/science.1259172

Chen, F., Wu, D., Chen, J., Zhou, A., Yu, J., Shen, J., et al. (2016). Holocene Moisture and East Asian Summer Monsoon Evolution in the Northeastern Tibetan Plateau Recorded by Lake Qinghai and its Environs: A Review of Conflicting Proxies. *Quat. Sci. Rev.* 154, 111–129. doi:10.1016/j.quascirev.2016.10.021

Chen, X. H. (2005). The Human Activity in the Region of the Qinghai Lake and Environment. *J. Qinghai Nationalities Inst. (Social Sciences)* 31, 38–43. (in Chinese with English abstract). doi:10.3969/j.issn.1674-9227.2005.01.010

Cui, Y. H., Zhang, D. Z., and Du, C. S. (1999). *The History of Qinghai Provinve*. Xining: Qinghai People Press. (in Chinese).

Cunningham, A. C., and Wallinga, J. (2010). Selection of Integration Time Intervals for Quartz OSL Decay Curves. *Quat. Geochronol.* 5, 657–666. doi:10.1016/j.quageo.2010.08.004

Daniels, F., Boyd, C. A., and Saunders, D. F. (1953). Thermoluminescence as a Research Tool. *Science* 117, 343–349. doi:10.1126/science.117.3040.343

Dong, G., Liu, H., Yang, Y., Yang, Y., Zhou, A., Wang, Z., et al. (2016). Emergence of Ancient Cities in Relation to Geopolitical Circumstances and Climate Change during Late Holocene in Northeastern Tibetan Plateau, China. *Front. Earth Sci.* 10, 669–682. doi:10.1007/s11707-015-0575-7

Guérin, G., Mercier, N., Nathan, R., Adamiec, G., and Lefrais, Y. (2012). On the Use of the Infinite Matrix assumption and Associated Concepts: A Critical Review. *Radiat. Measurements* 47, 778–785. doi:10.1016/j.radmeas.2012.04.004

Hou, G. L., Lai, Z. P, Cao, G. C., E, C. Y., Sun, Y. J, Rhode, D., et al. (2015). The Earliest Prehistoric Pottery in the Qinghai-Tibetan Plateau and its Archaeological Implications. *Quat. Geochronol.* 30, 431–437.

Huang, S. Z., and Fang, Y. (1962). The Ancient Capital of Tuyuhun-Discovery of Fuxi City. *Archaeology* 8, 436–440. (in Chinese).

Huang, X.-Z., Liu, S.-S., Dong, G.-H., Qiang, M.-R., Bai, Z.-J., Zhao, Y., et al. (2017). Early Human Impacts on Vegetation on the Northeastern Qinghai-Tibetan Plateau during the Middle to Late Holocene. *Prog. Phys. Geogr. Earth Environ.* 41, 286–301. doi:10.1177/0309133317703035

Huo, W. (2017). Ancient Qinghai and the Silk Road from Relics and Archaeology Study. *J. Qinghai Nationalities Univ. (Social Sciences)* 43, 10–15. (in Chinese with English abstract). doi:10.3969/j.issn.1674-9227.2017.01.002

Lai, Z. P., Hou, G. L., Cao, G. C., Sun, Y. J., Wang, Y. X., et al. (2015). Age Determination for a Neolithic Site in Northeastern Qinghai-Tibetan Plateau Using a Combined Luminescence and Radiocarbon Dating. *Quat. Geochronol.* 30, 411–415. doi:10.1016/j.quageo.2015.01.007

Li, Z. X. (1995). *The Examination of Ancient Cities in Qinghai Province*. China, Xi'an: Northwestern University Press. (in Chinese).

Liu, S. S., Huang, X. Z., Qiang, M. R., Lin, X. R., Bai, Z. J., and Peng, W. (2016). Vegetation and Climate Change during the Mid-Late Holocene Reflected by the Pollen Record from Lake Genggahai, Northeastern Tibetan Plateau. *Quat. Sci.* 36, 247–256. doi:10.11928/j.issn.1001-7410.2016.02.01

Liu, X., Lai, Z., Yu, L., Sun, Y., and Madsen, D. (2012). Luminescence Chronology of Aeolian Deposits from the Qinghai Lake Area in the Northeastern Qinghai-Tibetan Plateau and its Palaeoenvironmental Implications. *Quat. Geochronol.* 10, 37–43. doi:10.1016/j.quageo.2012.01.016

Liu, Z. H., Henderson, A. C. G., and Huang, Y. S. (2006). Alkenone-Based Reconstruction of Late-Holocene Surface Temperature and Salinity Changes in Lake Qinghai, China. *Geophys. Res. Lett.* 33, 370–386. doi:10.1029/2006gl026947

Murray, A. S., and Wintle, A. G. (2000). Luminescence Dating of Quartz Using an Improved Single-Aliquot Regenerative-Dose Protocol. *Radiat. Measurements* 32, 57–73. doi:10.1016/s1350-4487(99)00253-x

Prescott, J. R., and Hutton, J. T. (1994). Cosmic ray Contributions to Dose Rates for Luminescence and ESR Dating: Large Depths and Long-Term Time Variations. *Radiat. Measurements* 23, 497–500. doi:10.1016/1350-4487(94)90086-8

Rhode, D., Haiying, Z., Madsen, D. B., Xing, G., Jeffrey Brantingham, P., Haizhou, M., et al. (2007). Epipaleolithic/Early Neolithic Settlements at Qinghai Lake, Western China. *J. Archaeological Sci.* 34, 600–612. doi:10.1016/j.jas.2006.06.016

Sun, M. P. (2019). *Luminescence Dating on Ceramic of Nuomuhong Talitaliha Site and Tianjun Karst Cave Site*. master's thesis. Xining, Qinghai provincce: Qinghai Normal University.

Sun, M., Sun, Y., E, C., Hou, G., Zhang, J., and Shi, Y. (2021). Luminescence Dating of Nuomuhong Culture Ceramics at Talitaliha Site on the Northeastern Qinghai-Tibetan Plateau. *Geochronometria*. doi:10.2478/geochr-2020-0034

Sun, Y., Chongyi, E., Lai, Z., and Hou, G. (2018). Luminescence Dating of Prehistoric Hearths in Northeast Qinghai Lake and its Paleoclimatic Implication. *Archaeol Anthropol. Sci.* 10, 1525–1534. doi:10.1007/s12520-017-0472-y

Sun, Y., Lai, Z., Madsen, D., and Hou, G. (2012). Luminescence Dating of a Hearth from the Archaeological Site of Jiangxigou in the Qinghai Lake Area of the Northeastern Qinghai-Tibetan Plateau. *Quat. Geochronol.* 12, 107–110. doi:10.1016/j.quageo.2012.01.010

Thomas, P. J., Nagabhushanam, P., and Reddy, D. V. (2008). Optically Stimulated Luminescence Dating of Heated Materials Using Single-Aliquot Regenerative-Dose Procedure: A Feasibility Study Using Archaeological Artefacts from India. *J. Archaeological Sci.* 35, 781–790. doi:10.1016/j.jas.2007.06.015

Wang, S., and Zhao, X. (2013). Re-Evaluating the Silk Road's Qinghai Route Using Dendrochronology. *Dendrochronologia* 31, 34–40. doi:10.1016/j.dendro.2012.05.001

Wang, W. D. (2008). The Correct Estimation of Palaeodose in Porcelain Thermoluminescence Dating. *Sci. China Press* 38, 460–468. doi:10.1088/0953-8984/20/42/425208

Wang, W. D. (1993). Thickness Response of β Dose Rate in Pottery Fragments. *Nucl. Tech.* 16, 228–231.

Wei, H., E, C., Zhang, J., Sun, Y., Li, Q., Hou, G., et al. (2020). Climate Change and Anthropogenic Activities in Qinghai Lake basin over the Last 8500 Years Derived from Pollen and Charcoal Records in an Aeolian Section. *Catena* 193, 104616. doi:10.1016/j.catena.2020.104616

Wintle, A. G., and Murray, A. S. (2006). A Review of Quartz Optically Stimulated Luminescence Characteristics and Their Relevance in Single-Aliquot Regeneration Dating Protocols. *Radiat. Measurements* 41, 369–391. doi:10.1016/j.radmeas.2005.11.001

Yang, B., Qin, C., Wang, J., He, M., Melvin, T. M., Osborn, T. J., et al. (2014). A 3,500-Year Tree-Ring Record of Annual Precipitation on the Northeastern Tibetan Plateau. *Proc. Natl. Acad. Sci.* 111, 2903–2908. doi:10.1073/pnas.1319238111

Zhang, J., E, C. Y., and Zhao, Y. J. (2018). A High-Density Optical Stimulated Luminescence (OSL) Dating at Heima He Loess Section in Qinghai Lake Area. *J. Earth Environ.* 9, 557–568. (in Chinese with English abstract).

Conflict of Interest: The authors declare that the research was conducted in the absence of any commercial or financial relationships that could be construed as a potential conflict of interest.

frontiers in Earth Science

ORIGINAL RESEARCH
published: 08 September 2021
doi: 10.3389/feart.2021.736895

Earth Ice Age Dynamics: A Bimodal Forcing Hypothesis

Zhongping Lai[1,2,3], Yantian Xu[1] and Peisong Zheng[1]*

[1]Institute of Marine Sciences, Guangdong Provincial Key Laboratory of Marine Biotechnology, Shantou University, Shantou, China, [2]School of Geography and the Environment, University of Oxford, Oxford, United Kingdom, [3]Southern Marine Science and Engineering Guangdong Laboratory (Zhuhai), Zhuhai, China

The Earth has gone through multiple ice ages in the past million years. Understanding the ice age dynamics is crucial to paleoclimatic study, and is helpful for addressing future climate challenges. Though ice ages are paced by variations in Earth's orbit geometry, how various climatic system components on the Earth respond to insolation forcing and interact with each other remains unclear. A prevailing view argues that the initial responses occur in the northern high latitudes (i.e. the northern high-latitude hypothesis, NHH). This opinion is challenged by recent reports, such as the lead of climate change in the Southern Hemisphere (SH) relative to that in the Northern Hemisphere (NH), the southern control on Atlantic meridional overturning circulations (AMOC), and the potential significance of Southern Hemisphere (SH). Alternatively, the tropical hypothesis (TH) argues for a leading role of the tropics. Both the NHH and the TH belong to a single-forcing mechanism, and have difficulty in interpreting phenomena, such as the saw-tooth pattern of the ice ages. Here we present a new proposal concerning the Earth's ice age dynamics: the bimodal forcing hypothesis (BFH). The essential assumption of this hypothesis is that for glacial-interglacial cycles, the cooling (glaciation) starts from the northern high latitudes, whereas the warming (deglaciations) starts from the SH. Particularly, the BFH emphasizes the significance of SH oceans in accumulating and transferring heat for deglaciations. Thus, it is capable to reasonably explain the saw-tooth pattern. We compiled 100 paleotemperature records globally for validation. The BFH is consistent with most of these records, and provides a straightforward and comprehensible way to interpret ice age on Earth.

Keywords: milankovitch theory, ice age cycles, forcing mechanisms, bimodal hypothesis, termination from the south, cooling from the north

Edited by:
Shiyong Yu,
Jiangsu Normal University, China

Reviewed by:
Xiaodong Miao,
Linyi University, China
Qiong Chen,
Shandong University, China

***Correspondence:**
Zhongping Lai
zhongping.lai@yahoo.com

Specialty section:
This article was submitted to Quaternary Science, Geomorphology and Paleoenvironment, a section of the journal Frontiers in Earth Science

Received: *06 July 2021*
Accepted: *24 August 2021*
Published: *08 September 2021*

Citation:
Lai Z, Xu Y and Zheng P (2021) Earth Ice Age Dynamics: A Bimodal Forcing Hypothesis. Front. Earth Sci. 9:736895. doi: 10.3389/feart.2021.736895

INTRODUCTION

How the Earth's climate would respond to increasing anthropogenic atmospheric carbon dioxide concentration concerns the human society (IPCC and Stocker, 2013; Steffen et al., 2018). Resolving this problem requires insights from both the current and paleoclimatic studies (e.g. Zheng et al., 2021). Climate of the past ~2.6 million years (Myr) is characterized by repeated growth and decay of large continental ice sheets, with astronomical cycles at ~23 thousand years (kyr), ~41 kyr, and ~100 kyr (Milankovitch, 1941; Hays et al., 1976). Although variations in Earth orbital geometry have been widely accepted as the ultimate cause of glacial-interglacial cycles, the process that translates the insolation oscillations into periodic climate change is still in debate (Imbrie et al., 1992, 1993; Denton et al., 2010). A long-lasting enigma is the saw-tooth pattern of ice ages, i.e., relatively long periods of ice-sheet growth followed by relatively short periods of ice-sheet decay (Broecker and Donk, 1970; Lisiecki and Raymo, 2005). How do symmetric insolation fluctuations result in asymmetric ice age cycles? Internal feedbacks in Earth's climate system are

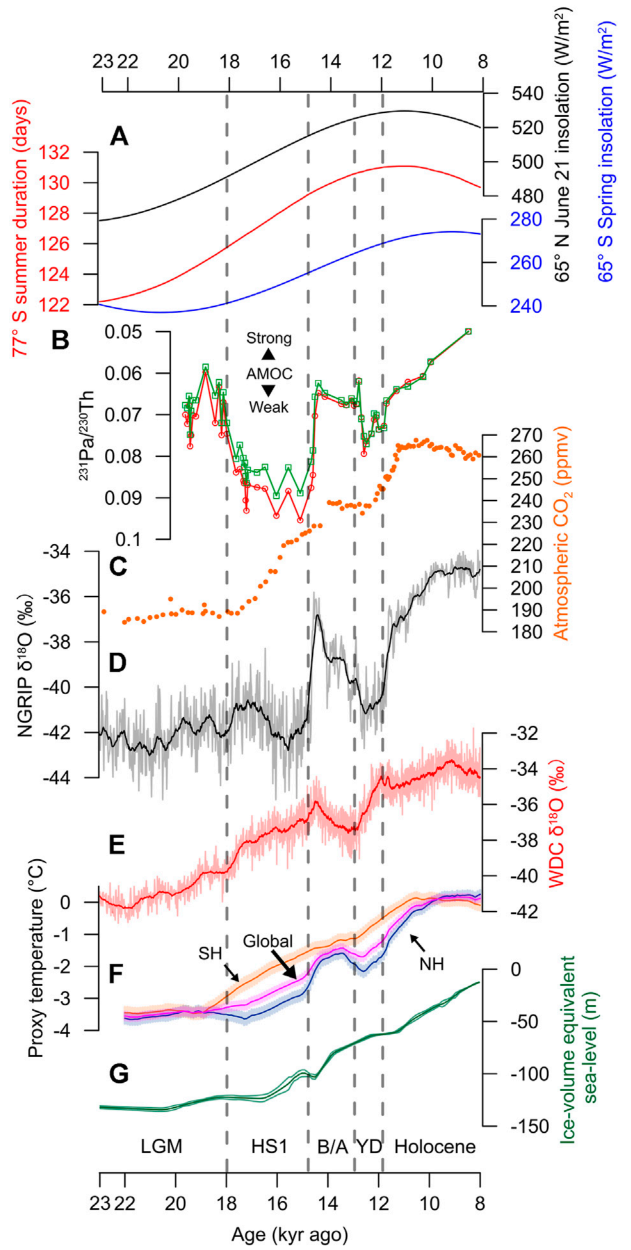

FIGURE 1 | Climatic records during the last deglaciation. **(A)** 65°N June 21 insolation (black) (Laskar et al., 2004). 65°S averaged mean longitude spring insolation (August 21 to November 20, blue) (Laskar et al., 2004; Stott et al., 2007). 77°S summer duration (red), which is measured as the number of days whose diurnal average insolation exceeds 250 W/m2 (Huybers and Denton, 2008). **(B)** North Atlantic core OCE326-GGC5 ^{231}Pa/^{230}Th ratios for the overall strength of AMOC. Red and green are ^{238}U-based value and ^{232}U-based results, respectively. Increasing values (plotted downward) indicate reduced overturning strength (McManus et al., 2004). **(C)** Atmospheric CO$_2$ from EPICA Dome C (EDC) ice core (Monnin et al., 2001). **(D)** δ^{18}O from North Greenland Ice Core Project (NGRIP) ice core (grey. Black for 20 points smoothed data). (Rasmussen et al., 2006). **(E)** δ^{18}O from West Antarctic Ice Sheet Divide (WDC) ice core, (grey. Black for 30 points smoothed data) (WAIS Divide Project Members, 2015). **(F)** Northern Hemisphere (NH; blue), Southern Hemisphere (SH; orange), and global (pink) surface temperature stacks with 1σ error range (Shakun et al., 2012). **(G)** Ice-volume equivalent sea level plotted with 2σ *(Continued)*

FIGURE 1 | uncertainty (Lambeck et al., 2014). All data are on their published timescale. Periods of Last Glacial Maximum (LGM), Henrich stadial 1 (HS1), Bølling-Allerød (B/A), Younger Dryas (YD) and Holocene are separate by grey dashed lines.

believed to be the answer. Different understandings of internal feedbacks with emphasis on different climate components lead to multiple climate hypotheses, such as the northern high-latitude hypothesis (NHH; e.g. Denton et al., 2010) and the tropical hypothesis (TH; e.g. Cane, 1998; Clement et al., 2001; Chiang, 2009; Beck et al., 2018; Wang, 2021). The NHH and the TH, both belong to a single-forcing mechanism (Ding, 2006), argue for a leading role of the northern high latitudes and the tropics, respectively. However, a single-forcing mechanism has difficulty in interpreting phenomena like the saw-tooth pattern.

The bimodal forcing hypothesis (BFH) we proposed here assumes cooling/glaciation starts from the northern high-latitudes while warming/deglaciation from the SH. We tested this hypothesis with a compilation of 100 global paleotemperature records. The BFH is compatible with most of them, and can better explain puzzles like the saw-tooth problem. In the following, we first outline the NHH and its drawbacks, then illustrate the logic of the BFH, and finally discuss future directions of this new hypothesis.

THE NORTHERN HIGH-LATITUDE HYPOTHESIS AND ITS DRAWBACKS

The Key Points of Northern High-Latitude Hypothesis

So far, the NHH has been the most prevailing ice age hypothesis. Essentially, it argues for a uniquely triggering role of the summer insolation at 65°N in both hemispheres (e.g. Kawamura et al., 2007). A concomitant assumption is that initial responses to insolation forcing happen in northern high latitudes, no matter in ice age onsets (e.g. Imbrie et al., 1992; 1993) or terminations (e.g. Denton et al., 2010). Besides, the ‘switch’ of Atlantic meridional overturning circulation (AMOC), which exerts an important effect on interhemispheric heat redistribution, is assumed to lie in the northern North Atlantic (e.g. Broecker and Denton, 1989; Clark et al., 2002). After the pioneering interpretation of glacial-interglacial cycles from a northern perspective (Imbrie et al., 1992; 1993), a comprehensive NHH-based picture of working processes during the last deglaciation was presented (Denton et al., 2010).

In summary, the rising NH summer insolation at the end of Last Glacial Maximum (LGM) (**Figure 1A**, black curve) initiated ice-sheet melting and delivered freshwater into the North Atlantic. This freshwater forcing shut down the AMOC during the Heinrich stadial 1 (HS1) interval (**Figure 1B**; Ganopolski and Rahmstorf, 2001; McManus et al., 2004; Liu et al., 2009), resulting in the deglacial warming in the SH through the bipolar seesaw mechanism (Crowley, 1992; Broecker, 1998; Stocker and Johnsen,

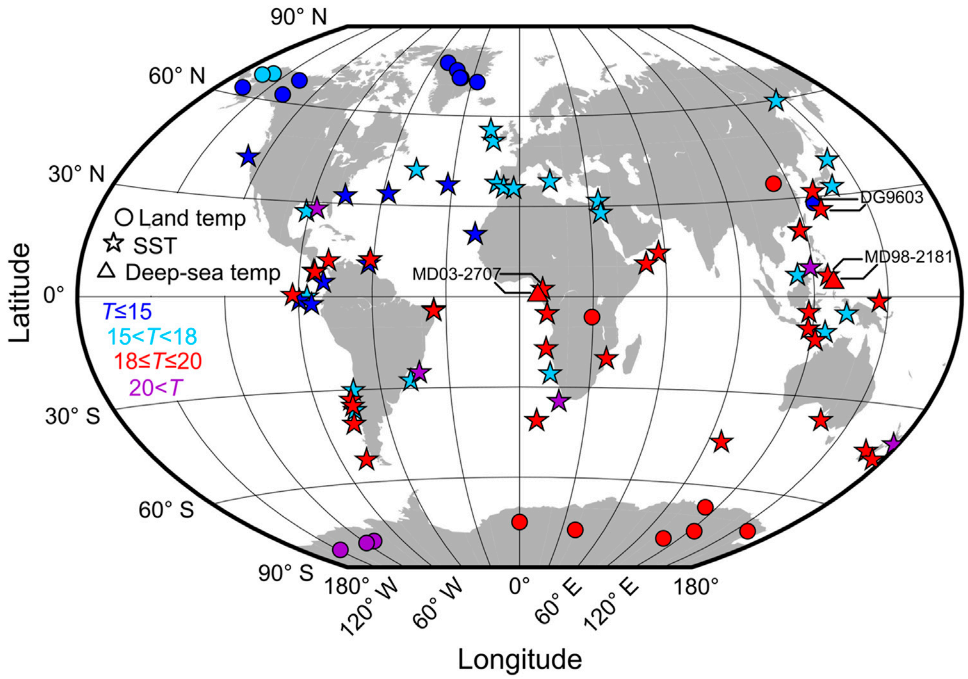

FIGURE 2 | Timings of initial warming from 100 climatic records worldwide. Different data shapes represent temperature records of land (circle), sea surface (pentacle), and deep-sea (triangle, only two), respectively. Different timings of initial warming (T) are differentiated by colors. Oceanic temperature records which are too close to or seriously overlapped with the land data points have been shifted slightly from their original positions. Note that core MD03-2707 and MD98-2181 contain both SST and deep-sea temperature records, and core DG9603 in Okinawa trough contains SST and pollen records which reflect adjacent land climate change. Most records in the SH show early initial warming (before 18 kyr), whereas records in the middle and high NH show either moderate (between 18 and 15 kyr) or late (after 15 kyr) initial warming. The early deglacial warming observed in some tropical and NH mid-latitude records (e.g. West Pacific) may partly arise from the influence of low-latitude insolation (Xu et al., 2013; Wang, 2021). Details about the database for this map can be found in supplementary materials.

2003). Meanwhile, reduced AMOC and expanded sea ice in North Atlantic caused the southward shift of SH westerlies and the release of CO_2 from the deep ocean to the atmosphere (**Figure 1C**; Toggweiler et al., 2006; Anderson et al., 2009). The last deglaciation was accomplished when atmospheric CO_2 was raised above threshold.

The seemingly self-consistent NHH actually has unsolvable problems, and there is an increasing number of studies challenging the NHH. We summarize three aspects of these challenges, i.e., the lead of climate change in the SH with respect to that in the NH, the southern control on AMOC variations, and the potential significance of SH insolation.

The Lead of Climate Change in the Southern Hemisphere with Respect to That in the Northern Hemisphere

Orbital-scale climate changes in the NH do not always lead those in the SH or the tropics (Shackleton and Pisias, 1985; Sowers et al., 1991, 1993; Pichon et al., 1992; Broecker and Henderson, 1998; Paillard and Parrenin, 2004; Bouttes et al., 2011, 2012; Paillard, 2015; Mariotti et al., 2016). Changes in sea surface temperature (SST) from the SH Indian Ocean (Hays et al., 1976) and the tropical Pacific (Lea et al., 2000; Visser et al., 2003) led variations in NH ice sheets by up to a few thousand years. Particularly, an early deglacial warming prior to the LGM has been observed from the SH mid/low-latitude SST records (Pahnke and Sachs, 2006; Santos et al., 2017).

Polar ice cores offer another opportunity to compare temporal relationship between hemispheres. A pioneering attempt to synchronize ice core records from the Antarctica and the Greenland showed that the onset of warming in Antarctica occurred ~3 kyr prior to that in Greenland during the last deglaciation (14.7 kyr ago; **Figure 1D**; Sowers and Bender, 1995). A surface air temperature record from the West Antarctic Ice Sheet Divide ice core (WDC; **Figure 1E**) revealed that significant warming in West Antarctica began by 20 kyr ago during the last deglaciation, confirming an earlier deglacial warming in Antarctica (WAIS Divide Project Members, 2013). Additionally, Antarctic Vostok temperature rising occurred ~4–9 kyr prior to the ice-sheet melting during the last four ice age terminations (Petit et al., 1999).

Compilations of surface temperature reconstructions during the last termination further confirm early warming in the SH and the tropics. Assessment of deglacial SST development in the Pacific Ocean revealed that the timing of initial deglacial warming was generally early (before 18 kyr ago) in the south, late (later than 15.5 kyr ago) in the north, and mixed with both early and intermediate (between 18 and 15.5 kyr ago) signals in the tropics (Kiefer and Kienast, 2005; Tachikawa et al., 2009). A lead of deglacial warming in the SH relative to that in the NH was confirmed at a global scale as well (**Figure 1F**; Shakun et al., 2012).

We also compile 100 paleotemperature records during the last deglaciation (see Material and Methods), including land/sea surface and deep ocean temperatures, and compare their initial timings of the last deglacial warming (**Figure 2**). Two points stand out from this temporal-spatial warming pattern of the last deglaciation. First, initial warming in the SH (mostly centered between 20 and 18 kyr ago) is earlier than in the NH (mostly centered after 18 kyr ago). Second, warming started prior to 20 kyr ago in some SH surface records, and prior to 18 kyr ago in two deep ocean records. This early and strong warming is inconsistent with the NHH view that bipolar seesaw initiates deglacial warming in the SH.

The Southern Control on Atlantic Meridional Overturning Circulations Variations

An ^{213}Pa/^{230}Th record recovered from the subtropical North Atlantic has demonstrated that a nearly total shutdown of AMOC occurred between 17.5 and 15 kyr ago, followed by an abrupt resumption at ~14.7 kyr ago (McManus et al., 2004; Böhm et al., 2015). The near-collapse of AMOC during the HS1 interval was regarded as the cause of SH warming in NHH, and was usually attributed to catastrophic iceberg discharge into the North Atlantic (e.g. Ganopolski and Rahmstorf, 2001; Liu et al., 2009). However, recent studies favor that episodic Heinrich events with huge iceberg discharge were the results rather than the causes of AMOC reduction. According to a sedimentary record from the northeast Atlantic, for the majority of abrupt climate changes over the past four glacial cycles, iceberg arrived too late to trigger cooling (Barker et al., 2015). And episodic ice-discharge events were probably a consequence of increased basal melting rate due to increased subsurface temperature caused by an inactive AMOC (Shaffer et al., 2004; Liu et al., 2009). A northwest Atlantic record showed that, for four Heinrich events (H1, H3, H5a and H6), the subsurface water started to warm approximately 1–2 kyr before each Heinrich event (Marcott et al., 2011). New evidence also suggested that the small amount of meltwater from ice-sheet margins during early deglaciation was unable to induce near-complete collapse of AMOC (e.g. Colin de Verdière et al., 2006; Sévellec et al., 2010).

In addition, the coupling of AMOC variations and sea level changes during the last deglaciation was at odds with a northern freshwater-forcing scenario, which predicts association of more freshwater input (i.e. larger sea level rise) with a less active AMOC. Within the duration when the AMOC was significantly reduced (17.5–15 kyr ago), a rise of ~25 m at a rate of ~12 m kyr^{-1} only occurred during the latter half of the interval (~16.5–15 kyr ago) after a period of near-constant sea level between ~18 and 16.5 kyr ago (**Figure 1G**; Lambeck et al., 2014). In contrast, the most prominent meltwater pulse (MWP-1A; ~20 m in less than

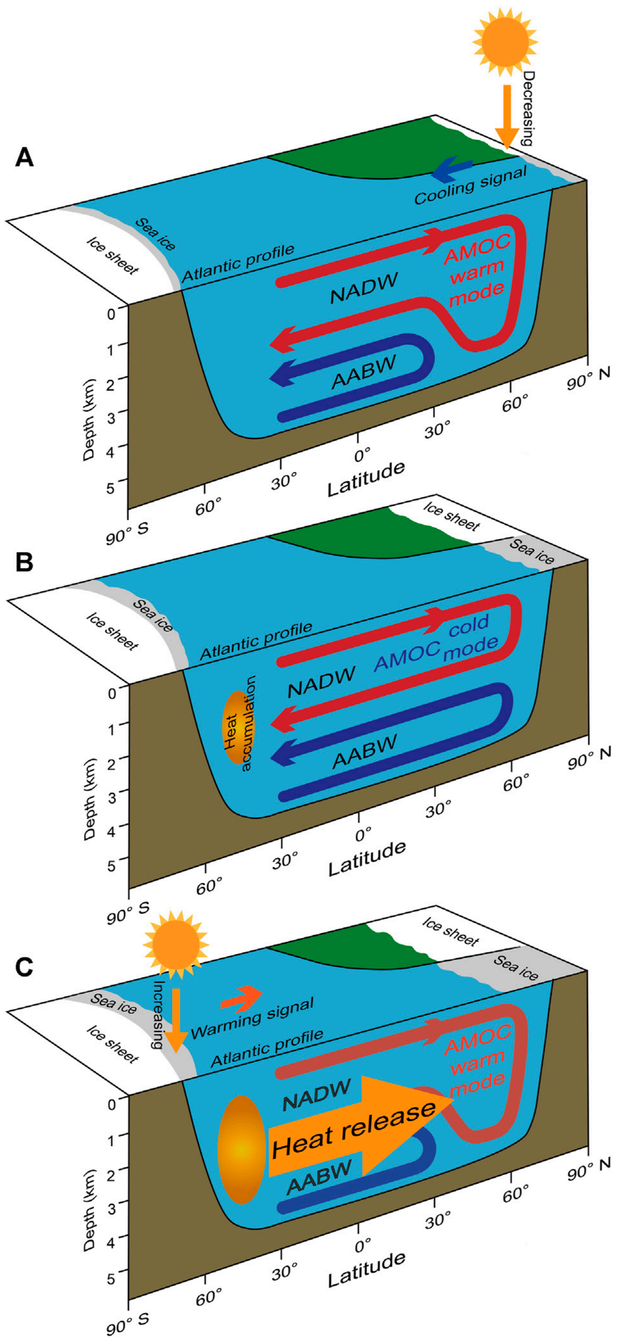

FIGURE 3 | Schematic of the bimodal forcing hypothesis. **(A)** During glacial inception, high northern latitudes first respond to decreasing insolation, and the coeval vigorous AMOC helps to deliver cooling signal to the rest of the Earth. **(B)** AMOC switches from a warm to cold mode when ice age is near its maximum, and this mode change results in heat accumulation in the SH. **(C)** The accumulated heat together with SH insolation cause the deglacial warming in the Southern Ocean and Antarctica. This warming and associated sea-ice retreat and CO$_2$ release terminate glacial conditions. Particularly, warming in the SH leads to AMOC resumption during deglaciations, this resumption is accompanied by AMOC overshoot (Skinner et al., 2013) and transported a huge amount of heat from the SH to the NH.

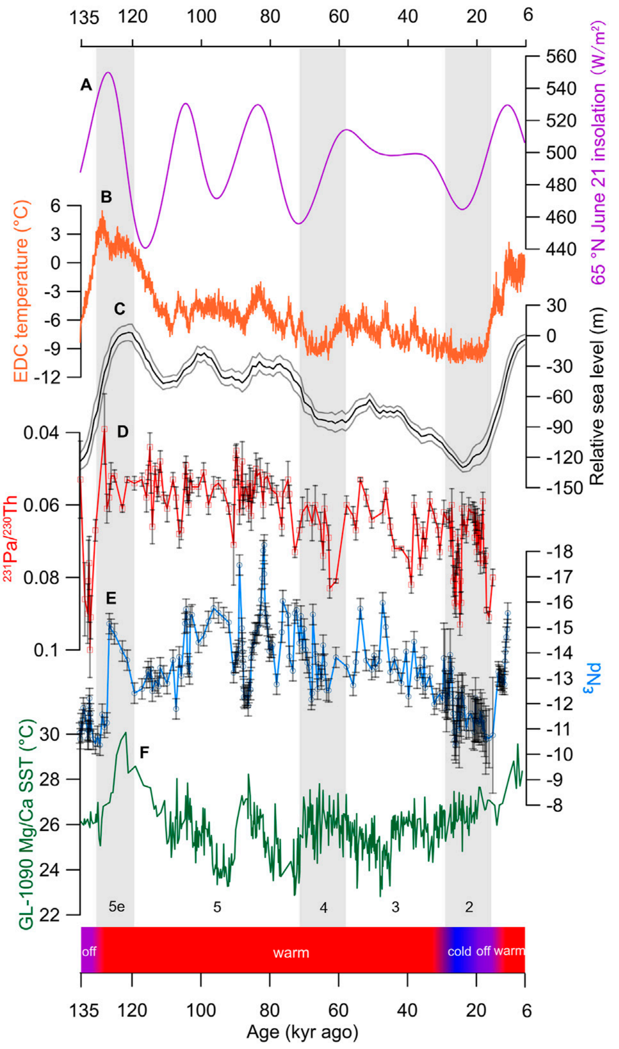

FIGURE 4 | Climatic records since the last interglacial period. **(A)** 65°N June 21 insolation (Laskar et al., 2004). **(B)** EDC temperature reconstruction based on ice δD (Jouzel et al., 2007). **(C)**. Composite sea level in one σ error (Spratt and Lisiecki, 2016). North Atlantic core ODP 1063 $^{231}Pa/^{230}Th$ **(D)** and $^{143}Nd/^{144}Nd$ (εNd) **(E**; Böhm et al., 2015) records. εNd is a proxy for changes in sources and mixing of water masses. Increasced values (plotted downward) indicate shoaling of the AMOC. **(F)** Western South Atlantic core GL-1090 SST data (Santos et al., 2017). All data are on their published timescale. The mode shifts of AMOC derived from the combined $^{231}Pa/^{230}Th$ and εNd records is showed in the bottom (Böhm et al., 2015). Grey and orange shadings mark cold periods (MIS 2, 4) and the last interglacial (MIS 5e), respectively.

500 years) coincided with a sharp resumption of AMOC at ~14.6 kyr ago (Deschamps et al., 2012).

To overcome deficiencies in modulating AMOC with a northern origin, some researchers argue for a southern control on the AMOC variability. A numerical simulation revealed that a gradual warming and sea-ice retreat in the Southern Ocean during deglaciations would induce an abrupt resumption of AMOC (Knorr and Lohmann, 2003). Another simulation also showed that freshwater perturbations to the regions of Antarctic Intermediate Water (AAIW) formation would induce a shift of North Atlantic Deep Water (NADW) formation from the "off" to the "on" mode (Weaver et al., 2003). This driving mechanism well explains the synchronicity of MWP-1A with AMOC resumption during the last deglaciation.

The Potential Significance of Southern Hemisphere Insolation

The NHH view that NH summer insolation drives terminations is questioned by recent proposals that local insolation is at least equally important in driving terminations in the SH. For example, due to the non-linear relationship between radiation and temperature, the seasonal distribution of the solar energy could control the annual temperature of the Antarctic (Huybers and Denton, 2008). This radiation-driven temperature (proportional to the local summer duration) was rising from about 25 kyr ago (Huybers and Denton, 2008). Alternatively, increased springtime insolation over the Southern Ocean (Stott et al., 2007) along with retreating sea ice due to the positive feedback between temperature and sea ice area (Levermann et al., 2007), could account for early onset of deglacial warming in the SH. Particularly, the retreat of sea ice would lead to decreased stratification in the Southern Ocean by inducing enhanced Ekman transport, both contributing to the subsequent rise in atmospheric CO_2 (Stephens and Keeling, 2000; Stott et al., 2007; Basak et al., 2018). Moreover, there are doubts that Antarctic temperature records derived from ice cores were biased, and the orbital component of the bias-corrected temperature record can be explained by local insolation without involving the NH (Laepple et al., 2011).

In summary, the astronomical-forcing theory nicely explains the dominant periods within glacial-interglacial cycles, but fails to illustrate explicitly the response of different climate system components to insolation forcing.

THE BIMODAL FORCING HYPOTHESIS

A single-forcing mechanism such as the NHH seems unsatisfactory in explaining ice age dynamics, thus we put forth the BFH. In this conceptual model, glaciations (cooling) start from the NH while deglaciations (warming) begin from the SH (**Figure 3**). Here we present an interpretation of the onset and termination of the last glacial period (~120–10 kyr ago) under the framework of BFH, which fits better with available paleoclimatic records and model simulations.

Cooling Down: Mechanism of the Onset of the Last Ice Age

The BFH assumes that northern high latitudes firstly responded to the decline of NH summer insolation beginning at ~128 kyr ago (**Figure 4A**), same as the NHH. Diminishing insolation triggered the Earth moving forward into the last ice age, assisted by a series of positive feedbacks such as vegetation and sea ice (Khodri et al., 2005). An early oceanic response to insolation to the south of Greenland indicated that SST started to decrease at ~119 kyr ago and a strong ice-rafted-deposit (IRD) input occurred at ~117 kyr ago, signaling the first regrowth of the Greenland Ice Sheet during the end of last interglacial period (Irvalı et al., 2016).

This initial cooling in the northern high latitudes was propagated through oceanic and atmospheric circulations towards the rest of the world. According to studies on oceanic circulations (e.g. Broecker, 1991; Marshall and Speer, 2012; Talley, 2013; Ferrari et al., 2014), once a cooling signal was imprinted on the northern North Atlantic, the formation regions of NADW, during the onset of last ice age, temperature of the whole ocean would begin to decrease within centuries. Reconstructions of deep ocean temperatures at various sites and with different methods all reveal a significant cooling during the MIS 5e-5 days transition (~115 kyr ago; e.g. Labeyrie et al., 1987; Shackleton, 2000; Cutler et al., 2003; Adkins, 2013). For instance, a deep ocean cooling of ~2°C was estimated between the MIS 5e and MIS 5c for two drilling cores in the Atlantic and Pacific (Cutler et al., 2003). Also, considerable temperature reductions around the MIS 5e-5 days transition were observed worldwide at sea (e.g. Labeyrie et al., 1996; Lea et al., 2000; Tachikawa et al., 2009; Koutavas, 2018), and land surface (e.g. Jouzel et al., 2007; **Figure 4B**). Compared to oceanic processes, atmospheric circulations played a relatively subordinate role during the onset of last ice age, because the contribution of atmosphere to rapid deep ocean cooling is limited, and the tropics is a barrier for *trans*-hemispheric atmospheric processes (Manabe and Broccoli, 1985; Chiang and Bitz, 2005). The aforementioned cooling trends are apparently synchronous at a global scale, which seems in contradiction with the BFH. However, this synchronicity could be misled by dating uncertainties and low sampling resolution.

Warming up: Mechanism of the Termination of the Last Ice Age

From its beginning at ~120 kyr ago, the last ice age lasted until the deglaciation at ~18 kyr ago (**Figure 4C**). Within the glacial period, the Earth experienced three NH summer insolation peaks but none triggered deglaciations (**Figure 4A**; Cheng et al., 2016), implying that apart from insolation, internal feedbacks are also needed to determine terminations. Simultaneous measurements of ^{231}Pa/^{230}Th and ^{143}Nd/^{144}Nd from North Atlantic evidenced a warm-to-cold mode shift of AMOC during the MIS three to two transition at ~27 kyr ago (**Figures 4D,E**; Böhm et al., 2015). As reduction in AMOC would lead to heat accumulation in SH through the bipolar seesaw, the mode shift of AMOC during the later part of last ice age was probably responsible for the early deglaciation warming registered in SH low/mid-latitudes (e.g. Pahnke and Sachs, 2006; Santos et al., 2017; **Figure 4F**). The rapid ice-sheet melting indicated by asymmetric saw-tooth pattern required huge amount of heat, which might partly source from the accumulated heat in the SH linked to reduced AMOC.

The deglacial warming in the Southern Ocean and Antarctica at ~20 kyr ago lagged that in the SH mid/low latitudes occurring at ~27 kyr ago, indicating a southward transmission of heat in the SH. The summer sea-ice edge around the Antarctica started to retreat at ~23 kyr ago (Collins et al., 2012), the surface air in the West Antarctica had felt the warming by ~20 kyr ago (WAIS Divide Project Members, 2013), and the Southern Ocean began to warm at ~19 kyr ago (Stott et al., 2007). This lag of deglacial warming possibly result from the existence of a thermal threshold between the Southern Ocean and the SH low/mid-latitudes, which was finally reached when the SH summer duration (Huybers and Denton, 2008; **Figure 1A**, red curve), and/or spring insolation (Stott et al., 2007; **Figure 1A**, blue curve), began to increase at ~23 kyr ago. The accumulated heat associated with reduced AMOC (Santos et al., 2017), or the heat accumulation in deep Southern Ocean during the long Greenland stadial starting from 27.6 kyr ago (Skinner et al., 2020) could contribute to this initial warming. Once Antarctic sea ice had retreated and the Southern Ocean had warmed, positive feedbacks worked to release CO_2 from the deep ocean to the atmosphere (e.g. Stephens and Keeling, 2000; Toggweiler et al., 2006; Watson et al., 2015), and CO_2 helped to drive the warming in the NH (Shakun et al., 2012). Moreover, heat carried by a Southern Ocean-origin water mass led to a 3°C warming in the deep North Atlantic during the HS1, possibly resulting in the reinvigoration of AMOC at ~14.7 kyr ago (Thiagarajan et al., 2014). Simulations also support a controlling role of the Southern Ocean warming in AMOC resumption (Knorr and Lohmann, 2003; Weaver et al., 2003; Buizert and Schmittner, 2015). The resumpted AMOC transported a considerable amount of heat from the SH to the NH at an unprecedented rate in the next few hundred years and caused a rapid melting of ice sheets, the MWP-1A (Deschamps et al., 2012). By this time, the transition from the LGM to Holocene on both hemispheres seemed irreversible.

In summary, the BFH is distinct from previous single-forcing hypotheses, in that it assumes the initial response of glacial onsets is different from that of glacial terminations. When the NH summer insolation starts to decline, it is the northern high latitudes that first react. The NH ice sheets begin to grow, and the high-latitude surface temperature begin to decrease. Subsequently, through a series of atmospheric and oceanic processes, especially the global oceanic overturning circulation, the cooling signal is transmitted towards the rest of the world. As the ice age proceeds near its maximum, the AMOC switches from a warm to a cold mode due to a few possible reasons, such as a threshold value has been reached by the volume of NH ice sheets, the temperature of NADW (Adkins, 2013), or the area of Antarctic sea ice (Ferrari et al., 2014). Then heat begins to accumulate in the SH as a result of reduced AMOC. Once the accumulated heat plus the SH local insolation attains a certain value, the Antarctic surface temperature starts to increase, the sea ice around the Antarctica starts to retreat, and the CO_2 preserved in deep ocean is added back to the atmosphere. Finally, the heat stored in the SH becomes so large that the AMOC switches back to the warm mode and both hemispheres move toward another interglacial period.

FUTURE DIRECTIONS

In general, the BFH differs from previous ice-age hypotheses in two aspects. First, it assumes that different climatic components drive glaciation and deglaciation, contrasting with single-forcing hypotheses which argue for a dominant role of a single climatic component during both ice-age onset and termination. This might benefit the understanding for the saw-tooth pattern, which indicates different processes of cooling and warming. Second, the BFH recognizes the significance of SH oceans in accumulating and transferring heat for terminations.

The BFH awaits further improvement, as many issues need to be resolved. For example, a crucial idea within the BFH, that reduced AMOC at the MIS three to two transition contributed to heat accumulation in the SH, is not yet consistent with traditional bipolar seesaw which is used to explain millennial-scale oscillations. Specific mechanisms transmitting heat from the SH low/mid latitudes to the Southern Ocean and Antarctica during ~27-~20 kyr ago remains unclear. And to which extent SH local insolation contributes to deglaciation is unsettled.

MATERIALS AND METHODS

In order to investigate the temporal-spatial distribution of the last glacial-interglacial transition (the time when temperature or proxy records have obviously shifted), we compiled 100 proxy records around the world (**Supplementary Table S1**, **Supplementary Figure S1**). Only proxy records with firm chronological control and high resolution have been collected. For records with the ^{14}C-based age model, we recalibrated all available ^{14}C dates using Intcal 13 and SHcal 13. Then the age model was built up by linear interpolation between ^{14}C-dated control points. We determine the start of deglaciation by visually identifying the first obvious shift in temperature or proxy curves since 34 kyr ago. Then this age is compared to the timing given by the original author(s) if available. In case that the result has apparent discrepancies (the difference between two ages is over 1,000 yr), we adopt the opinion of original author(s).

DATA AVAILABILITY STATEMENT

The original contributions presented in the study are included in the article/**Supplementary Material**, further inquiries can be directed to the corresponding author.

AUTHOR CONTRIBUTIONS

ZL proposed the hypothesis. ZL, YX, and PZ wrote the paper. PZ made figures. ZL, YX, and PZ have equal contributions.

FUNDING

This work was funded by National Natural Science Foundation of China (Grant No. 41877438, 41290252), and the STU Scientific Research Foundation for Talents (Grant No. NTF19003), both granted to ZL.

ACKNOWLEDGMENTS

Peter Clark and Joerg Lippold shared their published data. ZL thanks late Prof. Nicholas Shackleton for inspiring discussions many years ago when ZL was a DPhil student in Oxford, which triggered the thinking of this issue.

SUPPLEMENTARY MATERIAL

The Supplementary Material for this article can be found online at: https://www.frontiersin.org/articles/10.3389/feart.2021.736895/full#supplementary-material

REFERENCES

Adkins, J. F. (2013). The Role of Deep Ocean Circulation in Setting Glacial Climates. *Paleoceanography* 28 (3), 539–561. doi:10.1002/palo.20046

Anderson, R. F., Ali, S., Bradtmiller, L. I., Nielsen, S. H. H., Fleisher, M. Q., Anderson, B. E., et al. (2009). Wind-Driven Upwelling in the Southern Ocean and the Deglacial Rise in Atmospheric CO_2. *Science* 323 (5920), 1443–1448. doi:10.1126/science.1167441

Barker, S., Chen, J., Gong, X., Jonkers, L., Knorr, G., and Thornalley, D. (2015). Icebergs Not the Trigger for North Atlantic Cold Events. *Nature* 520 (7547), 333–336. doi:10.1038/nature14330

Basak, C., Fröllje, H., Lamy, F., Gersonde, R., Benz, V., Anderson, R. F., et al. (2018). Breakup of Last Glacial Deep Stratification in the South Pacific. *Science* 359 (6378), 900–904. doi:10.1126/science.aao2473

Beck, J. W., Zhou, W., Li, C., Wu, Z., White, L., Xian, F., et al. (2018). A 550,000-year Record of East Asian Monsoon Rainfall from10Be in Loess. *Science* 360 (6391), 877–881. doi:10.1126/science.aam5825

Böhm, E., Lippold, J., Gutjahr, M., Frank, M., Blaser, P., Antz, B., et al. (2015). Strong and Deep Atlantic Meridional Overturning Circulation during the Last Glacial Cycle. *Nature* 517 (7532), 73–76. doi:10.1038/nature14059

Bouttes, N., Paillard, D., Roche, D. M., Brovkin, V., and Bopp, L. (2011). Last Glacial Maximum CO_2 and δ^{13}C Successfully Reconciled. *Geophys. Res. Lett.* 38, L02705. doi:10.1029/2010gl044499

Bouttes, N., Paillard, D., Roche, D. M., Waelbroeck, C., Kageyama, M., Lourantou, A., et al. (2012). Impact of Oceanic Processes on the Carbon Cycle during the Last Termination. *Clim. Past* 8, 149–170. doi:10.5194/cp-8-149-2012

Broecker, W. S. (1991). The Great Ocean Conveyor. *Oceanography* 4 (1), 79–89.

Broecker, W. S., and Denton, G. H. (1989). The Role of Ocean-Atmosphere Reorganizations in Glacial Cycles. *Geochimica et Cosmochimica Acta* 53 (10), 2465–2501. doi:10.1016/0016-7037(89)90123-3

Broecker, W. S., and Henderson, G. M. (1998). The Sequence of Events Surrounding Termination II and Their Implications for the Cause of Glacial-Interglacial CO_2 changes. *Paleoceanography* 13 (4), 352–364. doi:10.1029/98pa00920

Broecker, W. S. (1998). Paleocean Circulation during the Last Deglaciation: a Bipolar Seesaw? *Paleoceanography* 13 (2), 119–121. doi:10.1029/97pa03707

Broecker, W. S., and van Donk, J. (1970). Insolation Changes, Ice Volumes, and the O^{18} record in Deep-Sea Cores. *Rev. Geophys.* 8 (1), 169–198. doi:10.1029/rg008i001p00169

Buizert, C., and Schmittner, A. (2015). Southern Ocean Control of Glacial AMOC Stability and Dansgaard-Oeschger Interstadial Duration. *Paleoceanography* 30, 1595–1612. doi:10.1002/2015pa002795

Cane, M. A. (1998). CLIMATE CHANGE: A Role for the Tropical Pacific. *Science* 282, 59–61. doi:10.1126/science.282.5386.59

Cheng, H., Edwards, R. L., Sinha, A., Spötl, C., Yi, L., Chen, S., et al. (2016). The Asian Monsoon over the Past 640,000 Years and Ice Age Terminations. *Nature* 534 (7609), 640–646. doi:10.1038/nature18591

Chiang, J. C. H., and Bitz, C. M. (2005). Influence of High Latitude Ice Cover on the marine Intertropical Convergence Zone. *Clim. Dyn.* 25 (5), 477–496. doi:10.1007/s00382-005-0040-5

Chiang, J. C. H. (2009). The Tropics in Paleoclimate. *Annu. Rev. Earth Planet. Sci.* 37, 263–297. doi:10.1146/annurev.earth.031208.100217

Clark, P. U., Pisias, N. G., Stocker, T. F., and Weaver, A. J. (2002). The Role of the Thermohaline Circulation in Abrupt Climate Change. *Nature* 415, 863–869. doi:10.1038/415863a

Clement, A. C., Cane, M. A., and Seager, R. (2001). An Orbitally Driven Tropical Source for Abrupt Climate Change. *J. Clim.* 14 (11), 2369–2375. doi:10.1175/1520-0442(2001)014<2369:aodtsf>2.0.co;2

Colin de Verdière, A., Ben Jelloul, M., and Sévellec, F. (2006). Bifurcation Structure of Thermohaline Millennial Oscillations. *J. Clim.* 19, 5777–5795. doi:10.1175/jcli3950.1

Collins, L. G., Pike, J., Allen, C. S., and Hodgson, D. A. (2012). High-resolution Reconstruction of Southwest Atlantic Sea-Ice and its Role in the Carbon Cycle during marine Isotope Stages 3 and 2. *Paleoceanography* 27, PA3217. doi:10.1029/2011pa002264

Crowley, T. J. (1992). North Atlantic Deep Water Cools the Southern Hemisphere. *Paleoceanography* 7 (4), 489–497. doi:10.1029/92pa01058

Cutler, S., Cutler, H., Matesic, D., Cheng, H., Adkins, J., Gallup, C. D., et al. (2003). Mode of Action of Phytotoxic Fungal Metabolites. *Earth Planet. Sci. Lett.* 206 (3–4), 253–270. doi:10.1201/9780203492789.ch13

Denton, G. H., Anderson, R. F., Toggweiler, J. R., Edwards, R. L., Schaefer, J. M., and Putnam, A. E. (2010). The Last Glacial Termination. *Science* 328, 1652–1656. doi:10.1126/science.1184119

Deschamps, P., Durand, N., Bard, E., Hamelin, B., Camoin, G., Thomas, A. L., et al. (2012). Ice-sheet Collapse and Sea-Level Rise at the Bølling Warming 14,600 Years Ago. *Nature* 483 (7391), 559–564. doi:10.1038/nature10902

Ding, Z. (2006). The Milankovitch Theory of Pleistocene Glacial Cycles: Challenges and Chances. *Quat. Sci.* 26 (5), 710–717. (In Chinese with English abstract). doi:10.3321/j.issn:1001-7410.2006.05.005

Ferrari, R., Jansen, M. F., Adkins, J. F., Burke, A., Stewart, A. L., and Thompson, A. F. (2014). Antarctic Sea Ice Control on Ocean Circulation in Present and Glacial Climates. *Proc. Natl. Acad. Sci.* 111 (24), 8753–8758. doi:10.1073/pnas.1323922111

Ganopolski, A., and Rahmstorf, S. (2001). Rapid Changes of Glacial Climate Simulated in a Coupled Climate Model. *Nature* 409, 153–158. doi:10.1038/35051500

Hays, J. D., Imbrie, J., and Shackleton, N. J. (1976). Variations in the Earth's Orbit: Pacemaker of the Ice Ages. *Science* 194, 1121–1132. doi:10.1126/science.194.4270.1121

Huybers, P., and Denton, G. (2008). Antarctic Temperature at Orbital Timescales Controlled by Local Summer Duration. *Nat. Geosci* 1, 787–792. doi:10.1038/ngeo311

Imbrie, J., Berger, A., Boyle, E. A., Clemens, S. C., Duffy, A., Howard, W. R., et al. (1993). On the Structure and Origin of Major Glaciation Cycles 2. The 100,000-year Cycle. *Paleoceanography* 8, 699–735. doi:10.1029/93pa02751

Imbrie, J., Boyle, E. A., Clemens, S. C., Duffy, A., Howard, W. R., Kukla, G., et al. (1992). On the Structure and Origin of Major Glaciation Cycles 1. Linear Responses to Milankovitch Forcing. *Paleoceanography* 7, 701–738. doi:10.1029/92pa02253

Irvalı, N., Ninnemann, U. S., Kleiven, H. F., Galaasen, E. V., Morley, A., and Rosenthal, Y. (2016). Evidence for Regional Cooling, Frontal Advances, and East Greenland Ice Sheet Changes during the Demise of the Last Interglacial. *Quat. Sci. Rev.* 150, 184–199. doi:10.1016/j.quascirev.2016.08.029

IPCC (2013). *Climate Change 2013: The Physical Science Basis. Contribution of Working Group I to the Fifth Assessment Report of the Intergovernmental Panel on Climate Change*. Editors T. F. Stocker (Cambridge: Cambridge Univ. Press), 11535. doi:10.1017/CBO9781107415324

Jouzel, J., Masson-Delmotte, V., Cattani, O., Dreyfus, G., Falourd, S., Hoffmann, G., et al. (2007). Orbital and Millennial Antarctic Climate Variability over the Past 800,000 Years. *Science* 317 (5839), 793–796. doi:10.1126/science.1141038

Kawamura, K., Parrenin, F., Lisiecki, L., Uemura, R., Vimeux, F., Severinghaus, J. P., et al. (2007). Northern Hemisphere Forcing of Climatic Cycles in Antarctica over the Past 360,000 Years. *Nature* 448 (7156), 912–916. doi:10.1038/nature06015

Khodri, M., Cane, M. A., Kukla, G., Gavin, J., and Braconnot, P. (2005). The Impact of Precession Changes on the Arctic Climate during the Last Interglacial-Glacial Transition. *Earth Planet. Sci. Lett.* 236 (1), 285–304. doi:10.1016/j.epsl.2005.05.011

Kiefer, T., and Kienast, M. (2005). Patterns of Deglacial Warming in the Pacific Ocean: a Review with Emphasis on the Time Interval of Heinrich Event 1. *Quat. Sci. Rev.* 24, 1063–1081. doi:10.1016/j.quascirev.2004.02.021

Knorr, G., and Lohmann, G. (2003). Southern Ocean Origin for the Resumption of Atlantic Thermohaline Circulation during Deglaciation. *Nature* 424, 532–536. doi:10.1038/nature01855

Koutavas, A. (2018). Temperature Correlations between the Eastern Equatorial Pacific and Antarctica over the Past 230,000 Years. *Earth Planet. Sci. Lett.* 485, 43–54. doi:10.1016/j.epsl.2017.12.041

Labeyrie, L. D., Duplessy, J. C., and Blanc, P. L. (1987). Variations in Mode of Formation and Temperature of Oceanic Deep Waters over the Past 125,000 Years. *Nature* 327 (6122), 477–482. doi:10.1038/327477a0

Labeyrie, L., Labracherie, M., Gorfti, N., Pichon, J. J., Vautravers, M., Arnold, M., et al. (1996). Hydrographic Changes of the Southern Ocean (Southeast Indian Sector) over the Last 230 Kyr. *Paleoceanography* 11 (1), 57–76. doi:10.1029/95pa02255

Laepple, T., Werner, M., and Lohmann, G. (2011). Synchronicity of Antarctic Temperatures and Local Solar Insolation on Orbital Timescales. *Nature* 471 (7336), 91–94. doi:10.1038/nature09825

Lambeck, K., Rouby, H., Purcell, A., Sun, Y., and Sambridge, M. (2014). Sea Level and Global Ice Volumes from the Last Glacial Maximum to the Holocene. *Proc. Natl. Acad. Sci.* 111, 15296–15303. doi:10.1073/pnas.1411762111

Laskar, J., Robutel, P., Joutel, F., Gastineau, M., Correia, A. C. M., and Levrard, B. (2004). A Long-Term Numerical Solution for the Insolation Quantities of the Earth. *Astron. Astrophys.* 428, 261–285. doi:10.1051/0004-6361:20041335

Lea, D. W., Pak, D. K., and Spero, H. J. (2000). Climate Impact of Late Quaternary Equatorial Pacific Sea Surface Temperature Variations. *Science* 289, 1719–1724. doi:10.1126/science.289.5485.1719

Levermann, A., Schewe, J., and Montoya, M. (2007). Lack of Bipolar See-Saw in Response to Southern Ocean Wind Reduction. *Geophys. Res. Lett.* 34, L12711. doi:10.1029/2007gl030255

Lisiecki, L. E., and Raymo, M. E. (2005). A Pliocene-Pleistocene Stack of 57 Globally Distributed Benthic $\delta^{18}O$ Records. *Paleoceanography* 20, PA1003. doi:10.1029/2004pa001071

Liu, Z., Otto-Bliesner, B. L., He, F., Brady, E. C., Tomas, R., Clark, P. U., et al. (2009). Transient Simulation of Last Deglaciation with a New Mechanism for Bolling-Allerod Warming. *Science* 325 (5938), 310–314. doi:10.1126/science.1171041

Manabe, S., and Broccoli, A. J. (1985). The Influence of continental Ice Sheets on the Climate of an Ice Age. *J. Geophys. Res.* 90, 2167–2190. doi:10.1029/jd090id01p02167

Marcott, S. A., Clark, P. U., Padman, L., Klinkhammer, G. P., Springer, S. R., Liu, Z., et al. (2011). Ice-shelf Collapse from Subsurface Warming as a Trigger for Heinrich Events. *Proc. Natl. Acad. Sci.* 108, 13415–13419. doi:10.1073/pnas.1104772108

Mariotti, V., Paillard, D., Bopp, L., Roche, D. M., and Bouttes, N. (2016). A Coupled Model for Carbon and Radiocarbon Evolution during the Last Deglaciation. *Geophys. Res. Lett.* 43, 1306–1313. doi:10.1002/2015gl067489

Marshall, J., and Speer, K. (2012). Closure of the Meridional Overturning Circulation through Southern Ocean Upwelling. *Nat. Geosci* 5 (5), 171–180. doi:10.1038/ngeo1391

McManus, J. F., Francois, R., Gherardi, J.-M., Keigwin, L. D., and Brown-Leger, S. (2004). Collapse and Rapid Resumption of Atlantic Meridional Circulation Linked to Deglacial Climate Changes. *Nature* 428, 834–837. doi:10.1038/nature02494

Milankovitch, M. (1941). *Kanon der Erdbestrahlung und seine Andwendung auf das Eiszeitenproblem*. Belgrade: Royal Serbian Academy Special Publication. (English translation published in 1969 by Israel Program for Scientific Translations, US Dept. Comm.).

Monnin, E., Indermühle, A., Dällenbach, A., Flückiger, J., Stauffer, B., Stocker, T. F., et al. (2001). Atmospheric CO_2 Concentrations over the Last Glacial Termination. *Science* 291, 112–114. doi:10.1126/science.291.5501.112

Pahnke, K., and Sachs, J. P. (2006). Sea Surface Temperatures of Southern Midlatitudes 0-160 Kyr B. *P. Paleoceanography* 21, PA2003. doi:10.1029/2005pa001191

Paillard, D., and Parrenin, F. (2004). The Antarctic Ice Sheet and the Triggering of Deglaciations. *Earth Planet. Sci. Lett.* 227, 263–271. doi:10.1016/j.epsl.2004.08.023

Paillard, D. (2015). Quaternary Glaciations: from Observations to Theories. *Quat. Sci. Rev.* 107, 11–24. doi:10.1016/j.quascirev.2014.10.002

Petit, J. R., Jouzel, J., Raynaud, D., Barkov, N. I., Barnola, J.-M., Basile, I., et al. (1999). Climate and Atmospheric History of the Past 420,000 Years from the Vostok Ice Core, Antarctica. *Nature* 399, 429–436. doi:10.1038/20859

Pichon, J.-J., Labeyrie, L. D., Bareille, G., Labracherie, M., Duprat, J., and Jouzel, J. (1992). Surface Water Temperature Changes in the High Latitudes of the Southern Hemisphere over the Last Glacial-Interglacial Cycle. *Paleoceanography* 7 (3), 289–318. doi:10.1029/92pa00709

Rasmussen, S. O., Andersen, K. K., Svensson, A. M., Steffensen, J. P., Vinther, B. M., Clausen, H. B., et al. (2006). A New Greenland Ice Core Chronology for the Last Glacial Termination. *J. Geophys. Res.-Atmos.* 111, 907–923. doi:10.1029/2005jd006079

Santos, T. P., Lessa, D. O., Venancio, I. M., Chiessi, C. M., Mulitza, S., Kuhnert, H., et al. (2017). Prolonged Warming of the Brazil Current Precedes Deglaciations. *Earth Planet. Sci. Lett.* 463, 1–12. doi:10.1016/j.epsl.2017.01.014

Sévellec, F., Huck, T., and Colin de Verdière, A. (2010). From Centennial to Millennial Oscillation of the Thermohaline Circulation. *J. Mar. Res.* 68, 597–624. doi:10.1357/002224011795977635

Shackleton, N. J., and Pisias, N. G. (1985). "Atmospheric Carbon Dioxide, Orbital Forcing, and Climate," in *The Carbon Cycle and Atmospheric CO_2: Natural Variations Archean to Present*. Editors E. Sundquist and W. Broecker (Washington DC: American Geophysical Union).

Shackleton, N. J. (2000). The 100,000-year Ice-Age Cycle Identified and Found to Lag Temperature, Carbon Dioxide, and Orbital Eccentricity. *Science* 289 (5486), 1897–1902. doi:10.1126/science.289.5486.1897

Shaffer, G., Olsen, S. M., and Bjerrum, C. J. (2004). Ocean Subsurface Warming as a Mechanism for Coupling Dansgaard-Oeschger Climate Cycles and Ice-Rafting Events. *Geophys. Res. Lett.* 31, L24202. doi:10.1029/2004gl020968

Shakun, J. D., Clark, P. U., He, F., Marcott, S. A., Mix, A. C., Liu, Z., et al. (2012). Global Warming Preceded by Increasing Carbon Dioxide Concentrations during the Last Deglaciation. *Nature* 484, 49–54. doi:10.1038/nature10915

Skinner, L. C., Scrivner, A. E., Vance, D., Barker, S., Fallon, S., and Waelbroeck, C. (2013). North Atlantic versus Southern Ocean Contributions to a Deglacial Surge in Deep Ocean Ventilation. *Geology* 41, 667–670. doi:10.1130/g34133.1

Skinner, L., Menviel, L., Broadfield, L., Gottschalk, J., and Greaves, M. (2020). Southern Ocean Convection Amplified Past Antarctic Warming and Atmospheric CO_2 Rise during Heinrich Stadial 4. *Commun. Earth Environ.* 1, 23. doi:10.1038/s43247-020-00024-3

Sowers, T., and Bender, M. (1995). Climate Records Covering the Last Deglaciation. *Science* 269, 210–214. doi:10.1126/science.269.5221.210

Sowers, T., Bender, M., Labeyrie, L., Martinson, D., Jouzel, J., Raynaud, D., et al. (1993). A 135,000-year Vostok-Specmap Common Temporal Framework. *Paleoceanography* 8 (6), 737–766. doi:10.1029/93pa02328

Sowers, T., Bender, M., Raynaud, D., Korotkevich, Y. S., and Orchardo, J. (1991). The $\delta^{18}O$ of Atmospheric O_2 from Air Inclusions in the Vostok Ice Core: Timing of CO_2 and Ice Volume Changes during the Penultimate Deglaciation. *Paleoceanography* 6 (6), 679–696. doi:10.1029/91pa02023

Spratt, R. M., and Lisiecki, L. E. (2016). A Late Pleistocene Sea Level Stack. *Clim. Past* 12, 1079–1092. doi:10.5194/cp-12-1079-2016

Steffen, W., Rockström, J., Richardson, K., Lenton, T. M., and Folke, D., (2018). Trajectories of the Earth System in the Anthropocene. *Proc. Natl. Acad. Sci. USA* 115 (33), 8252–8259. doi:10.1073/pnas.1810141115

Stephens, B. B., and Keeling, R. F. (2000). The Influence of Antarctic Sea Ice on Glacial-Interglacial CO_2 Variations. *Nature* 404 (6774), 171–174. doi:10.1038/35004556

Stocker, T. F., and Johnsen, S. J. (2003). A Minimum Thermodynamic Model for the Bipolar Seesaw. *Paleoceanography* 18 (4), 1087. doi:10.1029/2003pa000920

Stott, L., Timmermann, A., and Thunell, R. (2007). Southern Hemisphere and Deep-Sea Warming Led Deglacial Atmospheric CO_2 Rise and Tropical Warming. *Science* 318, 435–438. doi:10.1126/science.1143791

Tachikawa, K., Vidal, L., Sonzogni, C., and Bard, E. (2009). Glacial/interglacial Sea Surface Temperature Changes in the Southwest Pacific Ocean over the Past 360ka. *Quat. Sci. Rev.* 28, 1160–1170. doi:10.1016/j.quascirev.2008.12.013

Talley, L. (2013). Closure of the Global Overturning Circulation through the Indian, Pacific, and Southern Oceans: Schematics and Transports. *oceanog* 26 (1), 80–97. doi:10.5670/oceanog.2013.07

Thiagarajan, N., Subhas, A. V., Southon, J. R., Eiler, J. M., and Adkins, J. F. (2014). Abrupt Pre-bølling-allerød Warming and Circulation Changes in the Deep Ocean. *Nature* 511, 75–78. doi:10.1038/nature13472

Toggweiler, J. R., Russell, J. L., and Carson, S. R. (2006). Midlatitude Westerlies, Atmospheric CO_2, and Climate Change during the Ice Ages. *Paleoceanography* 21, PA2005. doi:10.1029/2005pa001154

Visser, K., Thunell, R., and Stott, L. (2003). Magnitude and Timing of Temperature Change in the Indo-Pacific Warm Pool during Deglaciation. *Nature* 421, 152–155. doi:10.1038/nature01297

WAIS Divide Project Members (2013). Onset of Deglacial Warming in West Antarctica Driven by Local Orbital Forcing. *Nature* 500, 440–444. doi:10.1038/nature12376

WAIS Divide Project Members (2015). Precise Interpolar Phasing of Abrupt Climate Change during the Last Ice Age. *Nature* 520, 661–665. doi:10.1038/nature14401

Wang, P. (2021). Low-latitude Forcing: A New Insight into Paleo-Climate Changes. *The Innovation* 2 (3), 100145. doi:10.1016/j.xinn.2021.100145

Watson, A. J., Vallis, G. K., and Nikurashin, M. (2015). Southern Ocean Buoyancy Forcing of Ocean Ventilation and Glacial Atmospheric CO_2. *Nat. Geosci* 8, 861–864. doi:10.1038/ngeo2538

Weaver, A. J., Saenko, O. A., Clark, P. U., and Mitrovica, J. X. (2003). Meltwater Pulse 1A from Antarctica as a Trigger of the Bolling-Allerod Warm Interval. *Science* 299, 1709–1713. doi:10.1126/science.1081002

Zheng, P., Pedro, J. B., Jochum, M., Rasmussen, S. O., and Lai, Z. (2021). Different Trends in Antarctic Temperature and Atmospheric CO_2 during the Last Glacial. *Geophys. Res. Lett.* 48, e2021GL093868. doi:10.1029/2021gl093868

Conflict of Interest: The authors declare that the research was conducted in the absence of any commercial or financial relationships that could be construed as a potential conflict of interest.

frontiers
in Earth Science

ORIGINAL RESEARCH
published: 14 September 2021
doi: 10.3389/feart.2021.713972

The Elements and Color of Lacustrine Record Revealed Lake Environmental Changes in Semiarid Northern China：A Case Study From Chagan Nur Lake of Southern Mongolian Plateau

Zhong Wang[1], *Guoqiang Li*[1]*, *Xiaoyan Wang*[1], *Siyi Gou*[1], *Yanqing Deng*[1], *Shuxian Tao*[1], *Yunian Zhang*[2], *He Yang*[1], *Wenwei Zhao*[3] and *Ming Jin*[1]

[1]Key Laboratory of Western China's Environmental Systems (Ministry of Education), College of Earth and Environmental Sciences, Lanzhou University, Lanzhou, China, [2]State Key Laboratory Breeding Base of Desertification and Aeolian Sand Disaster Combating, Gansu Desert Control Research Institute, Lanzhou, China, [3]School of Geographic Science, Nantong University, Nantong, China

Edited by:
Xiangzhong Li,
Yunnan University, China

Reviewed by:
Zheng Wang,
State Key Laboratory of Loess and Quaternary Geology, Institute of Earth Environment (CAS), China
Xiaonan Zhang,
Yunnan University, China
Xin Zhou,
University of Science and Technology of China, China

***Correspondence:**
Guoqiang Li
gqli@lzu.edu.cn

Specialty section:
This article was submitted to Quaternary Science, Geomorphology and Paleoenvironment, a section of the journal Frontiers in Earth Science

Received: 24 May 2021
Accepted: 29 July 2021
Published: 14 September 2021

Citation:
Wang Z, Li G, Wang X, Gou S, Deng Y, Tao S, Zhang Y, Yang H, Zhao W and Jin M (2021) The Elements and Color of Lacustrine Record Revealed Lake Environmental Changes in Semiarid Northern China：A Case Study From Chagan Nur Lake of Southern Mongolian Plateau. Front. Earth Sci. 9:713972. doi: 10.3389/feart.2021.713972

The lakes at the southern Mongolian Plateau are sensitive to the variation of EASM changes during the Holocene, and hence the lacustrine records of these lakes provide prospects for understanding how lake environmental changes respond to EASM variation at different timescales. The interpretation of proxy indexes of lacustrine sediments is complex due to the various climatic or/and environmental factors influencing the processes during deposition and after deposition. In this study, the elements and colors of an 11.7-m lacustrine record from Chagan Nur at the southern Mongolian Plateau of northern China were analyzed to constrain the lake environmental changes during the Holocene. The results show that stable elements of Al, Si, K, Ti, Fe, and Rb are more related to surface erosion or/and vegetation coverage, and the variation of Sr is related to the lake-level change in Chagan Nur. The element and color of the lacustrine records show that a small and shallow lake environment occurred at Chagan Nur during 11.7–10.5 ka, the lake level had increased during 10.5–7 ka, and then the lake shrank with strength surface erosion during 7–6.2 ka and from 2 ka to the present. The lake level and surface erosion changes of Chagan Nur have shown a direct response to EASM precipitation changes as reconstructed from the pollen record from the Chagan Nur Lake and other records from northern China.

Keywords: Northern China, elements, color, paleoenvironment, East Asia summer monsoon, Holocene

INTRODUCTION

East Asian summer monsoon (EASM) is the crucial atmospheric circulation system for East Asia, for it provided amounts of fresh water to all of the lives (An et al., 2015; Chen et al., 2015; Chen et al., 2020). The research of variations and mechanism of EASM is of significance for understanding how human beings adapt to the climatic changes in EASM dominance in the future. The southern Mongolian Plateau located at the margin of EASM is an ideal place to study the mechanism and variation of EASM. The lake sediments in these regions are the ideal carriers to reconstruct the variations of EASM intensity in the past period (Jin et al., 2006; An et al., 2012; Zhang et al., 2016; Goldsmith et al., 2017; Wen et al., 2017; Li et al., 2020; Chen et al., 2021).

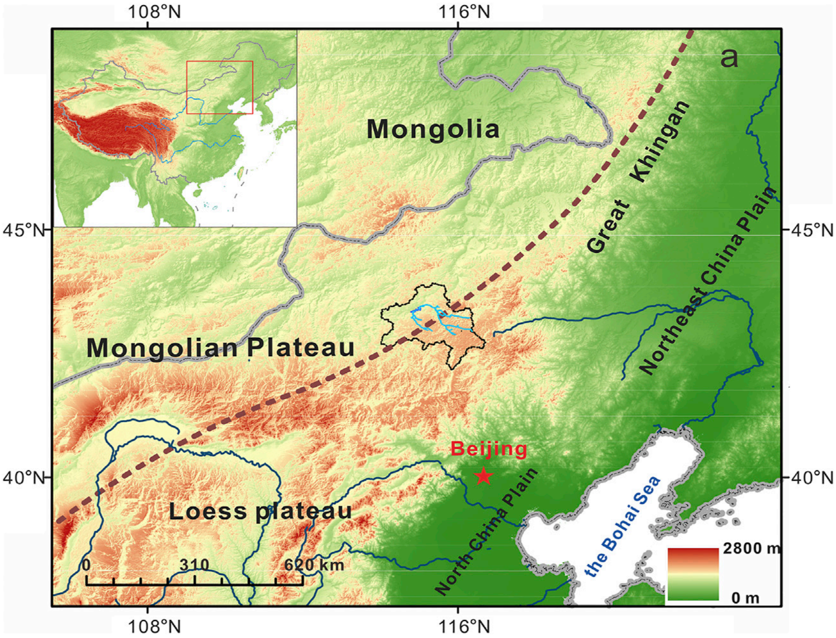

FIGURE 1 | Location of Chagan Nur basin in northern China.

Chagan Nur Lake locates at the southern Mongolian Plateau, which is exactly located at the fringe of the modern EASM. The lacustrine sediments in this lake provide reliable records for detecting the variation of EASM during the Holocene. For example, Jiang et al. (2016) and Han and Liu (2017) have reported that the paleoclimatic variations were affected by the changes of summer insolation using the proxies of grain size and pollen from west Chagan Nur over the past 2 ka and 7 ka, respectively. Liu and Ha (2015) has reconstructed the lake level since the past 6.8 ka by using paleolake shoreline records, and it showed that the paleolake level was at least 7 m higher than the present and gradually shrank till now. Chun et al. (2017) and Chun et al. (2018) has reported the variations of precipitation, temperature, and population in recent 50 years and further pointed out their effects on the changes of the lake level and vegetation coverage, and the results suggested that the variation of precipitation was the most fundamental factor for the recovery of vegetation and the rise of the lake level.

Element is one of the ideal proxies to detect the paleoclimate changes and can be superiorly and rapidly obtained by X-ray fluorescence (XRF) core scanning (Rothwell and Rack, 2006; Thomson et al., 2006; Liang et al., 2012). It has been widely applied in deep-sea sediments (Haug et al., 2001; Ziegler et al., 2008), lake sediments (Zhao et al., 2010; Li et al., 2016; Chen et al., 2021; Wu et al., 2012), and aeolian depositions (Liang et al., 2012; Liu et al., 2020). It has been proved to be well correlated with conventional XRF by contrast in lots of elements (Liang et al., 2012; Niu et al., 2019; Zhang X. et al., 2020). Different elements respond diversely to weathering, humidity, and temperature changes due to their own chemical and physical properties. The element ratio like Sr/Rb, Sr/Ca, Mg/Ca, Si/Fe, and Fe/Mn can be used to reflect the climate variation (Liang et al., 2012; Chen et al., 2021), and the single stable elements like Fe, Mn, Ti, Rb, and Zr also can be used to indicate the climate changes (Haug et al., 2001; Li et al., 2016). However, the paleoclimatic indications of elements under different climatic conditions are complicated and need to be further clarified or combined with other proxy indexes.

In this study, we presented the elements, color results of an 11.7-m lacustrine sediment core CG18B from Chagan Nur in the southern Mongolian Plateau. The changes of the lake level and surface erosion in the catchment during the Holocene were reconstructed. Furthermore, we discussed the relationship between lake environmental changes and the variation of EASM precipitation based on the pollen record from the same lake. Finally, it was figured out how the lake environment responded to EASM precipitation variation during the Holocene in northern China.

GEOGRAPHICAL SETTING

Chagan Nur (43° 26′ 11.68″ N, 115° 01′ 36.98″ E, 1,013 m a.s.l. **Figure 1** and **Figure 2**), an inland-closed lake situates on the southeastern Mongolian plateau, northern China. It covers a total area of ~ 108 km^2 consisting of two lakes, east and west, in which the west lake dried up in 2001 AD, only leaving the east lake with an area of 22 km^2. The elevation of the Chagan Nur basin is lower than 1,500 m, with the Otindag Sandy Land lying to the south and the Abaga Lava Platform to the north, basically appearing as the pattern of high in the south and low in the north. The Gogusty and Engeer rivers originating from the Otindag Sandy Land from the southern direction provide most of the fresh water to Chagan Nur Lake in the rainy season (June to September).

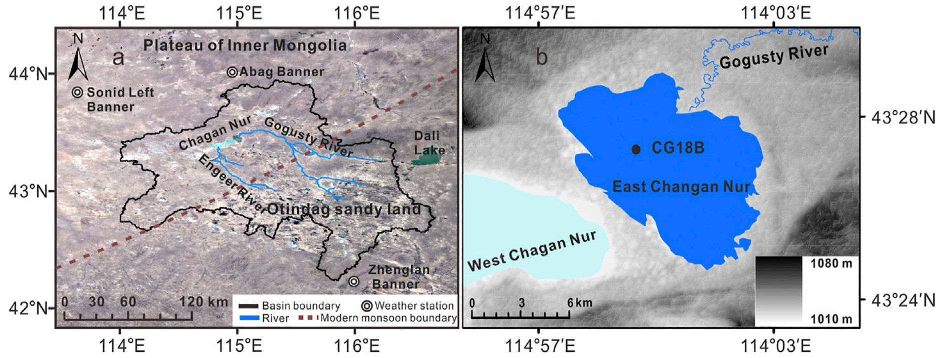

FIGURE 2 | Detailed information of Chagan Nur basin. **(A)** Li et al., (2020); **(B)** boundary of east Chagan Nur and the CG18B core.

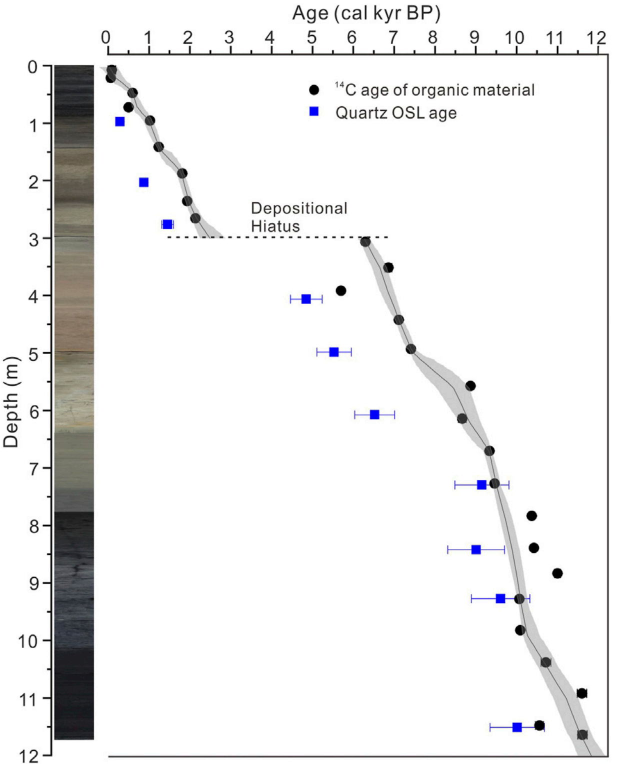

FIGURE 3 | Lithology, quartz OSL ages, ^{14}C ages of bulk organic materials, and age-depth model for sediment core CG18B from Chagan Nur (Redraw accorded by Li et al., 2020 with the IntCal20 curve).

The Chagan Nur basin is dominated by the typical semiarid temperate continental climate. The mean annual temperature is ~ 3.5°C. The annual precipitation in the basin is ~ 270 mm (Chun et al., 2017; Li et al., 2020), and more than 70% of the rainfalls occur in the rainy season (June to September) which is transported by the EASM from the Pacific and the Indian Ocean. The modern vegetation landscape in the region is typical dry steppes consisting primarily of grasslands, sandy deserts, and few forests.

MATERIALS AND METHODS

The X-ray Fluorescence Core Scanner

The 11.7 m sediment core (CG18B) was retrieved in September 2018 from the center of east Chagan Nur Lake at the water depth of about 2.5 m by the UWITEC platform produced by Austria and then split it down from the middle in the lab. Before the scanning XRF measurement, the fresh sample surface was flattened and smoothed to eliminate scanning errors and then was quickly covered with preservative film to isolate the sample from the pollution of atmospheric dust. After the preparatory work, the elemental counts of the lake's core were measured by the XRF Core Scanner at the Key Laboratory of Western China's Environmental Systems (Ministry of Education) of Lanzhou University. The CG18B core was scanned in the conditions of 10 kV–10 mA, 5 mm, no filter, and 10 s scanning time to get the elements of Al, Si, S, K, Ca, Ti, and Fe and 30 kV–20 mA, 5 mm, Pd-Thick filter, and 20 s scanning time to get the elements of Cu, Zn, Ga, Br, Rb, Sr, and Pb (Richter et al., 2006; Weltje and Tjallingii, 2008). The validity of parameter setting was carried out by the inspection of instrument parameters. All elements were recorded by counts per second (cps).

A total of 27 bulk sediment samples were collected from CG18B core for accelerator mass spectrometry (AMS) radiocarbon dating. We compounded the graphite in the ^{14}C dating laboratory in Lanzhou University by the normative approach and dated by accelerator mass spectrometry (AMS) in Peking University. All ^{14}C ages were recalibrated to calendar years using the IntCal20 calibration curve (Reimer et al., 2020). The ages are expressed as years before present (BP) where "present" is defined as AD 1950. The top two samples (2 and 14 cm) were 184 and 136 cal yr BP. Therefore, we employed the 136 yrs as the reservoir age to correct all the ages. 10 luminescence dating samples are collected from the core CG18B for chronology determination in Lanzhou University. The measured luminescence dating ages from 728 cm, 926 cm, and 1,150 cm of the core are consistent to ^{14}C age, while other luminescence dating ages have shown a systematic underestimation comparing to their ^{14}C ages primarily due to the exact water content is underestimated. As a result, the chronology of core CG18 is

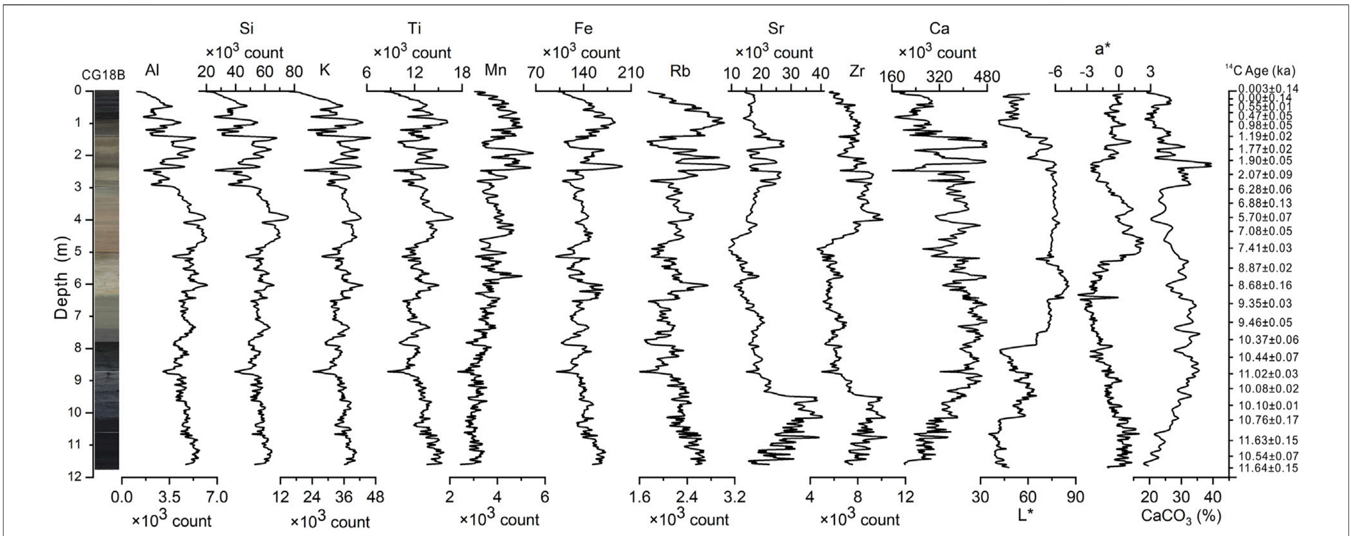

FIGURE 4 | Lithology, ^{14}C ages, elements, color, and carbonate indexes data of core CG18B.

established by using all ^{14}C ages with Bacon age-depth modeling (Blaauw and Christen, 2011) and the results are modified in **Figure 3** according to Li et al., 2020.

The Proxy Indexes of Color and Grain Size Measurement

The color and grain size from core CG18B are measured and analyzed at the Key Laboratory of Western China's Environmental Systems at Lanzhou University. The chroma of the samples was measured by using the Avaatech AV60626 XRF Core Scanner when the fresh samples were split immediately to avoid the influence of oxidation.

A total of 469 samples from the core were used for grain size measurement. We treated the samples in the lab of Lanzhou University and followed the ways of Peng et al. (2005). For each sample, the 0.2–0.25 g dry sample was treated with 10% H_2O_2 in the heating plate at 220°C to remove the organic material first, and then we added the 10 ml of 10% HCl to remove the carbonate content. The samples were soaked in distilled water to remove the acidic ions and stand for 10 h. After siphoning off the upper liquids by a rubber hose, we added 10 ml of 0.1 mol/L $(NaPO_3)_6$ with an ultrasonicator for 10 min to disperse the samples and then tested the dispersed samples using Malvern Master Sizer 2000.

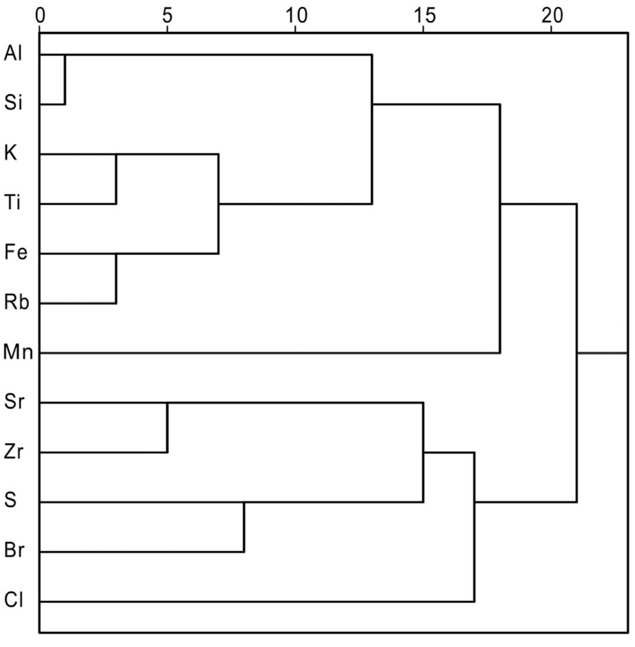

FIGURE 5 | Tree cluster analysis of elements, based on data correlation.

RESULTS

Lithology and Chronology

All of these sediments from the core CG18B are consisted of lacustrine clay and silty clay. The details of the sedimentary structure are as follows: the uppermost 2.4 m of the core is black clay interbedded with sandy clay layers at depths of 0.9–1.1 m and 1.7–2 m; the light brown to blue-gray clay is present at the depth of 2.4–6.4 m; at 6.4–11.7 m, there is black mud with no obvious structure but the color changes to light black in the upmost 7.4–6.4 m of the core; poorly sorted and poorly rounded gray sandy gravels occur at 11.7–11.8 m (Li et al., 2020).

Both the ^{14}C dating ages and luminescence dating ages show the lake sediments were deposited since the early Holocene (**Figure 3**, after 11.7 ka). An age jump occurred between the ^{14}C age of 2.086 ± 0.067 cal kyr BP at 264 cm and 6.274 ± 0.050 cal kyr BP at 305 cm in the core, indicating that the deposition hiatus occurred between the depths of 2.64–3.05 m. As a result, the age-depth

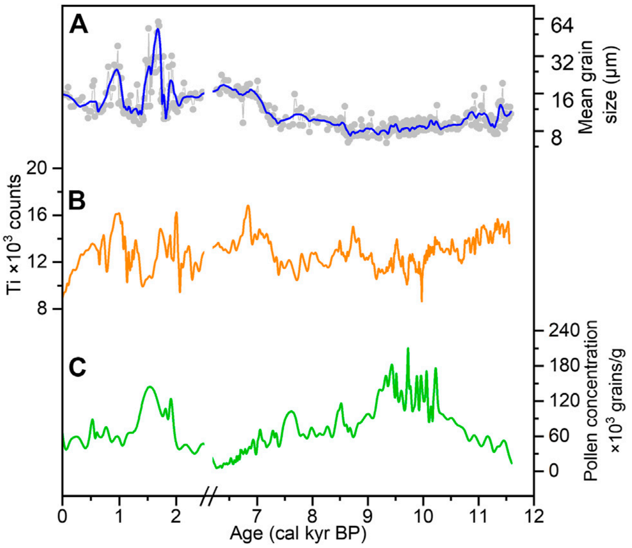

FIGURE 6 | Mean grain size, **(A)** the Ti content, **(B)** pollen concentration, and **(C)** (Li et al., 2020) of Chagan Nur.

model was established separately for the depths of 0–3 m and 3–11.7 m. The resulting age-depth model for core CG18B is illustrated in **Figure 3**.

The Results of Chroma and Elements

The measured elements of samples from the CG18B core are illustrated in **Figure 4**. The contents of Al, Si, K, and Ti vary with the depth. The relatively stable and high contents of Al, Si, K, and Ti occur at the depth of 11.7–5 m and then increase to the highest content in 5–3 m, whereas the contents of Al, Si, K, and Ti drop obviously at the depth of 3–0 m. Fe and Rb contents show the identical trend of the gradual decrease in 11.7–6.5 m and then appear as a slight peak at the depth of 6.5–5.5 m, and the contents keep stable and low in 5.5–3 m, followed by a distinct fluctuation at the depth of 3–0 m. The high values of Sr and Zr occur at the depth of 11.7–9.5 m and the contents slightly reduce at the depth of 9.5–5 m. The following variations of Sr and Zr at the depth of 5–0 m exhibit discrepancies, in which the highest Zr content occurs at the depth of 4–2.5 m, while the Sr content reaches the maximum at the depth of 3–1.5 m.

Correlation analysis of elements data indexes of core CG18B are further classified by tree cluster analysis (**Figure 5**). Al and Si (0.97), K and Ti (0.88), and Fe and Rb (0.86) are highly correlated ($R^2 > 0.8$); Zr and Sr (0.78) and S and Br (0.57) also have moderate correlations. Therefore, all the elements are divided into five branches by the tree cluster analysis initially, and then Al, Si, K, Ti, Fe, and Rb are classified as the same class according to their variation tendency and correlation.

For chroma analysis (**Figure 4**), the indices of a* are used to represent the degree of redness from green (negative value) to red (positive value), respectively. Chromas in Chagan Nur lake sediments showed different patterns. Two peaks of a* can be recognized in 11.7–9 m and 6.5–3 m and two low ebbs are in 9–6.5 m and 3–0 m.

DISCUSSION

The Variation of Stable Element Ti Recorded Surface Erosion at Chagan Nur Basin

Al, K, Ti, Fe, and Rb have the stable chemical property which is almost unaffected by surface chemical weathering and almost shows the same change (**Figure 4**), they are regarded as rock-forming elements and are enriched in coarse particle and only transported to the lake by surface erosion in semiarid and arid lake basin (Shen et al., 2013b; Li et al., 2016; Zhang et al., 2017; Zhang et al., 2020; Tao. 2020; Chen et al., 2021). The result of mean grain size proxy also shows the similar change with these stable elements (see **Figure 6**, Ti and mean grain size). In 10.5–7.5 ka, Ti shows a relatively low content (about 12 × 10^3 count) correspondingly with the decrease in mean grain size which indicated the weak surface erosion during this period. In 11.7–10.5 ka and 7–6.2 ka, the high content of Ti (15 × 10^3 count) correspondingly with the increase in mean grain size suggested that the surface erosion became strong. Over the past 2,500 years, the value of Ti becoming much more unstable indicated that the surface erosion process became more complex in this period.

The results of pollen concentration from core CG18B also supported the surface erosion result indicated by Ti. It has been reported that pollen concentration is one of the reliable proxies to reflect the vegetation coverage or humidity changes in the past period (Liu et al., 2002; Jiang et al., 2006; Zhao and Yu, 2012; Shen, 2013a). The vegetation recovery improvement in the Loess Plateau that had been reported could efficiently stop the water loss and soil erosion (Wang et al., 2016). At the same time, loess profiles also have revealed the degraded climate can result in vegetation reduction and desertification (mean grain size increase) and even cause the lack of loess sediments by the strong wind erosion (Stevens et al., 2018; Hao et al., 2013), so that the vegetation coverage variation is the appropriate proxies to reflect the change of surface erosion.

As illustrated in **Figure 6**, the Ti, mean grain size, and the pollen concentration show a similar trend. The low content of pollen concentration but the high value of mean grain size during 11.7–10.5 ka and 7–6.2 ka indicated the poor vegetation coverage, while the high pollen concentration and the low level of mean grain size during 10.5–7 ka indicated the lush vegetation. Correspondingly, the high content of Ti in 11.7–10.5 ka and 7–6.2 ka indicated strong surface erosion but low in 10.5–7 ka suggested surface erosion became low. The same situation also has been reported in Huahai Lake (Li et al., 2016) and Hurleg Lake (Zhao et al., 2010), which revealed that stable elements were abundant when the grain size turned coarse.

In the past 2,500 years, the instabilities and complexities of the pollen concentration and grain size might be caused by human activities. Zhang et al. (2012) has reported that a number of human activities have been recorded in the Chagan Nur basin such as the agricultural activities causing the vegetation degradation during the past 2000 years. In addition, human activities could cause the unconformity between the sand

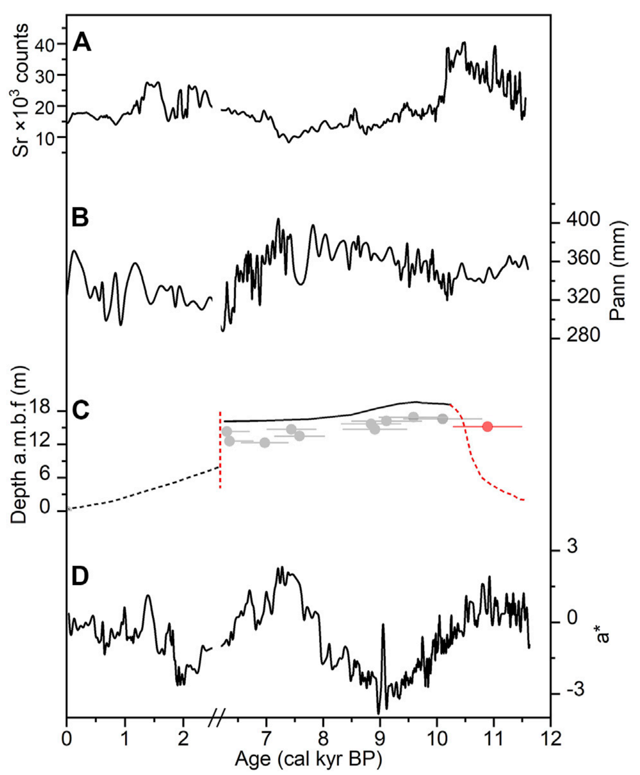

FIGURE 7 | Comparison of different climatic records in Chagan Nur lake. Sr content, **(A)** annual precipitation rebuilt by tree pollen (without pinus, Li et al., 2020), and **(B)** lake level (**C**, reorganize according Li et al., 2020), redness (a*, d).

storm and EASM like the abnormal sand storm during the wet period in northern China (Chen et al., 2021).

The Sr Element, Color (a*) in CG18B Core Revealed the Lake-Level Change of Chagan Nur Lake During the Holocene

Sr is a kind of active element which can be leaching from land surface during the wet and warm period by strong chemical weathering in typical monsoon area and then enrich in lake sediments (Liu et al., 2020; Liang et al., 2012; Jin et al., 2006; Wu et al., 2012). However, Sr in arid Chagan Nur Lake shows the opposite result since 11.7 ka (**Figure** 7) that high lake level correlated with low content of Sr or shallow lake level correlated with high content of Sr and it might be affected by lacking precipitation (Li et al., 2020) or weak chemical weathering. Zhang et al. (1994) have presented that the variations of Sr element and salinity that generally exists in the linear positive correlation in the arid Qinghai Lake, which indicates that the saltier the lake water, the higher the content of Sr, correspondingly, and Sr/Ca extracted from *Eucypris inflate* also used to rebuild the lake level change of Qinghai Lake. Therefore, Sr content in arid Chagan Nur Lake may be influenced by lake-level variation since 11.7 ka. a* (redness) also has some correspondence with Sr, for the value of a* varies synchronously with the content of ferric iron mineral (Ji et al., 2005) which could be influenced by oxidation environment caused by lake level in Chagan Nur Lake. As illustrated in **Figure** 7, the content of Sr exhibited high value during 11.7–10 ka in keeping with the small and shallow lake and less precipitation, leading to the lake water dissolving more oxygen and keeping the lake in strong oxidized condition, so that the low lake level not only provided enough oxygen content to the lake water but also promoted the enrichment of Sr in the lake water. In 10–6.2 ka, the Sr content decreased or attenuated in line with the rising of precipitation and the lake level, correspondingly, a* kept the lowest value in 10.5–8 ka, which meant the high lake level could reduce the oxygen in lake water and attenuate the concentration of Sr in lake water. The high a* value appeared in 8–6.2 ka might have been caused by the hiatus that happened during 2.5–6.2 ka, which caused the lake sediments formed in 8–6.2 ka to be exposed to the air and kept a highly oxidized state in the dried-up lake environment. The high values of Sr during 2–0 ka were corresponding with the shrunken lake level, high a* value, and poor precipitation during the late Holocene which was the same situation with 11.7–10 ka that the small-shallow lake level and precipitation enhanced the oxidized condition and enriched the content of Sr in lake water (**Figure** 7).

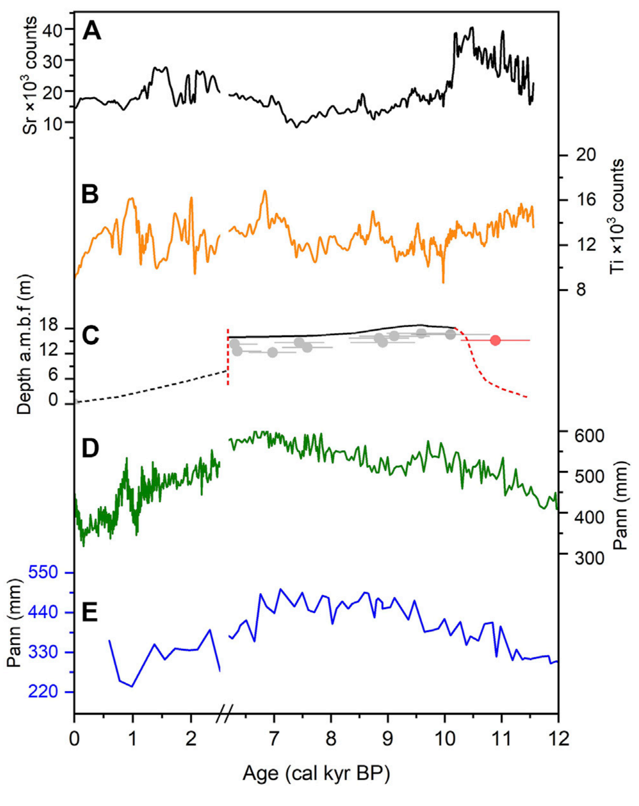

FIGURE 8 | Regional comparison by Sr content, **(A)** Ti content, and **(B)** lake level (**C**, reorganize according Li et al., 2020) with precipitation from Gonghai (**D**, Chen et al., 2015) and Bayan Chagan Nur (**E**, Jiang et al., 2006).

The Element Indicated Surface Erosion and Lake-Level Changes and Compared With Precipitation Recorded by Pollen and Lake Level Changes Rebuilt by Paleolake Shorelines

The lake environmental changes since 11.7 ka in Chagan Nur were reconstructed by proxy indexes of elements and color. The results suggested that the shallow lake with relatively strong surface erosion occurred during 11.7–10.5 ka. The weakening surface erosion, high lake level, and fresh lake water environment occurred during 10.5–7 ka. The strong surface erosion, relatively low lake level, and salinity lake water occurred in 7–6.2 ka and 2–0 ka of Chagan Nur Lake. The influence of human activities on the lake environmental changes has increased significantly during the past 2 ka.

As illustrated in **Figure 7**, the precipitation changes have been reconstructed by the pollen record from the Chagan Nur Lake. The results suggested that the variation of EASM dominated the paleoenvironmental changes in Chagan Nur basin at the margin of EASM dominance, which not only influenced the lake level but also influenced the vegetation coverage and surface erosion. The variations of precipitation reconstructed by pollen records from Chagan Nur (Li et al., 2020), Bayanchagan (Jiang et al., 2006), and Gonghai (Chen et al., 2015) are basically consistent (**Figure 8**) and show a spatial trend of decreasing from the south to north, which indicated that the strength of EASM is gradually reduced from southern China to northern China. During 11.7–10 ka, reconstructed precipitation by pollen showed a relatively low value, and the values of Sr and Ti kept at high level, indicating the EASM was weak and coarse grains were transported to the lake in this period. Pollen records from the Chagan Nur lake showed the herbaceous plant predominated in this region (Li et al., 2020), and the vegetation landscape was typical dry steppe. The less precipitation reduces runoff into the lake, and the poor vegetation coverage enhances surface erosion, both of which cause an increase in Ti and Sr contents in the lake. In 10–7 ka, the precipitation increased steadily and hit the peak in 8.5–7 ka, and the low values of Sr and Ti indicated that the EASM became strong, as a result of the rising lake level, the improved vegetation coverage, the fine mean grain size, and the higher ratio of tree pollen in the neighborhood area (Jiang et al., 2006; Wen et al., 2017; Han et al., 2020; Li et al., 2020). During 7–6.2 ka and 2.5–0 ka, the precipitation decreased rapidly and the content of Sr and Ti shot up which indicated the weakening of EASM, the degradation of vegetation, and the intensifying of surface erosion. Furthermore, the drought event happened in Chagan Nur during 6.2–2.5 ka which caused the depositional hiatus. When the lake reappeared in 2.5 ka, it might have been small and shallow as a result of the low lake water as indicated by the Sr value, shoreline record (Liu et al., 2017; Li et al., 2020), and strong surface erosion indicated by Ti value, which suggested the weakened EASM causing the diminishing precipitation during this period. Actually, the EASM intensity of the monsoonal region in northern China was weakest during the late Holocene because the northern Hemisphere summer insolation was minimum during the Holocene (Laskar et al., 2004).

CONCLUSION

Based on the chronology obtained by the radiocarbon and luminescence dating, in combination with the results of elements, color from an 11.7 m Chagan Nur lacustrine core, we have reconstructed variations of the surface erosion and lake level on the fringe of modern EASM dominance in northern China during the Holocene. The results show that the lake environment during the Holocene can be identified into four stages. The strong surface erosion and low lake water environment occurred at 11.7–10.5 ka. During 10.5–7 ka, the weakened surface erosion, rising lake level, and a better land coverage environment occurred at Chagan Nur lake basin. After that, the surface erosion gradually strengthened during 7–6 ka and from 2.5 ka to present, and lake level declined obviously during the Holocene period.

The variation in lake basin surface erosion, lake level, and land coverage of Chagan Nur have correlated with the EASM precipitation changes during the Holocene, indicating that the variation of EASM during the Holocene directly dominated the changes of surface erosion and lake level in arid northern China. During the past 2 ka, human activity has played a key role in the environmental changes at Chagan Nur Lake Basin.

DATA AVAILABILITY STATEMENT

The original contributions presented in the study are included in the article/Supplementary Material, and further inquiries can be directed to the corresponding author.

AUTHOR CONTRIBUTIONS

GL contributed to the conception and design of the study. ZW organized the database. ZW performed the statistical analysis. ZW wrote the first draft of the manuscript. ZW, XW, SG, YD, YZ, and ST did experiments. GL, ZW, WZ, and MJ discussed the data. All authors contributed to manuscript revision, reading, and approved the submitted version.

FUNDING

This work was supported by the National Natural Science Foundation of China (No. 41790423) and the Fundamental Research Funds for the Central Universities (No. lzujbky-2021-ey22).

REFERENCES

An, Z., Colman, S. M., Zhou, W., Li, X., Brown, E. T., Jull, A. J. T., et al. (2012). Interplay between the Westerlies and Asian Monsoon Recorded in Lake Qinghai Sediments since 32 Ka. *Scientific Rep.* 2, 619. doi:10.1038/srep00619

An, Z. S., Wu, G. S., Li, J. P., Sun, Y. B., Liu, Y. M., Zhou, W. J., et al. (2015). Global Monsoon Dynamics and Climate Change. *Sci. Rep.* 43, 29–77. doi:10.1038/srep00619

Blaauw, M., and Christen, J. A. (2011). Flexible Paleoclimate Age-Depth Models Using an Autoregressive Gamma Process. *Bayesian Anal.* 6, 457–474. doi:10.1214/ba/1339616472

Chen, C., Tao, S., Zhao, W., Jin, M., Wang, Z., Li, H., et al. (2021). Holocene lake Level, Vegetation, and Climate at the East Asian Summer Monsoon Margin: A Record from the Lake Wulanhushao basin, Southern Inner Mongolia. *Palaeogeogr. Palaeoclimatol. Palaeoecol.* 561, 110051. doi:10.1016/j.palaeo.2020.110051

Chen, F. H., Chen, S. Q., Zhang, X., Chen, J. H., Wang, X., Gowan, E. J., et al. (2020). Asian Dust-Storm Activity Dominated by Chinese Dynasty Changes since 2000 BP. *Nat. Commun.* 11, 992. doi:10.1038/s41467-020-14765-4

Chen, F. H., Xu, Q. H., Chen, J. H., Birks, H. J., Liu, J. B., Zhang, S. R., et al. (2015). East Asian Summer Monsoon Precipitation Variability since the Last Deglaciation. *Sci. Rep.* 5, 11186. doi:10.1038/srep11186

Chun, X., Su, R. G., Liu, J. Y., Liang, W. J., Yong, M., and Ulambadrakh, K. (2017). Climatic Implications on Variations of Qehan Lake in the Arid Regions of Inner Mongolia during the Recent Five Decades. *Environ. Monit. Assess.* 189, 14. doi:10.1007/s10661-016-5721-5

Chun, X., Yong, M., Liu, J. Y., and Liang, W. J. (2018). Monitoring Land Cover Change and its Dynamic Mechanism on the Qehan lake basin, Inner Mongolia, north China, during 1977–2013. *Environ. Monit. Assess.* 190, 205. doi:10.1007/s10661-018-6582-x

Goldsmith, Y., Broecker, W. S., Xu, H., Polissar, P. J., Demenocal, P. B., Porat, N., et al. (2017). Northward Extent of East Asian Monsoon Covaries with Intensity on Orbital and Millennial Timescales. *Proc. Natl. Acad. Sci. USA.* 114, 1817–1821. doi:10.1073/pnas.1616708114

Han, P., and Liu, X. Q. (2017). The Climate Evolution Inferred from Chagan Nuur in Middle East Part of Inner Mongolia since the Last 7000years. *Quat. Sci.* 37, 1382–1390. (In Chinese with English abstract). doi:10.11928/j.issn.1001-7410.2017.06.20

Han, Y., Liu, H. Y., Zhou, L. Y., Hao, Q., and Cheng, Y. (2020). Postglacial Evolution of forest and Grassland in southeastern Gobi (Northern china) - Sciencedirect. *Quat. Sci Rev* 248, 106611. doi:10.1016/j.quascirev.2020.106611

Hao, Q. Z., Wang, L., Oldfield, F., Peng, S. Z., Qin, L., Song, Y., et al. (2013). Delayed Build-Up of Arctic Ice Sheets during 400,000-year Minima in Insolation Variability. *Nature* 490, 393–396.

Haug, G. H., Hughen, K., Sigman, D., Peterson, L. C., and Röhl, U. (2001). Southward Migration of the Intertropical Convergence Zone through the Holocene. *Science* 293, 1304–1308. doi:10.1126/science.1059725

Ji, J., Ji, S., Balsam, W., Chen, J., Liu, L., and Liu, X. (2005). Asian Monsoon Oscillations in the Northeastern Qinghai-Tibet Plateau Since the Late Glacial as Interpreted From Visible Reflectance of Qinghai Lake Sediments. *Earth Planet. Sci. Lett.* 233, 61–70.

Jian, N., Wang, Y., Dong, J., Yang, J. S., Tian, F., Liu, J., et al. (2016). Sedimentary Record of Environmental Evolution since Ca 2000 Cal Yr B P Ago in Qehan Lake, Inner Mongolia. *Geol. Bull. China* 35, 953–962. (In Chinese with English abstract).

Jiang, W., Guo, Z., Sun, X., Wu, H., Chu, G., Yuan, B., et al. (2006). Reconstruction of Climate and Vegetation Changes of Lake Bayanchagan (Inner Mongolia): Holocene Variability of the East Asian Monsoon. *Quat. Res.* 65, 411–420. doi:10.1016/j.yqres.2005.10.007

Jin, Z., Cao, J., Wu, J., and Wang, S. (2006). A Rb/Sr Record of Catchment Weathering Response to Holocene Climate Change in Inner Mongolia. *Earth Surf. Process. Landforms* 31, 285–291. doi:10.1002/esp.1243

Laskar, J., Robutel, P., Joutel, F., Gastineau, M., Correia, A. C. M., and Levrard, B. (2004). A Long-Term Numerical Solution for the Insolation Quantities of the Earth. *A&A* 428, 261–285. doi:10.1051/0004-6361:20041335

Li, G., Wang, Z., Zhao, W., Jin, M., Wang, X., Tao, S., et al. (2020). Quantitative Precipitation Reconstructions from Chagan Nur Revealed Lag Response of East Asian Summer Monsoon Precipitation to Summer Insolation during the Holocene in Arid Northern China. *Quat. Sci. Rev.* 239, 106365. doi:10.1016/j.quascirev.2020.106365

Li, Z., Wang, N. a., Cheng, H., and Li, Y. (2016). Early-middle Holocene Hydroclimate Changes in the Asian Monsoon Margin of Northwest China Inferred from Huahai Terminal lake Records. *J. Paleolimnol* 55, 289–302. doi:10.1007/s10933-016-9880-8

Liang, L., Sun, Y., Yao, Z., Liu, Y., and Wu, F. (2012). Evaluation of High-Resolution Elemental Analyses of Chinese Loess Deposits Measured by X-ray Fluorescence Core Scanner. *Catena* 92, 75–82. doi:10.1016/j.catena.2011.11.010

Liu, H., Xu, L., and Cui, H. (2002). Holocene History of Desertification along the woodland-steppe Border in Northern china. *Quat. Res.* 57, 259–270. doi:10.1006/qres.2001.2310

Liu, M. P., and Ha, S. (2015). Mid Holocene Paleolake Fluctuation of the Qehan Lake, Inner Mongolia, China. *J. Desert Res.* 35, 306–312. (In Chinese with English abstract).

Liu, X., Sun, Y., Vandenberghe, J., Cheng, P., Zhang, X., Gowan, E. J., et al. (2020). Centennial- to Millennial-Scale Monsoon Changes since the Last Deglaciation Linked to Solar Activities and North Atlantic Cooling. *Clim. Past* 16, 315–324. doi:10.5194/cp-16-315-2020

Niu, J., Zhang, W. X., Zhang, H. C., Duan, L. C., Wu, M. J., and Wang, L. M. (2019). The Characteristics of Geochemical Elements in Fuxian Lake Sediments and its Environmental Significance Based on XRF Core Scanning. *Spectrosc. spectral Anal.* 39, 2223–2227. (In Chinese with English abstract).

Peng, Y., Xiao, J., Nakamura, T., Liu, B., and Inouchi, Y. (2005). Holocene East Asian Monsoonal Precipitation Pattern Revealed by Grain-Size Distribution of Core Sediments of Daihai Lake in Inner Mongolia of north-central China. *Earth Planet. Sci. Lett.* 233, 467–479. doi:10.1016/j.epsl.2005.02.022

Reimer, P., Austin, W., Bard, E., Bayliss, A., Blackwell, P., Bronk Ramsey, C., et al. (2020). The IntCal20 Northern Hemisphere Radiocarbon Age Calibration Curve (0–55 Cal kBP). *Radiocarbon* 62, 725. doi:10.1017/rdc.2020.41

Richter, T. O., van der Gaast, S., Koster, B., Vaars, A., Gieles, R., de Stigter, H. C., et al. (2006). The Avaatech XRF Core Scanner: Technical Description and Applications to NE Atlantic Sediments. *Geol. Soc. Lond. Spec. Publications* 267, 39–50. doi:10.1144/gsl.sp.2006.267.01.03

Rothwell, R. G., and Rack, F. R. (2006). New Techniques in Sediment Core Analysis: an Introduction. *Geol. Soc. Lond. Spec. Publications* 267, 1–29. doi:10.1144/gsl.sp.2006.267.01.01

Shen, J. (2013a). Spatiotemporal Variations of Chinese Lakes and Their Driving Mechanisms since the Last Glacial Maximum: a Review and Synthesis of Lacustrine Sediment Archives. *Chin. Sci. Bull.* 58, 17–31. doi:10.1007/s11434-012-5510-7

Shen, J., Wu, X., Zhang, Z., Gong, W., He, T., Xu, X., et al. (2013b). Ti Content in Huguangyan Maar lake Sediment as a Proxy for Monsoon-Induced Vegetation Density in the Holocene. *Geophys. Res. Lett.* 40, 5757–5763.

Stevens, T., Buylaert, J. P., Thiel, C., újvári, G., Yi, S., Murray, A. S., et al. (2018). Ice-volume-forced Erosion of the Chinese Loess Plateau Global Quaternary Stratotype Site. *Nat. Commun.* 9, 983. doi:10.1002/grl.50740

Tao, S. X. (2020). *Holocene lake Environmental Changes in the East Asian Summer Monsoon Limit Revealed by lake Geomorphy and Lacustrine Sediment Core Record from the Wulanhushao lake basin*. Lanzhou, China: Lanzhou University.

Thomson, J., Croudace, I. W., and Rothwell, R. G. (2006). A Geochemical Application of the ITRAX Scanner to a Sediment Core Containing Eastern Mediterranean Sapropel Units. *Geol. Soc. Lond. Spec. Publications* 267, 65–77. doi:10.1144/gsl.sp.2006.267.01.05

Wang, S., Fu, B., Piao, S., Lü, Y., Ciais, P., Feng, X., et al. (2016). Reduced Sediment Transport in the Yellow River Due to Anthropogenic Changes. *Nat. Geosci.* 9, 38–41. doi:10.1038/ngeo2602

Weltje, G. J., and Tjallingii, R. (2008). Calibration of XRF Core Scanners for Quantitative Geochemical Logging of Sediment Cores: Theory and Application. *Earth Planet. Sci. Lett.* 274, 423–438. doi:10.1016/j.epsl.2008.07.054

Wen, R., Xiao, J., Fan, J., Zhang, S., and Yamagata, H. (2017). Pollen Evidence for a Mid-holocene East Asian Summer Monsoon Maximum in Northern China. *Quat. Sci. Rev.* 176, 29–35. doi:10.1016/j.quascirev.2017.10.008

Wu, X., Zhang, Z., Xu, X., and Ji, S. (2012). Asian Summer Monsoonal Variations During the Holocene Revealed by Huguangyan Maar Lake Sediment Record. *Palaeogeo. Palaeoclimato. Palaeoeco.* 323-325, 13–21.

Zhang, E., Zhao, C., Xue, B., Liu, Z., Yu, Z., Chen, R., et al. (2017). Millennial-scale Hydroclimate Variations in Southwest China Linked to Tropical Indian Ocean since the Last Glacial Maximum. *Geology* 45, 435–438. doi:10.1130/g38309.1

Zhang, J., Tsukamoto, S., Jia, Y., and Frechen, M. (2016). Lake Level Reconstruction of Huangqihai Lake in Northern China since MIS 3 Based on Pulsed Optically Stimulated Luminescence Dating. *J. Quat. Sci.* 31, 225–238. doi:10.1002/jqs.2861

Zhang, P. X., Zhang, B. Z., Qian, G. M., Li, H. J., and Xu, L. M. (1994). The Study of Paleoclimatic Parameter of Qinghai Lake since Holocene. *Quat. Sci.* 03, 225–238. (In Chinese with English abstract).

Zhang, X. N., Zhou, A. F., Huang, Z. D., An, C. B., Zhao, Y. T., Yin, L. Y., et al. (2020b). Moisture Evolution in North Xinjiang (Northwest China) during the Last 8000 Years Linked to the Westerlies' winter Half-Year Precipitation. *Quat. Res.* 100. doi:10.1017/qua.2020.94

Zhang, X., Zhang, H., Chang, F., Ashraf, U., Peng, W., Wu, H., et al. (2020a). Application of Corrected Methods for High-Resolution Xrf Core Scanning Elements in lake Sediments. *Appl. Sci.* 10, 8012. doi:10.3390/app10228012

Zhang, X., Zhou, Y., Pang, J., Lu, H., Huang, C., Zhou, L., et al. (2012). The Relationship Between Environmental Changes and Human Activities during the medieval Warm Period and the Little Ice Age in Otindag Sandland by osl Dating. *Quater. Sci.* 32, 535–546. doi:10.3969/j.issn.1001-7410.2012.03.20

Zhao, C., Yu, Z., Zhao, Y., Ito, E., Kodama, K. P., and Chen, F. (2010). Holocene Millennial-Scale Climate Variations Documented by Multiple lake-level Proxies in Sediment Cores from Hurleg Lake, Northwest China. *J. Paleolimnol* 44, 995–1008. doi:10.1007/s10933-010-9469-6

Zhao, Y., and Yu, Z. (2012). Vegetation Response to Holocene Climate Change in East Asian Monsoon-Margin Region. *Earth-Science Rev.* 113, 1–10. doi:10.1016/j.earscirev.2012.03.001

Ziegler, M., Jilbert, T., de Lange, G. J., Lourens, L. J., and Reichart, G.-J. (2008). Bromine Counts from XRF Scanning as an Estimate of the marine Organic Carbon Content of Sediment Cores. *Geochem. Geophys. Geosyst.* 9, a–n. doi:10.1029/2007gc001932

Conflict of Interest: The authors declare that the research was conducted in the absence of any commercial or financial relationships that could be construed as a potential conflict of interest.

frontiers in Earth Science

ORIGINAL RESEARCH
published: 16 September 2021
doi: 10.3389/feart.2021.686677

Stepwise Weakening of Aeolian Activities During the Holocene in the Gannan Region, Eastern Tibetan Plateau

*Shengli Yang**, *Xiaojing Liu, Ting Cheng, Yuanlong Luo, Qiong Li**, *Li Liu and Zixuan Chen*

Key Laboratory of Western China's Environmental Systems (Ministry of Education), College of Earth and Environmental Sciences, Lanzhou University, Lanzhou, China

Aeolian sediments hold key information on aeolian history and past environmental changes. Aeolian desertification and extensive land degradation have seriously affected the eco-environment in the Gannan region on the eastern Tibetan Plateau. Understanding the history of aeolian activities can deepen our understanding of the impacts of climatic changes on aeolian activities in the future. This study uses a detailed chronology and multiple proxy analyses of a typical aeolian section in Maqu to reconstruct aeolian activities in the region during the Holocene. Our results showed that aeolian activities have occurred in the eastern Tibetan Plateau since the early Holocene. Magnetic susceptibility, grain size records, and paleosols formation indicated a trend of stepwise weakening in aeolian activities from the early Holocene to the present. The weakening of aeolian activities was divided into three stages: ~10.0–8.0 ka BP, ~8.0–4.0 ka BP, and ~4.0 ka BP to the present. Paleosols were primarily formed after ~8.0 ka BP, and episodically interrupted aeolian activities processes in the Gannan region. Aeolian activity may increase in the Gannan region as the climate gradually warms. Climatic changes and local hydrological conditions have jointly affected the history of aeolian activities in this region.

Keywords: loess, sand, aeolian activities, climate change, Holocence

Edited by:
Zhongping Lai,
Shantou University, China

Reviewed by:
Weiming Liu,
Institute of Mountain Hazards and Environment (CAS), China
Fuyuan An,
Qinghai Normal University, China

***Correspondence:**
Shengli Yang
shlyang@lzu.edu.cn
Qiong Li
leeqiong@lzu.edu.cn

Specialty section:
This article was submitted to Quaternary Science, Geomorphology and Paleoenvironment, a section of the journal Frontiers in Earth Science

Received: *27 March 2021*
Accepted: *01 September 2021*
Published: *16 September 2021*

Citation:
Yang S, Liu X, Cheng T, Luo Y, Li Q, Liu L and Chen Z (2021) Stepwise Weakening of Aeolian Activities During the Holocene in the Gannan Region, Eastern Tibetan Plateau. Front. Earth Sci. 9:686677. doi: 10.3389/feart.2021.686677

INTRODUCTION

The Tibetan Plateau (TP) is known as the third pole of the world with the highest altitude (Yao et al., 2012). The TP is a highly unique geological–geographical–ecological unit, with important geographical significance and high sensitivity to global environmental change and human disturbance (Dong et al., 2010; Kang et al., 2010; Chen et al., 2020). The Gannan region is situated on the eastern TP, and is the most important water conservation area in the upper reaches of the Yellow River (**Figure 1**). In recent decades, accelerating grassland degradation and aeolian desertification have caused severe environmental impacts in the region and its surrounding areas, and as a result, the area has received increased attention (Dong et al., 2010; Shen et al., 2011; You et al., 2014; Cao et al., 2019).

Most studies focus on the effects of modern climate change and human activities on aeolian desertification (Hu et al., 2013; Huo et al., 2013; Hu et al., 2015). However, an understanding of the history and process of desertification in the Gannan region over extended time scales would greatly help to assess the effects of climatic changes on desertification processes. Therefore, investigation of

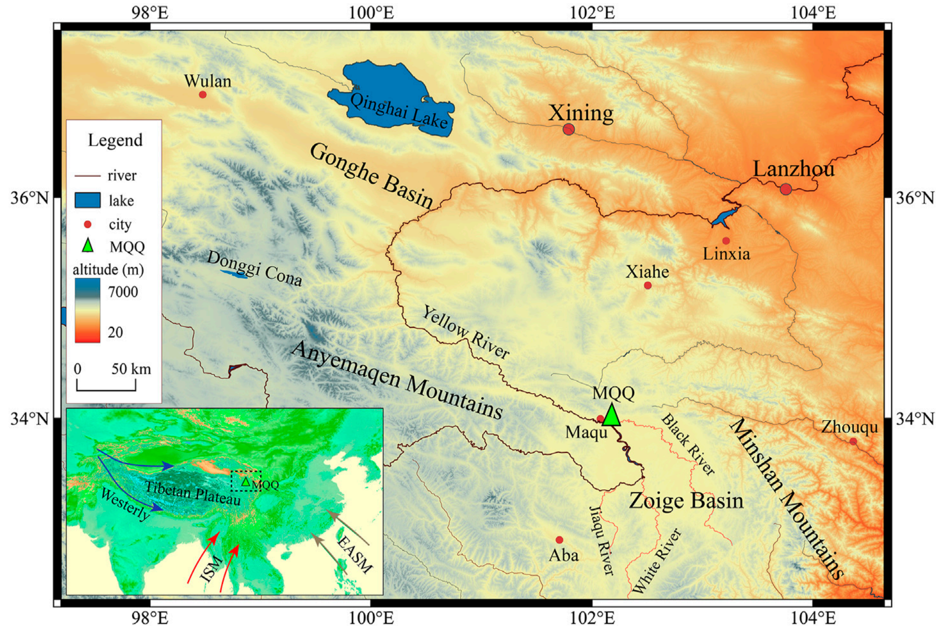

FIGURE 1 | Location of the Maquqiao (MQQ) profile and the terrain of the study area in the eastern Tibetan Plateau. (ISM: India summer monsoon; EASM: East Asian summer monsoon).

the aeolian processes in the Gannan region during the Holocene is essential to better understanding aeolian activities on the TP under global warming (Huo et al., 2013; Hu et al., 2018).

Aeolian sediments are widely distributed in the northeastern TP and can provide key information on aeolian history and past environmental changes (Stauch et al., 2012; Yu and Lai, 2014; Qiang et al., 2016). The aeolian deposits around Qinghai Lake indicate that aeolian activity and low effective moisture occurred at ~13 ka, ~10–9.1 ka, and ~8.9–7.8 ka and that the climate was wetter at ~4–3 ka (Lu et al., 2011). A subsequent study revealed that aeolian activity occurred episodically during the Holocene and that paleosols developed primarily from 9.5 to 4 ka in the Qinghai Lake Basin (Lu et al., 2015). In the Gonghe Basin, Qiang et al. (2013) found that the strongest aeolian activity occurred at 11.8–11.0 ka, 9.4 ka, 7.8 ka, and 5.7 (5.5) ka. The climate records of aeolian deposits reveal a relatively warm and wet climate in the early Holocene, dry conditions from 8.7 ka to 4.7 ka, and a warm and wet climate from 4.7 ka to 0.7 ka (Liu et al., 2013a). Aeolian deposition increased significantly in the Donggi Cona catchment during the early Holocene and from 3 ka to the present, which demonstrated that a drier and cooler climate caused the reactivation of dune sand and enhanced aeolian activity during the early Holocene (Stauch et al., 2012). On the basis of a summary of the published optically stimulated luminescence (OSL) ages from the TP, Stauch (2015) suggested that in most regions, the strongest aeolian sediment accumulation occurred during the late Glacial and in the early Holocene, which coincided with the strengthening of the Asian summer monsoon on the TP (Stauch, 2015). However, the history of aeolian activities in different regions is not consistent, and the relationship between aeolian activity and regional evironmental change is likely complex (Qiang et al., 2016).

Few studies have investigated the aeolian history in the Gannan region. Recently, Hu et al. (2018) analyzed OSL ages from three aeolian sand sections. They found that aeolian activity in the Zoige Basin had occurred since the early Holocene, whereas aeolian sediment deposition primarily had occurred after ~3.20 ± 0.33 ka with a very high sedimentation rate. However, the environmental records of aeolian sediments have not been reconstructed on the basis of detailed geochronology, and further investigations are needed. In this paper, detailed radiocarbon and OSL dating were conducted on a loess-sand profile near Maqu County in the Gannan region to obtain a reliable age framework. Multiple environmental proxies were employed to investigate the history of aeolian activities in the Gannan region and determine its relevance to environmental changes.

GEOGRAPHICAL SETTINGS AND METHODS

Study Area and Sampling

The Gannan region, with an altitude of ~3300–4800m, is situated in the northwest of the Zoige Basin in the eastern TP. It is surrounded by the Anymaqen Mountains to the west, the Minshan Mountains to the east, and the Xiqing Mountains to the north (**Figure 1**). The Yellow River flows northwest across the basin, and Maqu County is on the north bank. Wide, meandering river valleys of the Yellow River and its tributaries are the main

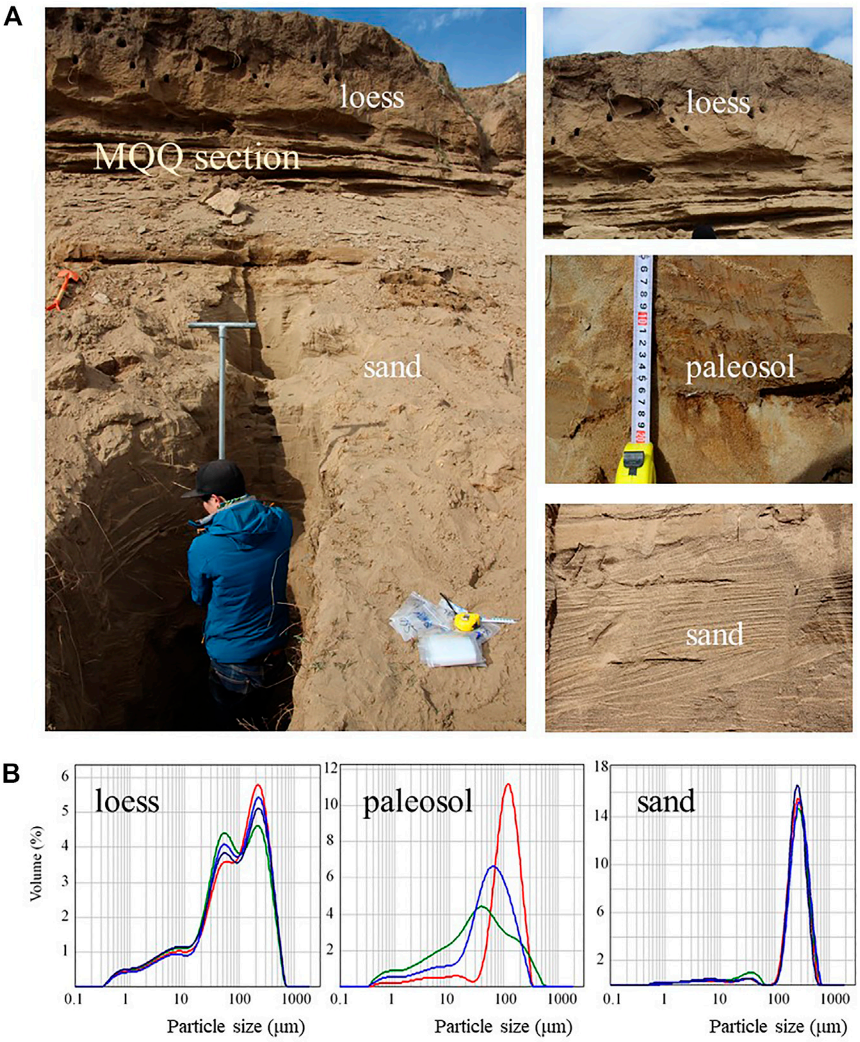

FIGURE 2 | (A) Photographs of the MQQ profile. **(B)** Grain size distributions in representative samples of loess, paleosol, and aeolian sand from the MQQ profile (different lines in color represent different samples).

rivers around this region, including the White River, the Black River, and Jiaqu River; and this region is the main water supply for the Yellow River (**Figure 1**). The Gannan region has a continental alpine and humid climate that is mainly affected by the westerlies and the Asian summer monsoon (ASM) (Yao et al., 2012; Yang et al., 2014). The annual average temperature of Maqu County is 1.26°C, the annual average precipitation is 606.5 mm, and the annual evaporation is 785.9 mm. More than 80% of the total annual precipitation occurs between May and October due to the influence of the ASM. The vegetation is dominated by alpine shrub meadows and alpine meadows, with mainly alpine meadow soil. Paleo-sand dunes and active dunes are widely distributed in the region. Thin aeolian deposits cover the various terraces and low-relief mountain slopes.

The Maquqiao (MQQ) profile (33.961° N, 102.078° E) is on the first terrace (T1) of the Yellow River at 3,422 m a.s.l. (**Figure 1**), south of Maqu County. The surface of the MQQ profile is ~13 m above the river level, and is composed of 1.3-m-thick sandy loess at the top and 7.2-m-thick aeolian sands with seven paleosol interbeds in the middle section (**Figure 2**). The multiple, weak, fine sandy-to-silty paleosol layers of light-grayish color were between 1.7 and 3.5 m. Samples were collected at different depths through the MQQ profile. In the upper 0–4 m, bulk samples for environmental proxies were collected at 2.5-cm intervals. From 4 to 8.5 m, samples were collected at 5-cm intervals because of high deposition rate and no distinct changes. A total of 249 bulk samples were collected, including 197 of sand and 52 of sandy loess. Owing to a lack of charcoal or macrofossils, we collected seven bulk sediments samples along the depth of the MQQ section for accelerator mass spectrometry (AMS) ^{14}C dating. Most samples were taken in or close to the paleosol layers. For the sample at 5 m, we collected bulk sands from the freshly cleaned section for radiocarbon dating. To collect

TABLE 1 | Accelerator mass spectrometry radiocarbon dating results of the MQQ profile by depth.

Lab. No	Depth(m)	Dating material	Age (cal. BP)	Error (2σ)	Dating lab
GN01	0.30	Organic sediments	388	81	Beta Analytic
GN02	1.30	Organic sediments	3,098	108	Beta Analytic
LZU16026	1.95	Organic sediments	4,843	72	Peking University
GN03	2.20	Organic sediments	5,953	42	Beta Analytic
LZU16027	2.55	Organic sediments	7,116	197	Peking University
GN04	3.30	Organic sediments	5,312	187	Beta Analytic
LZU16028	5.00	Organic sediments	8,387	34	Peking University

OSL dating samples, a stainless-steel tube was hammered into a freshly cleaned profile. Three samples were collected and then sealed in black plastic bags to avoid exposure to light.

AMS ^{14}C Dating

All samples were dried at room temperature before pretreatment. We first removed all rootlets and any visible contaminants from the sample by using tweezers, and then sieved the sediment to <180 microns to remove any plant remains or macrofossils. Following this, they were washed with HCl to remove all carbonates. The remaining samples were then dried at 60°C and combusted to extract organic sediment for AMS measurement. Carbon dioxide was obtained by step heating, and was then purified and synthesized into graphite. Four AMS ^{14}C samples were dated at Beta Analytic in Miami, United States, and three others were dated at Peking University in Beijing, China. Ultimately, seven AMS ^{14}C ages were obtained (**Table 1**).

Optically Stimulated Luminescence Dating

Three quartz samples were dated by the standard OSL SAR method. The pretreatment and equivalent dose (De) measurements were performed at the Key Laboratory of Western China's Environmental Systems (Ministry of Education), Lanzhou University, Lanzhou, China. All luminescence experimental were conducted in subdued red light. First, wet-sieving was used to separate the 90–125 µm size fraction. Then, HCl (10%) was added to remove carbonate, and hydrogen peroxide (30%) was added to remove organic matter. The quartz grains were then separated by 2.75 g/cm^3 and 2.62 g/cm^3 sodium polytungstate. Afterward, HF (10%) was added to etched quartz grains for approximately 40 min to remove the alpha-irradiated surface layer and weathering products, followed by HCl (10%) for 40 min to remove fluoride precipitation. The OSL measurements were performed on an automated Risø TL/OSL-20 reader equipped with blue (470 nm) and infrared (870 nm) LEDs. The laboratory irradiations were applied using a built-in calibrated ^{90}Sr/^{90}Y beta source, and the quartz OSL signal was detected using a 7.5-mm Schott U-340 filter. The equivalent dose was determined by using the single-aliquot regenerative-dose (SAR) protocol (Wintle and Murray, 2006), and 12 aliquots were measured for each sample. Some aliquots were omitted in the final calculations of De due to unsatisfactory criteria for the recycling ratio and recuperation. The water content was estimated to be 5 ± 2% based on measurement obtained by weighing the samples before and after drying, similar to a previous determination (Hu et al., 2018). The concentrations of uranium (U), thorium (Th), potassium (K), and rubidium (Rb) were determined using neutron activation analysis (NAA), and the element results were converted to α, β, and γ dose rates according to the conversion factors (Aitken, 1998).

Environment Proxy Analyses

Grain size and magnetic susceptibility were measured at the Key Laboratory of Western China's Environmental Systems (Ministry of Education), Lanzhou University. Grain size measurements were conducted on a Malvern Mastersizer 2000 laser diffractometer with a measurement range of 0.02–2,000 µm. In the pretreatment for grain size measurements, 10 ml of 10% H_2O_2 and 10 ml of 10% HCl were used to remove organic matter and carbonate, respectively. Samples were then rinsed with deionized water to remove acid ions. Before measurement, 0.1 mol/L $(NaPO_3)_6$ was added, and ultrasonic vibration was used to improve dispersion. Magnetic susceptibility was measured by a Bartington MS2 meter. Air-dried samples were mildly ground and wrapped with plastic film. Then, low frequency (470 Hz, χ_{lf}) and high frequency (4,700 Hz, χ_{hf}) magnetic susceptibility were measured. The frequency-dependent susceptibility (χ_{fd}) was calculated as $\chi_{fd} = \chi_{lf} - \chi_{hf}$.

RESULTS

AMS ^{14}C Ages

Seven samples were collected for AMS ^{14}C dating measurements along the MQQ profile (**Figure 3**). All calibrated AMS ^{14}C ages are listed in **Table 1**. The AMS ^{14}C ages ranged from 8,387 ± 34 cal. BP to 388 ± 81 cal. BP. Except for the age reversal at 3.30 m, all other AMS ^{14}C ages were consistent with the stratigraphic sequence. Although the AMS ^{14}C results were from two different laboratories, the age results were highly consistent in the stratigraphic sequence, which reflected the reliability of the AMS ^{14}C dating results. Because the age was 8,387 ± 34 cal. BP at the lowest depth of 5 m, and considering that there was 3.5 m of aeolian sand below, the bottom age of the MQQ profile was inferred to be in the early Holocene. Therefore, according the calibrated AMS ^{14}C dating, the aeolian sands of the MQQ profile have been deposited at least since the early Holocene, with deposits continuing to the present. The bottom

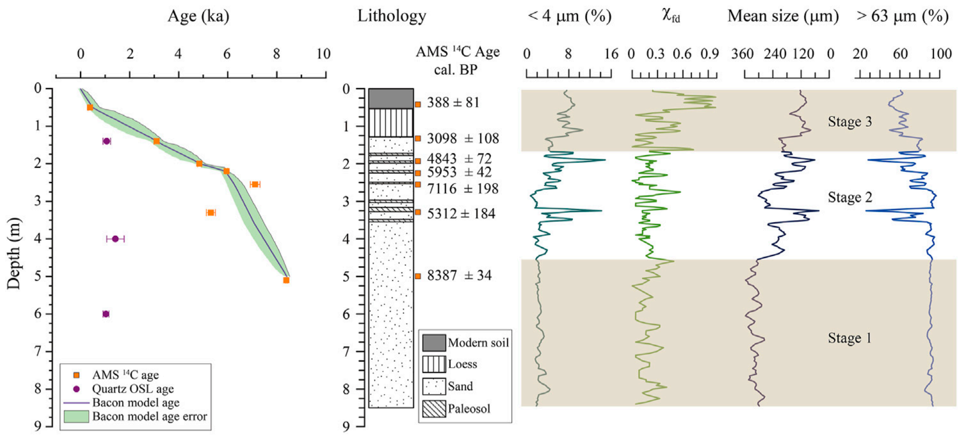

FIGURE 3 | Quartz optically stimulated luminescence (optically stimulated luminescence) and accelerator mass spectrometry (AMS) ^{14}C ages and Bacon age–depth model, lithology, grain size records, and the mass-specific frequency-dependent magnetic susceptibility along the depth of the MQQ profile.

TABLE 2 | Quartz optically stimulated luminescence (OSL) results at different depths, including equivalent dose (De), overdispersion (OD), contents of U, Th, K, Rb, and water content (WC), dose rate, and quartz OSL ages.

Depth (m)	Aliquots (n)	Grain size (μm)	De (Gy)	OD (%)	U (ppm)	Th (ppm)	K (%)	Rb (ppm)	WC (%)	Dose rate (mGy/yr)	OSL age (a)
1.4	9/12	90–125	2.52 ± 0.35	18 ± 5	1.16 ± 0.06	6.27 ± 0.21	1.45 ± 0.05	59.2 ± 4.74	5 ± 2	2.37 ± 0.07	1,065 ± 150
4.0	6/12	90–125	2.79 ± 0.68	0	0.99 ± 0.05	4.95 ± 0.17	1.23 ± 0.05	59.2 ± 4.74	5 ± 2	1.96 ± 0.06	1,420 ± 350
6.0	10/12	90–125	2.50 ± 0.26	0	1.02 ± 0.05	5.31 ± 0.18	1.71 ± 0.05	76.2 ± 5.33	5 ± 2	2.42 ± 0.07	1,035 ± 115

age of the sandy loess was 3,098 ± 108 cal. BP, which implied that there had been a significant weakening in aeolian activity in the Gannan region and a transition from aeolian sand to sandy loess. Thus, the AMS ^{14}C ages produced a reliable age framework for the MQQ profile, and aeolian processes during the Holocene in the Gannan region in the eastern TP could be evaluated (**Figure 3**).

Quartz Optically Stimulated Luminescence Ages

Supplementary Figure S1 shows the OSL decay curve and dose response curve of sample MQQ-1. The OSL signals were relatively bright and generally dominated by the fast component decreasing to background within the first 2 s of stimulation. However, the OSL signals were relatively low, which resulted in a poor signal-to-noise ratio and statistically imprecise doses. The fitted growth curve showed relatively large errors with the measured data points (**Supplementary Figure S1**). Because of the low overdispersion for all samples, the central age model was used to calculate the final De and apparent OSL ages (Galbraith et al., 1999). The OSL dating results are listed in **Table 2.** Three ages were obtained: 1,065 ± 155 a (1.4 m), 1,420 ± 355 a (4.0 m), and 1,035 ± 120 a (6 m) (**Table 2**). Thus, all OSL ages were between 1,035 a and 1,420 a, and these OSL ages do not increase with stratigraphic depth. Because the ages at different depths were within a similar range, OSL was not effective for dating the MQQ profile. Compared with the AMS ^{14}C ages, those derived from OSL were significantly younger and were inconsistent with the stratigraphic sequence.

Environmental Proxies

The particle size distribution characteristics were significantly different among loess, paleosol, and aeolian sand (**Figure 2B**). The particle size in the aeolian sand samples mainly varied from 0.4 to 600 μm. The peak size was between 200 and 400 μm, and the mean size was between 120 and 400 μm. The particle size in the loess samples varied from 0.2 to 600 μm. The peak size was between 60 and 300 μm, and the mean size was between 80 and 200 μm. The grain size of the paleosol samples varied from 0.2 to 500 μm. The mode grain size was between 40 and 120 μm, and the mean size was between 60 and 150 μm.

Figure 3 shows the change in magnetic susceptibility and particle size with depth in the MQQ profile. The frequency of magnetic susceptibility (χ_{fd}), the fraction <4 μm, the mean grain size, and the fraction >63 μm fluctuated significantly with depth (**Figure 3**). All environmental proxies were divided into two groups with 1.3 m as the boundary. The χ_{fd} values were highest from 0 to 1.3 m, and the average particle size was much finer than that of sands, with abundant clay content and less coarse fraction >63 μm. The aeolian sand sediments from 1.3 to 8.5 m were divided into two groups with 4.8 m as the boundary. Below 4.8 m, the variation in all proxies was relatively low, whereas above 4.8 m, all proxies showed high frequency and large amplitude variations. The χ_{fd} values in the paleosol layers of the sand deposits were relatively high but were lower than those in the loess. The fraction <4 μm in the paleosol interlayer within the aeolian sand was significantly higher than that in the aeolian sands, and the corresponding mean grain size and the fraction >63 μm were distinctly lower. Thus, grain size and magnetic susceptibility were good indicators of changes in the environment in both aeolian sand and loess deposits.

DISCUSSION

Timing of Aeolian Activities in the Gannan Region

For the MQQ section, the quartz OSL dating yielded significantly younger ages than those of AMS ^{14}C. Moreover, all OSL ages were concentrated between 1,035 and 1,420 a without stratigraphic order. By contrast, AMS ^{14}C dating results showed good stratigraphic order with depth in the MQQ profile with ages ranging from 388 ± 31 to 8,387 ± 34 cal. BP. However, there was a significant reversal at 3.3 m. The comparison of OSL and AMS ^{14}C ages showed that the luminescence ages were significant underestimations.

OSL dating is usually an effective dating method for aeolian deposits, but its reliability can be affected by a variety of factors, such as dim OSL signals and post-depositional disturbance (Bateman et al., 2003; Bateman et al., 2007; Ahr et al., 2013). The relatively low quartz OSL signals with poor signal-to-noise ratios likely led to the large uncertainties in the Des (**Supplementary Figure S1**). According to eleven quartz OSL ages of three aeolian sections in this region, the oldest OSL age of aeolian sands is 10.27 ± 0.81 ka (Hu et al., 2018). However, most of the OSL ages are younger than 3.32 ± 0.33 ka, indicating a high accumulation rate (Hu et al., 2018). Considering the depths of the two OSL ages of 10.27 ± 0.81 ka and 3.07 ± 0.30 ka from **Section 1** (1.5 m deep) in Hu et al., 2018, there may exist an erosion hiatus at this site. Although detailed information is lacking, in **Section 3** (4 m deep), the OSL age estimates ranged from 0.17 to 0.92 ka (Hu et al., 2018), and were close to our OSL results in this study. Moreover, many rodent burrows were observed along the MQQ profile (**Figure 2A**). Rodent activities can cause varying degrees of mixing of sediments, resulting in an underestimation of the OSL age (Bateman et al., 2007; Ahr et al., 2013). Thus, the significant underestimation of OSL ages might have been caused by post-deposition biological disturbances. Therefore, the three OSL results of the MQQ profile did not indicate its true stratigraphic age because of large uncertainties and underestimated ages. The concentration of the three OSL ages in the range of 1,035 a to 1,420 a might indicate a rodent-active period. Rodent activity remains prevalent in alpine pastures in the Gannan region, with its effects having appeared since at least 1,035 a to 1,420 a. However, further evaluations of OSL dating in this region are needed.

Owing to a lack of charcoal or macrofossils along the MQQ section, we used organic sediments for radiocarbon dating. Previous studies have shown that the dating of bulk organic matter of aeolian loess can yield a reliable AMS ^{14}C age for the past 25 cal kyr BP (Song et al., 2018; Cheng et al., 2020). Only one radiocarbon age at 3.3 m was out of line with the stratigraphic order, showing younger ages than its upper sample. This might have resulted from young carbon contaminations or post-deposition mixing. Most of the AMS ^{14}C samples were collected in paleosol layers that were relatively stable, whereas the OSL samples were taken from aeolian sand layers. As a result, bioturbation likely had greater effects on the OSL results than on those of AMS ^{14}C dating. In addition, the results from the two laboratories were in good agreement, which also illustrates the reliability of AMS dating (**Table 1**). According to the AMS ^{14}C results and field observations, no prominent sedimentary hiatus was identified in the Maqu section. Thus, the results of AMS ^{14}C dating with good stratigraphic order were used to build the age control for the MQQ section.

Based on AMS ^{14}C results, the Bacon software package was used to establish a Bayesian-based age–depth model for the upper 5 m of the MQQ profile (Blaauw and Christen, 2011) (**Figure 3**). The Bacon model converted depth into a time scale (**Figure 4**). The age of the bottom of the MQQ profile at a depth of 5 m was 8,387 ± 34 a BP. According to the results of the Bacon age–depth model and considering an average accumulation rate of 2.2–5.0 m of aeolian sand, the estimated age at the bottom of the MQQ profile was approximately 11 ka in the early Holocene. This result showed that aeolian sand activities in the Gannan region have occurred since the early Holocene and continued to the late Holocene. Moreover, multiple paleosol interlayers occurring episodically among the aeolian sands indicated that soil formation processes during humid stages punctuated the aeolian sand activity (Stauch, 2015).

Variations in climate and local hydrological conditions might jointly have influenced the history of aeolian activity in the region. Previous studies have found that significant accumulation of aeolian sediments in the northeastern TP began in the early Holocene (Lu et al., 2011; Qiang et al., 2013; Stauch, 2015). Drilling records of the Zoige Basin demonstrate that it was a paleo lake before the Holocene and that it began to dry out gradually between 40 and 22 ka (Wang et al., 1995). According to OSL dating, aeolian sand around the Zoige Basin was not deposited earlier than the early Holocene, and aeolian deposition primarily occurred in the late Holocene (Hu et al., 2018). The shrinkage and disappearance of ancient lakes provide abundant supplies of sediments, and in addition to climate warming in the early Holocene, may have led to enhanced aeolian activities in the Gannan region.

Stepwise Weakening of Aeolian Activities During the Holocene

The mass-specific frequency-dependent susceptibility (χ_{fd}) is an important indicator of pedogenesis-related effective moisture in aeolian deposits (Kukla et al., 1988; Zhou et al., 1990; An et al., 1991; Liu et al., 2004). Grain size is an important environmental indicator of paleoclimate, especially for aeolian sediments (Vandenberghe et al., 1997; Sun et al., 2002; Prins et al., 2007). The χ_{fd} and the mean grain size records showed clear upward,

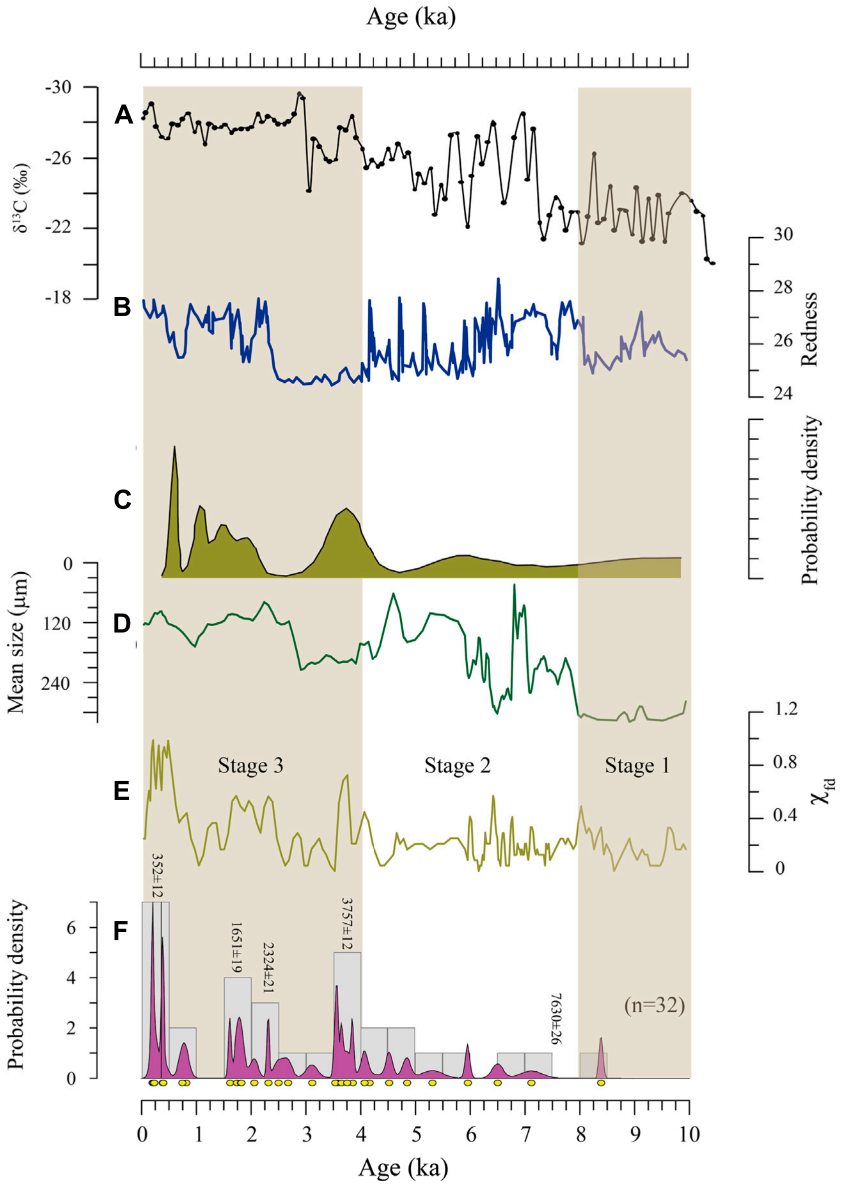

FIGURE 4 | (A) Organic δ^{13}C records indicating the variation in water depth (Liu et al., 2013b) and **(B)** Redness-inferred precipitation at Qianghai Lake (Ji et al., 2005). **(C)** OSL ages probability density for sandy loess from the Anyemaqen Mountains (Stauch, 2015). **(D)** Mean grain size and **(E)** Mass-specific frequency-dependent susceptibility (χ_{fd}) from the MQQ profile. **(F)** Probability density function of radio carbon ages for paleosols since the early Holocene in the eastern Tibetan Plateau. Radio carbon ages of paleosols are from (Xu, 1994; Zou and Wang, 1995; Fang et al., 1998; He et al., 2006; Lehmkuhl et al., 2014; Hu et al., 2016), and this study.

increasing trends, which indicated a stepwise wetting history since the early Holocene to the present (**Figure 4**). The process was divided into three steps based on the grain size and χ_{fd} records: ~10.0–8.0 ka, ~8.0–4.0 ka, and ~4.0 ka to the present (**Figure 4**). Most multiple paleosol interlayers of the MQQ section occurring after 8 ka also implied a trend of wetting in the Gannan region (**Figure 3**). Aeolian sands represent the expansion and accumulation of aeolian landforms, whereas paleosols are an indication of the stability of aeolian landforms, accompanied by increases in vegetation cover. Therefore, aeolian sediments and the formation of paleosols indicate dry and wet phases, respectively (Stauch, 2015). The probability density function (PDF) was calculated, and each age was regarded as an individual accumulation event (Lai et al., 2009; Stauch, 2015). The PDF of radiocarbon ages of paleosols around the Gannan region can reflect the periods of paleosol development. Paleosols were formed mainly after ~8.0 ka and indicated increasing effective moisture and episodic interruptions of aeolian desertification processes in the eastern TP (**Figure 4F**). The proxy records in this study agree well with the aeolian activities indicated by the probability density of OSL ages of aeolian sediments from the northeastern TP and

Anyemaqen Mountain area (**Figure 4C**) (Stauch, 2015) and by the organic $\delta^{13}C$ records indicating variation in water depth and the redness-inferred precipitation at Qinghai Lake (**Figures 4A,B**) (Ji et al., 2005; Liu et al., 2013b).

Based on the records in this study, the stepwise weakening of aeolian activities was divided into three stages that coincided with increasing moisture since the early Holocene (**Figure 4**). In stage 1 (~10–8.0 ka BP), according to AMS ^{14}C dating, the age in the MQQ profile was approximately 8 ka BP at 5 m and approximately 11 ka at the bottom. Coarse grain size and rare paleosol development implied strong aeolian activities with strengthened winds and suggested that aeolian activity in the Gannan region occurred at least since the early Holocene. This result is consistent with previous results in this region and the northeastern TP (Lu et al., 2011; Stauch et al., 2012; Qiang et al., 2013; Chen et al., 2016). The level of the lake was low and the climate was very dry in basins in the northeastern TP during the early to middle Holocene (Chen et al., 2016; Wu et al., 2020). In the Gonghe Basin in the northwest of the Gannan region, aeolian activity had occurred from 11.8 to 11.0 ka and at approximately 9.4 ka (Qiang et al., 2013); and in the Donggi Cona catchment to the west of the Gannan region, aeolian activity began at ~10.5 ka (Stauch et al., 2012). Strong aeolian activity in the early Holocene has also been reported in Qinghai Lake and the Qaidam Basin (Lu et al., 2011; Yu and Lai, 2014).

Stage 2 (~8.0–4.0 ka BP) corresponded to the mid-Holocene. Compared with the first stage in the early Holocene, the χfd value increased and the mean grain size decreased. Moreover, multiple, weak fine sand to silty paleosol layers were formed during this stage, indicating relatively wet climate conditions. Therefore, the aeolian activity weakened, and sand accumulation was interrupted by pedogenesis due to increases in humidity. Other studies also report a relatively warmer and wetter climate in the mid-Holocene in the northeastern TP (An et al., 2006; Stauch, 2015; Li et al., 2017; Wei et al., 2020). Loess records from the southern Anyemaqen Mountains indicate the climate was relatively humid from 8 to 4 ka, and the formation of a distinct paleosol layer also implied more humid conditions than those in the early Holocene (Lehmkuhl et al., 2014). The pollen record indicated that the precipitation in the northern TP reached a maximum in the mid-Holocene (Li et al., 2017). Pollen records also reveal a strong summer monsoon in the mid-Holocene (Wei et al., 2020) and extensive paleosol development from 5 to 3 ka (Yang et al., 2019).

In stage 3 (~4.0 ka to the present), the weakest aeolian activity during the Holocene occurred. From 4.0 ka to the present, the χ_{fd} value generally increased and the mean grain size decreased, which demonstrated the enhanced precipitation and weakened wind circulation. A permanent shift from aeolian sands to loess deposits occurred at the MQQ, implying a further weakening of aeolian activity (**Figure 4**). A similar shift to a more humid climate was found in the northern TP (Stauch et al., 2017). The local topographic position has an important influence on loess and sand deposits (Stauch et al., 2017). Aeolian sand continued to be deposited on other suitable sites in this stage (Hu et al., 2018). Loess sediments on the TP are normally associated with a wetter climate, because in a humid climate, vegetation density increases and more silty sediments are trapped (Lu et al., 2011; Stauch, 2015). With increasing rainfall, the level of the lake rose, and the surface wind–sand supplies decreased largely owing to better vegetation fixation and soil development. Thus, there was a transition from wind–sand deposits to loess deposits in the Maqu region. This wetting trend of the climate also occurred in the surrounding areas. The level of the lake was higher than that in the early to mid-Holocene (Chen et al., 2016), and a humid period occurred from 4 to 3 ka in the Qinghai Lake Basin (Lu et al., 2011). The Gonghe Basin was warmer and wetter from 4.7 to 0.7 ka than in the mid-Holocene (Liu et al., 2013a). Intensified agricultural cultivation since 2.2 ka in the Qinghai Lake basin also indicates the climate was humid during the late Holocene (Wei et al., 2020). Therefore, loess accumulation at this time can be linked to increased vegetation cover acting as a sediment trap (Chen et al., 2020).

However, some studies suggest that the climate became dry again in the late Holocene and that aeolian activities strengthened again in the northeastern TP (Stauch et al., 2012; Lu et al., 2015; Stauch, 2015). These contradictions suggest that the history of aeolian activities in different regions is inconsistent, which may reflect the complex responses of different regions to climate change (Qiang et al., 2013; Lu et al., 2015). In addition, the Yellow River catchment could have greatly affected aeolian activities because of changes in sand supply and landforms. The Zoige Basin was infilled with plenty of fluvial–lacustrine sediments, and the abundant fine-grained materials were susceptible to deflation and redeposition. The shrinking of the river system and lakes in the northeastern TP significantly affected aeolian activities by increasing material supplies. Therefore, climate change and regional response together determined the history of wind–sand activities in the region. The stepwise weakening of aeolian activities in the eastern TP might have been caused by variations in climate and local hydrological conditions (Qiang et al., 2016; Stauch et al., 2017; Hu et al., 2018). Further investigations in a broader region are needed.

The stacked global paleotemperature demonstrated that the global annual temperature had reached a maximum in the early Holocene, and then had decreased through the middle to late Holocene (Marcott et al., 2013). The Gannan region is located in the eastern TP, where precipitation is mainly controlled by the ASM (Chen et al., 2020; Zhao et al., 2020). Peat sediment records suggest that the climate remained warm/wet during the early to mid-Holocene, and became relatively cold/dry in the late Holocene (Yu et al., 2006; Sun et al., 2017). The strong aeolian activities related to the high aridity of the early to middle Holocene in the Maqu area could have been caused by higher summer temperatures that drove enhanced evaporation (Wu et al., 2020). Climatic warming-enhanced evaporation has caused an enormous loss of water in the basins of the northeastern TP (Wu et al., 2016). Similar to the strong aeolian activities in the warm early Holocene, even if the precipitation increases, future global warming will enhance aeolian activities in the eastern TP.

In summary, a stepwise weakening in aeolian activities has occurred since the early Holocene in the Gannan region. Extreme aeolian sands were deposited mainly under the warm climate in the early to mid-Holocene, whereas the weakest deposition occurred after 4.0 ka. The history of aeolian activity was mainly controlled by climate change since the Holocene, but was also affected by the local geomorphology and regional hydrological conditions. The results of this study show that the relations between aeolian activity and regional climate change are complex. Future global warming could lead to increases in aeolian activities similar to those that occurred in the early Holocene.

CONCLUSION

In this study, detailed chronology and multiple proxy analyses were conducted on an MQQ aeolian section and used to reconstruct the history of aeolian activities during the Holocene in the eastern TP. Aeolian activities have occurred since the warm early Holocene in the eastern TP. Magnetic susceptibility, grain size records, and paleosol formation indicated a stepwise weakening in aeolian activities from the early Holocene to the present. The weakening of aeolian activities was divided into three stages: ~10.0–8.0 ka BP, ~8.0–4.0 ka BP, and ~4.0 ka BP to the present. Paleosols were formed primarily after ~8.0 ka BP and indicated episodic interruptions of aeolian desertification in the Gannan region. The results indicate that aeolian activity may increase in the Gannan region as the climate gradually warms. Variations in the Asian summer monsoon and local hydrological conditions may have caused environmental changes in the eastern TP. These results strengthen the understanding of the evolution of aeolian activities in the eastern TP.

DATA AVAILABILITY STATEMENT

The raw data supporting the conclusions of this article will be made available by the authors, without undue reservation.

AUTHOR CONTRIBUTIONS

SY and QL designed the study. SY, TC YL, LL, and ZC, carried out field work and collected samples. XL, TC, and LL performed laboratory analysis. SY, QL, and XL performed data interpretations. SY, XL, and QL wrote the manuscript. All authors discussed interpretations and commented on the manuscript.

FUNDING

This work was supported by the National Natural Science Foundation of China (41877447, 41472147), the Strategic Priority Research Program of the Chinese Academy of Sciences (XDA20090003), and the Fundamental Research Funds for the Central Universities (lzujbky-2015-k10; lzujbky-2015-bt01).

ACKNOWLEDGMENTS

We thank X. Meng, D. Yue, M. Liang, S. Li, and D. Li for their assistance in the field and with sample preparation.

SUPPLEMENTARY MATERIAL

The Supplementary Material for this article can be found online at: https://www.frontiersin.org/articles/10.3389/feart.2021.686677/full#supplementary-material

REFERENCES

Ahr, S. W., Nordt, L. C., and Forman, S. L. (2013). Soil Genesis, Optical Dating, and Geoarchaeological Evaluation of Two upland Alfisol Pedons within the Tertiary Gulf Coastal Plain. *Geoderma* 192, 211–226. doi:10.1016/j.geoderma.2012.08.016

Aitken, M. J. (1998). *An Introduction to Optical Dating*. Oxford, UK: Oxford University Press.

An, C.-B., Feng, Z.-D., and Barton, L. (2006). Dry or Humid? Mid-holocene Humidity Changes in Arid and Semi-arid China. *Quat. Sci. Rev.* 25, 351–361. doi:10.1016/j.quascirev.2005.03.013

An, Z., Kukla, G. J., Porter, S. C., and Xiao, J. (1991). Magnetic Susceptibility Evidence of Monsoon Variation on the Loess Plateau of central China during the Last 130,000 Years. *Quat. Res.* 36, 29–36. doi:10.1016/0033-5894(91)90015-w

Bateman, M. D., Boulter, C. H., Carr, A. S., Frederick, C. D., Peter, D., and Wilder, M. (2007). Detecting post-depositional Sediment Disturbance in sandy Deposits Using Optical Luminescence. *Quat. Geochronol.* 2, 57–64. doi:10.1016/j.quageo.2006.05.004

Bateman, M. D., Frederick, C. D., Jaiswal, M. K., and Singhvi, A. K. (2003). Investigations into the Potential Effects of Pedoturbation on Luminescence Dating. *Quat. Sci. Rev.* 22, 1169–1176. doi:10.1016/s0277-3791(03)00019-2

Blaauw, M., and Christen, J. A. (2011). Flexible Paleoclimate Age-Depth Models Using an Autoregressive Gamma Process. *Bayesian Anal.* 6, 457–474. doi:10.1214/ba/1339616472

Cao, J., Adamowski, J. F., Deo, R. C., Xu, X., Gong, Y., and Feng, Q. (2019). Grassland Degradation on the Qinghai-Tibetan Plateau: Reevaluation of Causative Factors. *Rangeland Ecol. Manage.* 72, 988–995. doi:10.1016/j.rama.2019.06.001

Chen, F., Wu, D., Chen, J., Zhou, A., Yu, J., Shen, J., et al. (2016). Holocene Moisture and East Asian Summer Monsoon Evolution in the Northeastern Tibetan Plateau Recorded by Lake Qinghai and its Environs: A Review of Conflicting Proxies. *Quat. Sci. Rev.* 154, 111–129. doi:10.1016/j.quascirev.2016.10.021

Chen, F., Zhang, J., Liu, J., Cao, X., Hou, J., Zhu, L., et al. (2020). Climate Change, Vegetation History, and Landscape Responses on the Tibetan Plateau during the Holocene: A Comprehensive Review. *Quat. Sci. Rev.* 243, 106444. doi:10.1016/j.quascirev.2020.106444

Cheng, P., Burr, G. S., Zhou, W., Chen, N., Hou, Y., Du, H., et al. (2020). The Deficiency of Organic Matter 14C Dating in Chinese Loess-Paleosol Sample. *Quat. Geochronol.* 56, 101051. doi:10.1016/j.quageo.2019.101051

Dong, Z., Hu, G., Yan, C., Wang, W., and Lu, J. (2010). Aeolian Desertification and its Causes in the Zoige Plateau of China's Qinghai-Tibetan Plateau. *Environ. Earth Sci.* 59, 1731–1740. doi:10.1007/s12665-009-0155-9

Fang, X., Li, J., Zhou, S., and Kang, S. (1998). Aeolian Sand Deposition in the Source Area of Yellow River and its Significance. *Acta Sedimentologica Sinica* 16, 40–44. doi:10.14027/j.cnki.cjxb.1998.01.007

Galbraith, R. F., Roberts, R. G., Laslett, G. M., Yoshida, H., and Olley, J. M. (1999). Optical Dating of Single and Multiple Grains of Quartz from Jinmium Rock Shelter, Northern Australia: Part I, Experimental Design and Statistical Models. *Archaeometry* 41, 339–364. doi:10.1111/j.1475-4754.1999.tb00987.x

He, W., Xiong, Z., Yuan, D., Ge, W., and Liu, X. (2006). Palaeo-earthquake Study on the Maqu Fault of East Kunlun Active Fault. *Earthquake Res. China* 22, 126–134. doi:10.3969/j.issn.1001-4683.2006.02.002

Hu, G., Dong, Z., Lu, J., and Yan, C. (2015). The Developmental Trend and Influencing Factors of Aeolian Desertification in the Zoige Basin, Eastern Qinghai-Tibet Plateau. *Aeolian Res.* 19, 275–281. doi:10.1016/j.aeolia.2015.02.002

Hu, G., Jin, H., Dong, Z., Lu, J., and Yan, C. (2013). Driving Forces of Aeolian Desertification in the Source Region of the Yellow River: 1975-2005. *Environ. Earth Sci.* 70, 3245–3254. doi:10.1007/s12665-013-2389-9

Hu, G., Yu, L., Dong, Z., Lu, J., Li, J., Wang, Y., et al. (2018). Holocene Aeolian Activity in the Zoige Basin, Northeastern Tibetan Plateau, China. *CATENA* 160, 321–328. doi:10.1016/j.catena.2017.10.005

Hu, M., Zuo, H., Pang, N., and Li, X. (2016). Evolution of Chemical Weathering Process since the Middle-Late Holocene in the Maqu Plateau. *J. Desert Res.* 36, 623–635.

Huo, L., Chen, Z., Zou, Y., Lu, X., Guo, J., and Tang, X. (2013). Effect of Zoige alpine Wetland Degradation on the Density and Fractions of Soil Organic Carbon. *Ecol. Eng.* 51, 287–295. doi:10.1016/j.ecoleng.2012.12.020

Ji, J., Shen, J., Balsam, W., Chen, J., Liu, L., and Liu, X. (2005). Asian Monsoon Oscillations in the Northeastern Qinghai-Tibet Plateau since the Late Glacial as Interpreted from Visible Reflectance of Qinghai Lake Sediments. *Earth Planet. Sci. Lett.* 233, 61–70. doi:10.1016/j.epsl.2005.02.025

Kang, S., Xu, Y., You, Q., Flügel, W.-A., Pepin, N., and Yao, T. (2010). Review of Climate and Cryospheric Change in the Tibetan Plateau. *Environ. Res. Lett.* 5, 015101. doi:10.1088/1748-9326/5/1/015101

Kukla, G., Heller, F., Ming, L., Chun, X., Sheng, L., and Sheng, A. (1988). Pleistocene Climates in China Dated by Magnetic Susceptibility. *Geology* 16 (9), 811. doi:10.1130/0091-7613(1988)016<0811:pcicdb>2.3.co;2

Lai, Z., Kaiser, K., and Brückner, H. (2009). Luminescence-dated Aeolian Deposits of Late Quaternary Age in the Southern Tibetan Plateau and Their Implications for Landscape History. *Quat. Res.* 72, 421–430. doi:10.1016/j.yqres.2009.07.005

Lehmkuhl, F., Schulte, P., Zhao, H., Hülle, D., Protze, J., and Stauch, G. (2014). Timing and Spatial Distribution of Loess and Loess-like Sediments in the Mountain Areas of the Northeastern Tibetan Plateau. *CATENA* 117, 23–33. doi:10.1016/j.catena.2013.06.008

Li, J., Dodson, J., Yan, H., Cheng, B., Zhang, X., Xu, Q., et al. (2017). Quantitative Precipitation Estimates for the Northeastern Qinghai-Tibetan Plateau over the Last 18,000 Years. *J. Geophys. Res. Atmos.* 122, 5132–5143. doi:10.1002/2016jd026333

Liu, B., Jin, H., Sun, L., Sun, Z., Su, Z., and Zhang, C. (2013a). Holocene Climatic Change Revealed by Aeolian Deposits from the Gonghe Basin, Northeastern Qinghai-Tibetan Plateau. *Quat. Int.* 296, 231–240. doi:10.1016/j.quaint.2012.05.003

Liu, Q., Jackson, M. J., Banerjee, S. K., Maher, B. A., Deng, C., Pan, Y., et al. (2004). Mechanism of the Magnetic Susceptibility Enhancements of the Chinese Loess. *J. Geophys. Res. Solid Earth* 109. doi:10.1029/2004jb003249

Liu, W., Li, X., An, Z., Xu, L., and Zhang, Q. (2013b). Total Organic Carbon Isotopes: A Novel Proxy of lake Level from Lake Qinghai in the Qinghai-Tibet Plateau, China. *Chem. Geology* 347, 153–160. doi:10.1016/j.chemgeo.2013.04.009

Lu, R., Jia, F., Gao, S., Shang, Y., Li, J., and Zhao, C. (2015). Holocene Aeolian Activity and Climatic Change in Qinghai Lake basin, Northeastern Qinghai-Tibetan Plateau. *Palaeogeogr. Palaeoclimatol. Palaeoecol.* 430, 1–10. doi:10.1016/j.palaeo.2015.03.044

Lu, H. Y., Zhao, C. F., Mason, J., Yi, S. W., Zhao, H., Zhou, Y. L., et al. (2011). Holocene Climatic Changes Revealed by Aeolian Deposits from the Qinghai Lake Area (Northeastern Qinghai-Tibetan Plateau) and Possible Forcing Mechanisms. *Holocene* 21, 297–304. doi:10.1177/0959683610378884

Marcott, S. A., Shakun, J. D., Clark, P. U., and Mix, A. C. (2013). A Reconstruction of Regional and Global Temperature for the Past 11,300 Years. *science* 339, 1198–1201. doi:10.1126/science.1228026

Prins, M. A., Vriend, M., Nugteren, G., Vandenberghe, J., Lu, H., Zheng, H., et al. (2007). Late Quaternary Aeolian Dust Input Variability on the Chinese Loess Plateau: Inferences from Unmixing of Loess Grain-Size Records. *Quat. Sci. Rev.* 26, 230–242. doi:10.1016/j.quascirev.2006.07.002

Qiang, M., Chen, F., Song, L., Liu, X., Li, M., and Wang, Q. (2013). Late Quaternary Aeolian Activity in Gonghe Basin, Northeastern Qinghai-Tibetan Plateau, China. *Quat. Res.* 79, 403–412. doi:10.1016/j.yqres.2013.03.003

Qiang, M., Jin, Y., Liu, X., Song, L., Li, H., Li, F., et al. (2016). Late Pleistocene and Holocene Aeolian Sedimentation in Gonghe Basin, Northeastern Qinghai-Tibetan Plateau: Variability, Processes, and Climatic Implications. *Quat. Sci. Rev.* 132, 57–73. doi:10.1016/j.quascirev.2015.11.010

Shen, M., Tang, Y., Chen, J., Zhu, X., and Zheng, Y. (2011). Influences of Temperature and Precipitation before the Growing Season on spring Phenology in Grasslands of the central and Eastern Qinghai-Tibetan Plateau. *Agric. For. Meteorology* 151, 1711–1722. doi:10.1016/j.agrformet.2011.07.003

Song, Y., Luo, D., Du, J., Kang, S., Cheng, P., Fu, C., et al. (2018). Radiometric Dating of Late Quaternary Loess in the Northern piedmont of South Tianshan Mountains: Implications for Reliable Dating. *Geol. J.* 53, 417–426. doi:10.1002/gj.3129

Stauch, G. (2015). Geomorphological and Palaeoclimate Dynamics Recorded by the Formation of Aeolian Archives on the Tibetan Plateau. *Earth-Science Rev.* 150, 393–408. doi:10.1016/j.earscirev.2015.08.009

Stauch, G., Ijmker, J., Pötsch, S., Zhao, H., Hilgers, A., Diekmann, B., et al. (2012). Aeolian Sediments on the north-eastern Tibetan Plateau. *Quat. Sci. Rev.* 57, 71–84. doi:10.1016/j.quascirev.2012.10.001

Stauch, G., Schulte, P., Ramisch, A., Hartmann, K., Hülle, D., Lockot, G., et al. (2017). Landscape and Climate on the Northern Tibetan Plateau during the Late Quaternary. *Geomorphology* 286, 78–92. doi:10.1016/j.geomorph.2017.03.008

Sun, D., Bloemendal, J., Rea, D. K., Vandenberghe, J., Jiang, F., An, Z., et al. (2002). Grain-size Distribution Function of Polymodal Sediments in Hydraulic and Aeolian Environments, and Numerical Partitioning of the Sedimentary Components. *Sediment. Geology* 152, 263–277. doi:10.1016/s0037-0738(02)00082-9

Sun, X., Zhao, Y., and Li, Q. (2017). Holocene Peatland Development and Vegetation Changes in the Zoige Basin, Eastern Tibetan Plateau. *Sci. China Earth Sci.* 60, 1826–1837. doi:10.1007/s11430-017-9086-5

Vandenberghe, J., An, Z. S., Nugteren, G., Lu, H., and Van Huissteden, K. (1997). New Absolute Time Scale for the Quaternary Climate in the Chinese Loess Region by Grain-Size Analysis. *Geology* 25, 35. doi:10.1130/0091-7613(1997)025<0035:natsft>2.3.co;2

Wang, Y. F., Wang, S. M., Xue, B., Ji, L., Wu, J. L., Xia, W. L., et al. (1995). Sedimentological Evidence of the Piracy of Fossil Zoige lake by the Yellow-River. *Chin. Sci. Bull.* 40, 1539–1544. doi:10.1360/csb1995-40-8-723

Wei, H., E, C., Zhang, J., Sun, Y., Li, Q., Hou, G., et al. (2020). Climate Change and Anthropogenic Activities in Qinghai Lake Basin over the Last 8500 Years Derived from Pollen and Charcoal Records in an Aeolian Section. *CATENA* 193, 104616. doi:10.1016/j.catena.2020.104616

Wintle, A. G., and Murray, A. S. (2006). A Review of Quartz Optically Stimulated Luminescence Characteristics and Their Relevance in Single-Aliquot Regeneration Dating Protocols. *Radiat. Measurements* 41, 369–391. doi:10.1016/j.radmeas.2005.11.001

Wu, D., Chen, F., Li, K., Xie, Y., Zhang, J., and Zhou, A. (2016). Effects of Climate Change and Human Activity on lake Shrinkage in Gonghe Basin of Northeastern Tibetan Plateau during the Past 60 Years. *J. Arid Land* 8, 479–491. doi:10.1007/s40333-016-0125-5

Wu, D., Zhou, A., Zhang, J., Chen, J., Li, G., Wang, Q., et al. (2020). Temperature-induced Dry Climate in Basins in the Northeastern Tibetan Plateau during the Early to Middle Holocene. *Quat. Sci. Rev.* 237, 106311. doi:10.1016/j.quascirev.2020.106311

Xu, S. (1994). Paleosols and Their Reflection of the Environmental Changes in the Northeast Region of the Qinghai-Xizang Plateau. *Chin. Geographical Sci.* 14, 225–232. doi:10.13249/j.cnki.sgs.1994.03.004

Yang, K., Wu, H., Qin, J., Lin, C., Tang, W., and Chen, Y. (2014). Recent Climate Changes over the Tibetan Plateau and Their Impacts on Energy and Water Cycle: A Review. *Glob. Planet. Change* 112, 79–91. doi:10.1016/j.gloplacha.2013.12.001

Yang, L., Long, H., Cheng, H., He, Z., and Hu, G. (2019). OSL Dating of a Mega-Dune in the Eastern Lake Qinghai basin (Northeastern Tibetan Plateau) and its Implications for Holocene Aeolian Activities. *Quat. Geochronol.* 49, 165–171. doi:10.1016/j.quageo.2018.02.005

Yao, T., Thompson, L., Yang, W., Yu, W., Gao, Y., Guo, X., et al. (2012). Different Glacier Status with Atmospheric Circulations in Tibetan Plateau and Surroundings. *Nat. Clim Change* 2, 663–667. doi:10.1038/nclimate1580

You, Q., Xue, X., Peng, F., Xu, M., Duan, H., and Dong, S. (2014). Comparison of Ecosystem Characteristics between Degraded and Intact alpine Meadow in the

Qinghai-Tibetan Plateau, China. *Ecol. Eng.* 71, 133–143. doi:10.1016/j.ecoleng.2014.07.022

Yu, L., and Lai, Z. (2014). Holocene Climate Change Inferred from Stratigraphy and OSL Chronology of Aeolian Sediments in the Qaidam Basin, Northeastern Qinghai-Tibetan Plateau. *Quat. Res.* 81, 488–499. doi:10.1016/j.yqres.2013.09.006

Yu, X., Zhou, W., Franzen, L. G., Xian, F., Cheng, P., and Tim Jull, A. J. (2006). High-resolution Peat Records for Holocene Monsoon History in the Eastern Tibetan Plateau. *Sci. China Ser. D.* 49, 615–621. doi:10.1007/s11430-006-0615-y

Zhao, Y., Tzedakis, P. C., Li, Q., Qin, F., Cui, Q., and Liang, C. (2020). Evolution of Vegetation and Climate Variability on the Tibetan Plateau Over the Past 1.74 Million Years. *Sci. Adv.* 6. doi:10.1126/sciadv.aay6193

Zhou, L. P., Oldfield, F., Wintle, A. G., Robinson, S. G., and Wang, J. T. (1990). Partly Pedogenic Origin of Magnetic Variations in Chinese Loess. *Nature* 346, 737–739. doi:10.1038/346737a0

Zou, X. Y., and Wang, G. (1995). A Study on Desertification since Late Holocene in Maqu Area, Upstream of Huanghe River. *J. Desert Res.* 15, 65–70.

Conflict of Interest: The authors declare that the research was conducted in the absence of any commercial or financial relationships that could be construed as a potential conflict of interest.

frontiers in Earth Science

ORIGINAL RESEARCH
published: 20 September 2021
doi: 10.3389/feart.2021.699693

OSL Chronology of the Siling Co Paleolithic Site in Central Tibetan Plateau

Lan Luo[1,2], *Zhongping Lai*[1,3]*, *Wenhao Zheng*[4], *Yantian Xu*[1]*, *Lupeng Yu*[5], *Chang Huang*[1,6] *and Hua Tu*[1]

[1]Institute of Marine Sciences, Guangdong Provincial Key Laboratory of Marine Biotechnology, Shantou University, Shantou, China, [2]Department of Physics, Purdue Rare Isotope Measurement Laboratory, Purdue University, West Lafayette, IN, United States, [3]Southern Marine Science and Engineering Guangdong Laboratory (Zhuhai), Zhuhai, China, [4]Zhejiang Institute of Geology and Mineral Resources, Hangzhou, China, [5]Shandong Provincial Key Laboratory of Water and Soil Conservation and Environmental Protection, School of Resource and Environmental Sciences, Linyi University, Linyi, China, [6]Department of Earth Sciences, The University of Hong Kong, Hong Kong, SAR China

Edited by:
Shiyong Yu,
Jiangsu Normal University, China

Reviewed by:
Shugang Kang,
Institute of Earth Environment (CAS), China
Weiming Liu,
Chinese Academy of Sciences (CAS), China
Luke Gliganic,
University of Wollongong, Australia

***Correspondence:**
Zhongping Lai
zhongping.lai@yahoo.com
Yantian Xu
xuyantian@hotmail.com

Specialty section:
This article was submitted to Quaternary Science, Geomorphology and Paleoenvironment, a section of the journal Frontiers in Earth Science

Received: *24 April 2021*
Accepted: *08 July 2021*
Published: *20 September 2021*

Citation:
Luo L, Lai Z, Zheng W, Xu Y, Yu L, Huang C and Tu H (2021) OSL Chronology of the Siling Co Paleolithic Site in Central Tibetan Plateau. Front. Earth Sci. 9:699693. doi: 10.3389/feart.2021.699693

When and how was the Tibetan Plateau (TP), one of the least habitable regions on Earth, occupied by humans are important questions in the research of human evolution. Among tens of Paleolithic archaeological sites discovered over the past decades, only five are considered coeval with or older than the Last Glacial Maximum (LGM, ~27–19 ka). As one of them, the Siling Co site in the central TP was previously announced to be ~40–30 ka based on radiocarbon dating and stratigraphic correlation. Given the loose chronological constraint in previous studies, we here re-examined the chronology of the Siling Co site with the optically stimulated luminescence (OSL) dating technique. Four sections from the paleo-shoreline at an elevation of ~4,600 m in southeastern Siling Co were investigated, with stone artifacts found from the ground surface. Dating results of nine samples delineated the age of ~4,600 m paleo-shoreline to be ~10–7 ka (~8.54 ± 0.21 ka in average). This age indicates that the Siling Co site is not earlier than the early Holocene, much younger than the former age. The revised age of the Siling Co site is consistent with the wet and humid climate conditions on the TP during the early Holocene.

Keywords: OSL, Siling Co, paleolithic site, Tibetan Plateau, paleo-shoreline

INTRODUCTION

With an average elevation of ~4,000 m, a mean annual temperature close to the freezing point of water, and only half the concentration of oxygen at the sea level, the Tibetan Plateau (TP) offers one of the most demanding and hostile living conditions to humans. For this reason, the timing and mechanism of human colonization of this region as well as the accompanying cultural and physiological responses to numerous environmental extremes are of high concern and heatedly debated (Zhang and Li, 2002; Madsen et al., 2006; Zhao et al., 2009; Brantingham et al., 2010; Simonson et al., 2010; Yi et al., 2010; Chen et al., 2015; Meyer et al., 2017; Zhang et al., 2018; Chen et al., 2019; Zhang et al., 2020).

Over the past six decades, at least 38 Paleolithic archaeological sites with ages earlier than the middle Holocene have been discovered on the TP, and five of them were even considered coeval with or prior to the Last Glacial Maximum (LGM) (**Figure 1A**): Baishiya Karst Cave (~190–17 ka) (Zhang et al., 2020), Nwya Devu (ND) (~40–30 ka) (Zhang et al., 2018), Siling Co (~40–30 ka) (Yuan et al., 2007), Xiao Qaidam (~30 ka) (Huang et al., 1987), and Chusang (or Quesang, ~20 ka) (Zhang and Li,

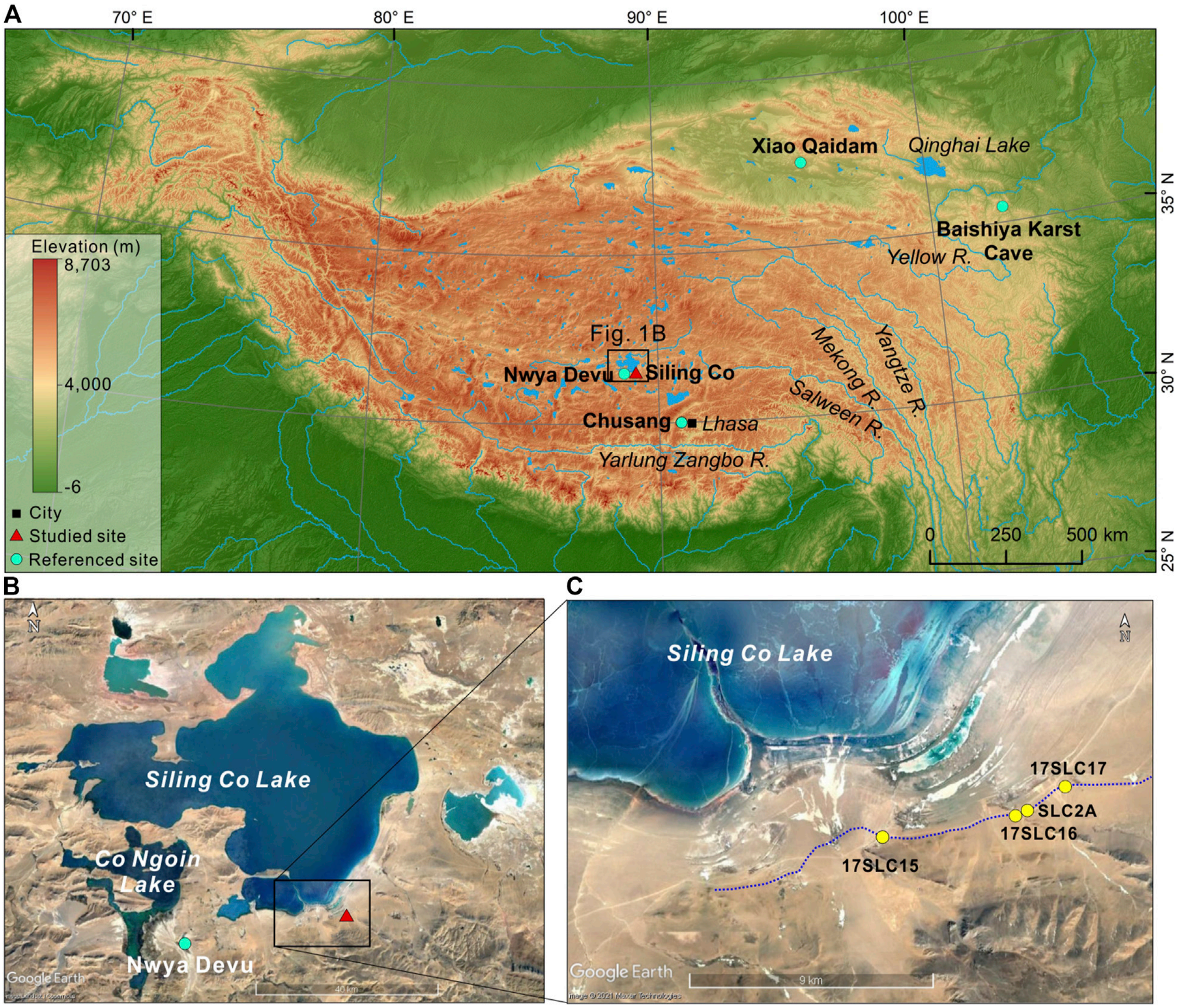

FIGURE 1 | The locations of the studied Siling Co Paleolithic site and sections. **(A)** Map showing the locations of the Siling Co site and four other Paleolithic sites (light blue dots) on the Tibetan Plateau with possible ages of the LGM or older. **(B)** Location of the Siling Co site in relation to Siling Co Lake, Co Ngoin Lake, and the Nwya Devu site. **(C)** Locations of the four investigated sections (yellow dots) along the paleo-shoreline at an elevation of ~4,600 m (blue dashed line). Artifacts were found on the ground surface of sections 17SLC16 and SLC2A. Digital elevation model data for **(A)** from http://vterrain.org/Elevation/global.html. Satellite imagery for **(B,C)** courtesy of Google Earth.

2002). However, recent re-examinations raised the possibility of age overestimation in some of these earliest sites. Based on 10 samples dated with the optically stimulated luminescence (OSL) method, Sun et al. (2010) deduced that the age of the Xiao Qaidam site was most likely between ~3 and 11 ka, much younger than the previously proposed ~30 ka according to radiocarbon dating, stratigraphic correlation, and speculation. Likewise, the age of the Chusang site, which consists of 19 human hand- and footprints found on the surface of fossil travertine, was revised from a previous OSL-derived timing of LGM (Zhang and Li, 2002) to no earlier than ~12.67 and 8.20 thousand calibrated years before present (ka cal. BP) by combined ^{14}C, ^{230}Th/U, and OSL dating (Meyer et al., 2017). Age overestimation of vital Paleolithic sites would cause serious misunderstanding of the pattern and driving mechanism of settlement on the TP. Therefore, chronological revisiting of more archaeological sites is necessary.

In this article, we focus on the Siling Co ("Co" means "lake" in Tibetan) site whose age was only loosely constrained by stratigraphic correlation with ^{14}C-dated lacustrine terraces (paleo-shorelines) (Yuan et al., 2007). Although some dating results obtained with OSL and cosmogenic nuclide techniques have been reported (Li et al., 2009; Kong et al., 2011; Shi et al., 2015, 2017), their stratigraphic relationship with stone artifact-bearing layers were vaguely described due to research emphasis on paleoclimate and/or tectonics. Thus, we re-investigated the chronology of the Siling Co site with the OSL method, which is suitable for coarse-grained, carbon-deficient shoreline deposits.

STUDY AREA AND SAMPLE COLLECTION

Regional Setting of Siling Co

Siling Co (88°31'–89°22'E, 31°30'–32°20'N) is a closed lake in the interior of the TP and is fed by precipitation and melting glaciers from a drainage area of 57,200 km^2. With a continued rise in the water level during the past few decades, it has become the largest endorheic lake in the central TP with a water area of 2,323.6 km^2 (Meng et al., 2012). Quaternary fluctuations of the lake level have left multiple paleo-shorelines, mainly composed of mixed gravel and sand, with the highest one lying at an elevation of ~4,600 m above the sea level (masl), nearly 50 m above the current lake level at ~4,550 m (Shi et al., 2015).

During a joint Sino–Japan expedition in 1988, some stone artifacts were found from the 4,600 m paleo-shoreline *in situ* and the surface of a natural alluvial cone near a rock hill (31°31′N, 89°14′E) in southeastern Siling Co (Yuan et al., 2007), about 39 km to the east of the latest reported Nywa Devu site situated on a terrace of Co Ngoin Lake (**Figure 1B**). As direct ^{14}C dating of carbonates failed due to severe contamination from "dead carbon," the stone artifact-yielding paleo-shoreline was assigned an age of ~40–30 ka based on stratigraphic correlation with nearby ^{14}C-dated paleo-shorelines (Yuan et al., 2007).

OSL Sample Collection

In our 2015–2017 fieldwork, an assemblage of 36 stone artifacts, including 15 flakes, 17 tools, and four micro-cores, were spotted on the surface of the ~4,600 m paleo-shoreline in southeastern Siling Co (**Figure 2**). The artifacts are mostly made of dark grey slate, and the raw materials could be readily found in surrounding areas. Surfaces and edges of the artifacts show little signs of erosion or rounding, suggesting that they were not transported from elsewhere. The allogenic possibility is further ruled out by the absence of higher paleo-shorelines around the site. Given similarities in geographic locations and lithic characteristics, we assume that this site is quite close to the one described in Yuan et al. (2007).

In the field, shoreline sediments can be distinguished by features such as bedding (e.g., foreset bedding), color, sorting, and rounding. At Siling Co, the shorelines are typically associated with sandy or gravelly deposits with cross-bedded layers. Four freshly cleaned sections from the ~4,600 m paleo-shoreline were chosen for a chronological study (**Figures 1C**, **3**), including three hand-excavated pits (17SLC16, 17SLC17, and SLC2A) and a section exposed by road construction (17SCL15). Among them, sections 17SLC16 and SLC2A are where the stone artifacts were discovered on the surface (**Figure 3**). Lithological details of these four sections are presented in **Table 1**. A total of nine OSL samples were collected, with one from 17SLC16, one from 17SLC17, two from SLC2A (duplicate samples), and five from 17SLC15 (**Figure 3**).

During the sample collection, stainless tubes (20–25 cm in length and 5 cm in diameter) were hammered into freshly cleaned vertical sections and then wrapped with black plastic bags and taped to avoid light exposure and moisture loss. For sediments rich in coarse-grained sand and gravel, two or three adjacent tubes were obtained for each sample to ensure enough materials for the following experiment. Additional sediments for dose rate determination were taken from the same positions of each sample.

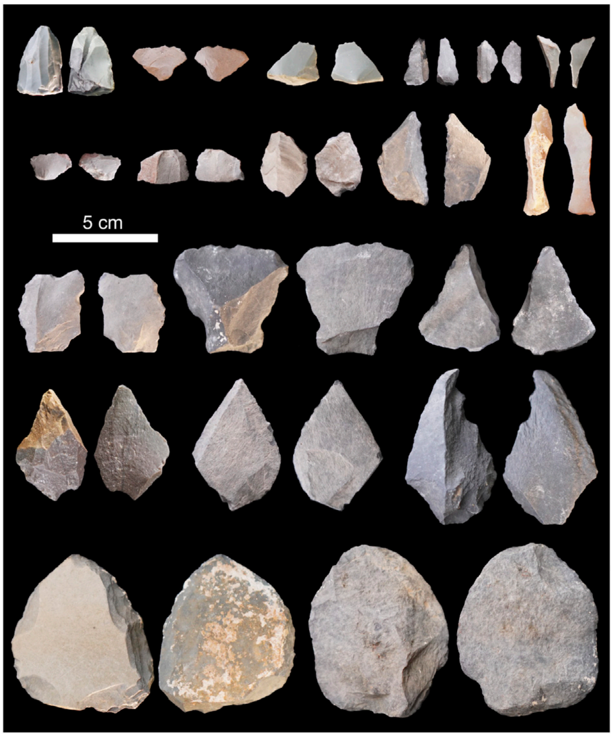

FIGURE 2 | Stone artifacts found in the Siling Co site. Artifacts were collected from the ground surface of sections 17SLC16 and SLC2A in this study.

OSL DATING

Sample Pretreatment

Sample preparation was conducted under subdued red light according to routine procedures. Coarse-grained quartz was used for equivalent dose (D_e) determination. First, 2–3 cm-thick sediments at both ends of the tube were discarded because of potential light exposure. The remaining part was wet sieved to remove >300 μm gravels, followed by treatment with 10% hydrochloric acid (HCl) and 30% hydrogen peroxide (H_2O_2) to eliminate carbonates and organic matter, respectively. Then, the coarse-grained component (90–125, 90–150, or 150–200 μm, depending on availability) was separated by wet sieving and treated with heavy liquid (aqueous sodium polytungstate, SPT) of 2.62 and 2.70 g/cm^3 to further isolate the quartz-rich fraction. Finally, this fraction was etched with 40% hydrofluoric acid (HF) for 40 min to corrode residual feldspars and the outer alpha-irradiated rind of quartz grains, followed by a 10% HCl rinse to eliminate fluoride precipitates. The purity of the isolated quartz fraction was checked by infrared light stimulation (IRSL), and repeated treatment with HF would be carried out if obvious IRSL signals were observed until passing

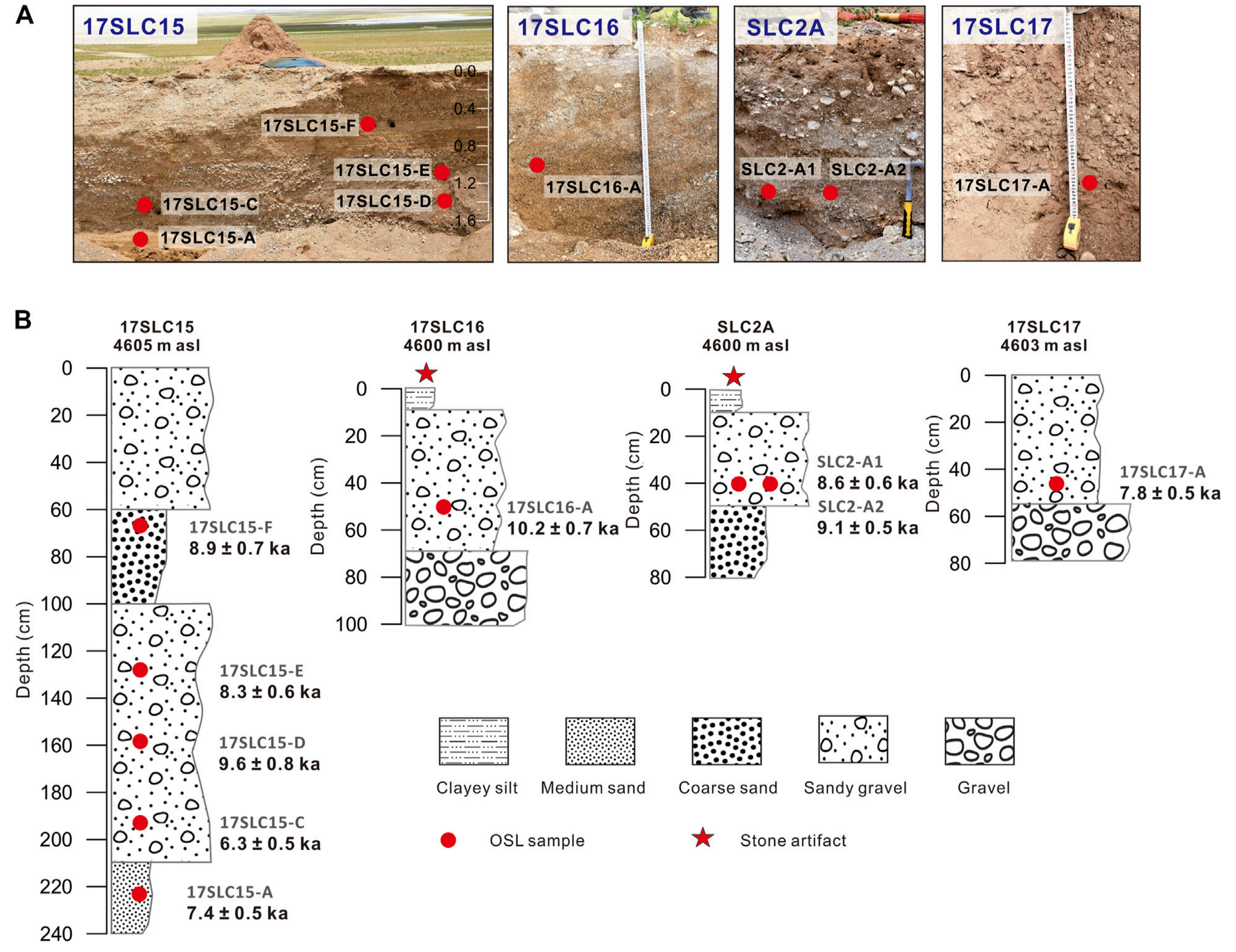

FIGURE 3 | (A) Photos showing the four studied sections and sampling positions. **(B)** Lithological logs of sections and OSL ages.

the test. After re-sieving with 90- or 150-μm sieves, the separated quartz grains were mounted as monolayers onto the central part (2–3 mm in diameter) of 9.7 mm-diameter steel discs with silicone oil adhesive.

OSL Measurement

Luminescence was measured by a Risø Model DA-20 TL/OSL reader equipped with blue LEDs (470 ± 20 nm), infrared LEDs (875 ± 80 nm), and a ^{90}Sr/^{90}Y beta source. The quartz OSL signals were stimulated by blue LEDs (90% diode power) for 40 s at 130°C and detected by a 9235QA photomultiplier tube after filtering through a 7.5 mm Hoya U-340 filter. The OSL signals of the first 0.64-s integral subtracted by the background (last 10 s) were used for growth curve construction.

The single aliquot regenerative dose (SAR) (Murray and Wintle, 2000) protocol combined with the standardized growth curve (SGC) method (Roberts and Duller, 2004; Lai, 2006; Lai et al., 2007) was employed for D_e determination. Prior to the routine experiment, preheat plateau and dose recovery tests were carried out on a representative sample SLC2A-1 to choose an appropriate preheat temperature and to assess the overall performance of the SAR protocol, respectively (Murray and Wintle, 2003). In the preheat plateau test, preheat temperatures varied from 220°C to 300°C at 20°C increments, while the cut-heat was fixed at 220°C for all the measurements; for each preheat temperature step, the mean D_e of four aliquots was calculated. 260°C was selected as an appropriate preheat temperature as was within the plateau region (**Figure 4A**). In the dose recovery test, four aliquots were bleached by blue light for 100 s before receiving a laboratory dose, and the SAR protocol was then used to recover this known dose. The resultant ratios of measured to given doses were within 10% uncertainty of unity, validating the overall protocol conditions in this study (**Figure 4B**).

In the SAR–SGC protocol for D_e determination, six or more aliquots were first measured by the SAR protocol and yielded 6 D_es and 6 growth curves, which were fitted by linear or single exponential functions. These D_es and growth curves were accepted only when *1*) the recycling ratio fell into the acceptance range of 0.9–1.1 and *2*) the recuperation, calculated by comparing the sensitivity-corrected OSL signal of 0 Gy (L_0/T_0) with the sensitivity-corrected natural OSL signal (L_n/T_n), was

TABLE 1 | Lithological details of studied sections from the paleo-shoreline at ~4,600 masl.

Section ID	Depth (cm)	Description
17SLC15 (31°30.6′N, 89°09.0′E, ground altitude: 4,605 m)	0–60	Grayish-brown sandy gravel with low-angle cross-beddings
	60–100	Brownish-gray coarse sand
	100–210	Brownish-gray sandy gravel with cross-beddings
	210–240	Brownish-yellow medium sand
17SLC16 (31°31.2′N, 89°12.0′E, ground altitude: 4,600 m)	0–10	Brownish-yellow clayey silt
	10–70	Grayish-yellow sandy gravel with low-angle cross-beddings
	70–100	Pale gray gravel with low angle cross-beddings, calcareously cemented in the surface
17SLC17 (31°31.8′N, 89°13.2′E, ground altitude: 4,603 m)	0–55	Yellowish-brown sandy gravel with horizontal beddings
	>55	Yellowish-brown gravel
SLC2A (31°31.3′N, 89°12.5′E, ground altitude: 4,600 m)	0–10	Reddish-brown clayey silt
	10–50	Grayish-yellow sandy gravel with ~10° cross-beddings
	>50	Brownish-gray coarse sand

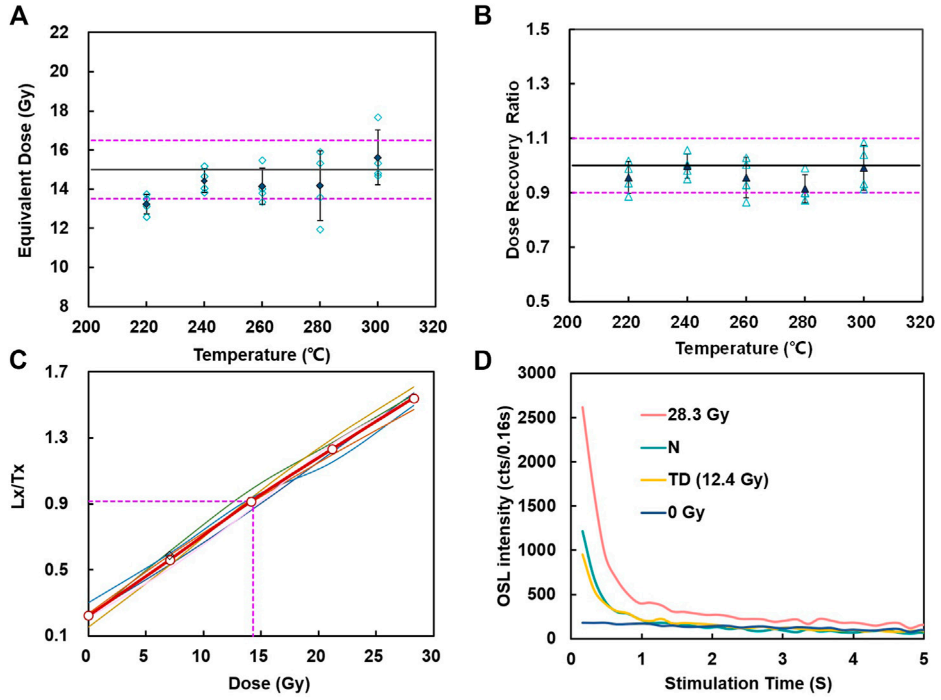

FIGURE 4 | Luminescence characteristics of sample SLC2A-1. **(A)** Preheat plateau test and **(B)** dose recovery test. **(C)** Growth curves of six aliquots and the standardized growth curve (SGC, the red line, and empty circles) averaged from them. Dashed lines indicate the projection of a sensitivity-corrected natural OSL signal onto the SGC to yield a D_e value. **(D)** Decay curves, where N is the natural dose and TD is the test dose.

$<$5%. The accepted growth curves were then averaged to give an SGC for the sample. Afterwards, the L_n/T_n of at least 12 more aliquots of this sample were measured under the same experimental conditions and projected onto the SGC to yield D_es. The difference in D_e errors determined by the SAR and SGC methods are minor and negligible. So, the SAR D_es and SGC D_es were treated equally in the following analysis after removing a few obvious outliers (at most 3) (**Table 2**).

The shoreline sediments are usually transported, washed, and sorted before deposition and thus should be well bleached. The overdispersion (OD) values of most samples were relatively low (20%) (**Table 2** and **Supplementary Figure S1**), suggesting that D_es of all aliquots were centering on some average value. Therefore, the central age model (CAM) was used to calculate the final D_e.

Dose Rate Measurement

The concentrations of uranium (U), thorium (Th), and potassium (K) of dose-rate samples were determined through either neutron activation analysis (NAA) or ICP-MS (for U and Th) and ICP-AES (for K). A water content value of 5% was assigned to all paleo-shoreline sediments

TABLE 2 | OSL dating results.

Sample ID	Depth (m)	Grain size (μm)	Aliquot No.		K (%)	Th (ppm)	U (ppm)	Dose rate[c] (Gy/ka)	D_e (Gy)	Over-dispersion (%)	Age (ka)
			Accepted[a]	Rejected[b]							
17SLC15-F	0.65	90–150	19 (6)	2	1.01 ± 0.04	5.73 ± 0.20	2.17 ± 0.09	2.22 ± 0.11	19.77 ± 1.28	23.0 ± 3.9	8.9 ± 0.7
17SLC15-E	1.30	90–150	19 (6)	2	0.75 ± 0.04	5.74 ± 0.20	3.43 ± 0.13	2.22 ± 0.10	18.52 ± 0.96	17.5 ± 3.0	8.3 ± 0.6
17SLC15-D	1.60	90–125	20 (7)	2	0.63 ± 0.03	5.02 ± 0.18	2.67 ± 0.10	1.88 ± 0.08	18.00 ± 1.18	26.1 ± 4.4	9.6 ± 0.8
17SLC15-C	1.95	90–125	19 (6)	2	1.36 ± 0.05	7.90 ± 0.25	2.39 ± 0.10	2.67 ± 0.13	16.69 ± 0.88	15.3 ± 2.8	6.3 ± 0.5
17SLC15-A	2.25	90–125	19 (6)	1	1.85 ± 0.06	10.90 ± 0.32	2.14 ± 0.09	3.25 ± 0.16	23.95 ± 1.29	19.5 ± 3.4	7.4 ± 0.5
17SLC16-A	0.50	90–150	19 (6)	1	0.59 ± 0.03	4.60 ± 0.16	2.23 ± 0.09	1.77 ± 0.09	18.50 ± 1.08	22.0 ± 3.8	10.2 ± 0.7
17SLC17-A	0.50	90–125	19 (6)	2	1.67 ± 0.06	10.80 ± 0.31	2.28 ± 0.09	3.22 ± 0.16	25.59 ± 1.44	19.3 ± 3.4	7.8 ± 0.5
SLC2-A1	0.40	90–150	19 (7)	2	0.57 ± 0.03	4.17 ± 0.15	2.29 ± 0.09	1.74 ± 0.08	15.01 ± 0.63	14.5 ± 2.6	8.6 ± 0.6
SLC2-A2	0.40	150–200	32 (12)	3	0.57 ± 0.03	4.17 ± 0.15	2.29 ± 0.09	1.72 ± 0.08	15.53 ± 0.50	18.1 ± 2.5	9.1 ± 0.5

[a] *Values in brackets are numbers of aliquots accepted by SAR.*

[b] *Number of aliquots rejected from the age calculation.*

[c] *Water contents of all samples were specified as 5 ± 3%.*

in consideration of their currently measured values, and an uncertainty of 3% was used to cover variations throughout the burial. The radioactive element concentrations were then converted to a dose rate according to the function of Aitken (1998). The cosmic ray contribution to the dose rate for each sample was estimated as a function of the density of cover deposits, depth, altitude, and geomagnetic latitude proposed according to Prescott and Hutton (1994).

DATING RESULTS

OSL Characteristics

Most of the OSL signals decreased to a level undistinguishable from the background within the first second of stimulation, indicating the dominance of the fast component, which is preferable for OSL dating (**Figure 4D**). The growth curves of different aliquots from the same sample, as exemplified by the sample SLC2A-1, were quite similar in shapes, corroborating the existence of SGC (**Figure 4C**).

Age of the Siling Co Site

Table 2 lists the OSL dating results of nine samples from four sections, and artifacts were found and collected from the surface of two sections (17SLC16 and SLC2A). Sample 17SLC16-A showed an age of 10.2 ± 0.7 ka. One sample from section 17SLC17 was dated at 7.8 ± 0.5 ka. In section 17SLC15, except sample 17SLC15-C at 1.95 m depth, the ages of other four samples range from 7.4 ± 0.5 to 9.6 ± 0.8 ka, which were consistent with each other at 2σ range. The duplicate samples from section SLC2A showed a similar age (8.6 ± 0.6 and 9.1 ± 0.5 ka) within 1σ uncertainties (**Figure 3B**), supporting the well-bleaching assumption in OSL dating. The anomalously young age of 17SLC15-C (6.3 ± 0.5 ka) may arise from the introduction of light-exposed sediments from the above through crevasses and was excluded in the following analysis.

Collectively, these dating results suggest an early Holocene age (~10–7 ka; ~8.54 ± 0.21 ka in average) for the 4,600 m paleo-shoreline. As stone tools in our field investigation were found on the surface of the 4,600 m paleo-shoreline, the age of the Siling Co site should be no earlier than the early Holocene.

DISCUSSION

Paleoclimatic Implications of the Age of the ~4,600 m Paleo-Shoreline

Thanks to their direct geomorphic indication of past water levels, paleo-shorelines have been widely used to reconstruct lake-level fluctuations, which in turn may shed light on climate changes (e.g. Liu et al., 2010; Goldsmith et al., 2017; Yu et al., 2019; Jonell et al., 2020) and lithospheric rheology (e.g. Shi et al., 2015; Henriquet et al., 2019). Previous studies have demonstrated that the amplitude of surface deformation due to changes in lake levels on the TP is no more than ~2–4 m (Shi et al., 2015; Henriquet et al., 2019), thus corrections for paleo-shoreline elevation were not made in this study.

The OSL dating of different protocols and the exposure dating with cosmogenic nuclides (^{36}Cl, ^{26}Al, and ^{10}Be) have been applied to multiple paleo-shorelines of Siling Co (Li et al., 2009; Xue et al., 2010; Kong et al., 2011; Shi et al., 2015, 2017; Hou et al., 2021), but consensus on the ages have yet to be reached. With the fine-grain (4–11 μm) quartz and polymineral OSL technique, Li et al. (2009) obtained different ages for two samples, that is, 18.6 ka for sample SW-L1/01 at 4,597 m asl and 9.6 ka for sample SW-L2/11 at 4,598 m asl. It is noted that only fractions <63 μm were used in U, Th, and K analysis, and the resultant bias in dose rate estimation may weaken the reliability of OSL ages. Shi et al. (2015) applied the coarse-grain (180–212 μm) quartz OSL dating to paleo-shorelines at 4,592 and 4,594 m asl, and seven of the nine results were approximately between 6 and 4 ka. As large overdispersion values were observed in nearly all samples, possibly due to a small aliquot size (2 mm) and test dose value (5 Gy), which led to a low signal intensity, they used the minimum age model and finite mixture model for age calculation. The reliability of their dating results awaits further examination. A recent OSL-based chronological study of paleo-shorelines <4,565.7 m asl, though not as high as 4,600 m asl, revealed a highstand of the lake level at ~10–7 ka (Hou et al.,

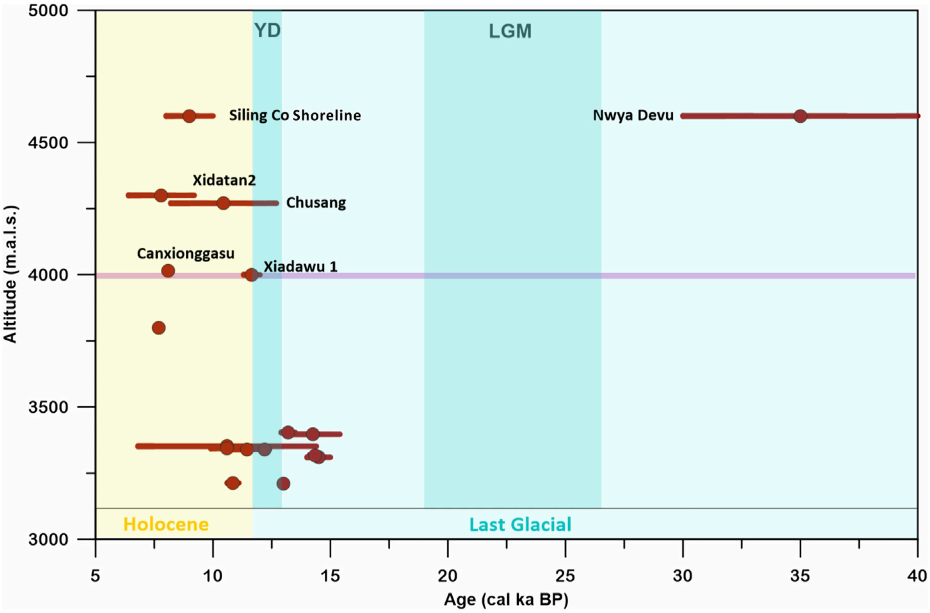

FIGURE 5 | The ages and altitudes of paleolithic–microlithic sites on the Tibetan Plateau. The names of sties at elevation >4,000 m (pink line) are indicated. Note that the Siling Co shoreline age here represents the maximum age of the Siling Co site.

2021), supporting the assignment of an early Holocene age to the ~4,600 m-paleo-shoreline in this study, which was the highest one in our field reconnaissance.

During the early Holocene, a warm and wet climate has been widely reported from the lake sediments (Wei and Gasse, 1999; Wu et al., 2006) and ice-core records (Thompson et al., 1989) on the TP. Previous studies on lake shorelines in the TP also show high lake levels during this period (e.g. Pan et al., 2012; Chen et al., 2013; Hudson et al., 2015). The ~10–7 ka shoreline in Siling Co indicates that this lake also achieved a high lake level in the early Holocene, which is consistent with the environment and climate change during this time. Compared with the extremely cold climate during the Last Glacial period, the warm and wet climate in the Holocene provided favorable conditions for ancient human activities, encouraging their expansion and occupation.

Archaeological Implications of the Age of the Siling Co Paleolithic Site

Climate change is considered an important driving factor in prehistoric human evolution. The basic coupling model of early human migration and climate change can be summarized as follows (Zhang et al., 2016; Madsen et al., 2017): During the warm climate, the living conditions at high latitudes/altitudes would gradually improve, and humans would spread to higher latitudes/altitudes due to internal competition or attraction from the external environment. When the climate becomes cold, humans would retreat from high to low latitudes/altitudes and then reinhabit the high latitudes/altitudes when the weather gets warmer.

The northeastern margin of the TP is widely considered as the main path for early human migration to the inner plateau. Here, we summarized the available paleolithic–microlithic sites with dating results (**Figure 5** and **Supplementary Table S1**). It can be seen that early humans were mainly active in the middle Yellow River during 35–20 ka (e.g., Shuidonggou) (Nian et al., 2014; Pei et al., 2014). They may temporarily reach the low-altitude areas at the edge of the TP during the warm climate. During LGM, the climate would be hard for early humans to explore further west (Sun et al., 2018). During the last deglacial interval (16–11.5 ka), with the improvement of climatic conditions, early humans re-entered the TP through the northwestern margin and reached the Qinghai Lake area (Sun et al., 2018). A series of archaeological sites of 14–11 ka have been found on the northeastern edge of the TP (~3,200 m asl) (e.g., Madsen et al., 2006; Brantingham et al., 2007; Sun et al., 2012; Madsen et al., 2017). At the beginning of Holocene, with the strengthening of the Asian monsoon (Dykoski et al., 2005), the climate of the TP turned warmer, the temperature and precipitation had risen to a similar level to that of today (Shen et al., 2006). Humans further expanded to the hinterland of the TP, including the high-altitude areas (>4,000 m asl). Several sites such as Xiadawu 1(Hou et al., 2016; Madsen et al., 2017), Xiao Qaidam (Sun et al., 2010), and Xidatan 2 (Brantingham et al., 2013) were discovered in this time. In this study, the age of the Siling Co site is revised from 40 to 30 ka to within the Holocene, making it consistent with this pattern of human settlement on the TP.

Recently, the ND Paleolithic site was reported from a terrace of Co Ngoin Lake at an elevation of ~4,600 m (Zhang et al., 2018) and is only ~39 km to the west of the Siling Co site. Considering age revisal at Chusang (Meyer et al., 2017) and Siling Co (this study) sites, an OSL-derived age of ~40–30 ka has made ND the unique evidence of human presence in the interior of the TP where the average elevation is above 4,000 m (Zhang et al., 2018). If the age is accurate, there are two questions to be considered. On the one hand, it triggered new thinking about the migration of early humans to the high altitudes of the TP. Considering the similarity of the stone tool technology at ND and Shuidonggou (~43 ka) (Nian et al., 2014; Zhang et al., 2018) along the middle Yellow River in the northeastern TP, it is possible that early humans rapidly migrated along the Yellow River and reached the high-altitude areas of the TP. However, the two sites are geographically apart with a linear distance of ~1,800 km and an altitude difference of ~3,400 m, and it would be a considerable challenge for early humans to migrate between them. Therefore, there may be other paths from the western or southern TP for early humans to reach the hinterland of the TP (Lv, 2014; Qiu, 2015; Wang et al., 2018). On the other hand, the age of the ND site is interesting in the context of climatic setting. Around the late period of the last ice age at 40–30 ka, climate over most of the regions on Earth was much colder and drier than today (Jouzel et al., 2007; Beck et al., 2018). Some studies (e.g. Lai et al., 2014; Yu et al., 2019) also suggested that the TP experienced the same climate as the rest of the world. Therefore, why did humans step into the interior of the TP under such a severe climatic condition? And what happened with these humans during the following LGM period? Were they locally extinct due to the extreme severe climate condition, or did they retreat to the lower area? More systematic survey combined with careful dating is needed to solve these problems.

CONCLUSION

Through dating nine samples from four sections along the paleo-shoreline at ~4,600 masl, where stone artifacts were found previously and in this study, we postulate that the age of the Siling Co Paleolithic site, which was previously assumed to be ~40–30 ka, should be no earlier than the early Holocene (~10–7 ka; ~8.54 ± 0.21 ka in average). The revised age of the Siling Co site is consistent with a current model that assumes that humans did not widely occupy the interior of the TP until the Holocene. We call for further examination on the age of other high-elevation Paleolithic sites dated to the LGM or earlier.

DATA AVAILABILITY STATEMENT

The original contributions presented in the study are included in the article/**Supplementary Material**; further inquiries can be directed to the corresponding authors.

AUTHOR CONTRIBUTIONS

ZL organized the project. ZL, LY, and CH collected the OSL samples. WZ and CH conducted the experiments in the laboratory. LL and ZL performed data analysis. LL, ZL, and YX wrote the manuscript. ZL, YX, and HT reviewed the manuscript and contributed to data interpretation. HT took photos for the artifacts. ZL proofread the manuscript. All authors contributed to discussions.

FUNDING

This study was supported by CNSF (41290252) and STU Scientific Research Foundation for Talents (NTF19003). The authors would like to thank Zhixiang Wang, Weitao Yuan, and Yanqing Deng for help in the field and Peisong Zheng and Qinjing Shen for constructive discussions.

SUPPLEMENTARY MATERIAL

The Supplementary Material for this article can be found online at: https://www.frontiersin.org/articles/10.3389/feart.2021.699693/full#supplementary-material

REFERENCES

Aitken, M. J. (1998). *An Introduction to Optical Dating*. Oxford, UK: Oxford University Press.

Beck, J. W., Zhou, W., Li, C., Wu, Z., White, L., Xian, F., et al. (2018). A 550,000-year Record of East Asian Monsoon Rainfall from10Be in Loess. *Science* 360, 877–881. doi:10.1126/science.aam5825

Brantingham, P. J., Gao, X., Olsen, J. W., Ma, H., Rhode, D., Zhang, H., et al. (2007). A Short Chronology for the Peopling of the Tibetan Plateau. *Dev. Quat. Sci.* 9, 129–150. doi:10.1016/s1571-0866(07)09010-0

Brantingham, P. J., Rhode, D., and Madsen, D. B. (2010). Archaeology Augments Tibet's Genetic History. *Science* 329, 1467. doi:10.1126/science.329.5998.1467-a

Brantingham, P. J., Xing, G., Madsen, D. B., Rhode, D., Perreault, C., Van Der Woerd, J., et al. (2013). Late Occupation of the High-Elevation Northern Tibetan Plateau Based on Cosmogenic, Luminescence, and Radiocarbon Ages. *Geoarchaeology* 28, 413–431. doi:10.1002/gea.21448

Chen, F. H., Dong, G. H., Zhang, D. J., Liu, X. Y., Jia, X., An, C. B., et al. (2015). Agriculture Facilitated Permanent Human Occupation of the Tibetan Plateau after 3600 B.P. *Science* 347, 248–250. doi:10.1126/science.1259172

Chen, F., Welker, F., Shen, C.-C., Bailey, S. E., Bergmann, I., Davis, S., et al. (2019). A Late Middle Pleistocene Denisovan Mandible from the Tibetan Plateau. *Nature* 569, 409–412. doi:10.1038/s41586-019-1139-x

Chen, Y., Zong, Y., Li, B., Li, S., and Aitchison, J. C. (2013). Shrinking Lakes in Tibet Linked to the Weakening Asian Monsoon in the Past 8.2 Ka. *Quat. Res.* 80, 189–198. doi:10.1016/j.yqres.2013.06.008

Dykoski, C., Edwards, R., Cheng, H., Yuan, D., Cai, Y., Zhang, M., et al. (2005). A High-Resolution, Absolute-Dated Holocene and Deglacial Asian Monsoon Record from Dongge Cave, China. *Earth Planet. Sci. Lett.* 233, 71–86. doi:10.1016/j.epsl.2005.01.036

Goldsmith, Y., Broecker, W. S., Xu, H., Polissar, P. J., deMenocal, P. B., Porat, N., et al. (2017). Northward Extent of East Asian Monsoon Covaries with Intensity on Orbital and Millennial Timescales. *Proc. Natl. Acad. Sci. USA* 114, 1817–1821. doi:10.1073/pnas.1616708114

Henriquet, M., Avouac, J.-P., and Bills, B. G. (2019). Crustal Rheology of Southern Tibet Constrained from Lake-induced Viscoelastic Deformation. *Earth Planet. Sci. Lett.* 506, 308–322. doi:10.1016/j.epsl.2018.11.014

Hou, G., Cao, G., Chongyi, E., Ren, X., Wuennemann, B., and Li, F. (2016). New Evidence of Human Activities at an Altitude of 4000 Meters Area of Qinghai-Tibet Plateau. *Acta Geogr. Sinica* 71, 1231–1240. doi:10.11821/dlxb201607011

Hou, Y., Long, H., Shen, J., and Gao, L. (2021). Holocene Lake-level Fluctuations of Selin Co on the central Tibetan Plateau: Regulated by Monsoonal Precipitation or Meltwater? *Quat. Sci. Rev.* 261, 106919. doi:10.1016/j.quascirev.2021.106919

Huang, W. W., Chen, K. Z., and Yuan, B. Y. (1987). "Paleolithics of Xiao Qaidam Lake in Qinghai Province in China," in Proceedings of the Sino–Australian Quaternary Meeting, (Beijing: Sciences Press), 168–172.

Hudson, A. M., Quade, J., Huth, T. E., Lei, G., Cheng, H., Edwards, L. R., et al. (2015). Lake Level Reconstruction for 12.8-2.3 Ka of the Ngangla Ring Tso Closed-Basin Lake System, Southwest Tibetan Plateau. *Quat. Res.* 83, 66–79. doi:10.1016/j.yqres.2014.07.012

Jonell, T. N., Aitchison, J. C., Li, G., Shulmeister, J., Zhou, R., and Zhang, H. (2020). Revisiting Growth and Decline of Late Quaternary Mega-Lakes Across the South-central Tibetan Plateau. *Quat. Sci. Rev.* 248, 106475. doi:10.1016/j.quascirev.2020.106475

Jouzel, J., Masson-Delmotte, V., Cattani, O., Dreyfus, G., Falourd, S., Hoffmann, G., et al. (2007). Orbital and Millennial Antarctic Climate Variability Over the Past 800,000 Years. *Science* 317, 793–796. doi:10.1126/science.1141038

Kong, P., Na, C., Brown, R., Fabel, D., Freeman, S., Xiao, W., et al. (2011). Cosmogenic 10Be and 26Al Dating of Paleolake Shorelines in Tibet. *J. Asian Earth Sci.* 41, 263–273. doi:10.1016/j.jseaes.2011.02.016

Lai, Z.-P., Brückner, H., Zöller, L., and Fülling, A. (2007). Existence of a Common Growth Curve for Silt-sized Quartz OSL of Loess from Different Continents. *Radiat. Measurements* 42, 1432–1440. doi:10.1016/j.radmeas.2007.08.006

Lai, Z., Mischke, S., and Madsen, D. (2014). Paleoenvironmental Implications of New OSL Dates on the Formation of the "Shell Bar" in the Qaidam Basin, Northeastern Qinghai-Tibetan Plateau. *J. Paleolimnol.* 51, 197–210. doi:10.1007/s10933-013-9710-1

Lai, Z. (2006). Testing the Use of an OSL Standardised Growth Curve (SGC) for Determination on Quartz from the Chinese Loess Plateau. *Radiat. Measurements* 41, 9–16. doi:10.1016/j.radmeas.2005.06.031

Li, D., Li, Y., Ma, B., Dong, G., Wang, L., and Zhao, J. (2009). Lake-level Fluctuations since the Last Glaciation in Selin Co (lake), Central Tibet, Investigated Using Optically Stimulated Luminescence Dating of beach Ridges. *Environ. Res. Lett.* 4, 045204. doi:10.1088/1748-9326/4/4/045204

Liu, X., Lai, Z., Fan, Q., Long, H., and Sun, Y. (2010). Timing for High lake Levels of Qinghai Lake in the Qinghai-Tibetan Plateau Since the Last Interglaciation Based on Quartz OSL Dating. *Quat. Geochronol.* 5, 218–222. doi:10.1016/j.quageo.2009.03.010

Lv, H. (2014). Trans-Himalaya Cultural Interactions in Western Tibetan Neolithic Age. *Archaeology* 12, 77–89.

Madsen, D. B., Haizhou, M., Brantingham, P. J., Xing, G., Rhode, D., Haiying, Z., et al. (2006). The Late Upper Paleolithic Occupation of the Northern Tibetan Plateau Margin. *J. Archaeological Sci.* 33, 1433–1444. doi:10.1016/j.jas.2006.01.017

Madsen, D. B., Perreault, C., Rhode, D., Sun, Y., Yi, M., Brunson, K., et al. (2017). Early Foraging Settlement of the Tibetan Plateau highlands. *Archaeological Res. Asia* 11, 15–26. doi:10.1016/j.ara.2017.04.003

Meng, K., Shi, X., Wang, E., and Liu, F. (2012). High-altitude Salt lake Elevation Changes and Glacial Ablation in Central Tibet, 2000-2010. *Chin. Sci. Bull.* 57, 525–534. doi:10.1007/s11434-011-4849-5

Meyer, M. C., Aldenderfer, M. S., Wang, Z., Hoffmann, D. L., Dahl, J. A., Degering, D., et al. (2017). Permanent Human Occupation of the Central Tibetan Plateau in the Early Holocene. *Science* 355, 64–67. doi:10.1126/science.aag0357

Murray, A. S., and Wintle, A. G. (2000). Luminescence Dating of Quartz Using An Improved Single-Aliquot Regenerative-Dose Protocol. *Radiat. Measurements* 32, 57–73. doi:10.1016/s1350-4487(99)00253-x

Murray, A. S., and Wintle, A. G. (2003). The Single Aliquot Regenerative Dose Protocol: Potential for Improvements in Reliability. *Radiat. Measurements* 37, 377–381. doi:10.1016/s1350-4487(03)00053-2

Nian, X., Gao, X., and Zhou, L. (2014). Chronological Studies of Shuidonggou (SDG) Locality 1 and Their Significance for Archaeology. *Quat. Int.* 347, 5–11. doi:10.1016/j.quaint.2014.03.050

Pan, B., Yi, C., Jiang, T., Dong, G., Hu, G., and Jin, Y. (2012). Holocene Lake-level Changes of Linggo Co in Central Tibet. *Quat. Geochronol.* 10, 117–122. doi:10.1016/j.quageo.2012.03.009

Pei, S., Niu, D., Guan, Y., Nian, X., Kuman, K., Bae, C. J., et al. (2014). The Earliest Late Paleolithic in North China: Site Formation Processes at Shuidonggou Locality 7. *Quat. Int.* 347, 122–132. doi:10.1016/j.quaint.2014.03.052

Prescott, J. R., and Hutton, J. T. (1994). Cosmic Ray Contributions to Dose Rates for Luminescence and ESR Dating: Large Depths and Long-Term Time Variations. *Radiat. Measurements* 23, 497–500. doi:10.1016/1350-4487(94)90086-8

Qiu, J. (2015). Who Are the Tibetans? *Science* 347, 708–711. doi:10.1126/science.347.6223.708

Roberts, H. M., and Duller, G. A. T. (2004). Standardised Growth Curves for Optical Dating of Sediment Using Multiple-Grain Aliquots. *Radiat. Measurements* 38, 241–252. doi:10.1016/j.radmeas.2003.10.001

Shen, C., Liu, K.-b., Tang, L., and Overpeck, J. T. (2006). Quantitative Relationships Between Modern Pollen Rain and Climate in the Tibetan Plateau. *Rev. Palaeobotany Palynology* 140, 61–77. doi:10.1016/j.revpalbo.2006.03.001

Shi, X., Furlong, K. P., Kirby, E., Meng, K., Marrero, S., Gosse, J., et al. (2017). Evaluating the Size and Extent of Paleolakes in Central Tibet During the Late Pleistocene. *Geophys. Res. Lett.* 44, 5476–5485. doi:10.1002/2017gl072686

Shi, X., Kirby, E., Furlong, K. P., Meng, K., Robinson, R., and Wang, E. (2015). Crustal Strength in Central Tibet Determined from Holocene Shoreline Deflection Around Siling Co. *Earth Planet. Sci. Lett.* 423, 145–154. doi:10.1016/j.epsl.2015.05.002

Simonson, T. S., Yang, Y., Huff, C. D., Yun, H., Qin, G., Witherspoon, D. J., et al. (2010). Genetic Evidence for High-Altitude Adaptation in Tibet. *Science* 329, 72–75. doi:10.1126/science.1189406

Sun, Y., Chongyi, E., Lai, Z., and Hou, G. (2018). Luminescence Dating of Prehistoric Hearths in Northeast Qinghai Lake and its Paleoclimatic Implication. *Archaeol Anthropol. Sci.* 10, 1525–1534. doi:10.1007/s12520-017-0472-y

Sun, Y., Lai, Z., Long, H., Liu, X., and Fan, Q. (2010). Quartz OSL Dating of Archaeological Sites in Xiao Qaidam Lake of the NE Qinghai-Tibetan Plateau and its Implications for Palaeoenvironmental Changes. *Quat. Geochronol.* 5, 360–364. doi:10.1016/j.quageo.2009.02.013

Sun, Y., Lai, Z., Madsen, D., and Hou, G. (2012). Luminescence Dating of a Hearth from the Archaeological Site of Jiangxigou in the Qinghai Lake Area of the Northeastern Qinghai-Tibetan Plateau. *Quat. Geochronol.* 12, 107–110. doi:10.1016/j.quageo.2012.01.010

Tang, H., Zhou, C., Li, Y., and Liang, Z. (2013). A New Discovery of Microlithic Information at the Entrance to the Northern Qingzang Plateau of the Kunlun Mountains of Qinghai. *Chin. Sci. Bull.* 58, 247–253. doi:10.1360/972012-550

Thompson, L. G., Mosley-Thompson, E., Davis, M. E., Bolzan, J. F., Dai, J., Klein, L., et al. (1989). Holocene--Late Pleistocene Climatic Ice Core Records from Qinghai-Tibetan Plateau. *Science* 246, 474–477. doi:10.1126/science.246.4929.474

Wang, J., Xia, H., Yao, J., Shen, X., Cheng, T., Wang, Q., et al. (2020). Subsistence Strategies of Prehistoric Hunter-gatherers on the Tibetan Plateau During the Last Deglaciation. *Sci. China Earth Sci.* 63, 395–404. doi:10.1007/s11430-019-9519-8

Wang, S., Zhang, X., and Chen, Z. (2018). Acheulian-like Tools Found at Nyade Site in North Tibet—With Discussions on Human Occupation of Tibetan Plateau in Late Pleistocene. *Acta Anthropol. Sinica* 37, 253–269. doi:10.16359/j.cnki.cn11-1963/q.2018.0006

Wei, K., and Gasse, F. (1999). Oxygen Isotopes in Lacustrine Carbonates of West China Revisited: Implications for Post Glacial Changes in Summer Monsoon Circulation. *Quat. Sci. Rev.* 18, 1315–1334. doi:10.1016/s0277-3791(98)00115-2

Wu, Y., Lücke, A., Jin, Z., Wang, S., Schleser, G. H., Battarbee, R. W., et al. (2006). Holocene Climate Development on the Central Tibetan Plateau: A Sedimentary Record from Cuoe Lake. *Palaeogeogr. Palaeoclimatol. Palaeoecol.* 234, 328–340. doi:10.1016/j.palaeo.2005.09.017

Xue, L., Zhang, Z., Liu, W., Lv, T., and Sun, J. (2010). The Shrinking Process of Siling Co in the Past 12 Ka: Based on OSL Dating of Past Shorelines. *Chin. J. Geol.* 45, 428–439.

Yi, M., Gao, X., Zhang, X., Sun, Y., Brantingham, P. J., Madsen, D. B., et al. (2011). A Preliminary Report on Investigations in 2009 of Some Prehistoric Sites in the Tibetan Plateau Marginal Region. *Acta Anthropol. Sinica* 30, 124–136.

Yi, X., Liang, Y., Huerta-Sanchez, E., Jin, X., Cuo, Z. X. P., Pool, J. E., et al. (2010). Sequencing of 50 Human Exomes Reveals Adaptation to High Altitude. *Science* 329, 75–78. doi:10.1126/science.1190371

Yu, S.-Y., Colman, S. M., and Lai, Z.-P. (2019). Late-Quaternary History of 'great lakes' on the Tibetan Plateau and Palaeoclimatic Implications - A Review. *Boreas* 48, 1–19. doi:10.1111/bor.12349

Yuan, B., Huang, W., and Zhang, D. (2007). New Evidence for Human Occupation of the Northern Tibetan Plateau, China During the Late Pleistocene. *Chin. Sci Bull* 52, 2675–2679. doi:10.1007/s11434-007-0357-z

Zhang, D. D., and Li, S. H. (2002). Optical Dating of Tibetan Human Hand- and Footprints: An Implication for the Palaeoenvironment of the Last Glaciation of the Tibetan Plateau. *Geophys. Res. Lett.* 29, 1072. doi:10.1029/2001gl013749

Zhang, D., Dong, G., Wang, H., Ren, X., Ha, P. u., Qiang, M., et al. (2016). History and Possible Mechanisms of Prehistoric Human Migration to the Tibetan Plateau. *Sci. China Earth Sci.* 59, 1765–1778. doi:10.1007/s11430-015-5482-x

Zhang, D., Xia, H., Chen, F., Li, B., Slon, V., Cheng, T., et al. (2020). Denisovan DNA in Late Pleistocene Sediments from Baishiya Karst Cave on the Tibetan Plateau. *Science* 370, 584–587. doi:10.1126/science.abb6320

Zhang, X. L., Ha, B. B., Wang, S. J., Chen, Z. J., Ge, J. Y., Long, H., et al. (2018). The Earliest Human Occupation of the High-Altitude Tibetan Plateau 40 Thousand to 30 Thousand Years Ago. *Science* 362, 1049–1051. doi:10.1126/science.aat8824

Zhao, M., Kong, Q.-P., Wang, H.-W., Peng, M.-S., Xie, X.-D., Wang, W.-Z., et al. (2009). Mitochondrial Genome Evidence Reveals Successful Late Paleolithic Settlement on the Tibetan Plateau. *Pnas* 106, 21230–21235. doi:10.1073/pnas.0907844106

Conflict of Interest: The authors declare that the research was conducted in the absence of any commercial or financial relationships that could be construed as a potential conflict of interest.

Advantages of publishing in Frontiers

OPEN ACCESS
Articles are free to read
for greatest visibility
and readership

FAST PUBLICATION
Around 90 days
from submission
to decision

HIGH QUALITY PEER-REVIEW
Rigorous, collaborative,
and constructive
peer-review

TRANSPARENT PEER-REVIEW
Editors and reviewers
acknowledged by name
on published articles

Frontiers
Avenue du Tribunal-Fédéral 34
1005 Lausanne | Switzerland

Visit us: www.frontiersin.org
Contact us: frontiersin.org/about/contact

REPRODUCIBILITY OF RESEARCH
Support open data
and methods to enhance
research reproducibility

DIGITAL PUBLISHING
Articles designed
for optimal readership
across devices

FOLLOW US
@frontiersin

IMPACT METRICS
Advanced article metrics
track visibility across
digital media

EXTENSIVE PROMOTION
Marketing
and promotion
of impactful research

LOOP RESEARCH NETWORK
Our network
increases your
article's readership